e-FILING REPORT COVER SHEET

Send completed Cover Sheet and the Report in an email addressed to:
PUC.FilingCenter@state.or.us

REPORT NAME: 2019 Smart Grid Report

COMPANY NAME: Idaho Power Company

DOES REPORT CONTAIN CONFIDENTIAL INFORMATION? ☒No ☐Yes

If yes, please submit only the cover letter electronically. Submit confidential information as directed in OAR 860-001-0070 or the terms of an applicable protective order.

If known, please select designation: ☒RE (Electric) ☐RG (Gas) ☐RW (Water) ☐RO (Other)

Report is required by: ☐OAR
☐Statute
☒Order 12-158 and 18-266
☐Other

Is this report associated with a specific docket/case? ☐No ☒Yes

If yes, enter docket number: UM 1460 and UM 1675

List applicable Key Words for this report to facilitate electronic search:

DO NOT electronically file with the PUC Filing Center:

- Annual Fee Statement form and payment remittance or
- OUS or RSPF Surcharge form or surcharge remittance or
- Any other Telecommunications Reporting or
- Any daily safety or safety incident reports or
- Accident reports required by ORS 654.715

Please file the above reports according to their individual instructions.

Lisa D. Nordstrom
Lead Counsel
lnordstrom@idahopower.com

October 1, 2019

Public Utility Commission of Oregon
Filing Center
201 High Street SE, Suite 100
P.O. Box 1088
Salem, Oregon 97301

RE: UM 1675 - Idaho Power Company's *2019 Smart Grid Report*

Attention Filing Center:

Idaho Power Company submits for filing its *2019 Smart Grid Report* in compliance with Order No. 12-158 in Docket No. UM 1460 and Order No. 18-266 in UM 1675. The Smart Grid Report includes the following documents:

- Appendix A Stakeholder Input
- Appendix B Dynamic Line Ratings in Southern Idaho
- Appendix C PSERC Final Reports
- Appendix D Oregon Schedule 5 – Time-of-Day Pilot Plan
- Appendix E Effects of Solar Intensity Variations on Distribution Feeder Load Report
- Appendix F Smart Grid Metrics

Please address all data requests and other communication to:

Electronic: lnordstrom@idahopower.com
dockets@idahopower.com

Regular Mail: Lisa Nordstrom
Idaho Power Company
1221 W. Idaho Street
Boise, Idaho 83702

Informal substantive questions concerning this filing may be directed to Regulatory Analyst Kristy Patteson at 208-388-2982 or kpatteson@idahopower.com.

Sincerely,

Lisa D. Nordstrom

Lisa D. Nordstrom

LDN:kkt
Enclosures
cc: Service List – UM 1675
Service List – UM 1460
Service List – LC 74
Service List – UE 233

P.O. Box 70 (83707)
1221 W. Idaho St.
Boise, ID 83702

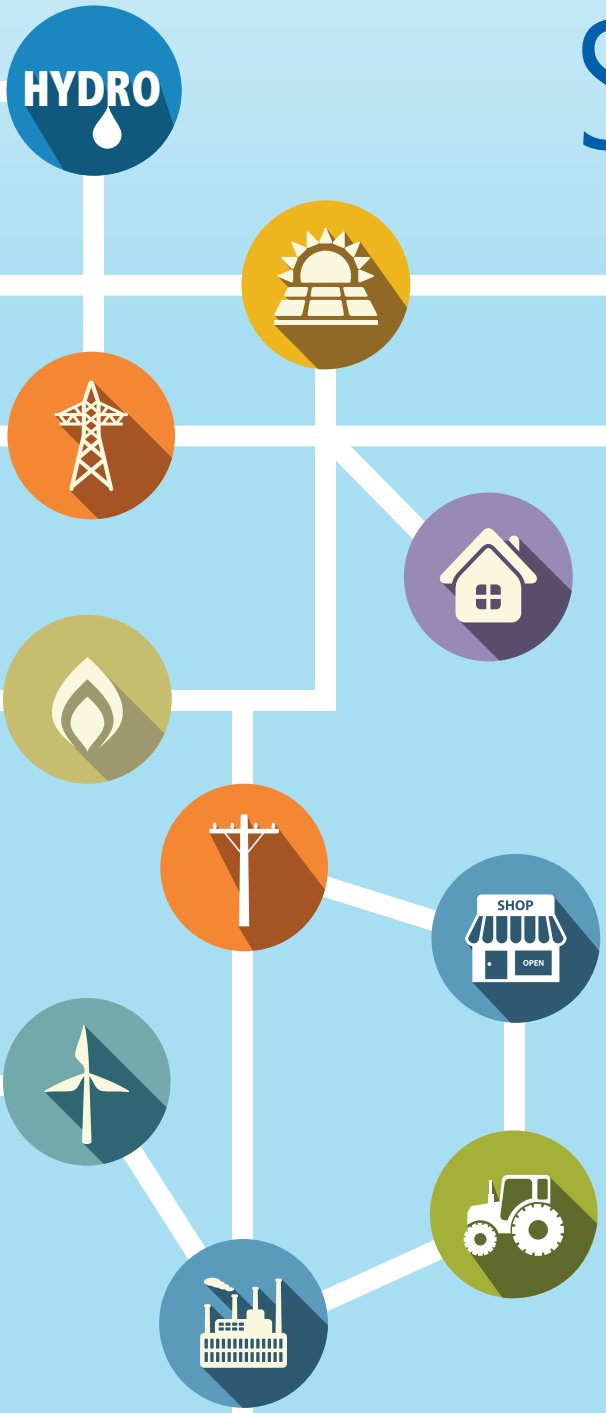

SMARTgrid Report

September 27, 2019

IDAHO POWER®
An IDACORP Company

TABLE OF CONTENTS

LIST OF TABLES

LIST OF FIGURES

LIST OF APPENDICES

LIST OF ACRONYMS

A/C—Air Conditioning
ACC—Automated Capacitor Control
AMI—Advanced Metering Infrastructure
ANSI—American National Standards Institute
BESS—Battery Energy Storage System
CAISO—California Independent System Operator
CAN-SPAM—Controlling the Assault of Non-Solicited Pornography and Marketing Act of 2003
CIM—Common Information Model
CIGRÉ—International Council on Large Electric Systems
CR&B—Customer Relationship and Billing
CRM—Customer Relationship Management
CVR—conservation voltage reduction
DC—Direct Current
DLR—Dynamic Line Ratings
DOE—Department of Energy
DR—Demand Response
DRU—Demand Response Unit
DSM—Demand-Side Management
EIM—Energy Imbalance Market
ESK—Energy Savings Kit
ESS—Energy Storage System
EV—Electric Vehicle
FAN—Field Area Network
FIDVR—Fault-Induced Delayed Voltage Recovery
GLASS—General Line Ampacity State Solver
GOMCA—Grid Operator's Monitoring & Control Assistant
GWh—Gigawatt-Hours
HAA—Hosted Advanced Applications
HVAC—Heating, Ventilation, and Air Conditioning
IED—Intelligent Electronic Devices
IEEE—Institute of Electrical and Electronics Engineers
INL—Idaho National Lab
IROL—Interconnection Reliability Operating Limits
IRP—Integrated Resource Plan
iSTEM—Idaho Science, Technology, Engineering, and Mathematics
IT—Information Technology
IVR—Interactive Voice Response
IVVC—Integrated Volt/VAr Control
kV—Kilovolt
kW—Kilowatt
kWh—Kilowatt-hour
LED—Light Emitting Diode
LSE—Linear State Estimator
LTC—Load Tap Changer

MHz—Megahertz
MWh—Megawatt-hour
MVA—Megavolt Ampere
MVAr—Megavolt Ampere Reactive
NDA—Non-Disclosure Agreement
O&M—Operation & Maintenance
OAR—Oregon Administrative Rule
OLTC—On-Load Tap Changers
OMS—Outage Management System
OPF-LI—Optimal Power Flow-Loading Limit
OPUC—Public Utility Commission of Oregon
ORS—Oregon Revised Statute
PALM—Phase Angle Limit and Monitoring
PDC—Phasor Data Concentrator
pf—Power Factor
PLC—power line carrier
PMU—Phasor Measurement Unit
PNNL—Pacific Northwest National Laboratories
PPA— Phasor Measurement Unit Performance Analyzer
PRSP—Peak Reliability Synchrophasor Program
PSERC —Power System Engineering Research Center
PUC—Public Utility Commission
PV—Photovoltaic
QoS—Quality of Service
RAS—Remedial Action Scheme
RC—Reliability Coordinator
RIT—Renewable Integration Tool
ROSE—Region of Stability Existence
SAIDI—System Average Interruption Duration Index
SCADA—Supervisory Control and Data Acquisition
SDGE—San Diego Gas and Electric
SE—State Estimator
SGIG—Smart Grid Investment Grant
SGM—Smart Grid Monitoring
SOL—System Operating Limit
SOW—Scope of Work
STEM—Science, Technology, Engineering, and Mathematics
SVIR—Sun Valley Institute for Resiliency
T&D—Transmission and Distribution
TE—Transportation Electrification
TES—Thermal Energy Storage
TOD—Time of Day
TSS—Test Suite Specification
UAS—Unmanned Aircraft Systems
V—Voltage
V&R—V&R Energy

VAr—Volt Ampere Reactive
VSAI—Voltage Stability Assessment Index
VVMS—Automated Volt/VAr Management System

EXECUTIVE SUMMARY

Idaho Power Company (Idaho Power or the company) is pleased to present its *2019 Smart Grid Report* in compliance with Order Nos. 12-158 and 18-266 issued by the Public Utility Commission of Oregon (OPUC) in Dockets UM 1460 and UM 1675. The OPUC's smart grid goal and objectives as set forth in Order No. 12-158 are as follows:

> *The Commission's goal is to benefit ratepayers of Oregon investor-owned utilities by fostering utility investments in real-time sensing, communication, control, and other smart-grid measures that are cost-effective to consumers and that achieve the following:*
>
> - *Enhance the reliability, safety, security, quality, and efficiency of the transmission and distribution network*
> - *Enhance the ability to save energy and reduce peak demand*
> - *Enhance customer service and lower cost of utility operations*
> - *Enhance the ability to develop renewable resources and distributed generation*

This document presents Idaho Power's sixth smart grid report and describes the company's efforts toward accomplishing the OPUC's goals. This report provides a review of current smart grid projects, initiatives, and activities being performed by the company and describes additional projects the company plans to undertake in the next five years. Opportunities the company has identified, as well as potential constraints, are also discussed.

Idaho Power evaluates new smart grid technologies and opportunities to solve existing problems, improve efficiency, increase reliability, improve safety or security, and enhance customer satisfaction. Opportunities for funding smart grid projects are evaluated using common criteria alongside other capital projects being considered by the company.

Actions Idaho Power has taken in response to the OPUC's specific recommendations for this report included in Order No. 18-266, Docket UM 1675, are presented in Section V. Targeted Evaluations.

SOLICITATION OF STAKEHOLDER INPUT

In preparation for filing this report, Idaho Power provides the public and other parties an opportunity to contribute information and ideas on smart grid investments and applications.

To solicit input from the general public, Idaho Power completed a draft report and made it available for review by the public and other stakeholders for a specific period. The company placed an advertisement—Share Your Ideas About Smart Grid—in the two newspapers with the best coverage in Idaho Power's Oregon service area, the *Argus Observer* (Ontario) and the *Hells Canyon Journal* (Halfway). Idaho Power included a web link in the newspaper ads that directed readers to a copy of the draft smart grid report.

Idaho Power also sent an email soliciting comments to all parties on the service lists of the initial smart grid docket, UM 1460; Idaho Power's last Oregon general rate case docket, UE 233; Idaho Power's last integrated resource planning docket, LC 74; and Idaho Power's 2017 smart grid report docket, UM 1675. Idaho Power requested comments be submitted by August 2, 2019.

Copies of the newspaper advertisements, the email solicitation, the informal comments received, and Idaho Power's responses will be provided in Appendix A of the final draft of the *2019 Smart Grid Report*. Also included is a screenshot of the smart grid landing page from Idaho Power's website. Idaho Power did not receive informal comments from any parties on the 2019 draft report. Therefore, no informal comments are included in the appendix.

I. SMART GRID GOALS, OBJECTIVES, STRATEGY, AND PROCESS

The smart grid is a concept whereby utilities deploy new technologies to reduce costs and improve the operation of the electrical power system. Idaho Power continues to evaluate new technological advancements and adopt these technologies as appropriate.

This document represents a vision of technology Idaho Power may deploy in the near to mid-term future. It presents various projects and programs Idaho Power is undertaking or may undertake. Some of the projects are already underway, while others are for future consideration. The *2019 Smart Grid Report* is a vision paper supported with concrete studies and analyses created by a working group of Idaho Power senior managers and their staff. The vision represented herein is forward looking and may be adjusted as years progress.

A. Goals and Objectives

The Smart Grid is Customer Centered

The smart grid concept provides customers easier access to their energy-use information and empowers them to act on that information. It provides information to customers and allows them to be more involved and proactive in managing their energy use. Idaho Power believes customers expect utilities to provide a different experience than the traditional paradigm of service. In part, this paradigm change is driven by the increasing use of technology in our everyday lives. Customers are likely to seek an interactive experience that enables them to make choices in their energy use.

Smart Grid is Data Rich

The smart grid is a data-rich environment with embedded sensing devices located throughout the electric system. These devices automate control and processes while providing information needed to more efficiently operate the system. It provides two-way flows of information between devices and Idaho Power and its customers. It gives the utility the ability to more efficiently integrate distributed resources. It provides resiliency in utility response to outages, speeding up restoration efforts.

Edge of Network

The smart grid is moving to the edge of the network—an area where utilities have traditionally not gone. This edge goes all the way to the secondary side of the service transformer and even down to the meters of the homes and businesses served by Idaho Power. The ability to control power quality at the customer level enables the system to become more efficient and responsive to customer needs while maintaining customer privacy.

The smart grid represents an opportunity to enhance the value customers receive from the electric system. Idaho Power is committed to helping customers realize this value through good planning and making wise investments, considering both costs and benefits associated with any smart grid project. Idaho Power must maintain the safety and reliability expected of it by both

customers and employees while implementing this vision. By optimizing and modernizing the power system, Idaho Power can enhance customer service, improve power reliability, promote energy efficiency, and more efficiently integrate renewable resources.

At Idaho Power, the smart grid vision consists of seven major characteristics:

1. Enhance customer participation and satisfaction
2. Accommodate generation/energy storage
3. Enable new products/services/markets
4. Improve power quality
5. Optimize asset efficiency
6. Anticipate and respond to disturbances
7. Provide resilient operation/robustness

B. Strategy

The company's strategy for realizing the smart grid vision consists of focusing investments on the following areas:

Operations

Idaho Power continues to invest in real-time sensing, diagnostic, communications, and control equipment to increase the efficiency and reliability of the system. Investments in the distribution system are progressing consistent with Idaho Power's distribution grid modernization roadmap and strategy. Specific investments and projects outlined in the roadmap are described in more detail later in this report. Two components of this roadmap, deployment of the field area network (FAN) and the integrated Volt/VAr control (IVVC), were accomplished during the last two years and are described further in this report.

The company has determined a strategy for communicating with the many devices already installed on the electrical system and new devices to be installed in the future. While Idaho Power has operated several communication systems for many years, a growing number of the systems are becoming outdated or have reached capacity. Idaho Power is deploying a field area network (FAN) that utilizes a frequency of 700-MHz to provide high-speed communications with considerable bandwidth for communicating with devices in the field. The 700-MHz FAN project is described in more detail later in this report.

Customer Systems

Idaho Power believes customers' expectations continue to increase, and they want more timely information about their energy use. To provide customers easier access to information about their energy use and enable them to take actions based on that information, many activities must occur.

Idaho Power continues to develop the My Account landing page so that customers can access their energy usage information and make informed choices about their energy use. Idaho Power recently launched "account alerts" for residential customers to keep customers updated on account information important to them. Account alerts are described later in this report under My Account.

C. Process

The Transmission and Distribution Strategies department is the primary department responsible for assessing new grid technologies, including smart grid opportunities. This department is responsible for tracking and evaluating industry technologies, guiding technology pilots, and assessing pilot-project outcomes.

Plans for utility-wide deployment of successful technologies are evaluated with all other capital-funding requests.

II. Status of Smart Grid Investments

The following sections describe the smart grid projects, initiatives, and activities underway and the results to date.

A. Transmission Network and Operations Enhancements

Transmission Situational Awareness—Grid Operator's Voltage Stability Monitoring and Control Assistant

Idaho Power system operators rely on a day-ahead power flow analysis and real-time analysis tools to manage the grid.

The goal of this project was to develop an application that enhances grid reliability by improving the quality and use of the synchrophasor data received from nearly 600 western interconnection phasor measurement units (PMU).

As reported in the *2017 Smart Grid Report*, Idaho Power, Southern California Edison, Peak Reliability, California Independent System Operator, Bonneville Power Administration, San Diego Gas and Electric (SDGE), and V&R Energy (V&R) received a U.S. Department of Energy (DOE) research and demonstration grant for a new synchrophasor-based software application named the Grid Operator's Monitoring & Control Assistant (GOMCA), another term for the PMU-ROSE (Region of Stability Existence) linear state estimator (LSE) tool. The funding matched dollars committed by the seven participants to extend and deploy synchrophasor technologies. Peak Reliability used the grant to improve the quality and use of the synchrophasor data it receives from the PMUs referenced above.

Idaho Power's current version of the GOMCA includes a near real-time analysis program (ROSE), as well as an off-line version of the same program to allow planners to review past events and develop more effective power system scenarios. The program acquires a state estimator solution from the Peak Reliability Coordinator (RC) every five minutes and computes

real power margins for selected paths, under normal and contingency conditions, to voltage collapse for pre-determined scenarios.

Peak RC's primary use of the tool has been calculation of voltage stability based interconnection reliability operating limits (IROL) in real-time using near real-time data. Peak has been actively calculating IROLs using this tool since its deployment in 2015.

Other utilities use the tool to ensure situational awareness with respect to their IROL. They compare the results provided by their tool with those generated by CAISO and PEAK RC to ensure consistency and to validate the results of the analysis.

Peak RC will cease operations by the end of the year 2019, and therefore, Idaho Power's participation in this project is complete for now. The GOMCA relies on the availability of Peak RC state estimator cases made available at regular intervals to Idaho Power and industry partners; without Peak RC, the project is not able to function. When Peak RC ceases operations, Idaho Power will utilize RC West as its new reliability coordinator. The GOMCA vendor, V&R, in coordination with SDGE, is working with RC West to enable the reading of RC West cases into the tool. Idaho Power is currently monitoring this effort.

Dynamic Line Rating Pilot

As originally described in the *2014 Smart Grid Report* and updated in the *2017 Smart Grid Report*, Idaho Power and the Idaho National Laboratory (INL) collaborated on a system that predicts wind speed and direction along a transmission line from an area-specific wind model using real-time weather station information located along the same transmission line.

The software program developed by the INL, General Line Ampacity State Solver (GLASS), calculates the actual line limits based on the measured ambient conditions and wind model results. The original pilot system with 15 weather stations was installed in a test area monitoring a portion of the 230-kilovolt (kV) and 138-kV transmission lines between Hagerman, Bliss, and Glenns Ferry, Idaho. This pilot system was expanded to include 46 weather stations covering the entire line corridor from the Midpoint Substation north of Twin Falls to the Boise Bench Substation in Boise, Idaho. The original pilot system weather stations were upgraded, and the additional weather stations were installed in 2016.

Idaho Power's Planning and Engineering and Operations department has access to review real-time line-limit capacity calculations from GLASS for the lines in this project. Additionally, Idaho Power and the INL gathered data to assess the potential to dynamically rate transmission line operating limits in the Hells Canyon area along the Oregon–Idaho border. Due to the extreme topology of the Hells Canyon area, installation and data gathering has proved to be a challenging endeavor.

A paper, provided in Appendix B, was submitted to the International Council on Large Electric Systems (CIGRÉ) US National Committee 2018 Grid of the Future Symposium by INL. In the paper, transmission corridor collected field weather data coupled with computational fluid dynamics results were used to calculate local dynamic line ratings (DLR) for every midpoint span along a transmission line. The GLASS software developed by INL was used to process the large amount of historical information gathered in a yearlong span to calculate DLR for several

transmission lines. The field data alone showed that for this region, the summer temperature assumptions and solar irradiance assumptions used in static ratings are often too conservative. For short transmission lines, the benefit of DLR was shown to be quite large during summer when more congestion would be expected from heating, ventilation, and air conditioning (HVAC) load, the DLR value is above static ratings approximately 95 percent of the time during summer. For the long line that was analyzed, the raw value of the ampacity was not as generous towards the benefits of DLR.

The Dynamic Line Rating Pilot is complete. The concept of using computational fluid dynamics augmented weather based dynamic line rating was proven successful as documented in the paper submitted by INL to the CIGRÉ US National Committee 2018 Grid of the Future Symposium. The results of the pilot were presented to Idaho Power in 2018. The usefulness of DLR has been demonstrated and has the potential to be a tool to be used by the Idaho Power System Planning and Load Serving Operations departments when additional line capability is needed.

Power System Engineering Research Center

The Power System Engineering Research Center (PSERC)—an industry-university cooperative, draws on university capabilities to creatively address challenges facing the electric power industry. PSERC conducts research for innovative solutions to these challenges using multidisciplinary research expertise in a multi-campus work environment and facilitates the interchange of ideas and collaboration among academia, industry, and government. This also helps educate the next generation of power system engineers.

The following PSERC projects are complete and their associated final reports are in Appendix C:

- (T-57HI) Life-Cycle Management of Mission-Critical Systems through Certification, Commissioning, In-Service Maintenance, Remote Testing, and Risk Assessment
- (S-70) Leveraging Conservation Voltage Reduction for Energy Efficiency, Demand-Side Control, and Voltage Stability Enhancement in Integrated Transmission and Distribution Systems
- (S-64) Monitoring and Maintaining Limits of Area Transfers with PMUs
- (S-65) Real-Time Synchrophasor Measurements-Based Voltage Stability Monitoring and Control

Transmission and Distribution Line Inspections using Unmanned Aircraft Systems

Idaho Power's current methods for transmission and distribution line inspections consist of patrolmen visiting each pole to visually identify reliability defects from the ground. The patrolman inspects transmission and distribution conductors, equipment, and poles by driving across the territory and assessing equipment visually using binoculars or a spotting scope. Often, the patrolmen are traversing uneven and difficult terrain, exposing themselves to hazardous and unsafe conditions. This process does not provide a full view of the elevated equipment and can lead to an incorrect assessment of equipment conditions. If the patrolmen

determine that there is a need to inspect the questionable equipment, they need to access the equipment using a bucket truck or a helicopter.

The use of Unmanned Aircraft Systems (UAS) in the line inspection process allows patrolmen to more safely inspect more infrastructure in a shorter amount of time. Additionally, the use of UAS saves money and improves safety, which can be advertised to customers and may improve the company's brand. Safety is improved by reducing the time in manned helicopters and exposure to hazardous terrain during inspections of the transmission and distribution infrastructure, communications, and transmission towers.

In 2017, Idaho Power piloted the use of UAS in the line inspection process. The transmission and distribution line patrolmen were trained in the use of UAS equipment to use as an additional tool to visually assess the condition of the transmission and distribution conductor, equipment, and poles. It was determined the use of this equipment improved safety, reliability, and efficiency. At the completion of the pilot program, the use of UAS equipment became a permanent part of the transmission and distribution line inspection process.

B. Substation and Distribution Network and Operations Enhancements

Solar End-of-Feeder Project

Figure 1
Solar installation as part of the Solar End-of-Feeder Project

The Solar End-of-Feeder Pilot Project is a small-scale proof-of-concept photovoltaic (PV) system which was evaluated as a non-wire alternative to traditional methods of mitigating low voltage near the end of a distribution feeder. The purpose of the pilot project was to evaluate its operational performance and its cost-effectiveness compared to traditional low voltage mitigation methods. In this project, low voltage is defined by voltage measurements lower than American National Standards Institute (ANSI) C84.1 standard for steady state range A voltage (V). This is defined as 114 V (normalized) measured at the customer's meter. Traditional methods for mitigating low voltage include the addition of capacity banks, voltage regulators,

or reconductoring feeder sections. Capacitor banks and voltage regulators are relatively inexpensive solutions in comparison to reconductoring.

During the spring of 2018, the firmware in the inverters at the End-of-Feeder PV was updated to be able to perform advanced functions and operate at a power factor other than unity to provide volt-ampere reactive support. Data analysis shows a fixed power factor (pf) of 0.95 leading results in an enhanced performance compared to the unity power factor. The data shows that the PV system operating with a leading pf was able to mitigate the low voltage at the end of the feeder by effectively reducing the number of the low voltage reads as shown in Table 1.

The Solar End-of-Feeder Project is installed and is in operation. The project has operated as expected, with the voltages maintained within ANSI C84.1 standards. Through the first two years of operation, the project resulted in effectively mitigating low voltage occurring during daylight hours.

Table 1 shows the results of the analysis pre-project (2016) and post-project (2017 and 2018). Low-voltage count includes how many 1-minute voltage reads were recorded less than 114 V. Percent low voltage is the percentage of total voltage reads that were less than 114 V. One-minute average voltage measurements from the smart grid monitor during summer 2016 and 2018.

Table 1
Low-voltage statistics from April 23, 2016, to August 12, 2018

	2016	2017	2018
Low-Voltage Count	436	33	4
Percent Low Voltage	0.270%	0.020%	0.002%
Minimum Voltage	111.80	112.68	112.68
Average Voltage	118.71	119.67	119.20

Figure 2 shows the voltage duration curve for the summers of 2016, 2017, and 2018. The data is 1-minute average voltage measurements from a smart grid monitor located near the solar site.

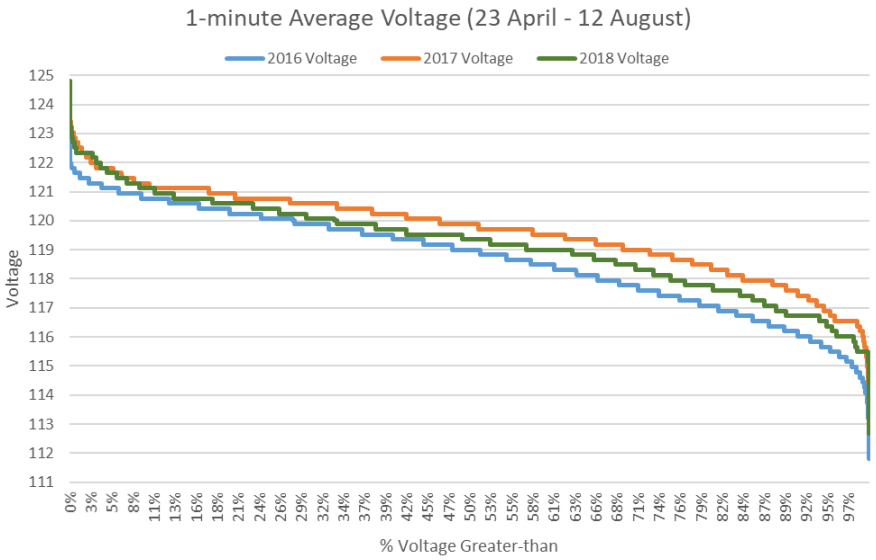

Figure 2
Voltage duration curve for summer 2016, 2017, and 2018

The time of the day of the low voltage measurements occurred are shown in Figure 3. It can be seen that most of the low voltage measurements post project happened during the late hours of the day, when the solar irradiance is reduced.

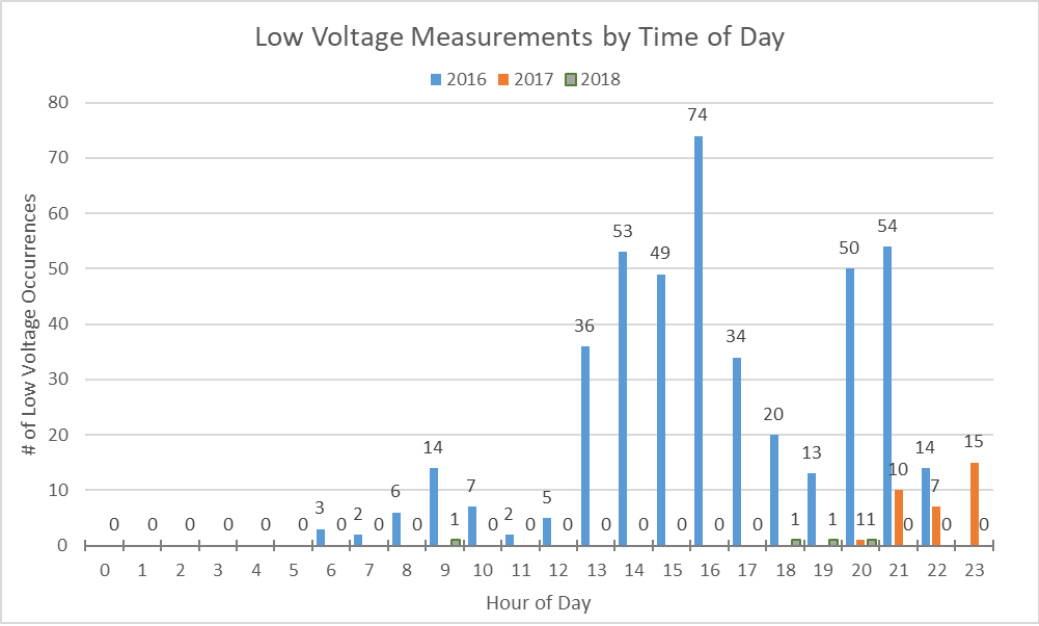

Figure 3
Low-voltage occurrences plotted by time of day

The pilot project successfully mitigated the low voltage issues at the end of the feeder. The voltage reads outside the allowable range decreased from 436 in 2016 to only 4 in 2018. The Solar End-of-Feeder Pilot Project is considered completed and will be monitored internally in the following years.

Volt/VAr InterTechnology Control Pilot

Idaho Power initiated the InterTechnology Control Pilot project in 2016 as a lead up to the IVVC system (formerly the Volt/VAr Optimization) project. Through the InterTechnology Control Pilot, Idaho Power hopes to enhance its experience controlling feeder voltages using substation transformer load tap changers (LTC), line voltage regulators, and line capacitors in a coordinated fashion and assisting in determining the scope of the IVVC project, as well as the strategy and requirements associated with an IVVC system. This project can validate or invalidate the feasibility of applying various control strategies.

The scope of the Volt/VAr InterTechnology Control Pilot is to accomplish the following:

- Determine a strategy or set of strategies that can be used for optimizing the Volt/VAr characteristics on a distribution circuit (i.e., flatten circuit voltage profile, improve VAr support for the transmission system, or other strategies).
- Determine a strategy for coordinating the actions of LTCs, voltage regulators, and capacitors on a distribution circuit or set of circuits fed from one distribution transformer.
- Install a small pilot project to test the identified strategies.
- Make recommendations concerning individual devices to be used in a Volt/VAr optimization system.

The outcome of this project is a coordinated Volt/VAr management strategy involving two circuits. Intelligent line devices were installed on two circuits served out of Aiken (AIKN) Substation near Blackfoot, Idaho. The new capacitor bank controllers and voltage regulator controllers with two-way communications installed can be used for monitoring various line quantities, as well as send out signals to the line devices to change control set points. The new line capacitor banks will more evenly distribute the circuit's VAr support.
Additionally, the substation LTC controller has been connected to the supervisory control and data acquisition system (SCADA), so control can be remotely performed.

An analysis was performed comparing pre-pilot values from the winter of 2015/2016 (December 15, 2015, to February 16, 2016) to post-pilot values from the winter of 2016/2017 (December 16, 2016, to February 17, 2017) and from the summer of 2016 (May 2016, to August 2016) to post-pilot values from the summer of 2017 (May 2017, to August 2017).

A summary of the circuits where the pilot project was implemented is presented in Table 2.

Table 2
Circuit summary

Circuit	Total Customers	Peak Load, Winter 2015–2016	Peak Load, Winter 2016–2017	Peak Load, Summer 2016	Peak Load, Summer 2017
AIKN-011	1,167	4.0 MW	4.4 MW	5.27 MW	5.65 MW
AIKN-013	205	5.1 MW	5.2 MW	5.36 MW	5.48 MW

Collected data includes the following:

- One-hour load data for each advanced metering infrastructure (AMI) customer connected at the AIKN substation
- One-hour load data for each MV90 (large industrial) customer connected to the AIKN substation
- One-hour average load data measured at the substation breaker for each circuit

Loss Calculation

The losses of each circuit were determined by the following equation:

$$E_{loss} = E_{breaker} - E_{load}$$

Where:

E_{loss} = Energy losses on the circuit at each hour

$E_{breaker}$ = Energy leaving the substation measured at the circuit breaker

E_{load} = Total energy serving the load measured at the meter

The total energy loss during the three-month period was calculated by the following equation:

$$E_{loss-total} = \sum_{n=1}^{n} E_{loss}$$

Results

Table 3 shows the total energy and calculated losses for both circuits associated with the InterTechnology Control Pilot.

Table 3
Analysis of losses

	Circuit		Total Energy (megawatt-hour [MWh])	Total Losses (MWh)	Percent Losses
Winter	AIKN-011	Pre-Pilot	5,252	318	6.1%
		Post-Pilot	5,752	323	5.6%
	AIKN-013	Pre-Pilot	8,504	158	1.9%
		Post-Pilot	8,797	162	1.8%
Summer	AIKN-011	Pre-Pilot	6,027	543	8.3%
		Post-Pilot	6,288	138	2.1%
	AIKN-013	Pre-Pilot	5,039	275	5.2%
		Post-Pilot	5,095	271	5.1%

The change in losses in each of the circuits is shown in Table 4.

Table 4
Change in losses

	Circuit	Pre-Project	Post-Project	Change
Winter	AIKN-011	6.056%	5.622%	- 7.166%
	AIKN-013	1.905%	1.803%	- 5.350%
Summer	AIKN-011	8.265%	2.140%	-74.1%
	AIKN-013	5.175%	5.050%	-2.41%

The data indicates a small reduction in technical losses for the circuits involved in the pilot during the winter and a significant reduction in technical losses for one of the feeders during the summer. It is surmised this reduction is due to circuit voltage flattening and more refined reactive power flow control.

LTC Operations

It was important the pilot's control regime not significantly increase the operation of the substation transformer LTC. Increased tapping operation can lead to additional wear on the LTC's electrical contacts, which can lead to premature LTC failure. Because LTCs are high value and difficult to replace, Idaho Power attempts to minimize LTC operations beyond those necessary to maintain adequate circuit voltages.

Idaho Power keeps monthly records of the total number of LTC operations for the transformer associated with the pilot. The number of LTC operations for the three-month period during the winter of 2015/2016 was compared with the same three-month period for the winter of 2016/2017. The number of LTC operations for the summer of 2016 (April 28, 2016 to

August 5, 2016) was compared to the post-project number of operations on the summer of 2017 (April 24, 2017 to July 25, 2017). Table 5 shows the results of the analysis.

Table 5
Results of analysis

	Pre-Project (Winter 2015–2016)	Post-Project (Winter 2016–2017)	Pre-Project (Summer 2016)	Post-Project (Summer 2017)
Number of operations	625	464	838	852
% difference	–	-25.8%	–	1.64%

The data indicates a significant reduction in LTC tap operations during the winter period, which can be attributed to the flatter voltage profile on the circuits connected to the transformer and an insignificant increase in operations during the summer. Because more voltage control was performed further out on the circuit, the LTC did not have to operate as often for voltage control.

This project was used as a lead up to the IVVC system. Idaho Power has now started implementation of the IVVC system. This project shows by controlling the interaction between capacitor banks and voltage regulation devices it is possible to flatten the voltage profile of the feeder and reduce the losses. This project is complete.

Electric Vehicle Activities

Home Electric Vehicle Charging Incentive Pilot

The Sun Valley Institute for Resiliency (SVIR), located in Blaine County, Idaho, launched a bulk electric vehicle (EV) buy-down program named RevUp Blaine. SVIR negotiated significant vehicle discounts (up to $7,000) from Nissan, BMW, and Chevrolet. Their goal was to recruit residents and businesses in Blaine County to purchase an EV.

In partnership with RevUp Blaine, Idaho Power offered an additional customer incentive of $300 toward the purchase and installation of a home Level 2 charging station. By offering this incentive, Idaho Power hoped to collect data on home charging infrastructure installation, costs, customer experience, and also evaluate opportunities for program expansion. The incentive was limited to the first 30 participants. Unfortunately, only one customer chose to participate. This may have been the result of most vehicles sold through the program being plug-in hybrids or shorter range pure EVs.

EV Workplace Charging Station Incentive Program

Idaho Power extended its 2016 EV Workplace Charging Station Incentive program into 2017/2018 and expanded it in 2019. Business customers may apply for an incentive to offset the costs of installing EV charging stations for employees, fleet vehicles, or customers. Those eligible may apply for an incentive for up to 50 percent of the project costs (equipment and labor) for installing one or more EV charging stations, up to a maximum of $7,500 per company or municipality, per site. In 2019, the pilot was expanded to include incentives for charging infrastructure for other electrification technologies such as electric buses, trucks, and electric forklifts (as shown in Figure 4).

Figure 4
Electric forklift

Oregon EV Awareness and Education Program

As directed by Senate Bill 1547, the OPUC opened Docket AR 599 to establish a rulemaking regarding transportation electrification (TE) program applications. The goals of Senate Bill 1547 and Docket AR 599 are to accelerate TE to reduce petroleum use, achieve optimum levels of energy efficiency and carbon reduction, meet federal and state air-quality standards, meet Oregon's greenhouse gas emissions reduction goals described in Oregon Revised Statute (ORS) 468A.205, and improve public health and safety. As detailed in the AR 599 Rulemaking, Idaho Power was required to file an Application for a TE Program by December 31, 2016.

On December 30, 2016, Idaho Power filed an application, in Docket UM 1815, to implement an EV Awareness & Education Program in its Oregon service area. The program is intended to increase the awareness of EVs and educate customers on the potential benefits of EVs, including lower fuel costs, lower maintenance costs, little to no emissions, vehicle performance benefits, energy independence, and local economic benefits. The program will also help customers understand vehicle and charging technology and the available options. By providing awareness and education, Idaho Power will address key barriers to EV adoption within its Oregon service area, including driving range, price, charging, and other technical concerns. On July 27, 2017, the OPUC issued Order No. 17-286 approving the company's EV Awareness & Education Program and ordering Idaho Power to implement the program beginning in 2018 and ending in 2020. In 2018, Idaho Power conducted two educational events for residential customers and one training for first responders about the safety features of electric vehicles and how they differ from internal combustion engines. Idaho Power is in the second year of program implementation.

In Docket No. AR 599, a set of rules was proposed for adoption by the Commission governing both TE programs and long-term TE plans. In Order No. 16-447 issued in that case,

the Commission adopted the individual programs rules but declined to adopt the plan rules as proposed and established a requirement that the electric companies eventually develop long-term transportation electrification plans. In lieu of requiring the electric companies to submit a full-scale transportation electrification plan with their initial program applications, the Commission directed Staff to open a new docket to work with utilities and stakeholders to develop the requirements for long-term transportation electrification plans.

After a collaborative process, the Commission adopted the new rule OAR 860-087-0020 for the development of TE Plans through Order No. 19-134. Idaho Power is currently working with Commission Staff and stakeholders to finalize the timing of its inaugural long-term TE plan.

ChooseEV Website

In 2018, Idaho Power added the ChooseEV web platform to its website to provide basic information about EV models to help customers understand the various performance attributes they should consider when making a purchase. The web platform includes information about electric vehicles, charging, a vehicle comparison tool, station locator, and tax incentive information including the $2,500 Oregon state rebates and Charge Ahead rebates. The web platform can be found at idahopower.chooseev.com.

Jordan Valley Energy Storage Project

A transformer located in the Jordan Valley Substation (Jordan Valley, Oregon) is currently operating around nameplate capacity during summer peak load. The transformer serves both residential and commercial customers in the city of Jordan Valley. The highest observed peak load was in the summer of 2016 when phase B of the transformer was overloaded by more than 12 percent for a short duration. A project was approved to replace the transformer with a 4-megavolt ampere (MVA) transformer bank with an in-service date of May 2021. Idaho Power currently maintains a spare transformer and has mobile transformers that can be used in case of transformer failure. The project also includes upgrading the voltage regulator.

A Battery Energy Storage System (BESS) was proposed as a cost-effective alternative to the original transformer replacement project with a scheduled in-service date of October of 2018. When proposals were received during a competitive bid process, they were at a higher cost than originally estimated. This made the BESS proposal no longer cost-effective at that time. Load balancing on the transformer has postponed the need to upgrade the transformer until 2021. The project is under further cost review as a potentially viable option.

700-MHz Field Area Network

Idaho Power purchased a band of 700-MHz radio spectrum in October of 2016 to build a system-wide FAN. The FAN will be Idaho Power's preferred field-to-station device communication network and will provide visibility into the distribution system and field device control, creating a flexible system to meet, monitor, and adapt to changing conditions in the future. Prior to the installation of the FAN, Idaho Power's communications to field devices were limited to commercial cellular systems which were difficult to secure, had high operation and maintenance (O&M) costs, and were subject to technology changes (e.g., constant evolution from 2G to 3G to 4G and now to 5G mobile telecommunications or cellular technology).

Installation of the FAN began with phase 1 in 2017, with the installation of master radio stations in the Boise area. Idaho Power is currently working to complete the installation of radio stations across its service area to support the IVVC system and expects to have all installations complete by the end of 2020. Future additions to the FAN will be based on project need, coverage requirements and costs, and bandwidth requirements.

Integrated Volt/VAr Control System Phase 1 Project (formerly known as Automated Volt/VAr Management)

Idaho Power has operated an automated capacitor control (ACC) system that controls reactive power flow at substation transformers by controlling distribution circuit capacitor banks. In place since the late 1990s, the ACC system is installed at 78 Idaho Power distribution substations. It uses one-way radio communications to command capacitor banks on and off with the goal to be near unity power factor at the substation transformer with a slightly leading power factor at heavy load and a slightly lagging power factor at light load. Control is performed via computers at each substation; the system is not currently centrally controlled.

Direct replacement of aging ACC components is difficult because many are obsolete and no longer supported by vendors. Additionally, the current software system will soon become unsupportable in Idaho Power's cyber secure information technology (IT) environment. The ACC system is not designed to operate with two-way power flow, nor does it provide visibility or control of the distribution system to optimize the voltage profile and minimize distribution system losses.

Installation of an Integrated Volt/VAr Control (IVVC) system to replace ACC began with phase 1 in 2017. Idaho Power is scheduled to fully replace ACC by the end of 2021 with a new IVVC system that provides integrated control of capacitors, voltage regulators, and station LTCs and also provides a higher level of visibility into the distribution system. In previous smart grid reports, this was referred to as Automated Volt/VAr Management System (VVMS).

Phase 1 of the IVVC project was completed in 2018 and included installing a vendor supported IVVC software system along with underlying IT infrastructure, new FAN, and modern device controllers at a substation near Boise. Control and communications to the field devices were established through the new Idaho Power 700-MHz FAN discussed previously. New intelligent line devices were installed with the capability to communicate over the FAN and act autonomously if communications are lost. After the successful phase 1 implementation, full replacement of ACC with the new IVVC will occur across the service territory (77 remaining substations) in a structured, multi-year approach.

Results from phase 1 of IVVC are illustrated below in Figure 5 and Figure 6. These figures show how the new IVVC system efficiently manages the Megavolt Ampere reactive (MVAr) power flow on the distribution system during reverse power flow conditions that occur from large PV installations. Each graph shows a one-week time period in early summer with the daylight hours (PV producing reverse power) highlighted with the gold bars. The trace in each figure is the reactive power flow at the substation transformer. The grey highlighted area is the optimal range for the reactive power flow. Figure 5 shows the reactive power flow was outside the optimal range when managed by the legacy, pre-IVVC control system, during the summer of 2017.

This is particularly evident during the daytime hours (highlighted by gold bars) at this substation when there is reverse power flow on the system from the large PV plant connected to one of the phase 1 distribution feeders.

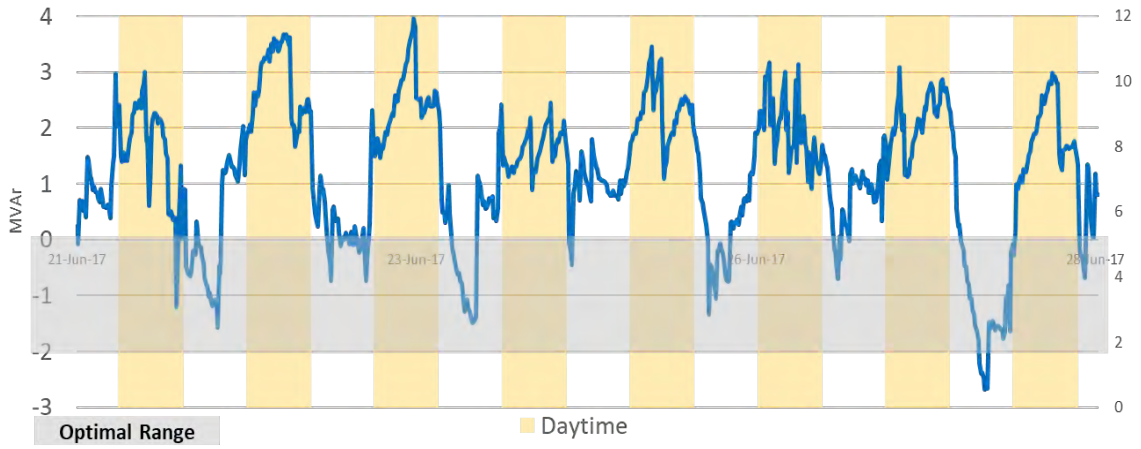

Figure 5
MVAr flow at IVVC phase 1 substation transformer pre-IVVC (2017)

Figure 6 shows the reactive power trace from the same week of time during the summer of 2018 when the phase 1 substation is under IVVC control. The new system efficiently manages the reactive power flow to the optimal range both during non-reverse power flow conditions (i.e., at night) and during the day when reverse power conditions occur from the PV generation (daytime hours highlighted with gold bars). This resulted in a 15 percent average reduction in losses in the distribution system during the first summer of operation for phase 1 of IVVC.

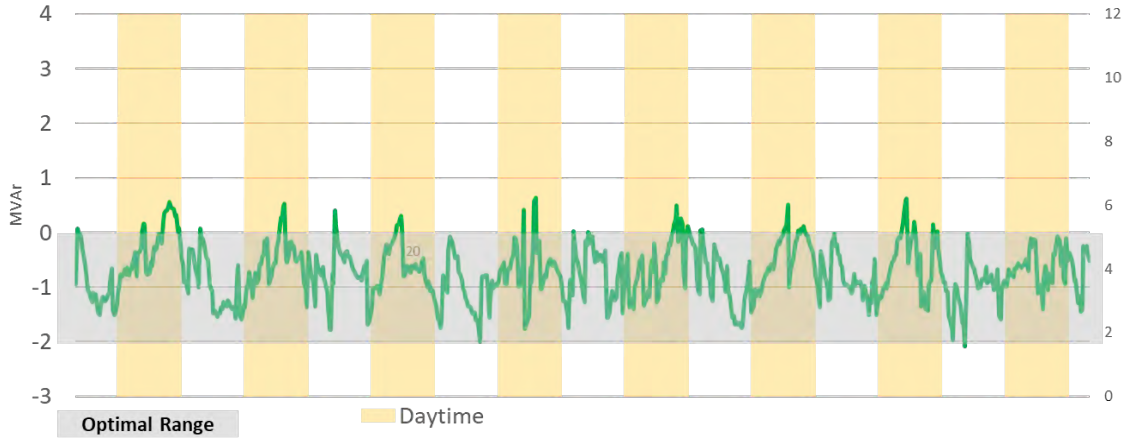

Figure 6
MVAr flow at IVVC phase 1 substation transformer post-IVVC (2018)

Phased Implementation of Distribution Circuit Fault Locating

Implementing fault-locating technologies can help Idaho Power achieve better system reliability by reducing the duration of outages through automation and provide greater situational awareness of the distribution system for grid operators and engineers. Operational benefits such as real-time fault locating, remote indication, and control to isolate faults are also realized, which result in shorter response times.

Successful reliability programs focus on reinforcing under-performing distribution circuits and targeting upgrades to reduce outages for relatively large groups of customers. The current analysis shows the number of future projects with relatively low costs and high reliability impact are limited. Idaho Power began a project to achieve its future reliability performance goals by continuing cost-effective distribution circuit reinforcing and phased implementation of targeted distribution automation.

Phase 1 of the distribution circuit fault locating project began in 2018 with the installation of mid-line smart reclosers on prioritized distribution feeders. In the past, Idaho Power's recloser location process was primarily based on overcurrent protection requirements; however, a structured, analytics-based program was developed in 2018, and the installation of mid-line reclosers on prioritized distribution feeders began in 2019. Idaho Power will continue to install mid-line reclosers on prioritized distribution feeders as needed.

Future phases of the project include the following:

- Add communications via the 700-MHz radio system to reclosers on the distribution system. This will provide remote control and data gathering capabilities for our operators and engineers.
- Install communicating line sensor/fault indicators for fault locating and provide real-time data to SCADA.
- Add communications (700-MHz) to reclosers with a tie to SCADA for data acquisition and remote control.

C. Customer Information and Demand-Side Management Enhancements

My Account

The My Account landing page is the gateway for customers to access and manage their specific Idaho Power account and energy usage information. Once logged in, customers can view their bill, make payments, enroll in account alerts, paperless billing, and initiate online account transactions and inquiries. Additionally, customers can access detailed account and energy usage information, including their hourly energy usage data. The My Account portal enables customers to make informed choices about their energy use and provides information on how to use energy wisely. Idaho Power's website (idahopower.com) had approximately 4.3 million visits in 2018. The My Account customer portal within Idaho Power's website had approximately 3

million logins in 2018. The 2018 average monthly My Account logins increased approximately 20 percent over 2017.

A central component of the My Account landing page continues to be the next-estimated-bill feature. A bar chart is displayed so customers can quickly compare their previous month's energy usage and billed amount to their current month's estimated bill and compare the same month from the prior year. This graph gives customers a visual and insightful look at their current and historical energy use. The landing page includes icon-driven navigation, helping customers access the account information that is most important to them, including detailed energy use.

In March 2018, Idaho Power launched "account alerts" for residential customers. Residential customers can enroll in "Account Past Due" and "Bill Threshold" alerts. In early 2019 "Power Outage" alerts were implemented. These proactive account alerts keep customers updated on account information important to them. Alerts can be delivered to customers by email or text messaging.

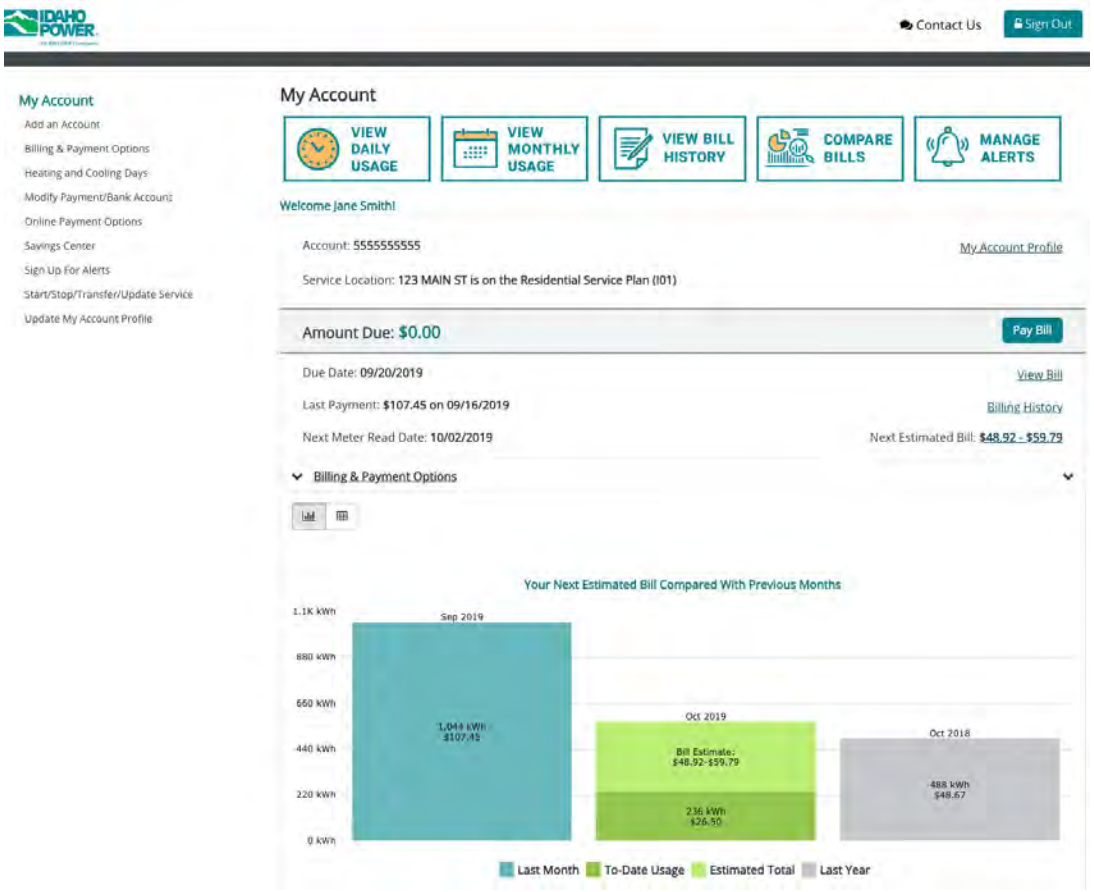

Figure 7
Idaho Power My Account webpage

Customer Relationship Management

Idaho Power reported in the *2017 Smart Grid Report* that it expected to fully implement a Customer Relationship Management (CRM) system by the first quarter of 2018. However, in late 2017 and early 2018, as Idaho Power further explored implementation of a CRM system integrated with the Customer Relationship and Billing (CR&B) system, the company found the expense of integration and the ongoing maintenance to be greater than expected. In order to pursue some of the benefits that would have been gained through the CRM, Idaho Power decided to develop a Customer Manager application in-house.

The Customer Manager application made it possible for Idaho Power to implement the following functionalities:

- Segmentation: The Segmentation function provides the ability to divide customers into groups for marketing and communications using demographics, housing characteristics, program participation, behavioral, and other data.

- Campaign Management: The Campaign Management tool will allow the company to better track and manage marketing campaigns, as well as analyze marketing effectiveness. It provides employees with visibility into these campaigns to help respond to customer inquiries.

- Enhanced Communications and Customer Preference Database: The addition of the Customer Manager supported the company's launch of email marketing and communications efforts, which also took place in 2018. The company uses an outside vendor to support its email marketing. The email marketing software includes tools to comply with Controlling the Assault of Non-Solicited Pornography and Marketing Act of 2003 (CAN-SPAM) and tracks which topics customers are interested in receiving emails about.

While Idaho Power now has a tool available for email marketing and communication, there may still be a broader need for a centralized CRM system to be integrated with the CR&B system. CRM systems are complex and evolving, and the company continues to review vendors and offerings. A CRM system would help Idaho Power to manage and track customer interactions related to energy efficiency and other customer relations activities, with the goal of increasing the effectiveness of Idaho Power's program and service offerings, provide a better customer experience, and enhance Idaho Power's capabilities of serve as an energy advisor to customers.

Demand Response

Idaho Power has offered optional demand response (DR) programs—two of which are direct load control—since 2004 to residential and irrigation customers, and to all of its customer segments since 2009. The company has offered an air conditioning (A/C) cycling program, A/C Cool Credit; an irrigation program, Irrigation Peak Rewards; and a commercial/industrial DR program, the Flex Peak Program. The A/C Cool Credit and Irrigation Peak Rewards programs use smart grid technology—more specifically, the power line carrier (PLC) technology to activate load-control devices installed on customer equipment. All three programs use the hourly load data made possible by AMI to help determine the load reduction achieved during a DR

event, and the company uses the hourly data to reconcile customer payments for some Irrigation Peak Rewards and Flex Peak Program participant payments.

Irrigation Peak Rewards

Since the AMI system deployment, Idaho Power has investigated and tested the AMI system as the primary communication channel for control devices on customer's irrigation pump panels for the Irrigation Peak Rewards program. In 2017, the company finished replacing existing third-party control devices with AMI Demand Response Units (DRU).

In 2017 and 2018, Idaho Power had 318 MW and 297 MW of peak capacity control in the Irrigation Peak Rewards Program from 2,307 and 2,335 participating pump locations, respectively. The change in capacity occurred primarily due to weather difference between the years. The capacity in the program is determined by looking at what the program could have achieved during program hours on the day when the most pumps were running concurrently. AMI technology provides the ability to turn off pumps during a demand response event by sending communication through the PLC to the DRU and allows the company to analyze the status of many participating pumps during load control events through an hourly usage report. These reports provide data to help determine which DRUs functioned properly and which pumps were off during the event.

In addition to using AMI technology, Idaho Power developed its own load control device. This device uses a secure cellular network signal to communicate with and shut off the pump during a load control event and are installed where AMI technology is not available. Approximately 89 percent of participating locations are controlled with the AMI system. The remaining 11 percent are controlled with a cellular device. The data available from the cellular device system allows the company to run circuit current and cellular communication data for each location, which enables the company to determine whether a pump is on or off.

In order to spread load reduction out over a period long enough to utilize full program capacity, Idaho Power splits the participating pump locations into four dispatch groups. Each group is a four-hour block of time overlapping in the 5 to 6 p.m. hour. The four dispatch groups are as follows: 2–6 p.m., 3–7 p.m., 4–8 p.m., and 5–9 p.m.

Flex Peak

The Flex Peak Program (Oregon Schedule 76) is a voluntary program designed for Idaho Power's industrial and large commercial customers who are capable of reducing their electrical energy loads for short periods of time during summer peak days. Idaho Power took over management of this program from a third-party aggregator in spring 2015. Participants are notified of a demand-reduction event two hours prior to the event, and in most cases reductions are achieved by the participants manually turning off equipment or otherwise changing their operations. The program objective is to reduce the demand on Idaho Power's system during periods of extreme peak electricity use.

For the 2017 and 2018 seasons, 141 and 140 service points were enrolled in the Flex Peak Program, 9 of which are located in Oregon. The enrolled capacity is just over 36 and 33 MW for 2017 and 2018, respectively. The Flex Peak Program was used three times during summer 2017

and three times during 2018. Preliminary results indicate the program's maximum peak reduction at generation level was approximately 36 MW in 2017 and 33 NW in 2018.

A/C Cool Credit

The A/C Cool Credit program (Oregon Schedule 74) is a voluntary, dispatchable DR program designed for residential customers. Using communication hardware and software, Idaho Power cycles participants' central A/C or heat pumps off and on via a direct load-control device installed on the A/C or heat pump unit. Participants receive a monthly monetary incentive for participating in the program during the summer season.

Approximately 26,000 PLC-controlled switches are installed on customers' A/C or heat pump units in Idaho Power's service area. Of these, about 350 are installed in Oregon. These switches allow Idaho Power to cycle customers' A/C or heat pumps during a cycling event. A/C Cool Credit was used three times during summer 2017 and four times during summer 2018. Preliminary results indicate the program's maximum peak reduction at generation level was approximately 29 MW in both 2017 and 2018.

D. Distributed Resource and Renewable Resource Enhancements

Renewable Integration Tool—Current Project Developments

The Idaho Power Smart Grid Investment Grant (SGIG) helped fund the Renewable Integration Tool (RIT) project. The RIT project was intended to develop tools to allow grid operators to more efficiently and reliably integrate variable renewable resources with baseload generation resources.

As reported in previous smart grid reports, the RIT was split into two tools in 2014: the Wind Forecast Tool and the Load Forecast Tool. Both tools are operational and benefit grid operators by allowing the system operators to more closely match supply and demand. A more balanced system in preschedule and in real time helps ensure there is sufficient supply to meet demand, and less energy may need purchased in the real-time market.

The Wind Forecast Tool was enhanced to provide forecast data required by Idaho Power's entry into the CAISO's Energy Imbalance Market. This included tailoring the forecasts according to Energy Imbalance Market's (EIM) definitions of generation resources as well as generation of wind forecast data at five-minute intervals.

In 2018, a third-generation Solar Forecast tool was developed. This was initiated primarily to fulfill the requirements of joining the EIM, but a desire to incorporate improvements was also a factor. Improvements included a refined method of incorporating persistence as well as theoretical sunrise and sunset times. In addition, new five-minute forecast data was created to fulfill EIM's requirements.

Activity on this project has been completed. The tools are part of the current operating procedures and are used daily.

III. FUTURE SMART GRID INVESTMENTS

This section describes smart grid investments Idaho Power is planning to undertake over the next five years (including pilots and testing). This section serves as a high-level strategic document for Idaho Power to plan its future smart grid projects. As such, the format of this section is different from the other sections in this report. The description for each of the following projects is laid out in the following format:

1. **Present**: What Idaho Power's present system looks like regarding the project described.
2. **Objective**: What the objective is of the individual project.
3. **Description**: A description of the proposed or existing pilot or project.
4. **Benefit**: How the investment will reduce costs, improve customer service, improve reliability, facilitate demand-side and renewable resources, or provide other system benefits.

A. Transmission Network and Operations Enhancements

There are no transmission network or operations enhancement projects to report.

B. Substation and Distribution Network and Operations Enhancements

Advanced Metering Infrastructure Expansion

Present

Idaho Power's current Advanced Metering Infrastructure (AMI) system covers approximately 99 percent of our service territory, leveraging about 560,000 AMI meters for billing, outage scoping and restoration, and usage data collection. Idaho Power also leverages the system for Demand Side Management (DSM) programs and has deployed approximately 20,000 automated remote connect/disconnect meters within our service territory. Idaho Power did not deploy AMI to approximately 1 percent (about 40 substations and 5,000 meters) of our service territory during the 2009–2011 deployment due to communication limitations and lower cost-benefit realized in these lower density areas. Idaho power continues to leverage manual meter reading for these segments of our service territory.

Objective

Deploy AMI in certain areas of Idaho Powers service territory where high O&M costs can be offset.

Description

Communications mediums have improved in some sparsely populated areas, enabling AMI to become a potential solution. While AMI equipment costs have stayed about the same,

other O&M costs continue to increase. Idaho Power is considering a project to expand its AMI footprint to include roughly 24 additional substations and 3,500 meters. Of those substations, roughly 12 are located in Idaho Power's Eastern Oregon service territory and about 12 substations in the South-Eastern Idaho area. This expansion will allow the company to off-set manual meter reading costs, enable the use of AMI for outage restoration assistance, facilitate DSM programs, and provide detailed usage information to our customers.

Benefit

The benefits associated with expanding AMI include the following:

- **Affordable**—Control/reduce O&M costs by reducing dependency on commercial cellular.
- **Improve Customer Information and Billing**—Collect hourly usage data for billing and customer presentment.
- **Enhance DSM Program Availability**—Expand areas where DSM is currently not available via AMI.
- **Improve Reliability**—Integration with Outage Management system allows operators to leverage AMI to determine outage scope and restoration activities.

Improvement in Momentary Interruptions and Frequency Monitoring

Present

Idaho Power tracks momentary interruptions to our customers. However, the company has limited data analytics and visualization of data to identify and prioritize for mitigation areas with a high number of momentary interruptions experienced by customers.

Objective

Maintain a high level of customer satisfaction by reducing the number of momentary interruptions experienced by our customers.

Description

Develop data analytics and visualization tools to track momentary interruptions that will be accessible to and easy to use by Idaho Power employees. Use the data to identify areas with a high number of momentary interruptions and identify and prioritize mitigations to reduce the number of interruptions.

Benefit

The benefits associated with this project are:

- Improve customer satisfaction by reducing momentary outages.
- Create efficient tools used to identify and manage momentary interruptions

Jordan Valley Microgrid

Present

As detailed in Section II Part B, a transformer located in the Jordan Valley Substation is capacity constrained.

Objective

Section II Part B describes an alternative to install a Battery Energy Storage System to shift peak load and defer a traditional transformer investment. Idaho Power is also considering the option to install a small, fully-functional microgrid. Operating a microgrid would allow Idaho Power to learn the true costs and benefits of a microgrid.

Description

The microgrid at Jordan Valley would provide critical loads with energy during transmission outages. It would operate independently from the rest of the grid for six hours during an average outage event. On a high level, the following elements are expected to be included in the microgrid:

- Battery Energy Storage System with a capacity of at least 200 kW and 500 kWh
- 70 kW solar project
- Microgrid controller
- 700 MHz communication system to signal the isolation of the microgrid and the reconnection to the main grid
- Reclosers to isolate from and reconnect to the main grid

Benefit

The benefits associated with installing a microgrid at Jordan Valley include the following:

- **Increased Resiliency**—A microgrid will provide power during transmission outage events to critical loads in a small, remote community.
- **Increased Reliability**—Customers within the microgrid will experience shorter outages.
- **Expertise**—The project presents an opportunity to gain expertise with Battery Energy Storage Systems. Idaho Power would also gain experience in coordinating generation, storage, and demand during islanded conditions. This expertise will be helpful as Idaho Power analyzes and implements future solutions.
- **Affordability**—The cost associated with the microgrid is estimated to be within 20% of the traditional alternative solution.

C. Customer Information and Demand-Side Management Enhancements

Personalized Customer Interaction and Customer Care Roadmap

Today, approximately 244,000 Idaho Power customers are registered My Account users. The My Account portal within Idaho Power's website is the gateway for customers to access and manage their specific Idaho Power account and energy use information. Idaho Power's customers using a desktop computer, tablet, or mobile phone can register and login to My Account.

Idaho Power continues to implement new functionality within My Account that improves the customer experience and engages customers on the account information most important to them. Examples of new functionality that improve the customer experience include paperless billing and auto pay options. These offerings make it easier for customers to enroll and manage their online billing and payment options.

Idaho Power has focused on providing customers with pro-active account information. In 2018, Idaho Power launched the alert center within My Account. Residential customers can enroll in account past due, bill threshold, and power outage alerts. Business customers can enroll in account past due and outage alerts. When triggers are met, customers enrolled in these alerts will receive a text or email message regarding the specific alert.

Idaho Power's interactive voice response (IVR) call management platform is the gateway into Idaho Power for customers contacting Idaho Power by phone. In 2018, 1.3 million customers interacted with the IVR. Like other communication channels, Idaho Power continually makes improvements to the IVR. In 2018, a project to integrate the IVR with our new outage OMS was completed. Customers using the IVR can get current outage information specific to their home or business, report a power outage, and request an automated call or text message when power is restored. Integrating the IVR and OMS has made outage reporting a more personalized experience.

Idaho Power is preparing for continued growth in the multiple communication channels customers are using, and will use, to conduct business. Customers expect Idaho Power to be easy to do business with and provide information that is most important to them via the communication channel of their choice. These channels include email, text messaging, phone applications, and social media platforms.

Idaho Power is refreshing a three-year customer care roadmap. Initiatives in the roadmap include: improved outage communication tools, expanding account alerts to all customer classes, developing more sophisticated alerts, integrating customer online requests into Idaho Power's customer information system, and offering two-way texting capabilities for outage reporting and making payments. Idaho Power will continue to explore opportunities to leverage existing systems to more actively engage its customers using their preferred technologies.

IV. SMART GRID OPPORTUNITIES AND CONSTRAINTS

This section describes other smart grid opportunities Idaho Power is considering for investment in over the next five to 10 years and any constraints that affect the company's investment considerations.

A. Transmission, Substation, Operations, and Customer Information Enhancements

There are no transmission, substation, operations, or customer information enhancements to report.

B. Evaluations and Assessments of Smart Grid Technologies

There are no evaluations or assessments of smart grid technologies to report.

C. Smart Grid Pilots and Programs

Idaho Power actively monitors smart grid-related technology advancements, articles, research, reports, demonstration projects, and demonstration results. An example of this is the use of cross-functional teams to further research potential opportunities, and a monthly internal update by the Transmission and Distribution (T&D) Strategies team who track PV, energy storage, and EV technology.

As energy generation, consumption, and management technologies continue to improve, new opportunities for the deployment of smart grid-enabled devices/appliances will become available. As these technologies continue to improve and become cost effective, it may be possible to utilize these technologies to create new products and services. These could help Idaho Power manage and optimize its system operation and help its customers manage their energy use, consumption, and distributed generation preferences. Idaho Power continues to closely monitor cost as well as the management and integration of distributed resources such as PV and energy storage, as well as EVs and microgrids.

D. State of Key Technologies

Idaho Power's customers are increasing their use of new electrical technologies. There is also an increasing number of customers who desire to generate their own power. They want to know more about the energy they use and to be able to more finely control their usage. The enabling technologies that allow Idaho Power's customers to do this are available today and limited only by cost and maturity. As prices continue to decrease, the company expects these new technologies will be adopted. This may change Idaho Power's interactions and relationships with these customers from what they are today.

Key technologies Idaho Power is tracking include the following:

- Cost and technical maturity of PV generating resources
- Cost and technical maturity of battery energy storage systems
- Cost, technical maturity, and availability of EVs
- Smart inverters used for PV integration

V. TARGETED EVALUATIONS

This section responds to the six smart grid-related recommendations adopted in OPUC Order No. 18-266, Docket UM 1675.

Recommendation No. 1

> *Continue to include staff and stakeholder informal comments and corresponding company responses in the 2019 Smart Grid Report.*

Idaho Power continues to include stakeholder informal comments and the company's respective responses as an appendix. This information is provided in Appendix A.

Recommendation No. 2

> *Continue to work with staff and include other stakeholders for input in finalizing the program design of the TOD (Time-of-Day) pilot. Staff encourages the company to complete its design of the TOD pilot taking into consideration the new suggestions by staff in the April 2018 phone call. If determined feasible, staff recommends that the company file a tariff proposal with the Commission by December 31, 2018, and report any findings in the 2019 Smart Grid Report.*

During 2018, Idaho Power hosted a series of phone conversations with staff, discussing potential TOD structures that included suggestions made by staff in the April 2018 phone call. The company, Commission Staff, and the Oregon Citizens' Utility Board agreed that the Time-of-Day Pilot Plan (TOD Pilot Plan) should be offered on an optional, voluntary basis. On December 28, 2018, the company filed Tariff Advice No. 18-12 requesting approval to implement Schedule 05, TOD Pilot Plan, and on May 21, 2019, the Commission approved Schedule 5 in Tariff Advice No. 18-12, effective June 1, 2019. Oregon Schedule 5 is provided in Appendix D.

Because the preparation and finalization of Idaho Power's *2019 Smart Grid Report* occurred only a few months after commencement of the TOD Pricing Plan, the company expects to report initial results of the pilot in the *2021 Smart Grid Report*.

Recommendation No. 3a

> *Updates to the Jordan Valley Energy Storage Project and whether it was effective in reducing load on the transformer in the Jordan Valley Substation.*

Proposals received during the competitive bid process for the Jordan Valley Energy Storage Project came in at a higher cost than was originally estimated which resulted in the initially-developed project not being cost-effective. However, in Section III Part B, the company explains it is considering the option to install a small, fully-functional microgrid to shift peak load and defer a traditional transformer investment.

Recommendation No. 3b

> *Staff is interested in knowing more about the Transmission Situational Awareness Peak Reliability Hosted Advanced Application and comparing the cost of participation to the cost of a System Operating Limit exceedance. Page 14 of Appendix C indicates that the yearly cost of the program is $75,000 with 4 potential exceedances avoided. Staff is interested in knowing how the company knew what the cost of those exceedances were and how much the savings compare with investment in a yearly program. Staff is also interested in knowing how it was determined that an exceedance would occur, and whether this is a program the company will participate in indefinitely.*

The cost reported on page 14 of Appendix C of the *2017 Smart Grid report* was the cost associated with participation in the Hosted Advanced Applications (HAA) program. The company has not identified the cost associated with a System Operating Limit (SOL) exceedance.

To determine when an SOL exceedance would have potentially occurred, the company counted the number of times the HAA program was used to simulate next-day conditions (i.e., forecasted load and generation levels and planned transmission outages), and a calculated SOL exceedance was identified in the simulation. The company was then able to avoid the potential next-day SOL exceedance by making adjustments, such as cancelling a planned outage.

With the discontinuation of Peak Reliability, Idaho Power will cease being enrolled in the HAA program by the end of 2019.

Recommendation No. 3c

> *Whether or not the company will update the EV charging impacts study.*

There are no plans to update the EV charging impacts study.

Recommendation No. 3d

> *Staff is highly interested in the Photovoltaic and Feeder Peak Demand Alignment Pilot. Staff requests that the company explain the metrics in the table on page 22 of Appendix C and produce the results and benefits of that pilot.*

The metrics in the table on page 22 of Appendix C of the *2017 Smart Grid Report*, are in hours. These hours represent the time that the irradiance peak leads the distribution feeder load peak.

The southerly numbers show that a solar panel facing 180° tilted 35° from horizontal would see an irradiance peak 3.96 to 4.13 hour prior to the distribution feeder load peak. This orientation represents a common solar PV fixed panel installation.

The global numbers show that a solar panel facing 180° tilted 0° from horizontal would see an irradiance peak 4.00 to 4.02 hour prior to the distribution feeder load peak. This orientation represents a fixed panel facing straight up.

The westerly numbers show that a solar panel facing 269° tilted 53° from horizontal would see an irradiance peak 1.76 to 1.94 hour prior to the distribution feeder load peak. This orientation represents a panel mounted to point where the sun was located when the distribution feeder load peaked the previous year.

The results and conclusion of the pilot can be seen in the attached report included in Appendix E.

Recommendation No. 3e

> *Because a 2018 smart grid report is not required, staff requests that the company update the Direct Load Control Program for both 2017 and 2018 in the 2019 Smart Grid Report.*

The Direct Load Control portion of the report, now titled Demand Response, has been updated for both 2017 and 2018 in Section II Part C.

Recommendation No. 4

> *Continue to include updates, if any, on additional PMU installations and provide a summary of how the newly-installed PMUs have improved observability in Idaho Power's system.*

Idaho Power has not installed any additional PMUs.

Recommendation No. 5

> *Include a description of what the energy efficiency measures related to CRM are and how the company defines energy efficiency as it pertains to its CRM system. Describe the difference in customer activity as a result of the new marketing tools and tactics, in addition to descriptions, with screenshots and pictures, of how the marketing tools and tactics impact customers. The company might consider including this as an appendix in the 2019 Report.*

Please see Section II Part C for an update on the CRM project and the recently implemented Customer Manager.

There is no relationship between energy efficiency measures and a CRM. The company uses its Customer Manager application to help market its energy efficiency programs and pull customer mailing lists more efficiently.

With regard to the difference in customer activity as a result of the new marketing tools and tactics; it remains a challenge to tie an email campaign directly to customer participation as it is with all marketing and communication efforts. The average open rate for Idaho Power's emails is 36 percent with a 2.7 percent click-through rate (the percentage of people who click on a link within the email), which is similar to the industry average. The Customer Manager, however, provides the company a new way to connect with customers about energy efficiency programs and activities.

Below are two examples of Idaho Power's energy efficiency emails.

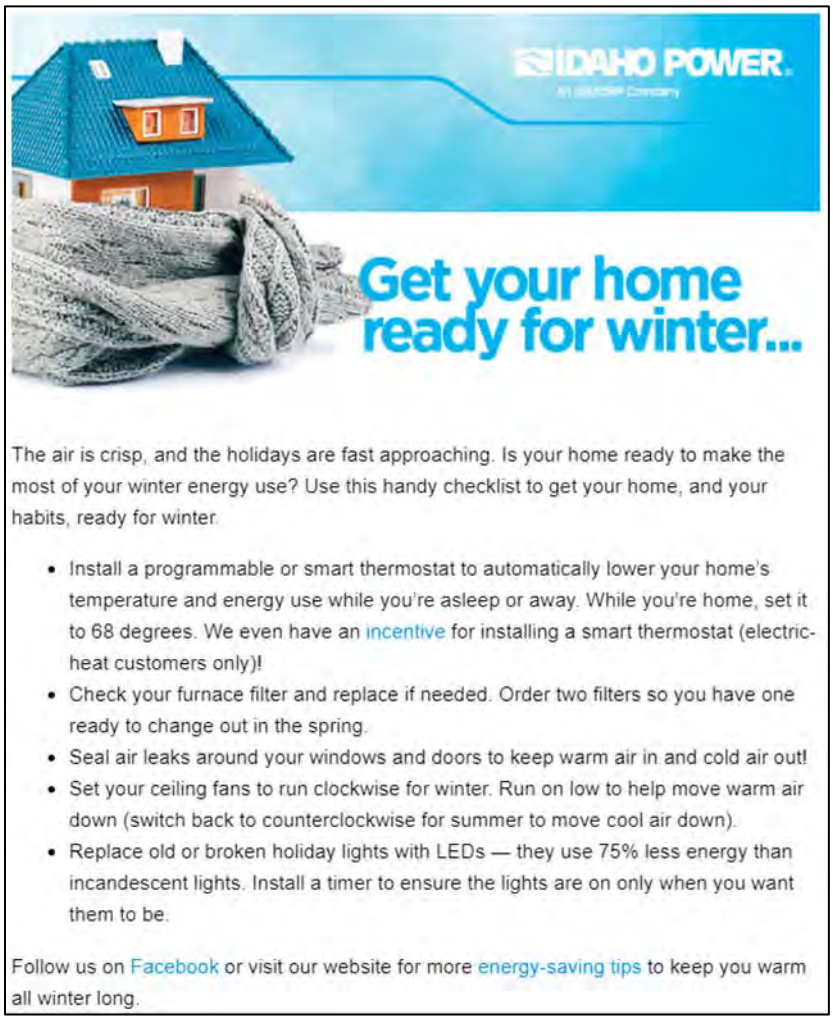

Figure 8
Winter tips and energy-saving information email sent to 25,580 homeowners in Idaho and Oregon who use 801 kWh or more per month

The winter tips email received an open rate of 30.2 percent and a click-through rate of 1.3 percent.

Figure 9
The introduction to the Energy Work electronic newsletter

The electronic newsletter was sent to 390 Oregon business customers. The open rate was 27.7 percent and the click-through rate was 1 percent. The newsletter included articles on Idaho Power's clean energy goal, energy efficiency offerings, rate changes, and more.

Recommendation No. 6

> *Continue updating all projects in Idaho Power's 2017 report and continue to include an updated version of Appendix C, with cost information, in the 2019 Smart Grid Report.*

An updated version of Appendix C is included in Appendix F of this report.

VI. RELATED ACTIVITIES

A. Cyber and Physical Security

All smart grid-related projects or plans conform to Idaho Power's Information Security standards, which are in place to secure its cyber assets. Idaho Power's aim is to strengthen its long-standing tradition of electric reliability while fostering a culture of compliance and satisfying a broad set of reliability standards.

Smart grid projects also conform to the requirements of Idaho Power's Physical Security program, protecting against unauthorized access to personnel, equipment, material, and documents while safeguarding against espionage, sabotage, acts of terrorism, damage, and theft. Physical security is an integral part of all critical infrastructure protection and safety, fire, and crime prevention programs.

Timing Intrusion Management Ensuring Resiliency Project

This DOE funded project involves Texas A&M University, Pacific Northwest National Laboratories (PNNL), and Idaho Power in the research, development, and demonstration of detection modules for timing intrusion management (both cyber and physical) in synchrophasor systems and other similar energy management systems to ensure resiliency of the systems.

Idaho Power will prepare its synchrophasor system to allow test access to a portion of the synchrophasor system as defined during the research phase of the project. Points of interest will include where the data processing and/or timing management is performed. Included in the research will be communication media and the protocols used to connect the equipment. While the Timing Intrusion Management Ensuring Resiliency Project team will undertake coordinated parallel efforts on the research, development, implementation, and testing of the timing intrusion modules, Idaho Power will participate in specifying the application requirements, field evaluation requirements, and field evaluation of the developed timing intrusion modules.

The ultimate goal of this project is to evaluate the solution developed by the Texas A&M Engineering Experimental Station team in the field environment at Idaho Power under attack scenarios to be defined by the PNNL team.

Project negotiations and contract work started in 2016, with the first in-person meeting of the project partners occurring in February 2017 at Texas A&M University. This project is expected to reach the field testing stage in October 2019, with final reports to be completed in December 2020.

B. Privacy

Idaho Power is committed to protecting the privacy of its customers and the data contained within company systems as stated in its *Corporate Security Policy* and evidenced by the company's Corporate Security program. For confidential data, such as customer information and energy usage data, Idaho Power limits access using a need-to-know approach enforced by

role-based access controls for employees and contractors and supported by periodic required training. The policies and controls undergo periodic reviews to ensure they support applicable mandates and guidance.

Idaho Power recognizes new risks are emerging from smart grid technologies, both from the increase in data and the increasing interconnectivity of systems. To stay current on these, Idaho Power has joined collaborative public/private partnerships, such as the National Institute of Standards and Technology Smart Grid Interoperability Panel Cyber Security Working Group.

Idaho Power customers can access their energy usage data electronically via a registered and password-protected login (My Account) on Idaho Power's website. Customers can also request that Idaho Power provide hard-copy usage information via fax, email, or mail.

Idaho Power provides protected customer information to entities other than the customer only under one of the following conditions:

- Receipt by Idaho Power of a court-ordered subpoena
- Presentation by a third-party of legal documentation substantiating the power of attorney for the customer of record
- Receipt by Idaho Power of written authorization from the customer of record identifying the third-party to whom information is to be released and specifying the information to be released
- Notification by a public utility commission that the customer of record has filed a complaint, at which point information will be provided to the Public Utility Commission (PUC) staff

In addition to the above conditions under which information for an individual customer may be provided, Idaho Power has several contractual business relationships with third parties for the procurement of services essential to the operation of the business (e.g., bill print services) that are subject to non-disclosure agreements and data security requirements.

C. General Customer Outreach and Education

Idaho Power recognizes the value of general energy efficiency awareness and education in creating behavioral change and customer demand for, and satisfaction with, its programs. The company achieves this through the Energy Efficiency Education Initiative by creating and delivering educational materials and programs that result in wise and informed choices regarding energy use and increased participation in Idaho Power's energy efficiency programs.

Kill A Watt Meter Program

The Kill A Watt™ Meter Program remained active in 2017 and 2018. Idaho Power's Customer Service Center and field staff continued to encourage customers to learn about the energy used by specific appliances and activities within their homes by visiting a local library to check out a Kill A Watt meter. The Kill A Watt meter brochure was updated in 2018. The Kill A Watt

meters were mentioned again on live television studio news programs on KTVB and KMVT in Idaho Power's monthly energy efficiency segments and highlighted in the *2018 Winter Energy Efficiency Guide*. Late in 2017, Idaho Power contacted participating libraries to determine what, if any, replacements were needed. Those communications continued into 2018. Forty-three libraries responded with requests for additional materials, including new meters, replacement kits, brochures, and/or *30 Simple Things You Can Do to Save Energy* booklets.

Idaho Science, Technology, Engineering, and Mathematics Steering Committee

Idaho Power continued to strengthen the energy education relationship with secondary school educators through continued participation on the Idaho Science, Technology, Engineering, and Mathematics (iSTEM) Steering Committee. In 2018, Idaho's Science, Technology, Engineering, and Mathematics (STEM) Action Center assumed the responsibility for overseeing the state's iSTEM Institutes.

In 2018, 13 teachers completed the four-day, two-credit professional development workshop offered at the College of Western Idaho's iSTEM Institute. The workshop *Electrons—Pushing, Using, and Saving Them!* was facilitated by Idaho Power and co-sponsored by Intermountain Gas and the INL. Among other things, participating teachers toured the Langley Gulch power plant and received a classroom kit containing Kill A Watt meters and other tools to facilitate student learning related to energy efficiency and wise energy use.

Idaho Power also used the 2018 workshop to introduce its five community education representatives to STEM practices and concepts. These employees regularly interact with students and teachers in schools and bring relevant STEM activities into classrooms in Idaho Power's service area. By participating in the 2018 workshop, teachers developed skills and relationships to help them engage middle school and high school students in activities and conversations around future energy needs, and energy efficiency options and choices.

Annual Student Art Contest

In 2018, Idaho Power held its eighth annual student art contest for grades K–9. Kindergarten through second grade completed a simple color page highlighting safety. Students in grades 3–9 were tasked with creating original artwork based on the themes *Ways to Save Energy* or *Environmental Stewardship*. Many students drew pictures of their favorite ways to save energy in the home. The student art contest provides a way for teachers and students to bring energy efficiency education into their classroom and inspire students and families to think more about energy.

With 4,654 submissions, over 30 students were recognized with first- and second-place awards. Over the years, student artwork has been displayed in local schools, libraries and city halls, and at events such as the annual Idaho Environmental Education Conference and elementary school STEM nights. Students in both Idaho and Oregon participated in 2019 (3,827 Idaho and 827 Oregon).

Energy Savings Kits

In 2018, 44,691 Energy Savings Kits (ESK) were shipped with a mini-home assessment to cross-market other energy efficiency programs, promote the use of My Account, and help families learn about other energy-saving behavior changes.

Idaho Power continued to coordinate light emitting diode (LED) lightbulb distributions aimed at providing the newest lighting technology to customers, along with education and answers to their common questions. At events and presentations, company staff distributed 9,450 LEDs in custom packaging that highlighted the advantages of energy-efficient lighting and encouraged participation in Idaho Power's My Account online portal. Customer representatives throughout the service area also handed out 700 Giveaway ESKs containing nine LED lightbulbs and other educational materials in conjunction with energy efficiency presentations and workshops.

Welcome Kit Program

In 2018, the company also implemented a Welcome Kit program with the goal of proactively introducing each first-time customer to sound, energy-saving practices along with Idaho Power's energy efficiency programs at a moment when they may be receptive to hearing and implementing change. In the first year, approximately 30,500 brand new customers received a Welcome Kit delivered to their home about 30–45 days after they moved in. Each kit contained four LED lightbulbs, a night light, a "Welcome to the Neighborhood" greeting card, and a small, easy-to-use, tabbed flip-book filled with helpful energy-saving tips and energy efficiency program information.

Energy Efficiency Guides

Idaho Power continued to produce semiannual *Energy Efficiency Guide*s in 2017 and 2018. Idaho Power distributed these guides primarily via insertion in local newspapers and at events across Idaho Power's service area. The winter *Energy Efficiency Guide* was published and distributed by 17 newspapers in Idaho Power's service area and the *Boise Weekly* also inserted the guide. The guide focused on providing answers to several interesting energy efficiency questions customers had recently asked. Along with useful energy-saving tips, the guide addressed hot tubs, programmable pressure cookers, high efficiency washers, portable space heaters, and ENERGY STAR® smart thermostats. The information was applicable to all residential customers and designed to be family friendly. Idaho Power included a story from the guide in January *News Briefs*, *News Scans*, and a promotional pod on the idahopower.com homepage.

The *Idaho Statesman* hosted Idaho Power's print ads, digital ads, and banner ads promoting the guide. This also included a one-day online homepage takeover on January 27, 2018, resulting in 173,223 impressions, 342 click throughs, and a click through rate of 20 percent. The newspaper hosted a 30-second energy efficiency commercial as a video pre-roll from January 28 to February 28. An Idaho Power Facebook boost was used to promote the guide to Idaho Power followers.

The summer *Energy Efficiency Guide* was delivered to over 194,000 homes the week of July 29, 2018. This guide highlighted efficient ways to stay comfortable during the sizzling summer months and specific room-by-room tips for reducing energy use at home and while on

vacation. It also discussed how to use landscaping to increase a home's comfort and boost energy efficiency.

The release of the summer guide received public relations support through numerous communication channels, including *News Briefs, News Scans*, on Idaho Power's social media accounts. It was also in digital ads on local newspaper websites, targeted to customers in the service area during the last week of July, including the *Times News, Idaho State Journal, Boise Weekly,* and *Idaho Press*. Both 2018 guides were translated into Spanish to help reach the larger Idaho Power customer base.

In 2018, the company distributed a total of 5,500 guides, including issues from past years, at energy efficiency presentations and events. The current library of guides continues to add value. Specific issues are often requested for distribution at events and presentations based on their relevance to the particular audience. On its website, Idaho Power provides a link to the most current seasonal guide and links to past guides.

Other Outreach Activities

Idaho Power continues to recognize that educated employees are effective advocates for energy efficiency and Idaho Power's energy efficiency programs. Idaho Power customer relations and energy efficiency staff reached out to each of Idaho Power's geographical regions and the Customer Service Center to speak with customer representatives and other employees to discuss educational initiatives and answer questions about the company's energy efficiency programs.

Idaho Power continued to participate in a select group of events impacting large audiences or audiences expected to have a higher receptivity to energy-efficient messaging and behavior change. In 2018, Idaho Power once again participated in *The Incredible Age Expo* (focused on customers preparing for retirement), Boise's *Treefort Music Fest* (focused on sustainably-minded younger people), St. Luke's FitOne Expo, and numerous home and garden shows throughout the service area.

Idaho Power participated in or sponsored an additional 45 outreach activities, including events, presentations, trainings, and other activities. Idaho Power customer representatives throughout the service area delivered numerous other presentations to local organizations addressing energy efficiency programs and wise energy use. In 2018, Idaho Power's community education team provided 118 presentations on *The Power to Make a Difference* to 3,063 students and 122 classroom presentations on *Saving a World Full of Energy* to 2,803 students. The community education representatives and other staff also completed 24 senior citizen presentations on energy efficiency programs and shared information about saving energy to 1,149 senior citizens in the company's service area. Additionally, Idaho Power's energy efficiency program specialists responded with detailed answers to 241 customer questions about energy efficiency and related topics received via Idaho Power's website.

Idaho Power will continue its customer outreach and education in 2019. Annually, the company assesses the effectiveness of it customer outreach and education efforts to insure its efforts are still reaching its target audiences, are current, and are wise expenditures of customer funds. Each year its activities will vary slightly some and events or activities will be changed or discontinued while others may be started.

Communications

Idaho Power communicates frequently with customers through a variety of channels, including, but not limited to, billing statements, bill messages, bill inserts, *Connections* articles, customer letters, door hangers, postcards, brochures, web content at idahopower.com, hold messaging on the company's 1-800-488-6151 phone line, social media, public events, and customer visits.

Idaho Power has successfully leveraged the functionality of AMI and especially the hourly meter data to enable most of its customers to learn more about their energy use and how to use energy wisely. The company has used events and other channels to provide customers with relevant information on a frequent basis about energy efficiency, company and program information, and updates about AMI metering. Idaho Power also sends a new-customer welcome letter inviting them to visit idahopower.com to learn more about their energy usage and to register on My Account.

VII. CONCLUSION

Idaho Power continues to refine its vision and strategy to anticipate what the future energy delivery system will look like and how it will meet customer needs and preferences, as well as improve company operations. The company is developing, testing, and deploying the technologies needed to facilitate the transition to a smart grid future and integrate renewable generation into the power system.

Idaho Power also continues work to improve customer care with future initiatives in place to improve outage communication tools, expand account alerts, integrate customer online requests into Idaho Power's customer information system, and offer two-way texting capabilities for outage reporting and making payments. Idaho Power will continue to explore opportunities to leverage existing systems to more actively engage its customers using their preferred technologies.

Idaho Power is dedicated to continuing efforts toward a smart grid system to provide its customers with an efficient, reliable, and safe power system that fits with customer expectations of a more interactive experience.

Appendix A.
Stakeholder Input

This page left blank intentionally.

IDAHO POWER®
An IDACORP Company

Share Your Ideas About **Smart Grid**

Idaho Power is preparing its annual smart grid investment report to the Public Utility Commission of Oregon (OPUC). We are seeking input, information and ideas from the public on smart-grid investments and applications.

Visit **idahopower.com/smartgrid** to review a draft version of the report. You'll also find information about what what the smart grid is, and how a smarter electrical grid can help move the energy industry into a new era of reliability, availability and efficiency.

Comments on the report will be accepted between July 15 and Aug. 2. To share your input, email **smartgrid@idahopower.com** or call Idaho Power Regulatory Analyst Kristy Patteson at 208-388-2982. A summary of customer comments will be provided to the OPUC with Idaho Power's report.

The smart grid represents energy innovation improvements that enhance customer service, power reliability, availability of renewable resources, and opportunities for time, energy and cost savings. The 2013, 2014, 2015, 2016 and 2017 reports can be found on our website.

idahopower.com/smartgrid

Patteson, Kristy

From: Towell, Kimberly
Sent: Tuesday, July 16, 2019 9:03 AM
To: 'dockets@oregoncub.org'; 'stephanie.andrus@state.or.us'; 'mike@oregoncub.org'; Nadine Hanhan; 'bob@oregoncub.org'; 'patrick.g.rowe@doj.state.or.us'; 'wendy.simons@oregon.gov'; 'rebecca.smith@oregon.gov'; 'oregondockets@pacificorp.com'; 'john@grid-net.com'; 'rfrisbee@si-two.com'; 'richard.george@pgn.com'; 'wendy@nwenergy.org'; 'royhemmingway@aol.com'; 'pkeisling@gmail.com'; 'keith@caporegon.org'; 'dockets@mrg-law.com'; 'adam@mrg-law.com'; 'douglas.marx@pacificorp.com'; 'wendy@mrg-law.com'; 'jesse.d.ratcliffe@doj.state.or.us'; 'adam.schultz@oregon.gov'; 'pge.opuc.filings@pgn.com'; 'john.volkman@energytrust.org'; 'michael.weirich@state.or.us'; 'sudeshna@oregoncub.org'; 'dockets@renewablenw.org'; 'greg@richardsonadams.com'; 'erik.colville@state.or.us'; 'jdj@racinelaw.net'; 'judy.johnson@state.or.us'; 'sarah.link@pacificorp.com'; 'etta.lockey@pacificorp.com'; 'dreading@mindspring.com'; 'peter@richardsonadams.com'; 'irion@sanger-law.com'; 'dws@r-c-s-inc.com'; 'stephens@eslerstephens.com'; 'ortez@eslerstephens.com'; 'doug.tingey@pgn.com'; 'tony@yankel.net'
Cc: Nordstrom, Lisa; Tatum, Tim; Larkin, Matt; Patteson, Kristy; Bearry, Christa; Aschenbrenner, Connie; White, Tami
Subject: Idaho Power Company's 2019 Oregon Smart Grid Report - Comments Solicited
Attachments: Draft 2019 Smart Grid Report.pdf; Newspaper ad for 2019 Smart Grid Report.pdf

Parties to Docket Nos. UM 1460, UE 233, LC 74, and UM 1675:

Idaho Power Company will be submitting its sixth annual Smart Grid Report to the Public Utility Commission of Oregon on October 1, 2019. As part of the annual report, Idaho Power is seeking public input and contributions from **July 15th - August 2nd**, on the attached Draft Smart Grid Report. To share your comments and ideas please email smartgrid@idahopower.com or call Kristy Patteson at (208) 388-2982.

Public input is being solicited through advertisements in the *Argus Observer* and *Hells Canyon Journal* newspapers. A copy of the advertisement is also attached.

For more information about smart grid, and Idaho Power smart grid reports and projects, go to www.idahopower.com/smartgrid.

Thank you,

--
Kimberly Towell
EXECUTIVE ASSISTANT
Idaho Power | Regulatory Affairs

Work 208-388-2558
Fax 208-388-6449

Email ktowell@idahopower.com

IDAHO POWER COMPANY'S RESPONSE TO INFORMAL COMMENTS ON IDAHO POWER'S DRAFT 2019 SMART GRID REPORT

Idaho Power did not receive informal comments from any parties on the 2019 draft report; therefore, no informal comments are included in this appendix.

Smart Grid

For Idaho Power, the Smart Grid represents energy innovation. It gives customers information they need to be wise energy consumers. It uses new technology to retrieve data and take actions that benefit electrical grid performance. And it leverages a combination of improvements that enhance customer service and power reliability, help integrate renewable resources, and create opportunities for time, energy and cost savings.

Smart Grid Benefits

- Enable customers to make more informed energy use decisions
- Reduce the time and impact of outages
- Limit effects of power line disturbances to strengthen the grid
- Support integration of renewable energy into our resource portfolio

Public Comment Period for Draft Report

Idaho Power is compiling its 2019 Oregon Smart Grid Report and would like your comments on the draft document. Comments are being solicited through Aug. 2, 2019. Submit comments to smartgrid@idahopower.com.

Company Reports

- 2017 Oregon Smart Grid Report
- 2016 Oregon Smart Grid Report
- 2015 Oregon Smart Grid Report
- 2014 Oregon Smart Grid Report
- 2013 Smart Grid Report
- 2011 Smart Grid Report

Appendix B.
Dynamic Line Ratings in Southern Idaho

This page left blank intentionally.

Using Computational Fluid Dynamics to Assess Dynamic Line Ratings in Southern Idaho

A.W. ABBOUD*, J.P. GENTLE, T.R. MCJUNKIN, B.A. FEHRINGER, J.P. LEHMER
Idaho National Laboratory
Idaho Falls, ID, USA

SUMMARY

The overall goal of the study is to combine computational fluid dynamics (CFD) simulations with weather data that is collected over a 1-year long period across southern Idaho to calculate the dynamic line ratings (DLR) of several transmission lines. These ratings can be compared to the static rating assumptions to show the potential for additional current carrying capacity along transmission lines through account for additional effects of convective cooling from the wind. The region of interest is quite large, sized at 144 km by 98 km; in order to cover this large region, the CFD simulations are split into four separate regions of over 80 million computational cells each. The weather data that was collected suggest initial assumptions used to make the static ratings were vastly over predicted with regards to summer temperatures and solar irradiance. The weather data is ran through the General Line Ampacity State Solver (GLASS) tool that was developed by Idaho National Laboratory (INL) to parse large quantities of weather data across thousands of transmission midpoint spans in the region. For shorter lines, the dynamic line ratings often show large improvement over static ratings. The case study here shows over 95% of the time DLR values are above static values on the short transmission lines. However, for long lines, a conundrum occurs, where due to the large number of weather stations associated with the line, there is often a single weather station which may read local wind speeds of zero. This often defaults the line rating to be limited by natural convective cooling and does not show as much improvement over static as might be expected from the weather data.

KEYWORDS

Computational Fluid Dynamics; Dynamic Line Rating; Transmission Lines

INTRODUCTION

Line ratings are typically calculated as constant values using conservative assumptions for the weather conditions in the calculations. While there are some adjusts that are made on seasonal or daily basis, there is likely a lot of unused head room on overhead conductors. Dynamic Line Ratings (DLR) have been identified by the United States Department of Energy as a distribution infrastructure solution to defer upgrades, support line outages, and increase yields of distributed generation [1,2].

The line ratings based on maximum conductor temperatures have standard models developed by the International Council on Large Electric Systems (CIGRE) [3,4,5], the International Electrochemical Commission (IEC) [6], and the Institute of Electrical and Electronics Engineers (IEEE) [7,8]. The conductor maximum temperature limits the ampacity of a transmission lines to avoid sagging or clearance issue of the line segments between structures due to thermal expansion. The conservative nature of transmission line standards can be hard to adjust, so research showing the benefits of DLR are important to prove that the method is acceptable. Case studies utilizing weather data in the field has shown potential for DLR to increase ampacity above static throughout several countries [9,10,11,12,13].

This study utilizes the coupling of field weather data collected within the transmission corridor with Computational Fluid Dynamics (CFD) results. For the wind field simulations, the steady-state Reynolds-Averaged Navier Stokes (RANS) approach was used for turbulent modelling of the wind flow [14]. The RANS approach has been used to validate wind flows in complex terrains [15], with adequate speed up predictions [16], and low-elevation mountains within acceptable error [17,18]. Due to the convective cooling calculation, the error in the cooling rate scales as approximate the square root of the wind speed, so a 10% error in wind speed is only a 5% error in the cooling rate. The site of interest in southern Idaho is 144km by 98 km. This study first goes through the theory for CFD and DLR, then discusses the CFD results, weather data comparisons to static assumptions, and finally DLR comparisons to static ratings.

THEORY

Computational Fluid Dynamics

In order to run the CFD simulations, the domain of interest must be linearized, this is done through projection into the Idaho Transverse Mercator Projection [19]. The domain is then split into four different regions which cover the space. The elevation map is shown in Figure 1a, where the plain area is mostly in light brown and green, and the darker brown in the north are the mountains. The roughness map of the terrain is shown in Figure 1b, this shows regions of low to high vegetation and cities where near ground wind fields would be affected. These regions are not explicitly modelled in the CFD, so the roughness layer is used to approximate slowdowns due to these subgrid effects. The division of this terrain into four sectors for CFD analysis is shown in Figure 1c. Only the regions with large transmission lines are selected, and some sparsely populated regions are ignored (as these likely have zero or no congestion).

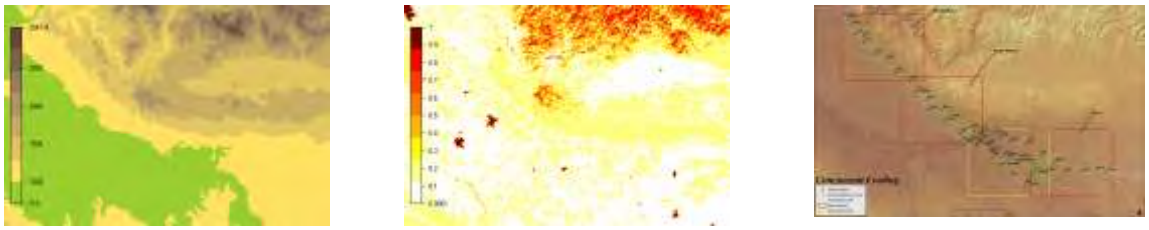

(a) (b) (c)

Figure 1. (a) The elevation map of the region, (b) the roughness map of the terrain, the division of the map into CFD domains around the transmission lines.

Each of the domains consists of 85 million computational cells, with 30-meter spatial resolution in the horizontal direction and varying spatial resolution vertically. The vertical resolution is spaced such that near the ground the resolution is in 5-meter increments to allow for accurate wind fields near the transmission lines, while above 100 meters a log scale is used up to the atmospheric boundary layer. For computing the wind speeds across the domain tiles the Wind Atlas methodology of Wind Sim is utilized [20].

The steady-state standard k-ε RANS model is used for modelling the turbulent kinetic energy and dissipation rate. The PDEs for the solution consist of the velocity vectors, continuity equation that equations for the turbulent kinetic energy and turbulent dissipation rates. The equation for the velocity vectors is

$$\rho U_i \frac{\partial U_j}{\partial x_i} = \frac{\partial}{\partial x_i}\left[(\mu + \mu_t)\left(\frac{\partial U_i}{\partial x_j} + \frac{\partial U_j}{\partial x_i}\right)\right] - \frac{\partial p}{\partial x_i} \tag{1}$$

The turbulent kinetic energy, k, equation is given by

$$\frac{\partial (U_i k)}{\partial x_i} = \frac{\partial}{\partial x_i}\left[\frac{\mu_t \partial k}{\sigma_k \partial x_i}\right] + P_k - \epsilon \tag{2}$$

And the equation for the turbulent dissipate rate, ϵ, is given by

$$\frac{\partial (U_i \epsilon)}{\partial x_i} = \frac{\partial}{\partial x_i}\left[\frac{\mu_t \partial \epsilon}{\sigma_\epsilon \partial x_i}\right] + c_{\epsilon 1}\frac{\epsilon}{k}P_k - c_{\epsilon 2}\frac{\epsilon^2}{k}P_k \tag{3}$$

Where the turbulent viscosity, μ_t is given by

$$\mu_t = \frac{C_\mu k^2}{\epsilon} \tag{4}$$

And the turbulent production term, P_k is given by

$$P_k = \mu_t\left(\frac{\partial U_i}{\partial x_j} + \frac{\partial U_j}{\partial x_i}\right)\frac{\partial U_i}{\partial x_j} \tag{5}$$

Where c_μ, c_{ϵ_1}, c_{ϵ_2}, σ_k, and σ_ϵ are the fixed constants for the $k - \epsilon$ model, with values set to 0.09, 1.55, 2.0, 1.0, and 1.3, respectively [14].

Dynamic Line Ratings

The dynamic ratings are calculated on 15-minute moving average intervals with 1-minute temporal resolution for the collected weather data. The heat balance equation is used to solve for the maximum current, *I*, to get [7]

$$I = \sqrt{\frac{q_c + q_r - q_s}{R(T_c)}} \tag{6}$$

Where q_c, q_r, and q_s are the convective, radiative and solar contributions, and *R* is the conductor resistance as a function of the conductor temperature T_c. The radiated heat loss per unit length in units of W/m is given by

$$q_r = 17.8D\epsilon\left[\left(\frac{T_c + 273.15}{100}\right)^4 - \left(\frac{T_a + 273.15}{100}\right)^4\right] \tag{7}$$

Where ϵ is the emissivity, T_a is the ambient air temperature and D is the conductor diameter. The heat gain through solar irradiance is given by

$$q_s = \alpha Q_{se} \sin(\theta) A' \tag{8}$$

Where α is the solar absorptivity, Q_{se} is the total solar and sky radiated heat flux corrected by elevation, θ is the effective angle of incidence of the sun's rays and A' is the projected area of the conductor. The convective heat loss is calculated using one of three equations for high wind speeds, low wind speed (below 3 mph) or natural convective cooling, these are given by high wind speed,

$$q_{c1} = \left[1.01 + 1.35\left(\frac{DV_w\rho_f}{\mu_f}\right)^{0.52}\right] k_f K_{angle}(T_c - T_a) \tag{9}$$

Low wind speed,

$$q_{c2} = 0.754\left(\frac{DV_w\rho_f}{\mu_f}\right)^{0.6} k_f K_{angle}(T_c - T_a) \tag{10}$$

Or natural convection

$$q_{cn} = 3.645\rho_f^{0.5} D^{0.75}(T_c - T_a)^{1.25} \tag{11}$$

Where V_w is the speed of air, with fluid parameters density ρ_f, viscosity μ_f and thermal conductivity k_f calculated at the ambient temperature. And K_{angle} is the wind direction factor which can varying form about 0.3 to 1.0 based on parallel or perpendicular wind flow to the transmission line, given by

$$K_{angle} = 1.194 - \cos(\phi) + 0.194\cos(2\phi) + 0.368\sin(2\phi) \tag{12}$$

Where ϕ is the angle of incidence between the wind and the transmission line midpoint. The GLASS code developed by INL does all of these calculations for every single transmission line midpoint of interest. The minimum value among all the midpoint calculation sis assumed to be the ampacity for each line.

RESULTS

Computational Fluid Dynamics

The results for the wind fields is shown in Figure 2 for each of the four domain decompositions. This is shown for both the north incoming and the south incoming sector. The direction of the incoming wind will impact where slower near-ground wind speeds occur. The northwest-1 and -2 sectors are closer to the large mountain ranges and show significant changes is speed due to that when wind comes from the north.

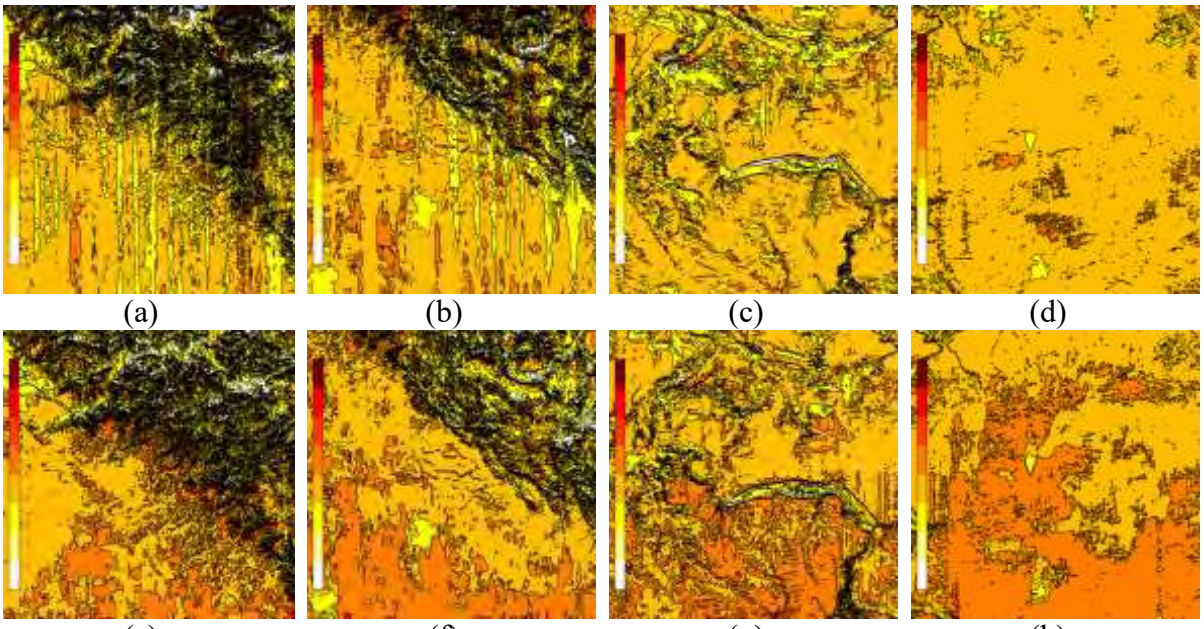

Figure 2. Wind field flow for the northwest-2, northwest-1, center, and east domain sections for north incoming (a-d) and south incoming wind (e-h), respectively. The color bar is scaled from 0 to 10 m/s.

Weather Data

A summary of one of the weather stations is shown, with comparison to the static assumptions. This weather station is located at the north-western portion of the terrain. Histograms for speed, temperature, and solar are shown in Figure 3a, 3b, and 3c, respectively. The difference from static as a percentage of time over the year is shown in Figures 3d, 3e and 3f for those same variables.

For this particular weather station, the wind speed is greater than the static assumption 63% of the time. This rating has both winter and summer seasonal adjustments on temperature and solar. For the ambient temperature, the values were below static 99% of the time in the summer, and below static 47% of the time in the winter. For the solar irradiance, the values were less than static assumptions 100% of the time in summer, and 95% of the time in winter. Trends are similar for the other 46 weather stations placed throughout the region.

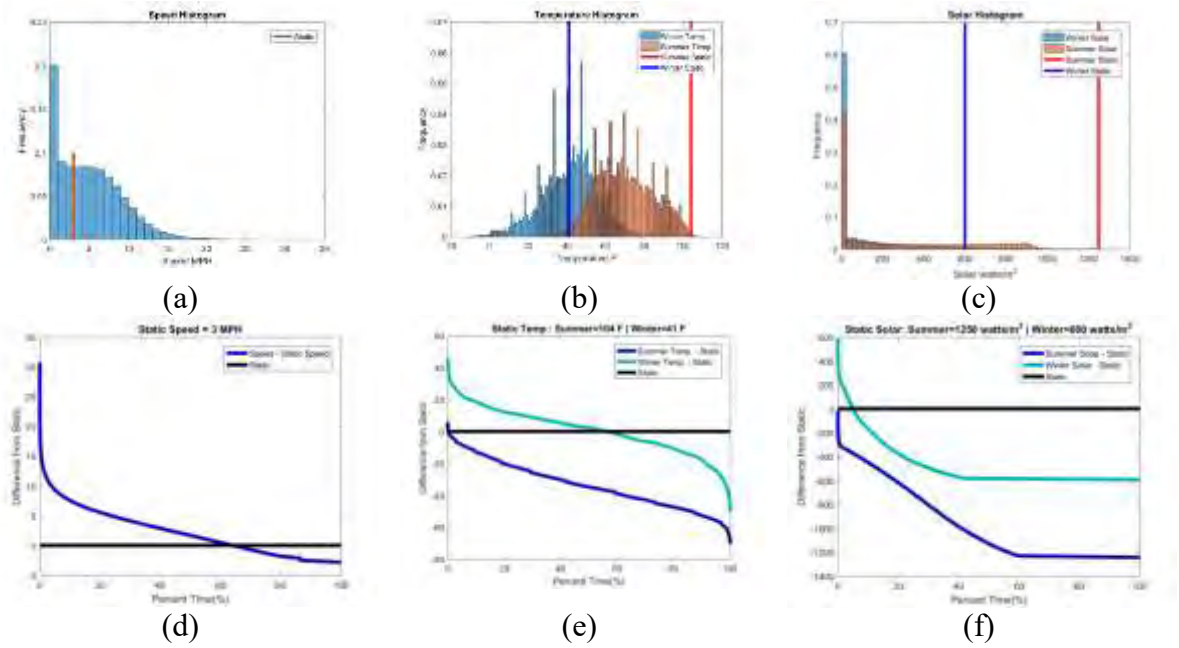

Figure 3. Example of weather data in the region, (a) histogram of wind speed, (b) histogram of temperature, (c) histogram of solar irradiance, and percentage of time above static for (d) wind speed (e) temperature and (f) solar irradiance.

Transferred Climatology

Example transfers are shown from the weather station to different midpoint spans using the wind fields from the CFD model. This transferred data gives updated wind speeds to use at the transmission line locations for the ampacity rating. Figure 4 shows how the data is processed though the CFD fields to different midpoint locations. The right side of this plot shows the wind data collected at three different weather station locations, while the left side shows the corresponding transferred wind rose after the CFD lookup table has been applied to each incoming wind direction. For flat regions of the terrain, the transferred wind rose may change only slightly – such as in the first row of transfers this weather station and midpoints are in a flat region of the terrain. While for hilly regions, the max wind speeds, and predominate wind directions can change the values, as shown in the second row in Figure 4. Nearby hills may block or redirect the wind incoming from the west and north western direction when comparing locations through locations along the foothills.

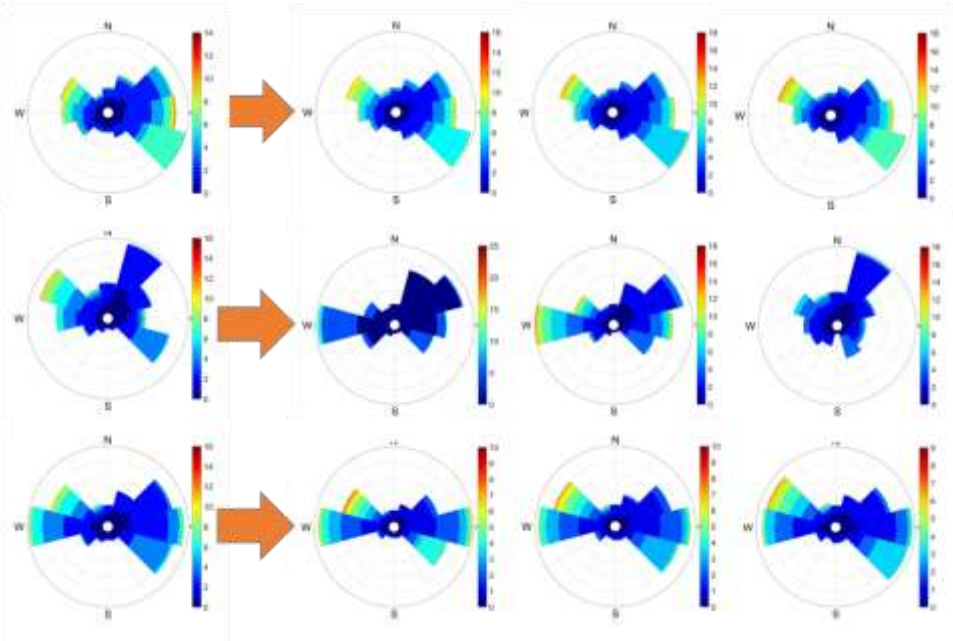

Figure 4. Example of transferred weather conditions of wind speed and direction based on the CFD lookup tables.

DLR Calculations

The dynamic line ratings are calculated for every major transmission line in the region using the GLASS code. For short lines with few weather stations, significant improvements are shown. In Figure 5a the 15-minute moving average of the ampacity for a short line for a small conductor of 3.1 miles with 2 weather stations is shown, with the summer and winter ratings shown with dotted overlay. Figure 5b shows the amount of time the rating is above static, in the winter the DLR rating is above the static rating nearly 80% of the time, and the DLR is above the summer rating is much better at about 95% of the time. From Figure 3a and 3b, this is likely that due to low wind speeds below static assumption occurring some of the time, as well as the winter temperature assumption as more of an average rather a conservative value such as in the summer. In Figure 5c the 15-minute average for a large conductor line is shown which is only 1 mile long with 2 nearby weather stations. For this line the DLR calculated above static is shown in Figure 5d, where the time above the winter rating is about 60%, and the time DLR is above the summer static rating is about 95%.

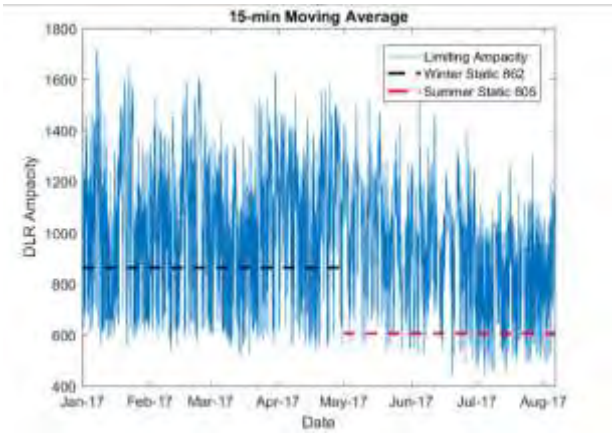

(a)

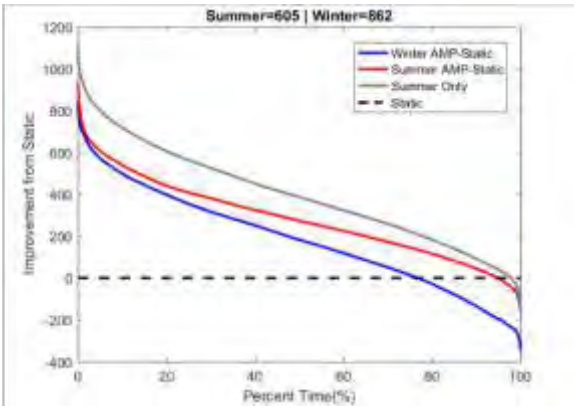

(b)

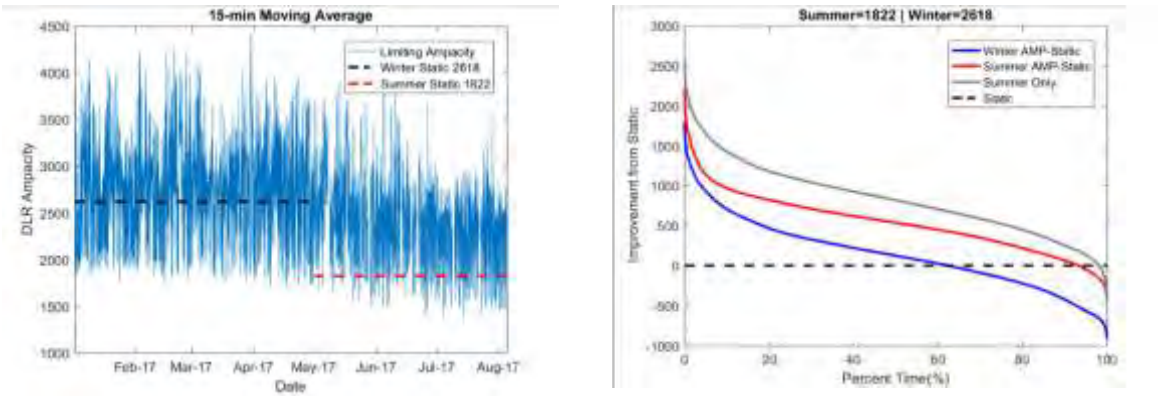

(c) (d)

Figure 5. The 15-minute moving average ampacity calculations for a (a) small conductor and (c) large conductor in the Boise-Twin Falls regions compared to static ratings, (c) small conductor DLR time above static and (d) large conductor DLR time above static rating.

For longer transmission lines, care needs to be taken in the applications of the DLR calculation. A large conductor which spans the entire region, of about 100 miles in length with 30 weather stations used for its DLR calculation has its 15-minute moving average of the ampacity plotted in Figure 6a. In the winter, the DLR ampacity is well below the static rating compared to the previous lines shown. The percentage of time above static plot for this long line is shown in Figure 6b, for this during the winter the DLR value is only above static 5% of the time, and for the summer, it is only 55% of the time.

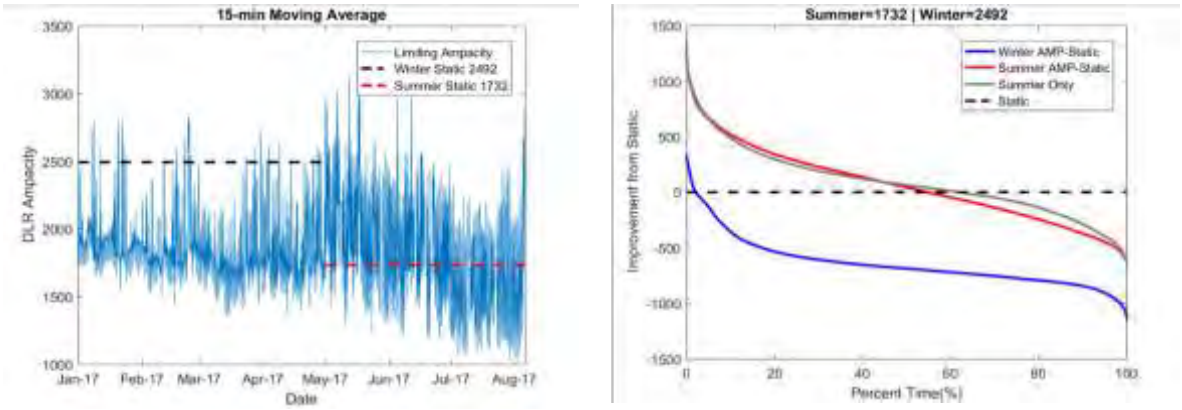

(a) (b)

Figure 6. The (a) 15-minute moving average for a large conductor of about 100 miles with 30 weather stations, and (b) the conductor time DLR is above the static rating.

In Figure 7a, the weather speed for all 30 weather stations associated with this long line are shown for a single day, along with the minimum at each timestamp. Figure 7b shows the wind speed histogram of a single station, where it seems as if the wind speeds should be on the higher side contributing much to the convective cooling effect. Figure 7c shows the histogram of the minimum wind speed (the black line in Figure 7a), which shows about 80% of the time the wind speed at one of the weather stations is near 0. For long lines with many weather stations, then the sheer number of values can cause a single weather station to show zero wind speed, which limits the DLR to natural convective cooling only. Although it still receives benefit from solar irradiance and ambient temperature conditions from static assumptions. Consider that, in general, weather stations in the region may read a near-zero value in the

wind speed 5% of the time such that the cooling is driven by natural convection, then the probability that a line with 30 weather stations on it all reading not zero values would be $P(>0) = 0.95^{30}$. Only 20% of the time the agglomeration of this weather data will every weather station read a non-zero value.

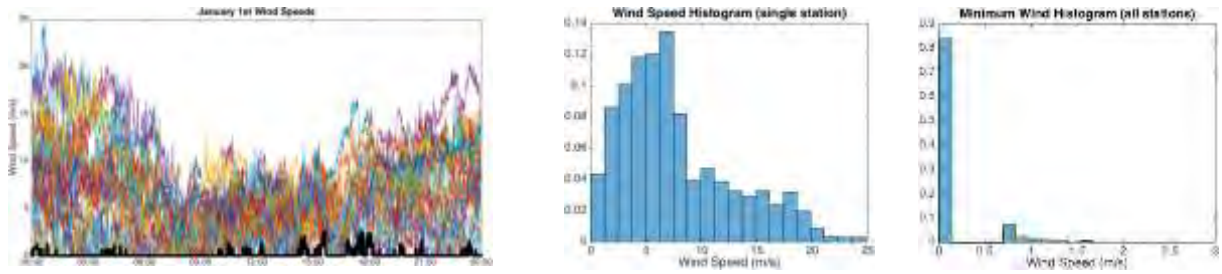

(a) (b) (c)

Figure 7. (a) The wind speed over a day long region for all the weather stations along the line, and the minimum speed of these 30 weather stations shown in the thick black line, (b) the histogram for a single weather station, and (c) the histogram for the minimum speed of all the weather stations.

CONCLUSION

Transmission corridor collected field weather data can be coupled with computational fluid dynamics results to calculate local DLR for every midpoint span along a transmission line. The GLASS software developed by INL was used to process the large amount of historical information gathered in a yearlong span to calculate dynamic line ratings for several transmission lines. The field data alone showed that for this particular region's summer temperature assumptions and solar irradiance assumptions used in static ratings are often too conservative. For short transmission lines, the benefit of DLR was shown to be quite large during summer when more congestion would be expected from HVAC load, the DLR value is above static ratings about 95% of the time in the summer.

For the long line that was analyzed, the raw value of the ampacity was not as generous towards the benefits of DLR. However, in actuality the entire 100-mile transmission line would not be expected to be at the same conductor temperature at every midpoint span due to different convective cooling rates – which was an assumption made in these DLR calculations. In the future, improved algorithms such as autoregressive–moving-average (ARMA) may be utilized for calculations for each midpoint and may alleviate the many weather station long line conundrum. Other methods for improving this issue have been hypothesized such as true dynamic line rating (TDLR) with individual temperature estimates, which will be examined in future studies.

ACKNOWLEDGEMENTS

This research was performed by Idaho National Laboratory with support from Idaho Power Company and funding from the U.S. Department of Energy Wind Energy Technologies Office. INL is operated by Battelle Energy Alliance under contract No. DE-AC07-05ID14517.

BIBLIOGRAPHY

[1] "Dynamic line rating systems for transmission lines: American recovery and reinvestment act of 2009," U.S. Department of Energy, Tech. Rep., 2014.
[2] "Smart grid system report," U.S. Department of Energy, Tech. Rep., 2010.
[3] CIGRE Working Group 22.12, "The thermal behaviour of overhead line conductors," Electra, vol. 114, no. 3, pp. 107–125, 1992.
[4] "Guide for selection of weather parameters for bare overhead conductor ratings," CIGRE WG 22.12, Tech. Rep., 2006.
[5] "Guide for thermal rating calculations of overhead lines," CIGRE WG B2.43, Tech. Rep., 2014.
[6] "Overhead electrical conductors calculation methods for stranded bare conductors," IEC Standard TR 1597, Tech. Rep., 1985.
[7] "Standard for calculating current-temperature relationship of bare overhead line conductors," IEEE Standard 738, Tech. Rep., 2012.
[8] IEEE PES WG Subcommittee 15.11, "Real-time over- head transmission line monitoring for dynamic rating," IEEE Transactions on Power Delivery, vol. 31, no. 3, 2016.
[9] D. Greenwood, J. Gentle, K. Myers, P. Davison, I. West, J. Bush, G. Ingram, and M. Troffaes, "A comparison of real-time thermal rating systems in the U.S. and the U.K." IEEE Trans. Power Delivery, vol. 29, no. 4, pp. 1849– 1858, August 2014.
[10] B. P. Bhattarai, J. P. Gentle, P. Hill, T. McJunkin, K. S. Myers, A. Abboud, R. Renwick, and D. Hengst, "Trans- mission line ampacity improvements of altalink wind plant overhead tie-lines using weather-based dynamic line ratings," in IEEE PES General Meeting, July 2017.
[11] B. P. Bhattarai, J. P. Gentle, T. McJunkin, P. J. Hill, K. Myers, A. Abboud, and D. Hengst, "Improvement of transmission line ampacity utilization by weather-based dynamic line ratings," IEEE Transactions on Power De- livery, 33(4), pp 1853-1863.
[12] S. Uski-Joutsenvuo and R. Pasonen, "Maximizing power line transmission capability by employing dynamic line ratings technical survey and applicability in finland, vtt- r-01604-13," Tech. Rep., 2013.
[13] B. J. L. Aznarte and N. Siebert, "Dynamic line rating using numerical weather predictions and machine learning: A case study," IEEE Trans. Power Delivery, vol. 32, no. 1, pp. 335–343, 2017.
[14] W. Jones and B. Launder, "The prediction of laminarization with a two-equation model of turbulence," International journal of heat and mass transfer, vol. 15, no. 2, pp. 301–314, 1972.
[15] T. Wallbank, "Windsim validation study: Cfd validation in complex terrain," Tech. Rep., 2008. [Online]. Available: http://www.windsim.com/documentation/paperspresentations/thesis/080512trw%20WindSim%20Write% 20Up%20-%20Validation%20study.pdf
[16] A. Dhunny, M. Loolchund, and S. Rughooputh, "Numerical analysis of wind flow patterns over complex hilly terrains: comparison between two commonly used cfd software," International Journal of Global Energy Issues, vol. 39, no. 3, pp. 181–203, 2016.
[17] A. Dhunny, M. Loolchund, and S. Rughooputh, "A high-resolution mapping of wind energy potentials for mauritus using computational fluid dynamics," Wind and Structures, vol. 20, no. 4, pp. 565–578, 2015.
[18] A. Dhunny, M. Loolchund, and S. Rughooputh, "Wind energy evaluation for a highly complex terrain using computational fluid dynamics (cfd)," Renewable Energy, vol. 101, pp. 1–9, 2017.

[19] Idaho Department of Water Resources. Idaho Transverse Mercator Projection. https://www.idwr.idaho.gov/GIS/IDTM/
[20] S. Koller and T. Humar, “Windpotentialanalyse fur windatlas jaresmittelwete der modellierten windgeschwindigkeit,” Energieschweiz, Bern, Switzerland, Tech. Rep., 2016. [Online]. Avail- able: http://www.bfe.admin.ch/geoinformation/05061/ 06675/index.html?lang=en&dossier id=06606

Appendix C.
PSERC Final Reports

This page left blank intentionally.

Life-Cycle Management of Mission-Critical Systems through Certification, Commissioning, In-Service Maintenance, Remote Testing, and Risk Assessment

Final Project Report

T-57HI

Power Systems Engineering Research Center
Empowering Minds to Engineer
the Future Electric Energy System

Life-Cycle Management of Mission-Critical Systems through Certification, Commissioning, In-Service Maintenance, Remote Testing, and Risk Assessment

Final Project Report

Project Team
Mladen Kezunovic, Project Leader
Tom Overbye
Pratyasa Bhui, Jinfeng Ren
Texas A&M University

Anurag K. Srivastava, David Bakken
Param Banerjee, Pratim Kundu
Washington State University

Sakis Meliopoulos, George Cokkinides
Georgia Institute of Technology

Graduate Students
Cheng Qian, Christoph Seidl, Ikponmwosa Idehen (Iyke)
Texas A&M University

Ren Liu, Hyojong Lee, Zhijie Nie,
Washington State University

Boqi Xie, Jiahao Xie, Yu Liu, Liangyi Sun
Yuan Kong, Chiyang Zhong, Orestis Vasios
Georgia Institute of Technology

Undergraduate Student
Alex Askerman
Washington State University

PSERC Publication 18-13

September 2018

For information about this project, contact:

Mladen Kezunovic
Texas A&M University
Department of Electrical and Computer Engineering
Wisenbaker Engineering Building 323C
College Station, TX 77843
Phone: 979-845-7509
Email: kezunov@ece.tamu.edu

Power Systems Engineering Research Center

The Power Systems Engineering Research Center (PSERC) is a multi-university Center conducting research on challenges facing the electric power industry and educating the next generation of power engineers. More information about PSERC can be found at the Center's website: http://www.pserc.org.

For additional information, contact:

Power Systems Engineering Research Center
Arizona State University
527 Engineering Research Center
Tempe, Arizona 85287-5706
Phone: 480-965-1643
Fax: 480-727-2052

Notice Concerning Copyright Material

Acknowledgements

We wish to thank the following companies and their representatives for supporting the project over the years:

- Entergy (Floyd Galvan, Angela Nelson)
- Idaho Power Company (Dave Angel, Orlando Ciniglio, Milorad Papic, Erik Schellenberg)
- ISONE (Eugene Litvinov, Tongxin Zheng, Frankie (Qiang) Zhang, Xiaochuan Luo)
- MISO (Mark Westendorf, Kevin Frankeny)
- NYISO (Rana Mukerji, Michael Swider, Ed Cano, Muhammad Marwali)
- NYPA (Saman Babaei, George Stefopoulos, Bruce Fardanesh)
- PowerWorld (Mark Laufenberg)
- RTE (Patrick Panciatici, Thibault Prevost, Gabriel Bareux)

Executive Summary

The overall research problem was to develop various tools and, methodologies to support life cycle management of mission-critical systems. The mission critical systems are represented with synchrophasor solutions, as well as the special protection schemes. The various evaluation stages included certification, commissioning, in-service maintenance, remote testing, and risk assessment. The tools have been developed for both laboratory and field-testing. The evaluation procedure assumed testing of individual components, as well as end-to-end system testing. With the developed tools, end-users will be able to maintain the system through the life-cycle from the initial selection of the system components and commissioning to the use throughout its life-time.

The project activities resulted in a PMU calibration lab developed at all participating universities, and other tools being developed as follows: a) Field test device and test protocols for device and system commissioning, acceptance, and in-service tests (M. Kezunovic, Texas A&M University), b) End-to-end remote testing of PMU and RAS (A. Srivastava and D. Bakken, WSU), c) PMU/MU Characterization and data validation via Substation Dynamic State Estimation, (Sakis Meliopoulos, GaTech), and d) Prototype algorithms and visualization for PMU data error identification and oscillation analysis (T. Overbye, Texas A&M University). The various tools have been tested mostly in the lab environment, and in some instances, actual utility data was used. The extension of this project in the future would be to use such tools and methodologies in specific utility applications.

Part I: Development of Field Test Devices and Test Protocols for Device and System Commissioning, Acceptance, and In-Service Tests

In this part of the study we focused on development of the various testing and evaluation tools to meet the acceptance and commissioning of the synchrophasor systems. The research method was to gradually proceed with testing various components starting from PMUs, then adding the communication channel, and PDCs, and finally adding an application for a complete end-to-end test. This approach was designated as “nested testing” approach. To facilitate such evaluation, we engaged in three developments: PMU field calibrator, “Gold PMU”, and Fault Location assessment procedure. Besides that, we develop a PMU test and evaluation setup that may be used for future certification of PMU products.

The implication of our work is in the ability of end-users to utilize such devices and methodologies in evaluating performance of their synchrophasor system and its components. Such a capability was not readily available in the past resulting in inability of the end-user to verify performance of their synchrophasor system, particularly in the case when system components are showing some malfunction or even failure. The PMU certification lab may be used to evaluate future purchases and make sure they meet the IEEE standards. The Gold PMU may be used to verify that a commercial PMU meets its in-service performance requirements by comparing the outputs from an installed PMU and Gold PMU installed in parallel. To create test inputs for in-service evaluation of synchrophasor systems, the field calibrator has automated waveform replay features allowing the test plan to be executed automatically. The Fault Location application is used to illustrate how all the mentioned tools may be used to perform an in-service evaluation of performance of an application.

The next step in this research would be to utilize the mentioned tools extensively for utility uses and develop user manuals for the utilization.

Part II: End-to-End Remote Testing of PMU and RAS

In addition to testing phasor measurement units before deployment following IEEE Test Suite Specification (TSS), it is important to test and validate PMU and associated real time critical applications in field. The proposed "PMU Performance Analyzer (PPA)" is capable of testing the PMU's in field by integrating it with middleware called Erkios. The PPA is a software application that makes PMU testing effortless and highly accurate. It is capable of analyzing the performance of a PMU (under test) during steady state and dynamic conditions as specified in the IEEE Standard and guidelines. The PPA may also include some tests that are not in the standard based on utility specific requirements.

Erkios is developed with an objective to provide a solution for remote PMU testing and in-field testing of RAS. Erkios is a middleware framework and utilizes a number of fault-tolerance techniques to provide in-field testing of PMU and Remedial Action Scheme (RAS).

The first step in building such a tool is to set up a testbed that emulates the real-world scenario so that the tool can be validated. Development and integration of real time testbed with Erkios to facilitate cyber-physical simulation of end-to-end in-field testing of PMU and RAS are presented here. The testbed involves a real time power system simulator that has the capability to integrate with power system sensors and controllers in a closed loop. Also, the testbed has the communication channels and data flow closer to real world scenario.

This project resulted in updated PPA and Erkios software for remote PMU and RAS testing as well as a cyber-physical testbed to test and validate the developed tools.

Part III: PMU/MU Characterization and Data Validation via Substation Dynamic State Estimation

Present day PMU and Merging Unit (MU) technologies offer the capability for better, accurate and faster monitoring of the power system. The data generated from these systems are utilized by many applications. These technologies are complex, and many things can cause deterioration of the performance of these systems. However, data from relays, PMUs, MUs, FDRs, and in general any IED in the substation are treated as separate entities without any tools to test their cross correlation and in general to provide automated checking of the validity of the data. If for some reason gaps and errors are generated in the data, these gaps/errors remain and propagate to higher level devices. Furthermore, if any physical anomalies occur (such as a blown fuse, a damaged wire, etc.) they will affect the quality and validity of the data, yet there is no mechanism to determine the root cause of these anomalies.

This project integrated technologies developed under previous projects into an integrated physical-and-protection co-model and analysis software that performs the following: (a) validate all data coming out of all relays, PMUs, and in general IEDs via the distributed state estimator, (b) detect anomalies and identify the root cause of these anomalies (hidden failures such as blown fuses, cut wires, etc. or human errors such as incorrect entry of system parameters such as CT and VT ratios, incorrect instrument transformer connection (delta/wye), etc.), (c) in case of temporary loss of

data, it creates the missing data from the state estimator and inserts the estimated data into the stream, and (d) it provides the validated data and the substation state up stream for further utilization, such as construction of the system wide real time model at the control center. These objectives have been achieved by a two parts process: (a) construction of a laboratory for the purpose of fully characterizing the individual components of the system, i.e. PMUs, merging units, digital fault recorders, etc. and (b) by constructing a laboratory that comprises the protective relaying scheme of a small substation, the substation automation infrastructure and a simulator to drive the system for the purpose of managing the data, identifying bad data and correcting bad data before the data are send upstream.

A field demonstration of the developed methods was planned. Specifically, the plan is to demonstrate these methods on the MARCY substation. Due to construction delays at MARCY substation, it was not possible to complete the demonstration before the end of the project. We do plan to complete this part of the project after the official completion of the project. Specifically, the required hardware at the substation for this demonstration will be installed in fall 2018 during a planned outage for the substation. Shortly after we plan to install the software at MARCY and test them in the field.

The work of this project will have substantial impact on future research activities. The developed methods and software will be critical components for many applications in the substation and control center. For example, we presently are extending these methods to be part of the protection and control system in the substation by making sure that all relays receive validated data. This application will solve a perennial problem in protection. Specifically, occasionally hidden failures occur in the instrumentation and data acquisition systems resulting in sending erroneous data to the relays and causing relay mis-operations. The data validation methods of this project can identify the hidden failures and correct data this avoiding relay mis-operations.

Another direction is to use the methods develop in this project to form the basic infrastructure of the next generation management systems. Note that a basic problem at control center operations is the accurate knowledge of the system in real time. The developed methods and software provide the validated data and model of each substation at speeds not possible before, specifically once per cycle. The validated data and validated real time model of each substation can be sent to the control center where the validated real time model of the entire system can be constructed by assembling the validated substation models at the same instant of time. This task can be achieved once per cycle. Thus, the control center can have the validated real time model of the entire system once per cycle and with a delay as short as much requires to stream the data from each substation, typically milliseconds. All the applications can now run on a validated real time model. In addition, the speed and accuracy open up a number of new applications such as full state feedback control of many fast responding resources in the power system such as universal power flow controller and other FACTS devises.

Part IV: Prototype Algorithms and Visualization for PMU Data Error Identification and Oscillation Analysis

An increased scale of power system interconnectivity and size poses challenges for operator visibility of the grid. Fast-measurement and high-reporting devices, known as phasor measurement unit (PMU) devices and used for monitoring grid health at high resolution scales, expand the

capabilities for grid data processing and analysis, whose results are then used to increase the awareness level of the power system. A growing interest in the use of these unique devices in large-scale systems prompts the development of newer, robust analysis methods fit enough to capture both local and holistic dynamic features of the system. For example, the integrity testing of huge amounts of data obtained from geo-spatially, distributed grid sensors prior to data usage by critical grid applications, such as stability monitoring, grid disturbance and oscillation monitoring, to assess the state of the system. In this report, the goal is to study mechanisms of PMU device failures, and prototype algorithms and visualizations for data error identification and oscillation analysis. A 2,000-bus synthetic large-scale system is used for the different case studies in this report.

Sections 2 and 3 present PMU device failure mechanism and data error analysis in large scale power systems. respectively Firstly, we ed error propagation models that allows for the study of different mechanisms of time issues associated with PMU device operation, which in turn affect the integrity of reported data measurements. Secondly, we developed an approach to measurement error analysis in large scale grids considering the spatial and temporal variations that could exist among device measurements. In addition, the use of a hybrid, multidimensional scaling (MDS) method is proposed for use to visualize all pairwise measurement error correlations among all buses in a test system. A Matlab user interface tool is developed to aid generation of artificial PMU data errors. Designed using the Matlab GUIDE program, the developed user interface accepts user input for a selected PMU error type. Also, a prototype visualization dashboard display designed in a rapid application development (RAD) studio, and using Delphi programming language, is developed for the presentation of PMU error information in the large-scale system. It uses MDS correlation plots, tables, trend and bar charts to present its information. To migrate these developed tools to an application level would require additional data processing modules (as some of the processes are still being implemented manually) and extensive debugging.

Sections 4 and 5 focus on methods for presenting information pertaining to system oscillation. This information is obtained from the processing of enormous amounts of PMU data measurements obtained from a large-scale power grid. The use of a one-line diagram of the 2,000-bus synthetic Texas system overlaid on a geographic map of Texas, small object representations (known as glyph objects) and a method in vector field visualization are used to visualize large-scale system oscillation information. A wide-area visualization method is intended to present large-scale system dynamics to an engineer in a condensed, easy-to-interpret, holistic view of the system. The proposed visualization method is currently implemented in the PowerWorld simulator software for field visualizations in geomagnetic disturbance (GMD) and oscillation monitoring studies.

In summary, the key contributions/takeaways from this project are:

- The formulation and use of model equations to explain some of the timing issues associated with PMU devices. In addition to other system dynamics, these model equations can be used to generate artificial data for research purposes.
- Assist engineers to better understand unique, PMU-reported data patterns attributable to timing issues in PMU device operation rather than supposedly actual events on the grid. This can help in the interpretation of data discrepancies, and further search for error source if patterns of time errors are observed in the data.

- Development of a hybrid, distributed analysis method to detect erroneous measurements from PMU data obtained from a large-scale power grid. The result of the proposed method shows a 100% accuracy, and greater improvement over a central error analysis method, in the detection of bad PMU data from measurements obtained from several measurement locations in a 2,000-bus, large-scale system.
- Implementation of data-layering techniques and vector field visualizations for the wide-area visualization of oscillation information obtained from the processing of large-scale system PMU data. Condensed and holistic views of system states will provide engineers with a better understanding of system dynamics.

Project Publications:

[1] C. Qian, M. Kezunovic. Dynamic Synchrophasor Estimation with Modified Hybrid Method. *2016 IEEE PES Conference on Innovative Smart Grid Technologies*,September 2016, Minneapolis, MN

[2] C. Qian, M. Kezunovic, "Spectral Interpolation for Frequency Measurement at Off-Nominal Frequencies," *IEEE PES General Meeting, July 2017*, Chicago IL.

[3] C. Qian, M. Kezunovic, "A Novel Time-Frequency Analysis for Power System Waveforms Based on "Pseudo-Wavelets," *IEEE PES T&D Conference and Exposition 2018,* Denver CO.

[4] C. Qian, M. Kezunovic, "A Power Waveform Classification Method for Adaptive Synchrophasor Estimation," *IEEE Transactions on Instrumentation and Measurement,* vol. 67, no. 7, pp. 1646-1658, July 2018.

[5] M. Zhou, Y. Wang, A. K. Srivastava, Y. Wu, P. Banerjee, "Ensemble based Algorithm for Synchrophasor Data. Anomaly Detection", *IEEE. Transactions on Smart Grid,* DOI 10.1109/TSG.2018.2816027,

[6] P. Banerjee, S, Pandey and A. K. Srivastava "Testing and Validation of Synchrophasor Devices and Applications for Power Grid Operation", book chapter in "Power System Grid Operation Using Synchrophasor Technology", Springer, 2018

[1] R. Liu, A. Srivastava, D. Bakken, A. Askerman, and P. Panciatici, "Decentralized State Estimation and Remedial Control Action for Minimum Wind Curtailment Using Distributed Computing Platform," *IEEE Transactions on Industry Applications*, 2017

[2] H. Lee, P. Banerjee, and A. K. Srivastava, "Synchrophasor Applications for Load Estimation and Stability Analysis", *IET Power and Energy Series, Synchronized Phasor Measurements for Smart Grids*, 2017

[3] H. Lee Tushar, P. Banerjee, and A. K. Srivastava, "Synchrophasor Applications for Load Estimation and Stability Analysis", *IET Power and Energy Series, Synchronized Phasor Measurements for Smart Grids*, 2017

[4] A. Srivastava and P. Banerjee, "Wide Area Close Loop Control in Smart Electric Grid", *Power and Energy Automation Conference*, Spokane, WA, March, 2016

[5] A. P.Meliopoulos, "Legacy SE to Distributed Dynamic State Estimators: Evolution and Experience," *Proceedings of the IEEE-PES 2015 General Meeting*, Denver, CO, July 26-30, 2015.

[6] A. P.Meliopoulos, "Dynamic State Estimation-Based Diagnostic Systems: Evolution and Experience," *Proceedings of the IEEE-PES 2015 General Meeting*, Denver, CO, July 26-30, 2015.

[7] H. Albinali and A. P. Meliopoulos, “Centralized Substation Protection Scheme to Detect Hidden Failures”, Accepted, *Proceedings of the IEEE-PES 2016 General Meeting*, Boston, MA, July 17-21, 2016.

[8] H. F. Albinali and A. P. S. Meliopoulos, "Resilient Protection System Through Centralized Substation Protection," in *IEEE Transactions on Power Delivery*, vol. 33, no. 3, pp. 1418-1427, June 2018.

[9] A. P. Meliopoulos, "Legacy SE to Distributed Dynamic State Estimators: Evolution and Experience," *Proceedings of the IEEE-PES 2015 General Meetin*g, Denver, CO, July 26-30, 2015.

[10] A. P. Meliopoulos, "Dynamic State Estimation-Based Diagnostic Systems: Evolution and Experience," *Proceedings of the IEEE-PES 2015 General Meeting*, Denver, CO, July 26-30, 2015.

[11] H. Albinali and A. P. Meliopoulos, “Centralized Substation Protection Scheme to Detect Hidden Failures”, Accepted, *Proceedings of the IEEE-PES 2016 General Meeting*, Boston, MA, July 17-21, 2016.

[12] R. Fan, A. P. S. Meliopoulos, G. J. Cokkinides, L. Sun and Yu Liu, "Dynamic state estimation-based protection of power transformers," *2015 IEEE Power & Energy Society General Meeting*, Denver, CO, 2015, pp. 1-5.

[13] S. Meliopoulos, G. J. Cokkinides, P. Myrda, Y. Liu, R. Fan, L. Sun, R. Huang and Z. Tan, “Dynamic State Estimation Based Protection: Status and Promise”, *IEEE Transactions on Power Delivery*, vol. 32, no. 1, pp 320-330, Feb. 2017.

[14] Y. Liu; A. P. Meliopoulos; R. Fan; L. Sun; Z. Tan, "Dynamic State Estimation Based Protection on Series Compensated Transmission Lines," *IEEE Transactions on Power Delivery* 32.5 (2017): 2199-2209.

[15] Y. Liu, S. Meliopoulos, L. Sun and R. Fan, “Dynamic State Estimation Based Protection on Mutually Coupled Transmission Lines”, *CSEE Journal of Power and Energy Systems*, vol.2, no.4, pp 6- 14, Dec. 2016.

[16] Y. Liu, S. Meliopoulos, Z. Tan, L. Sun and R. Fan, “Dynamic State Estimation Based Fault Locating in Transmission Lines”, *IET Generation, Transmission & Distribution*, in press.

[17] S. Meliopoulos, R. Huang, E. Polymeneas and G. Cokkinides, "Distributed dynamic state estimation: Fundamental building block for the smart grid," *2015 IEEE Power & Energy Society General Meeting*, Denver, CO, 2015, pp. 1-6.

[18] R. Huang, G. Cokkinides, C. Hendrington, and A. P. Meliopoulos, “Distribution System Distributed Quasi-Dynamic State Estimator”, *IEEE Transactions on Smart Grid*, Volume 7, No. 6, pp 2761-2770, November 2016

[19] Xie, A. P. S. Meliopoulos, Y. Liu and L. Sun, "Distributed quasi-dynamic state estimation with both GPS-synchronized and non-synchronized data," *2017 North American Power Symposium (NAPS)*, Morgantown, WV, 2017, pp. 1-6.

[20] L. Sun, A. P. S. Meliopoulos, Y. Liu and B. Xie, "Dynamic state estimation based synchronous generator model calibration using PMU data," *2017 IEEE Power & Energy Society General Meeting*, Chicago, IL, 2017, pp. 1-5.

[21] Xie, A. P. S. Meliopoulos, C. Zhong, Y. Liu, L. Sun, and J. Xie "Distributed Quasi-Dynamic State Estimation Incorporating Distributed Energy Resources," *2018 North American Power Symposium (NAPS)*, Fargo, ND, 2018, pp. 1-6.

[22] Idehen, T. Xu, and T. J. Overbye, "Subsequence dynamic time warping in the detection of PMU time errors," *IEEE Transactions on Smart Grid*, in preparation.

[23] Idehen, B. Wang, K. Shetye and T.J. Overbye, “Visualization of large-scale electric grid oscillation modes,” *2018 North American Power Symposium (NAPS)*, accepted.
[24] Idehen and T. J. Overbye, "A similarity-based PMU error detection technique," in *2017 19th International Conference on Intelligent System Application to Power Systems (ISAP)*, 2017, pp. 1-6.
[25] Idehen, Z. Mao, and T. J. Overbye, "An emulation environment for prototyping PMU data errors," in *2016 North American Power Symposium (NAPS*), 2016, pp. 1-6.

Student Theses:

[1] Cheng Qian. *Phasor Parameter Modeling and Time-Synchronized Calculation for Representation of Power System Dynamics*, PhD Dissertation, Texas A&M University.
[2] Christoph Seidl. *A comparison of end-to-end testing techniques for Synchrophasor Systems*, Master’s Thesis. Texas A&M University.
[3] Ren Liu. *Cyber Physical Security Analysis for Synchrophasor Applications*, PhD Dissertation, Washington State University, December 2017.
[4] Hyojong Lee. *Development, Modeling, and Applications of PMUs*, PhD Dissertation, Washington State University, December 2017.
[5] Ikponmwosa Idehen. *Data Analytics and Wide-Area-Visualization Associated with Power Systems Using Phasor Measurement*. PhD Dissertation, Texas A&M University, July 2019 (expected).

Part I

Development of Field Devices and Test Protocols for Device and System Commissioning, Acceptance, and In-Service Tests

Mladen Kezunovic
Pratyasa Bhui
Jinfeng Ren
Cheng Qian, Graduate Student
Christoph Seidl, Graduate Student

Texas A&M University

For information about this project, contact

Mladen Kezunovic
Texas A&M University
Department of Electrical and Computer Engineering
Wisenbaker Engineering Building 323C
College Station, TX 77843
Phone: 979-845-7509
Email: kezunov@ece.tamu.edu

Power Systems Engineering Research Center

The Power Systems Engineering Research Center (PSERC) is a multi-university Center conducting research on challenges facing the electric power industry and educating the next generation of power engineers. More information about PSERC can be found at the Center's website: http://www.pserc.org.

For additional information, contact:

Power Systems Engineering Research Center
Arizona State University
527 Engineering Research Center
Tempe, Arizona 85287-5706
Phone: 480-965-1643
Fax: 480-727-2052

Notice Concerning Copyright Material

Table of Contents

List of Figures

List of Tables

Nomenclature

FPGA	Field programmable gate array
GPS	Global positioning system
IED	Intelligent electronic device
IPC	Idaho power company
PDC	Phasor data concentrator
PMU	Phasor measurement unit
ROCOF	Rate of change of frequency
SCADA	Supervisory control and data acquisition
TSS	Test suite specifications
TVE	Total vector error
WAMPAC	Wide-area measurement, protection, and control
WAMS	Wide-area measurement system

1. Introduction

1.1 Background

Synchronized phasor measurement systems are becoming increasingly important in the modern power grid. Synchrophasor-based wide-area monitoring, protection, and control (WAMPAC) strategies have proven to be beneficial to the early detection and timely mitigation of emergencies in the power system. Despite the vital role of synchrophasor systems in the modern power grid, no standard tools for certification, commissioning, in-service maintenance, and risk assessment are available for synchrophasor infrastructure, which is composed of phasor measurement units (PMUs), intelligent electronic devices (IEDs), phasor data concentrators (PDCs), and end-use applications.

The mission-critical synchrophasor components are introduced to improve monitoring and control performances and are expected to operator correctly each time they are triggered. Because their design complexities, the components may have hidden design defects and imperfections that may cause trouble at any unpredictable time. As a result, it is crucial to closely monitor the performances of synchrophasor devices throughout their entire life-cycle. Especially, when the synchrophasor components are initially commissioned, when the components have been in-service for a long time, and when a potential abnormal operation is detected. In those cases, rigorous test procedures, reliable test tools to test different aspects of hardware and software design, from the individual synchrophasor component level, to overall end-to-end system level are the only solution to assure more reliable and robust operation of the mission-critical system. In order to test various levels of synchrophasor tools, a reference infrastructure is needed, which provides the reference operating conditions that the devices under test are tested against.

In Part I of the project, PMU calibration and certification lab, reference PMU, field calibrator test set, the integration tool for testing end-to-end synchrophasor system, as well as the test procedure for synchrophasor component testing are designed and implemented. The developed solutions can be used to perform lab acceptance, as well as field commissioning and in-service tests on the components of the synchrophasor systems, and the end-to-end system.

1.2 Summary of Chapters

This report is structured as follows. In chapter 2, the PMU calibration and certification lab is introduced. The lab is used to perform PMU performance testing according to standardized procedures.

Chapter 3 presents Gold PMU. Gold PMU is a device which is designed to provide accurate reference synchrophasor streams. Gold PMU hardware platform and accurate Gold PMU algorithm are implemented.

Chapter 4 discusses the development of a calibrator designed to perform PMU and end-to-end synchrophasor system calibration in the field.

Chapter 5 evaluates the integration of Gold PMU and field calibrator, where nested testing on synchrophasor system, including PMU, PDC, and end-use application can be performed and evaluated.

2. PMU Calibration and Certification Lab

2.1 Introduction

The Phasor Measurement Unit (PMU), introduced in the 80s, is an instrument capable of measuring amplitude and phase angle of voltage and current phasors, as well as the frequency and rate of change of frequency. Phasor angle is defined as a relative displacement at a given location compared to the reference cosine signal at another location, both synchronized to the Coordinated Universal Time. The synchronization is usually accomplished using the time reference signal from Global Positioning System of satellites. Fast calculation and reporting of the PMU data helps capture and track high-resolution real-time information for new advanced applications and improves situational awareness of the grid states.

PMU measurements can be employed in a large number of power system applications often implemented as Wide Area Monitoring, Protection and Control (WAMPAC) systems. PMU measurements are also applied in the model validation processes and are widely utilized in the system protection applications such as fault detection and location, out-of-step protection, oscillation detection, etc. To ensure the reliability and security of the infrastructure for synchrophasor-based end-use applications, good synchronization (better than 1 us), fast reliable communication network, and precise phase angle and magnitude measurements are needed.

Performance requirements of a PMU are specified in IEEE standards C37.118.1-2011 and C37.118.1a-2014 [1] [2]. Two classes of PMUs, namely the P and M performance class, are defined in the standards. The protection (P) class is focused more on the fast response rather than high precision. The opposite is required by the measurement (M) class PMUs. Each synchrophasor-capable Intelligent Electronic Device (IED) has to conform to at least one performance class. IEEE standard C37.118.1 specifies the type of the tests (i.e. steady state and dynamic state) and the maximum allowed measurements error, e.g., Total Vector Error (TVE), Frequency Error (FE) and Rate of Change of Frequency Error (ROCOF), which is defined for each reporting rate and performance class. The procedures and requirements for test equipment, e.g., timing reference, signal sources, calibration devices, and environmental conditions are specified in the IEEE Synchrophasor Measurement Test Suite Specification (TSS) report [3].

2.2 Design Specification

2.2.1 Calibration System Functional Requirements

According to IEEE TSS, a PMU Calibration System should have the following functions:

2.2.2 Signal generation/HIL system: generating test signals

- Timing reference: providing UTC-traceable timing signals (GPS, PSS, IRIG-B, etc.) to the calibration system.
- Receiver: to receive the synchrophasor measurement data from PMUs under test.

- Synchrophasor reference source: provide high precision reference synchrophasor to the system.
- Accuracy analysis: by comparing reference synchrophasor with PMU measurements, the calibration system performs calculations for total vector error (TVE), phasor magnitude error, phase angle error, frequency error, rate of change of frequency error, and additional calculations for dynamic step test results.
- The calibration system is able to determine the time of arrival of PMU data messages and comparing that time against the message timestamp. (Reporting latency test)
- The calibration system is able to document test result.

2.2.3 Calibration System Hardware Specifications

The specification includes:

- Hardware Specification for Timing Reference
- PMU under test may require various components to create the timing signals:
- GPS antenna
- IRIG-B (sometimes with 1 pps) (DC level or AM)
- Possibly with the addition of IEEE Std. 1344 extension
- Possibly with the IEEE Std. C37.118.1-2011 extension to the IEEE Std. 1344 extension.
- IEEE Std. 1588

For the purpose of the project three GPS antennas were located on the roof of the TAMU building where the PMU calibration lab is located. The PMU under test can be connected directly to either a GPS antenna or timing signal, that can be generated using available receivers (SEL-2407, Tekron TCG02-G, NI PXI 6683H module). A NI PXI 6683H is used as a synchronization PXI module to provide a synchronization signal for the signal generator as well as a timing reference for the acquisition module. The NI PXI-6683H has a GPS receiver which powers an active GPS antenna and receives and processes the RF signals (1.575 GHz) from the satellites. The GPS receiver then generates a very precise pulse-per-second (PPS) that the NI PXI-6683H uses to achieve sub-microsecond synchronization. This module is also capable of generating IRIG-B timing signal for the tested device.

In addition, two more devices are available for the purpose of generating timing reference:

- SEL-2407, Satellite-Synchronized Clock, provides time display, reliability, durability and high-accuracy timing to ± 100 nanoseconds.
- The TCG 02-G is a highly accurate fully featured GPS and GLONASS (GNSS) clock, offering multiple oscillator options, Time Code and Frequency outputs.

All three devices comply with the requirements defined in the IEEE standards.

1. Hardware Specification for Signal Source

The requirement of the signal source for a PMU Calibration System is:

- PMU calibrator shall provide three-phase voltage and current input signals to PMUs under test. The signals shall comply with both steady-state and dynamic test requirements.
- Total harmonic distortion plus noise of the input signal shall be less than 0.2% of the fundamental
- PMU calibrator shall be capable of supplying at least 120% of the selected nominal voltage (typically 84 V rms for V_{nom} = 70 V rms) and 200% of the selected nominal current per phase (10 A rms).
- Signal sources shall be capable of providing signal frequencies ranging from 45 Hz to 65 Hz.
- Bandwidth of the signal source should be at least 3 kHz. (down-limit is DC)

The available signal generator module in the PMU Calibration Lab at TAMU comprises of the NI PXI 7854R module as well as the power amplifiers.

The NI PXI 7845R module consists of:

- 8 analog inputs, independent sampling rates up to 750 kHz, 16-bit resolution, ±10 V
- 8 analog outputs, independent update rates up to 1 MHz, 16-bit resolution, ±10 V
- 96 digital lines configurable as inputs, outputs, counters, or custom logic at rates up to 40 MHz
- Virtex-5 LX110 FPGA programmable with the LabVIEW FPGA Module
- 3 DMA channels for high-speed data streaming

For generating voltage signals in range ±10 V, 6 analog outputs of NI PXI 7845R are used.
In order to amplify the generated signals from NI PXI 7854R, voltage and current amplifiers from AE Techron model TEC3600 and 7224 are selected and calibrated. Their performance meets the aforementioned standard requirements.

2. Hardware Specification for Receiver

PMUs may transmit their measurements over a variety of physical media (Ethernet via twisted pair copper using RG45 connector, or optimal Ethernet using ST or LC connectors, RS-232) using a variety of protocols (IEEE Std. C37.118-2005, IEEE Std. C37.118.2).

The NI PXI 6683H is equipped with the Gigabit 10/100/1000 Ethernet port used as the receiver interface for the stream of the device under test. In case that the Serial communication is required, NI PXIe-8105 embedded Controller can be used for interfacing the device under test. Our calibration lab is not equipped with ST or LC connectors.

3. Analyzer Tool

True (reference) values of the phasors are calculated in the course of time while being generated, and the tool for calculating the required errors (TVE, PE, ME, FE, RFE) is developed using NI LabVIEW software package and it is running on the NI PXIe-8105 embedded controller. All modules described above are parts of the NI PXIe1062Q chassis.

2.3 Implementation Features

2.3.1 Calibration System Overview

A PMU test and calibration platform used to verify the conformance of the evaluated PMUs under various static and dynamic tests according to the IEEE standards is shown in Figure 1. As shown in Figure 1. the PMU test system consists of a timing reference (GPS receiver), signal generator, power amplifier, and data management and results analytics tools. The timing reference provides GPS clock and time-code information to the calibration equipment and to the device under test so that the entire system is synchronized and time-stamped. Test signals are generated by the signal generator according to test types determined by the IEEE TSS [3]. The calculated and theoretical reference synchrophasor can be, hence, used for the comparison, and then followed by a result analysis and documentation.

The PMU test and calibration platform is implemented using National Instruments (NI) hardware as shown in Figure 1. The entire system consists of the PXI virtual instrument system with embedded Controller NI PXIe-8105,a user-programmable FPGA which is a part of NI PXI-7854R multifunctional reconfigurable I/O module to generate the required waveforms, and power amplifiers to generate 3-phase voltage and current signals feeding the PMU device under the test. As a part of the system, software based Phasor Data Concentrator (PDC) module that receives and parses the data is running on the PXI system. Measurements from the tested PMU are acquired through fast speed Ethernet communication ports, analyzed, and the reported using the NI LabVIEW software interface. Reports consist of all data reported by tested PMU as well as true values of phasors sent to the device, which allows extensive post-analysis of the collected results.

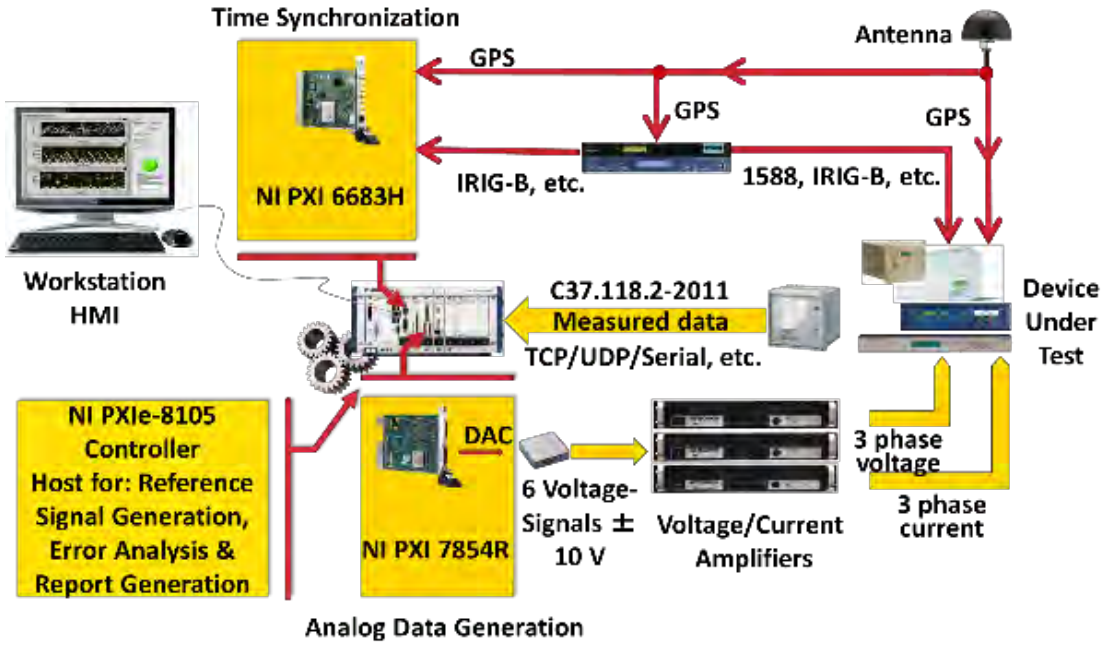

Figure 1. PMU Calibration System Platform

2.3.2 PMU Type Test and Application Test

- Type Test

PMUs provide different types of calculated values such as voltage and current magnitude, angle, frequency, rate of change of frequency, etc. According to the IEEE standard C37 118.1, each device that is capable of providing GPS synchronized measurements has to undergo various steady state and dynamic test scenarios while being calibrated. During the steady state tests, PMUs are exposed to various type-test scenarios where all variables are kept unchanged during each test and the measurements are captured according to the standard procedure. Such static type-tests include performance evaluation of PMUs over a range of frequency values, voltage/current amplitudes as well as influence of harmonic and inter-harmonic interferences. Dynamic type-tests involve testing PMUs with the modulated signals, checking their performance during the step occurrence in amplitude and angle, as well as testing the PMU response to the frequency ramp events. As a part of the standard requirements, latency of a PMU device has to be measured too (see Table 1). Table 2 shows a graphical representation of how the calibration lab at Texas A&M University for PMU calibration and testing is implemented.

Figure 2. Calibration Lab Implementation

Table 1. PMU Steady State Type-Test

Steady state tests					
Test subtype	Step	P (Protection) class		M (Measurement) class	
		Range	Error Requirements	Range	Error Requirements
Signal Frequency Range (test applied nominal + deviation $f_0 \pm f_{dev}$) Three temperatures (0,23,50)	0.1 Hz	$f_0 \pm 2$ Hz	1% TVE 0.005 Hz FE 0.44 Hz/s RFE	$f_0 \pm$ 2.0 Hz for Fs<10 ± Fs/5 for 10 ≤ Fs < 25 ± 5.0 Hz for Fs ≥25	1% TVE 0.005 Hz FE 0.1 Hz/s RFE
Signal Magnitude—Voltage	10% of nominal value	80 to 120 % of nominal	1% TVE	10 to 120 % of nominal	1% TVE
Signal Magnitude—Current	10% of nominal value	10 to 200 % of nominal	1% TVE	10 to 200 % of nominal	1% TVE
Phase Angle	No need for testing*	± π radians (+/- 180°)	1% TVE	± π radians (+/- 180°)	1% TVE
** The requirements of the phase angle test are satisfied by the signal frequency range test when the input frequency is nominal frequency ± 0.2 Hz and the test duration is 5 seconds. Therefore, no separate phase test need be performed.*					
Harmonic distortion (single harmonic)	50 measurements (each time just one harmonic)	1%, each harmonic up to 50th	1% TVE 0.005 Hz FE 0.44 Hz/s RFE	10%, each harmonic up to 50th	1% TVE (Fs ≤ 20) 0.005 Hz FE (Fs > 20) 0.025 Hz FE Limit suspended RFE
the harmonic sequence shall NOT be positive sequence for all harmonics but shall be in-phase with the fundamental frequency for all three phases					
Out-of-Band Interference	Form min In-Band to 10 Hz decrease fi exponentially (+0.1 Hz, +0.2 Hz, +0.4 Hz, +0.8 Hz…) From max In-Band to 120 Hz increase fi exponentially (+0.1 Hz, +0.2 Hz, +0.4 Hz, +0.8 Hz…)	/	/	10% of input signal magnitude, 10 Hz to 120 Hz	1.3% TVE 0.01 Hz FE Limit suspended RFE
Out-of-band compliance is to be checked with the frequency of the fundamental power signal at the nominal system frequency and also at nominal frequency ± 10% of the Nyquist frequency of the reporting rate (Fs) (test shall be repeated three times)					

Table 2. PMU Dynamic State Type-Test

Dynamic state tests									
Test subtype		P (Protection) class				M (Measurement) class			
		Range		Error Requirements		Range		Error Requirements	
$f_m = \omega/2\pi$ is the modulation frequency in Hz, k_x is the amplitude modulation factor, and k_a is the phase angle modulation factor The modulation frequency shall be varied in steps of 0.2 Hz or smaller over the range specified in the table									
Measurement Bandwidth—phase modulation $k_x = 0$ $k_a = 0.1$ radian	0.2 Hz	Fs	Modulation frequency (Fr)	3% TVE Max FE Hz	3% TVE Max RFE Hz/s	Fs	Modulation frequency (Fr)	3% TVE Max FE Hz	3% TVE Max RFE Hz/s
		10	1	0.03	0.6	10	2	0.12	2.3
		12	1.2	0.04	0.8	12	2.4	0.14	3.3
		15	1.5	0.05	1.3	15	3	0.18	5.1
		20	2	0.06	2.3	20	4	0.24	9
Measurement Bandwidth—amplitude modulation $k_x = 0.1$ $k_a = 0$ radian	0.2 Hz	25	2	0.06	2.3	25	5	0.3	14
		30	2	0.06	2.3	30	5	0.3	14
		50	2	0.06	2.3	50	5	0.3	14
		60	2	0.06	2.3	60	5	0.3	14
			min(Fs/10,2)	0.03 × Fr	$0.18 \times \pi \times Fr^2$		min(Fs/5,5)	0.06 × Fr	$0.18 \times \pi \times Fr^2$
Ramp of System Frequency Ramp rate = ± 1.0 Hz/s	More details in	± 2 Hz Exclusion interval = 2/Fs		1% TVE 0.01 Hz FE 0.4 Hz/s RFE		Lesser of ± (Fs /5) or ± 5 Hz Exclusion interval = 7/Fs		1% TVE 0.01 Hz FE 0.2 Hz/s RFE	
Step Change in Phase $k_x = 0$, $k_a = \pm \pi/18$		± 10° from nominal		Response time (s) Response delay (s) Overshoot (%) Frequency response time (s) ROCOF response time (s) See **Error! Reference source not found.**		± 10° from nominal		Response time (s) Response delay (s) Overshoot (%) Frequency response time (s) ROCOF response time (s) See **Error! Reference source not found.**	
Step Change in Magnitude $k_x = \pm 0.1$, $k_a = 0$		± 10% of nominal				± 10% of nominal			
PMU Reporting Latency		2 / Frequency of data reporting		0.002 second		7 / Frequency of data reporting		0.002 second	

- Application Test

Various applications for power system protection have different sensitivities to the data errors in the input measurements. Various PMU algorithms for synchrophasor estimations may have different responses to the input signals experienced during different protection application disturbances. The impacts of such input signal uncertainties and related application errors are largely unknown to the end-users and need to be fully investigated.

Even though the IEEE standards define the basic type-tests that PMUs have to undergo with certain precision, the test procedure does not reveal the impact of such results on the system-wide applications. In addition, the error impacts of the signal components present at the time of a specific protection event are not known. The performance is further affected by different requirements in terms of calculation speed, accuracy of estimated frequency, angle and magnitude measurements, etc., which are different for different protection applications. Hence, making meaningful trade-offs between such performance indicators to reduce the error impact is imperative. Since such decisions are made at the time of the PMU design, the user is primarily interested in evaluating the performance under various application scenarios. In order to build a trustworthy mindset for the protection end-users, the first step is to recognize the critical parameters of interest for a given application and then evaluate how the estimation algorithm matches the application requirements using the results acquired from the calibration tests. Such analyses could build the confidence about the quality of the synchrophasor application outputs. Figure 3 and Figure 4. demonstrate the end-to-end synchrophasor system and how it looks in real world scenarios as well as its implementation in Texas A&M University in the form of a synchrophasor-based test-bed.

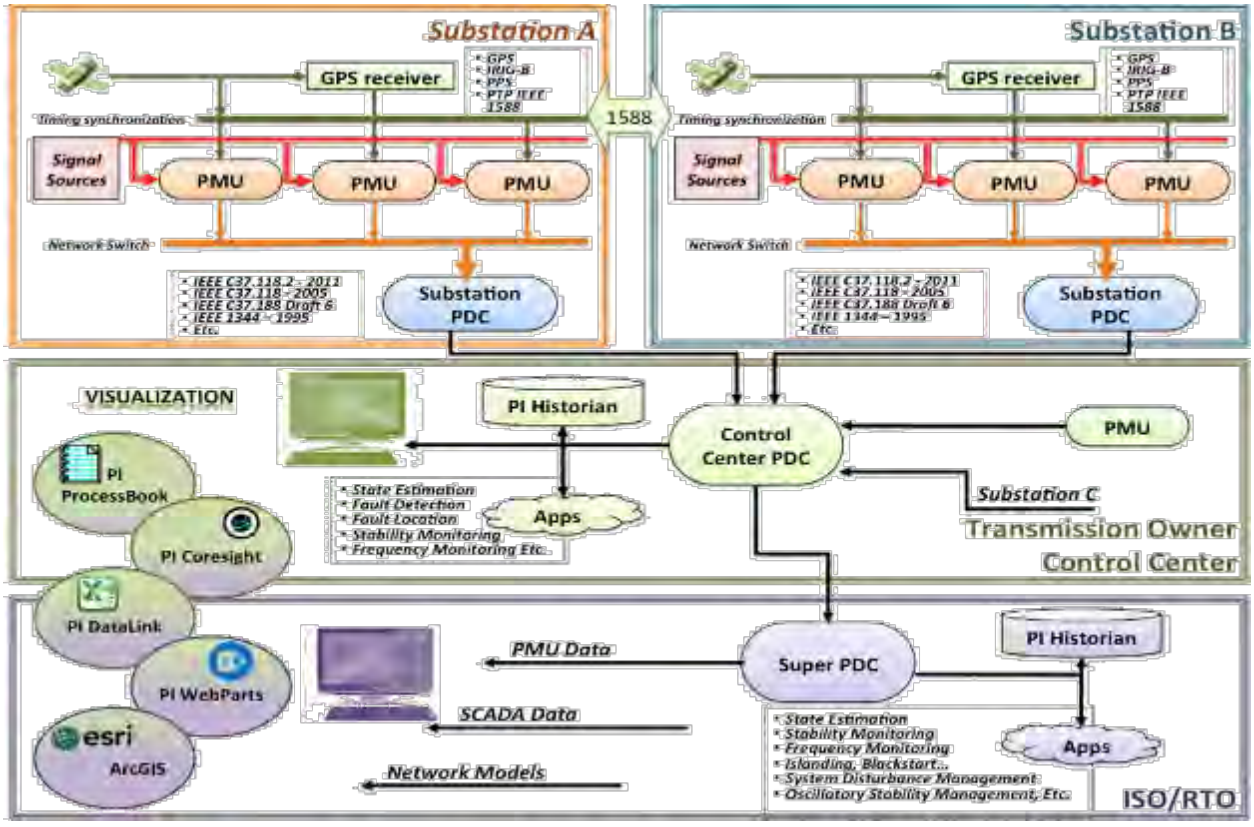

Figure 3. Synchrophasor applications in real world

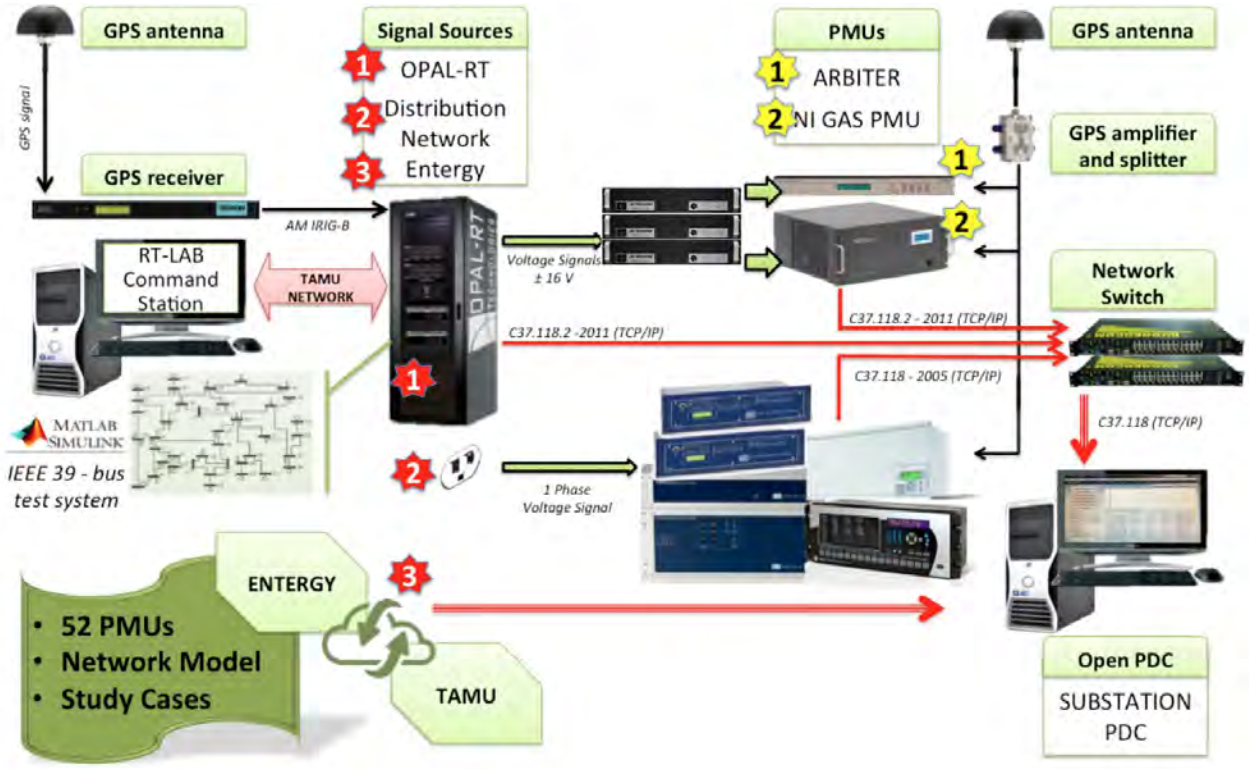

Figure 4. Synchrophasor-based test-bed setup

The test-bed platform used for characterizing the PMU response under fault (or other prevailing) conditions and evaluating the impact of the PMU errors on the end-use application outcome is implemented at Texas A&M University. The developed infrastructure is generic enough to be employed not only for quantifying the impact of PMU errors on fault scenarios, but also performing studies on trustworthy assessment of any end-use power system application that uses PMU measurements. General structure of the test setup is depicted in Figure 4. As shown in Figure 4. the synchrophasor system consists of timing references, signal generator, power amplifiers, and data management and analytic tools. Timing reference provides GPS clock reference to the PMUs so that measurements from different devices are synchronized and time-stamped. Model of the network under evaluation is built in the ATP-EMTP software package environment or from the digital simulators (OPAL-RT). Various fault (or other prevailing) scenario use cases can be simulated, and waveforms are generated using low voltage simulators. In order to have realistic measurements from the PMU, the applied signals must conform to the nominal level defined by the PMU device (i.e., normally 70 V rms and 5 A rms for voltage and current, respectively). Signals from the simulators are amplified to the nominal level using power amplifiers. Each PMU is connected to the GPS antenna for the synchronization purposes and measured data streams from the devices are collected and fed to a desired application algorithm for further evaluation purposes.

2.4 Use in Testing

2.4.1 Acceptance Testing and Certification of PMUs Using Laboratory Environment

A use case is identified when testing PMU devices and IEDs with synchrophasor capabilities in the Calibration Laboratory to check their compliance with latest IEEE Std. C37.118.1a-2014 and issuing of ICAP certificate if complied with the IEEE Standards.

1. The main scenario and implementation procedure is given below:
2. PMU testing is requested by the PMU manufacturer or owner (user).
3. Connect inputs of the PMU to the signal generator
4. Establish communication between tested device and calibration collector device through Ethernet interface.
5. Acquire the target IP address and PDC port (target port) from the PMU under test in case that UDP protocol is tested or acquire the PMU port number (host port) where the stream is sent.
6. Set the communication parameters on the local port of the calibrator system to match those of the PMU under test (the same net mask; and IP in the allowed range but different from the PMU's).
7. Ping the PMU under test in order to verify the communication connectivity.
8. Connect timing source to the PMU device (GPS antenna connection or IRIG-B signal generated by calibration equipment).
9. Wait until the tested PMU is synchronized to UTC and "Locked".
10. Set the communication protocol parameters, such as PDC port number and PMU IP address in the calibration PDC software.
11. Verify whether the communication is established between PMU and the calibration system using the PDC software.
12. Run the PDC software and obtain the phasors reporting order, and corresponding channel indices.
13. Set input parameters for the calibration software (PMU settings: nominal voltage, performance class, reporting rate, standard version; communication settings: PDC port, IP address of the PMU under test, communication protocol (UDP/TCP); phasor channel indices).
14. Run the calibration software.
15. When the tests are done, navigate to report folder and print the results.

The variations in this use case include:

2a. PMU device can be replaced with any synchrophasor-capable device that supports C37.118-2005 or C37.118.2-2011 communication protocols such as DFR, DPR, etc.;

3a. Establish communication between tested device and calibration collector device through RS-232 serial interface. (If the device under test does not have an Ethernet interface);

4a. Acquire information from PMU such as baud rate, data bits, parity, stop bits, and flow control;

5a. Update communication port (COM1 parameters) in the calibration system to match those of the PMU under test.

3. Gold PMU

3.1 Introduction

Gold PMU is defined as an absolutely accurate PMU. The functionality of Gold PMU can be described as a "Reference PMU". This PMU will be utilized to compare performance of the field PMU for the same inputs provided to the PMU under evaluation and the Gold PMU. A logical diagram of Gold PMU is shown in Figure 5 below.

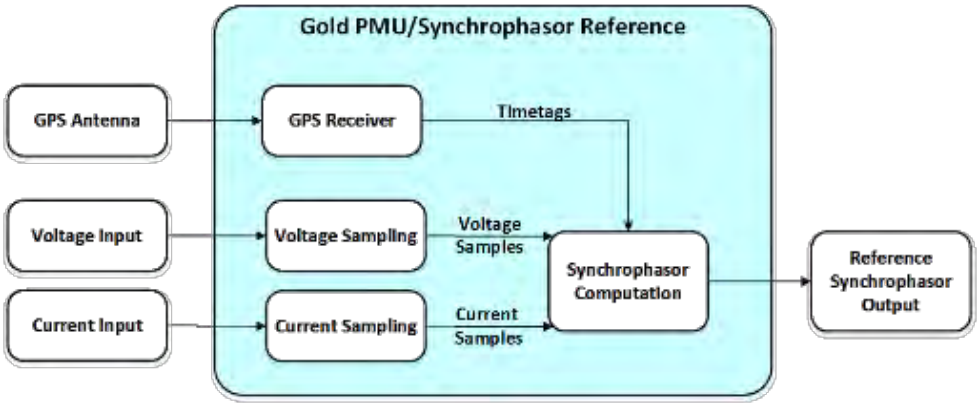

Figure 5. Functionality specification diagram of Gold PMU

The internal functionality specification of Gold PMU, marked in shaded blue block, is similar to a commercial PMU device. When used to test a commercial PMU, Gold PMU and PMU under evaluation will be connected in parallel, and both connected to the same signal generation source and GPS source, and the synchrophasor estimation results will be compared at embedded controller. This schematic is shown in Figure 6 below.

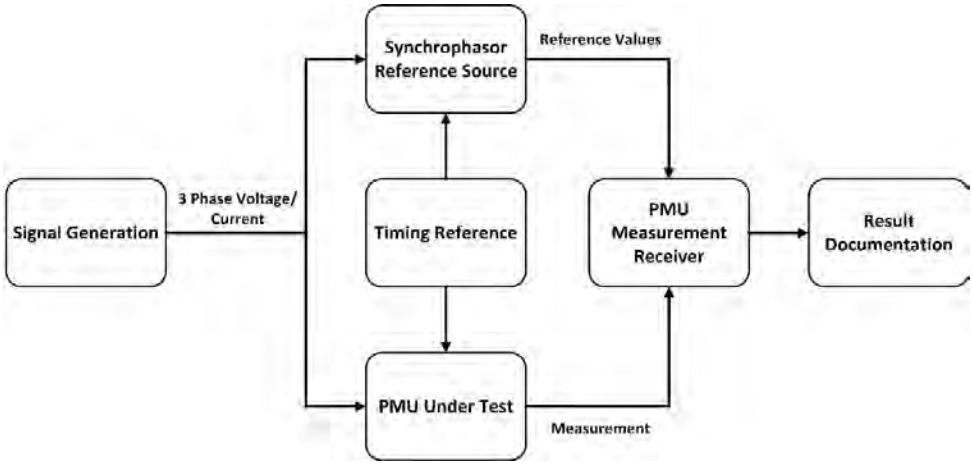

Figure 6. Use of Gold PMU as synchrophasor reference source in commercial PMU evaluation

3.2 Design Specification

3.2.1 Functionality Requirement Specification

As previously discussed, Gold PMU is designed as a more accurate PMU device, and thus should be equipped with the same hardware components that enable the same functionality of a commercial PMU device. The structure of Gold PMU functionality is shown in Figure 5, and a detailed description is listed in Table 3.

Table 3. Gold PMU Functionality Description

Functionality	**Requirement Specification**
Operating system, user interface, computation	CPU, hard drive, memory: in order to perform phasor estimation Control programs and user interface: enabling time-synchronized waveform sampling and user control
Phasor parameter calculation	Measurement algorithms for phasor parameters: the accuracy should be higher than IEEE standards.
Synchrophasor data transfer	Communication ports: streaming of calculated phasor.
Synchronized voltage waveform sampling	Voltage data acquisition module and synchronization of voltage samples
Synchronized current waveform sampling	Current data acquisition module and synchronization of current samples
Attenuators	When applicable, attenuate voltage and current inputs to acceptable level to data acquisition modules
Timing input	GPS antenna to receive timing signal from GPS satellites. Module/Program that decodes raw timing input signal (GPS, IRIG-B, etc.) Necessary peripheral cables to distribute timing information to voltage and current sampling modules.

3.2.2 Definition of Gold PMU Algorithm

At the core of the embedded controller lie Gold PMU algorithms, which ultimately enable the high synchrophasor estimation accuracy of Gold PMU.

A thorough literature survey has been performed to review available commonly used synchrophasor estimation algorithms. Synchrophasor estimation algorithms calculate phasor parameters from a vector of time-stamped samples. Benefited from interdisciplinary efforts such as signal processing technology, control theory, estimation theory, literature regarding synchrophasor estimation algorithms have proliferated since its inception three decades ago. A detailed literature survey document can be found on project website. And the basic scheme of Gold PMU algorithm to achieve high accuracy is shown in Figure 7.

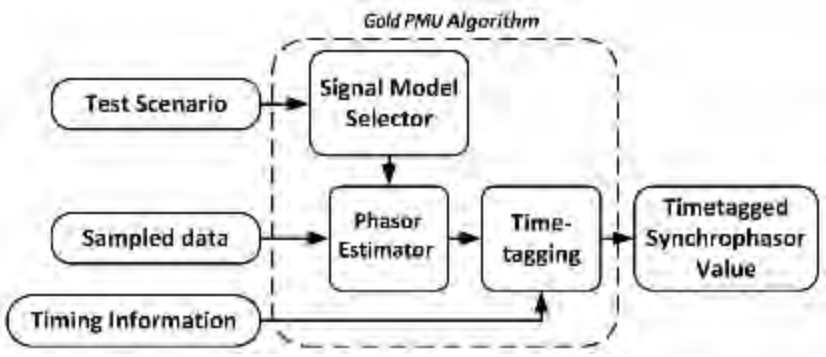

Figure 7. Gold PMU algorithm structure

From literature survey, it is concluded that none of the prior contributions in synchrophasor algorithms is able to be accurate for all types of input waveforms. Therefore, in this project, it is proposed that a "signal type classifier" be designed so that the "Test Scenario" can be identified. Then, in "Signal Model Selector", the fittest algorithm form will be selected to perform phasor paramter estimation. The fittest algorithm may be from current literature, or maybe a newly designed algorithm.

3.3 Implementation Features

3.3.1 Implementation of Hardware Functionality

The Gold PMU is implemented in National Instruments platform, which is composed of a chassis (embedded controller), and separate modules that can be inserted into the chassis slots.

The overall implementation strategy is shown from Table 4 to

Table 6.

Table 4. Voltage/Current Data Acquisition Modules for Gold PMU

Requirement	**Design**	**Hardware Specification**		
		Analog Input Level	**Sampling Rate**	**Resolution**
Voltage Input	NI 9225	300Vrms line to neutral	Max 50kHz/Ch,-3 channel	24-bit
Current Input	NI 9227	5Arms	Max 50kHz/Ch, 4-channel	24-bit

Table 5. Proposed Timing I/O Module of Gold PMU

Requirement	**Implementation**	**Hardware Specification**	
		Accuracy	**Voltage Level**
Timing I/O	NI 9467	±100ns	5VDC

Table 6. Proposed Embedded Controller Module of Gold PMU

Requirement	Implementation	Hardware Specification
Embedded Controller (CPU, hard drive, memory)	NI cRIO-9039[11]	1.91 GHz Quad-core CPU, 2GB DRAM, 16GB hard drive
Communication I/O	NI cRIO-9039	2 Ethernet, 2 serial ports

3.3.2 Implementation of Software Functionality

Gold PMU software, including user's interface, Gold PMU algorithms, data acquisition, timing acquisition, communication. All Gold PMU software is coded in NI LabVIEW for convenient implementation on NI hardware platform. The Gold PMU software hierarchy is shown in Figure 8.

The code that requires stable and efficient execution are programmed on the FPGA chip of NI 9039. Programs for data manipulation, signal processing, communication, and users' interface are coded in the Host Computer of NI 9039. The key is simultaneous acquisition of voltage waveform samples, current waveform samples, and absolute UTC time. The flowchart to achieve synchronized sampling is shown in Figure 9.

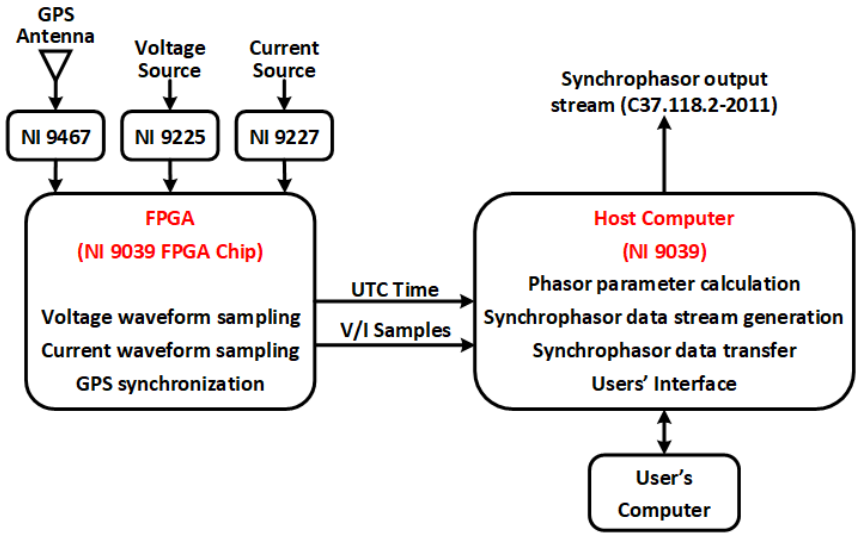

Figure 8. Overall hierarchy of Gold PMU software

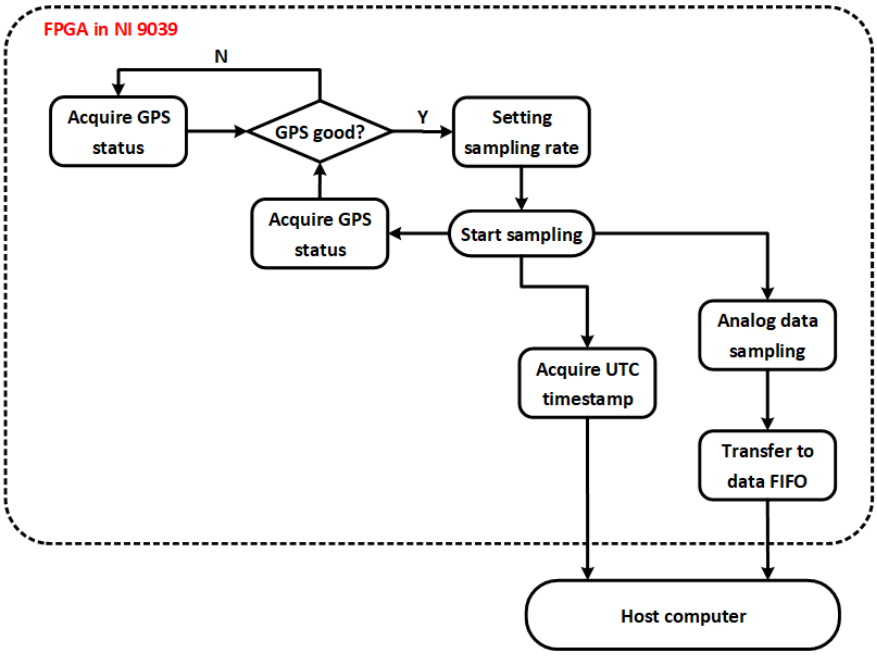

Figure 9. Hierarchy of FPGA implementation of synchronized voltage and current waveform sampling

3.3.3 Implementation of Gold PMU Algorithm

The approach for accurate synchrophasor estimation is discussed in Section 3.2.2. The input waveform type is first identified according to paper [4], which categorized input waveforms into steady-state, dynamic amplitude and frequency oscillations, and dynamic frequency ramping test scenarios.

For steady-state signals, frequency-domain algorithms, which are generally based on discrete Fourier transform (DFT) will be used. The fundamental frequency of a signal is first estimated [5], in an effort to reduce spectrum leakage, which is commonly observed in DFT-based methods when subjected to off-nominal frequency input. A typical DFT-based method, known as interpolated DFT (IpDFT) [6], is used to estimate synchrophasors from steady-state signals.

For dynamic waveforms with oscillatory phasor parameters, algorithm [7] is used. This algorithm is adopted to estimate the slow changing movement of magnitude and frequency, while effectively eliminating the impact of harmonic infiltration. For dynamic waveforms with non-oscillartory behaivors, noticeably frequency ramping up or down, algorithm [8] is used.

3.4 Use in Testing

Gold PMU is essentially used to provide synchrophasor reference. The input of Gold PMU, i.e. the test waveforms designed to evaluate commercial PMU performance, can be either be from standardized waveforms, or be generated by electromagnetic/electromechanical dynamic simulation software. In this project, the Gold PMU is intended to be used with Field End-to-End Calibrator to perform end-to-end application testing, shown in Figure 10. The accuracy of

commercial PMU is evaluated by comparing the synchrophasor estimation results from both the commercial PMU and Gold PMU; the performance of a given synchrophasor application is assessed by comparing the application results using the synchrophasor streams from both commercial PMU and Gold PMU. The details of "nested testing" strategy will be introduced in Section 4 along with Field End-to-End Calibrator.

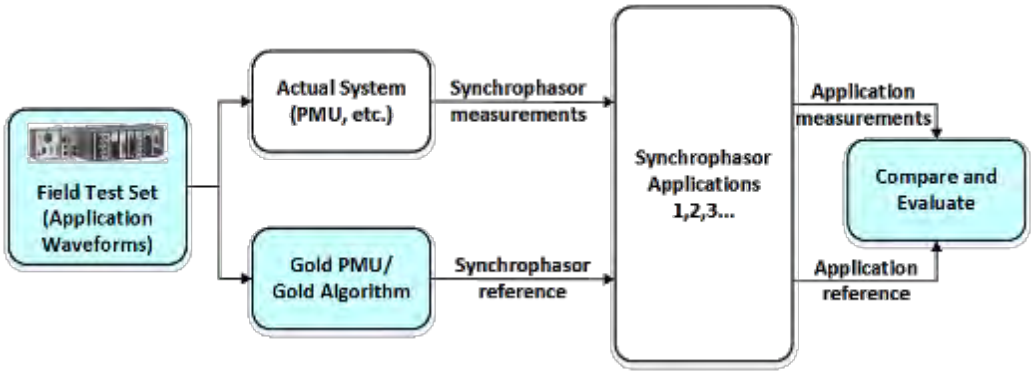

Figure 10. Gold PMU used in end-to-end application test

Gold PMU may be installed in a substation to perform troubleshooting test, as shown in Figure 11. In this approach, Gold PMU is permanently installed in a substation. When detection schemes trigger a troubleshooting command, a test switch will connect the Gold PMU, which will perform a reference synchrophasor estimation. In the meantime, phasor data streams from both PMU in field and Gold PMU will be collected by a field calibrator test set, where the performance of field PMU will be evaluated.

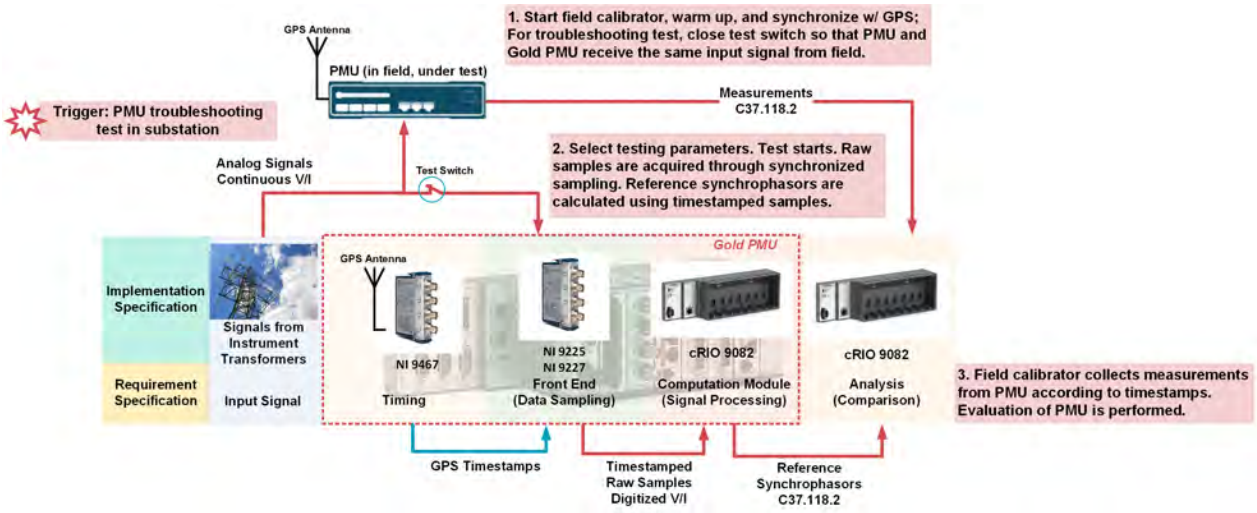

Figure 11. Using Gold PMU to perform troubleshooting test in a substation

4. Field Calibrator

4.1 Introduction

The entire synchrophasor system consists of multiple layers (see Figure 3): PMU devices, communication subsystem, applications and visualization. To evaluate synchrophasor systems as a complete solution it is necessary to confirm that all pieces work properly once they are connected. Even if all components pass the laboratory tests, there is no guaranty that everything will work properly after installation in the system. During the validation of PMU in a laboratory environment it is practically impossible to simulate conditions of a real network. Errors caused by instrumentation channel, cabling, GPS equipment, and cyber security solutions have to be studied and taken into account.

Field calibration consists of two sets of tests: field acceptance tests (commissioning tests) and periodic maintenance tests. PMU field commissioning tests include PMU calibration and basic system functionality check. It also verifies the correct phase sequence, GPS signal strength and correct interfacing, data sending/receiving sequences, and the communication link between PMUs and PDCs. As a part of the portable calibration system, a calibrated and accurate Gold PMU algorithm is used to provide a reference for testing. The output results from the reference PMU and PMU under test are compared so that corrective measures can be taken.

The Field Calibrator is a device capable of characterizing, calibrating and optimizing the performance of a given synchrophasor system and performing the aforementioned actions. Through performing a variety of standardized, so called *type tests*, as well as *application tests* based on simulated or observed power system data, the portable device captures and analyzes the behavior of Phasor Measurement Units (PMUs) and Phasor Data Concentrators (PDCs). By looping back the output streams of those devices and comparing them to the known generated input signals, various characteristics like time delay, fault uncertainty and design quality can be determined. This information may then be used for calibration to improve overall system performance and accuracy.
The procedure associated with the use of the Field Calibrator may be performed during initial calibration, periodic maintenance or trouble shooting when issues have already become apparent.

4.2 Design Specification

4.2.1 Objectives

- Provide field calibration tools for periodic maintenance tests
- Support end-to-end calibration of synchrophasor systems
- Enable in-service application testing using advanced synchrophasor algorithms
- Serve as a testbed for evaluation of new synchrophasor algorithms

4.2.2 Functional Overview

The following functions are required for the field calibrator purpose of periodic maintenance of a PMU in the field:

- Shall be run off an accurate timing source (IRIG-B/GPS/1PPS).
- Shall provide voltage and current input signals [Signal source(s)]
- Shall receive measurements from PMU under test (Receiver).
- Shall compare phasor magnitude and phase angle, frequency and rate of change of frequency (ROCOF) measurements from PMU to "true" (reference) phasor magnitude and phase angle, frequency and ROCOF represented by the signal source input to the PMU.
- Shall perform calculations for total vector error (TVE), phasor magnitude error (ME) and phase angle error (PE), frequency error (FE) and rate of change of frequency error (RFE), and additional calculations for the dynamic step test results.
- Shall have a means of determining the time of arrival of PMU data messages and comparing that time against the message timestamp.
- Shall provide test result documentation.

In addition, the following functions are required for end-to-end testing of the synchrophasor system:

- Required very accurate, with high precision measurements PMU algorithm – Gold PMU, as a reference measurement unit in case of unknown input signals.
- Shall provide an interface to analog voltage and current signals from the substation CTs and VTs (A/D converters).

4.2.3 Additional Settings and Instructions for Periodic Maintenance Test Set

For the purpose of maintenance testing, the inputs of the device under test must be de-energized from the substation signal source and connected to calibrator. The field calibrator performs testing by generating test signals based on the end-user preference that can be customized and analyzing the response to the generated signals using various software tools integrated in the calibrator. All the test signals are generated according to the user choice and sent to the amplifier (if applicable) and then to the PMU under test. Stream from the tested PMU is sent back to the field calibrator for further analysis.

4.2.4 Timing Reference

PMU under test may require one of the timing signals:

- GPS antenna
- IRIG-B (sometimes with 1 PPS) (DC level or AM)
    - Possibly with the addition of IEEE Std 1344 extension.

- Possibly with the IEEE Std C37.118.1-2011 extension to the IEEE Std 1344 extension.

- IEEE Std 1588 The timing reference shall have an uncertainty ≤ 1 microsecond (μs).

The calibration system need only provide one instance of each type of timing source accepted by the PMU being tested

4.2.5 Signal Source(s)

This functionality is required only for periodic maintenance.

- PMU calibrator shall provide three-phase voltage and current input signals to PMUs under test. The signals shall comply with both steady-state and dynamic test requirements as specified in the IEEE C37.118.1 standard.
- Total harmonic distortion plus noise of the input signal shall be less than 0.2% of the fundamental harmonic (except where otherwise specified by harmonic distortion or out-of-band interference tests)
- The voltage and current amplitudes must be at "nominal" value (except where specified in signal magnitude tests, and dynamic step tests).
- A common nominal voltage for testing PMUs is 70 V rms and current 5 A rms (except for small signal testing which is 5V for both cases).
- PMU calibrator shall be capable of supplying at least 120% of the selected nominal voltage (84 V for Vnom = 70 V) and 200% of the selected nominal current per phase (10 A).

4.2.5.1 Signal Sources for Steady-State Tests

- Signal frequency range test – signal sources shall be capable of providing signal frequencies from 45 Hz to 65 Hz.
- Signal magnitude tests – Voltage levels from 10% nominal level to 120% nominal level, and current levels from 10% nominal level to 200% nominal level shall be available from the signal source.
- Phase angle tests – constant phase at ±π radians or a "slowly varying" phase angle with the input frequency ≤0.25 Hz from the nominal frequency for a duration that allows at least 360◦ of phase rotation.
- Harmonic distortion tests – required harmonics from the second harmonic up to the 50th harmonic of the nominal frequency.
- Out-of-band interference test – require interfering signals from 10 Hz up to twice nominal frequency.

4.2.6 Signal Sources for Dynamic Tests

- Measurement bandwidth tests – require modulation of the input signals in phase and in amplitude individually.
- The modulation frequency range from 0.1 HZ to 5 Hz and the index of modulation is 0.10. Frequency ramp tests – require sweep (chirp) of frequency from up to 5 Hz below to 5 Hz above the nominal frequency at rates of ± 1 Hz per second.
- Step tests – require steps ± 10% nominal magnitude and ± 10^{o} of phase.

4.2.6.1 PMU Measurement Receiver

For PMUs that are able to use multiple protocols and over a variety of physical media full testing at all reporting rates shall be conducted using one protocol and limited testing shall be conducted at one reporting rate using the other protocol or protocols. The limited testing shall consist of the following:

- Dynamic step changes in phase and magnitude
- PMU latency

Protocols:

- IEEE Std C37.118-2005
- IEEE Std C37.118.2-2011

Physical media:

- TCP, UDP, or combined UDP/TCP Ethernet via:
    - twisted pair copper using RG45 connector
    - optical Ethernet using ST or LC connectors
- RS-232 (obsolete and may not be required for modern PMU calibration systems)

4.3 User Interface Specification

For the purpose of testing the entire synchrophasor system in the field environment, two different use cases were defined:

1. Test set for the periodic maintenance of PMU device employed in the field
2. Test set for testing the PMU device in-service

After the user has made a choice regarding the desired calibration procedure through the developed user interface, a short description of the procedure will pop-up including the required follow-up steps.

4.3.1 Common setting for all offered tests that are provided to the user

4.3.1.1 Communication Settings

- Communication protocol (TCP, UDP, Serial)
- PMU port (default value for TCP is 4712, and for UDP is 4713, but it can be customized based on the PMU internal settings)
- PMU address (IP address of the tested device; recommended to be a Static IP address)

4.3.1.2 PMU Settings

- Nominal frequency of the tested device (50 Hz/60 Hz; default value is 60 Hz)
- Performance class (M/P class)
- Reporting rate (all possible value defined in the standard are available; 60 is set as default value)
- Standard version (2011; for the old PMU devices 2005 standard version is also available)
- Nominal voltage and current values (default for voltage is 70 Vrms and for current is 5 Arms

4.3.1.3 Amplifier Settings (needs to be set according to data sheet)

The following parameters need to be configured to meet the nominal output values:

- Voltage Amplification Factor
- Current Amplification Factor
- Phase shift/delay of the amplifier

4.3.1.4 Test Settings

User can choose to either run one test, a group of tests or all tests.

Group 1 – Steady State Tests

- Steady Magnitude
- Steady Frequency
- Harmonic Distortion
- Out-of-band interference
- Latency

Group 2 – Dynamic Tests

- Amplitude Modulation
- Phase Modulation
- Frequency Ramp
- Amplitude Step
- Phase Step

Non-standard Tests

- Application Test

After choosing the desired settings, the communication between the portable calibrator and the PMU under test has to be established; all information about channel indices has to be gathered and updated in order to start the calibration procedure.

Subsequently, when tests are done, the user will get a notification on the screen and the reports will be generated in a pre-defined folder location.

4.3.2 Additional settings for in-service testing and instructions

For the purpose of in-service PMU testing and evaluation of the entire synchrophasor system as a whole, the Field Calibrator input needs to be connected to the Gold PMU, which references the substation signal source, and test PMU data for analysis and comparison. Multilayer testing of in-service PMUs consists of testing the timing reference, PMU device, communication layer, PDC and the application layer with visualization tools. For each level, separate groups of tests, for which selection options are provided, can be performed.

Test Set:

- Timing reference testing
- PMU basic performance test
- PDC test with the communication layer
- Application test with the visualization tools

4.4 Implementation Features

- 19” Rack mount capability
- Portable device
- In-service testing capability
- Periodic maintenance testing capability
- Standardized Type/Design testing capability

- Application testing capability
- PMU testing capability
- PDC testing capability
- Supports GPS/IRIG-B/1PPS
- Graphical User Interface

4.4.1 Hardware Modules

NI cRIO 9082:

- Controller Type: High Performance
- Number of Slots: 8
- Operating Temperature: 0..55°C
- CPU Clock Frequency: 1.33 GHz
- FPGA: Spartan-6 • Spartan-6 LX150

I/O slots: 6

- NI 9225 (Current Simultaneous Analog Input, 5 Arms, 50 kS/s, 4 Ch Module)

Current input for reference Gold PMU:

- NI 9225 (Voltage Simultaneous Analog Input, 300 Vrms, 50 kS/s, 3 Ch Module)

Voltage input for reference Gold PMU:

- NI 9263 x 2 (Analog Outputs: 4 DIFF • 100000 S/s/ch • 16 bits Measurement Type: Voltage range +-10V)

Output I/O cards for signals generated by portable calibrator:NI 9402 x 2 (Digital I/O: 4 DIO • 20 MHz Counter/Timers: 4 Measurement Type: Digital)

- Used as input for receiving IRIG-B/1 PPS

Digitals I/O for control signals:

- NI 9467 (GPS Timestamping and Synchronization Module)

4.5 Use in Testing

Figure 12 shows the development and its functionality to replay simulated waveforms as well as standardized type tests [2] with respect to the module outputs on the enclosure as a synchronized analog waveform. The graphs in this figure show the 1PPS signal (green) extracted from an IRIG-B signal in sync with two exemplary waveforms for both type and application waveform.

The Field Calibrator is used to fully evaluate a systems performance under predefined situations and test scenarios. An exemplary test setup can be observed in Figure 13. The Field Calibrator as well as the reference PMU (Gold PMU) are connected to an accurate timing source (IRIG-B connection) to ensure synchronous testing. The generated waveforms are distributed to all modules involved in the test circuit (U5 -> U3/U4/U6). As can be seen, for larger networks and test applications the Synchrophasor Comparison is being computed in a separate module (U11) that is capable of consolidating a multitude of synchrophasor data streams tapped at the outputs of the various PMUs and PDCs in the system (ET3 – ET8).

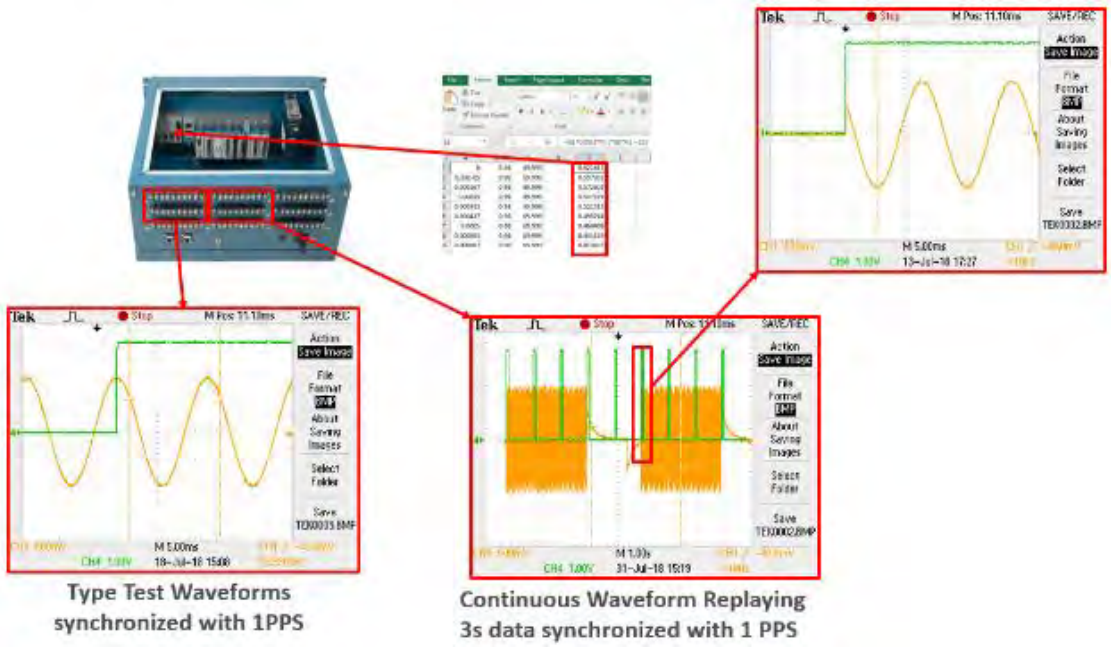

Figure 12. Module representation of TEES development with type/application test waveforms

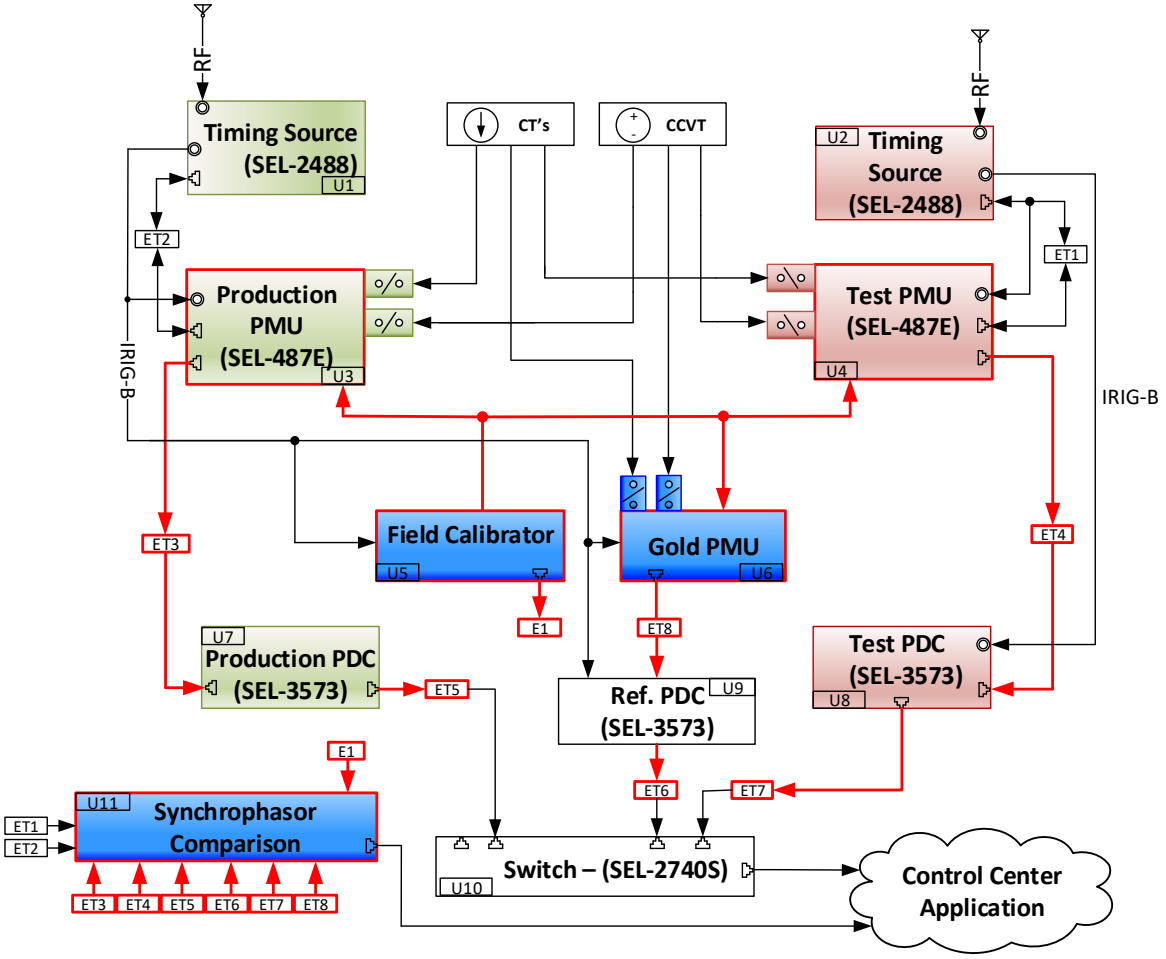

Figure 13. Exemplary test setup for End-to-end testing in synchrophasor applications

5. Integration of Gold PMU and In-Service Calibrator

5.1 Introduction

5.1.1 General

Power system is subjected to faults caused by various reasons such as different weather condition, animal or human contacts, vegetation contacts, etc. Once circuit breakers clear the fault following relays trip command, the fault point must be determined and proper action taken to expedite troubleshooting and minimize repair time [4]. Various fault location methods have been proposed in literature [5]–[11]. Single-end impedance based fault location methods are considered the most conventional scheme [5]–[11]. These methods utilize power frequency component of single-end voltage and (or) current measurements to locate faults on transmission lines. The main advantage of such methods is the simplicity and low cost of implementation. However, their accuracy might be affected by different factors, such as infeed current from remote end, fault resistance, variation of source impedance, loading conditions or fault incidence angle. Several methods were developed using unsynchronized two-end measurements [12]–[16]. In [12], post fault voltage and current phasor measurements are used to locate faults. The method is applicable even if line parameters are unknown. In [13], symmetrical components theory is used to formulate fault location scheme.

The method proposed in [14] is based on voltage magnitude at fault point and does not require phase angles. In [17], a time-domain method based on synchronized sampling of the voltage and current data from the two ends of the line is proposed. The line model equations are then solved to build the voltage and current profiles to accurately locate the fault. Improving the line model considering distributed line parameters led to more accurate results in [18]. In [19], the method proposed in [18] was modified to reduce the sampling rate from 20 kHz to 1 kHz. The main advantage of the mentioned two-end fault location methods comparing to single-end methods is their higher accuracy in locating faults. However, availability of measurements through the entire network might not be feasible due to the cost and installation concerns for foreseeable future [4]. Hence, a sparse measurement-based fault location method could be more practical due to its low implementation cost. In recent decades, development of phasor measurement units (PMUs) introduced various synchrophasor based methods [20]–[23]. In [20], [21], Clarke transformation is applied to the synchronized voltage and current phasors aligned with a discrete Fourier transform-based algorithm to calculate the location of fault.

Another fault detection/location technique is presented in [22], [23] with consideration of arcing fault discrimination based on synchronized fundamental phasor measurements. In [24], a bus-impedance matrix was utilized to calculate fault point with access to limited synchronized measurements at two remote buses in the network. Several methods utilize electromagnetic transient propagation in power system and are known as travelling wave based methods [25]–[28]. The method proposed in [25], [26] is based on measuring time of arrival (ToA) of electromagnetic traveling waves which propagate from the fault point to sparsely located synchronized measurement devices. Then, an optimization method is applied to calculate the location of fault. In [27], a wide area traveling wave-based method is proposed which determines faulty line and distance to fault by analyzing the traveling wave propagation times using the extended double end method. In [28], a traveling wave principle along with two graph theory-based lemmas is deployed

to sectionalize power system and locate faults within suspected sections. Despite the high accuracy of travelling wave-based methods, they require measurement device with high sampling rate to capture electromagnetic transient which increase cost of implementation.

Power system experiences electromechanical oscillations after fault clearing. The oscillation propagates through the system with certain speed based on network parameter, generator inertia etc. The time of arrival of oscillations at different measurement buses can be used to locate faults. A brief theory on electromechanical oscillation propagation has been given below.

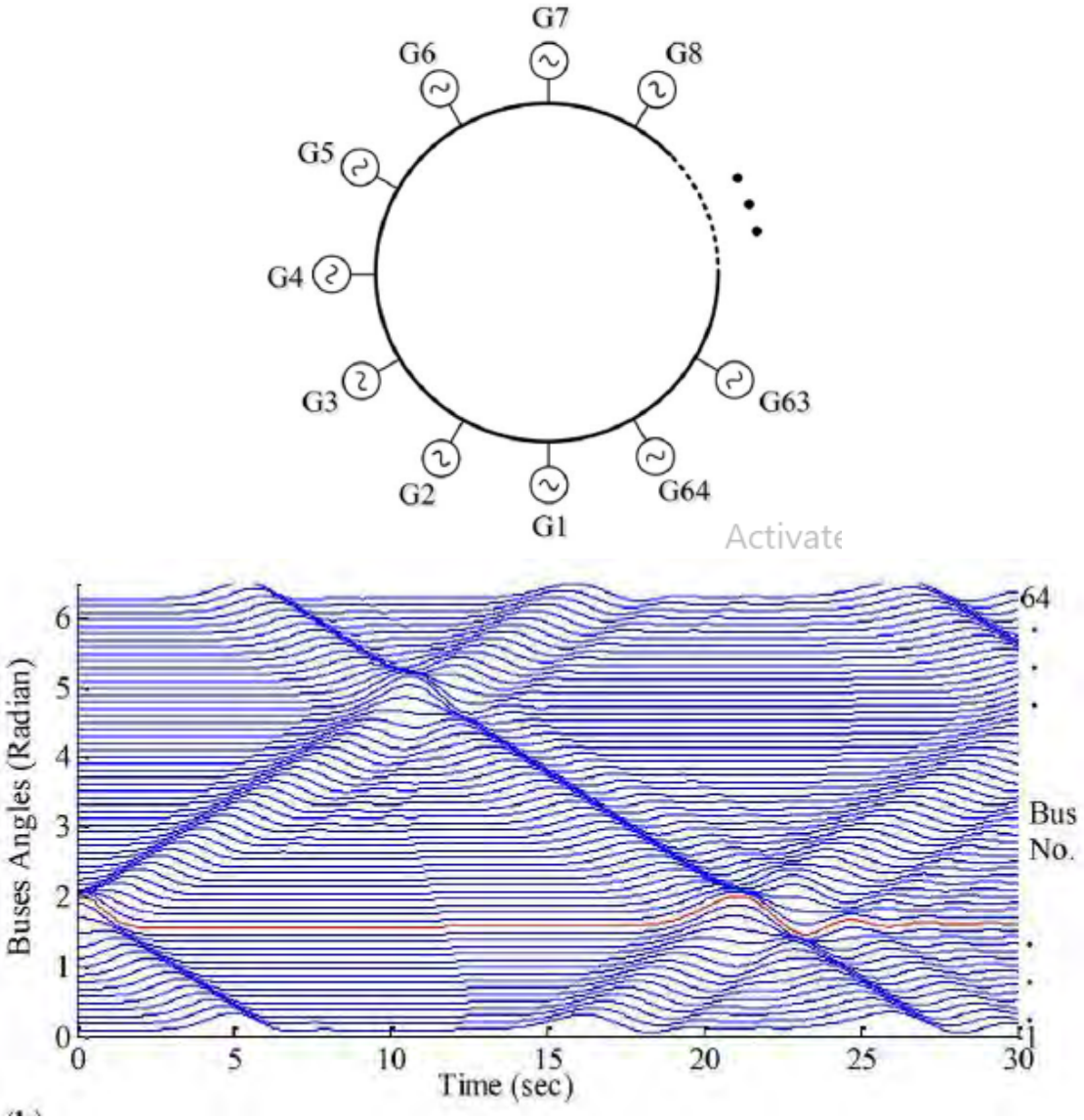

Figure 14. Understanding electromechanical-wave propagation. (a) 64-generator ring system, (b) Bus angle modulation following a fault at bus 16.

5.1.2 Continuum Modeling of Power System

A. Electromechanical-Wave Propagation Phenomena

When a disturbance occurs on a transmission line, electrical power flow changes in the network. This leads to a mismatch between electrical and mechanical torque of generators located in the vicinity. Therefore, each generator rotor angle changes to compensate the mismatch. Following the generators' rotor angle oscillations, the adjacent buses also encounter changes in their generators' rotor angle which again causes a mismatch in the electrical torque of the adjacent generators. In this fashion, the oscillation known as the electromechanical-wave propagation is "seen" throughout the entire network. Electromechanical oscillations could be detected by monitoring phasor angle of bus voltages and characterized with much lower frequency (0.1–10.0 Hz) than electromagnetic transients (kHz) [29]. To illustrate the concept, a simple power-system model in the form of a ring is used. Figure 14(a) shows the 64-generator ring system introduced in [29], which comprises 64 identical serially connected generators through identical transmission lines, forming a ring. The initial bus angles are evenly distributed from 0 to 360 degrees by steps equal to degrees. Due to homogeneity and ring shape of the 64-bus system, it is well-suited to study basic aspects of electromechanical-wave propagation phenomena. Figure 14(b) shows the phasor angle of 64-buses (in radian) with respect to time of a given disturbance occurring at bus 16 at. Following the change in the angle of bus 16 shown by the dashed line in Figure 14(b), the other generators react in a similar fashion, but with a certain time delay. Plotting all the bus angles together, this time delay can be represented as a wave modulated on buses' phasor angles, which travels away from the disturbance source into the network at a finite speed.

B. Continuum Modeling

Applying differential algebraic equations (DAEs) is the conventional way of modeling electromechanical-wave propagation in power system. Due to complexity, this approach could be time consuming and the result would be hard to analyze for large networks. Therefore, researchers introduced a much simpler method which embeds the effect of electromechanical wave propagation into power system behavior [29]–[33].

The so called continuum model, considers power system with spatially distributed parameters. The continuum model is based on applying partial differential equations (PDEs) describing the power systems to the infinitesimal element distributed along the power system. Due to generators rotor inertia, the timescale of electromechanical oscillations is large compared to the power system frequency. Therefore, the variables in continuum model can be considered as phasor parameters [33].

In the context of continuum modeling, any point in a power system could be represented by the incremental system as shown in Figure 15.

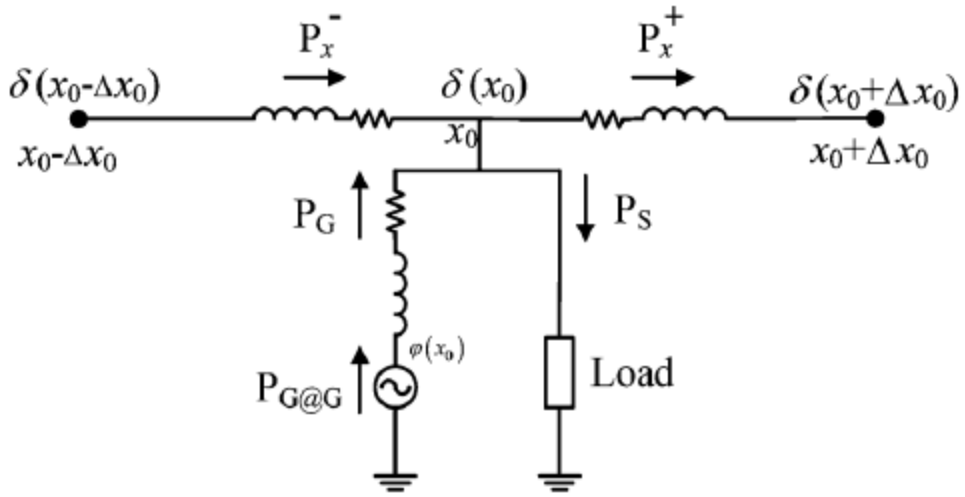

Figure 15. Incremental system used for continuum modeling of system

The model allows for representation of lines with different per-unit impedances, shunt reactances, generators and loads. The flexibility of the incremental model allows any arbitrary network topology to be modeled with continuum approach. Following is a brief summary of continuum formulation.

After several simplifications, the power flow and the swing equation for the continuum model can be obtained as:

$$G\left(\frac{\partial\delta(x_0)}{\delta x}\right)^2 - \frac{B\partial^2\delta(x_0)}{\partial x^2} = G_{int}\left[\cos\left(\delta(x_0)-\varphi(x_0)\right)-1\right] - B_{int}\sin\left(\delta(x_0)-\varphi(x_0)\right) - G_s \quad ..(1)$$

$$m(x_0)\frac{\partial^2\varphi(x_0,t)}{\partial t^2} + d(x_0)\frac{\partial\varphi(x_0,t)}{\partial t} = P_m(x_0) + B_{int}\sin\left(\delta(x_0)-\varphi(x_0)\right) - G_{int}[1-\cos(\delta(x_0)-\phi(x_0))] \quad .. \quad (2)$$

Where G, B, m, P_m represent the conductance, susceptance, inertia and the mechanical power of elementary length.

5.2 Design Specification

5.2.1 Functional Requirement

a) The simulation model, used for generating offline fault data base, should accurately represent the system and the operating condition during faults.

b) Accurate phasors of voltage and angle from different buses in the network

5.3 Implementation Features

5.3.1 IPC Model Calibration

The purpose of this task is to calibrate the model of Idaho Power Company power system data with field measurements. The detailed descriptions of the field measurement and the validation of the simulation model is given below:

Field Measurement: The measurements were recorded during a L-G fault on a series compensated line Hemingway (HMWY) – Midpoint (MPSN). Recording from the SEL relay (400 samples/s) and the DFR (12000 samples/s) were collected in COMTRADE ASCII 2005 format. The fault location and the midpoint substation configuration are shown in Figure 16.

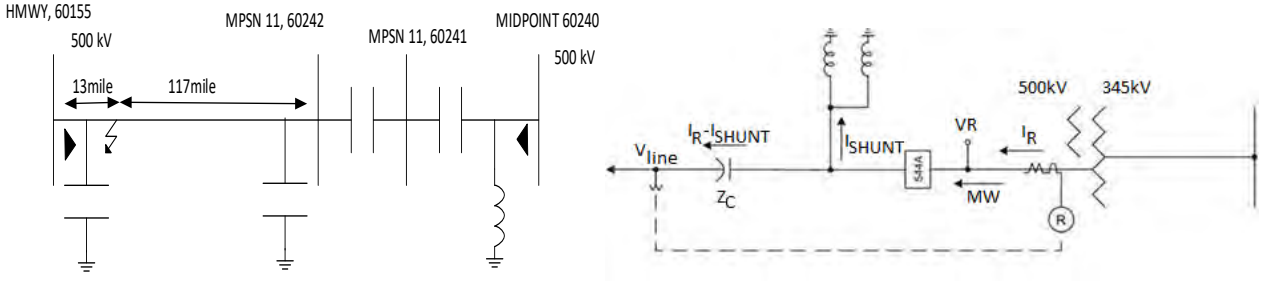

Figure 16. Fault location and the configuration of midpoint substation

Simplification the IPC Model: Original model collected from IPC was in PSS/E format which was obtained by converting the system model in PSLF format. There were several simplifications done to the model before it could be used for comparing with field measurements, as follows:

a) Removed shunt compensation in few buses to converge power flow,

b) Wind generators (only few MW) were converted to conventional generator as no suitable dynamic data was available,

c) System external to IPC was considered classical model while detail modelling of IPC was retained,

d) Net negative and zero sequence impedances were considered as equal and 1.5 times of positive sequence impedance.

Model Calibration: As PSS/E can provide only positive sequence measurement, positive sequence currents were computed from the SEL relay measurements using DFT. The comparison is shown Figure 17.

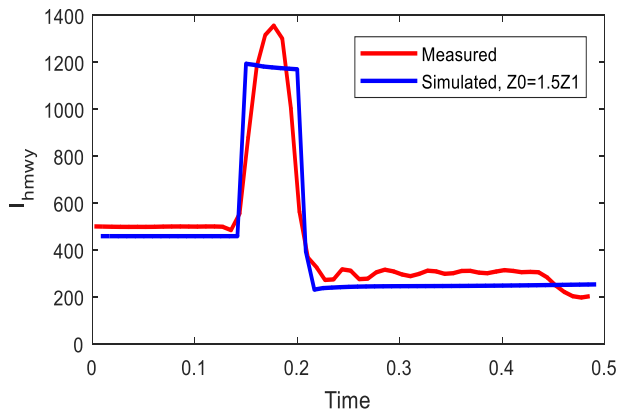

Simulated and measured currents at HMWY
Steady state: measured 499A, simulated 458A
Fault current: measured 1380A, simulated 1180A

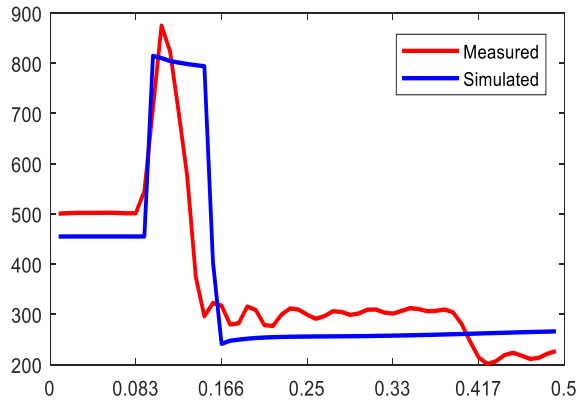

Simulated and measured currents at MPSN
Steady state: 501A, simulated 453A
Fault current: 890A, 809A.

Figure 17. Comparison between measured and simulated results

The difference between measured and simulated waveforms may be because of a) difference in operating condition, b) error in zero sequence impedance, c) smoothing effect of DFT in measured current, d) different fault clearing instances at two ends, e) neglecting L-C transients, sub-synchronous resonance (25 Hz oscillations in measured waveforms) in simulation in PSS/E.

5.3.2 Implementation of Fault Location Algorithm

The method works on the basic principle that electromechanical oscillations propagate in power system with certain speed depending on the generator inertia and line reactance. Time of arrival of oscillation at a location may be approximated using continuum modeling, $toa = \frac{distance}{velocity} = \frac{d}{\sqrt{\frac{\omega}{2h|z|}}}$ second, where d=distance from the fault location in mile, $\omega = 377\ rad/s$, $h = inertia/mile$, $z = line\ reactance\ per\ mile$. A decision tree is trained with four predictors ($v, \theta, \dot{\theta}\ and\ \ddot{\theta}$) where $v = bus\ voltage, \theta = bus\ angle$. Calculated toa as per the equation above is used for the target value in the decision tree training. When any fault occurs a 3second window is selected starting from one second before the fault and ($v, \theta, \dot{\theta}\ and\ \ddot{\theta}$) are computed. This is used in the trained decision tree to measure the toa of the oscillations. For each measurement locations (3 buses considered here), separate decision tree is used.

Minimum difference between measured toa and calculated toa indicates the fault location. It can be obtained with binary search method as shown in Figure 18.

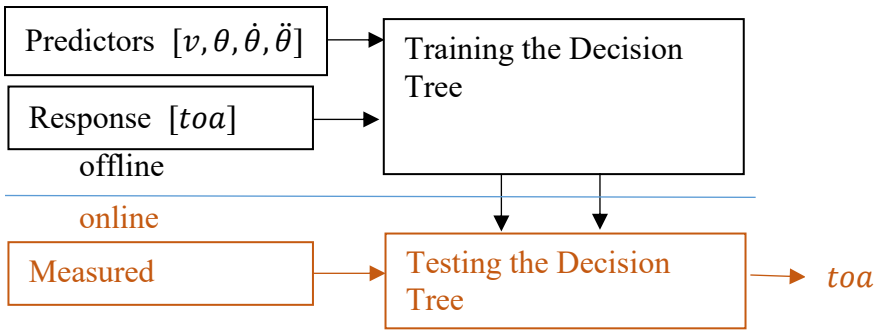

Figure 18. Block diagram for binary search method

The IPC Test System one-line diagram and parameters are given in Figure 19.

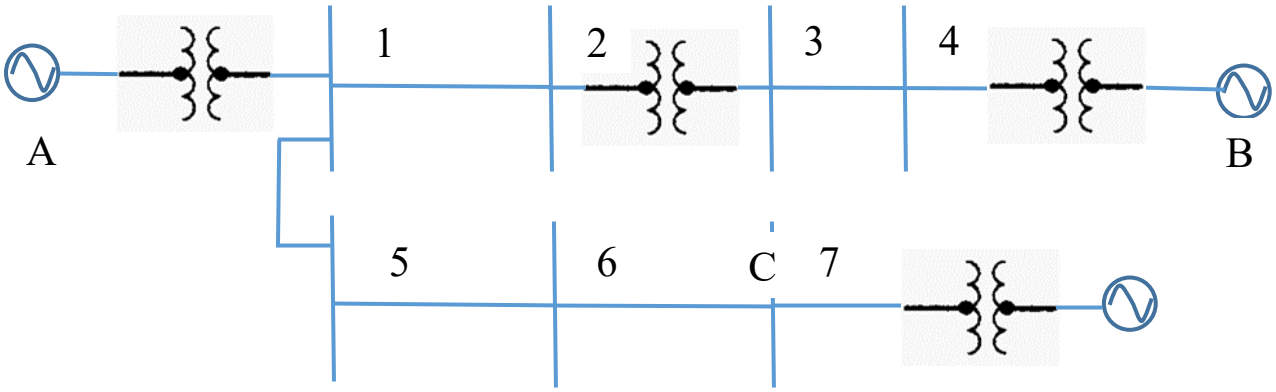

Figure 19. One-line diagram for IPC test system

Original bus number as per PSS/E is given within bracket as follows:

From Bus	To Bus	Brunch number	Branch Data
1 (60215)	2 (60250)	1	0.0481+j0.1518
2 (60250)	3 (61805)	2	0.00667+j0.07303
3 (61805)	4 (61800)	3	0.036818+j0.109717
1 (60215)	5 (61223)	4	0.0481+j0.1518
5 (61223)	6 (60225)	5	0.00014+j0.00117
6 (60225)	7 (60040)	6	0.00198+j0.01138

Inertia of generators is 6s for each generator.

Transformer reactance of each generator: A: 0.0025+j0.1798, B: 0.0147+j0.4363, C: 0.0037+j0.1363

5.4 Use in Testing

The complete connection diagram for the end to end application test has been shown in Figure 20. PSSE has been used to simulate faults and store voltage phasors and angles of different buses. A field calibrator may be used to generate analog waveforms which is used in the PMU to compute

phasors. Phasors are passed through the synchrophasor systems and finally the FL algorithm is run in the control center. The fault location obtained from the WAMS based algorithm can be compared with the actual location obtained from manual inspection or any highly accurate reference fault location algorithm.

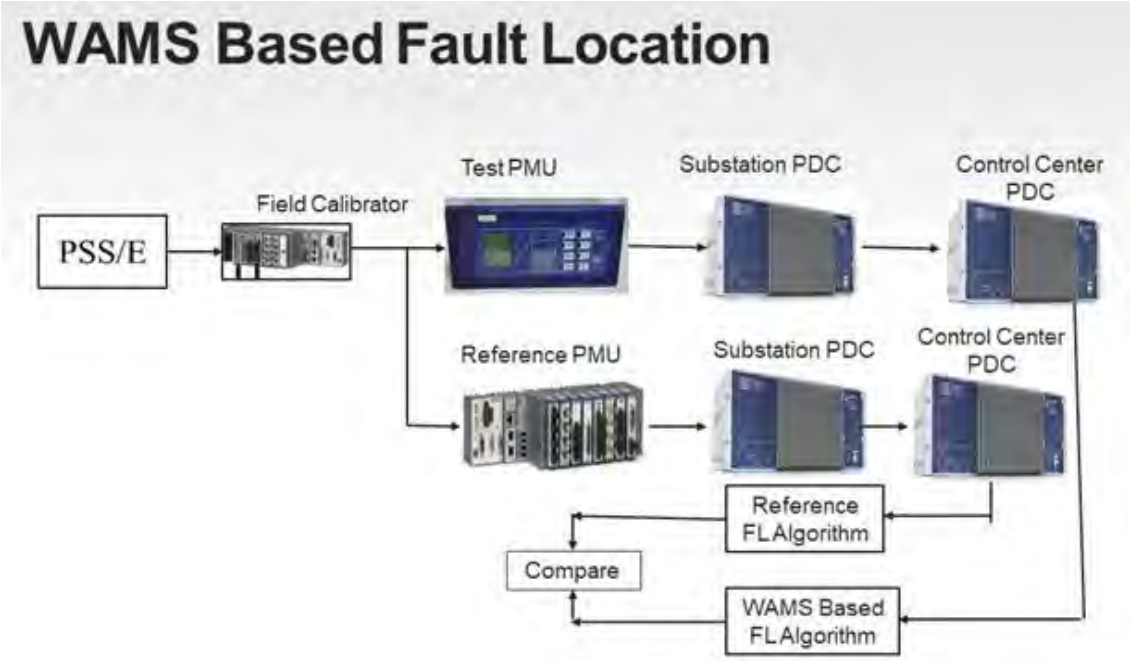

Figure 20. Diagram for End-to-End Application Test

6. Conclusions

The development of field test devices and protocols for commissioning, acceptance, and in-service testing procedures of synchrophasor devices and systems has been achieved. In particular, the PMU calibration and certification lab is constructed to perform standardized PMU acceptance tests; Field Calibrator performs commissioning and in-service testing on PMUs, PDCs, as well as synchrophasor applications, where Gold PMU is used as a reference synchrophasor source. The performance of Gold PMU is achieved by both robust physical hardware module selection, and accurate Gold PMU algorithms. The notion of nested testing is introduced so that the performance of synchrophasor system is tested device by device, and layer by layer. Then, the evaluation of a particular synchrophasor application, i.e. fault locations, is used as an example of the integration of Gold PMU and in-service field calibrator. The methodology is verified using IPC system data.

References

[1] "IEEE Standard for Syncrophasor Measurements for Power System, IEEE Std. C37.118.1-2011".

[2] "IEEE Standard for Syncrophasor Measurements for Power System, Amendment 1: Modification of Selected Performance Requirements, IEEE Std. C37.118.1a-2014".

[3] "IEEE Synchrophasor Measurement Test Suite Specification (TSS), version 2, 2015".

[4] C. Qian, M. Kezunovic. "A Power Waveform Classification Method for Adaptive Synchrophasor Estimation," *in IEEE Transactions on Instrumentation and Measurement,* vol. 67, no. 7, pp. 1646-1658, July 2018.

[5] C. Qian, M. Kezunovic, "Spectral Interpolation for Frequency Measurement at Off-Nominal Frequencies," in *IEEE PES General Meeting*, Chicago IL, July 2017.

[6] D. Macii, D. Petri and A. Zorat, "Accuracy Analysis and Enhancement of DFT-Based Synchrophasor Estimators in Off-Nominal Conditions," *in IEEE Transactions on Instrumentation and Measurement,* vol. 61, no. 10, pp. 2653-2664, Oct. 2012.

[7] C. Qian, M. Kezunovic, "Dynamic Synchrophasor Estimation with Modified Hybrid Method.," in *2016 IEEE PES Conference on Innovative Smart Grid Technologies North America*, Minneapolis, MN, September 2016.

[8] C. Qian, M. Kezunovic, "Synchrophasor Reference Algorithm for PMU Calibration System," in *2016 IEEE PES Transmission & Distribution Conference and Exposition*, Dallas, TX, May 2016.

[9] Z. Galijasevic and A. Abur, "Fault location using voltage measurements,"IEEE Trans. Power Del., vol. 17, no. 2, pp. 441–445, Apr. 2002.

[10] M. S. Sachdev and M. A. Baribeau, "A new algorithm for digital impedance relays," IEEE Trans. Power App. Syst., vol. PAS-98, no. 6, pp. 2232–2239, Dec. 1979.

[11] A. A. Girgis, "A new Kalman filtering based digital distance relay," IEEE Trans. Power App. Syst., vol. PAS-101, no. 9, pp. 3471–3480, Sep. 1982.

[12] T. Kawady and J. Stenzel, "A practical fault location approach for double circuit transmission lines using single end data," IEEE Trans. Power Del., vol. 18, no. 4, pp. 1166–1173, Oct. 2003.

[13] H. Ha, B. H. Zhang, and Z. L. Lv, "A novel principle of single-ended fault location technique for EHV transmission lines," IEEE Trans. Power Del., vol. 18, no. 4, pp. 1147–1151, Oct. 2003.

[14] C. E. M. Pereira and L. C. Zanetta, "Fault location in transmission lines using one-terminal post-fault voltage data," IEEE Trans. Power Del., vol. 19, no. 2, pp. 570–575, Apr. 2004.

[15] Z. Qingchao et al., "Fault location of two-parallel transmission line for non-earth fault using one-terminal data," IEEE Trans. Power Del., vol. 14, no. 3, pp. 863–867, Jul. 1999.

[16] M. Farshad and J. Sadeh, "Accurate single-phase fault-location method for transmission lines based on k-nearest neighbor algorithm using one-end voltage," IEEE Trans. Power Del., vol. 27, no. 4, pp. 2360–2367, Oct. 2012.

[17] Y. Liao and S. Elangovan, "Unsynchronized two-terminal transmission- line fault-location without using line parameters," Proc. Inst. Elect. Eng., Gen. Transm. Distrib., vol. 153, no. 6, pp. 639–643, Nov. 2006.

[18] J. Izykowski et al., "Accurate noniterative fault location algorithm utilizing two-end unsynchronized measurements," IEEE Trans. Power Del., vol. 25, no. 1, pp. 72–80, Jan. 2010.

[19] E. G. Silveira and C. Pereira, “Transmission line fault location using two-terminal data without time synchronization,” IEEE Trans. Power Del., vol. 22, no. 1, pp. 498–499, Feb. 2007.
[20] M. Davoudi, J. Sadeh, and E. Kamyab, “Parameter-free fault location for transmission lines based on optimization,” IET Gen., Transm. Distrib., vol. 9, no. 11, pp. 1061–1068, Aug. 2015.
[21] M. Davoudi, J. Sadeh, and E. Kamyab, “Time domain fault location on transmission lines using genetic algorithm,” in Proc. 11th Int. Conf. Environment Elect. Eng., May 2012, pp. 1087–1092.
[22] M. Kezunovic and B. Perunicic, “Automated transmission line fault analysis using synchronized sampling at two ends,” IEEE Trans. Power Syst., vol. 11, no. 1, pp. 441–447, Feb. 1996.
[23] A. Gopalakrishnan et al., “Fault location using the distributed parameter transmission line model,” IEEE Trans. Power Del., vol. 15, no. 4, pp. 1169–1174, Oct. 2000.
[24] P. Dutta, A. Esmaeilian, and M. Kezunovic, “Transmission-line fault analysis using synchronized sampling,” IEEE Trans. Power Del., vol. 29, no. 2, pp. 942–950, Apr. 2014.
[25] J. A. Jiang et al., “An adaptive PMU based fault detection/location technique for transmission lines part I: Theory and algorithms,” IEEE Trans. Power Del., vol. 15, no. 2, pp. 486–493, Apr. 2000.
[26] J. A. Jiang et al., “An adaptive PMU based fault detection/location technique for transmission lines. II. PMU implementation and performance evaluation,” IEEE Trans. Power Del., vol. 15, no. 4, pp. 1136–1146, Oct. 2000.
[27] Y. H. Lin et al., “A new PMU-based fault detection/location technique for transmission lines with consideration of arcing fault discrimination— Part I: Theory and algorithms,” IEEE Trans. Power Del., vol. 19, no. 4, pp. 1587–1593, Oct. 2004.
[28] Y. H. Lin et al., “A new PMU-based fault detection/location technique for transmission lines with consideration of arcing fault discrimination—Part I: Theory and algorithms,” IEEE Trans. Power Del., vol. 19, no. 4, pp. 1594–1601, Oct. 2004.
[29] Y. Liao, “Fault location for single-circuit line based on bus-impedance matrix utilizing voltage measurements,” IEEE Trans. Power Del., vol. 23, no. 2, pp. 609–617, Apr. 2008.
[30] M. Korkali, H. Lev-Ari, and A. Abur, “Traveling-wave-based fault location technique for transmission grids via wide-area synchronized voltage measurements,” IEEE Trans. Power Syst., vol. 27, no. 2, pp. 1003–1011, May 2012.
[31] M. Korkali and A. Abur, “Optimal deployment of wide-area synchronized measurements for fault-location observability,” IEEE Trans. Power Syst., vol. 28, no. 1, pp. 482–489, Feb. 2013.
[32] Y. Chen, D. Liu, and B. Xu, “Wide-area traveling wave fault location system based on IEC61850,” IEEE Trans. Smart Grid, vol. 4, no. 2, pp. 1207–1215, Jun. 2013.
[33] S. Azizi et al., “A traveling-wave-based methodology for wide-area fault location in multi-terminal DC systems,” IEEE Trans. Power Del., vol. 14, no. 3, pp. 863–867, Jul. 1999.
[34] J. S. Thorp et al., “Electromechanical wave propagation in large electric power systems,” IEEE Trans. Circuits Syst. I, Fundam. Theory Appl., vol. 45, no. 6, pp. 614–622, Jun. 1998.
[35] A. Semlyen, “Analysis of disturbance propagation in power systems based on a homogeneous dynamic model,” IEEE Trans. Power App. Syst., vol. PAS-93, no. 2, pp. 676–684, Mar. 1974.

[36] P. Dersin and A. Levis, “Feasibility sets for steady-state loads in electric power networks,” IEEE Trans. Power App. Syst., vol. PAS-101, no. 1, pp. 60–70, Jan. 1982.
[37] A. J. Arana, “Analysis of electromechanical phenomena in the power-angle domain,” Ph.D. dissertation, Elect. Eng. Dept., Virginia Polytechnic Institute and State University, Blacksburg, VA, USA, Dec. 2009.
[38] M. Parashar et al., “Continuum modeling of electromechanical dynamics in large-scale power systems,” IEEE Trans. Circuits Syst. I, Reg. Papers, vol. 51, no. 9, pp. 1848–1858, Sep. 2004.

Part II

End-to-End Remote Testing of PMU and RAS

Anurag K. Srivastava
David Bakken
Param Banerjee
Pratim Kundu
Ren Liu, Graduate Student
Hyojong Lee, Graduate Student
Zhijie Nie, Graduate Student
Alex Askerman, Undergraduate Student

Washington State University

For information about this project, contact

Anurag K. Srivastava
Washington State University
School of Electrical Engineer and Computer Science
Pullman, WA 99164
Phone: 5093352348
Email: anurag.k.srivastava@wsu.edu

Power Systems Engineering Research Center

The Power Systems Engineering Research Center (PSERC) is a multi-university Center conducting research on challenges facing the electric power industry and educating the next generation of power engineers. More information about PSERC can be found at the Center's website: http://www.pserc.org.

For additional information, contact:

Power Systems Engineering Research Center
Arizona State University
527 Engineering Research Center
Tempe, Arizona 85287-5706
Phone: 480-965-1643
Fax: 480-727-2052

Notice Concerning Copyright Material

Table of Contents

List of Figures

List of Tables

1. Introduction

1.1 Background

The critical component in Wide Area Measurement System (WAMS) is the Phasor Measurement Unit (PMU), which converts the point on wave signal of voltage and current to corresponding magnitude and phase angle. The magnitude and phase angle of voltage and current are time stamped using Global Positioning System (GPS) synchronized clock. The phase angle of voltage and current at a bus or a line are evaluated with reference to GPS synchronized sinusoid. The time stamped magnitude and angle (collectively called phasors) of voltage and current are transmitted to successive hierarchical archival mechanism using Phasor Data Concentrator (PDC), super PDC and control center PDC, where the end application retrieves the phasor for computation [1-4].
The PMUs installed in the field are subject to drift in performance, inaccurate wiring due to scheduled maintenance in the substation and inconsistent anomalies in settings due to human interaction. Hence, PMUs installed in the field are required to be calibrated in a scheduled manner (every 2 years or after major substation upgrade suggested). The extension of the local PMU testing in the lab is performing calibration and testing of PMUs installed at the substation. The task of uninstalling all the PMUs and transporting them to a PMU testing lab, performing testing and reinstall them in the field, discourage utilities to perform regular calibration. It is Imperative to develop a framework for testing the PMUs installed in a substation remotely for which tools are being developed in this work.

The synchrophasor application or wide area application mainly undergoes three stages before field deployment. The first stage is the algorithm development based on Differential and Algebraic Equation (DAE) model of the power system. In this stage, the validation of the application is performed using offline simulators. The offline simulators provide same simulation time increment for both the system and the controller model in the same simulation framework. The second stage is real-time testing and validation using hardware in the loop (HIL) test bed. The application or the controller implemented in hardware setup, cannot be validated using offline simulators. The simulation time of the system model in the offline simulators are not synchronized with the actual time used by the hardware controller, resulting in time skew of the controller output to the system or system response to the controller. The real-time simulators using HIL test bed simulate the test system in real-time and synchronization with the actual time of the hardware controller is guaranteed. The real-time HIL test bed emulated input output equivalent of the true power system. The synchrophasor based control application consists of a large number of interacting components in the power system network. The overall application can degrade the system performance, even if one or more devices are individually tested and validated. Even each device may be validated satisfactorily, there are chances that the system consisting of one or more devices may fail to achieve the desired objective. Validation and testing of the application with one or more devices as a single entity are also desirable before field deployment. The requirement of end-to-end testing of such control application is discussed in this chapter. The Remedial Action Schemes (RAS) are considered as an example synchrophasor based control application for performing end-to-end testing. The requirements of a RAS test bed are enlisted and architecture of middleware called Erkios for RAS testing developed at WSU. The developed testbed is evaluated for single substation and multiple substations RAS.

Validation and conformance testing of PMU performed at South California Edison (SCE) using the PMU Performance Analyzer (PPA), a software tool developed at WSU is presented as a part of device testing. The specification of testing equipment and architecture of a testbed for the PMU testing and associated applications is also presented in this chapter. Validation of PMU based anomaly detection and PMU based event detection are the two monitoring application presented in this chapter.

The phasors estimated using different PMUs might have variation in accuracy depending on the type of signal. This variation affects the performance of WAMS based monitoring and control applications running in the control centers. In view of this, a set of test scenarios and error metrics are enlisted in IEEE standard C37.118.1 for synchrophasors [3], amended in C37.118.1a.2014. PMU vendors are expected to provide compliance testing of their PMUs accuracy before deploying them in the field. However, PMU testing is carried out by limited agencies as it is expensive and requires a significant amount of manual labor.

Remedial Action Scheme (RAS) is a special control action that minimizes the impact of contingencies that cannot be constrained in time with normal protection and control devices. They are typically designed to stop events that would lead to cascading effects and cause a major blackout. The Western Electricity Coordinating Council (WECC) and North American Electric Reliability Corporation (NERC) have adopted certain standards for implementation, operation and performance of RAS. The standards are listed for various aspects like RAS logic, hardware involved, arming, detection and initiating devices, logic processing, transfer trip equipment, test switches, etc. Based on these standards, the following aspects of the RAS and standard have to be incorporated into the real time testbed to emulate real world scenario.

1. Maximum Allowable Time: The response time depends basically on the type of scenario. For angular stability, short-term voltage stability and other similar problems, the response time should be from a few cycles to a second. For slow stability problems, the response time can be up to several seconds. For thermal overloading of transmission lines, the response time can range from several seconds to minutes based on the line rating and operating state. The testbed should make sure that the delay caused by the test process and test network is not included in the evaluation. Further, the testing should also note the fact that the time taken for the actuator to react is not being included in the process. The RAS system could include more than one utility and so the response time for the action can includes the time taken to communicate between different utilities. To handle this, issue the NERC and WECC standards clearly state the starting point to evaluate the performance of the RAS.
2. Communication Channels: The standards state that the requirements should meet the Communication Systems Performance Guide for Protective Relaying Applications" and Critical Communications Circuits-Guidelines for Design". The main requirement is that the scheme logic should be designed so that the loss of the channel, noise or other failure will not result in a false operation of the scheme. This necessitates the need for a similar communication design in the testbed.
3. Cyber Security: The NERC adopted the standards CIP-002-1 through CIP-009-1 to address both physical and electronic security for critical assets. Erkios should abide these standards when doing an end-to-end in-field testing

4. Redundancy: This is a very important standard for implementing RAS as it addresses failure and maintenance issues. The WECC standard illustrates all scenarios and requirements in depth. The standard states that, except for a few components like substation batteries, PT/CTs (potential transformer/current transformer), breaker, and communication towers, all other equipment involved in RAS implementation should be redundant and especially the RAS logic. Also, the standard states that any mis-operation of RAS should not have an adverse effect on the power grid at the system level.

Results demonstrate that testing and validation of synchrophasor devices and applications is an iterative process to keep improving the performance of devices and applications involving all the stakeholders before the field deployment and even after field deployments for maintenance.
The mentioned tools will be demonstrated on synchrophasor WAMPAC solutions, but the mentioned test protocols and equipment/software will be made available in a modular design that can be utilized for a full evaluation and testing of any mission-critical systems including SPS and EMS. The testbeds are:

- Synchrophasor system
- EMS/SCADA
- SPS/ RAS for a given application

The testbed should resemble actual system displacement where the measurement equipment may be in substations, data concentrators in a control center, and displays at ISOs and/or TOs, and everything is connected through a communication network.

2. PMU Lab development

2.1 Background

Large deployment of PMUs in the field mandates that they are tested for compliance with IEEE TSS. The PMUs are tested for different parameters subject to different testing scenario for voltage and current. The PMU testing lab aims to provide all the necessary hardware and software infrastructure for carrying out the performance evaluation of PMUs under test. The Real Time Digital Simulator from RTDS is used for generating the time stamped analog signals which accurately follow the test cases mentioned in IEEE TSS. The RSCAD model controls the analog signal generation by RTDS and transmits the GPS time stamp of the signal events to the PMU Performance Analyzer (PPA) software. The PPA reconstructs the true value of the phasor for comparing with the PMU phasors using the GPS time stamps. The analog signals generated by the RTDS are amplified using voltage and current amplifiers and given to the PMU under test. The PMU under test estimate the time stamped voltage and current phasors using the GPS clock for the amplified signal given as input. The time stamped phasors from the PMU are archived by the Phasor Data Concentrator (PDC) and fed to the PPA for comparison with the time stamped true phasor. The PPA generates a detailed report for all the test cases performed by the user.

The test scenario listed requires generation of sinusoidal test signal with specific values of amplitude, frequency and harmonics. The signal generated by the test equipment needs to be validated for parameter accuracy before performing PMU testing using those signals. In this work, PMU testing using low cost NI-cRIO is proposed. The investigation demonstrates that the built-in signal generation using Labview is not suitable for PMU testing application.

The IEEE standard for synchrophasors mentions Total Vector Error (TVE) for comparing the accuracy of PMUs from different vendors. The TVE is the vector difference of the estimated phasor and the actual phasor, expressed as the percentage of the actual phasor. Apart from TVE, several other error metrics are also used for compliance testing of PMU. These include Frequency Error (FE) and Rate of Change of Frequency Error (RFE) [5-7].

The static test scenario mentioned in includes off-nominal frequency, static variation in magnitude and phase, and harmonic distortion along with out of band interference. The synchrophasor standard C37.118.1mention different sets of tests for P and M class PMUs. The P- class PMUs utilize a shorter window length (in the range of one or two cycles) and provide less filtering of the phasors. P class PMUs are typically used for faster operation with limited accuracy of the phasor measurements during dynamic and transients. The M- class PMUs uses larger data window and larger filters to eliminate aliased signal from the fundamental component and, hence, out of band interference test is required to be performed for M class PMUs. To filter out interference signals from the fundamental, the required length of the data window is typically greater than 5 cycles of the fundamental component, which results in larger reporting delays but more accurate phasor measurements. The Frequency Error (FE) and Rate of Change of Frequency Error (RFE) are the additional performance criteria mentioned in this standard for the performance evaluation of the PMUs. The dynamic signal variation added for testing the PMUs are amplitude and phase modulation, frequency ramp and step change of amplitude and phase. The response time, delay time and overshoot for a typical step response test case are shown in Figure 2.1. The maximum

TVE specified for different test cases includes a summation of time synchronization error, instrumentation error and processing error. The response time of FE and RFE for the PMUs of different classes are also separately specified for each of the test cases in the standard [8, 9].

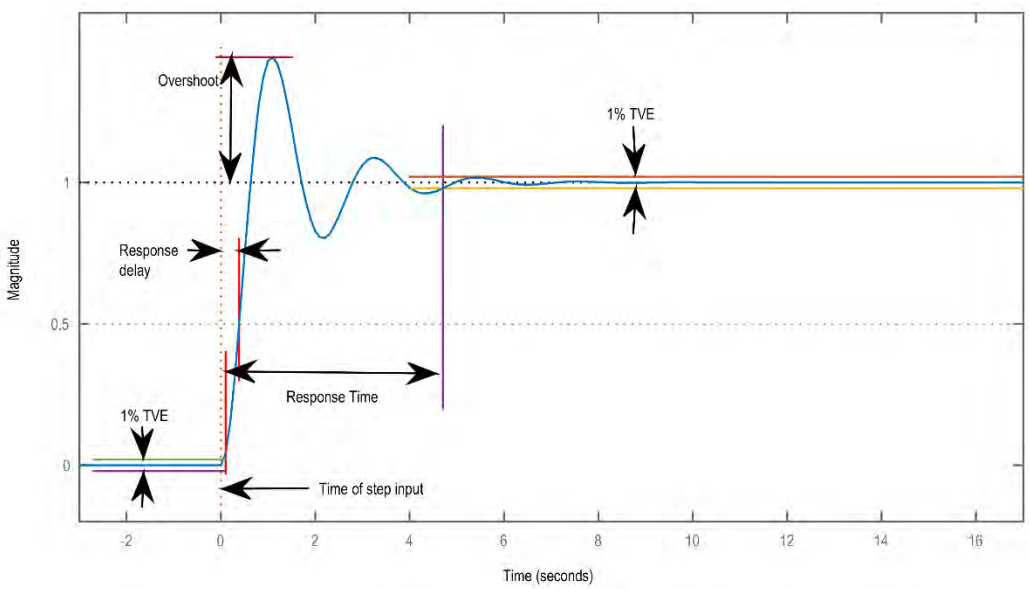

Figure 2.1 Parameters for step response

The IEEE synchrophasor standard was further amended in C37.118.1a.2014, in which the RFE values for most of the test cases are revised. The oscillation test signal, which was previously carried out by using a signal having joint amplitude and phase oscillation, has been changed to two separate signals for the amplitude and phase oscillations in the revised version of the standard. The reporting latency of the M- class PMUs has also been increased in the revised version of the standard.

The PMU estimates the magnitude and angle of the voltage and current signal samples buffered for a window length. The PMU uses the GPS time stamp at the center of the data window to report the magnitude and angle. The true value of phasor at the center of the data window is required to report the accuracy of the estimated phasor by the PMU. The magnitude and angle of the voltage and current signal mandated for PMU testing, may be constant with respect to time for static test cases or may be a simple function of time for dynamic test cases. In view of this, the PMU testing setup should have mechanism to obtain the GPS time and establish the true value of magnitude and phase, which may be dependent on GPS time stamp, particularly in the dynamic test cases. This specification is for testing Phasor Measurement Unit (PMU) according to IEEE TSS. It describes the specification of equipment required for setting up a PMU testing lab.

2.2 Purpose

The testing procedure of PMU for different static and dynamic scenarios is presented in this specification document. The PMU under test is given analog input of voltage and current with different parameters. The phasor outputs of the PMU are compared with the true phasors to obtain

different metrics and check for compliance with the limits mentioned in the IEEE C37.118.1-2011 standard.

2.3 Summary of the Test cases

The IEEE TSS specifies the detail of the testing procedure for different test cases carried out for testing a Phasor Measurement Unit (PMU).

The procedure for PMU testing for magnitude range test:

a) Start the voltage and current at a lower magnitude at a nominal frequency for 5sec.

b) Increase the input magnitudes by 10% of the nominal value and wait for 5sec.

c) Repeat step 2 till the upper magnitude limit is reached.

The procedure for PMU testing for frequency range test:

a) Start the voltage and current at rated magnitude at the lower frequency limit for 5sec.

b) Increase the input frequency by 0.1Hz of the nominal value and wait for 5sec.

c) Repeat step 2 till the upper frequency limit is reached.

The procedure for PMU testing for harmonic distortion test:

a) Start the voltage and current at rated magnitude with 1% (for P Class) or 10% (for M Class) second harmonic at rated frequency for 5sec.

b) Increase the harmonic number by 1 and wait for 5sec.

c) Repeat step 2 till the upper harmonic limit is reached.

The procedure for PMU testing for out of band interfering test:

a) Start the voltage and current at rated magnitude at rated frequency with 10% rated magnitude of the first lower frequency limit of interfering signal for 5sec.

b) Increase the interfering signal frequency in exponential steps and wait for 5sec.

c) Repeat step 2 till the interfering signal frequency reaches the first upper out of band limit.

d) Change the interfering signal frequency to second lowest out of band limit and wait for 5sec.

e) Increase the interfering signal frequency in exponential steps and wait for 5sec.

f) Repeat step 5 till the interfering signal frequency reaches the second upper out of band limit.

g) Repeat steps 1-6 for input signal frequency at a nominal frequency plus and minus 10% of the PMU reporting rate divided by two.

The procedure for PMU testing for step change of magnitude and phase test:

a) Start the voltage and current at rated magnitude and phase at a nominal frequency for 5sec.

b) The voltage and current magnitude are changed to +10% and -10% of the initial value and remain for 1 sec.

c) The voltage and current magnitude are changed to nominal value after 1 sec.

d) The step 2 and 3 are repeated 10 times with the starting of the step shifted by PMU reporting time interval divided by ten w.r.t to the first step instant.

e) The steps 1-4 are repeated for +10deg and -10deg phase change keeping the magnitude of rated value.

The procedure for PMU testing of positive and negative frequency ramp test:

a) Start the voltage and current at rated magnitude at the lower frequency limit for 5sec.

b) The frequency of the voltage and current are changed from the lower limit to the upper limit at 1Hz/s.

c) Wait for 5sec at the upper frequency limit

d) Decrease the frequency from the upper limit to lower frequency limit at -1Hz/s.

The procedure for PMU testing for AM, PM and Joint AM-PM test:

a) Start the voltage and current with a modulation magnitude of 10% of nominal and modulation frequency of 0.1Hz for 5sec.

b) Increase the modulation frequency of 0.2Hz and wait for 5sec.

c) Repeat step 2 till the upper modulation frequency limit is reached.

d) Repeat steps 1-3 for phase modulation keeping the magnitude of rated value.

Repeat steps 1-3 for combined magnitude and phase modulation.

2.4 Specification of the Equipment for PMU testing lab

Signal source: The PMU should be given input from a programmable voltage and current signal source.

a) The Signal source should have at least 1 three phase output for voltage and 1 three phase output for the current.

b) The voltage magnitude range of the Signal source should be in the range of 12V to 600V.

c) The current magnitude range of the Signal source should be in the range of 1A to 15A.

d) The Signal source should generate the fundamental signal frequency from 45Hz to 65Hz.

e) The magnitude of the voltage and current signal should be controllable using mathematical functions like level shifter, trigonometric functions and algebraic equations.

f) The phase of the voltage and current signal should be controllable using mathematical functions like level shifter, trigonometric functions and algebraic equations.

g) The Signal Source should also be able to inject at least one harmonics with 10% of the rated voltage and current magnitude. The single harmonic frequency should be variable from 100Hz to 3000Hz.

h) The Signal source should be controllable at required instances of the GPS pulses.

GPS time source: The time input to the PMU and the Signal source.

a) The GPS time source should be obtained from a GPS antenna.

b) The option to generate 1PPS, IRIG-B through copper or fiber should be present in the GPS clock receiver.

PMU measurement receiver: The Phasor Data Concentrator (PDC) is typically used for archiving the C37.118 phasor data from a PMU

a) The PDC should be configurable to receive C37.118 phasor data from Ethernet port or Serial port.

b) The PDC should have sufficient memory to archive three phase voltage, current, frequency and rate of change of frequency data.

c) The PDC should be able to export the archived phasor data in computer processing data file like .xlsx or .csv files.

Ethernet Switch: Connecting PMU, PDC and test report generator.

Calibrator: PMU are designed to calibrate before commissioning.

a) The calibrator should be able to remove any magnitude error in the reading of the PMU at rated voltage, current, and frequency.

b) The calibrator should be able to remove any angle error in the reading of the PMU at rated voltage, current, and frequency.

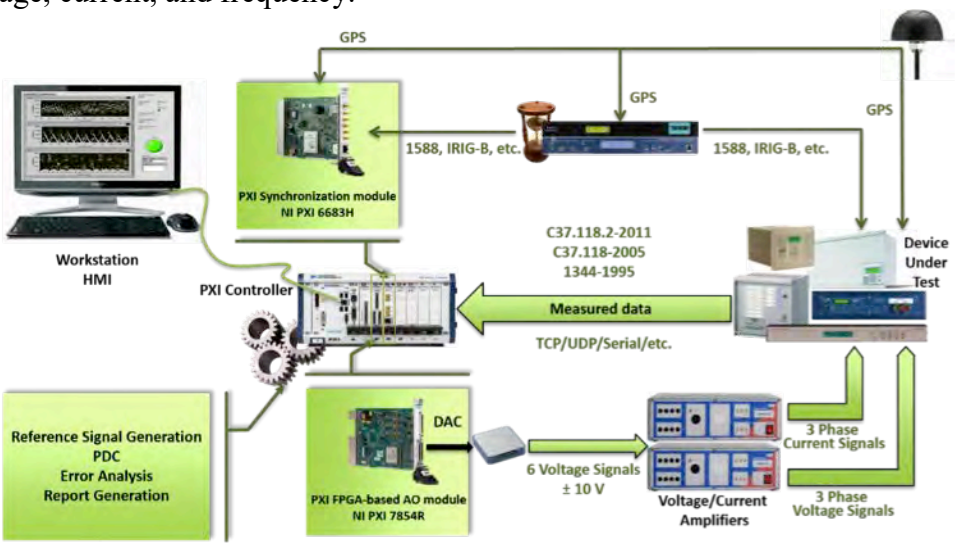

Figure 2.2a Test Suite: A software application for testing PMU using NI device.

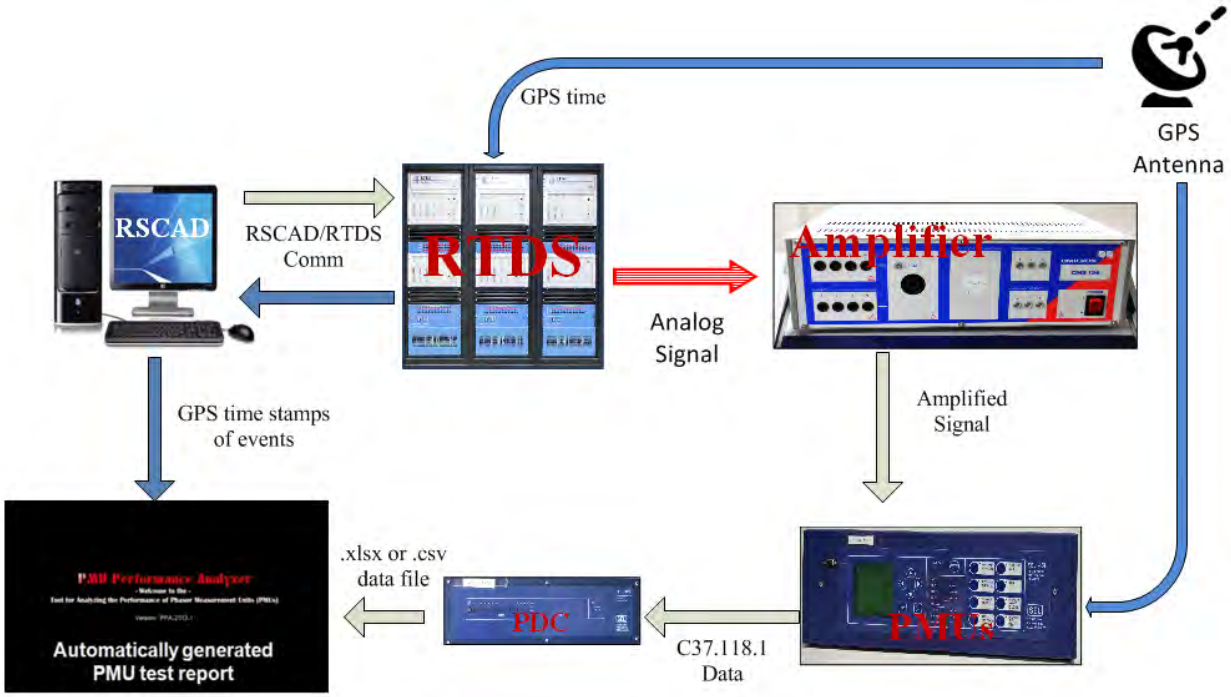

Figure 2.2b. Test Suite: A software application for testing PMU using RTDS.

The PMU testing lab development involves the implementation procedure for PMU testing mentioned in IEEE TSS. The list of equipment required for PMU testing is decided based on the previous document "Review of the IEEE TSS test plan requirements and lab specification requirements". The different scenario mentioned in the IEEE TSS for PMU testing are required to be implemented in RSCAD/RTDS for generating the analog test signal having changing parameters at known GPS time stamps. The test PMU is to be put in a setup consisting of RTDS, signal amplifier, PDC and communication network. The testing procedure is evaluated by loop back testing of the GPS time stamp generated analog signals. The analog signals generated by the analog output channels are connected to the analog input channels. The analog outputs generated are transferred back inside the RSCAD simulation and is compared with the digital signal generated using arithmetic components undergoing similar parameter change. Close similarity between these two signals validates the PMU testing procedure. The amplifier is a source of noise and non-linearity in the setup for PMU testing lab. The amplifier is validated using the NI Compact Rio platform. The analog (RTDS, amplifier and PMU) and networking connections (PMU, PDC and PPA) are finalized for the prototype testing. The amplifier is tested using the analog output and input modules available in the NI Compact Rio platform. The DC voltage at different values is provided to the input of the amplifier and the amplifier outputs are recorded using the analog input of the NI Compact Rio. The standard deviation of the recorded output gives the noise uncertainty of the amplifier. In this test the uncertainty of the analog input of the NI Compact Rio is assumed to be negligible. The linearity and step test are also carried out using the signals similar to the PMU testing, mentioned in the IEEE TSS document. The standard deviation of the power amplifier for static test is obtained for few DC voltage values. They are compared with standard deviation of the analog output module of the NI Compact Rio at low voltage. A typical result shows that the standard deviation of the amplifier for 50 V output is 0.0026v and that of the NI

Compact Rio is 0.0017v at 1V output. Large difference in the standard deviation of the amplifier and NI Compact Rio indicates higher noise injected by the amplifier. The response of step and dynamic test signals are also acquired and compared with the mathematically generated signals by super imposition.

The different modules of the NI-cRIO platform are tested for linearity, noise and frequency accuracy for PMU calibration application. The NI-cRIO platform uses "Sine Wave Generator Express VI" for generating dynamic sine wave with varying magnitude, phase and frequency. As the phase and frequency are related to each other (phase is the integration of frequency deviation), hence, the frequency error largely affects the phasor estimation accuracy.
The linearity study reveals that the NI-cRIO platform is largely linear within the working precision up to 4 decimal places. The given settings resulted in typical SNR below 160dB as shown in Figure 2.3.

The phase angle plot of RTDS signal with different frequency and NI-cRIO is shown in Figure 2.4. The target frequency from NI-cRIO platform is 59.9958Hz. The phase angle of the GT-NET PMU, which matches with the NI-cRIO angle (green curve) is RTDS signal having frequency 59.9957568Hz (purple curve). This resulted that the frequency accuracy of the NI-cRIO is accurate upto third decimal place. This frequency accuracy is not sufficient for PMU calibration application and we are actively coordinating with NI to solve this issue.

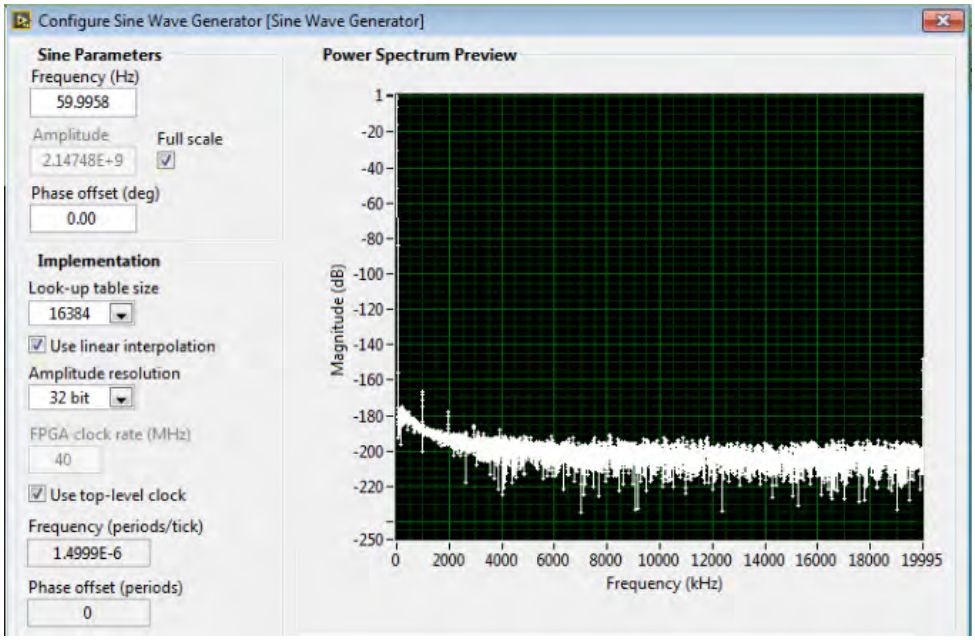

Figure 2.3: SNR of the "Sine Wave Generator Express VI" block in NI-cRIO platform

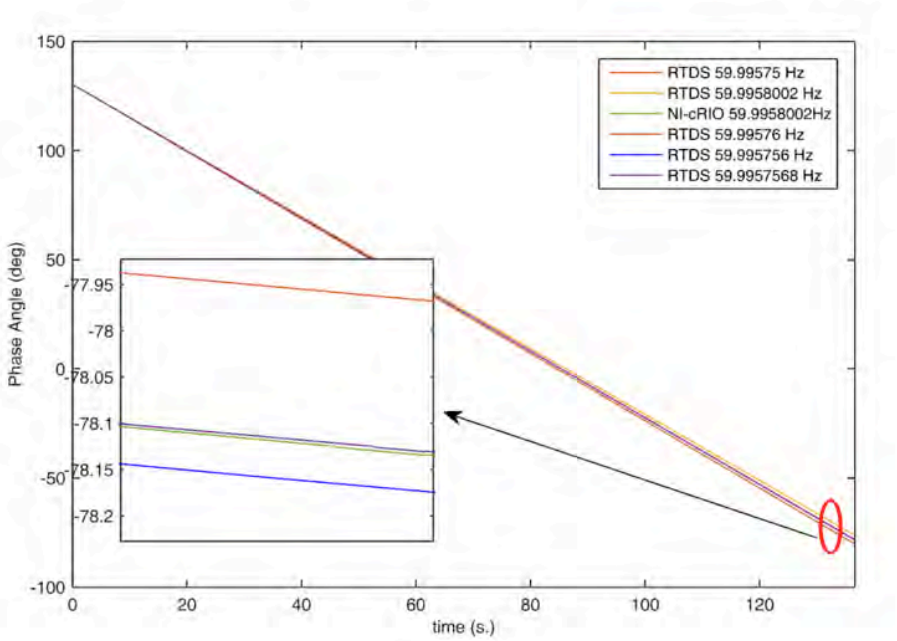

Figure 2.4: Phase angle difference resulted due to the slight difference in frequency.

2.5 Results

A DFR PMU is tested according to the error metric mentioned in for P class PMU. The testing is performed for different PMU phasor reporting rates of 30fps and 60fps. The results of the PMU testing are shown in Table I.

Table 1.1: Summary of PMU testing results

Static Tests				
Error	Magnitude Change (30/60 fps)	Angle Change (30/60 fps)	Signal Frequency Change (30/60 fps)	Harmonic Distortion (30/60 fps)
V Phasor TVE	P	P	F	P
I Phasor TVE	P	P	F	P
FE	P	P	F	F
RFE	P	P	F	F
Test Results (30/60 fps)				
# of Tests	16			
# of Test Passed	10			
Success Rate	62.50%			

The static state test of magnitude change and angle change are complied by the PMU for all the error metric for both 30 and 60 fps. The frequency change test is not complied by the PMU for all the error metric at 30fps and 60 fps. The harmonic distortion test is complied by voltage and current TVE for both 30 and 60fps. The FE and RFE for 30 and 60 fps are also not complied for the harmonic distortion test. The Dynamic test are also performed, but not presented due to space limitation.

The frequency uncertainty of the built-in function is observed to be more resulting in incorrect TVE evaluation. The frequency uncertainty of the generated signal is minimized using the combination of LUT and CORDIC blocks and hence, generating more accurate signals for PMU testing. The harmonic content of the signal generated using proposed method is also observed to be less than the threshold mentioned in the standard. The TVE, FE and RFE of a PMU for static tests are also performed using the proposed method. The proposed method demonstrates that a low-cost computing platform can be used for PMU calibration. The COMTRADE module section presents an alternative method of sinusoid signal generation for PMU calibration for static tests. The accurate signal will be generated by NI module using method provided by the COMTRADE module.

2.6 Summary

The PPA is used for testing PMU using various test signals as mentioned in the IEEE TSS specification. The PPA is used to perform steady state and dynamic testing of the PMU following IEEE TSS and IEEE C37.118.1-2011. The PPA generates the testing sequence and compares the error of the measurement obtained from PMU. The installer of the PPA is launched to deploy the tool in a system and all the steady state and dynamic test sequence are selected to perform the testing. The PPA is expected to perform the testing and generate the report for the magnitude error, phase error, total vector error, frequency error and rate of change of frequency error for all the steady state test. The TVE response time and overshoot under shoot are tested for the step change test of magnitude and phase. The magnitude error, phase error, total vector error, frequency error and rate of change of frequency error are tested for other dynamic test case, which are frequency ramp and amplitude and phase modulation test case.

The error metrics presented in the test report are obtained by running all the static and dynamic test case on a commercial PMU. The error metrics consist of Total Vector Error of voltage signal, Total vector error of current signal, Frequency error and Rate of change of frequency error for all the phase and positive sequence component of voltage and current signal. The TVE response time and magnitude and phase overshoot of voltage signal for magnitude and phase step change test case is also presented in the test report.

3. PMU Lab testing using the PMU Performance Analyzer

3.1 Background

The phasors obtained for different test scenario from the PMU under test is compared with the true phasor using PPA. The PPA gets the time stamps of all the events, which are associated with the change in parameters of analog signals. The PPA calculates the true value of the phasor for the corresponding variation in the analog signal and stores them internally. The user is expected to provide the time stamped phasor from the PDC in a specified .xlsx or .csv data format. The user specifies the PMU class (P or M class) and the PMU reporting rate in the PPA. The user also mentions the list of test cases for which the PMU under test is required to be evaluated. The PPA imports the test PMU phasors from the .xlsx or .csv file and generates the plots of total vector error (TVE), phasor magnitude error (ME) and phase angle error (PE), frequency error (FE) and rate of change of frequency error (RFE), and additional metrics for the dynamic step test results. The PPA also generates the PDF report for all the test cases conducted by the user [11,12].

The purpose of the software is to evaluate the percentage of conformity of the test PMU with the metrics mentioned for different scenario in Standard IEEE-C37.118.1. This process consists of the following steps:

1. The user selects a group of phasor data pertaining to different test cases under which the PMU is tested.
2. The user selects the PMU class and reporting rate for which the test is to be carried out.
3. The user selects the list of tests that has to be conducted from the all the test cases mentioned in StandardIEEE-C37.118.1.
4. The PPA scans the phasor data and reports if it is useable and free of any synchronization errors.
5. The PPA is expected to give the results in the final step.

3.2 Required features of PPA

a) True Value: It is assumed that the test PMU is provided with time synchronized analog signal having parameter variation at different time instants. The signal generator changes one analog signal parameter at a known time instants and continue that parameter for a fixed time interval. The PPA should be able to generate true value of the phasor using the GPS time stamps of the phasor data.

b) The PPA should be able to process the exported.xlsx or .csv data file from the PDC.

c) The PPA should be able to calculate the total vector error (TVE), phasor magnitude error (ME) and phase angle error (PE), frequency error (FE) and rate of change of frequency error (RFE), and additional calculations for the dynamic step test results.

d) The PPA shall have a means of determining the time of arrival of PMU data messages and comparing that time against the message timestamp.

e) The PPA should be able to generate test result documentation and pie-charts of the success rates of the PMU testing

3.3 Validity Checking

If errors are found in the input values, the program should provide an error message to the user that gives the reason for the error and its location in the input file. The locations can be recorded in either a log file or an on-screen window for the user's reference.

3.4 Interface Requirements

Users will interact with the program via a graphical user interface. To use the program, a user selects the data files using the **Browse** button. The file is then checked to determine the valid time range of the data.

The user is expected to either load the pre-saved configuration file or manually change the test configuration and PMU settings (PMU type, and the PMU reporting rate).

Next, the user selects a folder where the output results should be placed. Clicking on the **Compute Results** button causes the analysis to run, during which time the status bar at the bottom of the screen is updated to provide the user with some idea of what the program is doing. Once the analysis has completed, the list of results available for plotting becomes enabled, and the first test result is plotted automatically. The user can then click the **Save plot** button to enter a filename for the exported image [13-16].

Before exiting the program, the user can save the configuration settings used in the analysis process. This file can be loaded in the future, if the user wishes to repeat the analysis with different data sets from different PMU.

3.5 "About" window

An "About" screen is also required, which must display the copyright and contact information.

3.6 Pre-Production Splash Screen

This screen shows, the releases of the software with a disclaimer. It also allows the user to accept or decline the terms contained therein. Acceptance of the terms allows the software to continue launching; declining the terms causes the program to exit.

- **Configuration Management**: Software source code must be stored in a suitable revision control system, such as git or Team Foundation Server. (Note: Source code **cannot** be placed on a publicly available server, such as GitHub.)

3.7 Test Plan

- **Testing Approach**:
  - **Input validity** – Ensure that data files exist before trying to open them. Test program with input files that are improperly formatted, missing required columns, or that contain invalid entries. The user must be provided with a meaningful error message that describes the type and location of the error in the file.
  - **Output validity** – PPA will be tested using RTDS-produced results of GTNET-PMU and compared with the known test results. Documents from Inter Lab Comparison report may be referred for output testing.

3.8 Installation

The software must include an installer executable that installs the program in the user's desired location. In addition, the installer must also check for any missing required prerequisites and prompt the user to install them prior to beginning the installation process.

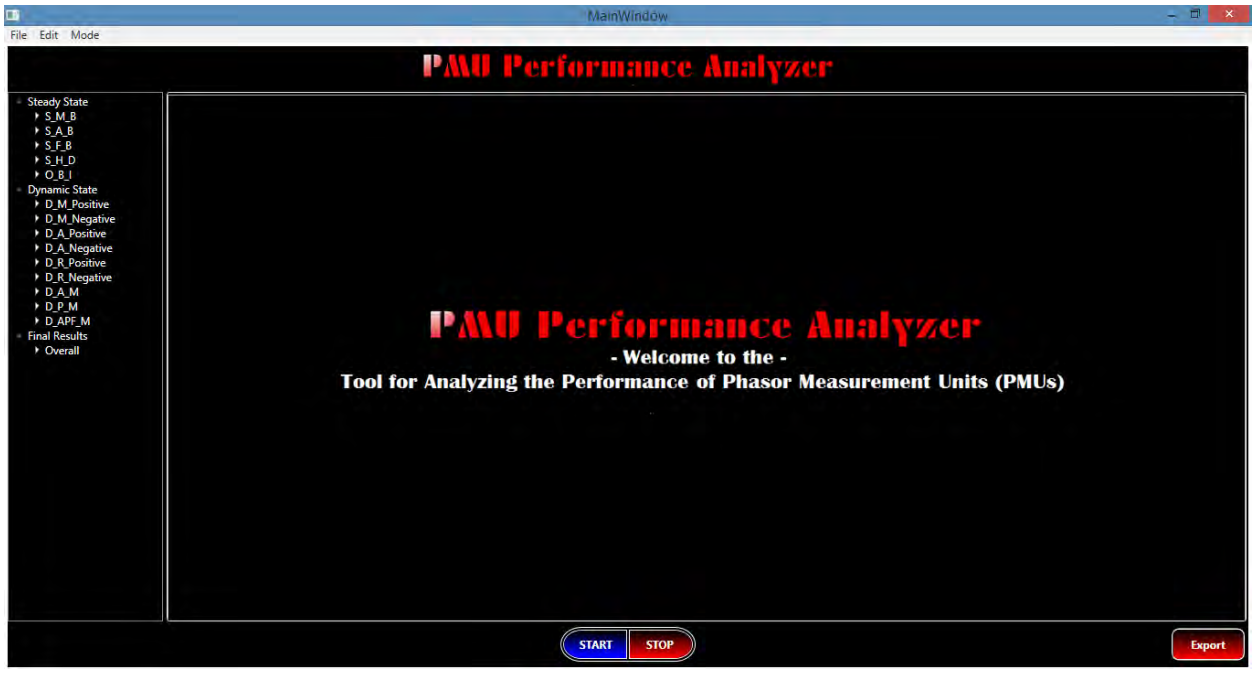

(a)

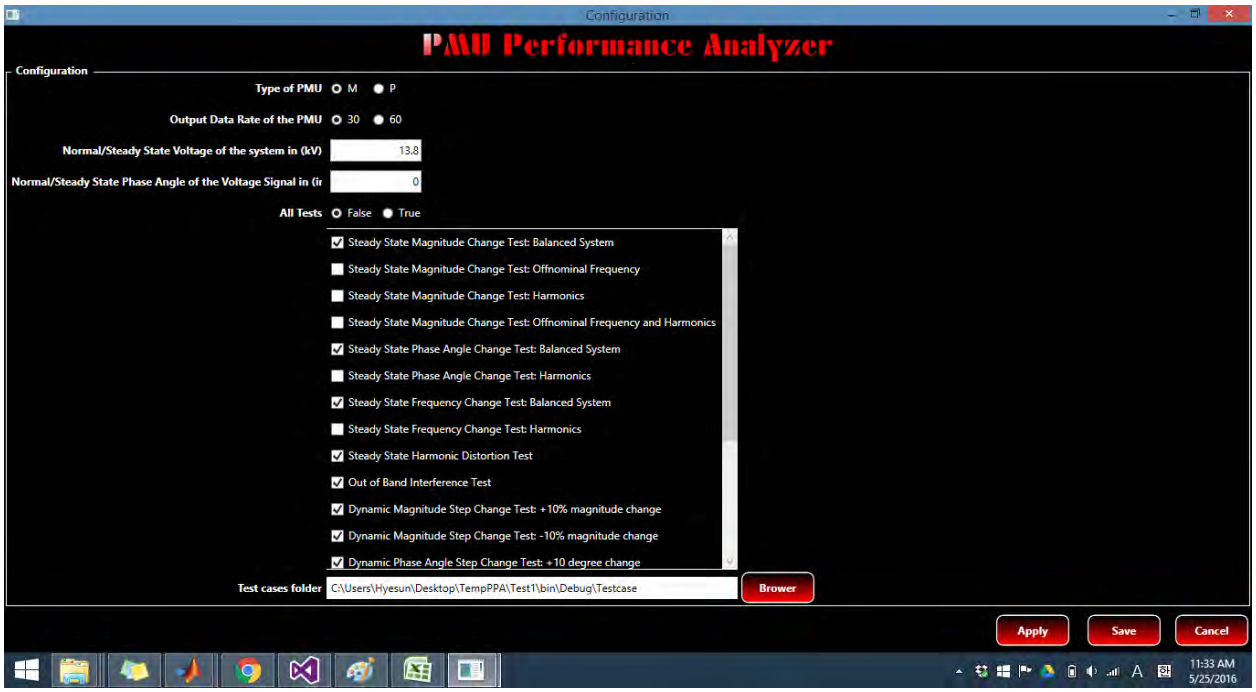
Configuration
PMU Performance Analyzer
Configuration
Type of PMU
M
P
Output Data Rate of the PMU
30
60
Normal/Steady State Voltage of the system in (kV)
13.8
Normal/Steady State Phase Angle of the Voltage Signal in (r
0
All Tests
False
True
Steady State Magnitude Change Test: Balanced System
Steady State Magnitude Change Test: Offnominal Frequency
Steady State Magnitude Change Test: Harmonics
Steady State Magnitude Change Test: Offnominal Frequency and Harmonics
Steady State Phase Angle Change Test: Balanced System
Steady State Phase Angle Change Test: Harmonics
Steady State Frequency Change Test: Balanced System
Steady State Frequency Change Test: Harmonics
Steady State Harmonic Distortion Test
Out of Band Interference Test
Dynamic Magnitude Step Change Test: +10% magnitude change
Dynamic Magnitude Step Change Test: -10% magnitude change
Dynamic Phase Angle Step Change Test: +10 degree change
Test cases folder
C:\Users\Hyesun\Desktop\TempPPA\Test1\bin\Debug\Testcase
Brower
Apply
Save
Cancel
11:33 AM
5/25/2016

(b)

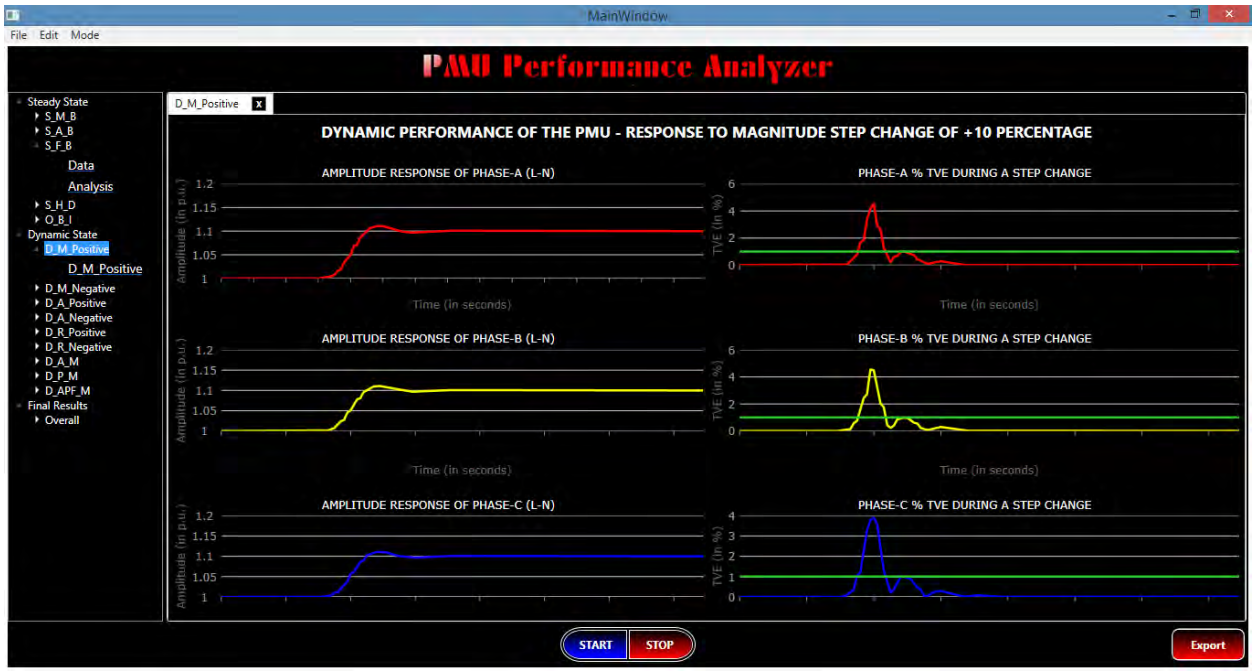
MainWindow
File
Edit
Mode
PMU Performance Analyzer
Steady State
S_M_B
S_A_B
S_F_B
Data Analysis
S_H_D
O_B_I
Dynamic State
D_M_Positive
D_M_Positive
D_M_Negative
D_A_Positive
D_A_Negative
D_R_Positive
D_R_Negative
D_A_M
D_P_M
D_APF_M
Final Results
Overall
D_M_Positive
DYNAMIC PERFORMANCE OF THE PMU - RESPONSE TO MAGNITUDE STEP CHANGE OF +10 PERCENTAGE
AMPLITUDE RESPONSE OF PHASE-A (L-N)
PHASE-A % TVE DURING A STEP CHANGE
AMPLITUDE RESPONSE OF PHASE-B (L-N)
PHASE-B % TVE DURING A STEP CHANGE
AMPLITUDE RESPONSE OF PHASE-C (L-N)
PHASE-C % TVE DURING A STEP CHANGE
Amplitude (in p.u.)
TVE (in %)
Time (in seconds)
START
STOP
Export

(c)

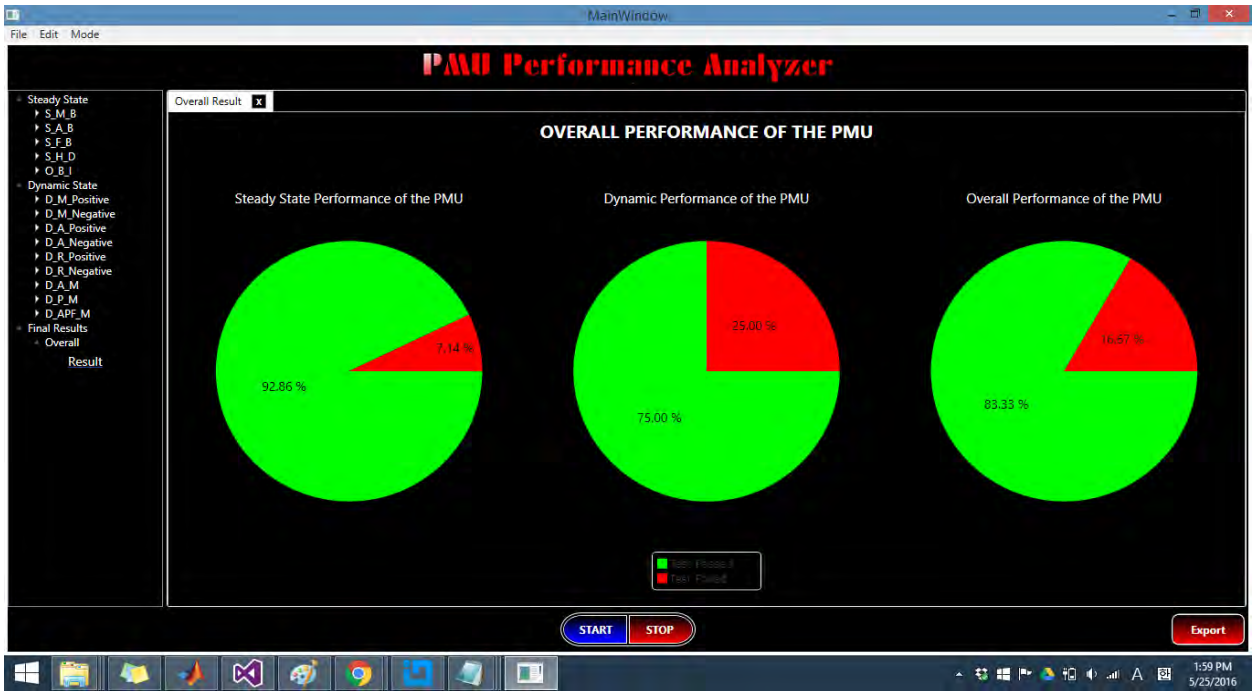

(d)

Figure 3.1 Installation and results reporting of the PMU performance analyzer

3.9 Highlights

- IEEE C37.118.1-2011 compliance test for P (Protection)-type PMU has been carried out for a 2 PMU device using PPA (PMU Performance Analyzer) s/w developed by WSU (Washington State University).
- The delay time, frequency response time and ROCOF in *dynamic* step change tests are carried out using multiple simulations run.
- For *steady-state* signal magnitude (voltage and current) tests, FE and RFE values were recorded for additional measures, although they are not required for IEEE compliance tests. DFR_PMU passed all of those additional tests.
- Test Procedures:
  - The PPA internally generates the true phasor and also utilizes PDC (Phasor Data Concentrator) to store the PMU data during the simulation of test cases. The PMU data collected from the PDC are in turn to be run and analyzed by PPA s/w and graphs and report are auto-generated instantly.

Interfacing PPA with NI CRIO platform

The time stamp of the change in signal parameter in NI-cRIO platform is required by the PPA for generating the true phasor.

The overall architecture of the lab with NI-cRIO and PPA is shown in Figure 3.2. The Labview system generates a log file, which contains the time stamp of the instances when signal parameter changes. The PPA read this log file and internally generates the true phasor.

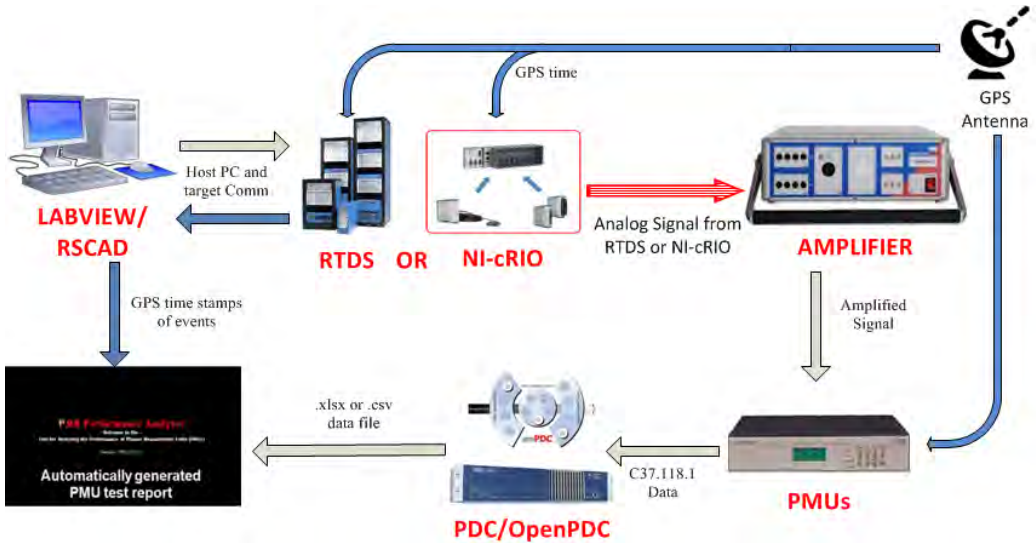

Figure 3.2: PMU Testing Lab

3.10 Test Results

Results of steady state performance of PMU - magnitude change: balanced system

Status of time synchronization of the ideal pmu & the test pmu: The test pmu is in perfect time synchronization with the ideal pmu.

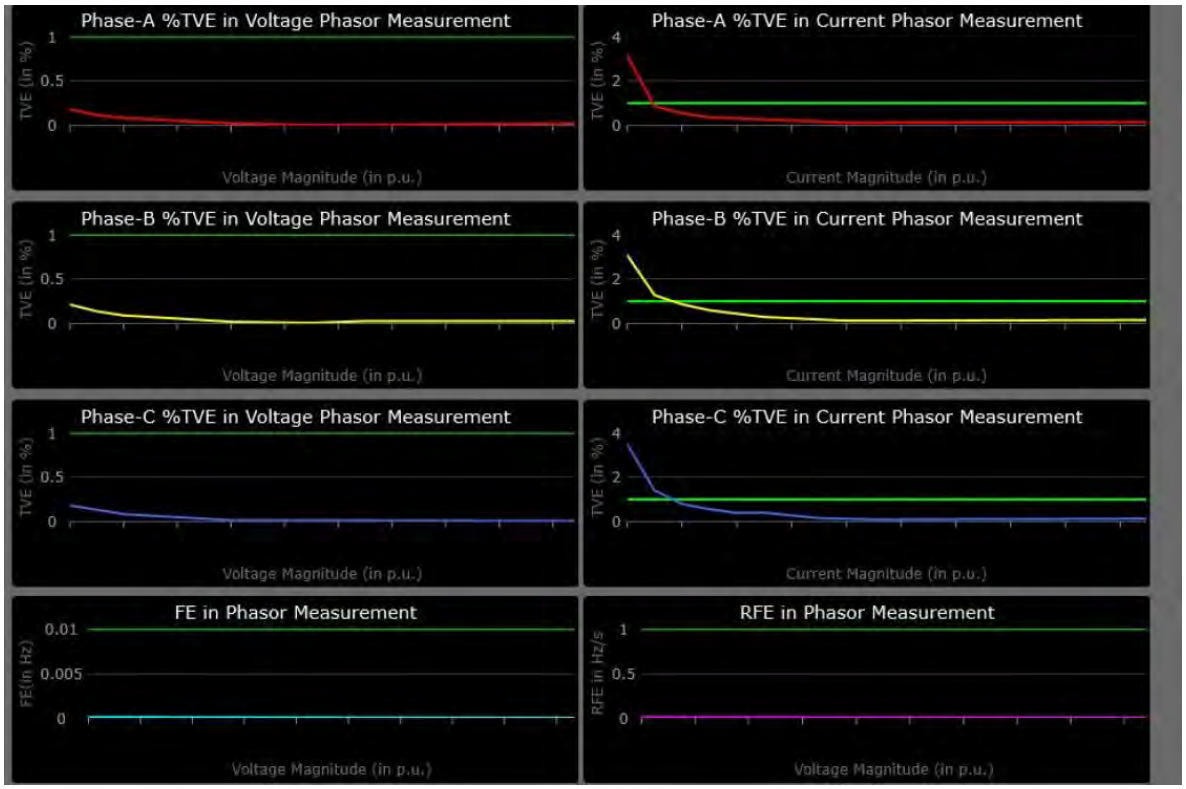

Figure 3.3: Magnitude Change for balanced system

Additional results are available in Appendix A.

3.11 Summary

This chapter presents the need and procedure for testing synchrophasor devices and applications before the field deployment. The specification of the testing equipment required for the PMU testing lab is discussed in detail. The architecture of the test bed and the features of the software called PPA used for automatic PMU testing is presented. The successful implementation of PMU testing performed in the Southern California Edition (SCE) using PPA is presented. The result of the PMU testing shows that the compliance of the standard for 30 fps and 60 fps can be different for some of the test scenarios.

4. COMTRADE Module

4.1 Introduction of COMTRADE Module

The COMmon format for TRAnsient Data Exchange for power systems (COMTRADE) module is a set of integrated equipment, which includes a local host computer, compactRIO system, and amplifier. The local host computer has faster data processing rate, which responses for reading, scaling and preparing a large amount of data. The cRIO system is made up of a low cost National Instrument cRIO with a GPS that is used to generate accurate analog output signals. Using the COMTRADE input module is a suitable algorithm, that can convert digital data source to accurate and stable analog output signal for further use by PMU testing, remotely PMU testing or further remotely RAS testing. An amplifier in the system is used to amplify and restore the voltage amplitude to original scale. The architecture of system algorithm is shown in Figure 4.1.

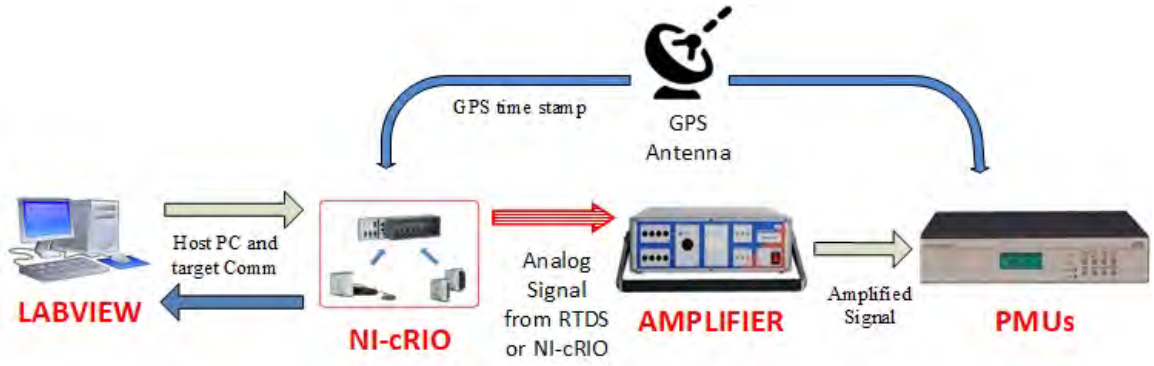

Figure 4.1: COMTRADE Module Algorithm Architecture

The analog output signal is generated using a reference COMTRADE file by Direct Memory Access (DMA) First In First Out (FIFO) method with GPS PPS correction for increased accuracy. A DMA channel consists of two FIFO buffers: one on the host computer and one on the Field-Programmable Gate Array (FPGA) target. After creating the DMA FIFO, the data can be read from COMTRADE file and write into buffer, depending on programming block diagram code on the host PC side, transfer using DMA channel to FPGA side, then read and processed by the FPGA. The DMA FIFO working illustration is shown as below.

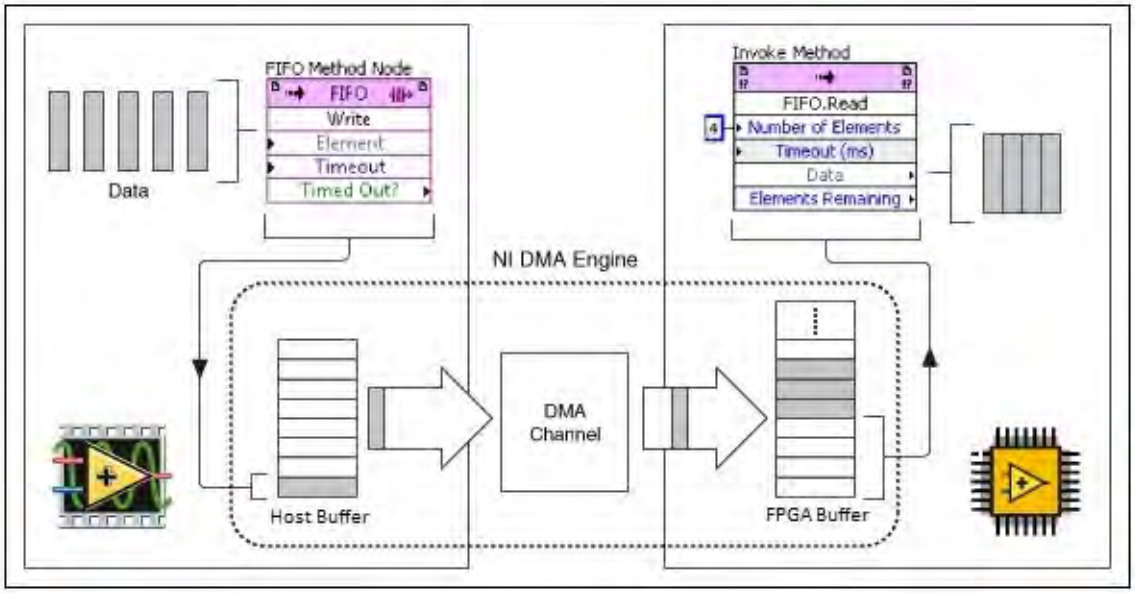

Figure 4.2: DMA FIFO Working Diagram

4.2 Work Statement of Host Computer VI

COMTRADE file includes digitally sampling measurement DATa file (.dat) and signal information ConFiGuration file (.cfg). On the Host computer side, 20 second length buffer is created depends on data sampling rate by using an invoke method. Labview host VI firstly reads data file from assigned path, shrinks the data amplitude, and shifts to FiXed Point (FXP) (±, 20, 5) that is FPGA specify available resolution. The FXP notation representation indicates (Sign, Bit length, Integer length) and allows for minimal approximation error. Then transfers prepared data through the DMA channel to cRIO-9068. A local host VI example is shown in Figure 4.3.

Figure 4.3: Local Host VI Example

In Figure 4.3, highlight blocks are:

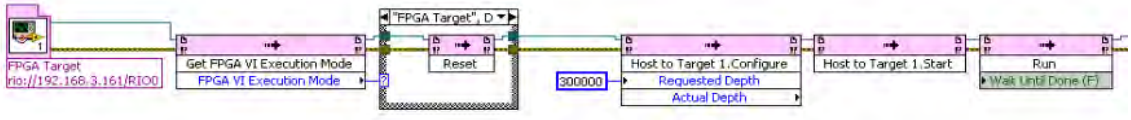

*Block1: Initialize FPGA VI and Create Host Buffer Using Invoke Method

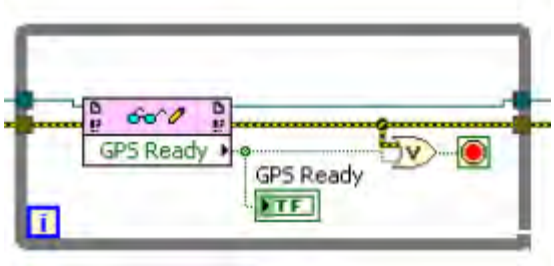

*Block2: Check GPS Status

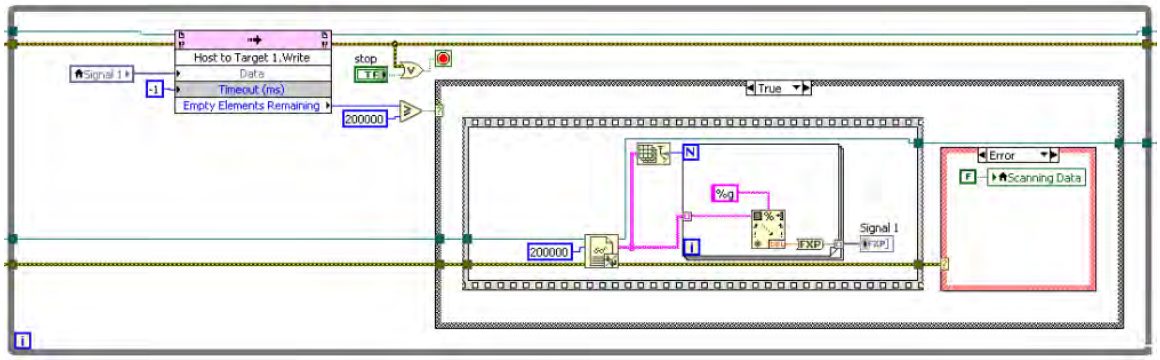

*Block3: Invoke Method Write and Transfer Data to DMA

The host VI is communicating with FPGA VI continuously. In this example host VI, it firstly initialized the FPGA VI, and then prepared host buffer for DMA transferring as *Block1. When the host VI checked that GPS signal was ready and stable from FPGA VI as *Block2, it would immediately warp data in buffer and send them to the FPGA by DMA channel using invoke method as *Block3. A logic flow chart of host VI work is shown as below.

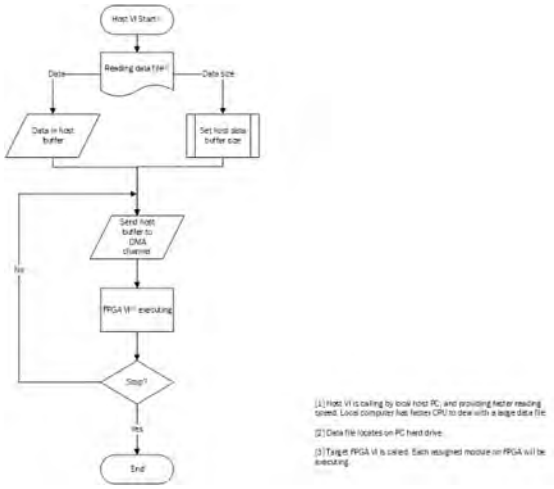

Figure 4.4: Host VI Flowchart

4.3 CompactRIO System and FPGA VI

CompactRIO System is one important part of the COMTRADE module, which important, it includes a cRIO-9068 compactRIO controller, NI-9467 GPS C series synchronization module, and a NI-9264 C series voltage output module. The assembled entity compactRIO system is shown in Figure 4.5.

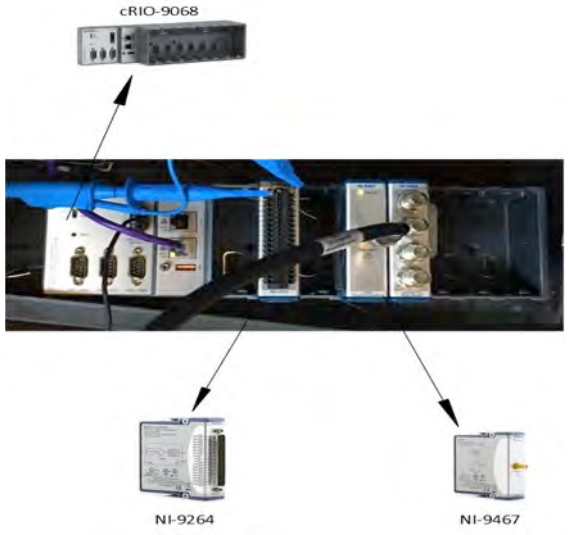

Figure 4.5: Assembled compactRIO System

In this part of the system, cRIO-9068 is embedded controller that contains a programmable Zynq-7020 FPGA that provides 2 slots for a GPS module and a digital-to-analog converter (DAC) module. The NI-9467 module provides accurate time synchronization for the compactRIO system, which be used for calibration of FPGA oscillator in every GPS Pulse-per-second signal (PPS), and accurate data time stamping, thus to get reliable analog signal output. The NI-9264 is a simultaneously updating analog output module. It contains 16 DAC channels, which can be used to generate ± 10 V voltage.

The programmed embedded FPGA is based on Labview FPGA VI to read data from DMA buffers. The NI-9264 analog output (AO) module then samples the resulting values at an assigned update rate to match the AO module at a base 60 Hz frequency. Meanwhile, the GPS will correct the oscillator depends on its time stamp. A Labview FPGA VI logic flowchart is shown in Figure 4.6, and an FPGA VI Block diagram is shown in Figure 4.7.

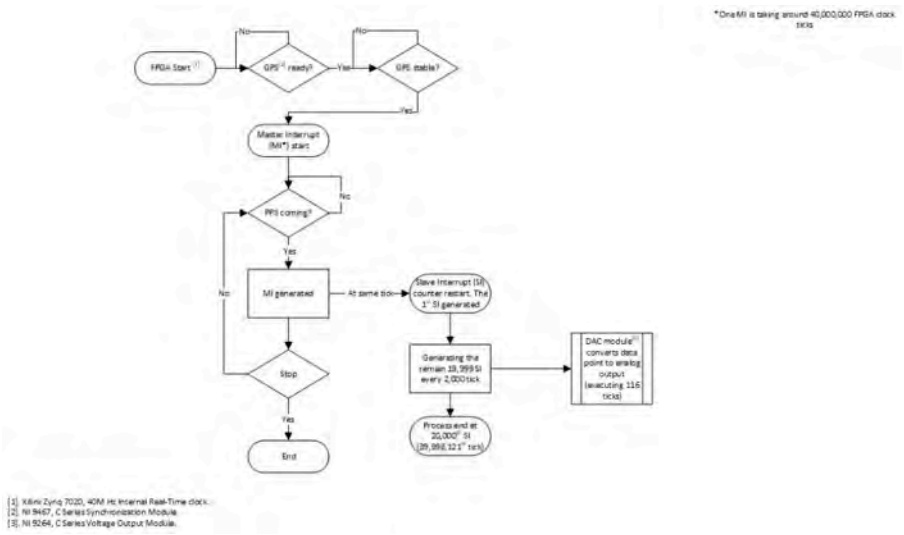

Figure 4.6: FPGA VI Flowchart

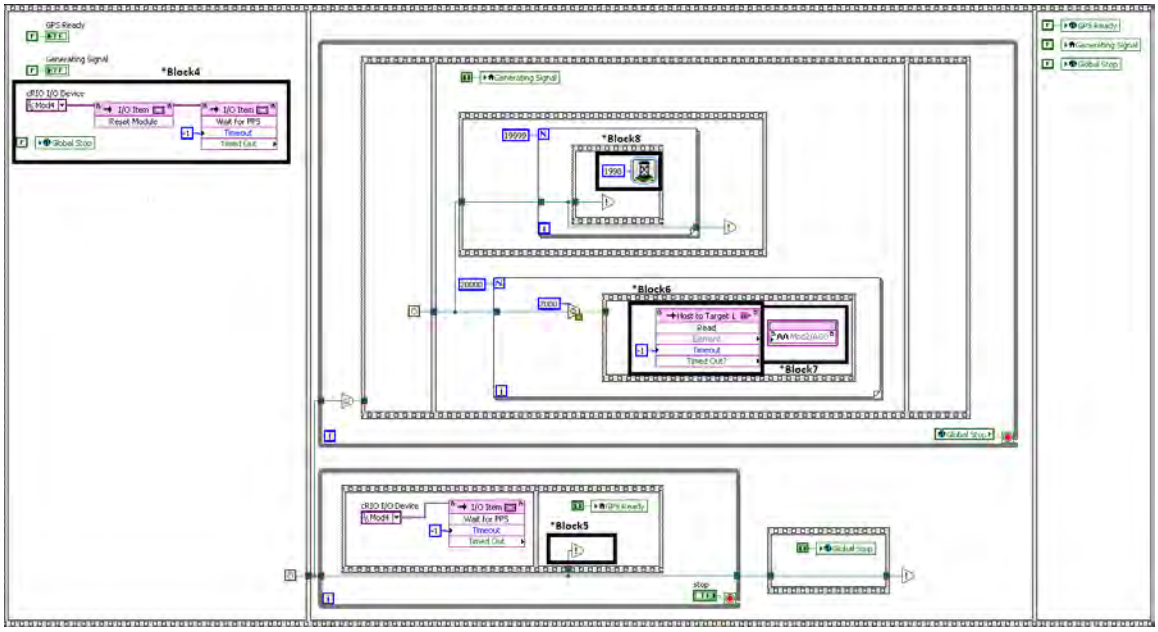

Figure 4.7: FPGA VI Block Diagram

In Figure 4.7, highlight blocks are:

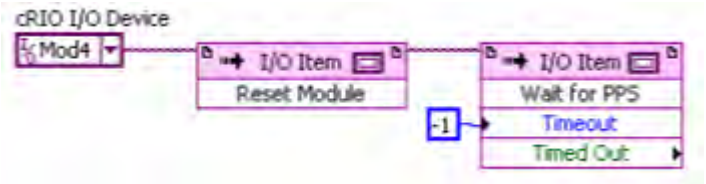

*Block4: Initialize GPS Module by FPGA I/O Method Node (NI-9467)

*Block5: Generate Interrupt & Waiting for Interrupt

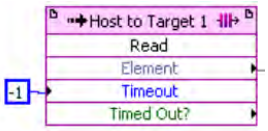

*Block6: Read FIFO Method Read Data from DMA Channel

*Block7: FPGA I/O Node - Analog Output (DAC NI-9264)

*Block8: Wait Express VI (Unit: ticks)

After data buffer transfer to FPGA target, the FPGA waits for GPS initialize as *Block4, and then generates interrupt as *Block5 to nested loop to read an element from buffer one by one in every 2,000 ticks. Labview FPGA VI read data buffer from the DMA channel using read FIFO method as *Block6, and send each element to the DAC module to generate analog output by the FPGA I/O Node function as *Block7. In this example, data sampling rate was 20,000 Hz. According to the 40 MHz top-level clock, to generate 60Hz frequency signal, the buffer-reading rate was ideally set at 2,000 ticks per element. Actually, the reading, executing speed of FPGA is one tick per element, and for loop executing speed is one tick per cycle. Therefore, wait clock VI was set to 1,998 ticks (*Block8) to get appropriate performance. Since the first PPS generated by I/O item function has deviated, and will cost a tiny oscillator error, the GPS module reset and initialized at beginning, thus to skip those errors and get further steady time stamps.

4.4 Error Correction by GPS

The NI cRIO-9068 has a 40MHz top level clock. According to tests, the internal clock cannot generate a constant number of ticks during each GPS PPS, since the instability of FPGA oscillator. The top-level clock has a timing accuracy of 5ppm.The missed or additional tick, causes a potential drift of 0.000299998 Hz. Therefore, adding GPS PPS interrupt during the signal generating can help to increase the signal accuracy. The algorithm and FPGA working time line is shown in Figure 4.8 as below.

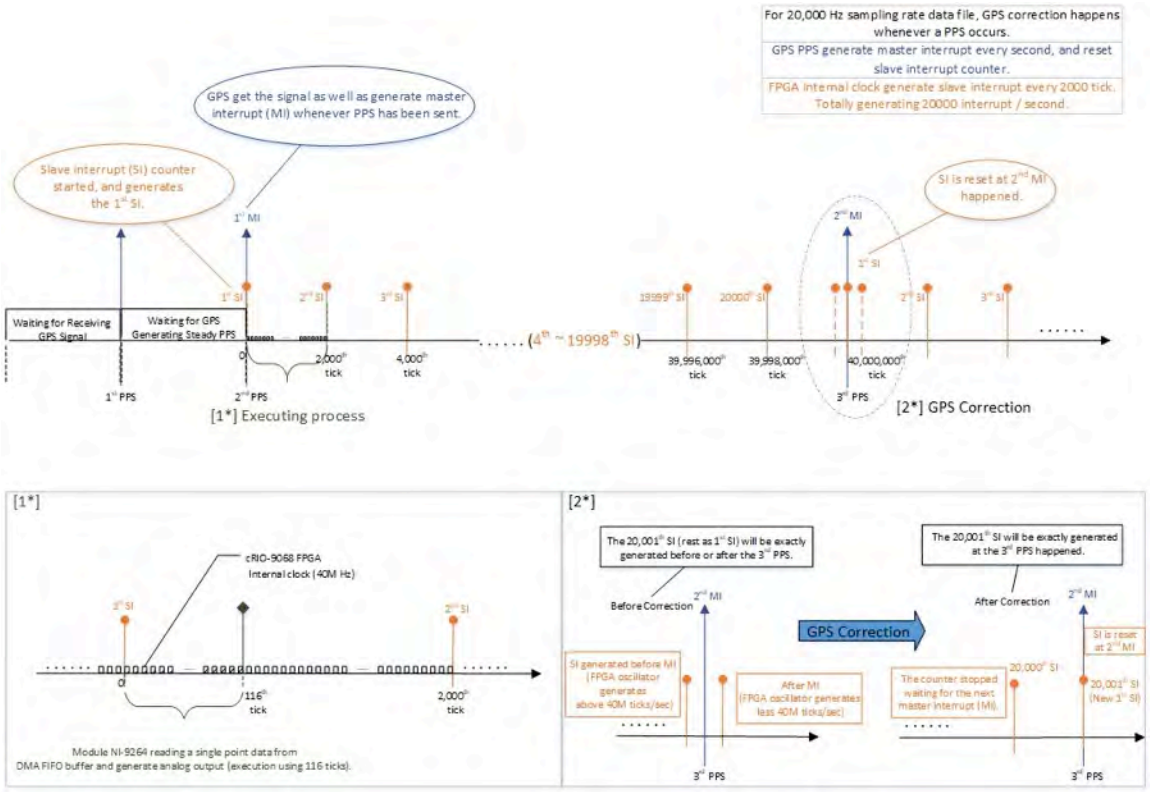

Figure 4.8: GPS Correction Algorithm

4.5 Results

The synchrophasor standard C37.118.1-2011 mention that phase error of 0.01 radian results in 1% TVE provided there is no error in the magnitude. The standard C37.118.1a-2014 also mentions that the test uncertainty ratio (TUR) of the calibrator must be greater than 10, which implies that the phase angle of the calibrator must be at least 10 times more accurate than the threshold value of 0.01 radian. The IEEE TSS mentions that most of the static test is 5 sec long along. On this basis, the frequency accuracy of the calibrator must be greater than 0.01/ (2pi 10) = 0.000159 Hz. The measuring frequency accuracy of a sinusoidal signal in the range of 0.00015 Hz, require a spectral resolution of 0.00007Hz. The frequency of interest of the sinusoid is 50Hz or 60Hz, which mandates that the sampling frequency must be more than the Nyquist rate. The sampling frequency for this study is fixed at 200Hz and the spectral resolution selected is 0.00001Hz. The length of the sinusoid required for this study is given by

$$L = Fs/R = 200/0.00001 = 20000000$$

Where Fs is the sampling frequency of the oscilloscope, R is required frequency resolution and L is the length of signal required for spectral estimation. The signal length required is around 27 hours of data at 200Hz sampling frequency.

The lower limit of FE specified for static state tests in C37.118.1-2011 and C37.118.1a-2014 is 0.005Hz, which require the calibrator to be accurate up to 0.0005 Hz, with a TUR of 10. The

spectral resolution of 0.00001 Hz is also sufficient to measure the frequency accuracy of the calibrator at 0.0005 Hz range.

The synchrophasor standard C37.118.1-2011 also mentions that the Total Harmonic Distortion (THD) of the calibrator must be less than 0.2% of the fundamental. The upper limit of frequency used for evaluating THD is not specified in C37.118.1-2011, which is limited to 50xbase freq, where base frequency is the fundamental frequency in Hz.

The step change test mentioned in C37.118.1-2011 requires the magnitude of the signal to change by 10% of the nominal value each step. The magnitude of the calibrator need to be accurate up to 1% with a TUR of 10. This demands that the minimum magnitude resolution of the analog output of the calibrator is accurate up to 0.5% at around 50% of the range of the calibrator output. For a calibrator output of ±10 volt and 16-bit resolution, the magnitude resolution at 50% of the output is 0.0015%, which is sufficient to detect accuracy of 0.5%.

The frequency accuracy of the proposed method is demonstrated in Figure 4.9, in which the spectral estimation of the fundamental component is shown. The spectral resolution for the fundamental component is fixed at 0.00001 Hz, which is obtained using 27hours of data using the Yokogawa DL850 ScopeCorder. The fundamental frequency of the sinusoid evaluated using Labview built-in function is 59.99538Hz and that of the CORLUT method from previous work is 60.00211Hz and proposed method is 59.99971946 Hz with error of ±0.00001Hz. However, the bandwidth of the fundamental component having magnitude more than 0.002 p.u. using CORLUT is 0.000222Hz, while that of Labview built-in function 0.00273Hz and proposed method is 0.00066Hz. This means that the fundamental frequency using Labview built-in function varies over a wide range over cycle to cycle, whereas the clock correction using CORLUT and the proposed method reduces the swing of the fundamental frequency component to a narrow band and improves the frequency uncertainty of the fundamental component over each cycle.

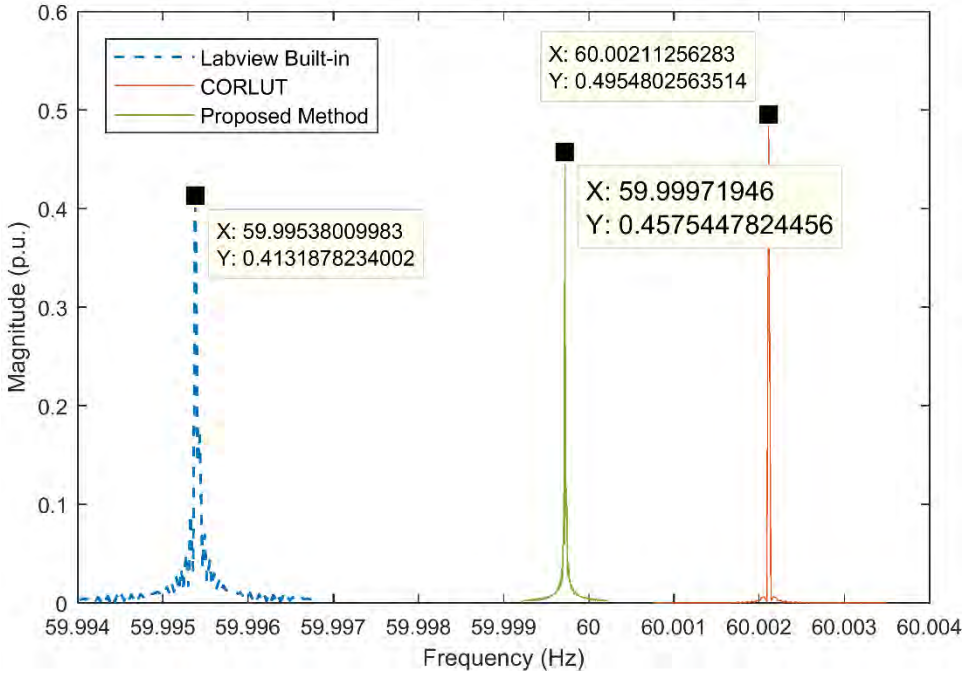

Figure 4.9: Spectral estimation of fundamental component

The spectral estimation of harmonic component of the proposed method is shown in Figure 4.10. The THD of the proposed method is evaluated as 8.8228e-07%, which is less than the threshold value of 0.2% mentioned in the standard.

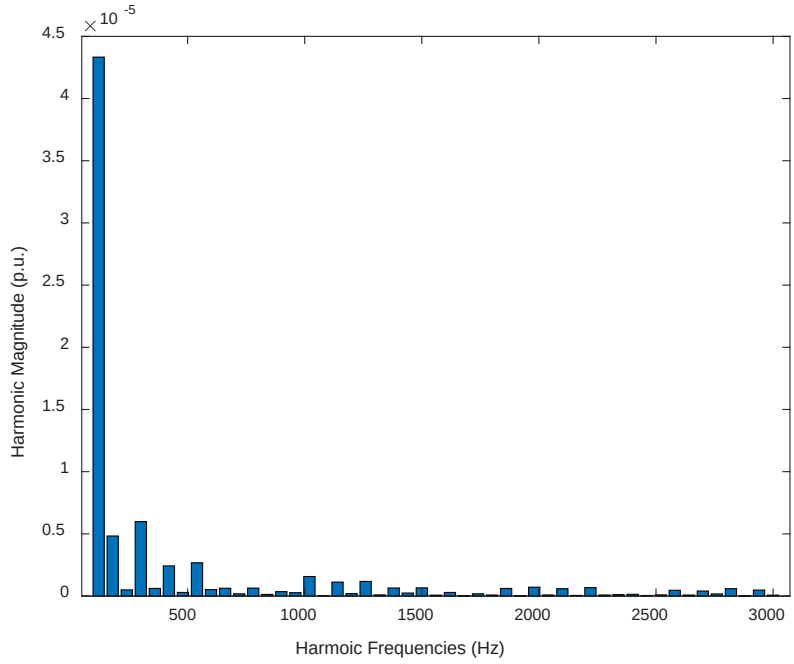

Figure 4.10 Spectral estimation of harmonic frequencies

4.6 Summary

The PMU testing system is developed to ensure the security, accuracy, and reliability of synchrophasor based applications in the power grids. The PMU testing method aims at a better solution for PMU calibration, and involves the implementation procedure for PMU testing, which mentioned in IEEE TSS. The necessary devices can be used for PMU testing includes analog signal generated by RTDS, GPS time stamps, low cost NI-cRIO, Phasor Analyzer (PPA) software. According to the simulation, analog output from RTDS, the time stamped phasors from the PMU are archived by the Phasor Data Concentrator (PDC), and then fed to the PPA software for comparison with the time stamped true phasor. Then the PPA generates a detailed report for all the test cases performed by the user. The Frequency Error (FE) and Rate of Change of Frequency Error (RFE) are the additional performance criteria mentioned in this standard for the performance evaluation of the PMUs.

For the PMU Testing Lab, outcome was all the necessary hardware and software infrastructure for carrying out the performance evaluation of PMUs under test, and details of the PMU testing lab setup.

For the PMU Lab testing using the PMU Performance Analyzer (PPA), the developed software evaluates the percentage of conformity of the test PMU with the metrics mentioned for different scenario in Standard IEEE-C37.118.1.

For the Comtrade Module part, it is one update and accurate method for NI-cRIO setup for PMU testing lab.

5. Erkios Middleware Software

5.1 Erkios software for end-to-end testing

The regular testing of equipment installed in the field is desirable because no more testing is carried out during the lifetime after initial testing and installation. Hence, correct working of these equipment's in case of a triggering event is uncertain after 5-10 years of commissioning. Therefore, in-field remote testing of equipment's becomes necessary to guarantee that they perform accurately at all times and will not be affected by any sort of software/hardware error that develop with time or hidden failure that was not captured before commissioning. In view of this, Erkios is developed for end-to-end and in-field testing of mission critical systems and equipment. The Erkios is a middleware, which is currently developed for in field-testing of PMUs and Remedial Action Schemes (RAS). The Erkios is capable of testing the field equipment, communication network and control logic without the need for de-commissioning. The Erkios is capable of remotely managing such test over a large number of substations [17-18].

In the Erkios architecture as depicted by Figure 5.1, there are four important modules or building blocks: Central Test System (CTS), Local Test System-Initiator (LTI), Local Test System-Collector (LTC) and Operation Wide-Area Network (or Op WAN). The CTS plays the role of a coordinator during tests. It is responsible for the creation of a test signal that consists of data regarding the test, transmitted to other modules. LTI is responsible for disabling the PT/CT inputs to sensor and disabling the actuator (or breakers) before the testing starts. After the testing is complete, it enables the sensor and actuator for normal operation. LTC is responsible for collecting the control actions and measurement data, and forwards it to the CTS. Op WAN transmits data between CTS, LTI, and LTC. Signal Generator and Amplifier are used to convert the digital signal sent out by LTI into analog signals suitable for the sensor inputs.

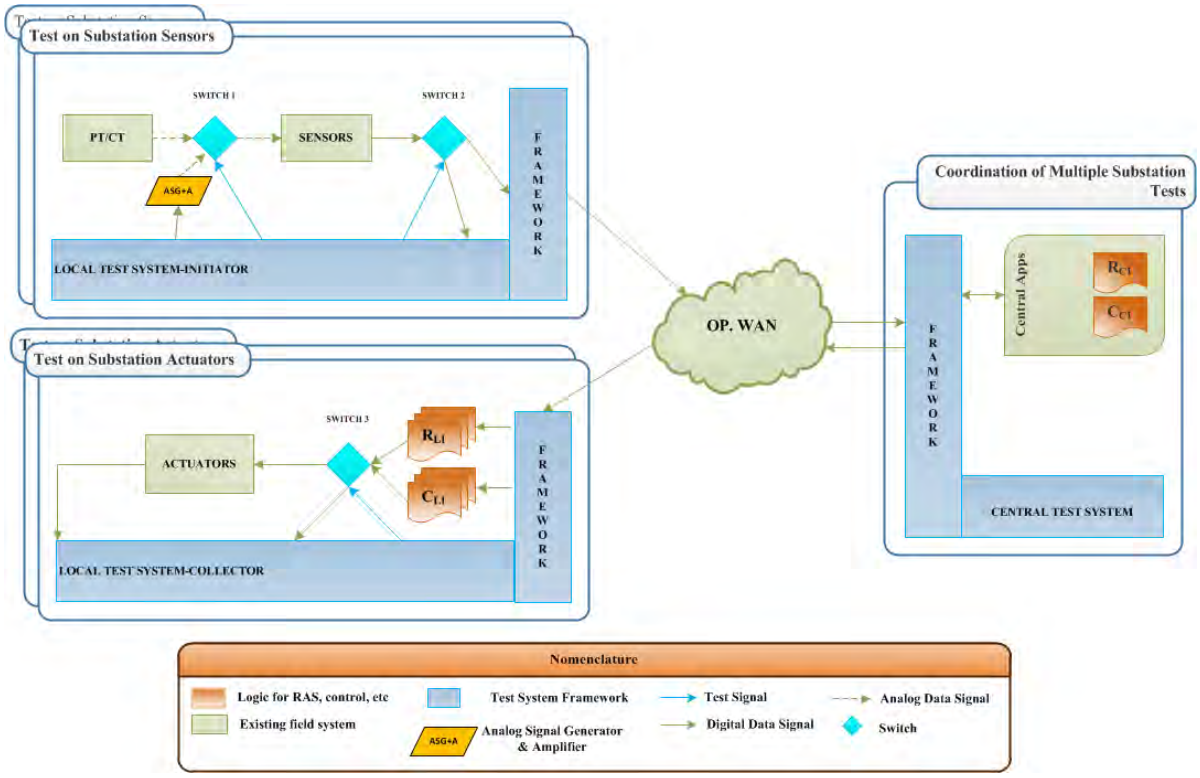

Figure 5.1: Erkios architecture for remote resting

Remote PMU testing is done by the middleware ERKIOS, which consists of several modules. This document provides some requirements for having a middleware glue layer to perform PMU testing. To ensure that the requirements for performing IEEE standardized tests on PMUs are met by ERKIOS. This document specifies the salient features required for designing middleware to test PMUs in a standard compliant manner. The lists of modules required in the substation for remote PMU testing are mentioned in "Specification and Middleware Requirements for Substation implementation with PMU". It is assumed that device specific requirements will be known and understood by the operator, and will subsequently be entered correctly at configuration time. The ERKIOS substation located modules, in specific the LTS initiator and collector will interact with PMUs.

5.2 Functional Requirements for ERKIOS

The following features need to be incorporated in the middleware to carry out the remote PMU testing:

a) Maximum Allowable time- The time taken by the test process and the test network should not be included in the PMU latency reporting

b) Break time between two tests- There are several tests mentioned in the IEEE Synchrophasor TSS, which takes sufficiently long time (in the range of minutes). The starting of such test will affect the performance of the EMS software running in the control centers. It is possible to break longer test scenario in multiple parts such that the LTI and Programmable Router can be coordinated to transmit some measurements from CT/PT to

make least effect on the EMS software. The EMS software takes several seconds to update the screen. Hence, the switching between PMU inputs from CT/PT to Signal Generator could be optimized to make the PMU testing process transparent to the EMS software in the Control center.

c) Authentication- The different modules in the middleware should communicate with the test PMU, Programmable Router and other modules using secure communication protocol.

d) Fault Tolerant- The middleware should have fault tolerant features within its own modules and the test bed. The crashing of any client and servers of the different components in the substation need to be handled during testing by abort, restart or notifying operators for human intervention.

e) Database management- The middleware is designed to test PMUs installed in multiple substations. The CTS interaction with the database for archiving the test results of multiple PMU and maintains a log of the testing carried out at each PMU.

f) Mask heterogeneity – The middleware should abstract many of the procedural steps of testing a device down with a uniform interface independent of device types. Once an LTS is setup for the devices in a substation an operator should be able to test any of them by following a simple process.

5.3 Validity checking

If errors are found in the input values, the program should provide an error message to the user that gives the reason for the error and its location in the input file. The locations can be recorded in either a log file or an on-screen window for the user's reference. ERKIOS should be able to check that the settings are within an expected sane interval of values.

5.4 Interface Requirements

An operator should be able to enter required information through a configuration window. A complete list of device types and necessary rules for each specific device as well as the overarching type should be enterable by the operator and validated by the ERKIOS central test system.

5.5 Security, Availability, Reliability, Recoverability and Business Continuity

Components should communicate only to authenticated ERKIOS modules. Only an authorized trained operator should be able to update device specific settings.

5.6 Maintenance and Support

It is anticipated that WSU personnel will maintain the software for the next two years.

5.7 Quality Plan

- **Change Control**: Changes in the ERKIOS architecture are to be done based on the feedback of the PSERC industry members.

- **Configuration Management**: Software source code must be stored in a suitable revision control system, such as git or subversion or Team Foundation Server. (Note: Source code **cannot** be placed on a publicly available server, such as GitHub.)

5.8 Test Plan

- **Testing Approach**:
  - **Input validity** – Ensure that data files exist before trying to open them. Test program with input that is improperly formatted, missing required variables, or that contain invalid entries. The user must be provided with a meaningful error message that describes the type and location of the error.
  - **Output validity** – Devices should be confirmed to function with the settings applied.

5.9 Installation

The software must include an installer executable that installs the program in the user's desired location or be able to run as a portable app from any location. In addition, the installer must also check for any missing required prerequisites and prompt the user to install them prior to beginning the installation process.

This document is the specification for the ERKIOS signal interface. It describes the requirements for data input from RAS test suites. ERKIOS v0.2 supports data interfacing from a user to the internal RAS simulator. Going forward, ERKIOS will interface with third party RAS test suites.

5.10 Purpose

To provide an outline on how ERKIOS will be designed to connect into existing simulation tools aware of the grid's network of devices. By using a third party tool, the feature set of ERKIOS is instead focused on the distributed test initiation and collection process.

5.11 Need for this specification

An operator will use the RAS test suite to generate analog or digital signals that is expected to trigger a specific action from a RAS controller deployed into a substation. This standard action and signal will be passed to ERKIOS, along with a source of the signal. The information required for ERKIOS to formulate the test cases is listed under this section of the specification.

5.12 Related Standard

The requirements for specific devices such as PMU and PPA testing can be found under the respective sections. Usage of this data at the substation is mentioned in "Requirement specification for alternative interfacing architecture with RAS at Substation"

5.13 Assumptions

A standalone test suite exists with knowledge of the grid assets that can accurately simulate the complete impact of specific signals when measured at any given device. The RAS test suite should be able to output, either directly to ERKIOS or through the actions of an operator.

5.14 General System Description

5.14.1 System Context

The software is non-self-contained; it must interact with test suites or provide contextually clear prompts for an operator to bridge the gap.

5.14.2 System Environments and Modes

The prototype software will be used in a research environment under normal operating conditions.

5.14.3 User Characteristics

It is assumed that users will be comfortable performing basic computer tasks such as locating and selecting files saved on disk. In addition, users are assumed to be capable of operating the testing utility with a high level of proficiency, so as to be able to incite actions at specific devices desired to be tested.

5.14.4 Operational Scenarios

Only a “normal” operational mode needs to be supported.

5.15 Functional Requirements for ERKIOS

The ERKIOS local test system should be able to transfer a signal representation into an appropriate analog or digital signal generator for the destination device in the substation via the Local Test System Initiator (LTS-initiator)

Device designations are common names recognized by ERKIOS to map to a specific device located at the substation, for example by hostnames. Additionally, ERKIOS local test systems must understand devices common names and possess knowledge of the device type and input format so as to be able to perform the appropriate signal switchover from real to test signals.

ERKIOS should seamlessly transition from the specified origin, source input on the destination test device and pass the test signal.

The ERKIOS local test system collector can intercept the resulting action before it is performed and can compare it to the expected resulting action.

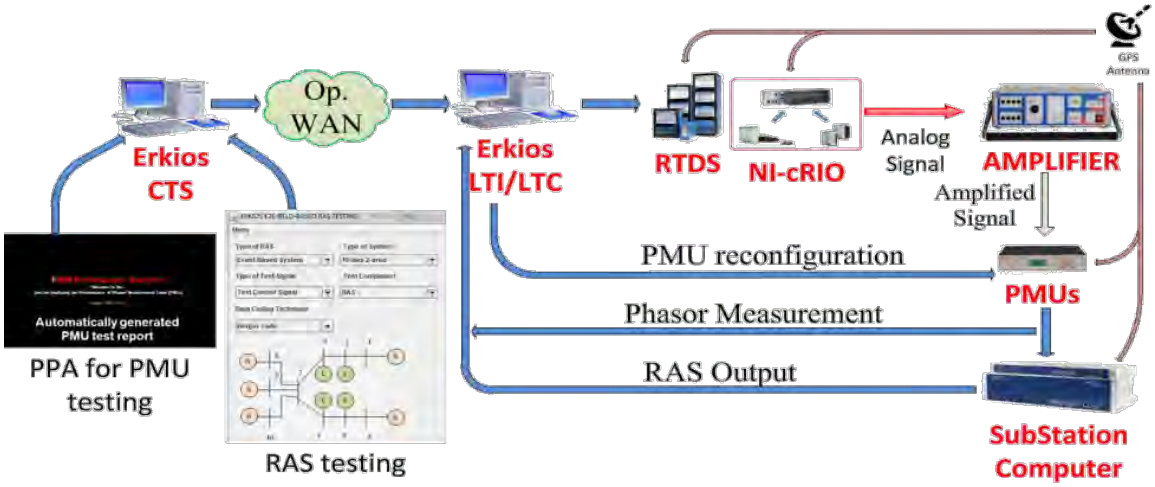

Figure 5.2: ERKIOS Middleware based Remote Testing of PMU and RAS

6. Remote PMU testing

6.1 Integration of PMU Performance Analyzer and Erkios Software

The Erkios can be used for remotely testing the PMUs in the field as shown in Figure 6.1, without the need to remove them from service and bring them in the PMU testing lab. The PMU testing lab is primarily designed for testing the new PMU before commissioning in the field. However, periodic testing of large number of PMUs, which are already in service is a difficult task. The proposed solution to this problem is integrating Erkios and PPA for carrying out remote testing of the PMUs installed in the substations. The PPA establishes the connection with the Erkios CTS and sends the lists of the test cases need to be performed on the remote PMU. The LTI generates the analog signal using the GPS time stamps and send the GPS time stamps to the LTC. The LTC also receives the time stamped phasor data from the test PMU through the programmable router. The GPS time stamps of the events and the time stamped phasor data in .xlsx or .csv format are transmitted to the PPA via CTS. The PPA generates the true phasor for all the testing scenarios and compares with the test PMU phasors.

The testing of PMUs installed at the substation is carried out using the middleware ERKIOS. The different modules of ERKIOS are mentioned in this specification.

6.2 Purpose

The remote testing of PMUs is carried out using the ERKIOS middleware. The limits given in the IEEE C37.118.1-2011 and sequence of parameters varied to the voltage and current signal for System Context

The remote PMU testing infrastructure consists of different modules of the middleware ERKIOS and the PMU Performance Analyzer (PPA). The modules of ERKIOS communicate with each other through Ethernet network using server client architecture.

6.3 System Environments and Modes

The remote PMU testing is required to work in unreliable communication network over long distances. The normal operating condition involves fault tolerant features of ERKIOS for reliable operation.

6.4 User Characteristics

It is assumed that users will be comfortable performing basic computer tasks such as locating and selecting files saved on disk. In addition, users are assumed to be capable of manipulating the layout of a spreadsheet using Excel or a similar tool. The middleware typically takes care of the underlying communication and switching function for remote PMU testing.

6.5 Substation Specification

The specification of the substation capable of remote PMU testing are briefly described as follows

a) The substation should have a GPS antenna and a GPS clock receiver similar to “Review of the IEEE TSS test plan requirements and lab specification requirements”.

b) The substation should be able to communicate with a Central test system (CTS), which is responsible for carrying out the PMU testing.

c) The substation should have a Local test system initiator (LTI), which disables CT/PT input to PMU and connects PMU input to the Signal source.

d) LTI should also be capable to receive the data from the CTS, unpacks the test signal data and transmits them to the Signal source.

e) LTI should also be able to control Programmable Router to transmit C37.118 data to Local test system collector (LTC).

f) The substation should have a Signal source similar to “Review of the IEEE TSS test plan requirements and lab specification requirements”, which can generate voltage and current signal for the test signal received from LTI at appropriate GPS time instants.

g) The substation should have a Programmable Router, which can transmit the C37.118 phasor data to the LTC during testing and switch back to substation PDC during normal operation.

h) The substation should have a LTC, which receives the C37.118 phasor data during the test and transmits to CTS for reporting, analysis and archiving.

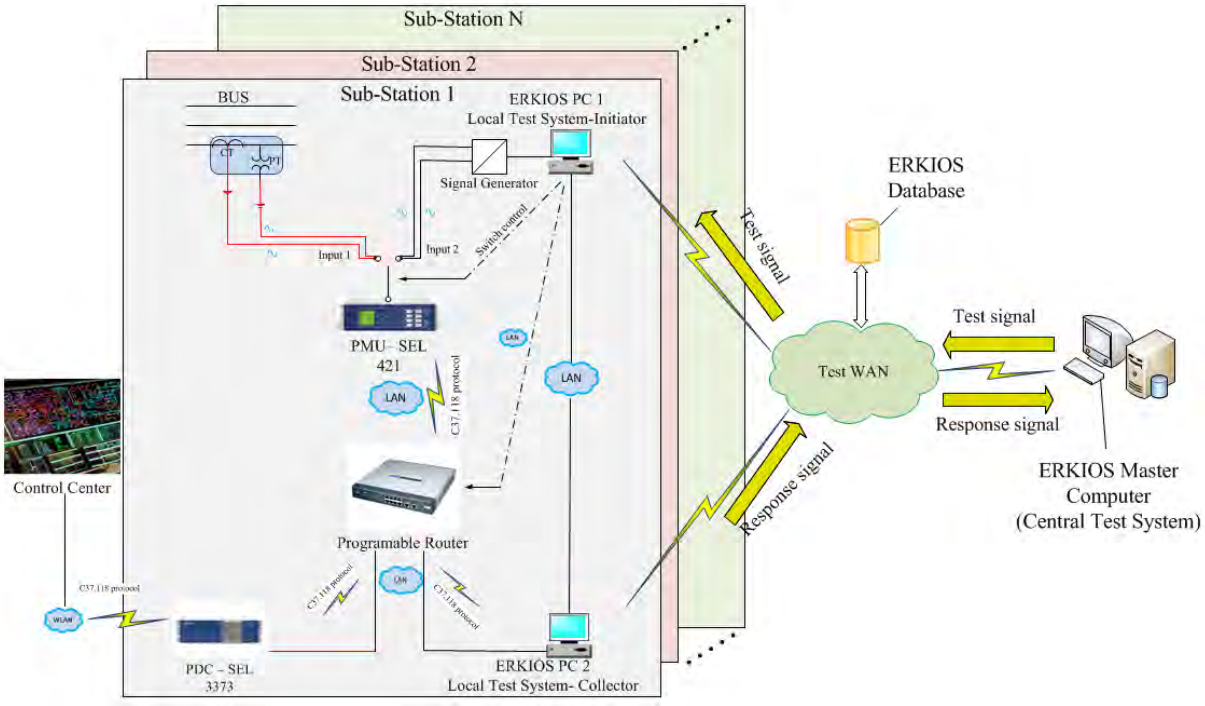

Figure 6.1: ERKIOS Architecture

The PMU installed at the substation may require recalibration following maintenance of other equipment in the substation. Apart from that, PMU may also require calibration in the interval of 2-3 years due to drifting of parameters resulting from temperature variations. The expansion of power system may also require the PMU installed at the substation to recalibrate.

The Erkios consists of different modules, which communicate with each other for achieving the goal of in-service and end-to-end testing of synchrophasor equipment and RAS schemes. The Erkios module communicates with each other over insecure networks, which demands robust algorithms for handling delays, data drop and data corruption. The issue of security is also needed to be addressed for communication of Erkios modules. The different methodology available for timing coordination, data drop and security are reviewed and are under implementation stage. These algorithms can be tested using cyber physical test bed consisting of NS3 network simulator for communication and RTDS, PMUs and relays for power system. The statistical metrics are required for evaluating the methods implemented in Erkios for handling delays, drop and corruption of the data packets. The "Requirement specification for timing coordination, data dropped and other issues" is prepared for implementation in Erkios tool. The different failure models are identified in the specification document with the details of each Erkios modules that may be associated with some kind of failures. The specification also mentions different failures and security handling mechanisms, which are required to be implemented in the Erkios. The procedure for interfacing PPA with Erkios is explored in this deliverable. The remote testing of PMU is carried out using Erkios middleware. The PPA has interface for local testing and remote testing of PMUs installed at the substation. The protocol, authentication and error detection features are discussed in this specification document. The procedure for remote testing of PMU is done by transmitting the test signals to the Erkios PC in the substation known as Local Test System Initiator. The LTI plays back the test signals following the IEEE TSS guidelines and captures the result as data files. The Erkios transfer the data file to the PPA for performance evaluation of the remote PMU. The communication of the PPA and Erkios is finalized by following server client architecture with authentication and implementing error detection mechanism. The infield calibration of PMU either requires a physical switch or configuration change for providing a test signal to the PMU. The physical connection requires an extra switch to change the connection between the real system and testing system. However, the configuration change only requires access of PMU via communication layer. The configuration change uses the software of the PMU to switch the signal for phasor estimation from the grid to the signal generator. By changing PMU configuration setting, the PMU data packet is redirected to ERKIOS system. The ERKIOS system transfers the collected PMU data and sends to the PPA system for testing. The configuration of PMU can change using either configuration software provided by manufacture or TELNET communication. To integrate with ERKIOS, locally TELNET commands are being used to transfer new configuration parameters for in-field PMU calibration.

6.6 Results

The PMU from one vendor is tested for changing the configuration using the TELNET command. The TELNET command is generated by ERKIOS Local Test System Initiator and verifies the transfer of the configuration files to the target PMU.

Using the FILE command in TELNET session, the PMU configuration file can transfer between test PMU and ERKIOS as shown in Figure 6.1 to back up the pre-test configuration.

```
=>File Read CFG.TXT
#000 Ready to send file
#001 Transfer Complete

=>


=>

=>

=>

=>File Read SETTINGS\SET_S1.TXT
#000 Ready to send file
#001 Transfer Complete

=>

=>

=>File Read SETTINGS\SET_S2.TXT
#000 Ready to send file
#001 Transfer Complete
```

Figure 6.2: FILE command in TELNET session

The ERKIOS system is a general remote testing platform catering to both PMU and RAS remote testing by controlling substation equipment. The ERKIOS can control substation equipment to enable/disable testing mode for remote PMU testing. Most of the substations are unmanned substation that is not controlled manually. The ERKIOS uses TELNET session to redirect PMU data using a local testing system (LTS) for the PMU Performance Analyzer. The configuration files of controlling substation devices are updated by control command from ERKIOS master computer via TELNET session. The redirecting data are most important step for security point of view. The ERKIOS also uses secure communication layer such as SSH to transfer the configuration file. The SEL PMU used to test ERKIOS system for controlling substation equipment as shown in Figure 6.2.

```
$ scp ERKIOS@/conf/SEL421/SET_S5.txt LTS@conf/SEL/SET_S5.txt
```

Figure 6.3: SCP command to transfer configuration file using SSH session

Once the configuration file is transferred in the LTS, it sends the configuration file to target PMU locally via TELNET session as shown in Figure 6.3.

```
=>>File Write SETTINGS\SET_S5.TXT
CCC#001 Transfer Complete

=>>
```

Figure 6.4: File command to send a configuration file from LTS to target PMU

6.7 Summary

ERKIOS is developed to test RAS systems in the field. Its deployment has the potential to enhance the reliability of RAS systems, which can possibly avoid power blackouts if they work properly. The given approach was applied as a middleware framework prototype; which goal is to detect the

existence of hidden or dormant failures to verify the correct operation in the field of the power grid system. The analysis focused on Self-Testing coding techniques and Remedial Action Schemes: Impacts on the System and Input Variables Schemes. The approach proposed was applied at different levels to hardware and/or software of the End-to-End composition of modules to improve robustness.

7. Remote RAS Testing

7.1 Introduction

Remedial Action Scheme (RAS) is an automatic control mechanism designed to detect the abnormal system conditions and take fast control action for maintaining the system reliability. A new RAS is developed to minimize the wind power curtailment and protect the transmission lines from overload/ congestion problems, which can be easily extended for voltage stability or other related problems. Distributing this RAS logic to multiple computers located near the edge improves the robustness and remedial action response times. To highlight this, how we run RAS logic in the testbed will evolve through a variety of configurations. Initially curtailment logic is run in a standard single, centralized style as a baseline comparison point. Distributed schemes, each have unique redundancy and fault-tolerance capabilities compared to a centralized system, often with measurable performance tradeoffs [19-23].

The specifications of the RAS test suite are briefly listed:

- The RAS test suite should be able to test Relays, Instrument transformers, and communication network, PMU, and RAS controller for the end-to-end remote testing.
- The RAS test suite should be able to generate appropriate testing signals based on the test target.
- The data format of packets, which transmit from the control center to the substation, should contain a time stamp, voltage phasor values, current phasor value, frequency values, and couple reserved bits.
- The ERKIOS should be able to send the testing signals from the control center to substations and send the control actions back to control center from the substation.
- The ERKIOS should be able to control the signal switch based on the test signal.
- The Analog Signal Generator and Amplifier should be able to receive the testing signals from the ERKIOS substation PC and convert them to appropriate testing power signal.
- The RAS test suite should be able to intercept the control actions from relays.
- All the signals should have the time stamps, which can utilize for analyzing communication latency, possible packet drop and the speed of the RAS.
- The RAS test suite should be able to generate the test result report based on the received control actions and the related time stamps.

The test result report should contain 1) Whether the RAS give the correct control action 2) How is the performance of communication network 3) Whether the Instrument transformers work well 4) Whether the PMU/PDC work well 5) Whether the RAS controller works as expected 6) Whether the relays work correctly

In the normal operation mode, the PMU measures voltage and current phasors based on the signal from CT/PT, which connects on the power grids. Then, PMU sends the measurements to substation computer, which is implementing the RAS algorithm. In the RAS testing mode, the input signal

must be generated before the PMU by an Analog Signal Generator and Amplifier, which generate the test analog signal based on the trigger signal from ERKIOS. The analog signal is delivered to an amplifier, which will convert it into a high-power analog signal to replicate a standard grid measurement. The high-power analog signal will be measured by PMU and the PMU measurements will be sent to the substation computer, which is then the same with the normal operation mode.

The interface of the RAS output should also be controlled by another signal switch. In the normal operation mode, the signal switch should connect to the RAS action performing actuator, which is the circuit breaker in the power grid. In the RAS testing mode, the signal is switched to connect to the ERKIOS local test system collector, which can collect the control actions from the substation computer and send them back to ERKIOS Master Computer. This switching can be a physical switch or a network switch performing the collection.

An operator setting up an ERKIOS local test system must establish a device specific connection, either with analog switched connectors, alternative connection, or digital network traffic rerouting. In addition to a device's specific input connections general requirements, such as device maximum allowable time for testing should be specified along with device types. Specific details about timing and test requirements can be found under the IEEE TSS review sections.

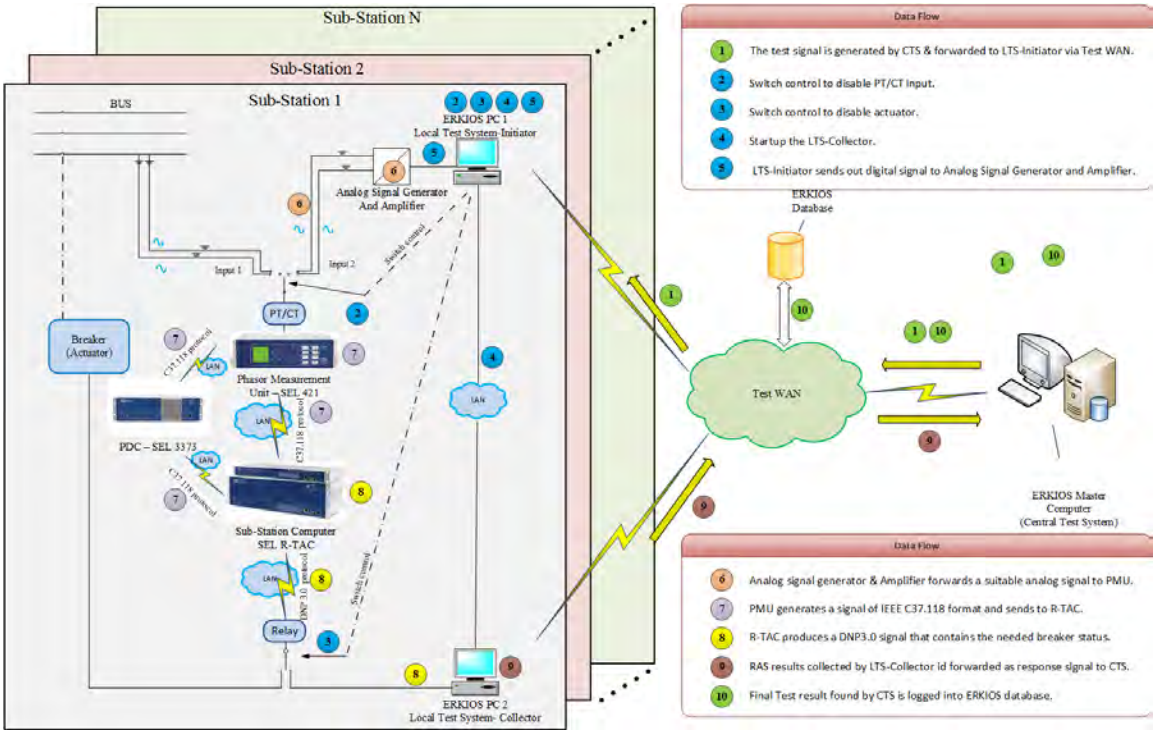

Figure 7.1: Interfacing Architecture with RAS at Substation

In order to enable the end-to-end and in field remote testing for RAS, a middleware framework called ERKIOS is developed. ERKIOS was designed to test a very wide range of RAS schemes in the field in order to ensure that the distributed components in a RAS scheme are functioning property. ERKIOS also supports a very wide range of failure models, handling failures of both

grid components as well as pieces of ERKIOS itself. The architecture of end-to-end in-field testing of RAS by ERKIOS is shown in the Figure 7.1. There are two different operation modes for this architecture: 1) Normal Operation 2) RAS testing.

In the Normal Operation mode, all the substations are connected to the rest of the power grid through the transmission lines. The sensor, which is Phasor Measurement Unit in this case, measures the different parameters, such as voltage and current phasors, in all the substations. The measurements are delivered to the substation computer, which implements the RAS algorithm, based on C37.118 communication protocol. The substation computer runs the RAS algorithm and generates the appropriate control actions, which is sent to the respective relay, breaker, or actuator. The control actions are transmitted by DNP 3.0 communication protocol.

In the RAS testing mode, ERKIOS is involved as a middleware framework for RAS testing. There are five main components for the RAS testing mode: 1) ERKIOS Master Computer 2) LTS-Initiator 3) Analog Signal Generator and Amplifier 4) Sensor and Substation Computer 5) LTS-Collector.

7.2 Test plans of wind curtailment RAS

Since the installation of wind farm is increasing rapidly, wind power has become an important renewable source of power generation in smart grids. Based on [1], the wind energy consumption occupies 19% of the total renewable energy consumption in 2015, and the percentage is keeping increasing. However, the wind generation highly depends on local weather condition. Intermittency and uncertainty in wind generation may cause exceeding the line ratings of the low voltage transmission lines, which requires wind generation curtailment to protect the transmission line from overload conditions.

Table 7.1: Facts on Wind Curtailment Issues

Regions	Curtailment Facts
ERCOT, US	Wind generation is curtailed approximately 45-50% of the days from Jan. to Aug. 2008. From Dec. 2008 to Dec. 2009, daily wind curtailment is between 500MW and 2000MW, sometimes up to 3900 MW. Monthly averages ranged from about 24-28% of potential wind generation.
Midwest ISO, US	About 200,000 MWh wind energy were curtailed in 2009.
SCE, US	About 3-4 hours curtailment every two days (or 6-8% of the time).
China	30% of installed wind capacity hasn't been connected to the grid by end-2011. Moreover, according to data from China Electricity Council (CEC), approximately 11% of wind power generated in China was not procured by grid operators.
Alberta, Canada	From Jan. to Dec. 2010: 3055 hours of wind curtailment period and 155 facilities were affected.
Spain	In 2010, wind curtailment totaled 315,230 MWh. Between Jan. 2011 and Apr. 2011, wind curtailment totaled 23,994 MWh

Table 7.1 shows some of the wind curtailment conditions all over the world. In order to keep increasing the integration of wind renewable energy and maintain the reliability and stability of power system, innovative automation and information technologies need to be deployed for the power system operation and control.

This demonstration includes eight test-plan for the wind curtailment remedial action scheme (RAS). These RAS tests are conducted based on the measurements collected from PMUs. The optimal RAS solution is calculated for the minimal curtailment of wind generation based on DC power flow model. The RAS controllers should be able to collect measurement data, analyze the system status, propose control strategy, and execute control actions of wind farm generation curtailment. For implementation, this project deploys a real-time hardware-in-the-loop (HIL) testbed, which involves with RTDS as a power system simulator, BeagleBone programmed controller, SEL-421 hardware PMU, and GTNET software PMU.

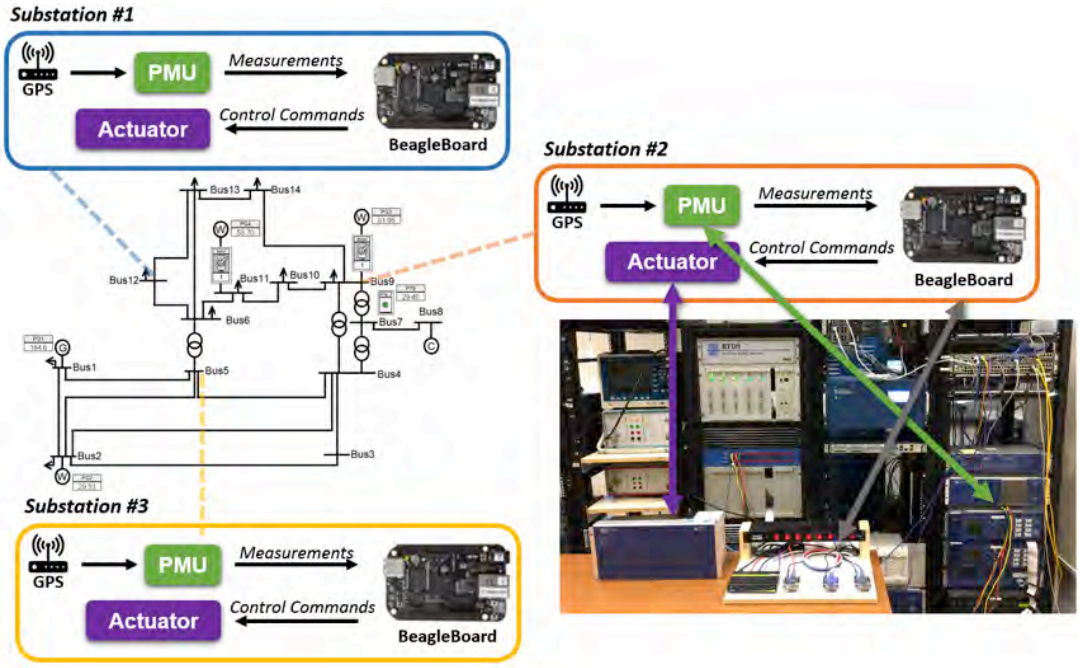

Figure 7.2: Real-Time Implementation Testbed

Table 7.2: Test Plan Objectives of Wind Curtailment Ras

Test	Operating Condition	Objectives
1	Normal	Verify if the RAS controller can remain stable when there is no operational violation detected
2	Alert	Verify if the RAS controller can execute RAS control action of wind curtailment when there exists ***one*** transmission line violating the preset line ratings
3	Alert	Verify if the RAS controller can execute RAS control action of wind curtailment when there exists ***one*** transmission line violating the modified line ratings

4	Alert	Verify if the RAS controller can execute RAS control action of wind curtailment when there exists ***two*** transmission line violating the modified line ratings

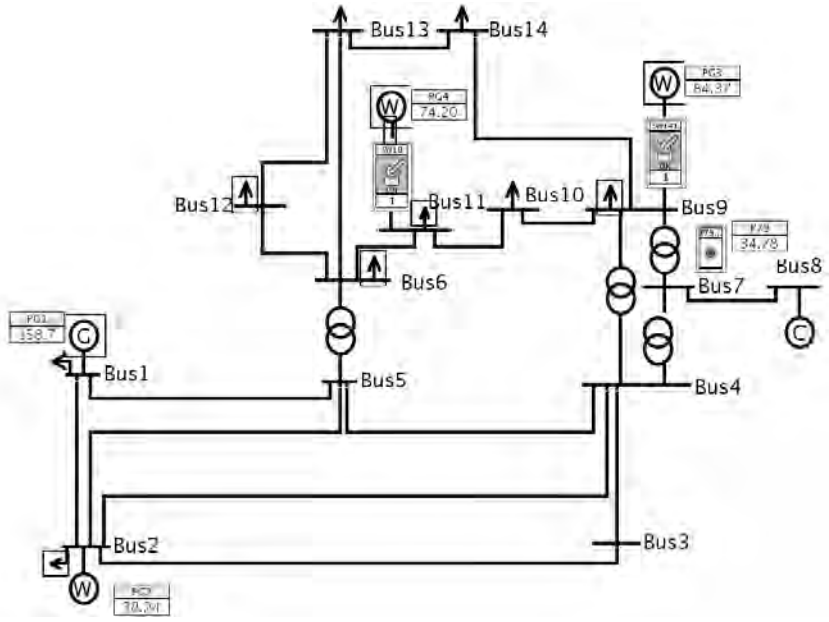

Figure 7.3: One Line Diagram of IEEE 14-Bus Test System with 3 Wind Farms

Table 7.3 demonstrates the basic information of the Ras testing system in details.

Table 7.3 Descriptions of Base Case

Property	**Configurations**
Test System Model	Extended IEEE 14-Bus System
Total Load for Base Case	347.8 MW
Number of Wind Farms	3
Wind Farm Locations	Bus #2, #9 and #11
Preset Slack Bus Generator Output	P_S = 148.7 MW
Preset Wind Farm Output	P_1 = 100 MW, P_2 = 50 MW, P_3 = 50 MW
Number of Regulated Transmission Lines	20
Preset Line Ratings (MW)	[100, 50, 100, 35, 50, 50, 50, 50, 50, 50, 70, 50, 50, 50, 35, 30, 50, 70, 30, 30]
Line Ratings Regulation #1 (MW)	[100, 50, 100, 35, 50, 50, 50, 50, 50, 50, 70, 50, 50, 50, 35, 30, 50, 70, 30, 30]
Line Ratings Regulation #2 (MW)	[100, 50, 100, 35, 50, 50, 50, 50, 50, 50, 70, 50, 50, 50, 30, 30, 50, 70, 30, 30]
Line Ratings Regulation #3 (MW)	[100, 50, 100, 35, 50, 45, 50, 50, 50, 50, 70, 50, 50, 50, 35, 30, 50, 70, 30, 30]

Line Ratings Regulation #4 (MW)	[100, 50, 100, 35, 50, 45, 50, 50, 50, 50, 70, 50, 50, 50, 30, 30, 50, 70, 30, 30]

Demonstration of Test Plans

Test 1: Verify if the RAS controller can remain stable when there is no operational violation detected

Case #1 (Base Case)

Base Case with Wind Farm Outputs (P1 = 100 MW, P2 = 50 MW, P3 = 50 MW)

↓

System Status: ***Normal***

↓

No RAS action should be executed

Case #2 (Modified Wind Farm Outputs& Line Ratings)

Base Case with Wind Farm Outputs (P1 = 100 MW, P2 = 50 MW, P3 = 50 MW)

↓

↓ Modify Wind Farm Outputs
↓ (P1 = 100 MW, P2 = 60 MW,
↓ P3 = 60 MW)

↓

↓ Set line rating configuration to
↓ Line Ratings Regulation #2 (MW)

↓

System Status: ***Normal***

↓

No RAS action should be executed

Test 2: Verify if the RAS controller can execute RAS control action of wind curtailment when there exists ***one*** transmission line violating the preset line ratings

Case #3 (Violation on Preset Line Rating Limit #1)

Base Case with Wind Farm Outputs (P1 = 100 MW, P2 = 50 MW, P3 = 50 MW)

↓

↓ Modify Wind Farm Outputs
↓ (P1 = 100 MW, P2 = 90 MW,
↓ P3 = 90 MW)

↓

Detected violation in line ratings:
Line #15 (7-9) is overloaded: 39.203 MW > 35.000 MW

↓

System Status: ***Alert***

↓

RAS action executed within 10 seconds:
Wind farm P2 output is curtailed to 70.482 MW

↓

Violation is eliminated:
Line #15 (7-9) is within the line rating limit: 35.000 MW

↓

System Status: ***Normal***

Test 3: Verify if the RAS controller can execute RAS control action of wind curtailment when there exists ***one*** transmission line violating the modified line ratings

Case #5 (Line Rating Regulation #2)

Base Case with Wind Farm Outputs (P1 = 100 MW, P2 = 50 MW, P3 = 50 MW)

↓

↓ Set line rating configuration to
↓ Line Ratings Regulation #2 (MW)

↓

System Status: ***Normal***

↓

↓ Modify Wind Farm Outputs
↓ (P1 = 100 MW, P2 = 80 MW,
↓ P3 = 80 MW)

↓

Detected violation in line ratings:
Line #15 (7-9) is overloaded: 31.852 MW > 30.000 MW

↓

System Status: ***Alert***

↓

RAS action executed within 10 seconds:
Wind farm P2 output is curtailed to 69.977 MW

↓

Violation is eliminated:
Line #15 (7-9) is within the line rating limit: 30.000 MW

↓

System Status: ***Normal***

Test 4: Verify if the RAS controller can execute RAS control action of wind curtailment when there exists ***two*** transmission lines violating the modified line ratings

Case #7 (Line Rating Regulation #3)

Base Case with Wind Farm Outputs (P1 = 100 MW, P2 = 50 MW, P3 = 50 MW)

↓ Set line rating configuration to Line Ratings Regulation #3 (MW)

System Status: ***Normal***

↓ Modify Wind Farm Outputs (P1 = 100 MW, P2 = 90 MW, P3 = 90 MW)

Detected violation in line ratings:
Line # 6 (3-4) is overloaded: 45.013 MW > 45.000 MW
Line #15 (7-9) is overloaded: 39.203 MW > 35.000 MW

↓

System Status: ***Alert***

↓

RAS action executed within 10 seconds:
Wind farm P2 output is curtailed to 70.482 MW

↓

Violation is eliminated:
Line #6 (3-4) is within the line rating limit: 45.000 MW
Line #15 (7-9) is within the line rating limit: 35.000 MW

↓

System Status: ***Normal***

7.3 Idaho Power RAS

The 179 bus WECC system was modified to include the geographical area involved in one of the RAS scheme implemented by Idaho Power. The model was built on Opal-RT to study the test cases for the implemented RAS. The primary function of the RAS is to prevent thermal damages to the lines following any contingency or if a line is removed for maintenance activities. It also helps to optimize the transfer along critical corridors.

This simulation considers an event where remediation is being taken by the RAS. A 345 kV line outage is considered. The power flow monitored at another line gets overloaded during this line outage. The RAS takes control action by adding a shunt capacitor, which limits the line flow in the overloaded line as shown in the simulation results below.

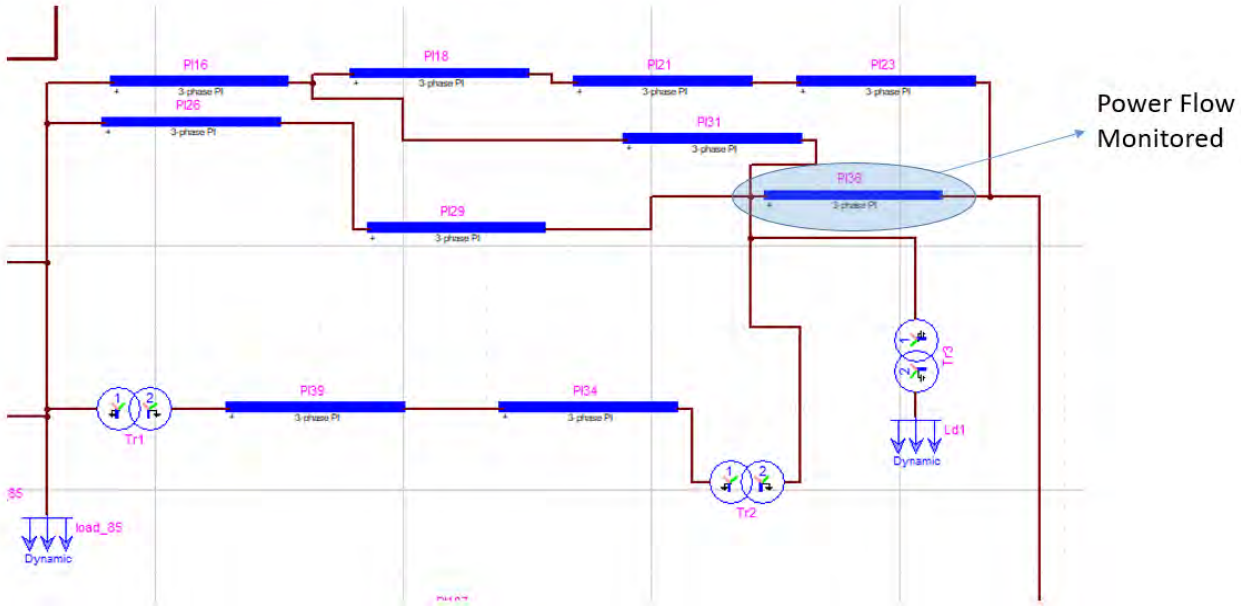

Figure 7.4: OPAL-RT SLD Idaho RAS geographic area involved

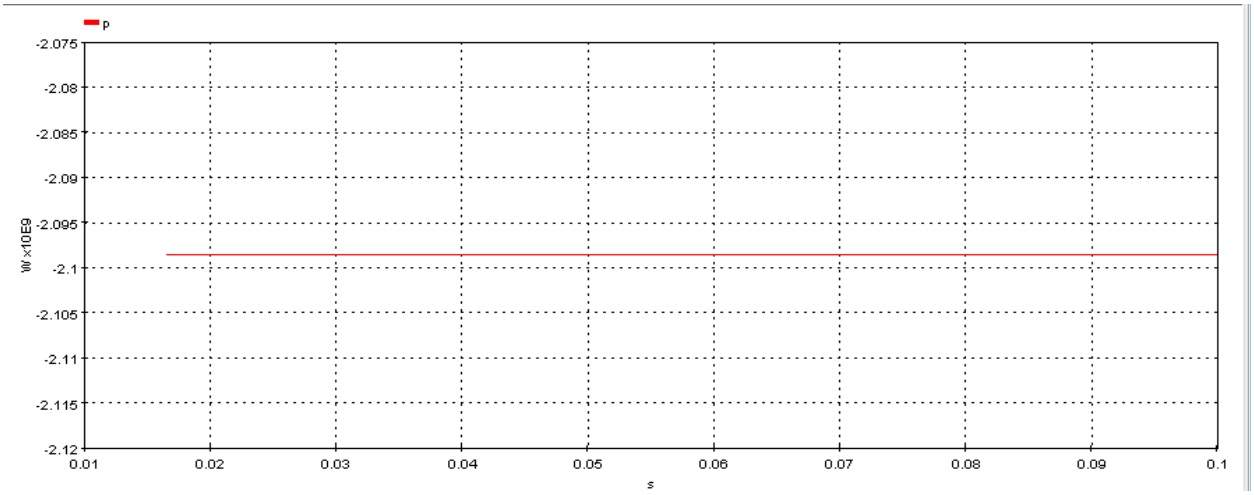

Figure 7.5: Power flow in the monitored line

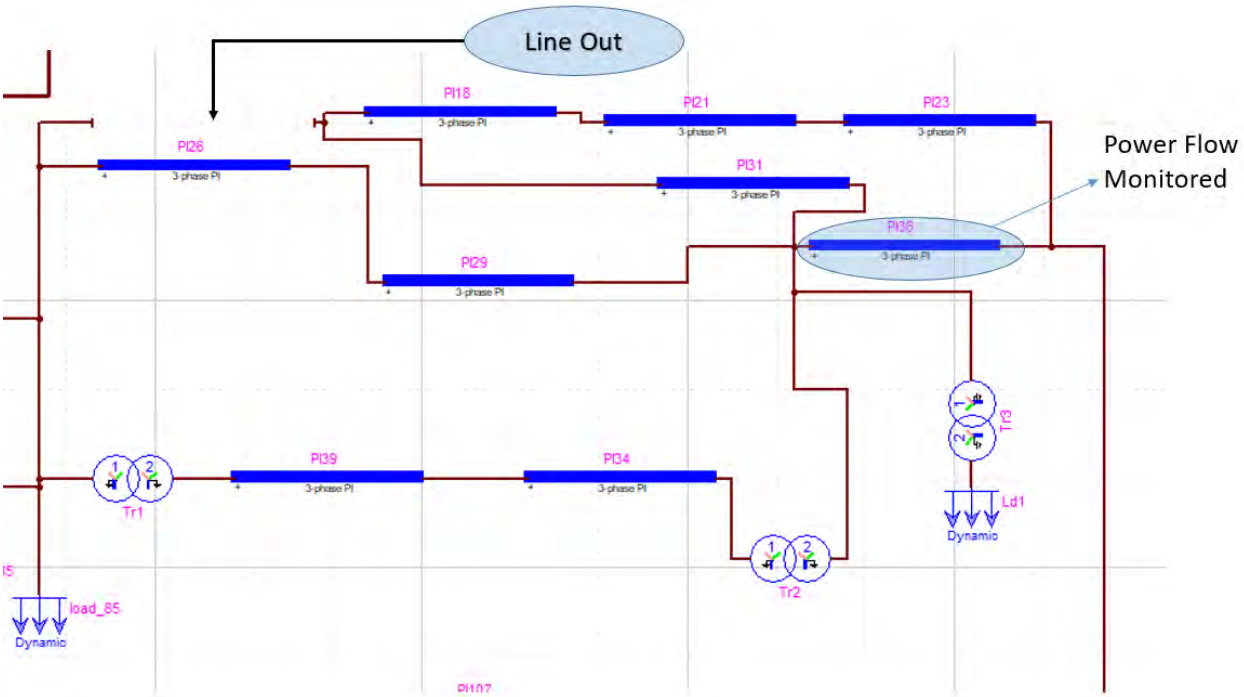

Figure 7.6: 345kV line outage

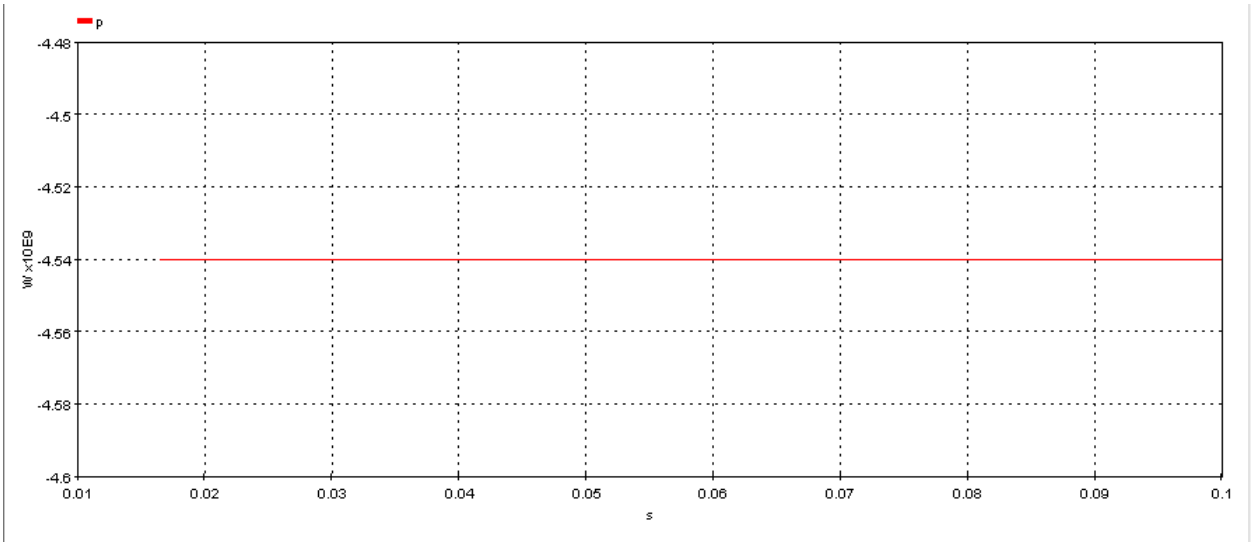

Figure 7.7: Monitored power flow during line outage

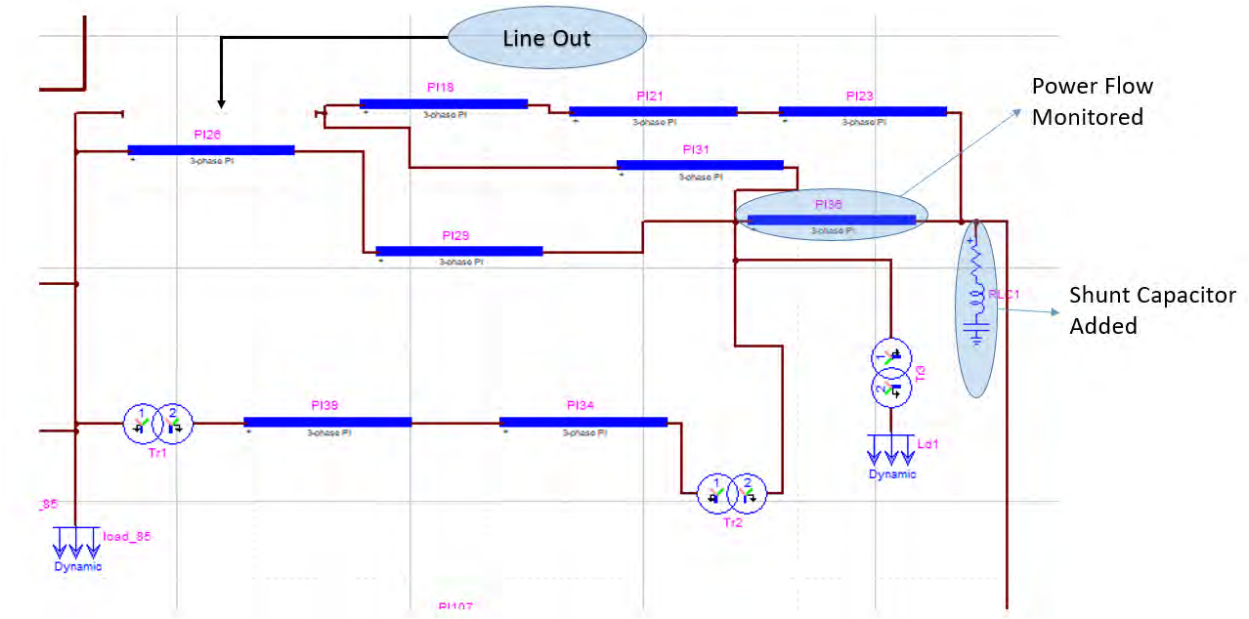

Figure 7.8: RAS control action by adding shunt capacitor during line outage

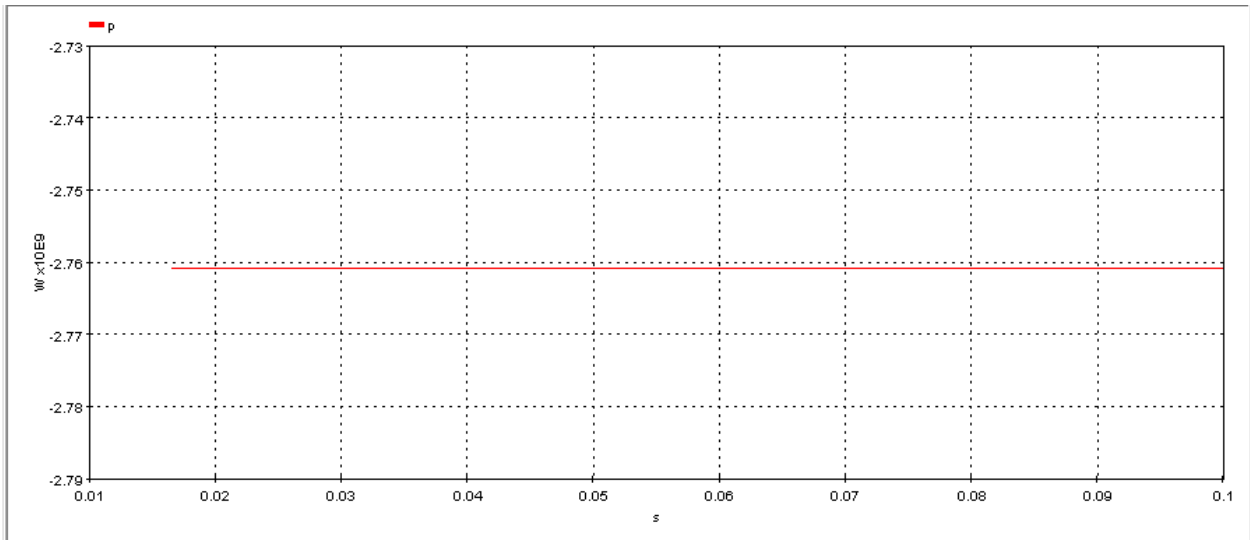

Figure 7.9: Power flow after RAS control action

Future Testing

Future testing involves validating the remediation taken by RAS for contingencies, which include loss of line from service and overload condition in monitored lines and transformers. The control actions implemented by RAS include adding of shunt capacitors, bypassing series capacitors and shedding of generation at the power plants.

7.4 Summary

The RAS test suite is a software & hardware hybrid platform, which is designed for remote testing the specific RAS. The standalone RAS test suite is integrated with ERKIOS middleware for the data management of RAS testing and communication between the substation and control center. Erkios is developed to provide in-field and end-to-end testing of RAS system. The RAS test suite and ERKIOS is capable of end-to-end remote testing in-field RAS without interrupting them from operation for a long time. The operation of the setup will prove the feasibility and reliability of the Erkios framework in a real power grid. Further, it will enrich Erkios by helping to build functionality and libraries to test different RAS. The testbed also paves the niche for implementing other in-field testing applications like PMU and relay testing.

8. Conclusions

The specification of the testing equipment required for the PMU testing lab is discussed in this report. The architecture of the test bed and the features of the software called PPA used for automatic PMU testing are presented. The successful implementation of PMU testing performed at the Southern California Edition (SCE) using PPA is presented. The result of the PMU testing shows that the compliance of the standard for 30 fps and 60 fps can be different for some of the test scenarios. The process of integrating a middleware like Erkios for Remedial Action Scheme (RAS) testing with the simulated power grid and connected hardware in the loop is discussed. The infrastructure and other requisites to build such an integration and data management are clearly described with the implementation of the testbed. The operation of the prototype testbed integration provides the insight for the feasibility and reliability of the Erkios framework in a real power grid. Further, it will enrich Erkios by helping to build functionality and libraries to test different RAS.

Appendix A

- Result for PMU performance analyzer

Test results of steady state performance of pmu - angle change: balanced system.

[A.1] Status of time synchronization of the ideal pmu & the test pmu:

Input Voltage Magnitude (in p.u.)	*TVE of Phase-A (in percentage)*	*TVE of Phase-B (in percentage)*	*TVE of Phase-C (in percentage)*
20.000	*0.007*	*0.022*	*0.016*
40.000	*0.006*	*0.030*	*0.016*
60.000	*0.015*	*0.038*	*0.016*
80.000	*0.008*	*0.019*	*0.015*
100.000	*0.016*	*0.017*	*0.015*
120.000	*0.022*	*0.015*	*0.026*
140.000	*0.008*	*0.013*	*0.023*
160.000	*0.005*	*0.015*	*0.012*
180.000	*0.006*	*0.007*	*0.009*
200.000	*0.006*	*0.009*	*0.023*
220.000	*0.004*	*0.019*	*0.019*
240.000	*0.015*	*0.023*	*0.018*
260.000	*0.012*	*0.009*	*0.016*
280.000	*0.009*	*0.012*	*0.015*
300.000	*0.016*	*0.012*	*0.024*
320.000	*0.009*	*0.014*	*0.020*
340.000	*0.010*	*0.020*	*0.015*

[A.2] Analysis of Average TVE in Voltage Phasor Measurement:

Average TVE of Phase-A (in percentage)	Average TVE of Phase-B (in percentage)	Average TVE of Phase-C (in percentage)	Average TVE of + Seq. (in percentage)
0.010	0.017	0.018	0.008

Standard Deviation of TVE of Phase-A (in percentage)	Standard Deviation of TVE of Phase-B (in percentage)	Standard Deviation of TVE of Phase-C (in percentage)	Standard Deviation of TVE of + Seq. (in percentage)
0.005	0.008	0.004	0.002

[A.3] Analysis of Maximum & Minimum TVE in Voltage Phasor Measurement:

Maximum TVE of Phase-A (in percent-age)	Minimum TVE of Phase-A (in percentage)	Maximum TVE of Phase-B (in percent-age)	Minimum TVE of Phase-B (in percent-age)	Maximum TVE of Phase-C (in percent-age)	Minimum TVE of Phase-C (in percentage)	Maximum TVE of + Seq. (in percent-age)	Maximum TVE of + Seq. (in percent-age)
0.022	0.004	0.038	0.007	0.026	0.009	0.012	0.003

[A.4] Verification of PMU Performance - Maximum TVE in Voltage Phasor Measurement:

Maximum TVE (in percentage)	Allowed Maximum TVE (in percentage)	Test Result
0.038	1.000	PASS

[A.5] Magnitude Error in Voltage Phasor Measurement:

Mean M_E of Phase-A (in percentage)	Stand. Dev. of M_E of Phase-A (in percentage)	Minimum M_E of Phase-A (in percentage)	Maximum M_E of Phase-A (in percentage)
0.003	0.001	0.002	0.005
Mean M_E of Phase-B (in percentage)	Stand. Dev. of M_E of Phase-B (in percentage)	Minimum M_E of Phase-B (in percentage)	Maximum M_E of Phase-B (in percentage)
0.004	0.001	0.003	0.005
Mean M_E of Phase-C (in percentage)	Stand. Dev. of M_E of Phase-C (in percentage)	Minimum M_E of Phase-C (in percentage)	Maximum M_E of Phase-C (in percentage)
0.003	0.001	0.002	0.004

Mean P_E of Phase-C (in degrees)	Stand. Dev. of P_E of Phase-C (in degrees)	Minimum P_E of Phase-C (in degrees)	Maximum P_E of Phase-C (in degrees)
0.010	0.003	0.005	0.015

Mean M_E of + Seq. (in percentage)	Stand. Dev. of M_E of + Seq. (in percentage)	Minimum M_E of + Seq. (in percentage)	Maximum M_E of + Seq. (in percentage)
0.003	0.000	0.002	0.003

[A.6] Phasor Error in Voltage Phasor Measurement:

Mean P_E of Phase-A (in degrees)	Stand. Dev. of P_E of Phase-A (in degrees)	Minimum P_E of Phase-A (in degrees)	Maximum P_E of Phase-A (in degrees)
0.006	0.003	0.002	0.012

Mean P_E of Phase-B (in degrees)	Stand. Dev. of P_E of Phase-B (in degrees)	Minimum P_E of Phase-B (in degrees)	Maximum P_E of Phase-B (in degrees)
0.010	0.005	0.004	0.022

Mean P_E of + Seq. (in degrees)	Stand. Dev. of P_E of + Seq. (in degrees)	Minimum P_E of + Seq. (in degrees)	Maximum P_E of + Seq. (in degrees)
0.004	0.002	0.000	0.007

[B.1] Analysis of TVE in Current Phasor Measurement:

Input Voltage magnitude (in p.u.)	TVE of Phase-A (in percentage)	TVE of Phase-B (in percentage)	TVE of Phase-C (in percentage)
20.000	0.111	0.099	0.178
40.000	0.131	0.123	0.199
60.000	0.137	0.145	0.142
80.000	0.148	0.150	0.131
100.000	0.137	0.114	0.165
120.000	0.147	0.126	0.192
140.000	0.139	0.112	0.145
160.000	0.137	0.136	0.117
180.000	0.122	0.141	0.111
200.000	0.134	0.118	0.166
220.000	0.166	0.125	0.139
240.000	0.148	0.115	0.152
260.000	0.149	0.146	0.133
280.000	0.135	0.109	0.167
300.000	0.147	0.135	0.143
320.000	0.177	0.116	0.148
340.000	0.152	0.128	0.153

[B.2] Analysis of Average TVE in Current Phasor Measurement:

Average TVE of Phase-A (in percentage)	Average TVE of Phase-B (in percentage)	Average TVE of Phase-C (in percentage)	Average TVE of + Seq. (in percentage)
0.142	0.126	0.152	0.087

Standard Deviation of TVE of Phase-A (in percentage)	Standard Deviation of TVE of Phase-B (in percentage)	Standard Deviation of TVE of Phase-C (in percentage)	Standard Deviation of TVE of + Seq. (in percentage)
0.015	0.015	0.024	0.008

[B.3] Analysis of Maximum & Minimum TVE in Current Phasor Measurement:

Max. TVE of Phase-A (in %)	Min. TVE of Phase-A (in %)	Max. TVE of Phase-B (in %)	Min. TVE of Phase-B (in %)	Max. TVE of Phase-C (in %)	Min. TVE of Phase-C (in %)	Max. TVE of + Seq. (in %)	Max. TVE of + Seq. (in %)
0.177	0.111	0.150	0.099	0.199	0.111	0.096	0.066

[B.4] Verification of PMU Performance - Maximum TVE in Current Phasor Measurement:

Maximum TVE (in percentage)	Allowed Maximum TVE (in percentage)	Test Result
0.199	1.000	PASS

[B.5] Magnitude Error in Current Phasor Measurement:

Mean M_E of Phase-A (in percentage)	Stand. Dev. of M_E of Phase-A (in percentage)	Minimum M_E of Phase-A (in percentage)	Maximum M_E of Phase-A (in percentage)
0.110	0.021	0.080	0.137

Mean M_E of Phase-B (in percentage)	Stand. Dev. of M_E of Phase-B (in percentage)	Minimum M_E of Phase-B (in percentage)	Maximum M_E of Phase-B (in percentage)
0.104	0.014	0.075	0.131

Mean M_E of Phase-C (in percentage)	Stand. Dev. of M_E of Phase-C (in percentage)	Minimum M_E of Phase-C (in percentage)	Maximum M_E of Phase-C (in percentage)
0.078	0.015	0.063	0.092

Mean M_E of + Seq. (in percentage)	Stand. Dev. of M_E of + Seq. (in percentage)	Minimum M_E of + Seq. (in percentage)	Maximum M_E of + Seq. (in percentage)
0.057	0.006	0.049	0.068

[B.6] Phasor Error in Current Phasor Measurement:

Mean P_E of Phase-A (in degrees)	Stand. Dev. of P_E of Phase-A (in degrees)	Minimum P_E of Phase-A (in degrees)	Maximum P_E of Phase-A (in degrees)
0.071	0.012	0.052	0.097
Mean P_E of Phase-B (in degrees)	Stand. Dev. of P_E of Phase-B (in degrees)	Minimum P_E of Phase-B (in degrees)	Maximum P_E of Phase-B (in degrees)
0.063	0.009	0.047	0.084

Mean P_E of Phase-C (in degrees)	Stand. Dev. of P_E of Phase-C (in degrees)	Minimum P_E of Phase-C (in degrees)	Maximum P_E of Phase-C (in degrees)
0.083	0.014	0.057	0.111

Mean P_E of + Seq. (in degrees)	Stand. Dev. of P_E of + Seq. (in degrees)	Minimum P_E of + Seq. (in degrees)	Maximum P_E of + Seq. (in degrees)
0.045	0.013	-0.001	0.055

[C.1] Analysis of FE in Frequency Measurement:

Input Voltage Magnitude (in p.u.)	FE (in Hz)
20.000	0.000
40.000	0.000
60.000	0.000
80.000	0.000
100.000	0.000
120.000	0.000
140.000	0.000
160.000	0.000
180.000	0.000
200.000	0.000
220.000	0.000
240.000	0.000
260.000	0.000
280.000	0.000
300.000	0.000
320.000	0.000
340.000	0.000

Mean FE (in Hz)	Stand. Dev. of FE (in Hz)	Minimum FE (in Hz)	Maximum FE (in Hz)
0.000	0.000	0.000	0.000

[C.2] Verification of PMU Performance - Maximum FE in Frequency Measurement:

Maximum FE (in Hz)	Allowed Maximum FE (in Hz)	Test Result
0.000	0.010	PASS

[D.1] Analysis of RFE in Frequency Measurement:

Input Voltage Magnitude (in p.u.)	RFE (in Hz/s)
20.000	0.001
40.000	0.002
60.000	0.001
80.000	0.002
100.000	0.001
120.000	0.002
140.000	0.002
160.000	0.001
180.000	0.002
200.000	0.001
220.000	0.001
240.000	0.002
260.000	0.001
280.000	0.001
300.000	0.002
320.000	0.001
340.000	0.001

Mean FE (in Hz/s)	Stand. Dev. of FE (in Hz/s)	Minimum FE (in Hz/s)	Maximum FE (in Hz/s)
0.002	0.000	0.001	0.002

[D.2] Verification of PMU Performance - Maximum RFE in ROCOF Measurement:

Maximum RFE (in Hz/s)	Allowed Maximum RFE (in Hz/s)	Test Result
0.002	1.000	PASS

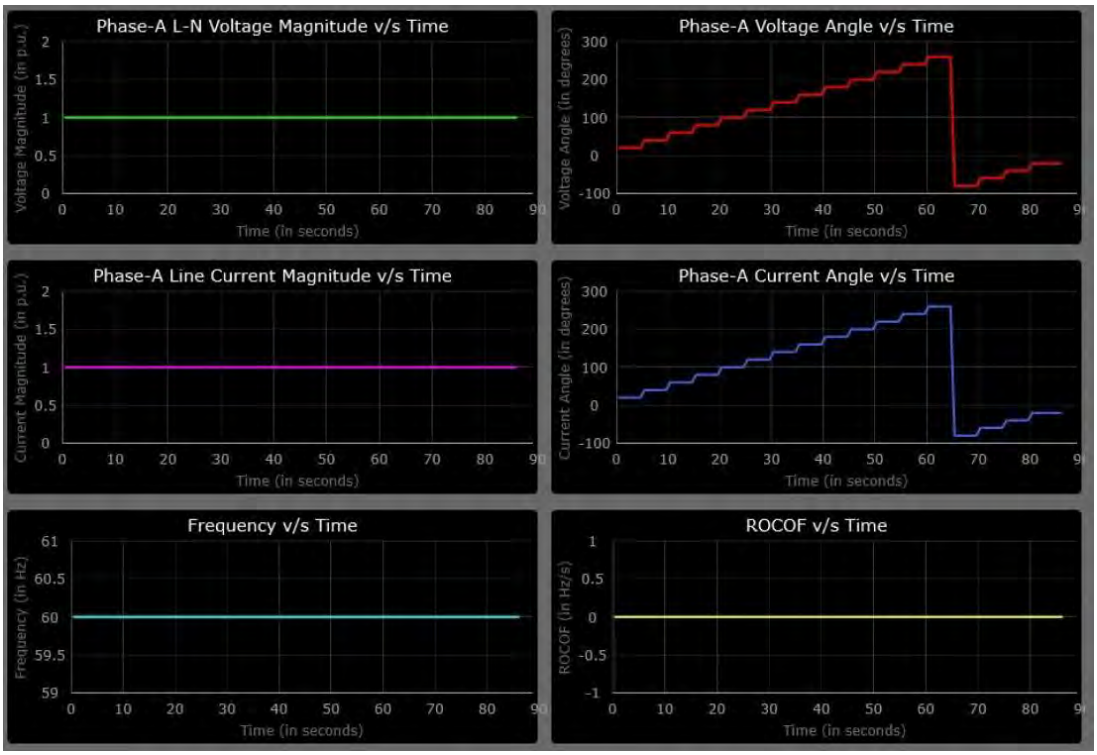

Figure A1.1 PPA test for balanced system with angle change.

References

[1] Real-time applications of phasor measurement units (PMU) for visualization, reactive power monitoring and voltage stability protection," The New York State Energy Research and Development Authority, Nov 2010. [Online]. Available: https://www.nyserda.ny.gov/-/media/Files/Publications/Research/Electic-Power-Delivery/real-time-applications-PMU.pdf

[2] "IEEE standard for synchrophasor measurements for power systems," IEEE Std. C37.118.1-2011 (Revision of IEEE Std. C37.118-2005), Dec. 2011.

[3] "IEEE standard for synchrophasor measurements for power systems-Amendment 1: modification of selected performance requirements," IEEE Std. C37.118.1a-2014 (Amendment to IEEE Std. C37.118.1-2011), Apr. 2014.

[4] "Advancement of synchrophasor technology in projects funded by the american recovery and reinvestment act of 2009," U.S. Department of Energy, Mar 2016. [Online]. Available: https://www.smartgrid.gov/files/ 20160320 Synchrophasor Report.pdf

[5] "Phasor measurement units gain credibility through improved test and calibration standards," Fluke Calibration, 2017. [Online]. Available:http://download.flukecal.com/pub/literature/3780120C EN w.pdf

[6] S. S. Biswas, A. K. Srivastava, J. S. Park, and J. Castaneda, "Tool for testing of phasor measurement units: Pmu performance analyser," IET Generation, Transmission Distribution, vol. 9, no. 2, pp. 154–163, 2015.

[7] P. Komarnicki, C. Dzienis, Z. A. Styczynski, J. Blumschein, and V. Centeno, "Practical experience with pmu system testing and calibration requirements," in 2008 IEEE Power and Energy Society General Meeting - Conversion and Delivery of Electrical Energy in the 21st Century, July 2008, pp. 1–5.

[8] Y. H. Tang, G. N. Stenbakken, and A. Goldstein, "Calibration of phasor measurement unit at nist," IEEE Transactions on Instrumentation and Measurement, vol. 62, no. 6, pp. 1417–1422, June 2013.

[9] D. Georgakopoulos and S. Quigg, "Precision measurement system for the calibration of phasor measurement units," IEEE Transactions on Instrumentation and Measurement, vol. 66, no. 6, pp. 1441–1445, June 2017.

[10] OPENPDC, "OPENPDC." [Online]. Available: http://www. gridprotectionalliance.org

[11] S. S. Biswas, A. K. Srivastava, J. S. Park, and J. Castaneda, "Tool for testing of phasor measurement units: Pmu performance analyser," IET Generation, Transmission Distribution, vol. 9, no. 2, pp. 154–163, 2015.

[12] A. Goldstein et al., "Ieee synchrophasor measurement test suite specification," New York: IEEE 2014

[13] M. Karimi-Ghartemani, B. T. Ooi, and A. Bakhshai, \Application of enhanced phase-locked loop system to the computation of synchrophasors," IEEE Transactions on Power Delivery, vol. 26, no. 1, pp. 22{32, Jan 2011.

[14] J. A. de la O Serna, \Synchrophasor estimation using prony's method," IEEE Transactions on Instrumentation and Measurement, vol. 62, no. 8, pp. 2119{2128, Aug 2013.

[15] A. G. Phadke, J. S. Thorp, and M. G. Adamiak, "A new measurement technique for tracking voltage phasors, local system frequency, and rate of change of frequency," IEEE Transactions on Power Apparatus and Systems, vol. PAS-102, no. 5, pp. 1025{1038, May 1983.

[16] A. E. Patel M., Aivolaitas S., \Real-Time Application of Synchrophasors for Improving Reliability ," NERC, Tech. Rep., October 2010.
[17] L. Chavez, D. Bakken, A. Bose, and P. Panciatici, "Erkios: End-to-end field-based RAS testing," in Innovative Smart Grid Technologies (ISGT), 2015 IEEE PES, Feb 2015.
[18] "WECC policy regarding extreme contingencies and umplanned events," Western Electric Coordinating Council, May 2002.
[19] "Special protection system criteria," North East Power Coordinating Council, p. 11, November 2002.
[20] D. Karlsson and X. Waymel, "System protection schemes in power networks," CIGRE Task Force 38.02.19, June 2001.
[21] M. Vaiman, P. Hines, J. Jiang, S. Norris, M. Papic, A. Pitto, Y. Wang, and G. Zweigle, "Mitigation and prevention of cascading outages: Methodologies and practical applications," in Power and Energy Society General Meeting (PES), 2013 IEEE, July 2013, pp. 1–5.
[22] "Minimum operating reliability criteria (morc)," Western Electric Coordinating Council, April 2005.
[23] J. Wen, W. Liu, P. Arons, and S. Pandey, "Evolution pathway towards wide area monitoring and protection - a real-world implementation of centralized RAS system," Smart Grid, IEEE Transactions on, vol. 5, no. 3, pp. 1506–1513, May 2014.

Part III

PMU/MU Characterization and Data Validation via Substation Dynamic State Estimation

Sakis A. P. Meliopoulos
George J. Cokkinides
Boqi Xie, Graduate Student
Jiahao Xie, Graduate Student
Yu Liu, Graduate Student
Liangyi Sun, Graduate Student
Yuan Kong, Graduate Student
Chiyang Zhong, Graduate Student
Orestis Vasios, Graduate Student

Georgia Institute of Technology

For information about this project, contact:

Sakis A.P. Meliopoulos
Georgia Institute of Technology
School of Electrical and Computer Engineering
777 Atlantic Dr. E164
Atlanta, Georgia 30332-0250
Phone: 404-894-2926
E-mail: sakis.m@gatech.edu

Power Systems Engineering Research Center

The Power Systems Engineering Research Center (PSERC) is a multi-university Center conducting research on challenges facing the electric power industry and educating the next generation of power engineers. More information about PSERC can be found at the Center's website: http://www.pserc.org.

For additional information, contact:

Power Systems Engineering Research Center
Arizona State University
527 Engineering Research Center
Tempe, Arizona 85287-5706
Phone: 480-965-1643
Fax: 480-727-2052

Notice Concerning Copyright Material

Table of Contents

List of Figures

List of Tables

1. Introduction

1.1 Background

Prior research by PSerc researchers have addressed a number of issues related to the future mission-critical systems. The authors of this part of the report have performed the following projects: (1) Real Time PMU-Based Stability Monitoring, S-50, (2) Adaptive and Intelligent PMUs for Smarter Applications, S-57, (3) Setting-less Protection: Laboratory Demonstrations, T-52G, (4) Setting-less Protection Methods, T-49G, and (5) Substation of the Future: A Feasibility Study, T-38.

The extensive PSerc body of knowledge acquired from these projects formed the basis for this project. The body of knowledge from these projects relate to the design and use of the mission-critical systems. Specifically, the following conclusions were reached. (1) Mission-critical systems heavily depend on the quality of service supplied by the measurement infrastructure that includes the sensors, as well as communications and software middleware, (2) To preserve quality of service, the systems need to be tested keeping in mind different aspects of its deployment: equipment selection, commissioning, in-service operation, and risk assessment, and (3) The techniques for testing and evaluation may range from substation test equipment to system-wide IT assessment tools, all needed to address different robustness issues and user awareness. It is clear that technology exists today to achieve the goal of monitoring and assessing the performance of these systems in real time. This in turn automates and simplifies the management of these important assets of the power system. The objective of this project is exactly that, to automate and simplify the management of these assets.

1.2 Overview of the Problem

Presently data from relays, PMUs, FDRs, and in general any IED in the substation are treated as separate entities without any tools to test their cross correlation and in general to provide automated checking of the validity of the data. If for some reason gaps and errors are generated in the data, these gaps/errors remain and propagate upstream to higher level devices. Furthermore, if any physical anomalies occur (such as a blown fuse, a damaged wire, etc.) they will affect the quality and validity of the data, yet there is no mechanism to determine the root cause of these anomalies. The idea is to integrate technologies developed under previous projects into an integrated physical-and-protection co-model and analysis software that will perform the following: (a) validate all data coming out of all relays, PMUs, and in general IEDs via the distributed state estimator, (b) detect anomalies and identify the root cause of these anomalies (hidden failures such as blown fuses, cut wires, etc. or human errors such as incorrect entry of system parameters such as CT and VT ratios, incorrect instrument transformer connection (delta/wye), etc.), (c) in case of temporary loss of data, it creates the missing data from the state estimator and inserts the estimated data into the stream, and (d) it provides the validated data and the substation state upstream for further utilization, such as construction of the system wide real time model at the control center. These objectives have been achieved by a two parts process: (a) construction of a laboratory for the purpose of fully characterizing the individual components of the system, i.e. PMUs, merging units, digital fault recorders, etc. and (b) by constructing a laboratory that comprises the protective relaying scheme of a small substation, the substation automation infrastructure and a simulator to

drive the system for the purpose of managing the data, identifying bad data and correcting bad data before the data are send upstream. These two developments are briefly described next.

1.3 PMU and Merging Unit Testing Lab Development

Phasor Measurement Units are instruments that can provide a precise and comprehensive view of the system. They can capture the state of the system in real time by measuring the voltage phasor, current phasor, frequency and rate of change of frequency at rates of 1 to 60 frames per second for 60 Hz systems. While PMUs are in general highly accurate instruments, they are subject to degradation for many reasons, such as loss of synchronizations, transients, connection to non-ideal instrumentation channels, hidden failures and manufacturer algorithmic inconsistencies. The characteristics of the PMUs are very important to the dynamic state estimator and a number of other applications. The correct model of the accuracy of PMUs can drastically improve the performance of the dynamic state estimator and result in well validated data. For this reason it is important to characterize PMUs by laboratory measurements.
In a present day substation it is possible that some or all of the data are collected with merging units. Merging units are pure data acquisition systems, GPS synchronized that provide the sampled values of voltage/current waveform. Application of the standard PMU on the sample values provides the voltage and current phasors, frequency and rate of frequency change. Therefore merging units coupled with phasor computation software act as Phasor Measurements Units. As such they must be characterized by measurement for the same reason as the legacy PMUs.

For the purpose of characterizing PMUs and Merging Units, an integrated testing platform based on the Standard PMU was developed. Previously developed technology was integrated into a laboratory set up for routine testing and characterization of PMUs and merging units for a variety of events such as steady state under nominal or off nominal frequency, frequency ramps, magnitude changes (smooth or abrupt), combination of frequency and magnitude changes, combination of above plus faults and others. The response of PMUs to these waveforms is tested against the standard PMU, a highly accurate algorithm to compute the phasors in real time when frequency changes occur as well as the waveform may be distorted with harmonics and transients. The standard PMU algorithm is based on (a) accurate tracking the frequency of the waveforms (b) representation of the waveform between two sample points as a quadratic function, and (c) computing the Fourier transform over a time window which is an integer number of cycles long; as the frequency changes the time window is accordingly adjusted. The standard PMU algorithm has been extensively tested and is more accurate than traditional methods. The developed hardware and software testing methods support and exceed the requirements of the standards, i.e. IEEE Std C37.118.1a™-2014 and IEEE Synchrophasor Test Suit Specifications [TSS].

The standard PMU algorithm is also used to convert merging units into phasor measurements units. Specifically, the sampled data from merging units are fed into the “standard PMU” which computes the phasors and creates a C37.118 stream of phasors. In addition, we develop software to communicate with multiple vendor merging units using IEC 61850 2-LE. This software is integrated into the overall testing platform. We have tested merging units from various manufacturers.

1.4 Dynamic State Estimation Based Data Validation and Correction

A laboratory has been developed that comprises the protective relaying scheme of a small substation, the substation automation infrastructure and a simulator to drive the system for the purpose of managing the data, identifying bad data and correcting bad data before the data are send upstream. The laboratory set up is shown in the Figure 1-1. The simulator is not shown in the figure. Note that the illustrated substation infrastructure combines the present technology of modern substations (numerical relays connected to a substation bus) and the most recent technology of merging units connected to process bus and protection computers connected between the process bus and substation bus. The laboratory enables research and development for in-service calibration and testing of relays, PMUs, merging units, etc., detection of physical system hidden failures, and data compression via the distributed dynamic state estimation. In addition, software products developed in this environment are readily transferable to actual substations. A brief description of the approach follows.

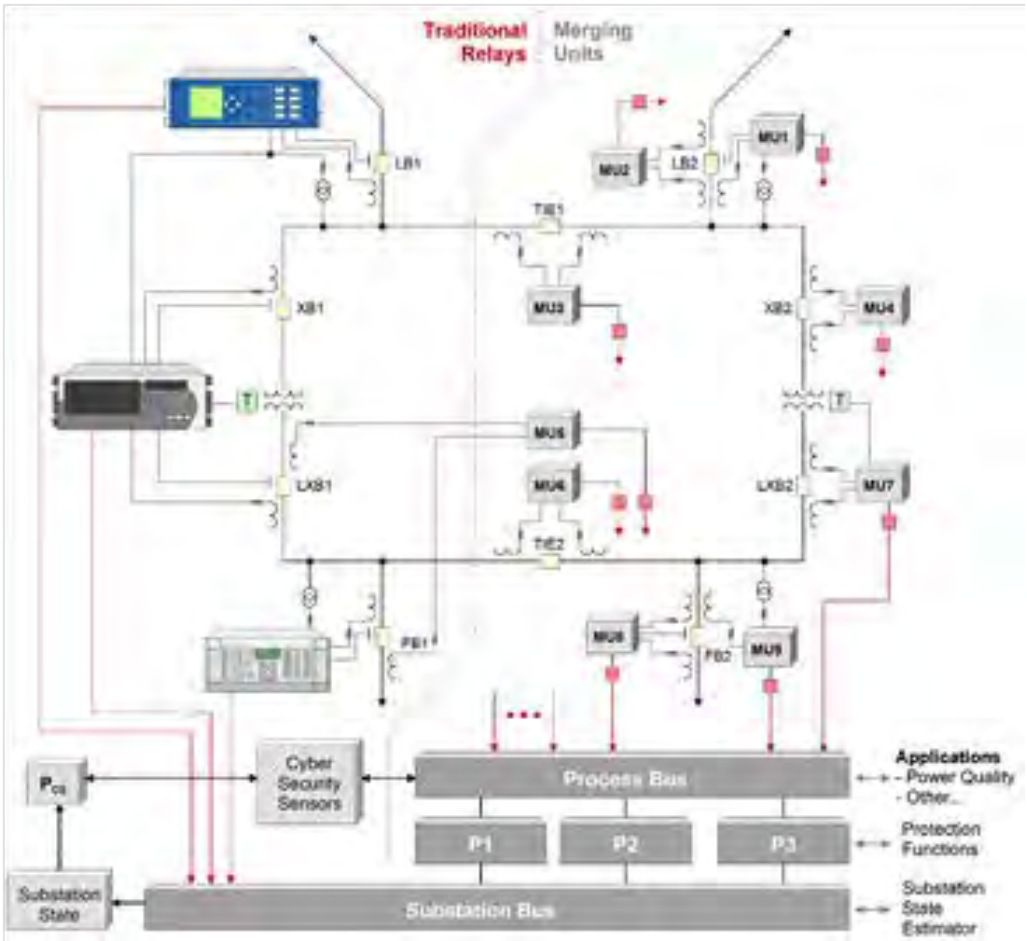

Figure 1.1: Laboratory Infrastructure for Testing the Distributed Dynamic State Estimation

The central component of the approach is the substation based distributed state estimator. This technology has been developed under a number of previous projects and was further improved under this project. This state estimator utilizes all available data from the relays, merging units, PMUs, meters and any IED in the substation and fits the data to a three-phase, breaker oriented

model of the substation including the circuits connected to the substation up to the next substation. Previous projects have demonstrated the ability of this state estimator to execute at rates of 60 times per second (each cycle). Details of the method and implementation issues have been described in a number of previous publications. In this project we utilized the statistical properties of the state estimator to fully characterize the validity of the data and the expected errors. Specifically, the statistical properties of the state estimator were used to detect and identify bad data. Bad data analysis determines the location and root cause of the bad data. Subsequently the bad data are removed and replaced with estimated values using the real time model of the substation. The end result is that all data are validated before are send to upstream devices and the system operator. The analysis identifies calibration issues, physical system failures (hidden failures), human errors (for example, incorrect entry of CT or VT ratios), subsystem failures (such as loss of GPS synchronization in some part of the system) and other. The overall process is illustrated in Figure 1-2.

Some of these sources of errors can be corrected in real time and automatically. For example, calibration errors can be corrected by resetting the appropriate parameters in the relays, human errors (incorrect entries) can be also corrected in real time and automatically. Other sources of error may require human intervention, such as blown fuses, etc.

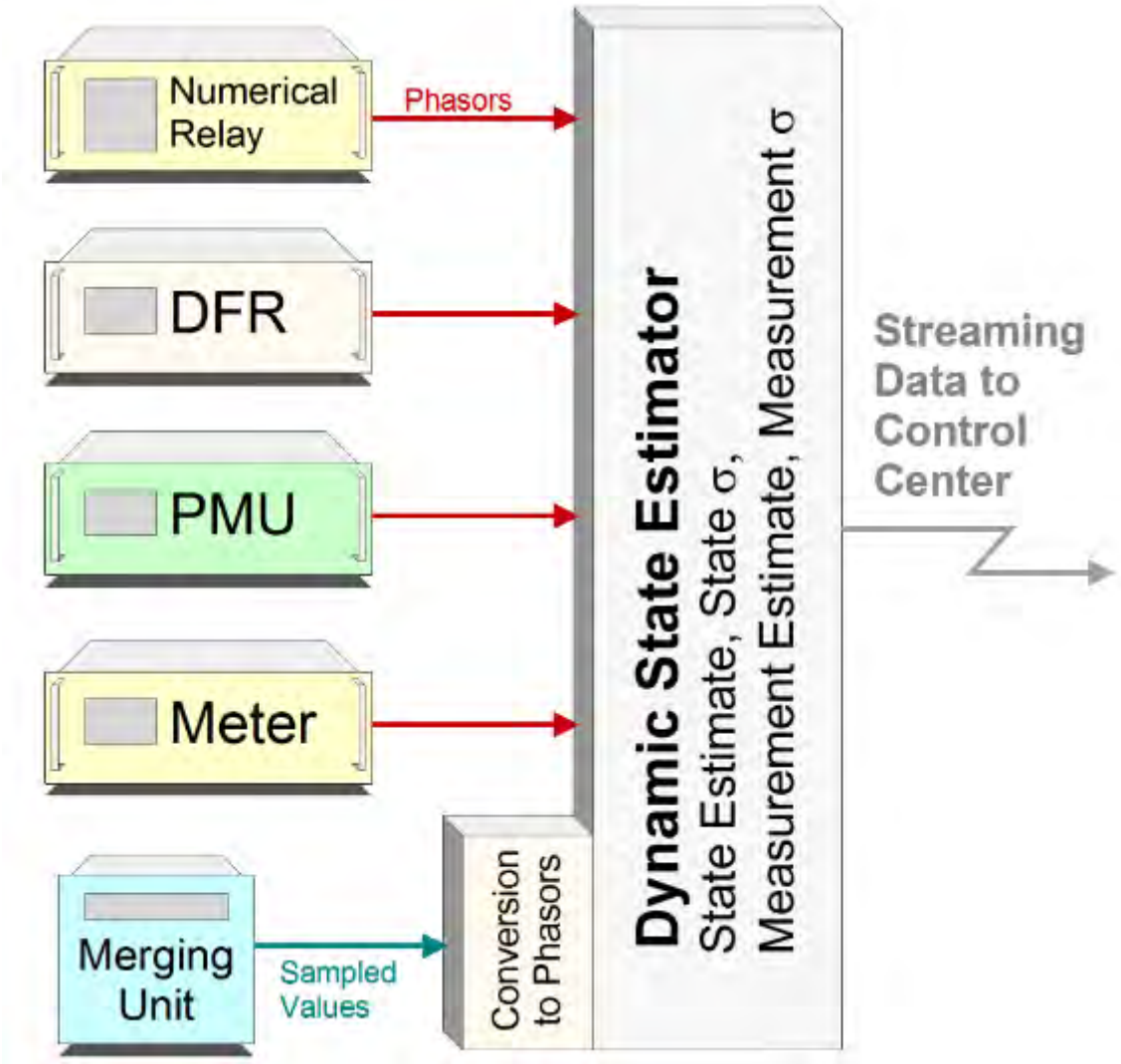

Figure 1.2: Connectivity and Data Flow of the Distributed Dynamic State Estimator

In summary, the substation based dynamic state estimation is used for validating all data collected in the substation and identify and correct any data anomalies. We integrated previously developed technology into an integrated data validation procedure for all PMUs and other relay, fault recorder, meter data in the entire substation. The data validation procedure is based on an integrated physical-and-protection co-model and dynamic state estimation methods. It requires high accuracy models of all components in the substation as well as the interconnecting transmission lines. This work was implemented at the Georgia Tech the laboratory and extensively tested with a model of the MARCY substation. The plan was to install the distributed dynamic state estimator in the field (MARCY substation). Because of delays in equipment installation at MARCY substation, we were unable to install the dynamic state estimator at MARCY. However, it appears that the installation of the equipment at MARCY will be completed in November of 2018. We plan to install the dynamic state estimator in the field at that time.

1.5 Field Demonstration

During this project we worked with the MARCY substation model of NYPA and the plan is to install the Dynamic State Estimation based data validation and correction on the MARCY substation. Preparations of this field demonstration have been completed (see section 5 of the report). However the installation of the required hardware for this demonstration has not been complete at NYPA as of the end of this project. It is expected that the hardware will be installed during the Fall 2018 planned outage at MARCY. We expect to install the Dynamic State Estimator with data validation and correction at that time.

1.6 Report Organization

This report describes the Georgia Tech work on project T-57HI. It is organized as follows: First a brief summary of the work is provided. Next, section 2 provides summary of the work towards the development of a PMU and Merging Unit Testing Laboratory. Section 3 provides summary of the work towards a substation based state estimator with capability to validate data and detect hidden failures. Section 4, a numerical example is used to demonstrate the substation based dynamic state estimator. In section 5, a use case for the application of the quasi-dynamic state estimator on the MARCY substation is described. In Appendix A, the object-oriented modeling approach used in state estimation is described, and an example is provided. Finally, the section “Papers Published” provides a list of publications resulted from this work.

2. PMU and Merging Unit Testing Lab Development

An integrated testing platform based on the Standard PMU is described in this section. We integrate previously developed technology into an integrated laboratory set up for routine testing and characterization of PMUs and merging units for a variety of events such as steady state under nominal or off nominal frequency, frequency ramps, magnitude changes (smooth or abrupt), combination of frequency and magnitude changes, combination of above plus faults and others. The approach used to achieve this goal is briefly described below. The method and techniques used support and exceed the requirements of the standards, i.e. IEEE Std C37.118.1a™-2014 and IEEE Synchrophasor Test Suit Specifications [TSS]. The method is also used to convert merging units into phasor measurements units. Specifically, the sampled data from merging units are fed into the "standard PMU" which computes the phasors and creates a C37.118 stream.

A laboratory infrastructure for high precision testing and characterization of PMUs and merging units is constructed. The performance metrics of the PMU accuracy or merging unit accuracy are: (a) Magnitude Accuracy, (b) Time or Phase Angle Accuracy, (c) Frequency Accuracy, (d) Communication Compliance to IEEE Standard C37.118, and (e) communication compliance with IEC 61850-LE-2. The functional laboratory infrastructure for testing PMUs is shown in Figure 2.1.

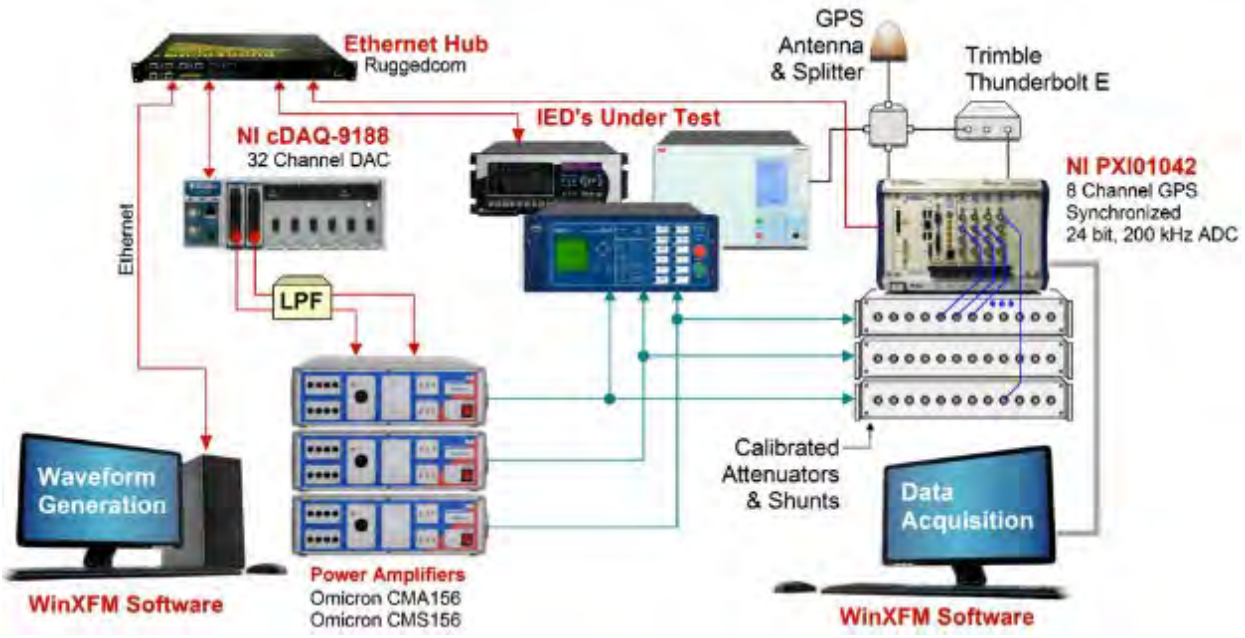

Figure 2.1: Functional Laboratory Setup for Testing and Characterizing PMUs (Similar Arrangement for Merging Units)

A similar setup is used for merging units. Photographs of the laboratory components are shown in Figures 2.2 and 2.3. Presently, the laboratory includes several PMUs (SEL, GE, USI, etc.) and several Merging Units (2 GE Hardfiber, 1 Alstom, 2 Siemens). The method is applicable to any manufacturer relays, PMU, merging units, and fault recorders. A short description of the laboratory work follows.

Figure 2.2: Photograph of Laboratory Equipment 1 – View 1

Figure 2.3: Photograph of Laboratory Equipment 2 – View 2

Testing and characterization of the PMUs: The basic approach is based on injecting signals into the PMU (or merging unit) through a simulator, a bank of D/A converters, and a bank of amplifiers, as shown in Figure 2.1; then capture the input to the PMU (or merging unit) via a high accuracy (magnitude and time) data acquisition system (the NI PXI01042, Trimble, GPS antenna) and compute the phasors with a high precision method (see the standard PMU); then capture the output of the PMU (or merging unit), and finally compute the errors of the PMU (or merging unit) versus the standard PMU. Multiple error metrics are used, examples are: (a) timing error (with precision 0.1 microsecond), (b) magnitude error on a sample by sample basis, (c) magnitude error over a user defined time interval, (d) total vector error, and others.

The PMU and MU testing lab consists of a signal generation system and a benchmark data acquisition system. The signal generation system consists of a personal computer running the WinXFM program which transmits streaming sampled value data stored in COMTRADE files to D/A converters. Specifically, the sample values are transmitted to a National Instrument 16 bit, 36 channel D/A converter unit (NI9188) via a local area network (Ethernet). The maximum D/A converter sampling rate is 25 ksps per channel. The local area network is based on a Ruggedcom Ethernet hub. The D/A converter analog output is a low power voltage signal with maximum amplitude of 10 Volts peak. These signals are fed into a bank of Omicron voltage and current amplifiers which raise the output voltage and current to standard levels required by relays, PMUs and MUs. The omicron voltage amplifiers peak output voltage is 250 volts, and the current amplifiers can generate peak output currents 5 amperes continuously, and up to 25 amperes for short periods of time (few seconds).

The benchmark data acquisition system is based on a national instrument PXI chassis containing 8 channels of high quality A/D converters which are synchronized to a GPS disciplined clock. The A/D converters sample the analog signals with 24-bit resolution using Sigma-Delta architecture. The clock driving the A/D converters is a 10 MHz signal generated by a Trimble Thunderbolt-E GPS disciplined oven-controlled crystal oscillator. The A/D converter digital filters are also periodically synchronized using the 1-PPS signal provided by the Trimble GPS receiver. This system achieves UTC synchronized sampling with typical accuracy of less than 100 nanoseconds. The PXI chassis also contains a Windows-based Quad-Core PC which processes the A/D converter data and computes phasors. The phasor computations are carried out in the WinXFM software running in this PC using the "Standard PMU" algorithm (The standard PMU algorithm is described in a technical paper). The Standard PMU algorithm generates a high quality synchro-phasor output which is used as a benchmark for evaluating the performance of the various devices under test.

At the same time, the WinXFM program captures the output of the device under test (in IEEE-C38.118 synchro-phasor stream format) and displays the discrepancies between the device under test and the standard PMU output. Various test signals are used, including steady state, frequency ramps, amplitude transients, etc. The results are displayed in plot format as phase, amplitude and frequency error versus time. Note that the WinXFM program includes a waveform calculator feature, which allows the user to define arbitrary functions of all captured waveforms, and thus various error metrics can be easily specified and displayed.

Note that the performance of the described evaluation system is solely determined by the accuracy of the benchmark data acquisition system, and not affected by the accuracy of the signal generation system. This is an important advantage of the described approach, since it is immune to the inevitable amplitude and phase errors inherent in power amplifiers and delays and other errors generated by free-running D/A converters.

A similar approach has been developed for merging unit evaluation. Note that the outputs of merging units are "point-of-time" sample values. Specifically, the evaluation of the merging units is performed in two ways: (a) direct comparison of the point-of-time samples from the merging unit under test to the corresponding point-of-time samples generated by the benchmark data acquisition system, and (b) comparison of the synchro-phasor data derived from the merging unit data using the standard PMU algorithm to synchro-phasors generated by the benchmark data acquisition system.

In order to facilitate merging unit characterization, a "Merging Unit Data Concentrator" (MUDC) software module has been developed and integrated into the WinXFM program. The MUDC collects sampled values from multiple MUs, time aligns the data, and adds time stamps. This process facilitates the proper processing of the sample values. The user interface of the Merging Unit Data Concentrator is shown in Figure 2.4. The sampling rate, the base frequency, maximum latency and buffer size can be user selected set. The merging units can be chosen from the "Merging Units" tab, and the available measurements from the selected merging units can be chosen in the "Measurements" tab. An example of the measurement selection user interface is shown in Figure 2.5. Any errors detected in the incoming merging unit data are reported in the "Error Counts" block.

A unique feature is that the system can test and characterize multiple Merging Units simultaneously. This allows comparisons of merging units by various manufacturers in order to determine interoperability characteristics.

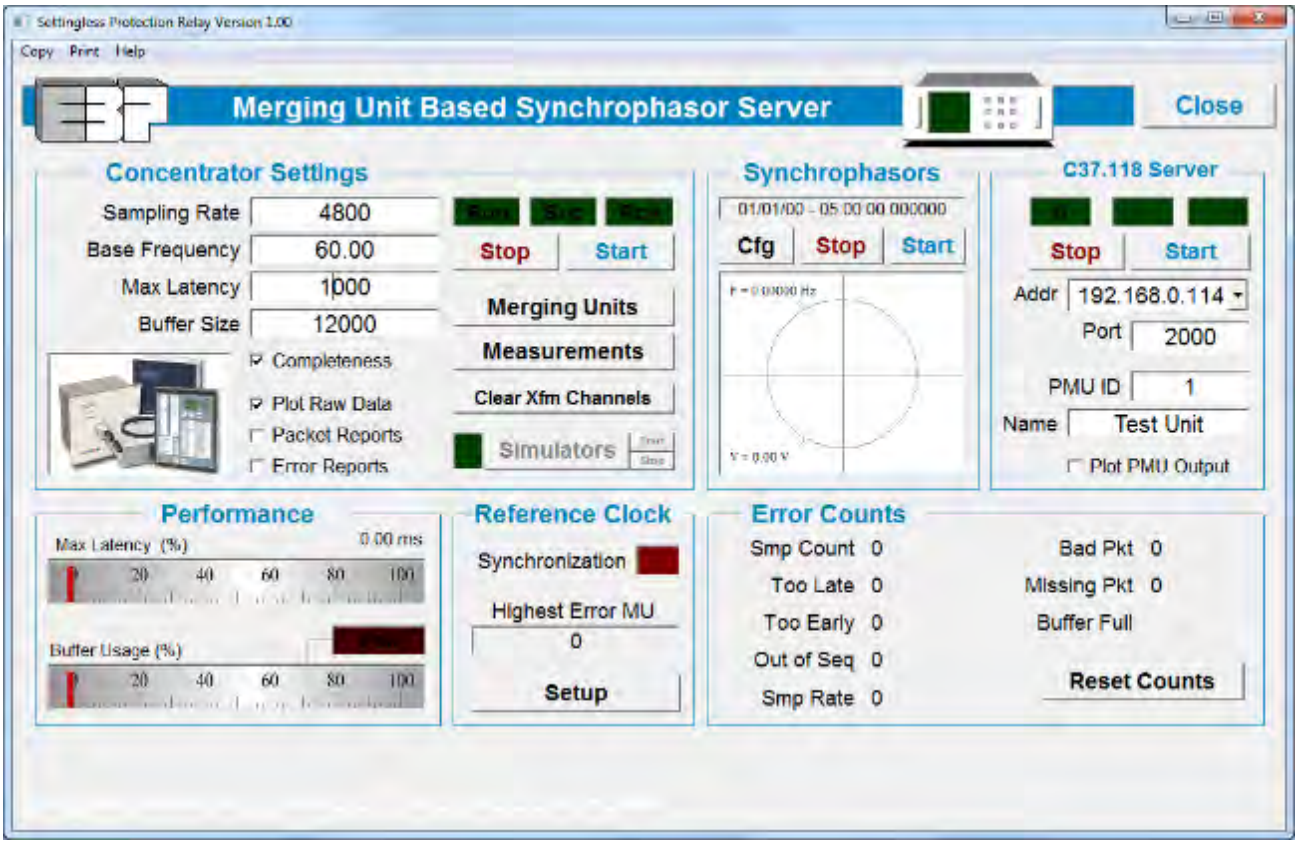

Figure 2.4: User Interface of the Merging Unit Data Concentrator

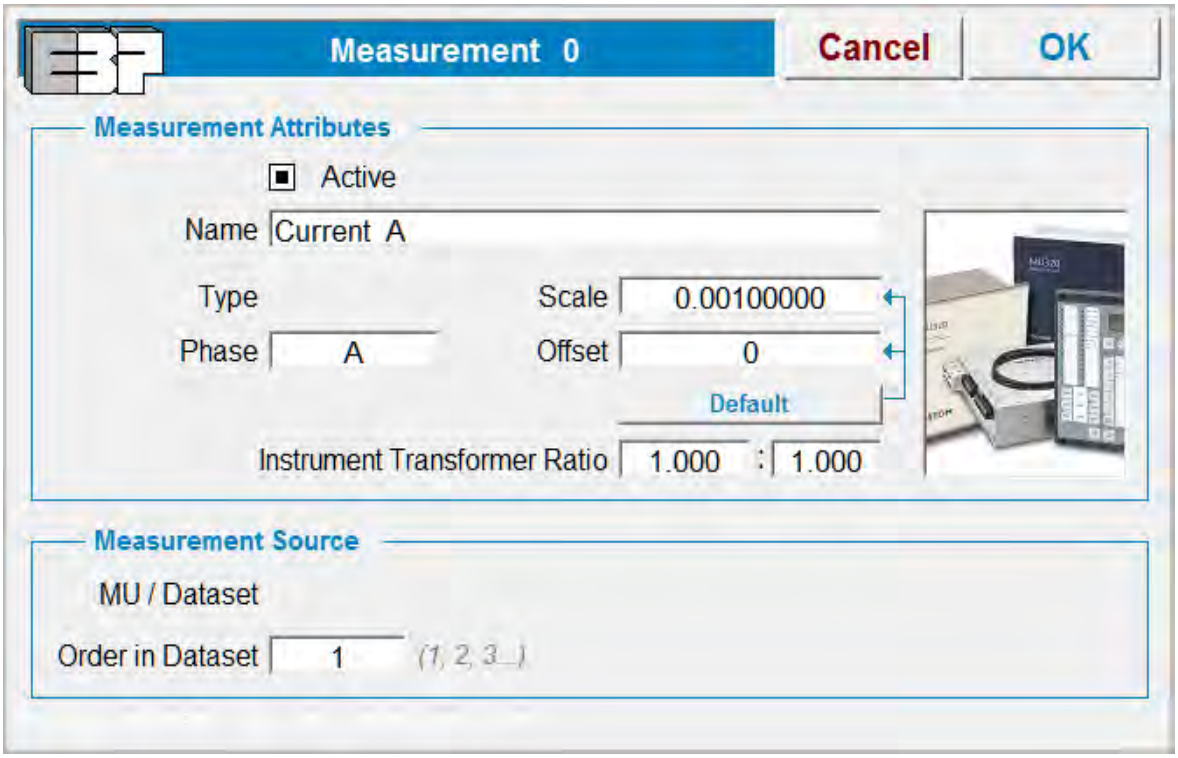

Figure 2.5: User Interface of the Measurement Selection

Processing of the sample data using the standard PMU and creating a C37.118 stream: The output of the merging units is sampled values with GPS time stamps. The standard PMU is used to convert the sampled values into streaming data in C37.118 format. The performance of the Merging Units is performed in two ways. First the timing accuracy of each sampled value is checked by comparing the input value and coincidental GPS time to the output sample and time tag. The GPS time and time tag should be less than 1 microsecond. The second test is to compare the input phasor captured with the method as described in the previous paragraph to the output phasor.

Organizing and Standardizing the Testing: A library of signals is generated and stored in COMTRADE format for testing PMUs and merging nits. The library contains various events. A sample of these events is: (a) steady state operation at various frequencies (nominal frequency, nominal frequency plus 0.1 Hz, 0.2 Hz, minus 0.1 Hz, etc., (b) events with frequency ramps of various rates, (c) events with abrupt and gradual magnitude changes, (d) events with combination of magnitude and frequency changes during a fault, and others. Figure 2.6 shows a test signal from the library. The test signal represents a frequency ramp from 60 Hz to 60.5 Hz. Note that the actual waveforms are not clear in the figure. However, the data are in COMTRADE format and are available to be viewed with any COMTRADE reader.

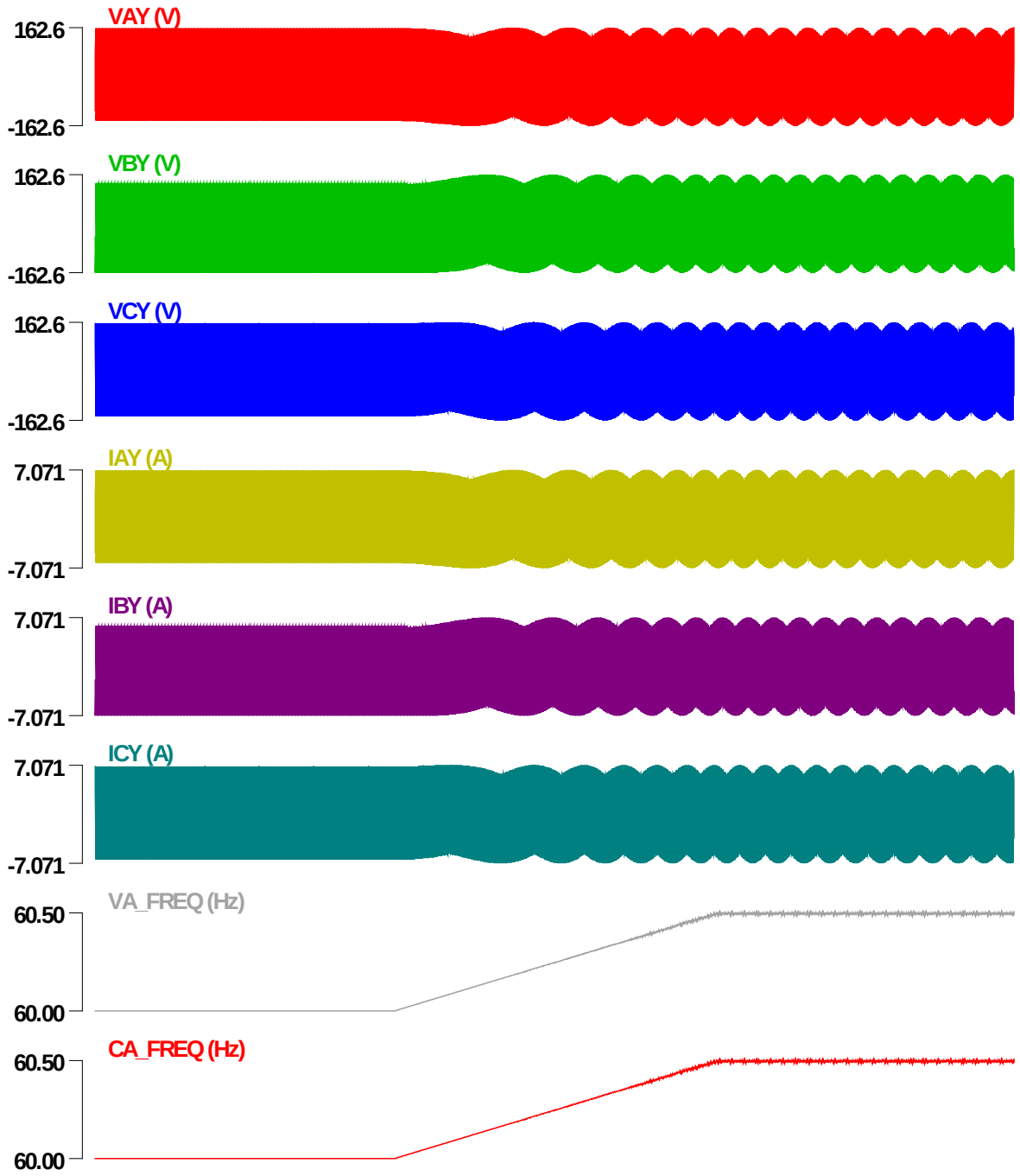

Figure 2.6: Example Test Signal: Total Time of graph: 15 seconds, Frequency Ramp of +0.1 Hz/sec for 5 secs Starting at time t=5 seconds

A basic characteristic of the testing method is its ability to (a) accurately capture the input signal and (b) accurately compute the phasors of the input signal. We have verified that the input signal is captured with accuracy: magnitude 0.01% and timing 0.1 microsecond. The accuracy of the computed input phasors is achieved with the Standard PMU. The Standard PMU algorithm uses an advanced method for estimating the frequency of the input signals and a quadratic fitting of the signal between samples. As the frequency changes, the time window changes as it is defined as an

integer number of cycles and the number of samples in the time window changes (non-integer number of cycles). The analog signal is recreated by a quadratic fitting as discussed earlier. The Fourier transform is applied to the signal over the time window which is an exact integer number of cycles (one cycle for 60 phasors/sec, two cycles for 30 phasors per sec, etc.). This approach eliminates spectral leakage, a well-known source of PMU errors. We also refer to this method as fractional sample correction method. The performance evaluation of this method is shown in Figure 2.7. This figure above shows the performance of the Standard PMU algorithm for a range of sampling rates (1 to 10 ks/s), different time windows (number of cycles) and different approximation methods for a 60 Hz waveform. The phase angle error of the quadratic integration method (the Standard PMU) is plotted (green curve) for sampling rates ranging from 1 to 10 kHz. For comparison purposes, the plot also includes the results of the discrete time phasor computation without any fractional sample correction (red curve), and phasor computation with fractional sample correction based on trapezoidal integration (blue curve). Note that if one standardizes to 128 samples per cycle (or 7.68 ks/s as suggested by IEC), the phase error of the Standard PMU is less than 0.00005 degrees. The Standard PMU is an integral part of the testing laboratory for PMUs and merging units.

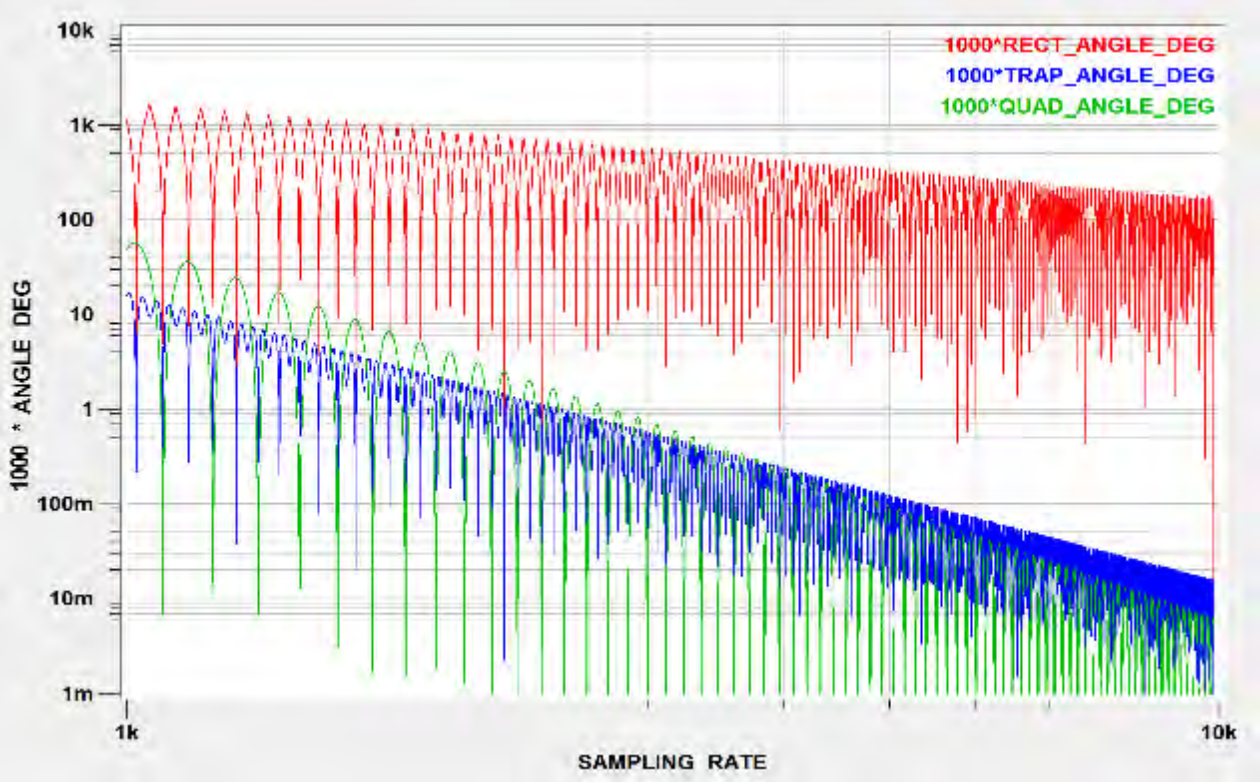

Figure 2.7: Performance evaluation of fractional sample correction method

Results of data capturing accuracy (hardware) and accuracy of phasor computation using the standard PMU (software) are presented in this section. As an example, Figure 2.8 shows the performance of a specific PMU (in this case a fault recorder) during testing with six test signals. Figure 2.9 shows the timing accuracy of the hardware. Note the accuracy exceeds 0.1 microsecond. The accuracy of the software has been evaluated with a number of numerical experiments.

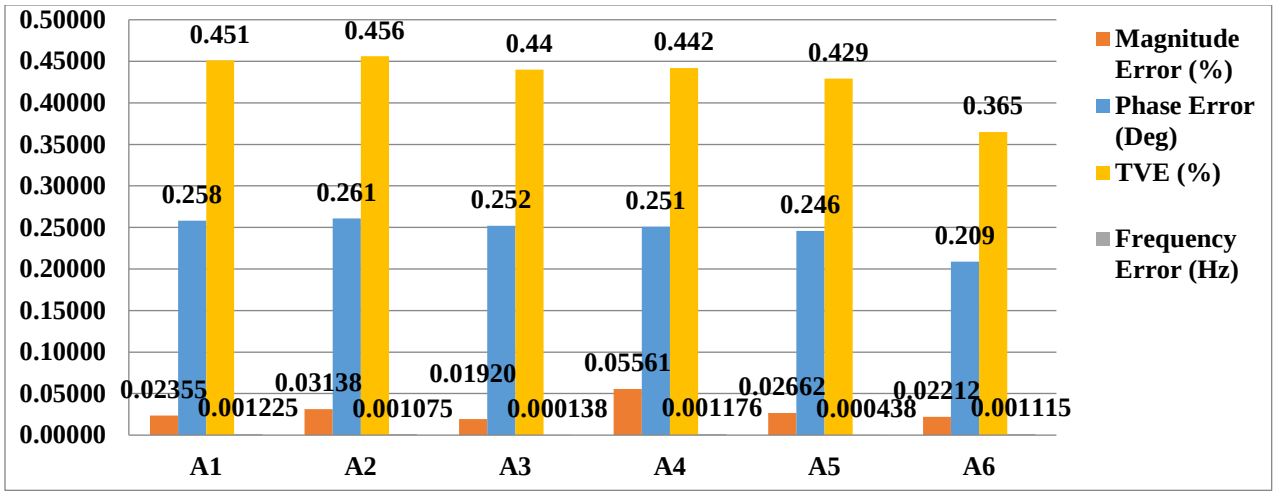

Figure 2.8: Example Maximum Absolute Error (Magnitude, Phase, and TVE) for Six Test Signals

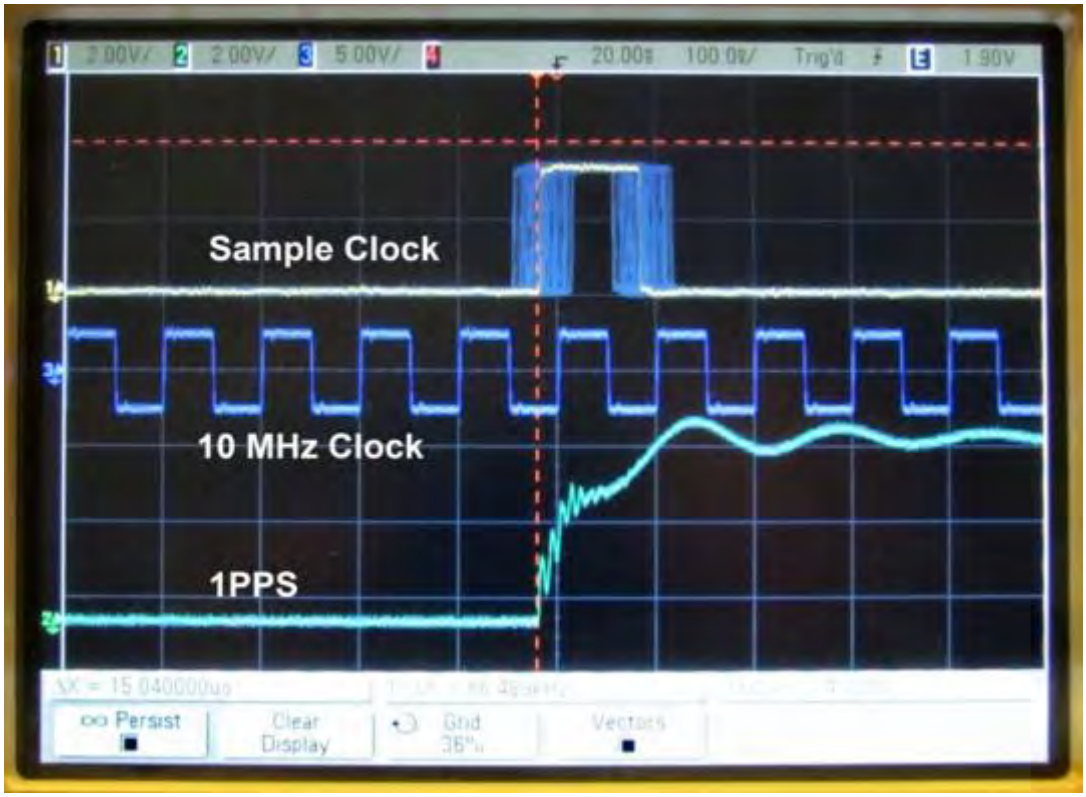

Figure 2.9: Verification of A/D Converter Sample Clock Synchronization

3. Substation Based Dynamic State Estimation

In this section, an integrated data validation procedure for all PMUs and other data in the entire substation is elaborated. The data validation procedure is model based using the distributed dynamic state estimation. It requires the model of all components in the substation as well as the interconnecting transmission lines. The validation provides quantitative characterization of the data, i.e. percent error, it detects and identifies bad PMU or other data, and it identifies the source of bad data, including hidden failures. The methodology is implemented in the laboratory before deploying it in the field. The laboratory setup will demonstrate the characterization of PMU and other data and the detection and identification of hidden failures.

We propose to integrate technologies developed under previous projects into an integrated physical-and-protection co-model and analysis software that performs the following: (a) validates all data coming out of all relays, PMUs, and in general all IEDs via the distributed state estimator, (b) detects anomalies and identifies the root cause of these anomalies (hidden failures such as blown fuses, cut wires, etc. or human errors such as incorrect entry of system parameters such as CT and VT ratios, incorrect instrument transformer connection (delta/wye), etc.), (c) in case of temporary loss of data, it will create the missing data from the state estimator and will insert the estimated data into the stream, and (d) provides the validated data and the substation state up stream for further utilization, such as construction of the system wide real time model at the control center. These objectives will be achieved by constructing a laboratory that will comprise the protective relaying scheme of a small substation, the substation automation infrastructure and a simulator to drive the system.

Presently data from relays, PMUs, FDRs, and in general any IED in the substation are treated as separate entities without any tools to test their cross correlation and in general to provide automated checking of the validity of the data. If for some reason gaps are generated in the data, these gaps remain and propagate to higher level devices. Furthermore, if any physical anomalies occur (such as a blown fuse, a damaged wire, incorrect settings in electronic meters or PMUs, etc.) they will affect the quality and validity of the data, yet there is no mechanism to determine the root cause of these anomalies. The evaluation method consists of comparing the collected data to the physical model of the system. To limit the size of the problem, this task is performed at each substation independently from other substations. A systematic and mathematically rigorous method is used for setting up the substation model and collecting the PMU data and data from other devices and correlating them to the model. Discrepancies will trigger a procedure to determine the level of discrepancy and the source of the discrepancy by backtracking on the physical model. This procedure will identify any hidden failures.

The central component of the approach is the substation based distributed state estimator. This technology has been developed under a number of previous projects and it is further improved to achieve the goals of this project. The state estimator utilizes all available data from the relays, merging units, PMUs, meters and any IED in the substation and fits the data to a three-phase, breaker-oriented model of the substation including the circuits connected to the substation up to the next substation. Previous projects have demonstrated the ability of this state estimator to execute at rates of 60 times per second (each cycle). The statistical properties of the state estimator is used to detect and identify bad data. The bad data are further analyzed to determine the root

cause of the bad data and to make corrections or send this information to the operator for further action. This analysis identifies any calibration issues, physical system failures (hidden failures), human errors (for example, incorrect entry of CT or VT ratios), subsystem failures (such as loss of GPS synchronization in some part of the system) and other. Some of these sources of errors can be corrected in real time and automatically. For example, calibration errors can be corrected by resetting the appropriate parameters in the relays, human errors (incorrect entries) can be also corrected in real time and automatically. Other sources of error may require human intervention, such as blown fuses, etc. Not that the system operates in real time and therefore any problems that may arise will be detected within a couple of cycles after their occurrence.

The initial laboratory set up is shown in the Figure 3.1. The simulator is not shown in the figure. Note that the proposed substation infrastructure combines present technology of modern substations (numerical relays connected to a substation bus) as well as recent technology of merging units connected to process bus and protection computers connected between the process bus and substation bus. Equipment for completing this laboratory set up has been procured as well as donated by the industry.

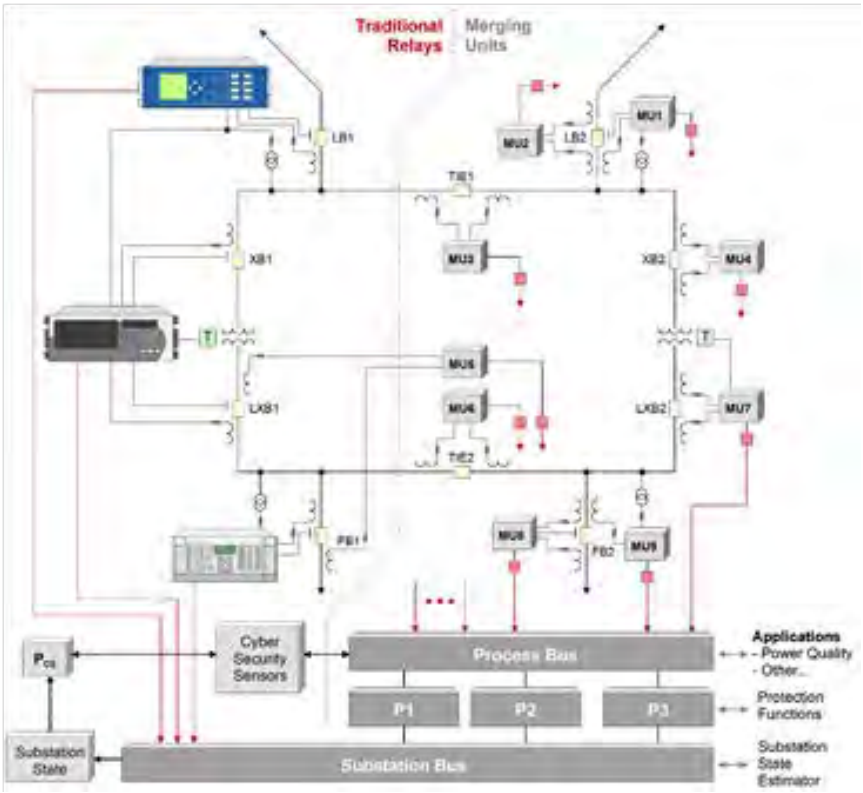

Figure 3.1: Laboratory Infrastructure for Testing the Distributed Dynamic State Estimation

The substation based dynamic state estimator collects the data and performs the dynamic state estimation. Specifically, all the data from all IEDs in the specific substation are first be collected into a data concentrator and converted to C37.118 data stream. Then the data stream run through the state estimator in each substation separately where the quasi-dynamic state estimation (QSE)

is performed. To be more specific, the dynamic state estimator uses the substation model and outputs estimated substation states, estimated measurements, expected errors on states and measurements and the corresponding confidence level. Furthermore, it detects and corrects bad data so that the streaming data outputs (in C37.118 format) to the control center contain only validated data. The overall structure is illustrated in Figure 3.2.
The estimator is defined in terms of models, states, measurement sets and estimation methods. The dynamic state estimation algorithm is object-oriented, i.e. all the models in the system are expressed in a standard format, namely the state and control algebraic companion form (SCAQCF) and the distributed dynamic state estimation operates directly on these object models. SCAQCF device model is derived from quadratic integration on quadratized physical device model, which describes all the physical laws that a specific component should satisfy. The detailed SCAQCF syntax is described in Appendix A.

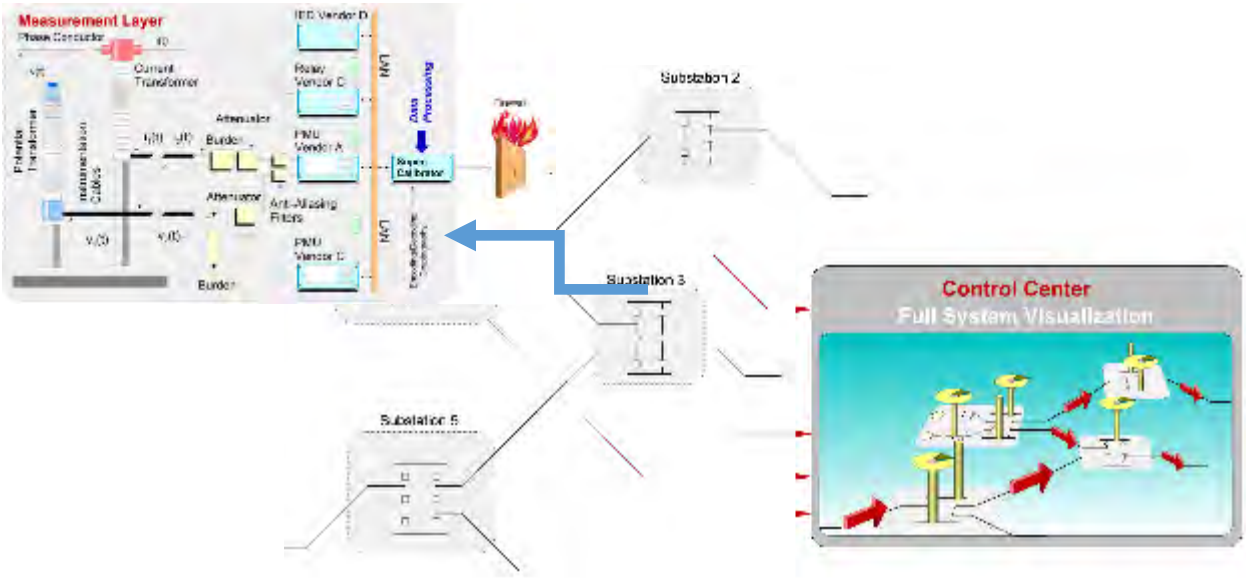

Figure 3.2: Architecture of the Distributed Quasi-Dynamic State Estimator

The QSE models the slow electro-mechanical transients of the power system with differential equations while the fast electrical transients are neglected and electrical quantities are represented with time varying phasors. The architecture illustrated in Figure 3.2 is described as follows: A local state estimator is installed in each substation and utilizes measurements only at the local substation for the purpose of avoiding the requirement of obtaining and transmitting via communication channels measurements from other substations. The quasi-dynamic state estimation is performed in each substation in parallel (i.e. substation level state estimation). The estimated states for each substation are produced and sent to the control center where the system wide estimated states are synthesized by combining all the substation estimated states of the same time instant. Note that for this approach, data from at least one GPS-synchronized device is required in each substation in order to synchronize all the data in the substation.

The measurements in a specific substation can be classified into four types: (a) Actual Measurements: measurements that come from actual measurement channels, i.e. any

measurements from any IEDs (relays, meters, FDR, PMUs, etc.); (b) Derived Measurements: measurements derived from actual measurements based on topology; (c) Pseudo Measurements: not directly measured, represent quantities for which their value is approximately known, such as missing phase measurements, neutral/shield voltage measurements, neutral currents, etc. (d) Virtual Measurements: mathematical quantities defined by physical laws, such as Kirchoff's current law, model equations, etc.

The dynamic state estimator uses three different methods to estimate the states and perform the protection: (a) Unconstrained Least Square Method; (b) Constrained Least Square Method; (c) Extended Kalman Filtering Method.

The unconstrained weighted least square (WLS) method is briefly presented below.

The measurements b are expressed as functions of the states:

$$\mathbf{b} = h(\mathbf{x}) \tag{3.2}$$

The WLS method minimizes the sum of the weighted squares of the components of the residual vector. Mathematically:

$$Minimize \;\; J = \sum_{i=1}^{n} \left(\frac{h_i(x) - z_i}{\sigma_i} \right)^2 = \sum_{i=1}^{n} s_i^2 = \eta^T W \eta \tag{3.3}$$

where $s_i = \frac{\eta_i}{\sigma_i}$, $W = diag\left\{ ..., \frac{1}{\sigma_i^2}, ... \right\}$ and σ_i is the standard deviation of the meter by which the corresponding measurement b is measured;

The solution is given with Newton's iterative algorithm:

$$\mathbf{x}^{\nu+1} = \mathbf{x}^{\nu} - (H^T W H)^{-1} H^T W (h(\mathbf{x}^{\nu}) - \mathbf{b}) \tag{3.4}$$

where H is the Jacobian matrix:

$$H = \frac{\partial h(\mathbf{x})}{\partial \mathbf{x}} \tag{3.5}$$

Once the solution is calculated by equation (3.4), chi-square test is applied. Chi-square test provides the probability that the measurements are consistent with the dynamic model. Chi-square test is applied as follows. First the quantity (errors of estimated data) ξ is computed:

$$\xi = \sum_{i} \left(\frac{h_i(x) - z_i}{\sigma_i} \right)^2 \tag{3.6}$$

The probability (confidence level) that the measurements and the model fit together within the accuracy of the meters is computed from:

$$\Pr[\chi^2 \geq \xi] = 1 - \Pr[\chi^2 \leq \xi] = 1 - \Pr(\xi, \upsilon) \quad (3.7)$$

where υ is the degree of freedom and it is the difference between the number of measurements and states.

A confidence level around 100% (small chi-square value) infers the measurements are highly consistent with the dynamic model of the system, while a confidence level around 0% (large chi-square value) means that measurements do not match the dynamic model of the system. In case a low confidence level is obtained, the next task is to identify the bad measurements.

The functionality of the state estimator components can be viewed in Figure 3.3 which illustrates the user interface of the substation based state estimator.

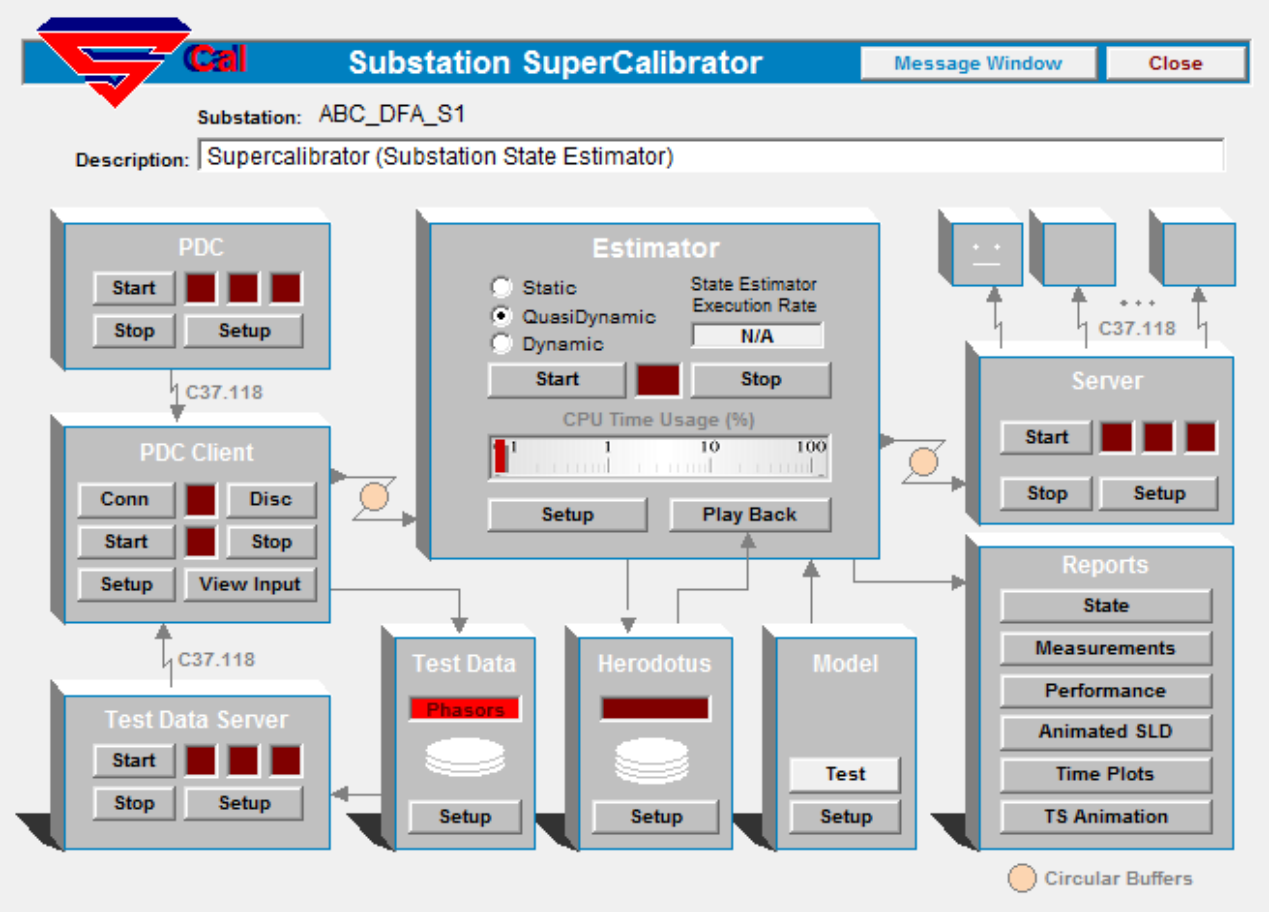

Figure 3.3: Substation Based Quasi-Dynamic State Estimator User Interface

The PDC client connects either to a Phasor Data Concentrator (PDC, for real time data) or to the Test Data Server (for simulation experiments) and receives a C37.118 synchrophasor data stream that may also be mixed with data from standard relays. The data are sent to a circular buffer which is accessed by the state estimator to perform the state estimation.

Before the execution of the state estimator, the user has to (a) enter the network model, and (b) map the measurements to the substation physical system. This is a necessary step because the

measurements must be linked to the model of the system for the purpose of extracting the mathematical model of the measurement.

Several reporting and visualization tools have been implemented for the state estimation results. Performance evaluation of the state estimation results is based on several metrics, and one of them is the parameterized (parameter k) chi-square test shown in Figure 3.4. The parameter k is defined as follows: if it is 1.0 then the standard deviation of each measurement is equal to the accuracy of the measurement error with which this measurement was obtained. If different than 1.0 then the standard deviation of the measurement error equals the accuracy of the measurement error times k.

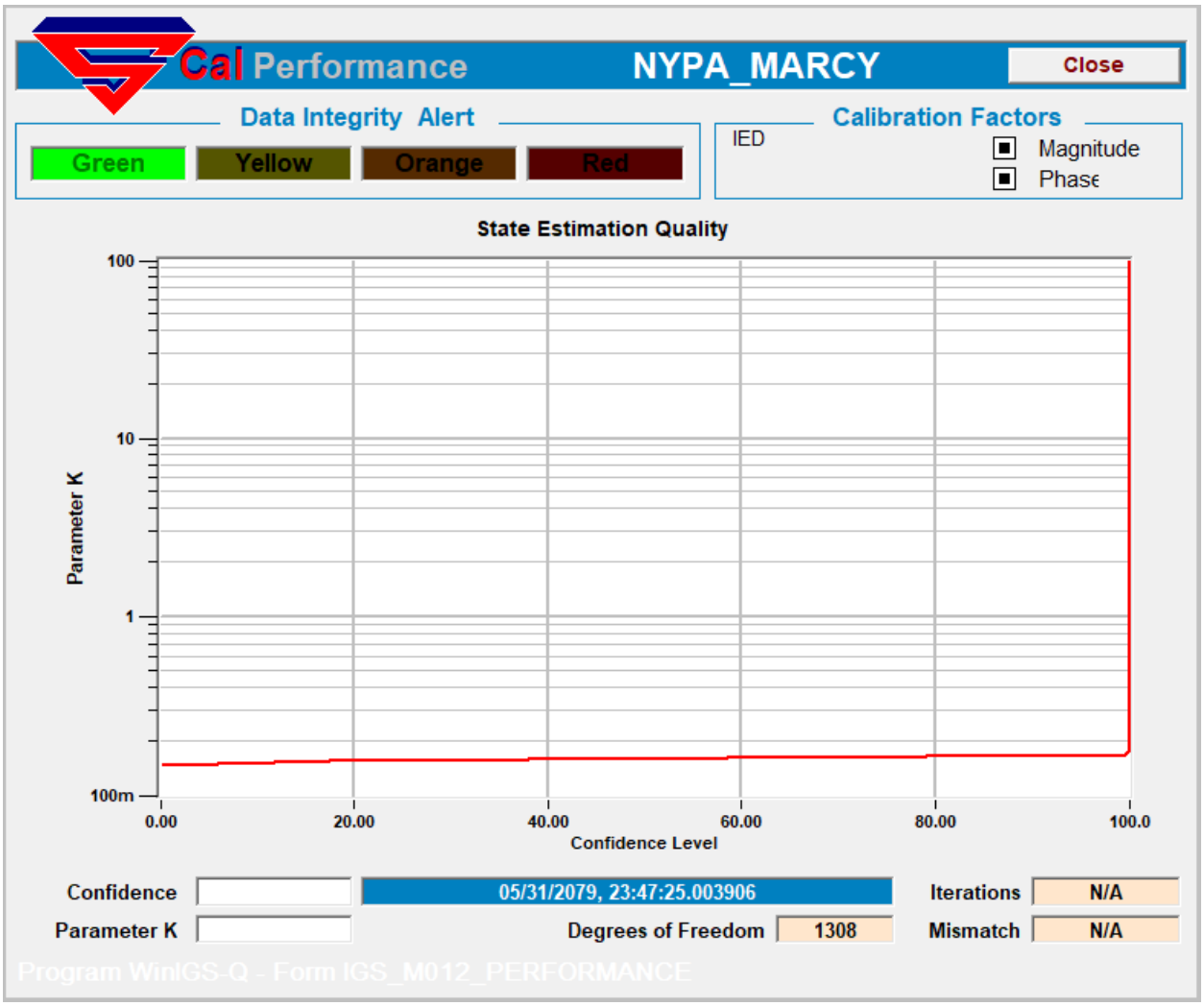

Figure 3.4: k Value versus Confidence Level for a Sample Run

A play back function is also under continuous development and integrated with the state estimator. The purpose of the play back capability is to enable high fidelity disturbance playback (or simply playback of normal operating conditions). For this purpose, it is necessary to store not only real time measurements data as well as state estimation data but also coincidental model of the system. The play back function also provides all the visualization options that are available in real time.

The execution time monitor (CPU Time Usage) in the state estimator monitors the portion of the time used by the state estimation calculations, where 100% corresponds to the time between two successive QSE computations. If the state estimation is set to execute 60 times per second, then 100% corresponds to 16.6 ms. The details of the developed state estimator with a use case can be found in section 5.

4. Substation Based Dynamic State Estimation: Numerical Example

This section uses a numerical example to demonstrate the substation based dynamic state estimator. The example system shown in Figure 4.1 consists of one substation and interconnected circuits. Note that some of the relays in this substation are GPS-synchronized, and others are not. The substation contains a local state estimator that performs quasi-dynamic state estimation. This numerical example demonstrates that the state estimator is able to accurately estimate the overall states of the substation and the states of interconnecting lines when the collected data contain both GPS-synchronized and non-synchronized measurements. In addition, we simulate measurement errors by injecting errors in the measurements from a Gaussian noise source.

4.1 System Configuration

The example substation consists of two buses (Bus 3, 115 kV and Bus 4, 13.8 kV) and a wye-delta transformer that connects them. Additionally, the substation is connected to two transmission systems (sections i1 and i2) and three distribution systems (sections j1, j2, and j3). The substation is protected by seven relays: Relays 1 and 4 are GPS-synchronized while relays 2, 3, 5, 6, and 7 are not. The measurement sampling rate is two phasor samples per cycle. The states of this example system are as follows: (1) 15 voltage phasors of phases A, B, C, N1, and N2 at Buses 1, 2, and 3 (the 115 kV transmission line has two neutral points); (2) 16 voltage phasors of phases A, B, C, and N at Buses 4, 5, 6, and 7; (3) three internal states (voltage phasors) in the transformer; and (4) five synchronous angle differences for non-synchronized relays (relays 2, 3, 5, 6, and 7). Since each phasor consists of a real part and an imaginary part and each synchronous angle difference is represented by cosine and sine functions, the substation consists of 78 states at time t in total.

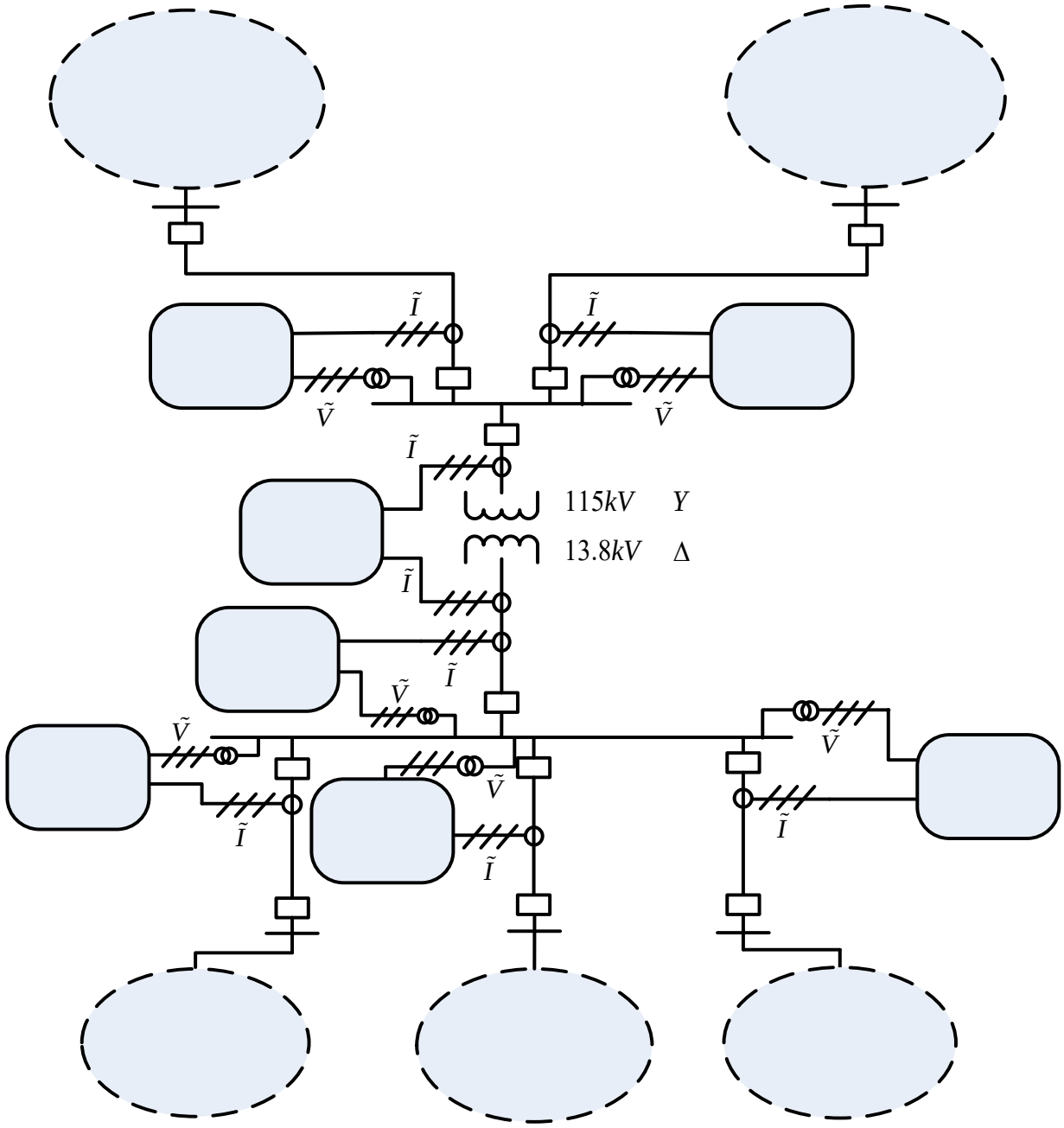

Figure 4.1: The Example Substation and Interconnected Circuits

4.2 Measurement Model Creation

The creation of the measurement model is straightforward. If the collected measurements are synchronized, the state estimator directly formulates the measurement equations in the SCAQCF syntax. For instance, synchronized voltage measurement equations are a linear combination of all related state variables:

$$\mathbf{z}_{\mathbf{V\_Syn}} = \mathbf{Y}_{\mathbf{V\_Syn}}\mathbf{x}_{\mathbf{abcn}} + \boldsymbol{\eta}\text{, and} \tag{4.1}$$

$$\mathbf{z}_{\mathbf{V\_Syn}} = \mathbf{Y}_{\mathbf{V\_Syn}}\mathbf{x}_{\mathbf{abcn}} + \boldsymbol{\eta} \tag{4.2}$$

Where $\mathbf{x}_{\mathbf{abcn}} = \left[\tilde{v}_a \quad \tilde{v}_b \quad \tilde{v}_c \quad \tilde{v}_n\right]^{\mathrm{T}}$, and $\boldsymbol{\eta}$ is the measurement error.

We obtain synchronized current measurement equations from the device model. For instance, the current measurement of the jth terminal of a device is:

$$\mathbf{Z}_{\mathbf{I\_Syn}} = \mathbf{Y}^{\mathbf{j}}_{\mathbf{x,I\_Syn}}\mathbf{x} + \mathbf{Y}^{\mathbf{j}}_{\mathbf{u,I\_Syn}}\mathbf{u} + \begin{Bmatrix} \vdots \\ \mathbf{x}^{\mathrm{T}}\mathbf{F}^{\mathbf{i}}_{\mathbf{x,I\_Syn}}\mathbf{x} \\ \vdots \end{Bmatrix} + \begin{Bmatrix} \vdots \\ \mathbf{u}^{\mathrm{T}}\mathbf{F}^{\mathbf{i}}_{\mathbf{u,I\_Syn}}\mathbf{u} \\ \vdots \end{Bmatrix} + \begin{Bmatrix} \vdots \\ \mathbf{u}^{\mathrm{T}}\mathbf{F}^{\mathbf{i}}_{\mathbf{ux,I\_Syn}}\mathbf{x} \\ \vdots \end{Bmatrix} - \mathbf{B}_{\mathbf{I\_Syn}} + \boldsymbol{\eta} \qquad (4.3)$$

where $\mathbf{x}$ is the corresponding device state vector shown in (1), $\mathbf{Y}^{\mathbf{j}}_{\mathbf{x,I\_Syn}}$ is the linear coefficient matrix consisting of rows corresponding to jth terminal obtained from $\mathbf{Y}_{\mathbf{eqx}}$, $\mathbf{Y}^{\mathbf{j}}_{\mathbf{u,I\_Syn}}$ is the linear coefficient matrix consisting of rows corresponding to jth terminal obtained from $\mathbf{Y}_{\mathbf{equ}}$, $\mathbf{F}^{\mathbf{i}}_{\mathbf{x,I\_Syn}}$ is the nonlinear coefficient matrix corresponding to jth terminal obtained from $\mathbf{F}^{\mathbf{i}}_{\mathbf{eqxx}}$, $\mathbf{F}^{\mathbf{i}}_{\mathbf{u,I\_Syn}}$ is the nonlinear coefficient matrix corresponding to jth terminal obtained from $\mathbf{F}^{\mathbf{i}}_{\mathbf{equu}}$, $\mathbf{F}^{\mathbf{i}}_{\mathbf{ux,I\_Syn}}$ is the nonlinear coefficient matrix corresponding to jth terminal obtained from $\mathbf{F}^{\mathbf{i}}_{\mathbf{equx}}$,and $\mathbf{B}_{\mathbf{I\_Syn}}$ is the measurement history-dependent vector.

However, if any measurement is collected from relays without the GPS synchronization functionality, an angle difference between the reference phase angle of this non-synchronized relay and the synchronized reference phase angle may exist. This difference is referred to as the "synchronous angle difference," which is added to the measurement equation as a new variable, θ.

In this case, equation (4.1) and (4.3) are modified as follows:

$$\mathbf{Z}_{\mathbf{V\_UnSyn}} = \mathbf{Y}_{\mathbf{V\_Syn}}\mathbf{x}_{\mathbf{abcn}}\left(\cos\theta - j\sin\theta\right) + \boldsymbol{\eta}, \text{ and} \qquad (4.4)$$

$$\mathbf{Z}_{\mathbf{I\_UnSyn}} = (\mathbf{Y}^{\mathbf{j}}_{\mathbf{x,I\_Syn}}\mathbf{x} + \mathbf{Y}^{\mathbf{j}}_{\mathbf{u,I\_Syn}}\mathbf{u} + \begin{Bmatrix} \vdots \\ \mathbf{x}^{\mathrm{T}}\mathbf{F}^{\mathbf{i}}_{\mathbf{I\_Syn}}\mathbf{x} \\ \vdots \end{Bmatrix} + \begin{Bmatrix} \vdots \\ \mathbf{x}^{\mathrm{T}}\mathbf{F}^{\mathbf{i}}_{\mathbf{x,I\_Syn}}\mathbf{x} \\ \vdots \end{Bmatrix} + \begin{Bmatrix} \vdots \\ \mathbf{u}^{\mathrm{T}}\mathbf{F}^{\mathbf{i}}_{\mathbf{u,I\_Syn}}\mathbf{u} \\ \vdots \end{Bmatrix} + \begin{Bmatrix} \vdots \\ \mathbf{u}^{\mathrm{T}}\mathbf{F}^{\mathbf{i}}_{\mathbf{ux,I\_Syn}}\mathbf{x} \\ \vdots \end{Bmatrix} - \mathbf{B}_{\mathbf{I\_Syn}}) \cdot \left(\cos\theta - j\sin\theta\right) + \boldsymbol{\eta} \qquad (4.5)$$

To suit the SCAQCF syntax, the measurement equations above need to be quadratized, so $x_{\cos\theta} = \cos\theta$ and $x_{\sin\theta} = \sin\theta$ are two new states and linear coefficient matrices $\mathbf{Y}_{\mathbf{V\_Syn}}$, $\mathbf{Y}_{\mathbf{x,I\_Syn}}$, $\mathbf{Y}_{\mathbf{u,I\_Syn}}$ become nonlinear coefficient matrices. In addition, as two new states obey mathematical rules, we add one more equation in the measurement model, shown in equation (4.6):

$$0 = x^2_{\cos\theta} + x^2_{\sin\theta} - 1 \qquad (4.6)$$

The measurements above, collected from IEDs, are actual measurements. With the purpose of increasing redundancy and improving state estimation performance, we create two other measurement types in this example: (1) virtual measurements and (2) pseudo-measurements. Virtual measurements are those that obey physical or mathematical laws of the system, such as

Kirchhoff's current law (KCL). Specifically, internal equations in all device models are virtual measurements. Furthermore, according to KCL, the sum of all currents from various devices connected to one common node is zero, which is also a virtual measurement. Pseudo-measurements are those with known expected values. For instance, the voltage of the neutral phase is close to zero in a normal operation, that is, a pseudo- measurement.

By combining all the measurement types mentioned above and substituting control variables by the values given from the control center, the state estimator is able to generate the measurement model of the entire system, expressed in a similar syntax as the device model syntax:

$$\mathbf{z} = \mathbf{Y}_{\mathbf{eqz}}\mathbf{x} + \begin{Bmatrix} \vdots \\ \mathbf{x}^{\mathrm{T}}\mathbf{F}_{\mathbf{eqz}}^{\mathbf{i}}\mathbf{x} \\ \vdots \end{Bmatrix} - \mathbf{B}_{\mathbf{eqz}} + \boldsymbol{\eta} = h(\mathbf{x}) + \boldsymbol{\eta}, \tag{4.7}$$

where $\mathbf{z}$ is the measurement vector of the system, $\mathbf{Y}_{\mathbf{eqz}}$ is the linear coefficient matrix regarding state vector $\mathbf{x}$, $\mathbf{F}_{\mathbf{eqz}}^{\mathbf{i}}$ is the nonlinear (quadratic) coefficient matrix, $\mathbf{B}_{\mathbf{eqz}}$ is the history-dependent vector, and $\boldsymbol{\eta}$ is the measurement error.

In this example system, each relay has two three-phase measurement channels, and each phasor measurement is divided into a real part and an imaginary part. As a result, the entire system has 84 actual measurements. As the voltage of the neutral phase is close to zero during a normal operation, the system measurement model contains 20 pseudo- measurements. In addition, 23 virtual measurements are available: (a) six represent internal equations for the transformer; (b) 12 obey KCL at Buses 3 and 4; and (c) the other five virtual measurements are the mathematical laws shown in (7) for each synchronous angle difference. In summary, the measurement vector contains 127 elements. Meanwhile, the standard deviation is introduced for each measurement to represent the measurement error. For actual measurements, the standard deviations are the meter errors of the corresponding IEDs. Since the virtual measurements are the equations obeying mathematical or physical laws, their errors are much smaller compared to those of actual measurements. Therefore, we set their standard deviations to be relatively low value (e.g., 0.001 p.u.). Similarly, as we only know the expected value of pseudo measurements, they have larger errors than the actual measurements. Thus, we set their standard deviation to be a relatively high value (e.g., 0.1 p.u.).

4.3 Evaluation Method

Unconstrained weighted least square (WLS) method is applied in dynamic state estimation. The problem is formulated as follows. The measurements $\mathbf{z}$ are expressed as functions of the states:

$$\mathbf{z} = h(\mathbf{x}), \tag{4.8}$$

The WLS method minimizes the sum of the weighted squares of the components of the residual vector. Mathematically:

$$\textit{Minimize} \quad J = \left(\mathbf{z}(\mathbf{t}) - h(\mathbf{x})\right)^{\mathrm{T}} \mathbf{W} \left(\mathbf{z}(\mathbf{t}) - h(\mathbf{x})\right) \tag{4.9}$$

where $\mathbf{W}$ is the weight matrix with the weights defined as the inverse of the squared standard deviation:

$$\mathbf{W} = \mathrm{diag}\left\{1/\sigma_1^2, 1/\sigma_2^2, \cdots, 1/\sigma_n^2\right\} \tag{4.10}$$

Unknown state vector $\mathbf{x}$ is obtained by the optimal condition:

$$dJ/d\mathbf{x} = 0 \tag{4.11}$$

To obtain the solution of the nonlinear optimization problem above, we linearize the nonlinear equations (the highest order is the second order in equation (4.8) at the point $\mathbf{x}^v$ by assuming that an initial guess $\mathbf{x}^v$ is very close to the optimal solution:

$$\mathbf{r} = h(\mathbf{x}^v) + \partial h(\mathbf{x})/\partial \mathbf{x}\Big|_{\mathbf{x}=\mathbf{x}^v}\left(\mathbf{x} - \mathbf{x}^v\right) - \mathbf{z} \tag{4.12}$$

After we set $\mathbf{H} = \partial h(\mathbf{x})/\partial \mathbf{x}\Big|_{\mathbf{x}=\mathbf{x}^v}$, and $\mathbf{z}' = -h(\mathbf{x}^v) + \mathbf{H}\mathbf{x}^v + \mathbf{z}$, the equation becomes

$$\mathbf{r} = \mathbf{H}\mathbf{x} - \mathbf{z}' \tag{4.13}$$

The optimization problem is now expressed as

$$\textit{Minimize} \quad J = \left(\mathbf{H}\mathbf{x} - \mathbf{z}'\right)^{\mathrm{T}} \mathbf{W}\left(\mathbf{H}\mathbf{x} - \mathbf{z}'\right) \tag{4.14}$$

Thus, we generalize the solution as an iterative equation:

$$\mathbf{x}^{v+1} = \left(\mathbf{H}^{\mathrm{T}}\mathbf{W}\mathbf{H}\right)^{-1}\mathbf{H}^{\mathrm{T}}\mathbf{W}\mathbf{z}' = \mathbf{x}^v - \left(\mathbf{H}^{\mathrm{T}}\mathbf{W}\mathbf{H}\right)^{-1}\mathbf{H}^{\mathrm{T}}\mathbf{W}\left(h\left(\mathbf{x}^v\right) - \mathbf{z}\right) \tag{4.15}$$

Once the solution is calculated by equation (4.15), chi-square test is applied. Chi-square test qualifies the goodness of fit between the model and measurements by providing the probability that the measurements are consistent with the dynamic model. Chi-square test is applied as follows. First the quantity ξ is computed:

$$\xi = \sum_i \left(\frac{h_i(x) - z_i}{\sigma_i}\right)^2 \tag{4.16}$$

The probability (confidence level) that the measurements and the model fit together within the accuracy of the meters is computed from:

$$\Pr[\chi^2 \geq \xi] = 1 - \Pr[\chi^2 \leq \xi] = 1 - \Pr(\xi, \upsilon) \tag{4.17}$$

where υ is the degree of freedom, defined as the difference between the number of measurements and states.

A confidence level around 100% (small chi-square value) infers the measurements are highly consistent with the dynamic model of the system, and the estimated states and measurements are trustworthy. A low confidence level (large chi-square value) implies the occurrence of some bad data or hidden failures in the system.

The computed best estimate of the substation state is utilized to compute the best estimate of the bad data, if any, and the best estimate of missing data, if any. The computation of the best estimate of bad data or missing data is calculated from the model of the system and the best estimate of the substation state:

$$\mathbf{z}_{bad} = \mathbf{Y}_{eqz\_bad}\mathbf{x} + \begin{Bmatrix} \vdots \\ \mathbf{x}^T\mathbf{F}^i_{eqz\_bad}\mathbf{x} \\ \vdots \end{Bmatrix} - \mathbf{B}_{eqz\_bad} + \boldsymbol{\eta} \tag{4.18}$$

$$\mathbf{z}_{miss} = \mathbf{Y}_{eqz\_miss}\mathbf{x} + \begin{Bmatrix} \vdots \\ \mathbf{x}^T\mathbf{F}^i_{eqz\_miss}\mathbf{x} \\ \vdots \end{Bmatrix} - \mathbf{B}_{eqz\_miss} + \boldsymbol{\eta} \tag{4.19}$$

where the model equations for the bad data and missing data are denoted with the subscript "bad" and "miss". Note the model is quadratic, at most, since the dynamic state estimator operates on the quadratized model of the substation. Finally, the best estimate of the state and data, including the filled-in-data, are sent to the substation UI and the control center as a C37.118 stream.

4.4 State Estimation Results

We create two events and apply quasi-dynamic state estimation to this system. The duration of these two events is 20 seconds each with load changes outside the substation. The results of the events follow.

Event 1: Quasi-dynamic state estimation using both GPS- and non-synchronized measurements

During the event, the measurements (phasors) "seen" by the relays in the substation have been stored in a COMTRADE file, and they are used to perform the dynamic state estimation algorithm. The system of the state estimator includes the substation, the two transmission lines, and the three distribution lines. The data generated by the event and by the state estimator are very large, so we present and discuss examples of some specific data. Figures 4.2 and 4.3 show the voltage and the current actual and estimated phasor measurements in relay 4.

Figures 4.2 and 4.3 indicate that the estimated measurements accurately track the actual measurements. In Figure 4.4, $\theta_1 \sim \theta_5$ are the estimated synchronous angle differences of non-synchronized measurements from relays 2, 3, 5, 6 and 7, respectively. Note that since the voltage channels of relays 5, 6, and 7 measure the voltage at the same node (Bus 4), the estimated synchronous angle differences θ_3, θ_4, and θ_5 are the same. The confidence level remains 100% during the entire event. Therefore, the measurements are consistent with the system model. The state estimator validates the measurements and streams the estimated states to the control center for further application.

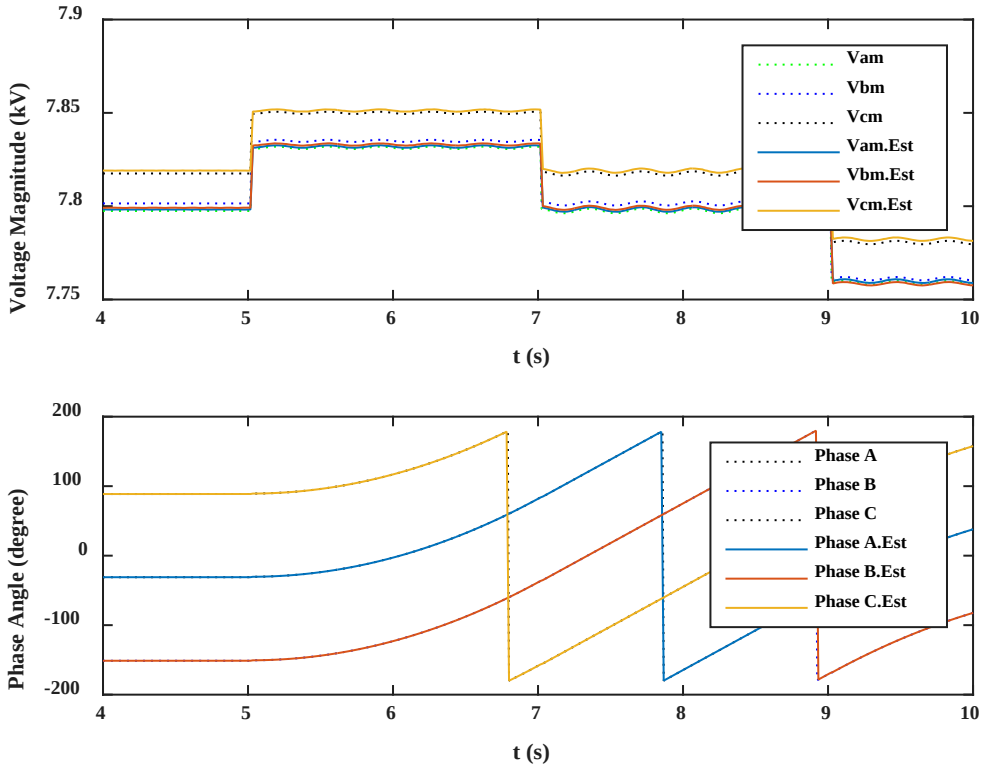

Figure 4.2: Voltage Actual and Estimated Phasor Measurements in Relay 4, Event 1

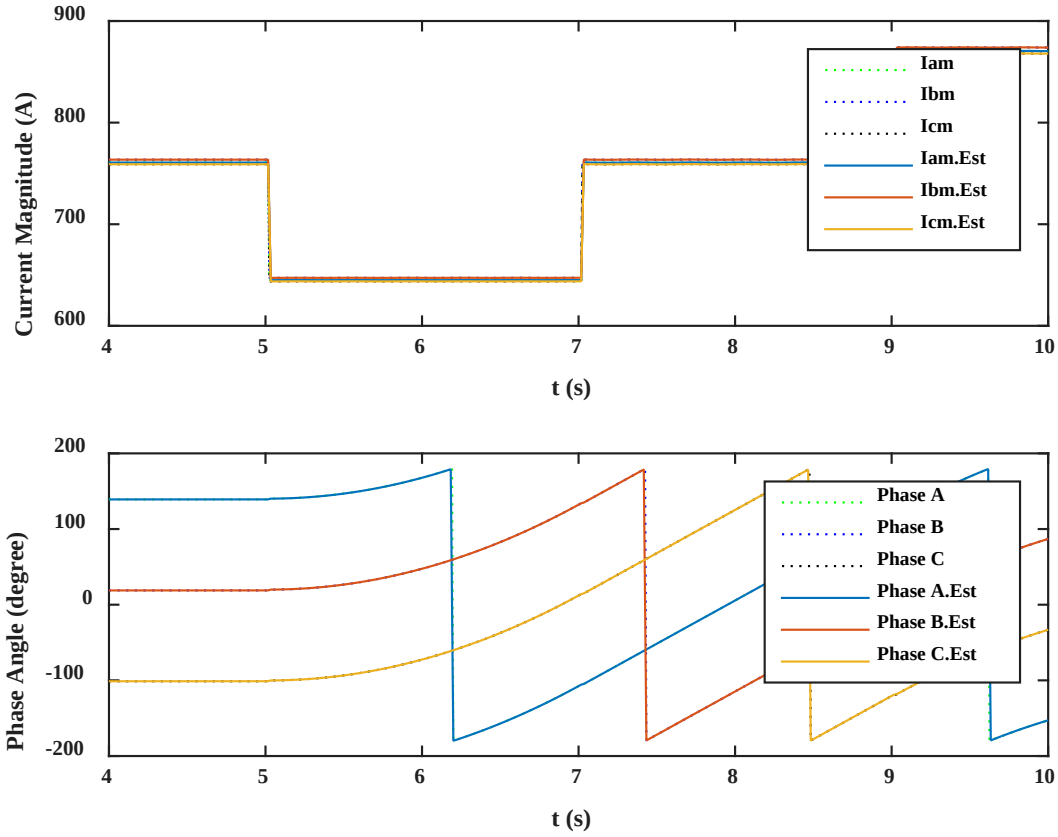

Figure 4.3: Current Actual and Estimated Phasor Measurements in Relay 4, Event 1

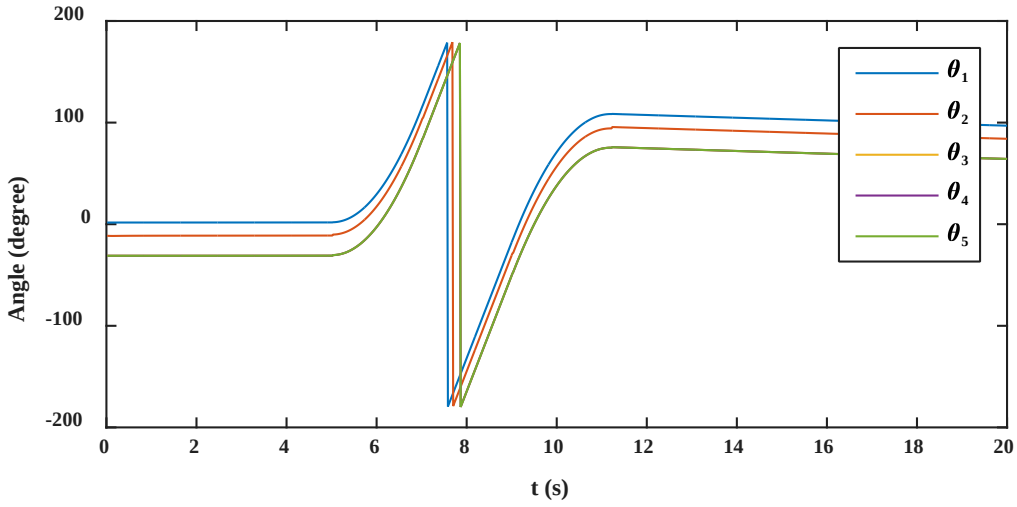

Figure 4.4: Estimated Angle Difference in Event 1

Event 2: Quasi-dynamic state estimation using both GPS- and non-synchronized measurements with 1% Gaussian noise

Applying the dynamic state estimation algorithm to Event 2, we add a 1% Gaussian noise source to the measurements from relays in the substation and store these measurements in a COMTRADE file. The system of the state estimator is the same as that of Event 1. We present and discuss examples of measurements and generated data from the state estimator. Figures. 4.5 and 4.6 illustrate the voltage and the current actual and estimated measurements of phase A in relay 4. Figures. 4.5 and 4.6 indicate that even with 1% Gaussian noise, estimated measurements can also track actual measurements. Figure 4.7 shows the estimated synchronous angle differences of non-synchronized measurements from relays 2, 3, 5, 6 and 7. The confidence level in Figure 4.7 indicates strong consistency between the measurements and the system model (the probability is always larger than 90%). The DQDSE validates the measurements of this event and streams the estimated states to the control center for further application. Figure 4.8 shows that the square roots of the variance of estimated measurements in relay 4 are close to 0.01 p.u., which reflects the addition of Gaussian noise to the measurements.

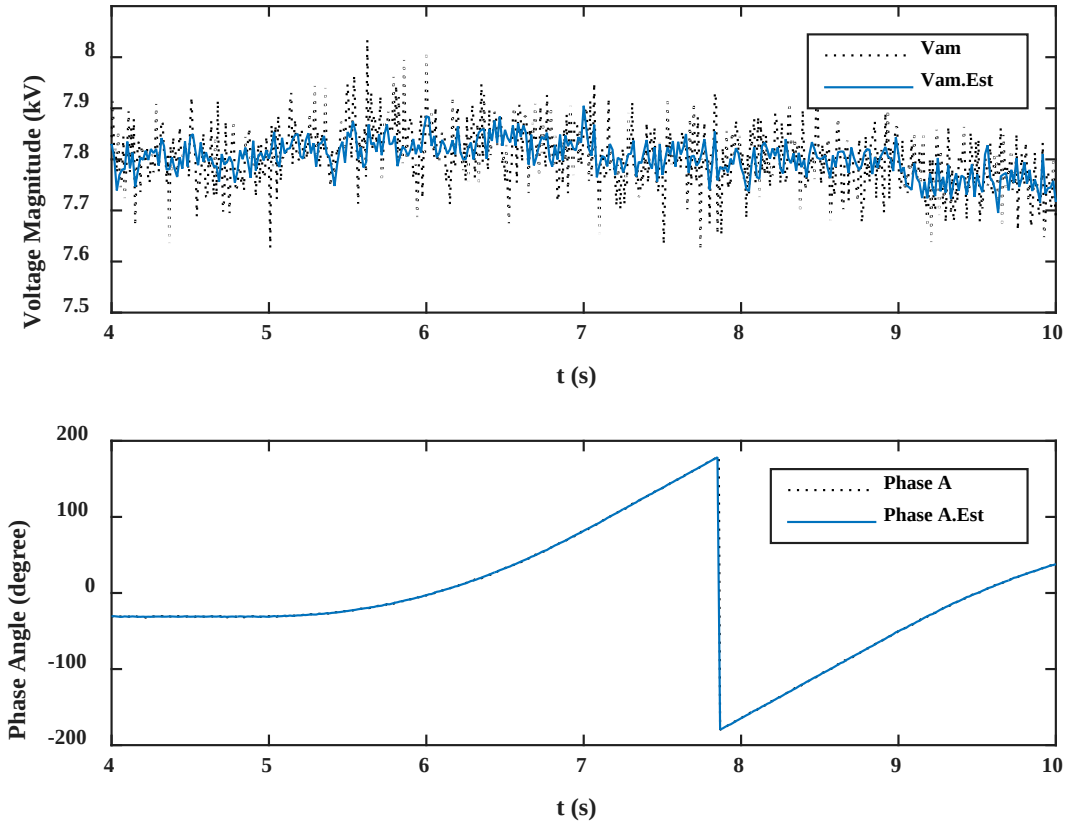

Figure 4.5: Voltage Actual and Estimated Phasor Measurements of Phase A in Relay 4, Event 2

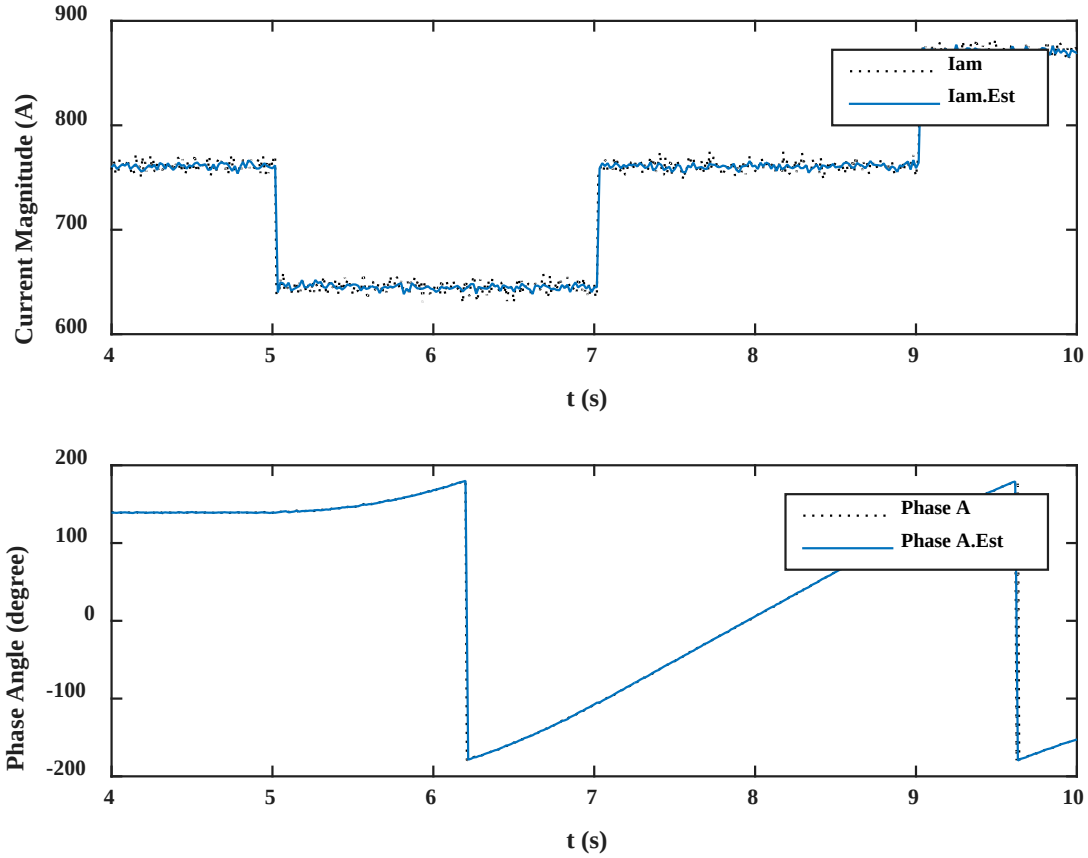

Figure 4.6: Current Actual and Estimated Phasor Measurements of Phase A in Relay 4, Event 2

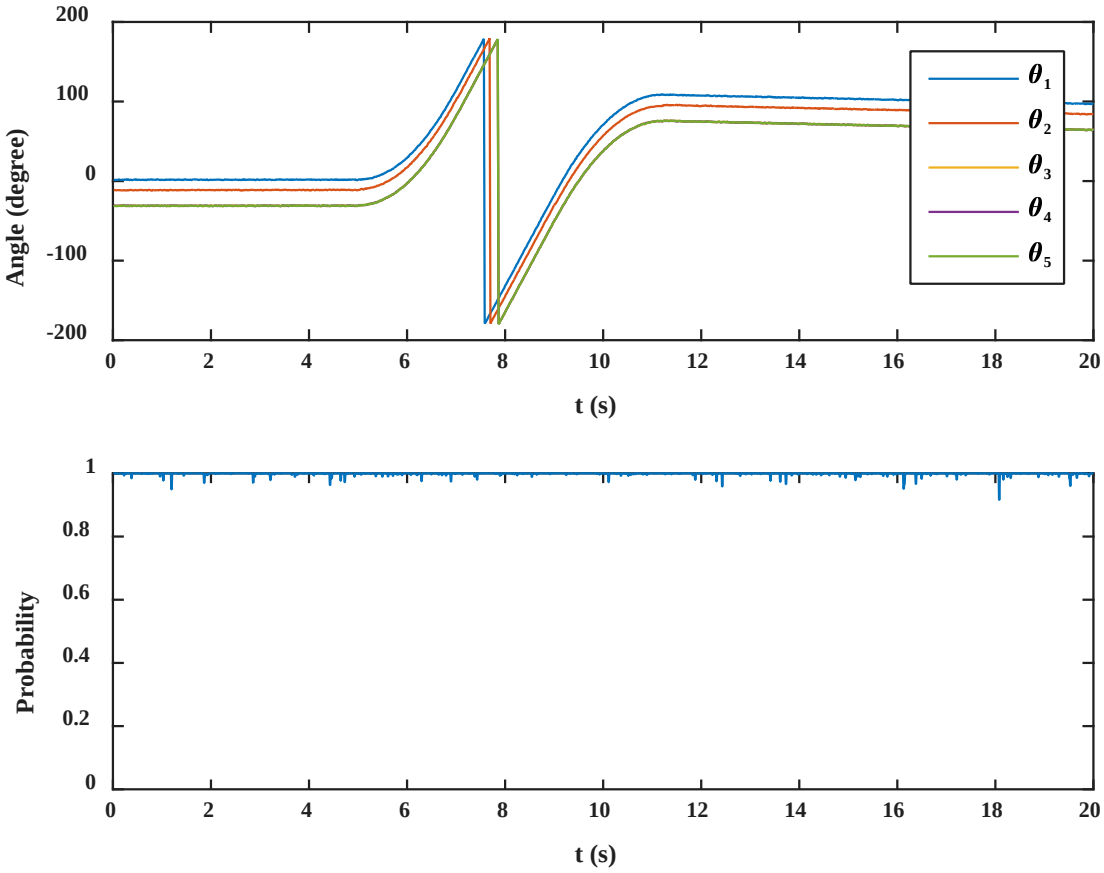

Figure 4.7: Estimated Angles and Confidence Level in Event 2

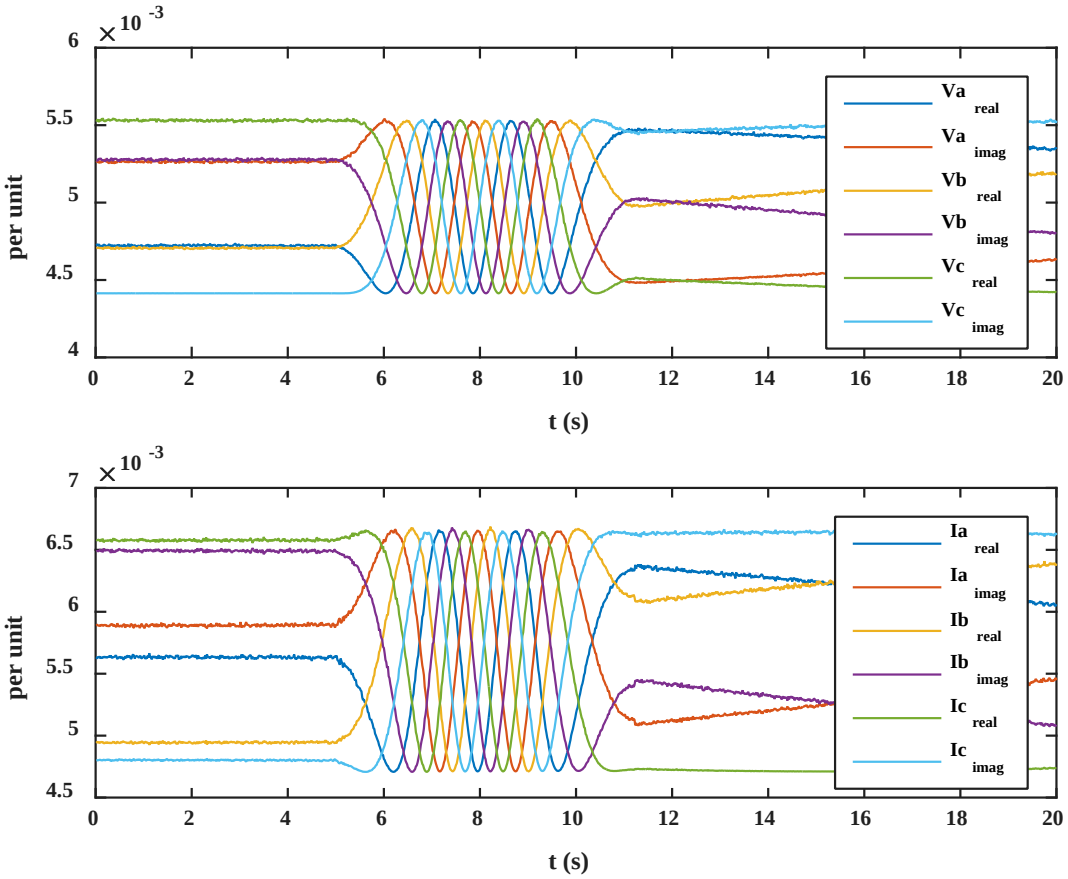

Figure 4.8: Square Root of the Variance of Voltage and Current Estimated Measurements in Relay 4, Event 2

5. Distributed System Quasi-Dynamic State Estimation: Use Case - Marcy Substation

5.1 Overview

This section describes a use case for the distribution system quasi-dynamic state estimator (DS-QSE). The use case is the Marcy substation of NYPA. The document describes: (a) preparing the example system (i.e., the Marcy substation) in WinIGS-Q, (b) modeling all IEDs providing measurements in this section, (c) simulating example events and store data in COMTRADE format, (d) setting up the state estimator for the system, and (e) executing DS-QSE and record performance.

5.2 Use Case System

We select Marcy substation as an example to perform the state estimation. The single-line diagram of the substation is shown in Figure 5.2.1. Marcy substation is connected to Massena substation, Volney substation, Edic substation, Coopers Corner substation, and New Scotland substation. It consists of six single-phase auto transformers with tertiary, two three-phase two-winding transformers, one three-phase three-winding transformer, two capacitor banks, one shunt reactor, four three-phase constant power loads, and nineteen breakers. The parameters of these devices are listed in Table 5.2.1. This substation has 23 buses. All of them are three-phase buses. The total number of states of this section is 74 at time t, and 74 at time tm.

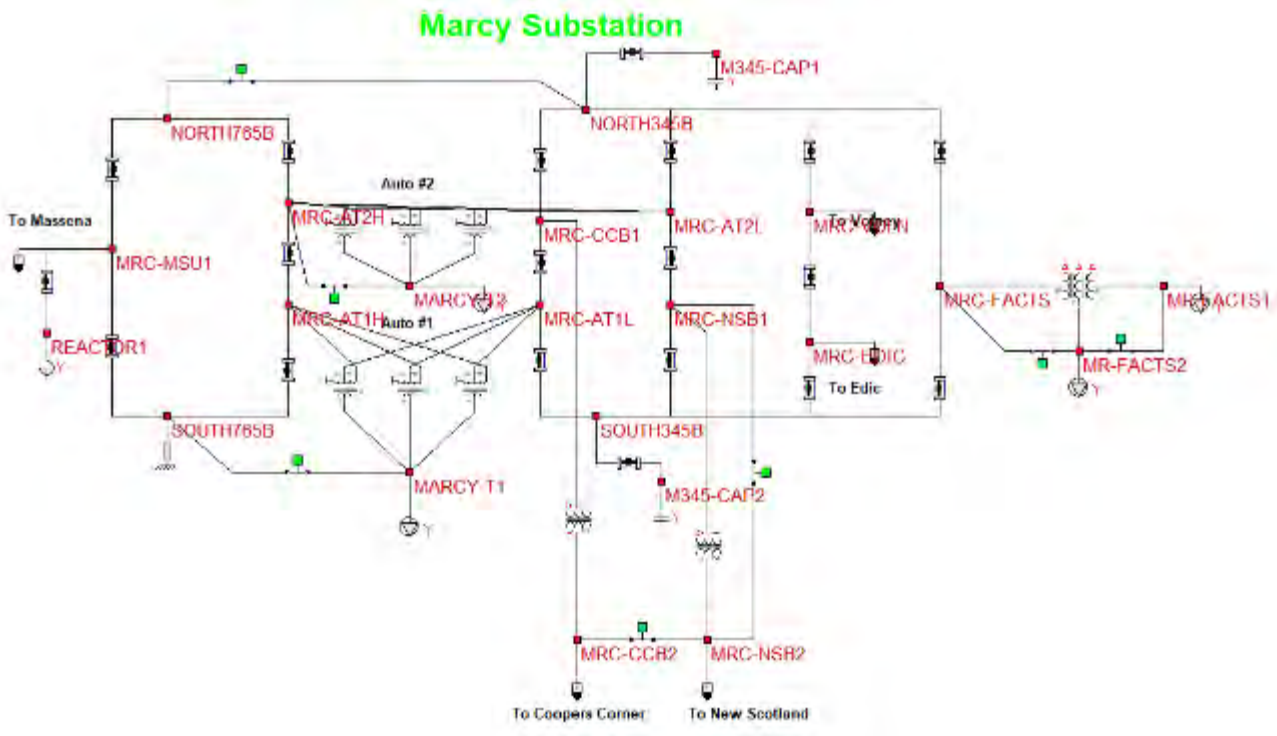

Figure 5.2.1: Marcy Substation

Table 5.2.1: Summary of Devices in Use Case Test System

Devices	Rated Voltage (kV)	Rated Power	# of States
AutoTransformer T-1, Phase A	765/345/13.8 (L-L)	300MVA (primary to secondary), 75MVA (primary to tertiary), 75MVA (secondary to tertiary)	12 at time t 12 at time tm
AutoTransformer T-1, Phase B	765/345/13.8 (L-L)	300MVA (primary to secondary), 75MVA (primary to tertiary), 75MVA (secondary to tertiary)	12 at time t 12 at time tm
AutoTransformer T-1, Phase C	765/345/13.8 (L-L)	300MVA (primary to secondary), 75MVA (primary to tertiary), 75MVA (secondary to tertiary)	12 at time t 12 at time tm
AutoTransformer T-2, Phase A	765/345/13.8 (L-L)	300MVA (primary to secondary), 75MVA (primary to tertiary), 75MVA (secondary to tertiary)	12 at time t 12 at time tm
AutoTransformer T-2, Phase B	765/345/13.8 (L-L)	300MVA (primary to secondary), 75MVA (primary to tertiary), 75MVA (secondary to tertiary)	12 at time t 12 at time tm
AutoTransformer T-2, Phase C	765/345/13.8 (L-L)	300MVA (primary to secondary), 75MVA (primary to tertiary), 75MVA (secondary to tertiary)	12 at time t 12 at time tm
Three-Phase Three-Winding Transformer	345kV/21.4kV/21.4kV	200MVA (primary to secondary), 100MVA (primary to tertiary), 100MVA (secondary to tertiary)	24 at time t 24 at time tm
Three-Phase Two-Winding Transformer #1	345kV (delta)/345kV (wye)	1000MVA	20 at time t 20 at time tm
Three-Phase Two-Winding Transformer #2	345kV (delta)/345kV (wye)	1000MVA	20 at time t 20 at time tm
Capacitor Bank #1	345 kV	100MVA	8 at time t 8 at time tm
Capacitor Bank #2	345 kV	100MVA	8 at time t 8 at time tm
Shunt Reactor	765 kV	-216MVAR	8 at time t 8 at time tm
Load #1 (MARCY-T1)	13.8 kV	1 kW 1 kVar	8 at time t 8 at time tm
Load #2 (MARCY-T2)	13.8 kV	1 kW 1 kVar	8 at time t

			8 at time tm
Load #3 (MR-FACTS1)	21.4 kV	10 kW 1 kVar	8 at time t 8 at time tm
Load #4 (MR-FACTS2)	21.4 kV	10 kW 1 kVar	8 at time t 8 at time tm

5.3 Marcy System Model in WinIGS - SCAQCF Standard

This section introduces the modeled components in this substation. We use WinIGS-Q to build physically based models. The detailed parameters of autotransformers with tertiary, three-phase three-winding transformers, three-phase two-winding transformers, capacitor/reactor banks, three-phase constant power loads, three-phase breakers, two-node connectors are shown in Table 5.3.1 to 5.3.7. And the model interfaces of these devices are shown in Figure 5.3.1 to 5.3.8.

Table 5.3.1: Parameters of Autotransformers with Tertiary

Single-Phase Autotransformer with Tertiary (M293)					
#	Device Name	Bus Name	Rated Power (MVA)	Rated Voltage (kV)	Tertiary Connection Type
1	AutoTransformer T-1, Phase A	MRC-AT1H MRC-AT1L MARCY-T1	300/75/75	765/345/13.8 (L-L)	DELTA
2	AutoTransformer T-1, Phase B	MRC-AT1H MRC-AT1L MARCY-T1	300/75/75	765/345/13.8 (L-L)	
3	AutoTransformer T-1, Phase C	MRC-AT1H MRC-AT1L MARCY-T1	300/75/75	765/345/13.8 (L-L)	
4	AutoTransformer T-2, Phase A	MRC-AT2H MRC-AT2L MARCY-T2	300/75/75	765/345/13.8 (L-L)	DELTA
5	AutoTransformer T-2, Phase B	MRC-AT2H MRC-AT2L MARCY-T2	300/75/75	765/345/13.8 (L-L)	
6	AutoTransformer T-2, Phase C	MRC-AT2H MRC-AT2L MARCY-T2	300/75/75	765/345/13.8 (L-L)	

Table 5.3.2: Parameters of Three-Phase Three-Winding Transformers

Three-Phase Three-Winding Transformer (M105)					
#	Device Name	Bus Name	Rated Power (MVA)	Rated Voltage (kV)	Connection Type
1	FACTS Shunt Transformer	MRC-FACTS MR-FACTS1 MR-FACTS2	200/100/100	345.0/21.4/21.4	DELTA DELTA DELTA

Table 5.3.3: Parameters of Three-Phase Two-Winding Transformers

Three-Phase Two-Winding Transformer (M104)					
#	Device Name	Bus Name	Rated Power (MVA)	Rated Voltage (kV)	Connection Type
1	FACTS Series Transformer - Coopers Corner Line	MRC-CCB1 MRC-CCB2	1000	345.0/345.0	DELTA WYE
2	FACTS Series Transformer - New Scotland Line	MRC-NSB1 MRC-NSB2	1000	345.0/345.0	DELTA WYE

Table 5.3.4: Parameters of Capacitor/Reactor Bank

Three-Phase Capacitor/Reactor Bank (M116)					
#	Device Name	Bus Name	Rated Power	Rated Voltage	Connection Type
1	Reactor Bank 1, Marcy 765 kV	REACTOR1	-216.0 MVar	765.0 kV	WYE
2	Capacitor Bank 1, Marcy 345 kV	M345-CAP1	100 MVar	345.0 kV	WYE
3	Capacitor Bank 2, Marcy 345 kV	M345-CAP2	100 MVar	345.0 kV	WYE

Table 5.3.5: Parameters of Load Models

Three-Phase Constant Power Load (M161)						
#	Device Name	Bus Name	Real Power (kW)	Reactive Power (kVar)	Rated Voltage	Connection Type
1	Load 1	MARCY-T1	1.0	1.0	13.8	WYE
2	Load 2	MARCY-T2	1.0	1.0	13.8	WYE
3	Load 3	MR-FACTS1	10.0	1.0	21.4	WYE
4	Load 4	MR-FACTS2	10.0	1.0	21.4	WYE

Table 5.3.6: Parameters of Three-Phase Breaker

Three-Phase Breaker (M192)				
#	Device Name	Bus Name	Phases	Open/Closed
1	Breaker 7203	MRC-MSU1 REACTOR1	A, B, C, N	Closed
2	Breaker 7214	NORTH765B MRC-MSU1	A, B, C, N	Closed
3	Breaker 7202	MRC-MSU1 SOUTH765B	A, B, C, N	Closed
4	Breaker 7414	NORTH765B MRC-AT2H	A, B, C, N	Closed
5	Breaker 7402	MRC-AT2H MRC-AT1H	A, B, C, N	Closed
6	Breaker 7302	MRC-AT1H SOUTH765B	A, B, C, N	Closed
7	Breaker 3202	NORTH345B MRC-CCB1	A, B, C, N	Closed
8	Breaker 3208	MRC-CCB1 MRC-AT1L	A, B, C, N	Closed
9	Breaker 3214	MRC-AT1L SOUTH345B	A, B, C, N	Closed
10	Breaker 3402	NORTH345B M345-CAP1	A, B, C, N	Closed
11	Breaker 3414	SOUTH345B M345-CAP2	A, B, C, N	Closed
12	Breaker 3302	NORTH345B MRC-AT2L	A, B, C, N	Closed
13	Breaker 7402	MRC-AT2L MRC-NSB1	A, B, C, N	Closed
14	Breaker 7302	MRC-NSB1 SOUTH345B	A, B, C, N	Closed
15	Breaker 3102	NORTH345B MRC-VOLN	A, B, C, N	Closed
16	Breaker 3108	MRC-VOLN MRC-EDIC	A, B, C, N	Closed
17	Breaker 3114	MRC-EDIC SOUTH345B	A, B, C, N	Closed
18	Breaker 3002	NORTH345B MRC-FACTS	A, B, C, N	Closed
19	Breaker 3014	MRC-FACTS SOUTH345B	A, B, C, N	Closed

Table 5.3.7: Parameters of Two-Node Connectors

Two-Node Connector (M191)				
#	Device Name	Bus Name	Phases	Open/Closed
1	Node Connector 1	NORTH765B NORTH345B	N	Closed
2	Node Connector 2	MRC-AT2H MARCY-T2	N	Closed
3	Node Connector 3	SOUTH765B MARCY-T1	N	Closed
4	Node Connector 4	MRC-CCB2 MRC-NSB2	N	Closed
5	Node Connector 5	MRC-NSB1 MRC-NSB2	N	Closed
6	Node Connector 6	MRC-FACTS MR-FACTS2	N	Closed
7	Node Connector 7	MR-FACTS2 MR-FACTS1	N	Closed

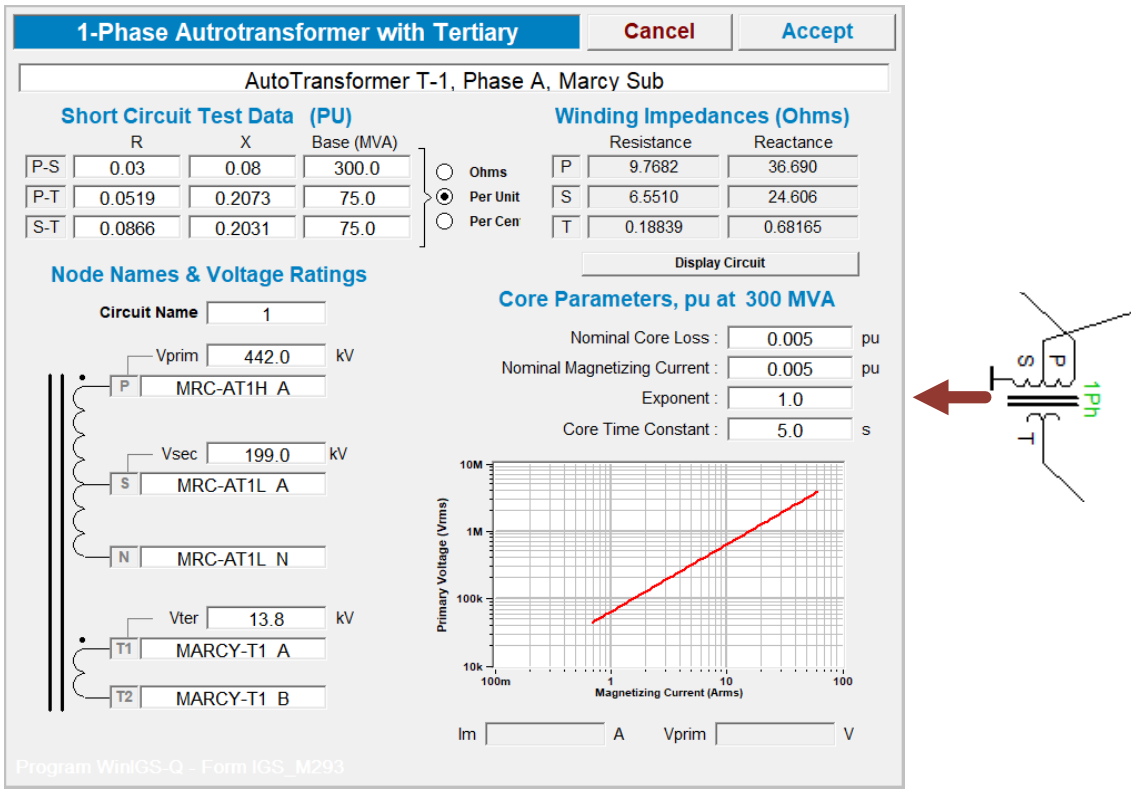

Figure 5.3.1: Three-Phase Autotransformer with Tertiary (M106)

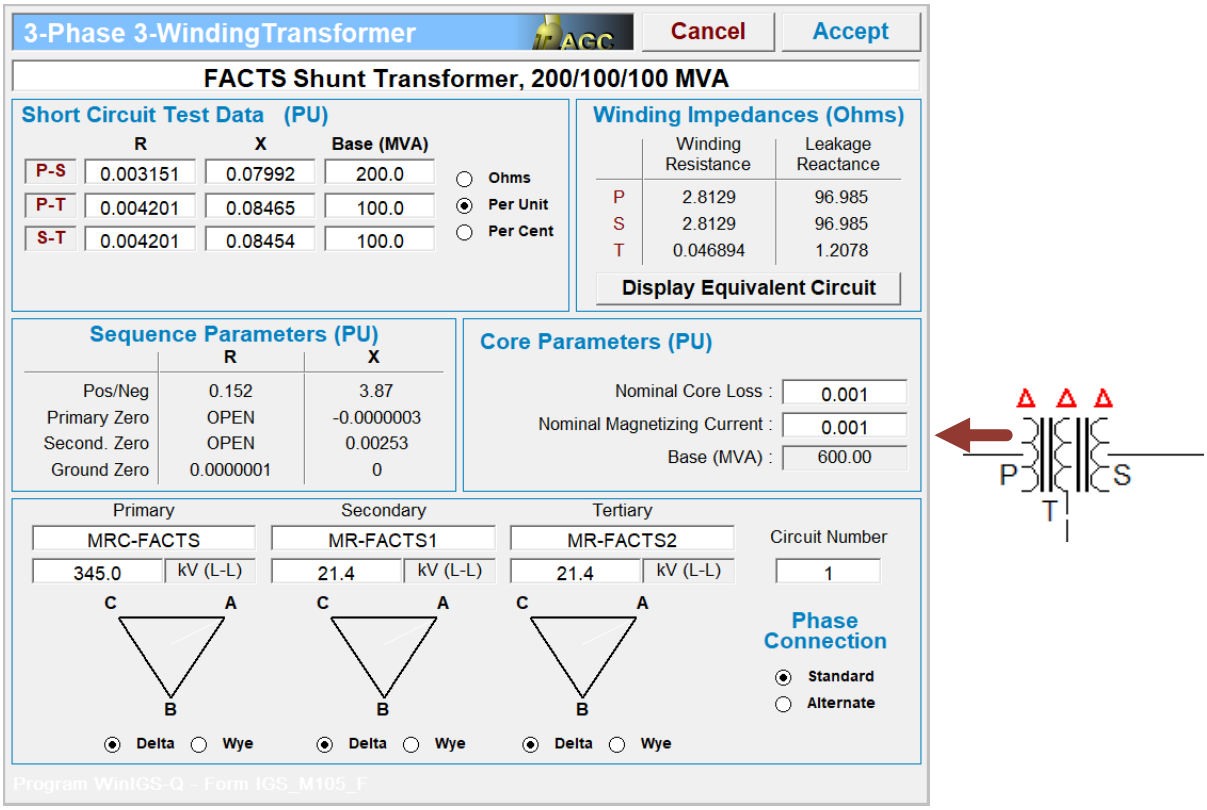

Figure 5.3.2: Three-Phase Three-Winding Transformer (M105)

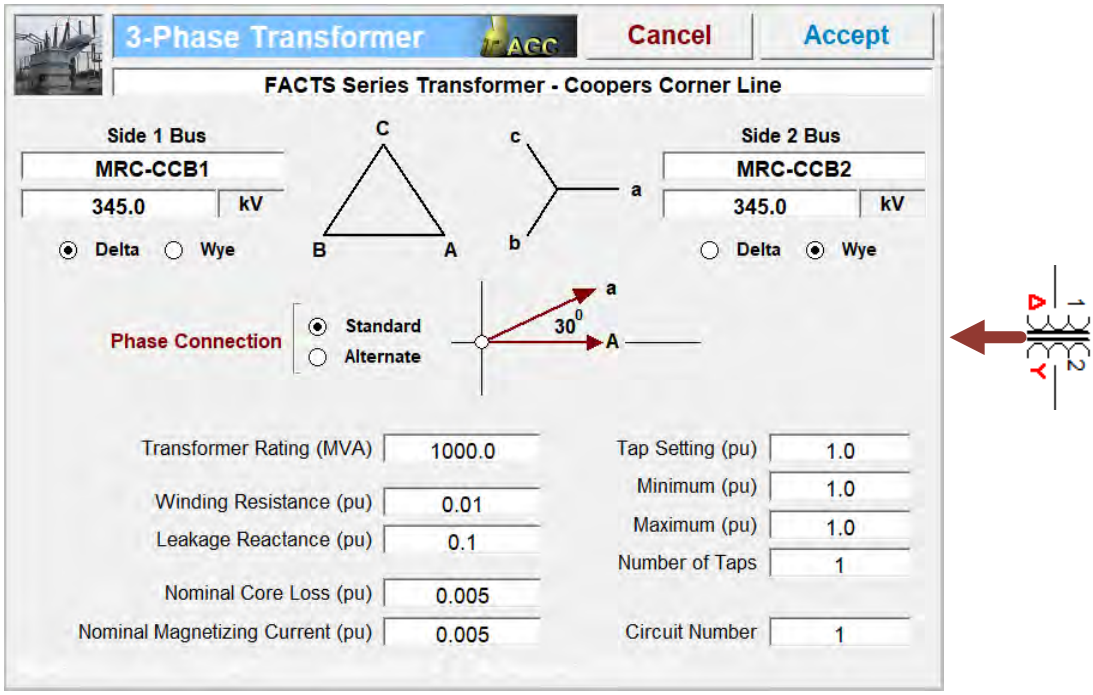

Figure 5.3.3: Three-Phase Two-Winding Transformer Model (M104)

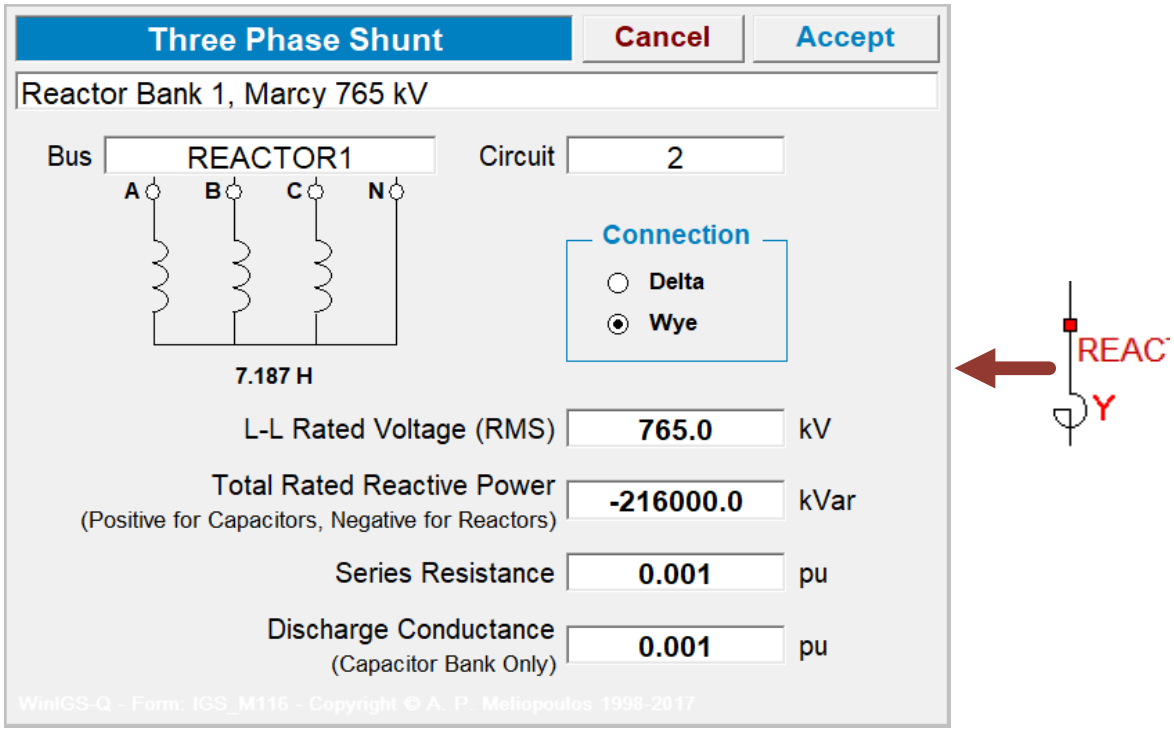

Figure 5.3.4: Reactor Bank Model (M116)

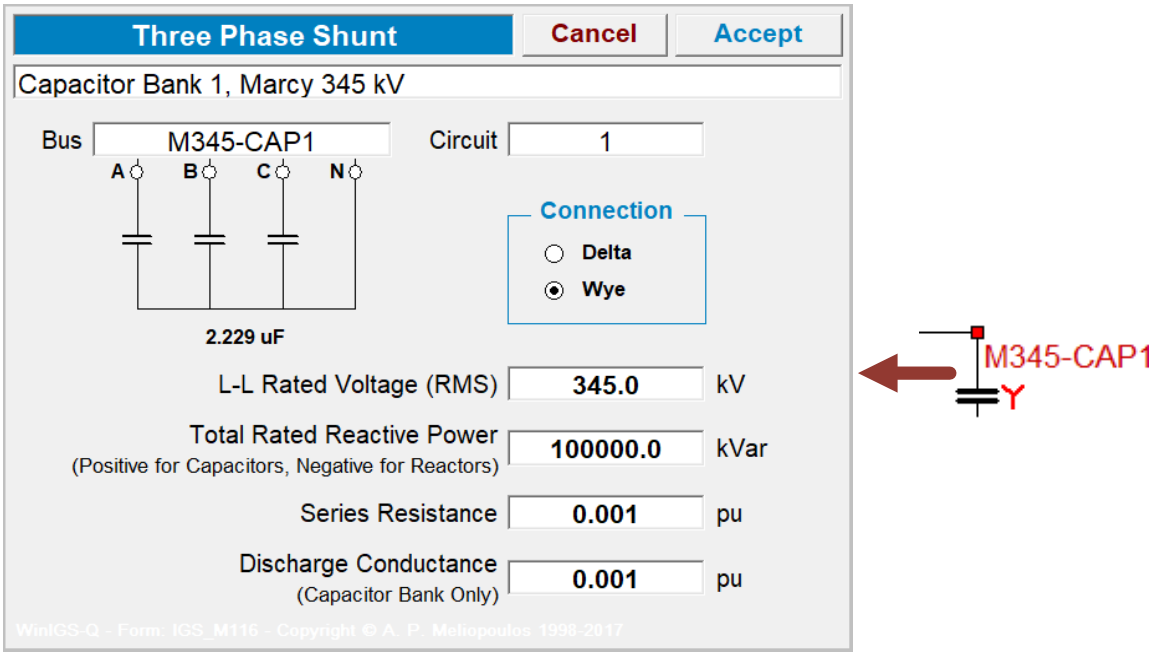

Figure 5.3.5: Capacitor Bank Model (M116)

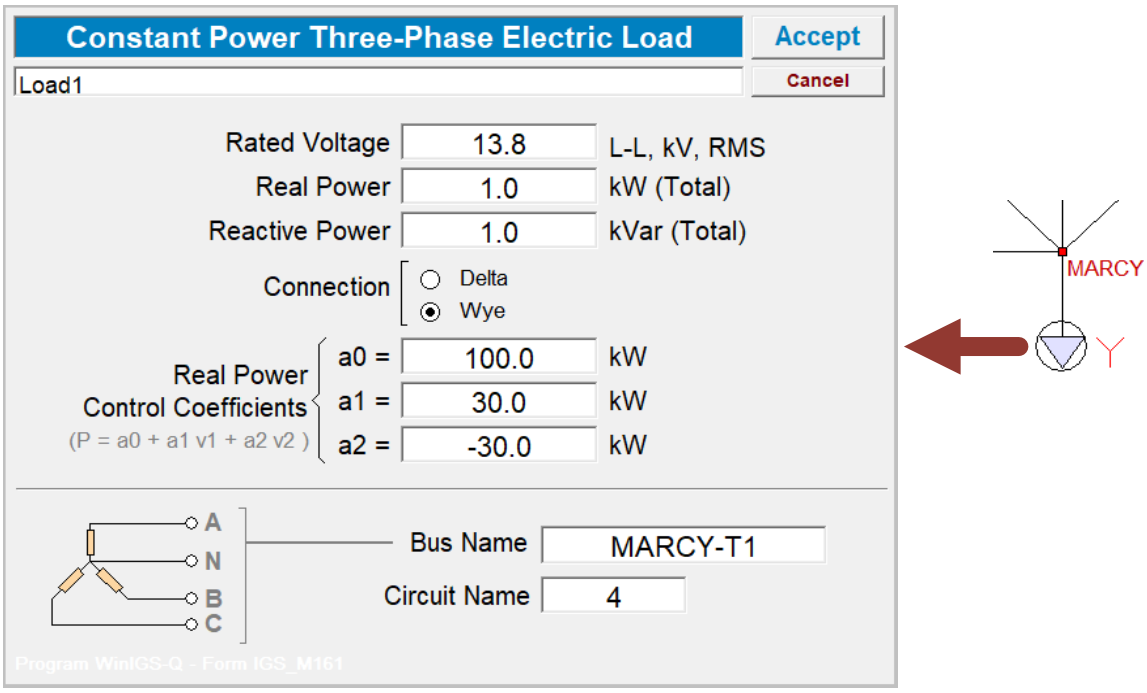

Figure 5.3.6: Three-Phase Constant Power Load Model (M161)

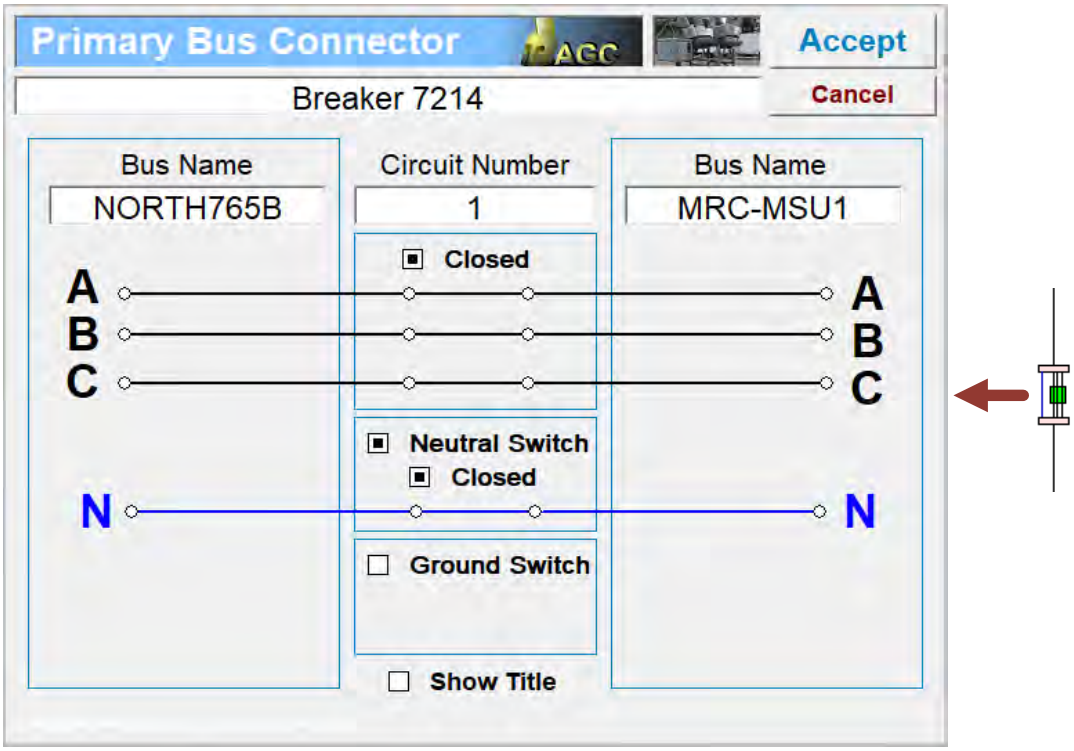

Figure 5.3.7: Three-Phase Breaker Model (M192)

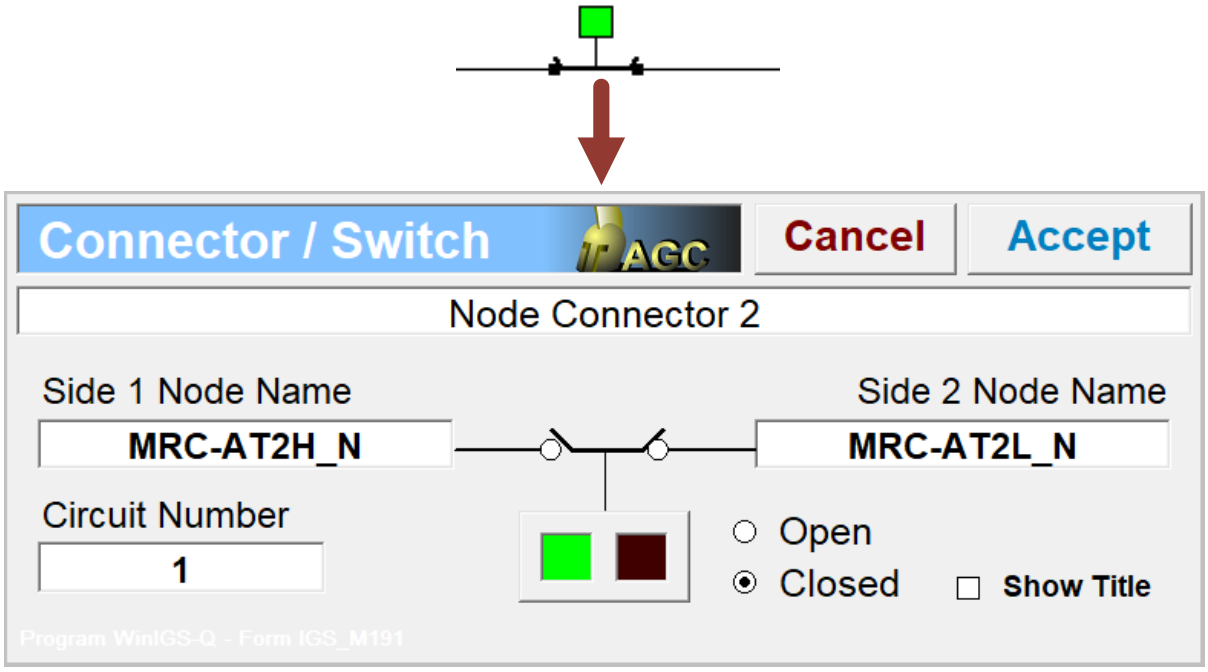

Figure 5.3.8: Node Connector Model (M191)

5.4 Marcy co-Model: Physical System and IEDs

This section introduces the procedure that we set up the IEDs in this substation. We use one IED setup as an example, and the other IEDs are set up in the same way. 46 IEDs are placed in this substation. The total number of phasor measurements is 360 (i.e., 720 measurements in real values) at time t. Since the substation consists of 74 states, the redundancy is 905%. The substation with setup IEDs is shown in Figure 5.4.1.

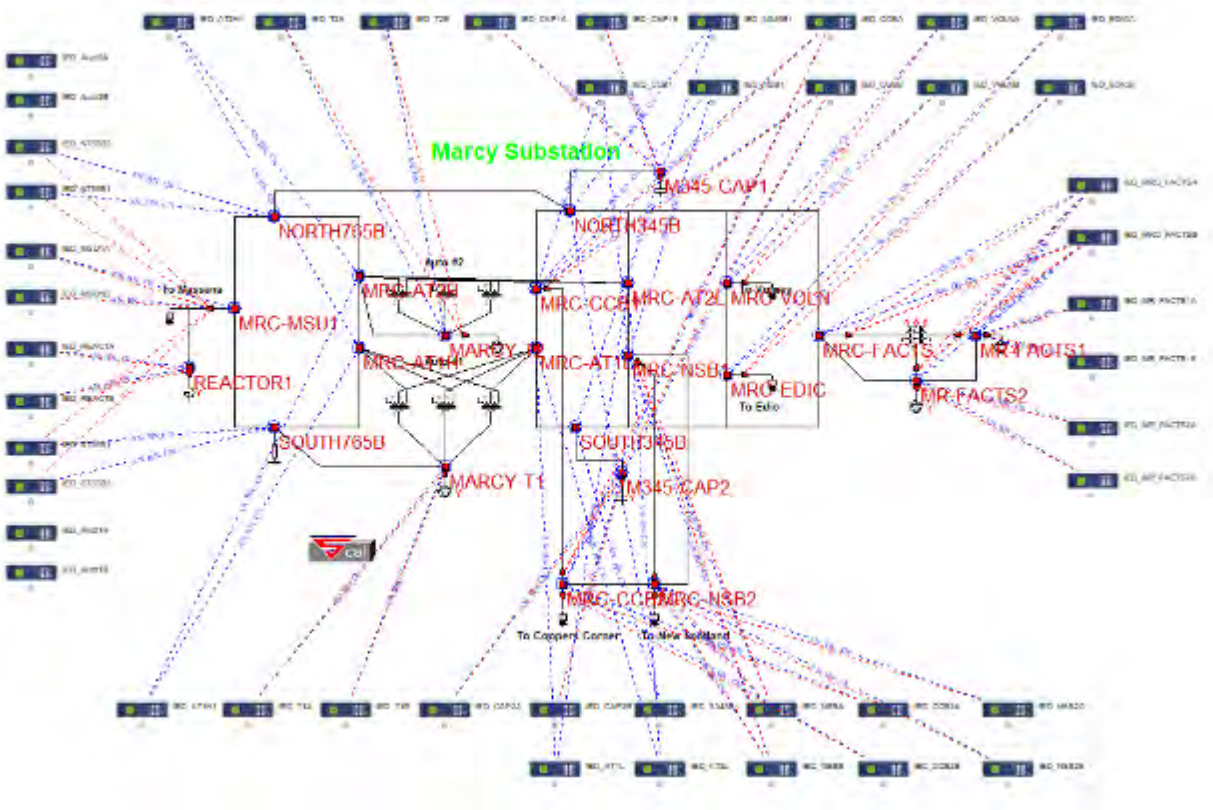

Figure 5.4.1: Marcy Substation with IEDs

5.4.1 Instrumentation Channels

The instrumentation channel and measurement parameters to be used by the state estimator are modelled in the IED model (M007, see icon in Figure 5.4.2).

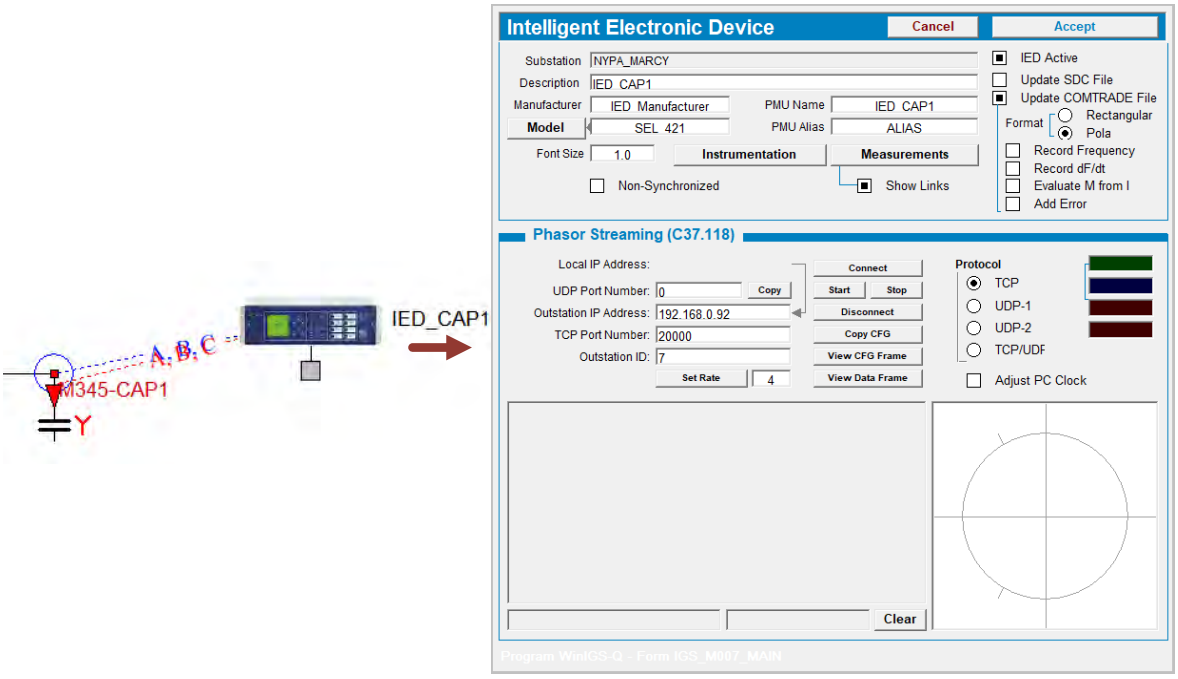

Figure 5.4.2: IED and its user interface

The IED model parameters and instrumentation channel list can be edited by clicking on the IED icon. This action will bring the user interface illustrated in Figure 5.4.2. The user is able to edit the IED name, manufacturer, etc. in this user interface. Click on the instrumentation button to open the instrumentation channel list dialog as shown in Figure 5.4.3.

Double click on each list table entry to inspect the instrumentation channel parameters. Figure 5.4.4 and 5.4.5 illustrate examples of a voltage phasor and a current phasor channel, respectively. Note that one instrumentation channel model includes models of the instrument transformer, instrumentation cable, burdens, and data acquisition device (i.e., a PMU in this example). The instrumentation channel parameters are listed in Table 5.4.1 with detailed descriptions.

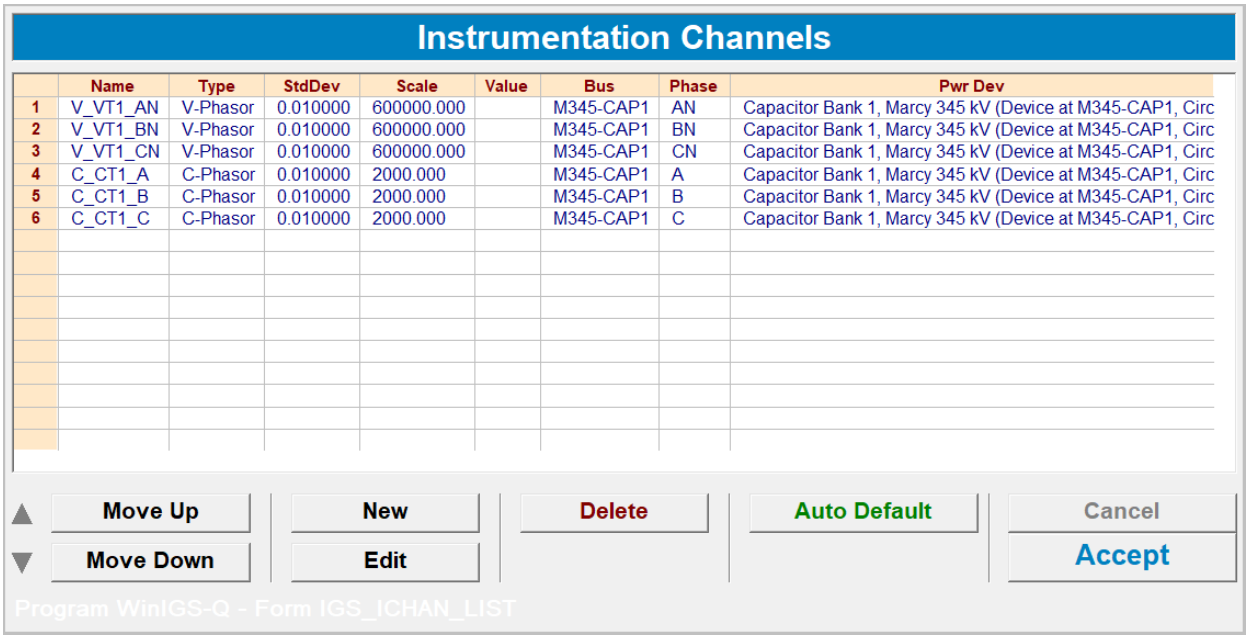

Figure 5.4.3: Instrumentation Channel List Dialog of One IED

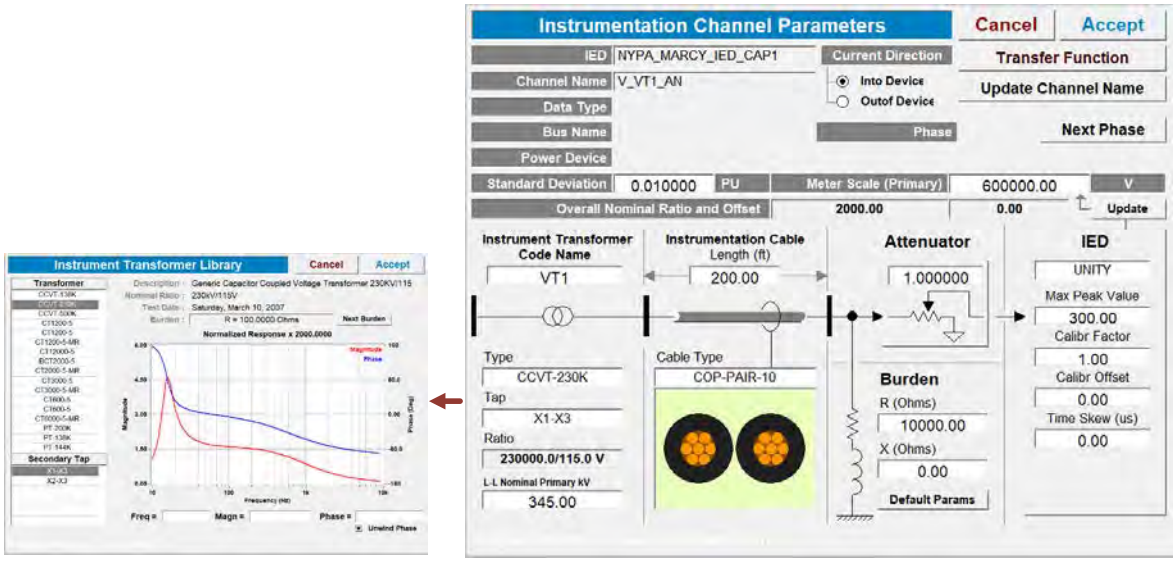

Figure 5.4.4: Example of a Voltage Phasor Instrumentation Channel Dialog

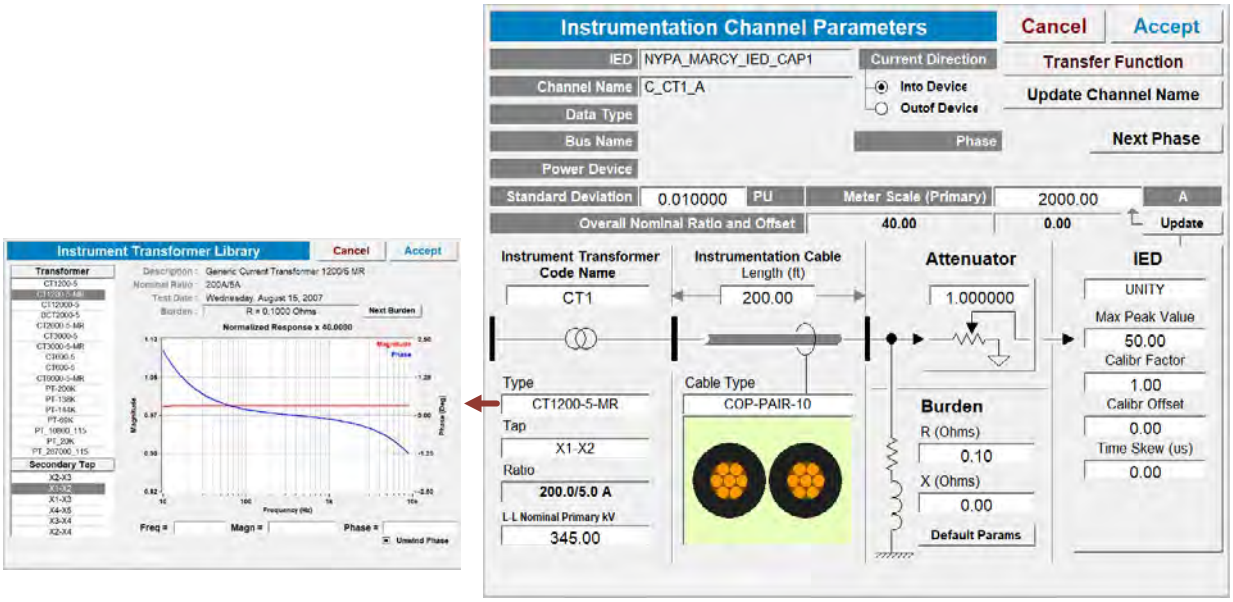

Figure 5.4.5: Example of a Current Phasor Instrumentation Channel Dialog

Table 5.4.1: Instrumentation Channel Parameters – User Entry Fields

Parameter	**Description**
Data Type	Specifies the type of the measured quantity.
Bus Name	The bus name where the measurement is taken
Power Device	Identifies the power device into which the current is measured (not used for voltage measurements)
Phase	The phase of the measured quantity (A, B, C, N, etc.)
Current Direction	The direction of current flow which is considered positive. For example, “into device” indicates that the positive current flow is into the power device terminal (See also Power Device parameter above)
Standard Deviation	Quantifies the expected error of the instrumentation channel in per unit of the maximum value that the channel can measure.
Meter Scale	The maximum peak value that the channel can measure defined at the instrument transformer primary side. Note that this value can be directly entered by the user, or automatically computed from the instrument transformer and data acquisition device characteristics. To automatically compute the, click on the **Update** button located below the Meter Scale field.
Instrument Transformer Code Name	An identifier of the instrument transformer associated with this channel. Note that WinIGS uses this identifier to generate the channel name. For example, the phase A voltage channel is

	automatically named V_VT_AN, if the instrument transformer name is set to VT.
Instrument Transformer **Type** and **Tap**	Selects instrument transformer parameters from a data library. The library includes parameters needed to create instrument channel models such as turns ratio, frequency response, etc. To select an instrument transformer model, click on the **type** or **tap** field to open the instrument transformer data library dialog (See also Figure 4.3 and 4.4)
L-L Nominal Primary Voltage	The line to line voltage at the instrument transformer primary side.
Instrumentation Cable Length	The length of the instrumentation cable connecting the instrument transformer secondary with the data acquisition device.
Cable Type	The instrumentation cable type and size. Clicking on this field opens the cable library selection window. Note that if the desired cable is not found in the library, a cable library editor is available allowing adding and modifying cable parameters. (See WinIGS-Q user's manual for details).
Attenuator	Attenuation value of any additional voltage or current reduction divider. Set to 1.0 if none.
Burden	The equivalent resistance of the burdens attached to the instrument transformer secondary.
IED	Selects data acquisition device from a IED library. This setting retrieved the data acquisition device frequency response for applying error correction. Set to UNITY if this information is not available.
Maximum Peak Value	Set to the maximum instantaneous (peak) voltage or current value that will not saturate the data acquisition device input. This value can be found in data acquisition device specifications
Calibration Factor	The channel output is multiplied by this value. Set to 1.0 if none required.
Calibration Offset	This value is added to the channel output. Set to 0.0 if none required.
Time Skew	Time delay in seconds of this channel with respect to time reference. Set to zero for no delay.

Note that the order of the instrumentation channels can be modified using the **Move Up** and **Move Down** buttons of the instrumentation channel list dialog (shown in Figure 4.2). Once the instrumentation channel parameter entry is completed, click on the Accept button of the instrumentation channel list dialog, to save the channel parameters. Note that the instrumentation channel parameters are saved in an ASCII file named:

CASENAME_Fnnnnn.ich
where case name is the WinIGS-Q network model file name root, and nnnnn is a 5-digit integer. Each IED has its own 'ich" file, and these files are stored in the same directory as the WinIGS-Q network model file.

In this example, 46 IEDs are placed in this substation for state estimation. The instrumentation channels of these IEDs are listed in Table 5.4.2. The total number of these channels is 360.

Table 5.4.2: Instrumentation Channels of IEDs in the Selected Section

IED Name	Voltage Channels	Current Channels	# of channels of this IED
IED_MRC_FACTSA	AN, BN, CN at MRC-FACTS	A, B, C at MRC-FACTS (into the transformer)	18
	AN, BN, CN at MR-FACTS1	A, B, C at MR-FACTS1 (into the transformer)	
	AN, BN, CN at MR-FACTS2	A, B, C at MR-FACTS2 (into the transformer)	
IED_MRC_FACTSB	AN, BN, CN at MRC-FACTS	A, B, C at MRC-FACTS (into the transformer)	18
	AN, BN, CN at MR-FACTS1	A, B, C at MR-FACTS1 (into the transformer)	
	AN, BN, CN at MR-FACTS2	A, B, C at MR-FACTS2 (into the transformer)	
IED_MR_FACTS1A	AN, BN, CN at MR-FACTS1	A, B, C at MR-FACTS1 (into the load)	6
IED_MR_FACTS1B	AN, BN, CN at MR-FACTS1	A, B, C at MR-FACTS1 (into the load)	6
IED_MR_FACTS2A	AN, BN, CN at MR-FACTS2	A, B, C at MR-FACTS2 (into the load)	6
IED_MR_FACTS2B	AN, BN, CN at MR-FACTS2	A, B, C at MR-FACTS2 (into the load)	6
IED_Auto1A	AN, BN, CN at MRC-AT1H	A, B, C at MRC-AT1H (into the transformer)	18
	AN, BN, CN at MRC-AT1L	A, B, C at MRC-AT1L (into the transformer)	
	AN, BN, CN at MARCY-T1	A, B, C at MARCY-T1 (into the transformer)	
IED_Auto1B	AN, BN, CN at MRC-AT1H	A, B, C at MRC-AT1H (into the transformer)	18
	AN, BN, CN at MRC-AT1L	A, B, C at MRC-AT1L (into the transformer)	
	AN, BN, CN at MARCY-T1	A, B, C at MARCY-T1 (into the transformer)	
IED_Auto2A	AN, BN, CN at MRC-AT2H	A, B, C at MRC-AT2H (into the transformer)	18

	AN, BN, CN at MRC-AT2L	A, B, C at MRC-AT2L (into the transformer)	
	AN, BN, CN at MARCY-T2	A, B, C at MARCY-T2 (into the transformer)	
IED_Auto2B	AN, BN, CN at MRC-AT2H	A, B, C at MRC-AT2H (into the transformer)	18
	AN, BN, CN at MRC-AT2L	A, B, C at MRC-AT2L (into the transformer)	
	AN, BN, CN at MARCY-T2	A, B, C at MARCY-T2 (into the transformer)	
IED_S765B1	AN, BN, CN at SOUTH765B	A, B, C at MRC-MSU1 (out of the substation)	6
IED_S765B2	AN, BN, CN at SOUTH765B	A, B, C at MRC-MSU1 (out of the substation)	6
IED_N765B1	AN, BN, CN at NORTH765B	A, B, C at MRC-MSU1 (out of the substation)	6
IED_N765B2	AN, BN, CN at NORTH765B	A, B, C at MRC-MSU1 (out of the substation)	6
IED_MSU1A	AN, BN, CN at MRC-MSU1	A, B, C at MRC-MSU1 (out of the substation)	6
IED_MSU1B	AN, BN, CN at MRC-MSU1	A, B, C at MRC-MSU1 (out of the substation)	6
IED_REACTA	AN, BN, CN at REACTOR1	A, B, C at REACTOR1 (into the reactor)	6
IED_REACTB	AN, BN, CN at REACTOR1	A, B, C at REACTOR1 (into the reactor)	6
IED_AT1H1	AN, BN, CN at MRC-AT1H	none	6
	AN, BN, CN at MRC-AT2H		
IED_AT2H1	AN, BN, CN at MRC-AT1H	none	6
	AN, BN, CN at MRC-AT2H		
IED_T1A	AN, BN, CN at MARCY-T1	A, B, C at MARCY-T1 (into the load)	6
IED_T1B	AN, BN, CN at MARCY-T1	A, B, C at MARCY-T1 (into the load)	6
IED_T2A	AN, BN, CN at MARCY-T2	A, B, C at MARCY-T2 (into the load)	6
IED_T2B	AN, BN, CN at MARCY-T2	A, B, C at MARCY-T2 (into the load)	6
IED_CAP1A	AN, BN, CN at M345-CAP1	A, B, C at M345-CAP1 (into the cap bank)	6
IED_CAP1B	AN, BN, CN at M345-CAP1	A, B, C at M345-CAP1 (into the cap bank)	6
IED_CAP2A	AN, BN, CN at M345-CAP2	A, B, C at M345-CAP2 (into the cap bank)	6
IED_CAP2B	AN, BN, CN at M345-CAP2	A, B, C at M345-CAP2 (into the cap bank)	6

IED_N345B1	AN, BN, CN at NORTH345B AN, BN, CN at SOUTH345B	none	6
IED_S345B1	AN, BN, CN at NORTH345B AN, BN, CN at SOUTH345B	none	6
IED_CCB1	AN, BN, CN at MRC-CCB1 AN, BN, CN at MRC-NSB1	none	6
IED_NSB1	AN, BN, CN at MRC-CCB1 AN, BN, CN at MRC-NSB1	none	6
IED_AT1L	AN, BN, CN at MRC-AT1L AN, BN, CN at MRC-AT2L	none	6
IED_AT2L	AN, BN, CN at MRC-AT1L AN, BN, CN at MRC-AT2L	none	6
IED_CCBA	AN, BN, CN at MRC-CCB1 AN, BN, CN at MRC-CCB2	A, B, C from MRC-CCB1 to MRC-CCB2 A, B, C from MRC-CCB2 to MRC-CCB1	12
IED_CCBB	AN, BN, CN at MRC-CCB1 AN, BN, CN at MRC-CCB2	A, B, C from MRC-CCB1 to MRC-CCB2 A, B, C from MRC-CCB2 to MRC-CCB1	12
IED_NSBA	AN, BN, CN at MRC-NSB1 AN, BN, CN at MRC-NSB2	A, B, C from MRC-NSB1 to MRC-NSB2 A, B, C from MRC-NSB2 to MRC-NSB1	12
IED_NSBB	AN, BN, CN at MRC-NSB1 AN, BN, CN at MRC-NSB2	A, B, C from MRC-NSB1 to MRC-NSB2 A, B, C from MRC-NSB2 to MRC-NSB1	12
IED_VOLNA	AN, BN, CN at MRC-VOLN	A, B, C at MRC-VOLN (out of the substation)	6
IED_VOLNB	AN, BN, CN at MRC-VOLN	A, B, C at MRC-VOLN (out of the substation)	6
IED_EDICA	AN, BN, CN at MRC-EDIC	A, B, C at MRC-EDIC (out of the substation)	6
IED_EDICB	AN, BN, CN at MRC-EDIC	A, B, C at MRC-EDIC (out of the substation)	6
IED_CCB2A	AN, BN, CN at MRC-CCB2	A, B, C at MRC-CCB2 (out of the substation)	6

IED_CCB2B	AN, BN, CN at MRC-CCB2	A, B, C at MRC-CCB2 (out of the substation)	6
IED_NSB2A	AN, BN, CN at MRC-NSB2	A, B, C at MRC-NSB2 (out of the substation)	6
IED_NSB2B	AN, BN, CN at MRC-NSB2	A, B, C at MRC-NSB2 (out of the substation)	6

5.4.2 Measurement Channel

The next step is to define the measurements to be used for the state estimator, in terms of the defined instrumentation channels. This is accomplished by clicking on the **Measurement** button of the IED user interface (shown in Figure 5.4.2). This action opens the measurement list dialog illustrated in Figure 5.4.6.

For most cases (including the example described in this document), the measurement parameters can be created automatically using the **Auto Create** button from the measurement list dialog.

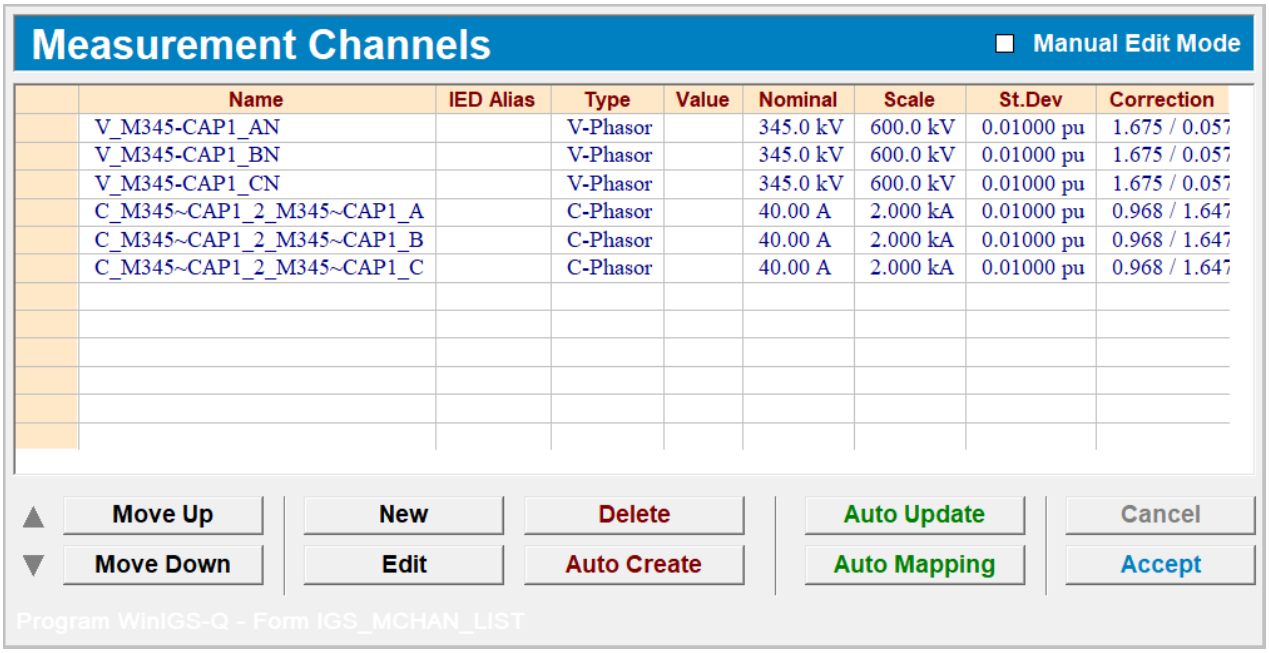

Figure 5.4.6: Measurement List Dialog

Measurement parameters can be manually created and edited using the New and Edit buttons of the measurement list dialog (shown in Figure 5.4.6), which open the measurement parameter dialog illustrated in Figure 5.4.7 and Figure 5.4.8. The fields in this dialog are briefly described in Table 5.4.2.

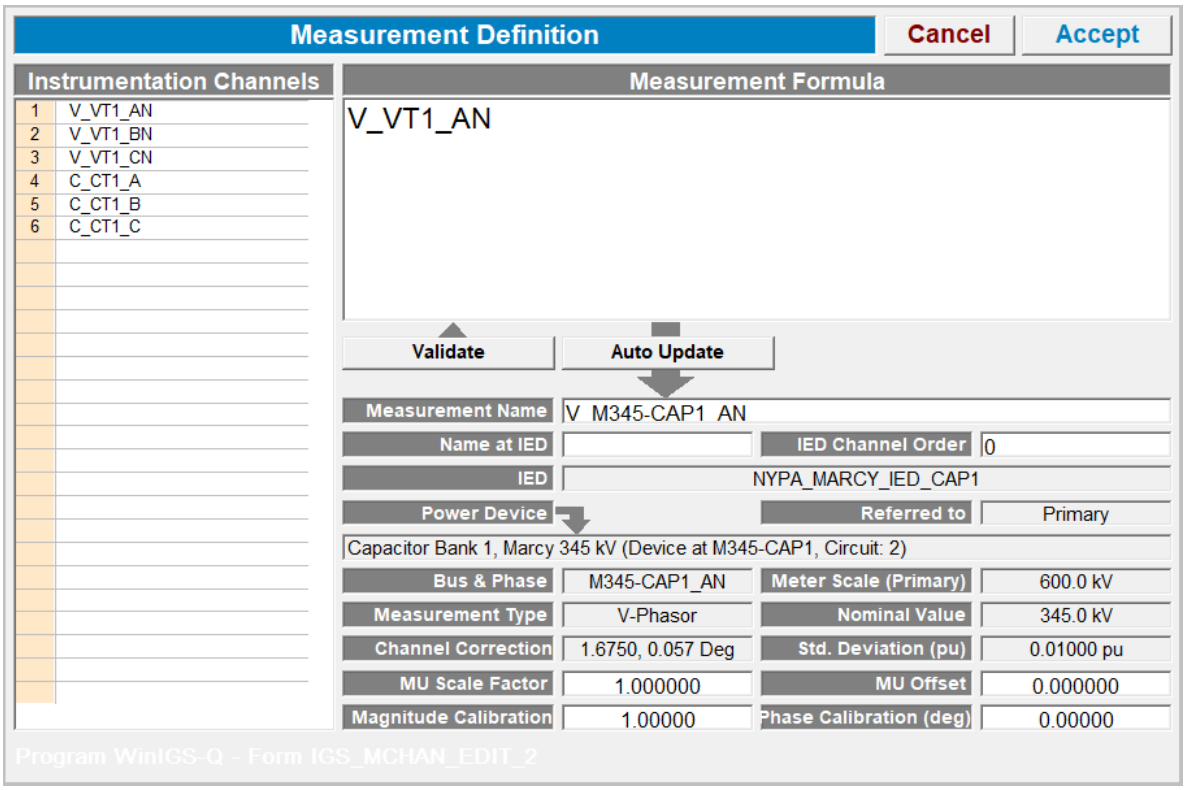

Figure 5.4.7: Voltage Phasor Measurement Parameters Dialog

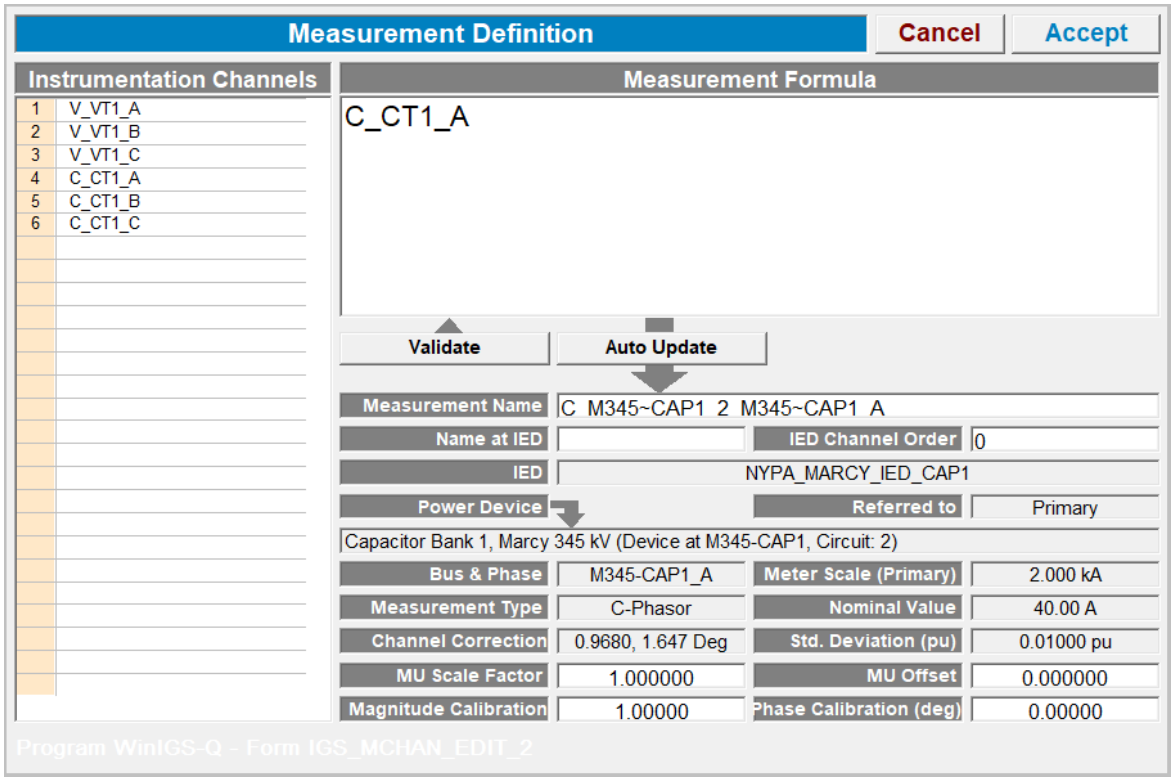

Figure 5.4.8: Current Phasor Measurement Parameters Dialog

Table 5.4.3: Measurement Parameters – User Entry Fields

Parameter	Description
Measurement Formula	Mathematical expression giving measurement value in terms of instrumentation channel values. Note that the measurement formula for automatically created measurements form instrumentation channels is simply the instrumentation channel name. However, a measurement can be manually defined as any expression involving all available instrumentation channels.
Measurement Name	***Voltage phasor measurements*** names are automatically formed based on the bus name, phase and measurement type. For example, a phase A to N voltage measurement on Bus M345-CAP1 is automatically named as V_M345-CAP1_AN. Similarly, ***current phasor measurements*** are automatically formed by identifying a power device and a specific terminal into which the measured current is flowing. For example, the phase A current into the capacitor bank connected at bus M345-CAP1 is named as C_M345~CAP1_2_M345~CAP1_A, where the part M345~CAP1_2 identifies the power device as circuit 2 connected at bus M345-CAP1, and the last part _M345~CAP1_A identifies the terminal into which the measured current is flowing. Note that the name part 1 is the user specified Circuit Name of the capacitor bank connected at bus M345-CAP1.
Name at IED	The measurement name as defined by the IED.
Meter Scale (Primary)	The maximum peak value that the channel can measure defined at the instrument transformer primary side. Note that this value is obtained from the corresponding instrumentation channel.
Standard Deviation (pu)	Quantifies the expected error of the measurement channel in per unit of the maximum value that the channel can measure.
Magnitude Calibration and Phase Calibration	Measurement magnitude and a phase angle correction values. Default values are 1.0 and 0.0 respectively.

5.5 Use Case: Normal Operation with Load VariationEvent Description and Sampled Data

We use WinIGS-Q to define events, simulate events and store the results in COMTRADE format. The WinIGS-Q case file is named as "NYPA_Q_Event1.NMT" and is provided with this report. Figure 5.5.1 shows the simulation user interface. The simulation is executed for a period of 1 minute. The measurements generated during the simulation are stored in a COMTRADE file. Figure 5.5.1 shows the quasi-dynamic domain simulation parameters dialog (click the "clock" button on the task bar) where the simulation time step, duration, as well as the COMTRADE output is specified. Note that the time step is selected to be 1 sample per cycle in this example, i.e., 60 samples per second. The simulation results are stored in COMTRADE files. The generated COMTRADE configuration and data files are named "NYPA_Q_Event1_MARCY.cfg" and "NYPA_Q_Event1_MARCY.dat", respectively.

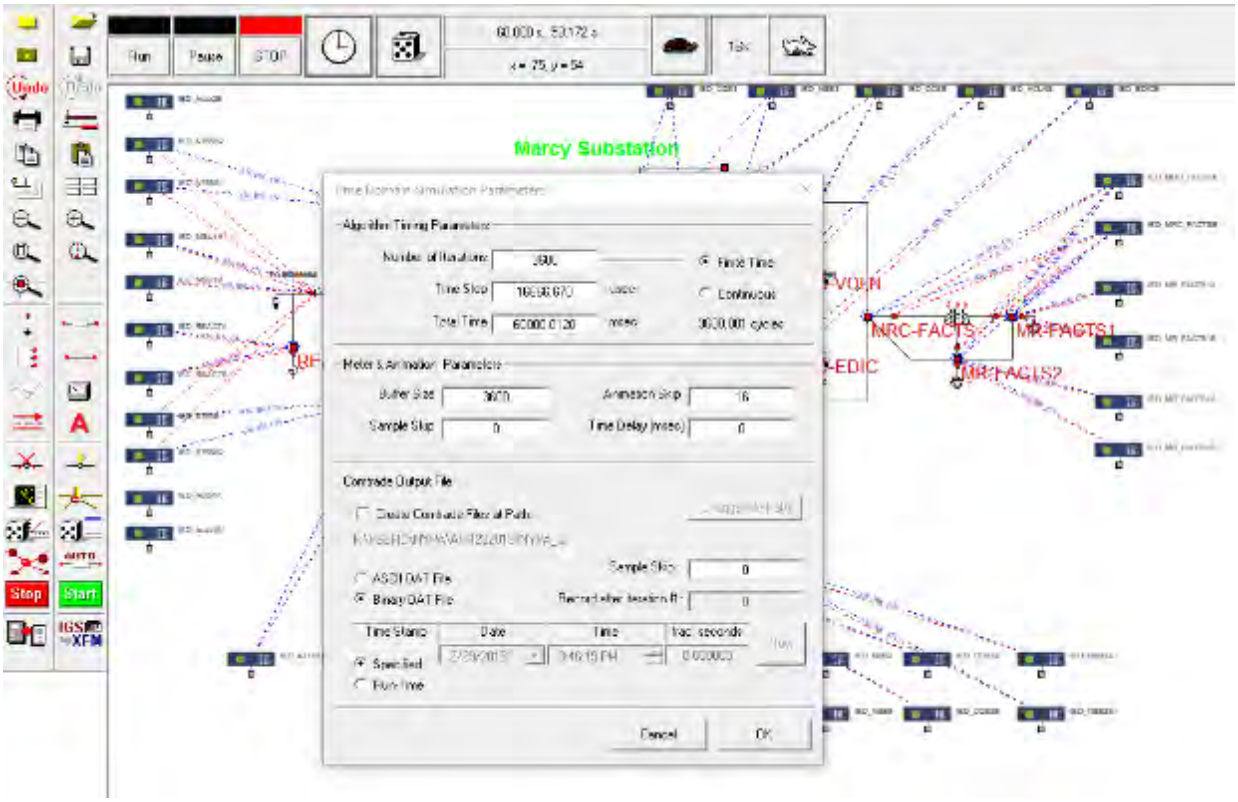

Figure 5.5.1: Perform Simulation for the Example System

In this event, the system is in normal operation with load variations outside the Marcy substation. The load variations are described as follows. At t=10.0s, a load with 80 MW, 30 MVar is disconnected to the system at Clay substation, and it is reconnected to the system at t=13.1s. Another load with 70 MW and 20 MVar at Clay substation is connected to the grid at 20.0s and disconnected at 23.1s. A load with 70 MW and 15 MVar is on and off at 28.0s and 30.1s in Edic Substation. Similarly, another load with 70 MW and 20MVar is disconnected at 35.05s and reconnected at 38.1s in Edic Substation. At t=45.05s, a load with 70 MW and 25 MVar is connected to the grid at Volney substation, and then it is disconnected at 47.1s. Another load with

80 MW and 30 MVar is then switched off at 53.05s, and switched on at 56.1s. Since the generated data is very large, we present the data obtained from some specific relays as shown from Figure 5.5.2 to 5.5.7.

Figure 5.5.2 shows the three-phase voltage phasor measurements at MRC-AT1H, MRC-AT1L, and MARCY-T1 obtained from IED_Auto1A. Figure 5.5.3 presents the three-phase current phasor measurements for the three single-phase autotransformers obtained from IED_Auto1A. Figure 5.5.4 shows the three-phase voltage phasor measurements at MRC-AT2H, MRC-AT2L, and MARCY-T2 obtained from IED_Auto2A. Figure 5.5.5 shows the three-phase current phasor measurements for the three single-phase autotransformers obtained from IED_Auto2A. Figure 5.5.6 depicts the three-phase voltage and current measurements for the capacitor bank at Bus M345-CAP1 obtained from IED_CAP1A. Figure 5.5.7 presents the three-phase voltage and current measurements for the three-phase two-winding transformer from MRC-CCB1 to MRC-CCB2 obtained from IED_CCBA.

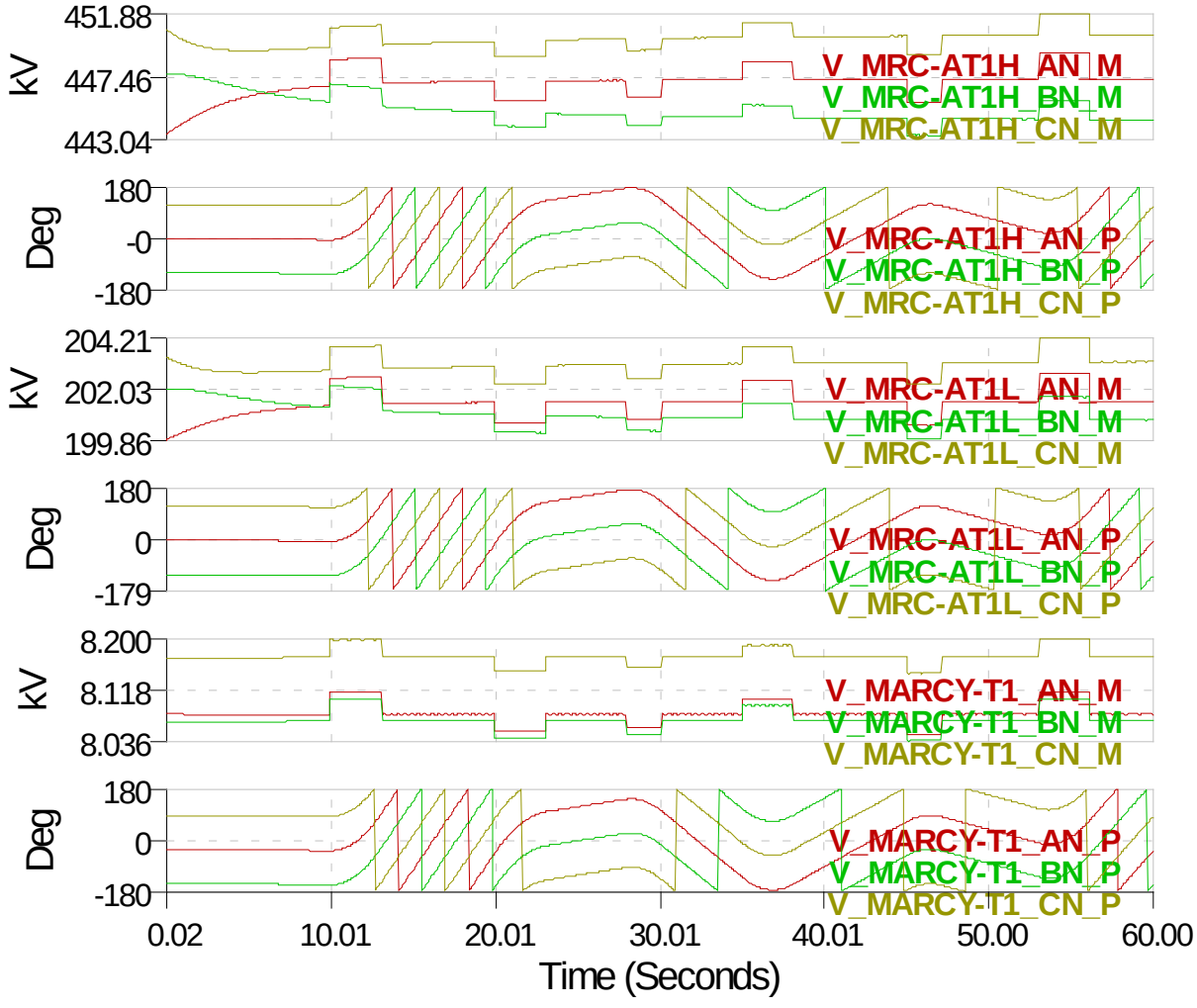

Figure 5.5.2: Three-phase Voltage Measurements at MRC-AT1H, MRC-AT1L, and MARCY-T1

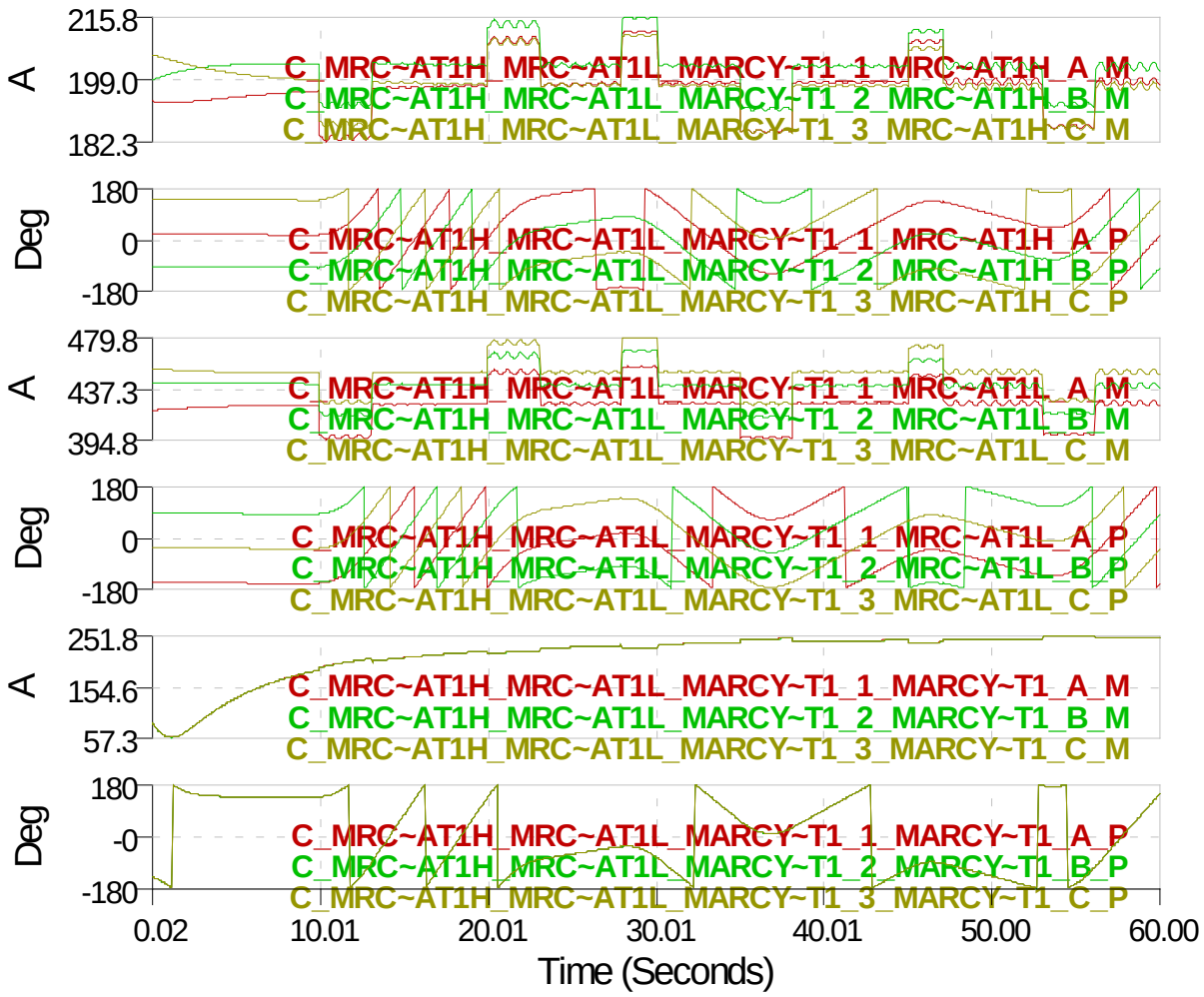

Figure 5.5.3: Three-phase Current Measurements for the Three Single-Phase Autotransformers at Auto Bank 1

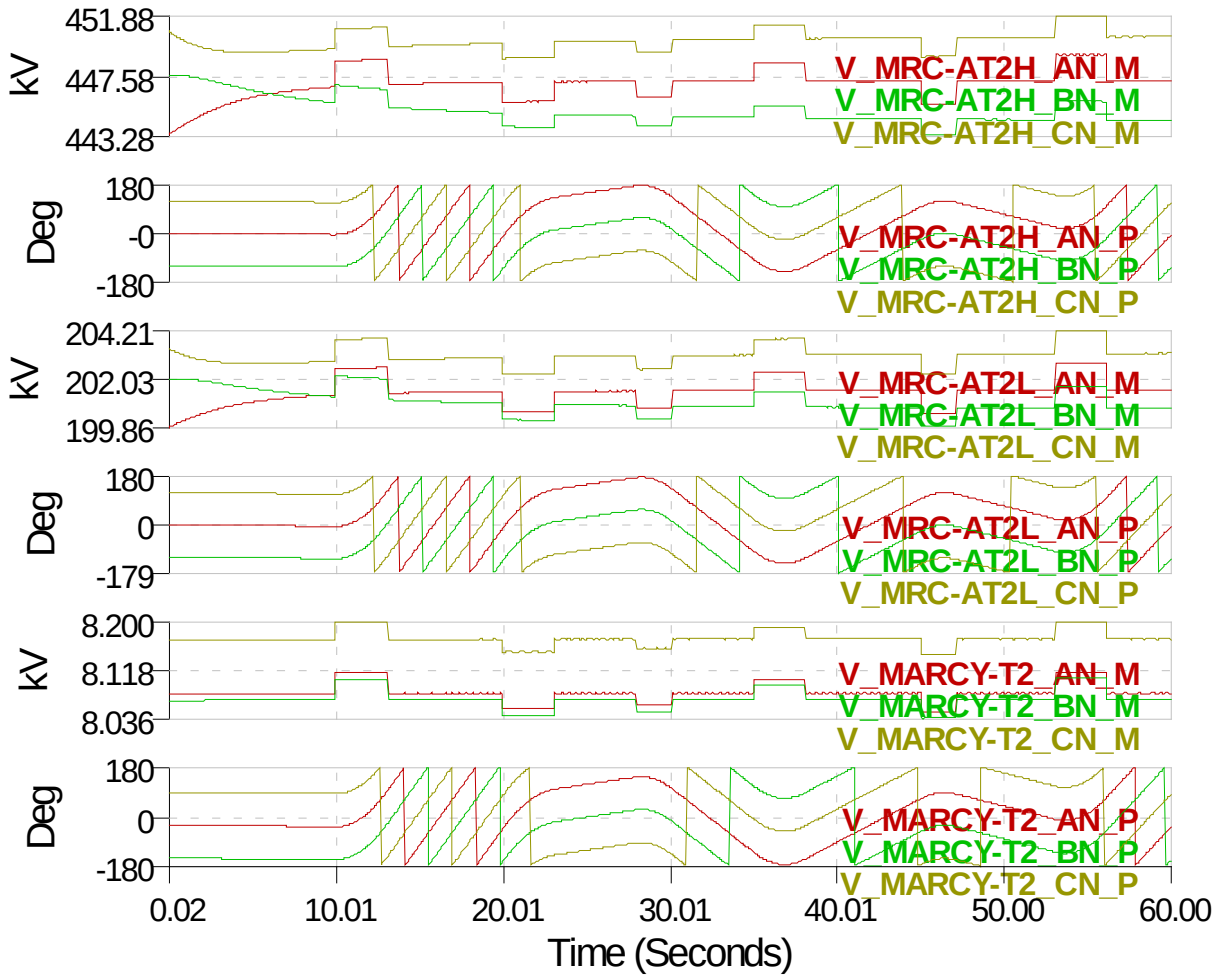

Figure 5.5.4: Three-phase Voltage Measurements at MRC-AT2H, MRC-AT2L, and MARCY-T2

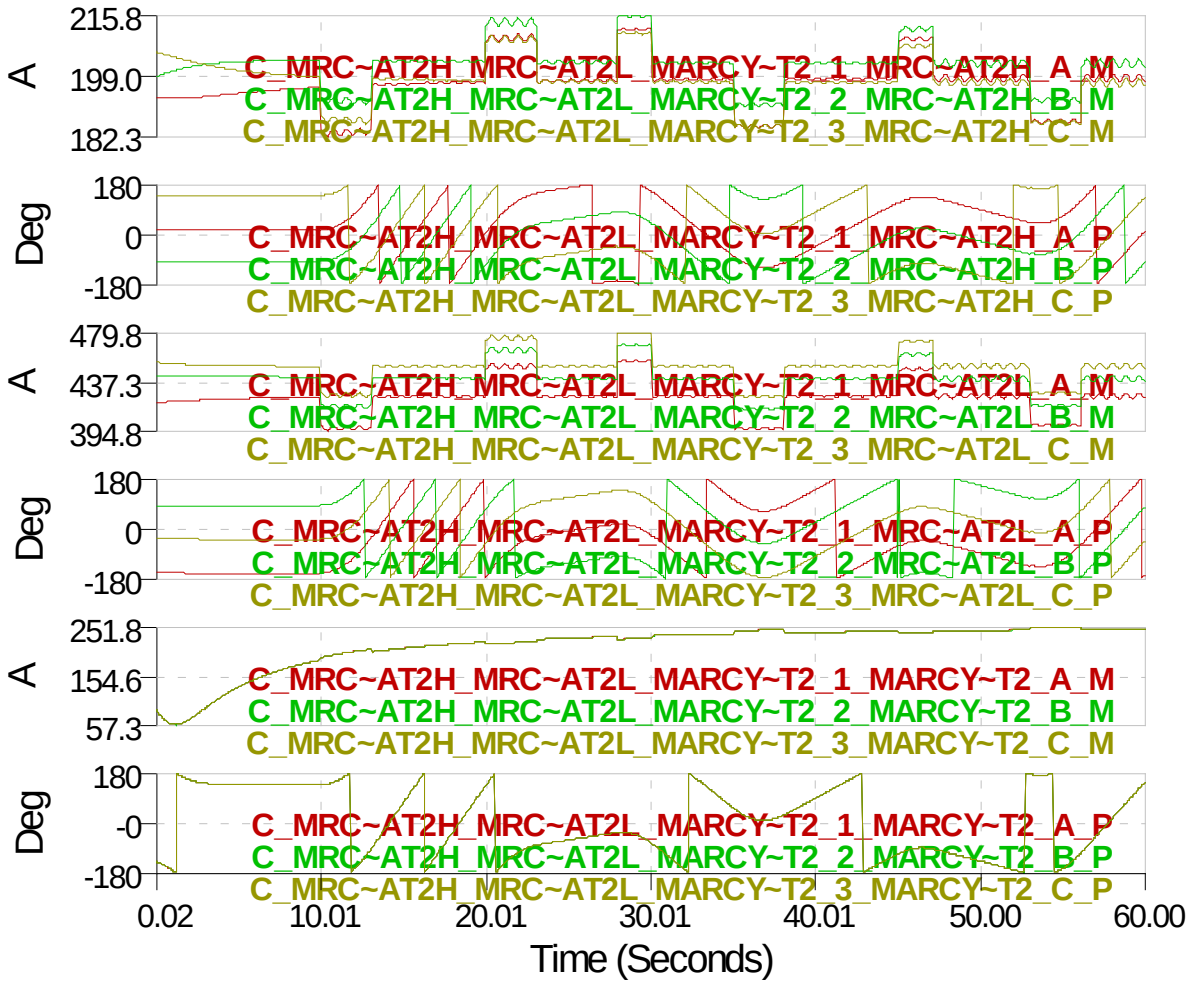

Figure 5.5.5: Three-phase Current MeasureFments for the Three Single-Phase Autotransformers at Auto Bank 2

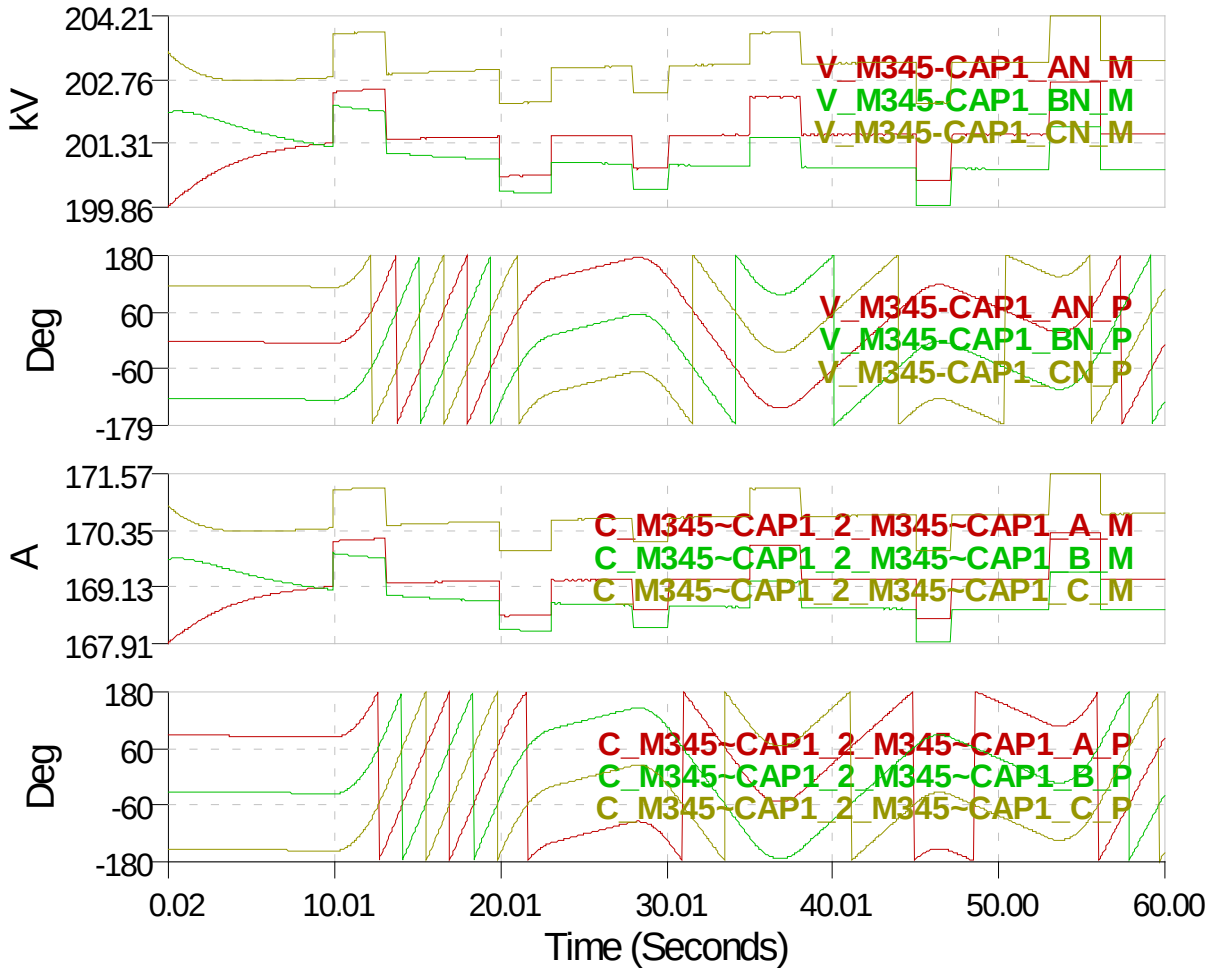

Figure 5.5.6: Three-phase Voltage and Current Measurements for the Capacitor Bank at Bus M345-CAP1

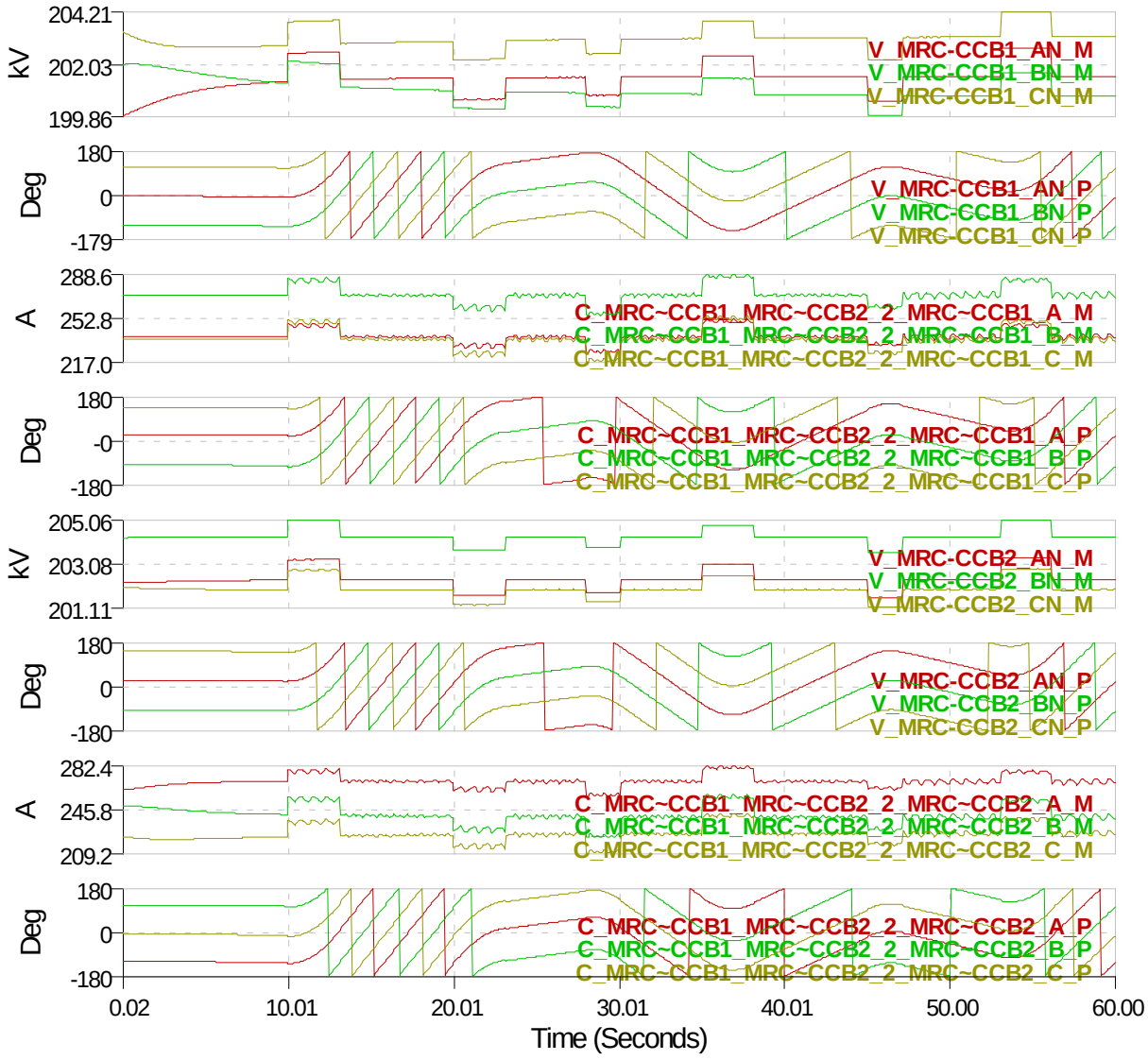

Figure 5.5.7: Three-phase Voltage and Current Measurements for the Transformer from MRC-CCB1 to MRC-CCB2

5.5.2 Setup DS-QSE for Marcy Substation

This subsection presents the procedure regarding to setting up the distributed state estimator for the use case. The state estimator has been implemented within the WinIGS-Q program. In order to setup the state estimator, we have to execute the WinIGS-Q program, open the use case, click the meter button  , and add the state estimator (M012) into the system. Figure 5.5.8 shows the procedure to add the state estimator icon into the system.

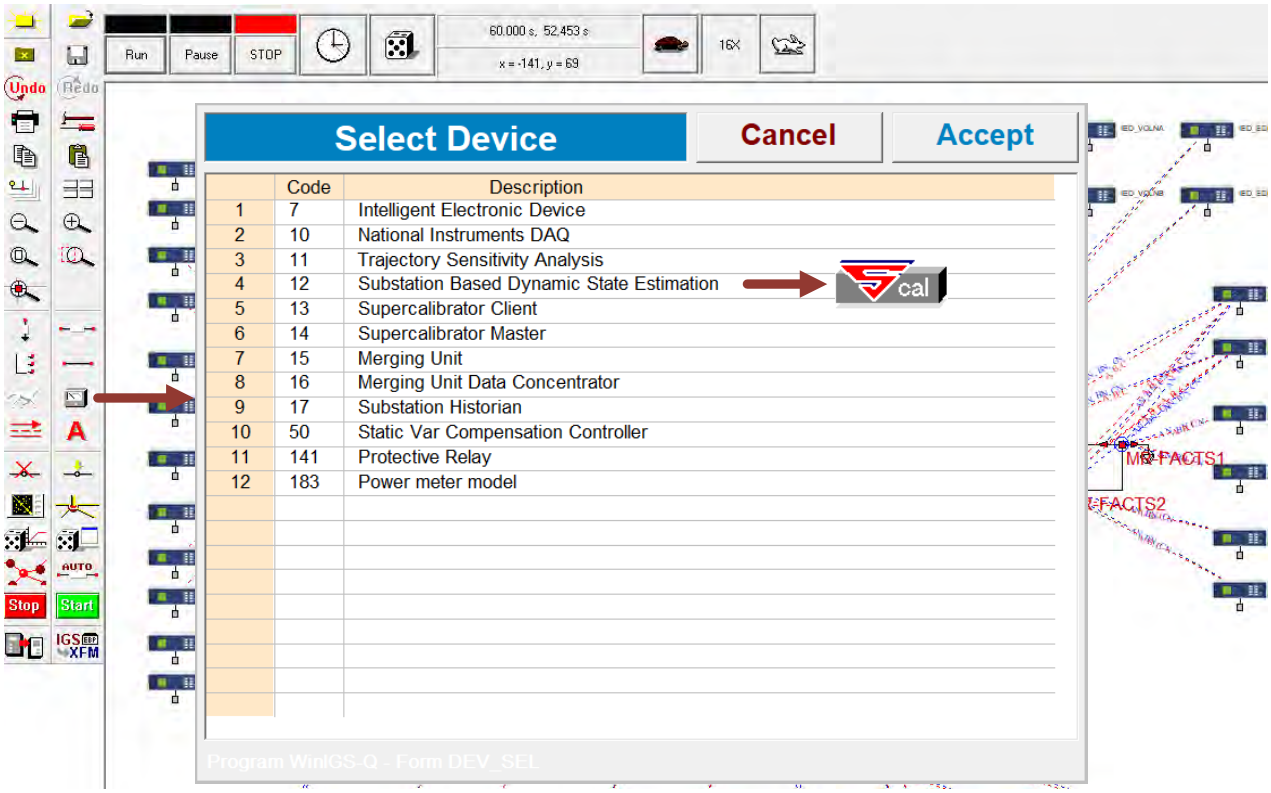

Figure 5.5.8: Add State Estimator Object

The next step is to set up the state estimator. The user interface of the state estimator is shown in Figure 5.5.9. The design of the state estimator supports the connection of the state estimator to a virtual PDC (for field demonstration) or to a phasor data concentrator client (PDC client, for simulation experiments). The PDC client connects to the test data server and receives a C37.118 synchro-phasor data stream. The test data server serves the purpose of numerical experimentation with the quasi-dynamic state estimation where a C37.118 data stream is created that is served to the PDC client. The user can define the data source to be synchro-phasor format or COMTRADE format that has been saved upon the simulation of the system. Notice that in this example, we use the COMTRADE file that is created in Section 5.5.1. The measurement data is streamed to the test data server and then PDC client before the state estimation, and the interface of the test data server and PDC client are shown in Figure 5.5.10 and 5.5.11, respectively.

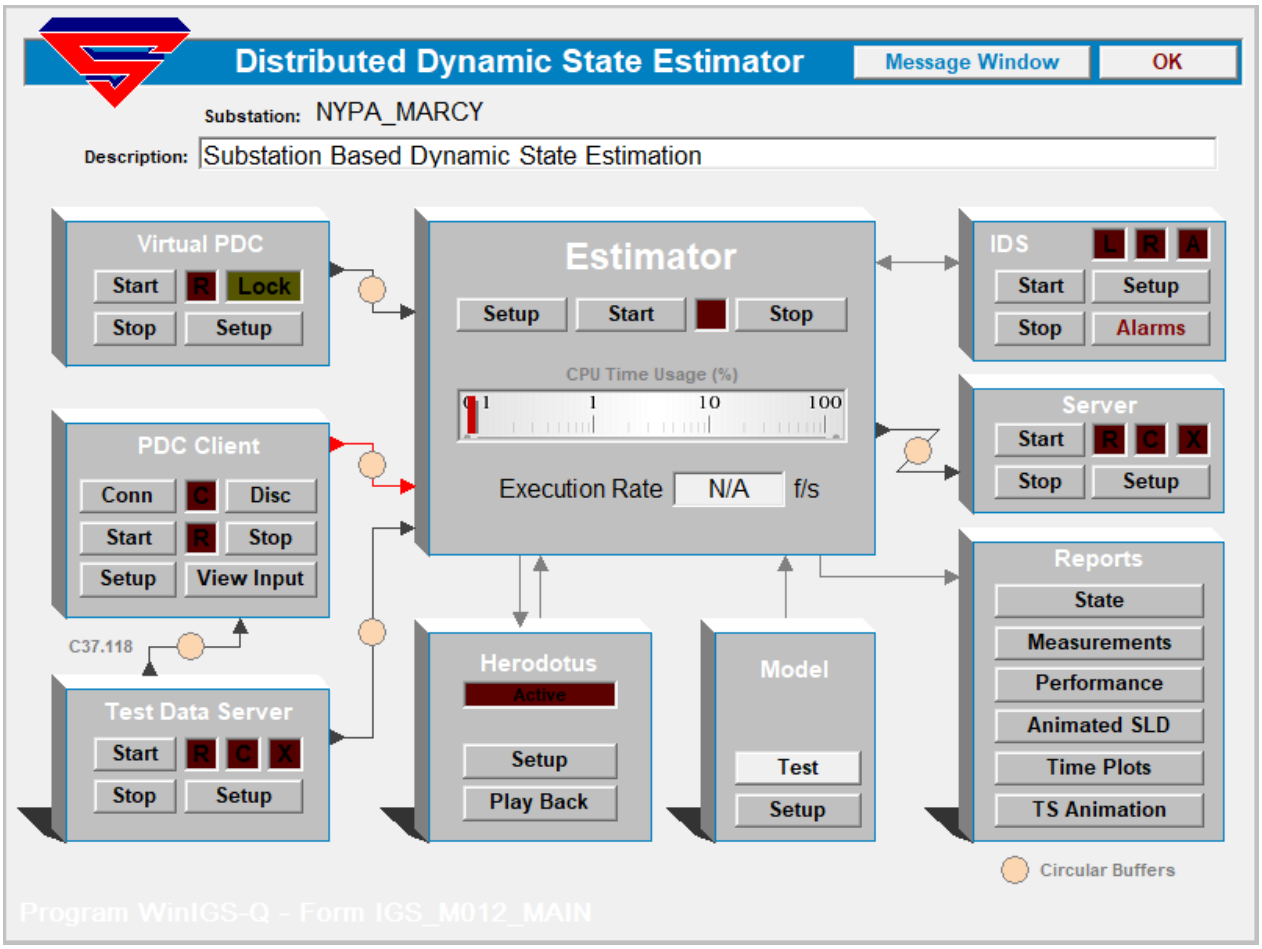

Figure 5.5.9: User Interface of State Estimator

The setup for test data server is as follows. First, we click the "**Setup**" button in the **Test Data Server** section on the lower left corner as shown in Figure 5.5.9. The user interface of the test data server is shown in Figure 5.5.10. Next, the user has to select the data file using the file path button in the middle of the user interface, and also define the data source and data format according to the data file. In this example, since we stream COMTRADE file to the test data server, we select the data source to be **COMTRADE** and data format to be **Phasors (Polar)**. Then we select **Stream (TCP)** in the streaming parameters and click **Play** button. Once all these steps are executed, we can see the streaming phasors on the right lower corner.

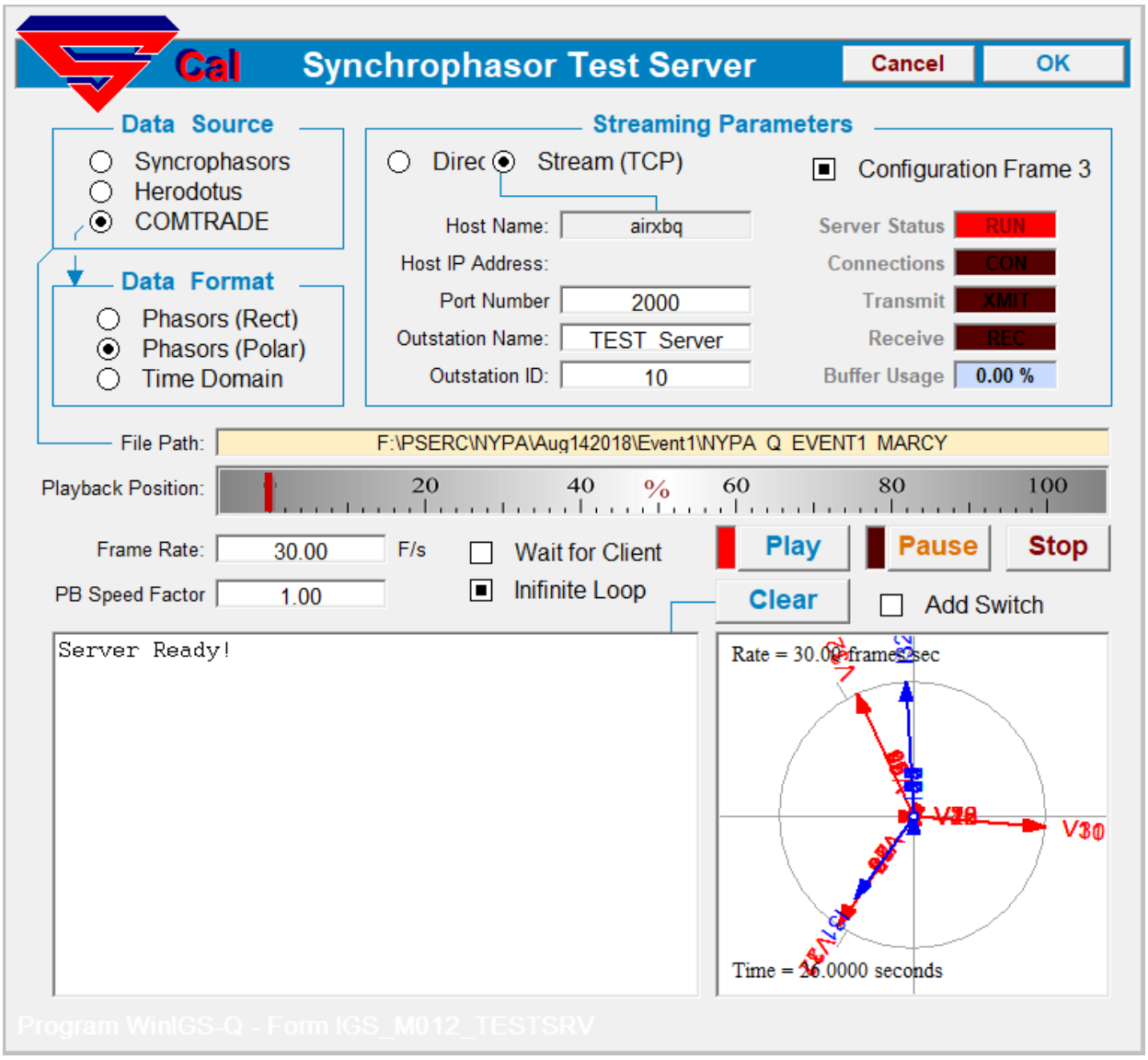

Figure 5.5.10: Test Data Server Interface

The next step is to setup the PDC client as shown in Figure 5.5.11. Notice that for the simulation experiment case as described in this example, the user has to set the **Outstation IP Address** as same as **Local IP Address**. Click **TCP** in protocol section, and then click "**connect**" and "**start**". And the streaming phasor diagram is shown in the upper right corner. The next step is to map the measurements to the corresponding state estimator measurement channels as shown in Figure 5.5.12. In the measurement mapping dialog, the user has to select the PDC measurement channel to the corresponding state estimator measurement channel one by one. Once all the measurement channels are set up, click "**Verify PDC Mapping**" to verify if all the measurement channels are mapped correctly. If all the measurements are mapped correctly, we will see the dialog as shown in Figure 5.5.13.

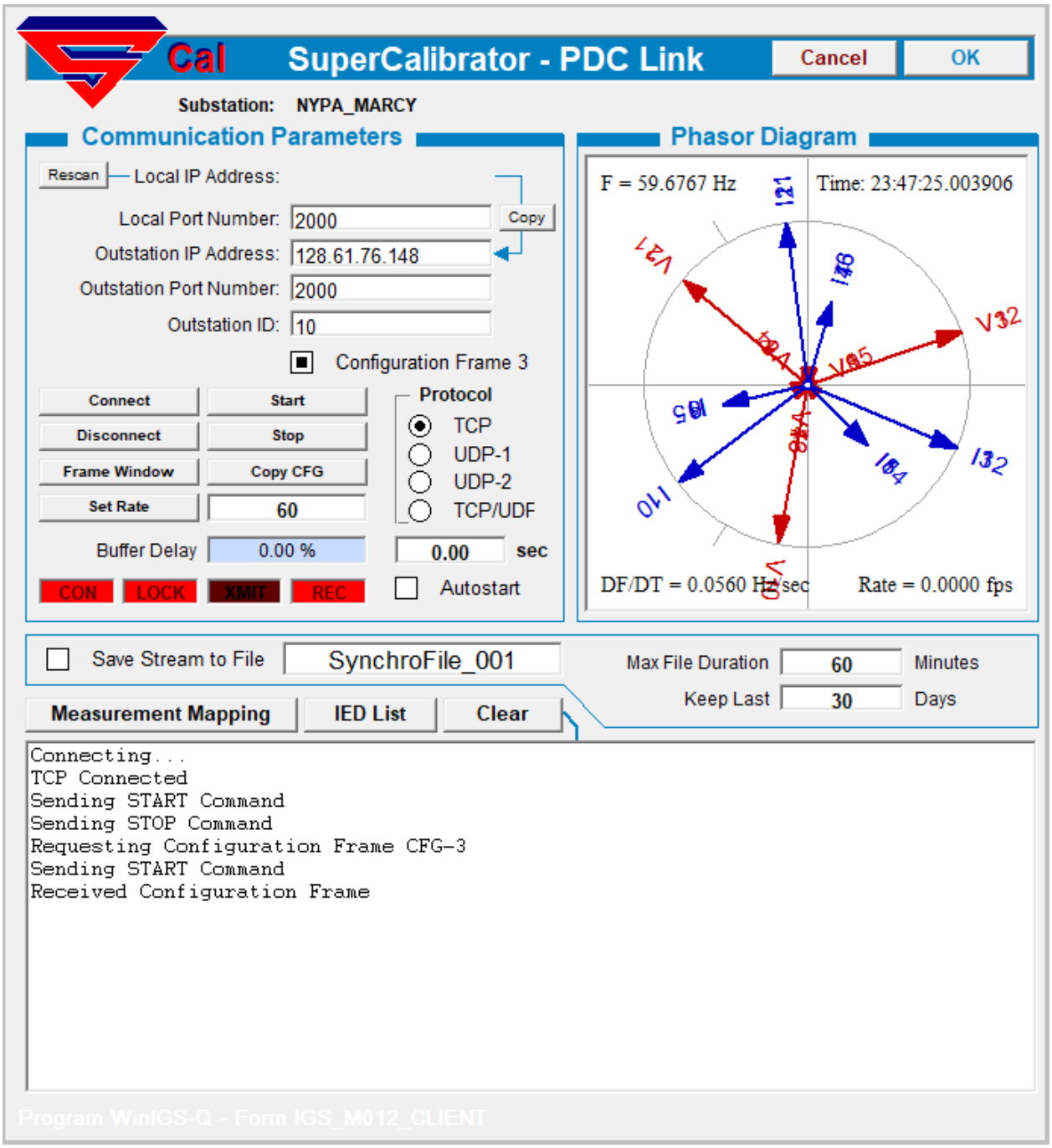

Figure 5.5.11: PDC Client Interface

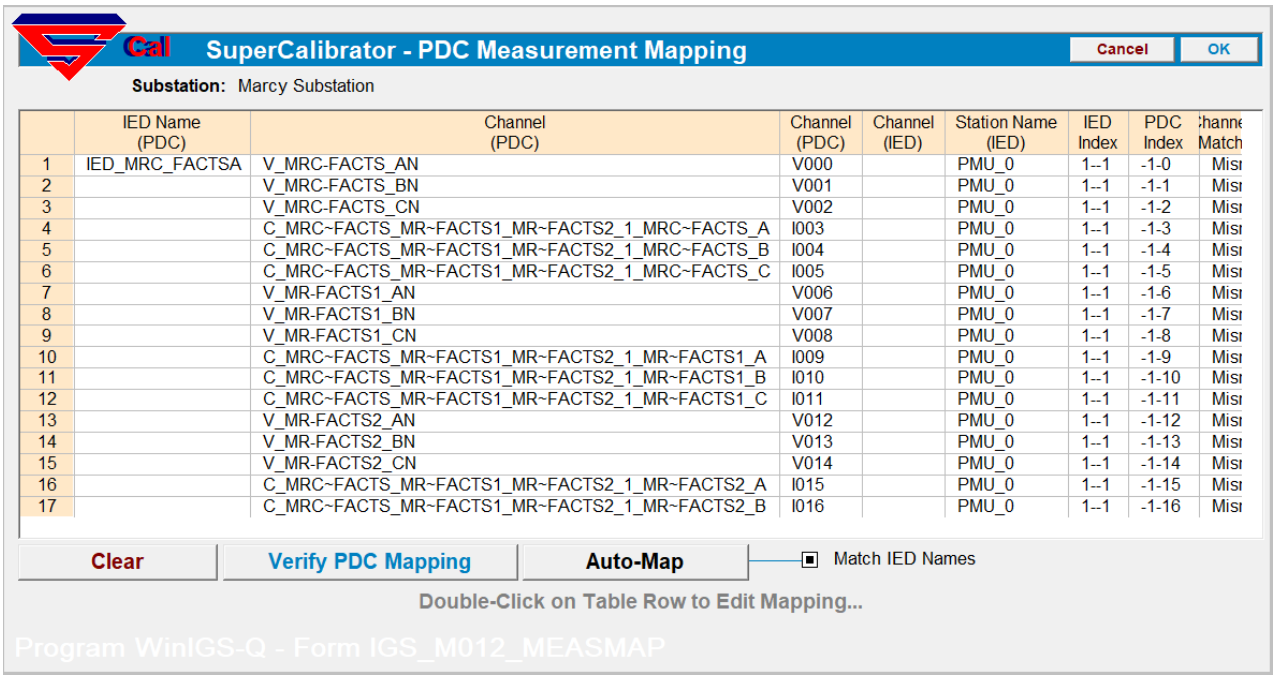

	IED Name (PDC)	Channel (PDC)	Channel (PDC)	Channel (IED)	Station Name (IED)	IED Index	PDC Index	Channe Match
1	IED_MRC_FACTSA	V_MRC-FACTS_AN	V000		PMU_0	1--1	-1-0	Misı
2		V_MRC-FACTS_BN	V001		PMU_0	1--1	-1-1	Misı
3		V_MRC-FACTS_CN	V002		PMU_0	1--1	-1-2	Misı
4		C_MRC~FACTS_MR~FACTS1_MR~FACTS2_1_MRC~FACTS_A	I003		PMU_0	1--1	-1-3	Misı
5		C_MRC~FACTS_MR~FACTS1_MR~FACTS2_1_MRC~FACTS_B	I004		PMU_0	1--1	-1-4	Misı
6		C_MRC~FACTS_MR~FACTS1_MR~FACTS2_1_MRC~FACTS_C	I005		PMU_0	1--1	-1-5	Misı
7		V_MR-FACTS1_AN	V006		PMU_0	1--1	-1-6	Misı
8		V_MR-FACTS1_BN	V007		PMU_0	1--1	-1-7	Misı
9		V_MR-FACTS1_CN	V008		PMU_0	1--1	-1-8	Misı
10		C_MRC~FACTS_MR~FACTS1_MR~FACTS2_1_MR~FACTS1_A	I009		PMU_0	1--1	-1-9	Misı
11		C_MRC~FACTS_MR~FACTS1_MR~FACTS2_1_MR~FACTS1_B	I010		PMU_0	1--1	-1-10	Misı
12		C_MRC~FACTS_MR~FACTS1_MR~FACTS2_1_MR~FACTS1_C	I011		PMU_0	1--1	-1-11	Misı
13		V_MR-FACTS2_AN	V012		PMU_0	1--1	-1-12	Misı
14		V_MR-FACTS2_BN	V013		PMU_0	1--1	-1-13	Misı
15		V_MR-FACTS2_CN	V014		PMU_0	1--1	-1-14	Misı
16		C_MRC~FACTS_MR~FACTS1_MR~FACTS2_1_MR~FACTS2_A	I015		PMU_0	1--1	-1-15	Misı
17		C_MRC~FACTS_MR~FACTS1_MR~FACTS2_1_MR~FACTS2_B	I016		PMU_0	1--1	-1-16	Misı

Figure 5.5.12: Measurement Mapping

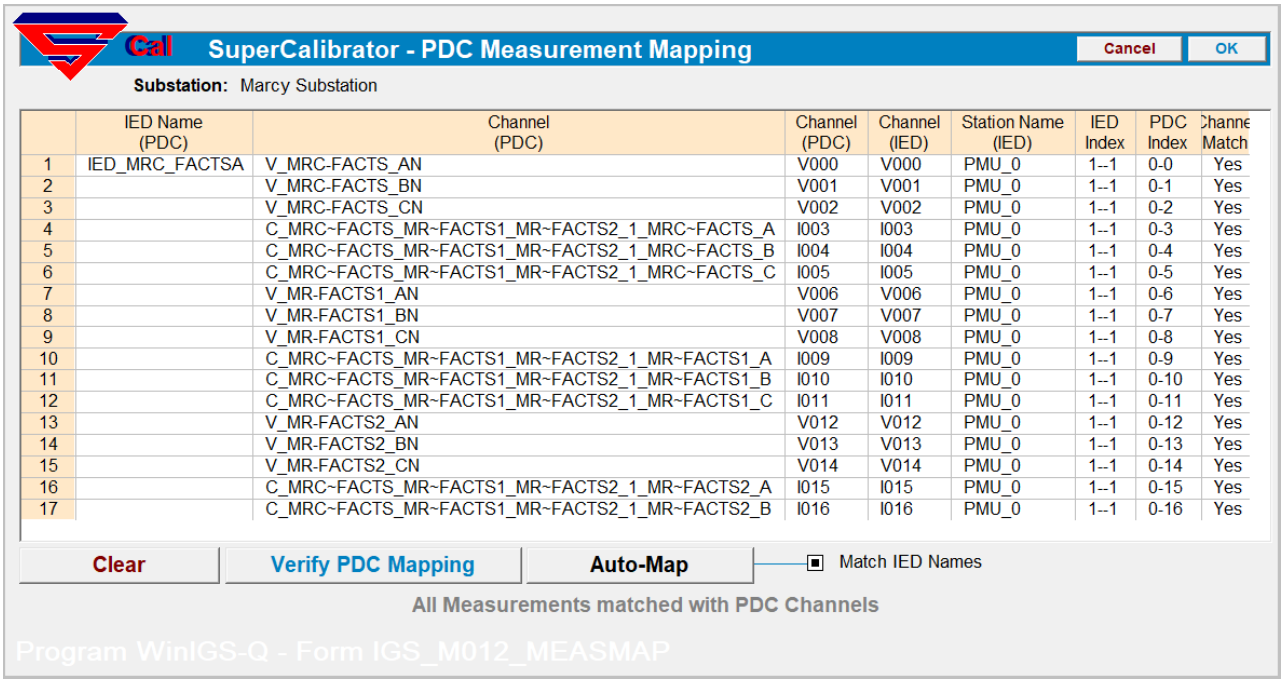

	IED Name (PDC)	Channel (PDC)	Channel (PDC)	Channel (IED)	Station Name (IED)	IED Index	PDC Index	Channe Match
1	IED_MRC_FACTSA	V_MRC-FACTS_AN	V000	V000	PMU_0	1--1	0-0	Yes
2		V_MRC-FACTS_BN	V001	V001	PMU_0	1--1	0-1	Yes
3		V_MRC-FACTS_CN	V002	V002	PMU_0	1--1	0-2	Yes
4		C_MRC~FACTS_MR~FACTS1_MR~FACTS2_1_MRC~FACTS_A	I003	I003	PMU_0	1--1	0-3	Yes
5		C_MRC~FACTS_MR~FACTS1_MR~FACTS2_1_MRC~FACTS_B	I004	I004	PMU_0	1--1	0-4	Yes
6		C_MRC~FACTS_MR~FACTS1_MR~FACTS2_1_MRC~FACTS_C	I005	I005	PMU_0	1--1	0-5	Yes
7		V_MR-FACTS1_AN	V006	V006	PMU_0	1--1	0-6	Yes
8		V_MR-FACTS1_BN	V007	V007	PMU_0	1--1	0-7	Yes
9		V_MR-FACTS1_CN	V008	V008	PMU_0	1--1	0-8	Yes
10		C_MRC~FACTS_MR~FACTS1_MR~FACTS2_1_MR~FACTS1_A	I009	I009	PMU_0	1--1	0-9	Yes
11		C_MRC~FACTS_MR~FACTS1_MR~FACTS2_1_MR~FACTS1_B	I010	I010	PMU_0	1--1	0-10	Yes
12		C_MRC~FACTS_MR~FACTS1_MR~FACTS2_1_MR~FACTS1_C	I011	I011	PMU_0	1--1	0-11	Yes
13		V_MR-FACTS2_AN	V012	V012	PMU_0	1--1	0-12	Yes
14		V_MR-FACTS2_BN	V013	V013	PMU_0	1--1	0-13	Yes
15		V_MR-FACTS2_CN	V014	V014	PMU_0	1--1	0-14	Yes
16		C_MRC~FACTS_MR~FACTS1_MR~FACTS2_1_MR~FACTS2_A	I015	I015	PMU_0	1--1	0-15	Yes
17		C_MRC~FACTS_MR~FACTS1_MR~FACTS2_1_MR~FACTS2_B	I016	I016	PMU_0	1--1	0-16	Yes

Figure 5.5.13: All Measurements Are Matched with PDC Channels

5.5.3 Execute DS-QSE and Record Performance

Once the test data server and PDC client are set up, we are ready to run the state estimator. First, click "**Setup**" in the "**Estimator**" section, and we will see a dialog as shown in Figure 5.5.14. Notice that we should select "**QuasiDynamic**" and "**Unconstrained**" in the Estimation Options section and select "**PDC Client**" in the input section. The state estimator after this step is shown in Figure 5.5.15.

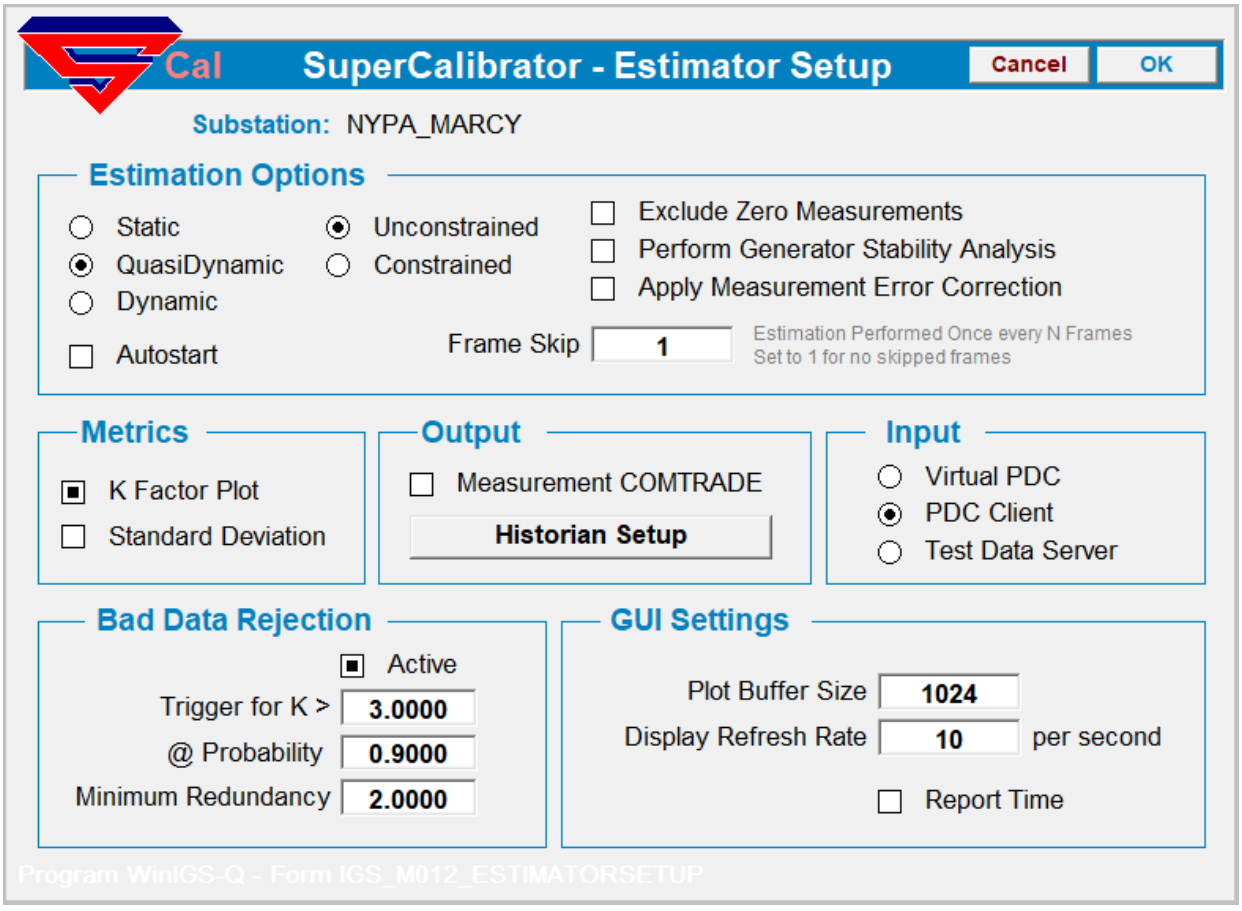

Figure 5.5.14: User Interface of Estimator Setup

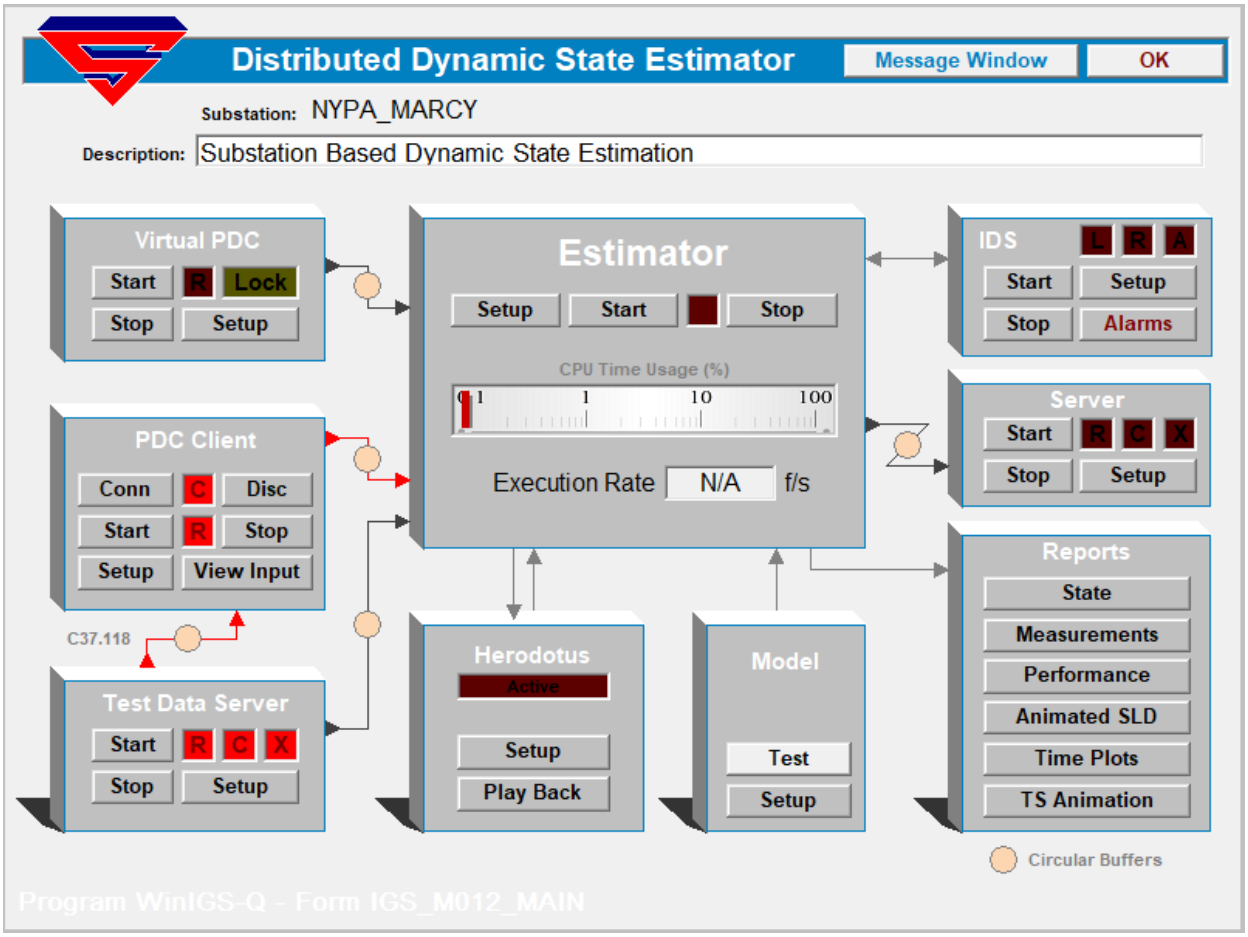

Figure 5.5.15: Ready to Run the State Estimator

Next, click "**Start**" in the "**Estimator**" section, and the estimator starts to perform the state estimation as shown in Figure 5.5.16. The user can view the performance metrics in the **Report** section, where estimated states, measurements, estimated measurements, performance evaluation, and animation are shown. The estimated states of the whole substation can be viewed by clicking the **States** button in the **Report** section as shown in Figure 5.5.17, where all the states of buses as well as the internal states of devices are shown. Notice that the name of an internal state starts from the device code and ends with the number of this internal state in the device.

The measurements and estimated measurements of Marcy Substation can be viewed by clicking the **Measurements** button in the **Report** as shown in Figure 5.5.18, where the user can select the table and diagram to show different measurement types (e.g., field measurement from IEDs, derived measurement, etc.). The user can also let the table and diagram show only the voltage/current measurements by clicking voltage/current option in Figure 5.5.18. Notice that if the user clicks "**S.E.**" option in Figure 5.5.18, a state estimator CSE measurement report is generated as shown in Figure 5.5.19, where all the measurement models (actual, derived, virtual, and pseudo measurements) processed in the state estimator are shown in the table. In this example, we have 774 measurements at time t and 774 measurements at time tm. Since the substation consists of 120 states at time t, the redundancy is (774-120)/120 = 545%. Also notice that all the errors between the measurements and estimated measurements are in very small values, which

substantiates the state estimator running successfully. In addition, the confidence level of this example can be viewed by clicking "**Performance**" button in the Report section shown in Figure 5.5.20. Notice that we use the performance evaluation, which is also called the parameterized (parameter k) chi-square test to validate the model, and it is generated as follows.

All the phasors are divided into real and imaginary parts so that the state estimator is able to manipulate the data in real number. The chi-square test is calculated as:

$$\zeta = \sum_{i=1}^{n} \left(\frac{r_i}{k\sigma_i} \right)^2 ,$$

where r_i is the residual between measurement and estimated measurement i, and σ_i is the standard deviation of the corresponding measurement. Note that the variable k enables to express the results of the chi-square test with only one variable.

And then we compute the confidence level as:

$$\Pr[\chi^2 \geq \zeta] = 1.0 - \Pr(\chi^2, \nu) .$$

A confidence level around 100% (small chi-square value) when k=1 infers that the measurements are highly consistent with the dynamic model of the system, i.e., the model is validated, while a confidence level around 0% (large chi-square value) when k=1 means that the measurements do not match the dynamic model of the system. As shown in Figure 5.5.20, the green light is on, and the confidence level is 100% when k=1, which implies the estimation results are trustworthy, i.e., the measurements are consistent with the system model.

In addition, 3D visualizations have been developed. A screenshot of the 3D visualization is shown in Figure 5.5.21. The estimated voltage magnitude for each node is visualized as a tube. The height of the tube is proportional to the voltage magnitude. The estimated voltage phase of a node is visualized as an arc. The angle of the arc is proportional to the voltage phase angle. Surface plots are also available as illustrated in Figure 5.5.21. The voltage estimated measurements are plotted as a contour map to reflect the magnitude of each measurement. The green surface denotes the bus voltages of this substation are around the rated voltage, and the maximum difference between the bus voltage and its rated value is within 0.025 p.u. error.

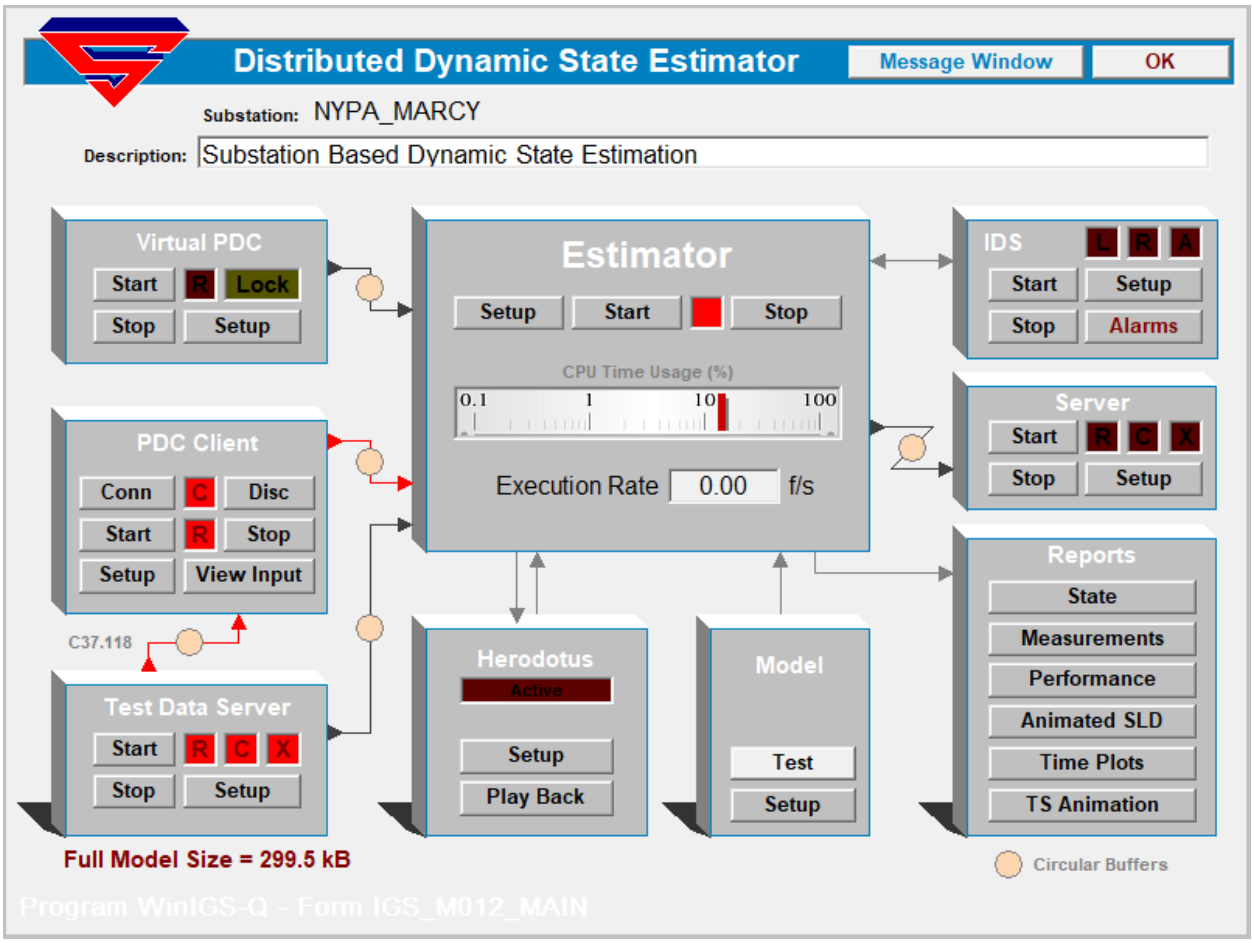

Figure 5.5.16: State Estimator is Running

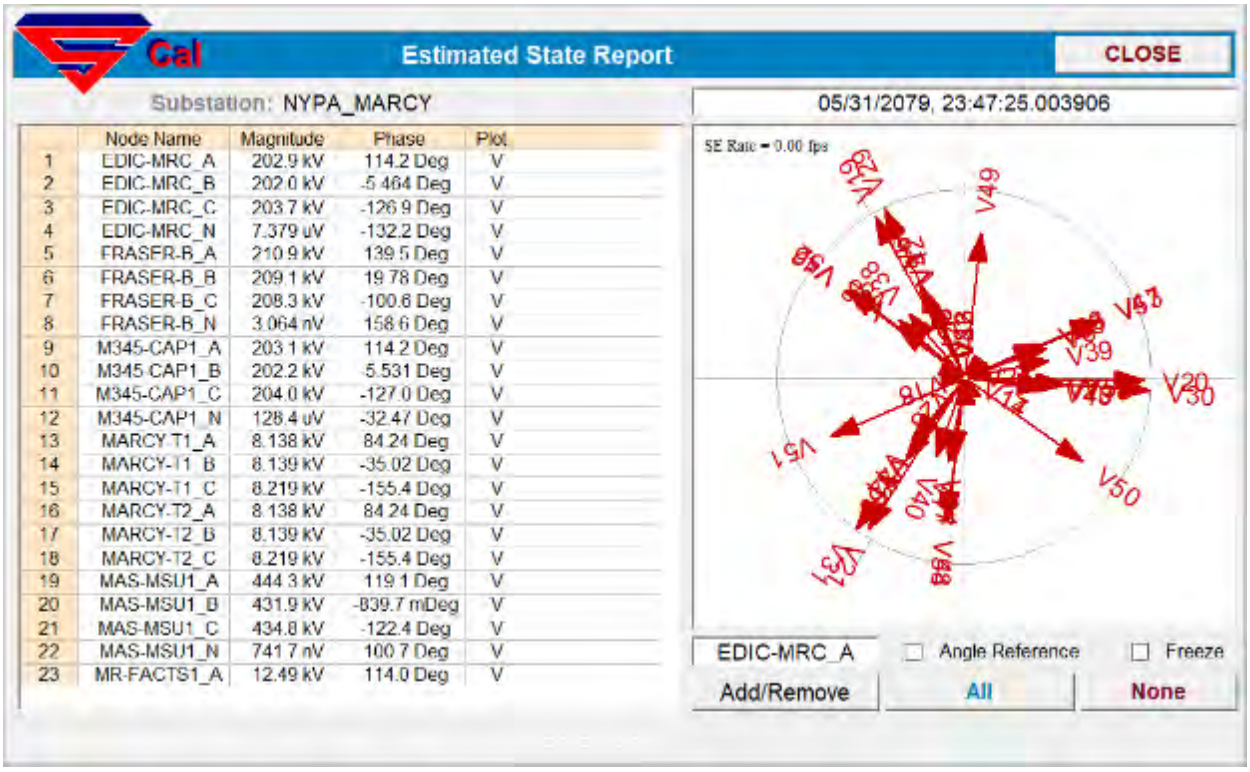

	Node Name	Magnitude	Phase	Plot
1	EDIC-MRC_A	202.9 kV	114.2 Deg	V
2	EDIC-MRC_B	202.0 kV	-5.464 Deg	V
3	EDIC-MRC_C	203.7 kV	-126.9 Deg	V
4	EDIC-MRC_N	7.379 uV	-132.2 Deg	V
5	FRASER-B_A	210.9 kV	139.5 Deg	V
6	FRASER-B_B	209.1 kV	19.78 Deg	V
7	FRASER-B_C	208.3 kV	-100.6 Deg	V
8	FRASER-B_N	3.064 nV	158.6 Deg	V
9	M345-CAP1_A	203.1 kV	114.2 Deg	V
10	M345-CAP1_B	202.2 kV	-5.531 Deg	V
11	M345-CAP1_C	204.0 kV	-127.0 Deg	V
12	M345-CAP1_N	128.4 uV	-32.47 Deg	V
13	MARCY-T1_A	8.138 kV	84.24 Deg	V
14	MARCY-T1_B	8.139 kV	-35.02 Deg	V
15	MARCY-T1_C	8.219 kV	-155.4 Deg	V
16	MARCY-T2_A	8.138 kV	84.24 Deg	V
17	MARCY-T2_B	8.139 kV	-35.02 Deg	V
18	MARCY-T2_C	8.219 kV	-155.4 Deg	V
19	MAS-MSU1_A	444.3 kV	119.1 Deg	V
20	MAS-MSU1_B	431.9 kV	-839.7 mDeg	V
21	MAS-MSU1_C	434.8 kV	-122.4 Deg	V
22	MAS-MSU1_N	741.7 nV	100.7 Deg	V
23	MR-FACTS1_A	12.49 kV	114.0 Deg	V

Figure 5.5.17: Estimated State Report

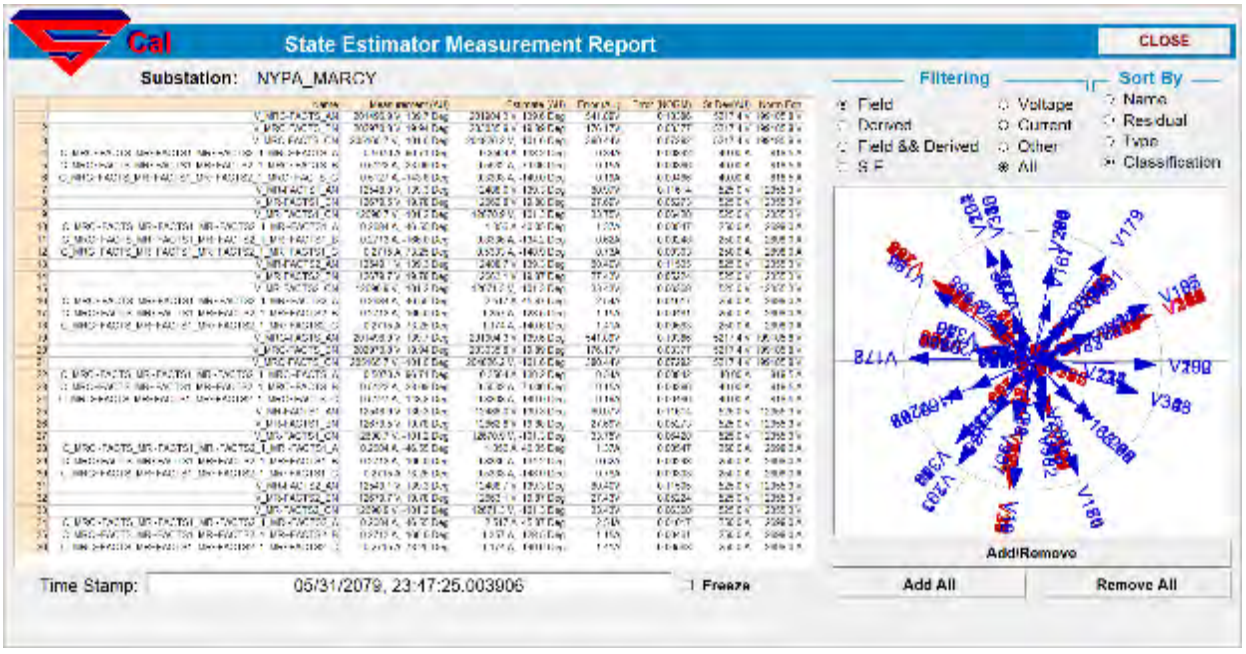

Figure 5.5.18: State Estimator Measurement Report

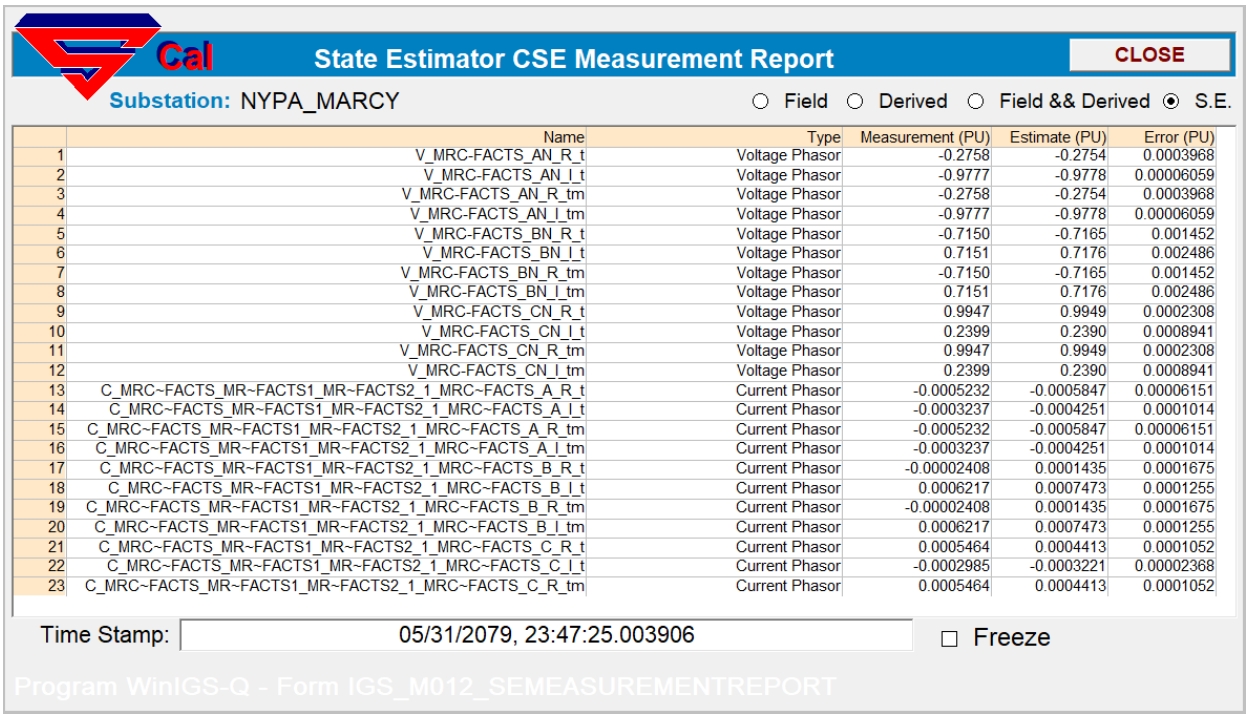

	Name	Type	Measurement (PU)	Estimate (PU)	Error (PU)
1	V_MRC-FACTS_AN_R_t	Voltage Phasor	-0.2758	-0.2754	0.0003968
2	V_MRC-FACTS_AN_I_t	Voltage Phasor	-0.9777	-0.9778	0.00006059
3	V_MRC-FACTS_AN_R_tm	Voltage Phasor	-0.2758	-0.2754	0.0003968
4	V_MRC-FACTS_AN_I_tm	Voltage Phasor	-0.9777	-0.9778	0.00006059
5	V_MRC-FACTS_BN_R_t	Voltage Phasor	-0.7150	-0.7165	0.001452
6	V_MRC-FACTS_BN_I_t	Voltage Phasor	0.7151	0.7176	0.002486
7	V_MRC-FACTS_BN_R_tm	Voltage Phasor	-0.7150	-0.7165	0.001452
8	V_MRC-FACTS_BN_I_tm	Voltage Phasor	0.7151	0.7176	0.002486
9	V_MRC-FACTS_CN_R_t	Voltage Phasor	0.9947	0.9949	0.0002308
10	V_MRC-FACTS_CN_I_t	Voltage Phasor	0.2399	0.2390	0.0008941
11	V_MRC-FACTS_CN_R_tm	Voltage Phasor	0.9947	0.9949	0.0002308
12	V_MRC-FACTS_CN_I_tm	Voltage Phasor	0.2399	0.2390	0.0008941
13	C_MRC~FACTS_MR~FACTS1_MR~FACTS2_1_MRC~FACTS_A_R_t	Current Phasor	-0.0005232	-0.0005847	0.00006151
14	C_MRC~FACTS_MR~FACTS1_MR~FACTS2_1_MRC~FACTS_A_I_t	Current Phasor	-0.0003237	-0.0004251	0.0001014
15	C_MRC~FACTS_MR~FACTS1_MR~FACTS2_1_MRC~FACTS_A_R_tm	Current Phasor	-0.0005232	-0.0005847	0.00006151
16	C_MRC~FACTS_MR~FACTS1_MR~FACTS2_1_MRC~FACTS_A_I_tm	Current Phasor	-0.0003237	-0.0004251	0.0001014
17	C_MRC~FACTS_MR~FACTS1_MR~FACTS2_1_MRC~FACTS_B_R_t	Current Phasor	-0.00002408	0.0001435	0.0001675
18	C_MRC~FACTS_MR~FACTS1_MR~FACTS2_1_MRC~FACTS_B_I_t	Current Phasor	0.0006217	0.0007473	0.0001255
19	C_MRC~FACTS_MR~FACTS1_MR~FACTS2_1_MRC~FACTS_B_R_tm	Current Phasor	-0.00002408	0.0001435	0.0001675
20	C_MRC~FACTS_MR~FACTS1_MR~FACTS2_1_MRC~FACTS_B_I_tm	Current Phasor	0.0006217	0.0007473	0.0001255
21	C_MRC~FACTS_MR~FACTS1_MR~FACTS2_1_MRC~FACTS_C_R_t	Current Phasor	0.0005464	0.0004413	0.0001052
22	C_MRC~FACTS_MR~FACTS1_MR~FACTS2_1_MRC~FACTS_C_I_t	Current Phasor	-0.0002985	-0.0003221	0.00002368
23	C_MRC~FACTS_MR~FACTS1_MR~FACTS2_1_MRC~FACTS_C_R_tm	Current Phasor	0.0005464	0.0004413	0.0001052

Figure 5.5.19: State Estimator Detailed Measurement Report

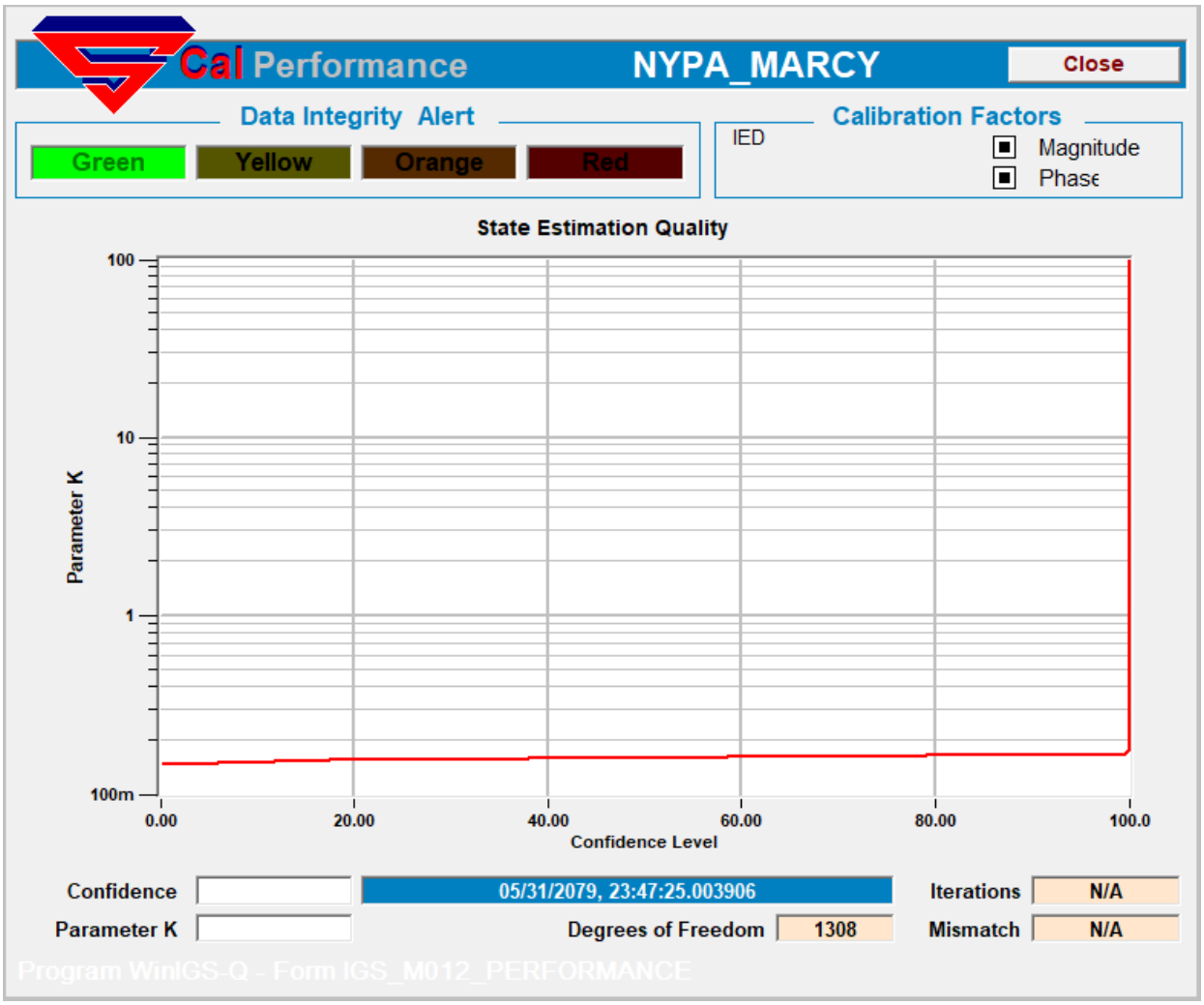

Figure 5.5.20: Performance of the State Estimator

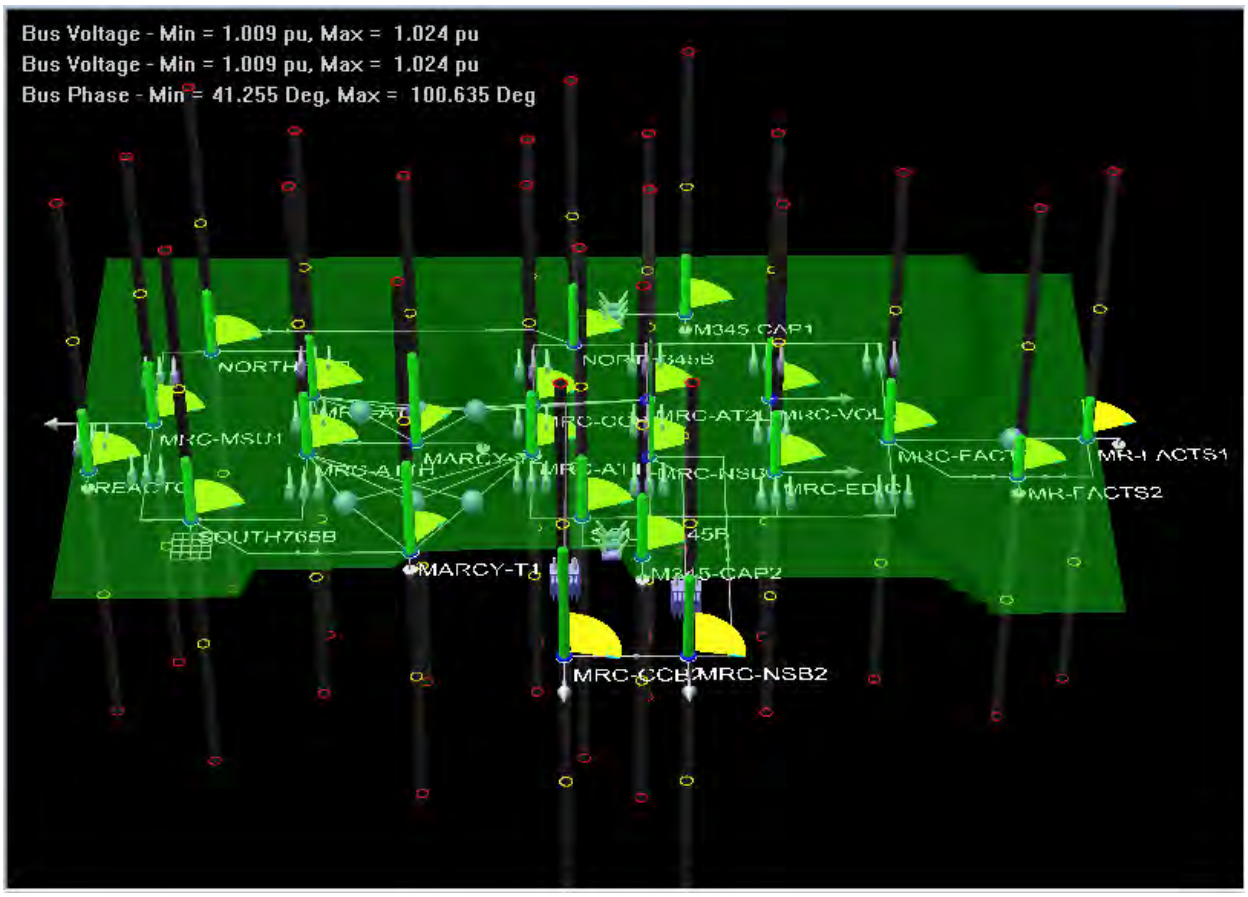

Figure 5.5.21: 3D Visualization Screenshot

6. Conclusions

Present day PMU and Merging Unit (MU) technologies offer the capability for better, accurate and faster monitoring of the power system. The data generated from these systems are utilized by many applications.

These technologies are complex and many causes can lead to deterioration of the performance of these systems. This project developed methods for the data validation from these systems in real time and in case of data errors and/or missing data it corrects the data and fills in missing data if any. The end result is that the developed technology monitors the entire data acquisition system in a substation and sends validated and corrected data upstream. This has been achieved by methods that characterize PMUs and MUs in the laboratory and (b) constructing a co-model of the physical system of the substation and the PMUs, MUs, relays, etc. in the substation on which the dynamic state estimation is run. The results of the dynamic state estimation are used to determine the accuracy of the data, detect and identify bad data, remove the bad data and replace them with estimated values using the validated substation model.

A field demonstration of the developed methods is planned. Specifically the methods will be demonstrated on the MARCY substation. The required hardware at the substation for this demonstration will be install in Fall 2018 during a planned outage for the substation.

The developed substation based dynamic state estimator operates on dynamic models of the power system and executes once per cycle. The dynamic models of the system are what we refer toi as quasi-dynamic models. These models capture the slow dynamics, such as electromechanical oscillations, control response of power electronic converters. They do not capture the fast electrical transients; as a result, electrical quantities are represented with their phasors. This formulation enables the dynamic state estimator to track the slow dynamics of the system with frequency 60 times per second. This is a brand new capability not available before. Tracking the slow dynamics of the power system provides higher accuracy of the operating conditions of the system and opens up new applications. In the next two paragraphs we discuss two important directions for utilization of this technology.

The developed methods and software will be critical components for many applications in the substation and control center. For example, we presently are extending these methods to be part of the protection and control system in the substation by making sure that all relays receive validated data. This application will solve a perennial problem in protection. Specifically, occasionally hidden failures occur in the instrumentation and data acquisition systems resulting in sending erroneous data to the relays and causing relay mis-operations. The data validation methods of this project can identify the hidden failures and correct data thus avoiding relay mis-operations.

Another direction is to use the methods developed in this project to form the basic infrastructure of the next generation management systems. Note that a basic problem at control center operations is the accurate knowledge of the system in real time. The developed methods and software provide the validated data and model of each substation at speeds not possible before, specifically once per cycle. The validated data and validated real time model of each substation can be sent to the control center where the validated real time model of the entire system can be constructed by assembling

the validated substation models of the same instant of time. This task can be achieved once per cycle. Thus the control center can have the validated real time model of the entire system once per cycle and with a delay as short as much time is required to stream the data from each substation to the control center, typically milliseconds. All the applications can now run on a validated real time model. In addition the speed and accuracy opens up a number of new applications such as full state feedback control of many fast responding resources in the power system such as universal power flow controller and other FACTS devises.

Appendix A. Object Oriented Modeling Standard

A.1 Quasi-dynamic Domain SCAQCF Device Model Description

Each device mathematical model should be also expressed in the generalized State and Control Algebraic Quadratic Companion Form (SCAQCF). The advantage of this SCAQCF device model is that it does not contain differential terms and the highest order is second order so that it is easy for computer to do simulation and computation. This SCAQCF model is derived by applying the quadratic integration method to the differential equation in the previous SCQDM.

The final expression for the Q model SCAQCF device model is:

Model Description: *Type*, *Code*, *ID*, *Title*

$$\begin{Bmatrix} i(t) \\ 0 \\ 0 \\ i(t_m) \\ 0 \\ 0 \end{Bmatrix} = elhs(t) = Y_{eqx}\mathbf{x} + \begin{Bmatrix} \vdots \\ \mathbf{x}^T \left\langle F^i_{eqxx} \right\rangle \mathbf{x} \\ \vdots \end{Bmatrix} + Y_{equ}\mathbf{u} + \begin{Bmatrix} \vdots \\ \mathbf{u}^T \left\langle F^i_{equu} \right\rangle \mathbf{u} \\ \vdots \end{Bmatrix} + \begin{Bmatrix} \vdots \\ \mathbf{u}^T \left\langle F^i_{equx} \right\rangle \mathbf{x} \\ \vdots \end{Bmatrix} - B_{eq}$$

$$B_{eq} = -N_{eqx}\mathbf{x}(t-h) - N_{equ}\mathbf{u}(t-h) - M_{eq}I(t-h) - K_{eq}$$

$$\mathbf{h}(\mathbf{x},\mathbf{u}) = Y_{feqx}\mathbf{x} + Y_{fequ}\mathbf{u} + \begin{Bmatrix} \vdots \\ \mathbf{x}^T \left\langle F^i_{feqxx} \right\rangle \mathbf{x} \\ \vdots \end{Bmatrix} + \begin{Bmatrix} \vdots \\ \mathbf{u}^T \left\langle F^i_{fequu} \right\rangle \mathbf{u} \\ \vdots \end{Bmatrix} + \begin{Bmatrix} \vdots \\ \mathbf{u}^T \left\langle F^i_{fequx} \right\rangle \mathbf{x} \\ \vdots \end{Bmatrix} + C_{feqc}$$

$$\textit{Constraints}: \quad \mathbf{h}(\mathbf{x},\mathbf{u}) \le \mathbf{0}$$

$$\mathbf{u}_{min} \le \mathbf{u} \le \mathbf{u}_{max}$$

$$|\mathbf{du}| \le \mathbf{u}_{llimit}$$

Model Dimensions: $n_{equ}, n_{state}, n_{control}, n_{Feqxx}, n_{Fequu}, n_{Fequx}, n_{fconst}, n_{Ffeqxx}, n_{Ffequu}, n_{Ffequx}$

Connectivity: nn_t, *ivn*, *inn*, *onn*, S_{st}

Normalization Factors: $x_{NF}, e_{NF}, u_{NF}, h_{NF}$

Units: *xUnit*, *eUnit*, *uUnit*, *hUnit*

The normalization factors, functional constraints and variable limits are the same as the time domain SCQDM.

The SCAQCF coefficients are derived from the SCQDM coefficients as follows:

$$Y_{eqx}=\begin{bmatrix} \frac{4}{h}D_{eqxd1}+Y_{eqx1} & -\frac{8}{h}D_{eqxd1} \\ \frac{4}{h}D_{eqxd2}+Y_{eqx2} & -\frac{8}{h}D_{eqxd2} \\ Y_{eqx3} & 0 \\ \frac{1}{2h}D_{eqxd1} & \frac{2}{h}D_{eqxd1}+Y_{eqx1} \\ \frac{1}{2h}D_{eqxd2} & \frac{2}{h}D_{eqxd1}+Y_{eqx2} \\ 0 & Y_{eqx3} \end{bmatrix}$$

$$Y_{equ}=\begin{bmatrix} Y_{equ1} & 0 \\ Y_{equ2} & 0 \\ Y_{equ3} & 0 \\ 0 & Y_{equ1} \\ 0 & Y_{equ2} \\ 0 & Y_{equ3} \end{bmatrix} \quad F_{eqx}=\begin{bmatrix} 0 & 0 \\ 0 & 0 \\ F_{eqxx3} & 0 \\ 0 & 0 \\ 0 & 0 \\ 0 & F_{eqxx3} \end{bmatrix} \quad F_{equ}=\begin{bmatrix} 0 & 0 \\ 0 & 0 \\ F_{equu3} & 0 \\ 0 & 0 \\ 0 & 0 \\ 0 & F_{equu3} \end{bmatrix} \quad F_{equx}=\begin{bmatrix} 0 & 0 \\ 0 & 0 \\ F_{equx3} & 0 \\ 0 & 0 \\ 0 & 0 \\ 0 & F_{equx3} \end{bmatrix}$$

$$N_{eqx}=\begin{bmatrix} -Y_{eqx1}+\frac{4}{h}D_{eqxd1} \\ -Y_{eqx2}+\frac{4}{h}D_{eqxd2} \\ 0 \\ \frac{1}{2}Y_{eqx1}-\frac{5}{2h}D_{eqxd1} \\ \frac{1}{2}Y_{eqx2}-\frac{5}{2h}D_{eqxd2} \\ 0 \end{bmatrix} \quad N_{equ}=\begin{bmatrix} -Y_{equ1} \\ -Y_{equ2} \\ 0 \\ \frac{1}{2}Y_{equ1} \\ \frac{1}{2}Y_{equ2} \\ 0 \end{bmatrix} \quad M_{eq}=\begin{bmatrix} I_{size(i(t))} \\ 0 \\ 0 \\ -\frac{1}{2}I_{size(i(t))} \\ 0 \\ 0 \end{bmatrix} \quad K_{eq}=\begin{bmatrix} 0 \\ 0 \\ C_{eqc3} \\ \frac{3}{2}C_{eqc1} \\ \frac{3}{2}C_{eqc2} \\ C_{eqc3} \end{bmatrix}$$

$$Y_{feqx}=\begin{bmatrix} Y_{hfeqx} & 0 \\ 0 & Y_{hfeqx} \end{bmatrix} \quad Y_{fequ}=\begin{bmatrix} Y_{hfequ} & 0 \\ 0 & Y_{hfeqx} \end{bmatrix} \quad C_{feqc}=\begin{bmatrix} C_{hfeqc} \\ C_{hfeqc} \end{bmatrix}$$

$$F_{feqxx}=\begin{bmatrix} F_{hfeqxx} & 0 \\ 0 & F_{hfeqxx} \end{bmatrix} \quad F_{fequu}=\begin{bmatrix} F_{hfequu} & 0 \\ 0 & F_{hfequu} \end{bmatrix} \quad F_{fequx}=\begin{bmatrix} F_{hfequx} & 0 \\ 0 & F_{hfequx} \end{bmatrix}$$

$$\mathbf{u}_{min}=\begin{bmatrix} \mathbf{u}_{hmin} \\ \mathbf{u}_{hmin} \end{bmatrix} \quad \mathbf{u}_{max}=\begin{bmatrix} \mathbf{u}_{hmax} \\ \mathbf{u}_{hmax} \end{bmatrix} \quad \mathbf{u}_{llimit}=\begin{bmatrix} \mathbf{u}_{hllimit} \\ \mathbf{u}_{hllimit} \end{bmatrix}$$

This quasi-dynamic domain SCAQCF device structure has the following items:

Table A.1: Definitions of Quasi-dynamic Domain SCAQCF Variables in Power Device Class Implementation

Term	Variable Name	Variable Type	Container Type	Description
Type	iQDSCAQCFModel_DeviceType	int		Device type (TA, TD, QA, QD, CONNECTOR)
Code	iQDSCAQCFModel_ModelCode	int		Model code
ID	iQDSCAQCFModel_ModelID	int		Model ID
Title	sQDSCAQCFModel_ModelTitle	CString		Model title
$i(t,t_m)$	vQDSCAQCFModel_i	double	vector	Through variable vector
$elhs(t)$	vQDSCAQCFModel_elhs	double	vector	Equation left hand side values
$x(t,t_m)$	vQDSCAQCFModel_x	double	vector	State variable vector
$u(t,t_m)$	vQDSCAQCFModel_u	double	vector	Control variable vector
Y_{eqx}	vQDSCAQCFModel_Yeqx	CTriplet	vector	Coefficients of the linear terms associated with state variables
Y_{equ}	vQDSCAQCFModel_Yequ	CTriplet	vector	Coefficients of the linear terms associated with control variables
F_{eqxx}	vQDSCAQCFModel_Feqxx	CCubelet	vector	Coefficients of the quadratic terms associated with state variables
F_{equu}	vQDSCAQCFModel_Fequu	CCubelet	vector	Coefficients of the quadratic terms associated with control variables
F_{equx}	vQDSCAQCFModel_Fequx	CCubelet	vector	Coefficients of the quadratic terms associated with the products of state and control variables
B_{eq}	vQDSCAQCFModel_Beq	double	vector	Past history vector
N_{eqx}	vQDSCAQCFModel_Neqx	CTriplet	vector	Coefficients associated with state variables in past history
N_{equ}	vQDSCAQCFModel_Nequ	CTriplet	vector	Coefficients associated with control variables in past history
M_{eq}	vQDSCAQCFModel_Meq	CTriplet	vector	Coefficients associated with through variables in past history
K_{eq}	vQDSCAQCFModel_Keq	CDoublet	vector	Constant terms
$h(x,u)$	vQDSCAQCFModel_h	double	vector	Functional constraints
Y_{feqx}	vQDSCAQCFModel_Yfeqx	CTriplet	vector	Coefficients of the linear terms associated with state variables in functional constraints

Y_{fequ}	vQDSCAQCFModel_Yfequ	CTriplet	vector	Coefficients of the linear terms associated with control variables in functional constraints
F_{feqxx}	vQDSCAQCFModel_Ffeqxx	CCubelet	vector	Coefficients of the quadratic terms associated with state variables in functional constraints
F_{fequu}	vQDSCAQCFModel_Ffequu	CCubelet	vector	Coefficients of the quadratic terms associated with control variables in functional constraints
F_{fequx}	vQDSCAQCFModel_Ffequx	CCubelet	vector	Coefficients of the quadratic terms associated with the products of state and control variables in functional constraints
C_{feqc}	vQDSCAQCFModel_Cfeqc	CDoublet	vector	Constant terms in functional constraints
u_{min}	vQDSCAQCFModel_umin	double	vector	Lower bounds of control variables
u_{max}	vQDSCAQCFModel_umax	double	vector	Upper bounds of control variables
u_{llimit}	vQDSCAQCFModel_uLnzLimit	double	vector	Maximum permissible control variable excursions to maintain linearization error below a threshold
n_{equ}	nQDSCAQCFModel_Equ	int		Number of equations
n_{state}	nQDSCAQCFModel_State	int		Number of state variables
$n_{control}$	nQDSCAQCFModel_Control	int		Number of control variables
n_{Feqxx}	nQDSCAQCFModel_Feqxx	int		Number of Feqxx terms
n_{Fequu}	nQDSCAQCFModel_Fequu	int		Number of Fequu terms
n_{Fequx}	nQDSCAQCFModel_Fequx	int		Number of Fequx terms
n_{fconst}	nQDSCAQCFModel_Fconstraint	int		Number of functional constraints
n_{Ffeqxx}	nQDSCAQCFModel_Ffeqxx	int		Number of Ffeqxx terms in functional constraints
n_{Ffequu}	nQDSCAQCFModel_Ffequu	int		Number of Ffequu terms in functional constraints
n_{Ffequx}	nQDSCAQCFModel_Ffequx	int		Number of Ffequx terms in functional constraints
nn_t	vQDSCAQCFModel_NodeName	CString	vector	Terminal node names
ivn	vQDSCAQCFModel_InternalVarNam	CString	vector	Internal state variable names

inn	vQDSCAQCFModel_InternalNodeNumber	int	vector	Internal node numbers
onn	vQDSCAQCFModel_OptimalNodeNumber	int	vector	Optimal numbers of all device states with external states placed first
S_{st}	vQDSCAQCFModel_SwitchStatus	int	vector	Switch status for each terminal pair (used in connector devices)
x_{NF}	vQDSCAQCFModel_StateNormFactor	double	vector	Normalization factors for state variables
e_{NF}	vQDSCAQCFModel_EquationNormFactor	double	vector	Normalization factors for equations
u_{NF}	vQDSCAQCFModel_ControlNormFactor	double	vector	Normalization factors for control variables
h_{NF}	vQDSCAQCFModel_ConstraintNormFactor	double	vector	Normalization factors for functional constraints
$xUnit$	vQDSCAQCFModel_xUnit	CString	vector	Units (metric) of state variables
$eUnit$	vQDSCAQCFModel_eUnit	CString	vector	Units (metric) of equations
$uUnit$	vQDSCAQCFModel_uUnit	CString	vector	Units (metric) of control variables
$hUnit$	vQDSCAQCFModel_hUnit	CString	vector	Units (metric) of functional constraints

A.2 Quasi-dynamic Domain SCAQCF Measurement Model Description

The quasi-dynamic domain SCAQCF measurement model is the matrix expression for each measurement in SCAQCF. The primary data that define a measurement are pointers and the measurement error. This model is also created by the program automatically.

The quasi-dynamic domain SCAQCF measurement model comes from two parts: 1) quasi-dynamic domain SCAQCF device model; 2) quadratic integration of quasi-dynamic domain SCQDM.

If the measurement equation is derived from quasi-dynamic domain SCAQCF device model, it just pulls equation from the quasi-dynamic domain SCAQCF device model.

If the measurement equation comes from the quasi-dynamic domain SCQDM, the quadratic integration algorithm should be applied to this equation. The procedure is the same as deriving the quasi-dynamic domain SCAQCF device model from quasi-dynamic domain SCQDM.

The above two steps are processed for each measurement. Then all the equations are stacked into the following standard quasi-dynamic domain SCAQCF measurement model:

$$\tilde{\mathbf{z}} = Y_{qm,x}\tilde{\mathbf{x}} + \begin{Bmatrix} \vdots \\ \tilde{\mathbf{x}}^T F^i_{qm,x}\tilde{\mathbf{x}} \\ \vdots \end{Bmatrix} + Y_{qm,u}\tilde{\mathbf{u}} + \begin{Bmatrix} \vdots \\ \tilde{\mathbf{u}}^T F^i_{qm,u}\tilde{\mathbf{u}} \\ \vdots \end{Bmatrix} + \begin{Bmatrix} \vdots \\ \tilde{\mathbf{u}}^T F^i_{qm,ux}\tilde{\mathbf{x}} \\ \vdots \end{Bmatrix} + C_{qm}$$

$$C_{qm} = N_{qm,x}\tilde{\mathbf{x}}(t-h) + N_{qm,u}\tilde{\mathbf{u}}(t-h) + M_{qm}\tilde{I}(t-h) + K_{qm}$$

Measurement noise error: dMeterScale, dMeterSigmaPU
Note: All the above variables are in metric system.

where:

$\tilde{\mathbf{z}}$: measurement variables at both time t and time t_m, $\tilde{\mathbf{z}} = [\tilde{\mathbf{z}}(t),\ \tilde{\mathbf{z}}(t_m)]$

$\tilde{\mathbf{x}}$: external and internal state variables of the measurement model, $\tilde{\mathbf{x}} = [\tilde{\mathbf{x}}(t), \tilde{\mathbf{x}}(t_m)]$

$\tilde{\mathbf{u}}$: control variables of the measurement model, i.e. transformer tap, etc. $\tilde{\mathbf{u}} = [\tilde{\mathbf{u}}(t), \tilde{\mathbf{u}}(t_m)]$

$Y_{qm,x}$: matrix defining the linear part for state variables,

$F_{qm,x}$: matrices defining the quadratic part for state variables,

$Y_{qm,u}$: matrix defining the linear part for control variables,

$F_{qm,u}$: matrices defining the quadratic part for control variables,

$F_{qm,xu}$: matrices defining the quadratic part for the product of state and control variables,

C_{qm} : history dependent vector of the measurement model,

$N_{qm,x}$: matrix defining the last integration step state variables part,

$N_{qm,u}$: matrix defining the last integration step control variables part,

M_{qm} : matrix defining the last integration step through variables part,

K_{qm} : constant vector of the measurement model,

dMeterScale : the scale that meters use (in metric units),

dMeterSigmaPU : the standard deviation for the measurements (in per. unit),

Quasi-dynamic Domain SCAQCF Measurement Model Structure

This quasi-dynamic domain SCAQCF measurement model structure has the following items:

int m_iMeasDeviceID;
Device ID from which the measurement is measured

BOOL m_bMeasLinearity;
Linearity of each measurement: 0(False) Nonlinear, 1(True) Linear

int m_iMeasType;
Measurement type: 0 Actual, 1 Derived, 2 Pseudo, 3 Virtual

int m_iMeasQuantity;
Measurement quantity: 14 Torque, 15 Speed, 16 Voltage, 17 Current

double m_dMeasMeterSigmaPU;
Standard deviation for the measurements (in per. unit system)

double m_dMeasMeterScale;
Meter scales (in metric unit system)

CString m_sMeasName;
Name for the measurement

CString m_sMeasUnit;
Unit for the measurement

double m_dMeasRatio;
Ratio for the derived measurement

vector<int> m_viMeasTerminals;
Terminal numbers where the measurement is measured

vector<CSting> m_vsMeasTerminals;
Terminal names where the measurement is measured

double m_dQDSCAQCFMeasValue;
Measurement value in metric system

double m_dQDSCAQCFMeasValuePU;
Measurement value in PU system

double m_dQDSCAQCFMeasScale;
system consistent scaling factor for measurement in metric system

double m_dQDSCAQCFMeasSigmaPU;
Standard deviation for the measurements (in per. unit system) in the measurement model

int m_iQDSCAQCFMeasDefinitionIndex;
Measurement definition index

int m_iQDSCAQCFMeasTime;
Measurement time: 0: time t, 1: time tm

BOOL m_iQDSCAQCFMeasVirtual;
Virtual measurement false/true

vector<SP_LINEAR> m_vlQDSCAQCFMeasLinTermX;
Coefficients of the linear state for the q domain SCAQCF measurement model
It stores the entry's corresponding state number and entry value.

vector< SP_LINEAR > m_vlQDSCAQCFMeasLinTermU;
Coefficients of the linear control for the q domain SCAQCF measurement model
It stores the entry's corresponding control number and entry value.

double m_dQDSCAQCFMeasConstantK;
Constant for the q domain SCAQCF measurement model

vector<SP_QUAD> m_vqQDSCAQCFMeasNonlinTermX;
Coefficients of the quadratic state variables for the q domain SCAQCF measurement model
It stores the entry's row number, column number and entry value.

vector<SP_QUAD> m_vqQDSCAQCFMeasNonlinTermU;
Coefficients of the quadratic control variables for the q domain SCAQCF measurement model
It stores the entry's row number, column number and entry.

vector<SP_QUAD> m_vqQDSCAQCFMeasNonlinTermUX;
Coefficients of the production of state and control variables for the q domain SCAQCF measurement model
It stores the entry's row number, column number and entry value.

double m_dQDSCAQCFMeasConstantC;
Constant containing past history for the q domain SCAQCF measurement model

vector< SP_LINEAR > m_vlQDSCAQCFMeasPastTermX;
Coefficients of the linear state past history for the q domain SCAQCF measurement model
It stores the entry's corresponding state number and entry value.

vector< SP_LINEAR > m_vlQDSCAQCFMeasPastTermU;

Coefficients of the linear control past history at time t for the q domain SCAQCF measurement model

It stores the entry's corresponding control number and entry value.

vector< SP_LINEAR > m_vlQDSCAQCFMeasPastTermI;

Coefficients of the through variable past history at time t for the q domain SCAQCF measurement model

It stores the entry's corresponding control number and entry value.

vector<SP_LINEAR> m_vlQDSCAQCFMeasLinTermX_PU;

Coefficients of the linear state for the q domain SCAQCF measurement model in per unit system

It stores the entry's corresponding state number and entry value.

vector< SP_LINEAR > m_vlQDSCAQCFMeasLinTermU_PU;

Coefficients of the linear control for the q domain SCAQCF measurement model in per unit system

It stores the entry's corresponding control number and entry value.

double m_dQDSCAQCFMeasConstantK_PU;

Constant for the q domain SCAQCF measurement model in per unit system

vector<SP_QUAD> m_vqQDSCAQCFMeasNonlinTermX_PU;

Coefficients of the quadratic state variables for the q domain SCAQCF measurement model in per unit system

It stores the entry's row number, column number and entry value.

vector<SP_QUAD> m_vqQDSCAQCFMeasNonlinTermU_PU;

Coefficients of the quadratic control variables for the q domain SCAQCF measurement model in per unit system

It stores the entry's row number, column number and entry.

vector<SP_QUAD> m_vqQDSCAQCFMeasNonlinTermUX_PU;

Coefficients of the production of state and control variables for the q domain SCAQCF measurement model in per unit system

It stores the entry's row number, column number and entry value.

double m_dQDSCAQCFMeasConstantC_PU;

Constant for the q domain SCAQCF measurement model in per unit system

vector< SP_LINEAR > m_vlQDSCAQCFMeasPastTermX_PU;

Coefficients of the linear state past history for the q domain SCAQCF measurement model in per unit system

It stores the entry's corresponding state number and entry value.

vector< SP_LINEAR > m_vlQDSCAQCFMeasPastTermU_PU;

Coefficients of the linear control past history for the q domain SCAQCF measurement model in per unit system

It stores the entry's corresponding control number and entry value.

vector< SP_LINEAR > m_vlQDSCAQCFMeasPastTermI_PU;

Coefficients of the through variable past history for the q domain SCAQCF measurement model in per unit system

It stores the entry's corresponding control number and entry value.

A.3 Modeling Example: Single-Phase Transformer Model

This section describes an example for the modeling approach via a single-phase transformer. First the model is provided in compact form. Subsequently its quadratic form is derived.

A.3.1 Single-Phase Transformer – Compact Form

Figure A-1 illustrates the physical model of a single-phase variable tap transformer. Three of these models can be used to construct four types of three-phase transformers, with connections of Y-Y, Y-Δ, Δ-Y, and Δ-Δ.

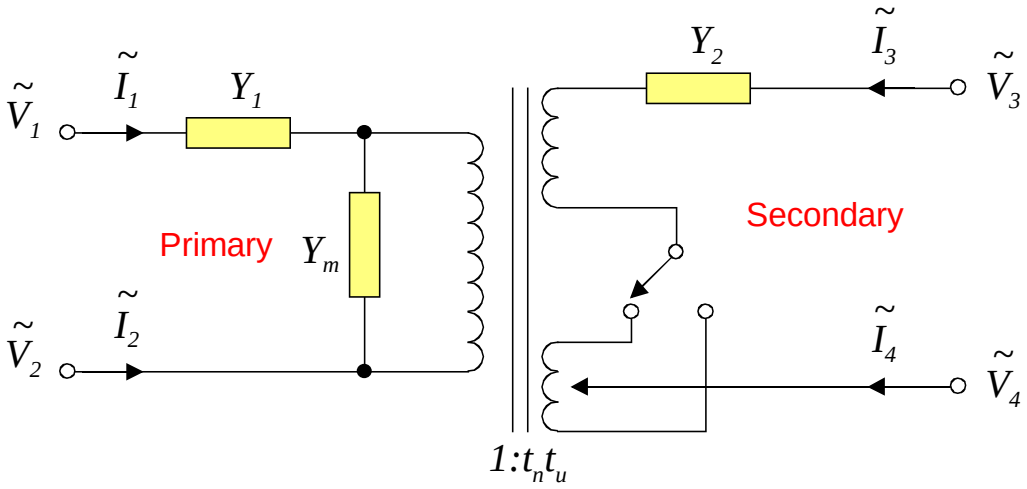

Figure A.1: Single-Phase Variable Tap Transformer

In Figure A-1, the turn ratio *t* consists of two parts. One is the nominal transformation ratio t_n and the other is the per-unit tap selection t_u. The overall turn ratio is $t = t_u t_n$. The primary, secondary, and shunt admittances Y_1, Y_2, and Y_m of the transformer when $t_u = 1$ are expressed as

$$Y_1 = 2Y_{pu}Y_{base1}$$
$$Y_2 = 2Y_{pu}Y_{base2}$$
$$Y_m = Y_{pu}^m Y_{base1}$$

where Y_{pu} is the per-unit series admittance and Y_{pu}^{m} is the shunt admittance of the transformer. Note that $Y_{base1} = t_n^2 Y_{base2}$. Considering t_u as a control variable in a more general sense, the single-phase transformer equivalent circuit is illustrated in Figure A-2.

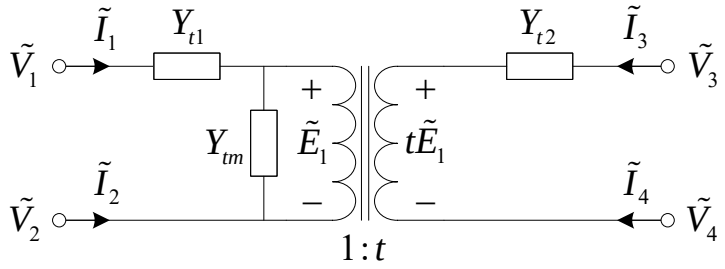

Figure A.2: Single-Phase Transformer Equivalent Circuit

With a variable t_u, the actual primary, secondary, and shunt admittances Y_{t1}, Y_{t2}, and Y_{tm} becomes:

$$Y_{t1} = Y_1$$
$$Y_{t2} = \frac{Y_2}{1+|1-t_u|}$$
$$Y_{tm} = Y_m$$

Applying Kirchoff's laws in the circuit of Figure A-2 and substituting Y_{t1}, Y_{t2}, Y_{tm} respectively with Y_1, Y_2, Y_m according to the above equations, the single-phase transformer equations are:

$$\tilde{I}_1 = Y_1\left(\tilde{V}_1 - \tilde{V}_2 - \tilde{E}_1\right)$$
$$\tilde{I}_2 = -\tilde{I}_1$$
$$\tilde{I}_3 = \frac{Y_2}{1+|1-t_u|}\left(\tilde{V}_3 - \tilde{V}_4 - t_n t_u \tilde{E}_1\right)$$
$$\tilde{I}_4 = -\tilde{I}_3$$
$$0 = -Y_1\left(\tilde{V}_1 - \tilde{V}_2 - \tilde{E}_1\right) - t_n t_u \frac{Y_2}{1+|1-t_u|}\left(\tilde{V}_3 - \tilde{V}_4 - t_n t_u \tilde{E}_1\right) + Y_m \tilde{E}_1$$

A.3.2 Single-Phase Transformer – Quadratized Form

The single-phase transformer quadratized device model (QDM) separates the real and imaginary parts. During this process, additional states w_1 and w_2 are introduced to eliminate $1 + |1 - t_u|$ from the denominator. They are defined as

$$y_1 = \frac{1}{1+\left|1-t_u\right|}$$
$$y_2 = t_u y_1$$

As a result, the following equation holds.

$$y_2^2 - 2y_1y_2 = 1 - 2y_1$$

In order to transform the single-phase transformer model into the standard QDM syntax, the following variables are required to move the quadratic terms out of the through equations.

$$w_1 = y_1V_{3r} - y_1V_{4r} - t_n y_2 E_{1r}$$
$$w_2 = y_1V_{3i} - y_1V_{4i} - t_n y_2 E_{1i}$$

The transformer quadratized model is given by

$$I_{1r} = Y_{1r}\left(V_{1r} - V_{2r} - E_{1r}\right) - Y_{1i}\left(V_{1i} - V_{2i} - E_{1i}\right)$$
$$I_{1i} = Y_{1r}\left(V_{1i} - V_{2i} - E_{1i}\right) + Y_{1i}\left(V_{1r} - V_{2r} - E_{1r}\right)$$
$$I_{2r} = -Y_{1r}\left(V_{1r} - V_{2r} - E_{1r}\right) + Y_{1i}\left(V_{1i} - V_{2i} - E_{1i}\right)$$
$$I_{2i} = -Y_{1r}\left(V_{1i} - V_{2i} - E_{1i}\right) - Y_{1i}\left(V_{1r} - V_{2r} - E_{1r}\right)$$
$$I_{3r} = Y_{2r}w_1 - Y_{2i}w_2$$
$$I_{3i} = Y_{2r}w_2 + Y_{2i}w_1$$
$$I_{4r} = -Y_{2r}w_1 + Y_{2i}w_2$$
$$I_{4i} = -Y_{2r}w_2 - Y_{2i}w_1$$
$$0 = -Y_{1r}\left(V_{1r} - V_{2r} - E_{1r}\right) + Y_{1i}\left(V_{1i} - V_{2i} - E_{1i}\right) + Y_{mr}E_{1r} - Y_{mi}E_{1i} - t_nY_{2r}t_uw_1 + t_nY_{2i}t_uw_2$$
$$0 = -Y_{1r}\left(V_{1i} - V_{2i} - E_{1i}\right) - Y_{1i}\left(V_{1r} - V_{2r} - E_{1r}\right) + Y_{mr}E_{1i} + Y_{mi}E_{1r} - t_nY_{2r}t_uw_2 - t_nY_{2i}t_uw_1$$
$$0 = y_1V_{3r} - y_1V_{4r} - t_ny_2E_{1r} - w_1$$
$$0 = y_1V_{3i} - y_1V_{4i} - t_ny_2E_{1i} - w_2$$
$$0 = 2y_1 - 2y_1y_2 + y_2^2 - 1$$
$$0 = t_uy_1 - y_2$$

where the state vector is:

$$\mathbf{x} = \left[V_{1r},\ V_{1i},\ V_{2r},\ V_{2i},\ V_{3r},\ V_{3i},\ V_{4r},\ V_{4i},\ E_{1r},\ E_{1i},\ w_1,\ w_2,\ y_1,\ y_2 \right]$$

and the control vector is:

$$\mathbf{u} = \left[t_u \right]$$

Above equations are cast in the standard SCQDM syntax. The syntax of the SCDQM is:

$$\tilde{I}(t) = Y_{eqx1}\tilde{\mathbf{x}}(t) + Y_{equ1}\tilde{\mathbf{u}}(t) + D_{eqxd1}\frac{d\tilde{\mathbf{x}}(t)}{dt} + C_{eqc1}$$

$$0 = Y_{eqx2}\tilde{\mathbf{x}}(t) + Y_{equ2}\tilde{\mathbf{u}}(t) + D_{eqxd2}\frac{d\tilde{\mathbf{x}}(t)}{dt} + C_{eqc2}$$

$$0 = Y_{eqx3}\tilde{\mathbf{x}}(t) + Y_{equ3}\tilde{\mathbf{u}}(t) + \left\{ \begin{matrix} \vdots \\ \tilde{\mathbf{x}}(t)^T \left\langle F^i_{eqxx3} \right\rangle \tilde{\mathbf{x}}(t) \\ \vdots \end{matrix} \right\} + \left\{ \begin{matrix} \vdots \\ \tilde{\mathbf{u}}(t)^T \left\langle F^i_{equu3} \right\rangle \tilde{\mathbf{u}}(t) \\ \vdots \end{matrix} \right\} + \left\{ \begin{matrix} \vdots \\ \tilde{\mathbf{u}}(t)^T \left\langle F^i_{equx3} \right\rangle \tilde{\mathbf{x}}(t) \\ \vdots \end{matrix} \right\} + C_{eqc3}$$

$$\mathbf{h}(\tilde{\mathbf{x}}(t), \tilde{\mathbf{u}}(t)) = Y_{fx}\tilde{\mathbf{x}}(t) + Y_{fu}\tilde{\mathbf{u}}(t) + \left\{ \begin{matrix} \vdots \\ \tilde{\mathbf{x}}(t)^T F^i_{fx} \tilde{\mathbf{x}}(t) \\ \vdots \end{matrix} \right\} + \left\{ \begin{matrix} \vdots \\ \tilde{\mathbf{u}}(t)^T F^i_{fu} \tilde{\mathbf{u}}(t) \\ \vdots \end{matrix} \right\} + \left\{ \begin{matrix} \vdots \\ \tilde{\mathbf{u}}(t)^T F^i_{fux} \tilde{\mathbf{x}}(t) \\ \vdots \end{matrix} \right\} + C_{fc}$$

Connectivity: *TerminalNodeName*
Normalization Factors: StateNormFactor, ThroughNormFactor, ControlNormFactor

$$\textit{subject to}: \quad \mathbf{h}_{\min} \le \mathbf{h}(\mathbf{x}, \mathbf{u}) \le \mathbf{h}_{\max}$$

$$\mathbf{u}_{\min} \le \mathbf{u} \le \mathbf{u}_{\max}, \quad \mathbf{x}_{\min} \le \mathbf{x} \le \mathbf{x}_{\max}$$

Note: All the above variables are in metric system.

Thus, the single-phase transformer model in the standard SCQDM is:

$$Y_{eqx1} = \begin{bmatrix} Y_{1r} & -Y_{1i} & -Y_{1r} & Y_{1i} & 0 & 0 & 0 & 0 & -Y_{1r} & Y_{1i} & 0 & 0 & 0 & 0 \\ Y_{1i} & Y_{1r} & -Y_{1i} & -Y_{1r} & 0 & 0 & 0 & 0 & -Y_{1i} & -Y_{1r} & 0 & 0 & 0 & 0 \\ -Y_{1r} & Y_{1i} & Y_{1r} & -Y_{1i} & 0 & 0 & 0 & 0 & Y_{1r} & -Y_{1i} & 0 & 0 & 0 & 0 \\ -Y_{1i} & -Y_{1r} & Y_{1i} & Y_{1r} & 0 & 0 & 0 & 0 & Y_{1i} & Y_{1r} & 0 & 0 & 0 & 0 \\ 0 & 0 & 0 & 0 & 0 & 0 & 0 & 0 & 0 & 0 & Y_{2r} & -Y_{2i} & 0 & 0 \\ 0 & 0 & 0 & 0 & 0 & 0 & 0 & 0 & 0 & 0 & Y_{2i} & Y_{2r} & 0 & 0 \\ 0 & 0 & 0 & 0 & 0 & 0 & 0 & 0 & 0 & 0 & -Y_{2r} & Y_{2i} & 0 & 0 \\ 0 & 0 & 0 & 0 & 0 & 0 & 0 & 0 & 0 & 0 & -Y_{2i} & -Y_{2r} & 0 & 0 \end{bmatrix}$$

$$Y_{equ1} = 0$$

$$D_{eqxd1} = 0$$

$$C_{eqc1} = 0$$

$$Y_{eqx2} = 0$$

$$Y_{equ2} = 0$$

$$D_{eqxd2} = 0$$

$$C_{eqc2} = 0$$

$$Y_{eqx3} = \begin{bmatrix} -Y_{1r} & Y_{1i} & Y_{1r} & -Y_{1i} & 0 & 0 & 0 & 0 & Y_{1r}+Y_{mr} & -Y_{1i}-Y_{mi} & 0 & 0 & 0 & 0 \\ -Y_{1i} & -Y_{1r} & Y_{1i} & Y_{1r} & 0 & 0 & 0 & 0 & Y_{1i}+Y_{mi} & Y_{1r}+Y_{mr} & 0 & 0 & 0 & 0 \\ 0 & 0 & 0 & 0 & 0 & 0 & 0 & 0 & 0 & 0 & -1 & 0 & 0 & 0 \\ 0 & 0 & 0 & 0 & 0 & 0 & 0 & 0 & 0 & 0 & 0 & -1 & 0 & 0 \\ 0 & 0 & 0 & 0 & 0 & 0 & 0 & 0 & 0 & 0 & 0 & 0 & 2 & 0 \\ 0 & 0 & 0 & 0 & 0 & 0 & 0 & 0 & 0 & 0 & 0 & 0 & 0 & -1 \end{bmatrix}$$

$$Y_{equ3} = 0$$

$$F^0_{eqxx3} = \{2,4,12,1\}$$
$$F^1_{eqxx3} = \{2,6,12,-1\}$$
$$F^2_{eqxx3} = \{2,8,13,-t_n\}$$
$$F^3_{eqxx3} = \{3,5,12,1\}$$
$$F^4_{eqxx3} = \{3,7,12,-1\}$$
$$F^5_{eqxx3} = \{3,9,13,-t_n\}$$
$$F^6_{eqxx3} = \{4,12,13,-2\}$$
$$F^7_{eqxx3} = \{4,13,13,1\}$$

$$F^i_{equu3} = 0$$

$$F^0_{equx3} = \{0,0,10,-t_n Y_{2r}\}$$
$$F^1_{equx3} = \{0,0,11,t_n Y_{2i}\}$$
$$F^2_{equx3} = \{1,0,10,-t_n Y_{2i}\}$$
$$F^3_{equx3} = \{1,0,11,-t_n Y_{2r}\}$$
$$F^4_{equx3} = \{5,0,12,1\}$$

$$C_{eqc3} = \begin{bmatrix} 0 \\ 0 \\ 0 \\ 0 \\ -1 \\ 0 \end{bmatrix}$$

$$u_{\min} = [0.9]$$

$$u_{\max} = [1.1]$$

References

[1] IEEE Standard for Synchrophasor Measurements for Power Systems," IEEE Std C37.118.1-2011 (Revision of IEEE Std C37.118-2005)

[2] IEEE Guide for Synchronization, Calibration, Testing, and Installation of Phasor Measurement Units (PMUs) for Power System Protection and Control," IEEE C37.242-2013.

[3] S. Biswas, F. Shariatzadeh, R. Beckstrom, A. Srivastava, AK., "Real time testing and validation of Smart Grid devices and algorithms," IEEE Power and Energy Society General Meeting (PES), pp.1-5, 21-25 July 2013

[4] S. Biswas, A. Srivastava, J. Park, J. Castaneda, "Tool for testing of phasor measurement units: PMU performance analyzer", IET Generation, Transmission & Distribution, 2014, DOI: 10.1049/iet-gtd.2014.0104

[5] S. Dutta and T. J. Overbye, "Information Processing and Visualization of Power System Time Varying Data," Proc. 2013 IEEE Symposium Series on Computational Intelligence (SSCI), Singapore, Apr. 16–19, 2013.

[6] S. Dutta and T.J. Overbye, "Feature Extraction and Visualization of Power System Transient Stability Results," Proc. IEEE Transactions on Power Systems, vol. 29, March 2014, pp. 966-973.

Part IV

Prototype Algorithms and Visualization for PMU Data Error Identification and Oscillation Analysis

Tom Overbye
Ikponmwosa Idehen (Iyke), Graduate Student

Texas A&M University

For information about this project, contact:

Tom Overbye
Texas A&M University
Department of Electrical and Computer Engineering
301 Wisenbaker Engineering Building
College Station, TX
77843-3128
Phone: 979-458-5001
Email: overbye@tamu.edu

Power Systems Engineering Research Center

The Power Systems Engineering Research Center (PSERC) is a multi-university Center conducting research on challenges facing the electric power industry and educating the next generation of power engineers. More information about PSERC can be found at the Center's website: http://www.pserc.org.

For additional information, contact:

Power Systems Engineering Research Center
Arizona State University
527 Engineering Research Center
Tempe, Arizona 85287-5706
Phone: 480-965-1643
Fax: 480-727-2052

Notice Concerning Copyright Material

Table of Contents

List of Figures

List of Tables

1. Introduction

1.1 Background

Synchrophasor data are now increasingly used for monitoring the health of power grids. After the 2003 U.S Northeastern blackout, recommendations for an improved wide-area situational awareness of the grid led to the development and deployment of phasor measurement units (PMUs) and other similar synchrophasor devices equipped to measure power system quantities – synchrophasor data – at rates as high as 120 samples per second in 60 Hz operating systems. Through the aid of a time reference provided by a global positioning system (GPS) signal, high resolution, synchrophasor data are time-synchronized phasor measurements which enable wide-area monitoring and control of the grid by making use of measurements obtained from remote locations. As of September 2017, it was reported that over 2,500 networked PMU devices had been installed on the North American grid [1]. Consequently, large amounts of data can now be generated, thus presenting several opportunities for monitoring personnel to have a higher level of visibility of the system.

Like most measurement devices, a failure in the operational mode of a PMU device introduces potential sources of errors in reported measurements. As a result, the level of data quality - which encompasses the aspects of data accuracy, timeliness and availability - is compromised. The synchrophasor network, comprising of PMU devices, data concentrators, communication links and the phasor applications, is exposed to a variety of errors which ultimately affect any of the reported PMU measurement quantities- voltage (or current) phasor magnitude and angle, frequency and rate of change of frequency (ROCOF). Electrical noise, due to harmonic distortions, wiring of input signals, leakage effect caused by phasor estimation windowing function, was discussed in [2-5]. Time mis-synchronization issues [6-10], caused by clock delays, intermittent reception of global positioning system (GPS) signals, loose cable wiring, spoof attacks, and which lead to phasor angle errors have also been mentioned in the literature. These error types are often attributed to the internal working mechanism of the device; are manifested in the data, and thus result in low quality data reported by the device. References [11, 12] also show that data quality issues result from low latency, low bandwidth, data drop-offs, wrong data alignment and limited capacities of the communication network. These errors are external, and reflect the limitations of the existing PMU network infrastructure. Finally, as observed from an application level, [13] reported on how an increased deployment of endpoint phasor applications can also reduce PMU data quality.

The distinct mode of PMU device operation (such as time synchronization and time stamping [2]), unfortunately, exposes reported data measurements to a new paradigm of time-based errors. For example, the ability to report phasor angle measurements makes the PMU a critical device in monitoring the stress level of the grid (by checking the phase angle differences between system nodes), which could not be done through the use of conventional devices like the remote terminal units (RTUs) and supervisory control and data acquisition (SCADA) devices [14]. However, it is important that PMU devices be accurately synchronized to an external reference, otherwise device time errors, which causes mis-synchronization and angle measurement errors, could cause Engineers to lose sight of the true stress levels on the grid.

These unique measurement errors pose newer data quality issues which must be handled by control center applications, and thus motivates the need to study data anomalies associated with PMU synchrophasor measurements. The report develops a framework used to study PMU data errors – the generation of synthetic errors based on known error mechanisms, utilization of intelligent analytic techniques to analyze data errors, and data visualization via the presentation of data error information in a large-scale system. Fig. 1.1. shows different implementation blocks in the developed framework used to achieving these goals.

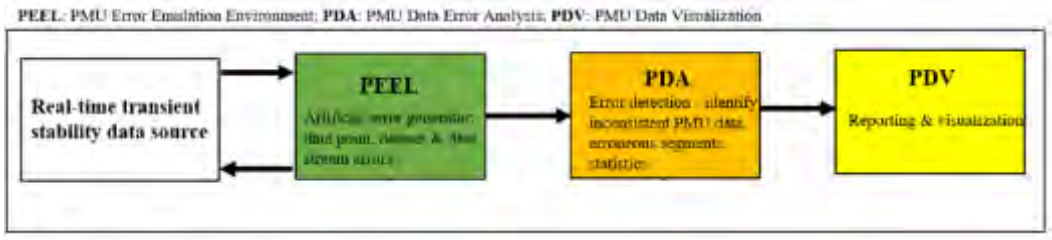

Fig.1.1. Framework for studying PMU data errors

The process of studying mechanisms of PMU data errors involved the study of actual, field synchrophasor data obtained from different utilities, and comparisons drawn with the physical processes associated with these errors as described in the literature. For further research purposes, developed error propagation models were then used to synthesize prototype data errors used in subsequent research activities.

Large amounts of PMU data have enabled online oscillation monitoring and control [15, 16] - a critical task in preserving the safe and secure operation of the power grid. Through visualization, current methods often used to present oscillation information to engineers display oscillation information on a bus node or limited area basis, and do not capture the overall state of the grid. Reference [17] emphasizes the need for engineers to have a comprehensive picture of system states when monitoring grid trends and dynamics. Moreover, as the grid becomes more interconnected and larger in scale, it becomes more imperative for data presentation methods to provide holistic perspectives of the grid to system operators.

1.2 Summary of Chapters

This report is structured as follows. In chapter 2, data quality issues due to associated PMU data errors are presented. In particular, the mechanisms of time-related, PMU errors are used to develop error propagation models for the prototyping of synthetic errors.

In chapter 3, an analytic method for the study of data errors in a large-scale system, using a 2,000-bus synthetic network, is developed. Thereafter, effectiveness of the proposed technique is assessed by carrying out different simulation studies on the test, large-scale system.

In chapter 4, error metrics obtained for the large-scale system is presented through the use of MDS visualization – it provides a comparative assessment of error levels in measurements obtained from different buses in the system.

In chapter 5, wide-area visualization methods are used to present system-based, large-scale oscillation mode information which are obtained from the modal analysis and processing of synchrophasor data. Currently, these methods are being implemented in the PowerWorld simulator software [18], and the case studies presented in this chapter demonstrate the application of these wide-area visualization techniques.

Finally, the conclusions are presented in chapter 6.

2. Categorization of Data Error Sources and Mechanisms of Time-Related Issues in Phasor Measurement Units

In this chapter, different data errors and quality issues associated with PMU and other synchrophasor devices are presented. Error mechanisms and time error propagation models of PMUs, which are used to generate the synthetic data errors used in this work, are then discussed. Finally, the use of synthetic networks for artificially generating data in research studies, followed by the presentation of prototype and actual time errors in data measurements are discussed These constitute the PMU data error emulation (PEEL) block in the proposed framework of Fig. 1.1.

2.1 Categorization of PMU Error Sources

Reference [19] identified groups of PMU data using three levels of attributes: attributes of single data points, dataset and data stream availability. Attributes of single data point are concerned with the accuracy of the individual, time-stamped measurements, while data set attributes relate to the accuracy and logical consistency of a group of data points or an entire set of PMU data. Data set attributes are related to the condition of the underlying communication network through which PMU data are transmitted. Based on these attribute levels, [20] divided PMU error sources into three categories, and shown in Table 2.1.

Table 2.1. Categorization of PMU error sources

Categories	Error Sources
Data point	Accuracy, noise, phase-error, harmonic distortion, estimation algorithms, asynchronous local behaviors (e.g. time-skew), instrument error
Dataset	Status code error, improperly configured PMUs, abnormal or loss of PDC configuration, frequency calculation discrepancies, mislabeling due to erroneous timestamps, CRC error, invalid timestamp
Data stream	Network limitations - Data loss or drop-outs, network latency; increase in endpoint applications

2.2 PMU Error Mechanisms

The unique time-synchronization aspect of PMU operation requires a prior knowledge of the operation mechanisms associated with data errors before prototype synthetic errors can be generated. Based on the developed models, the appropriate modifications are effected on bus phasor values (magnitude or/and angle). This is in addition to other no-time based errors (e.g., noise, repeated values and dropped data frames).

2.2.1 Time Errors and Error Propagation Models

A loss of synchronism between a reference coordinated universal time (UTC) signal, obtained via the use of a global positioning system (GPS) receiver, and a PMU device internal sampling clock

causes time-skew errors [6, 21], and have been observed to manifest as phasor angle biases in reported measurements. However, they are observed not to affect the phasor magnitude [21]. Assuming an off-nominal, system frequency of f_i Hz, the phase angle deviation $\Delta\delta_\varepsilon$ due to a time error Δt_ε, is computed as,

$$\Delta\delta_\varepsilon = 360\Delta t_\varepsilon f_i \tag{2.1}$$

where $f_i = f_o + \Delta\varepsilon$, f_o is the nominal frequency and $\Delta\varepsilon$ is the deviation from f_o. The component of $\Delta\delta_\varepsilon$ due to $\Delta\varepsilon$ is $360\Delta t_\varepsilon\Delta\varepsilon$. Δt_ε is in the order of microseconds, and in normal operating conditions, $\Delta\varepsilon \in (0,0.05)$. Ignoring $\Delta\delta_{\Delta\varepsilon}$, the updated equation becomes,

$$\Delta\delta_\varepsilon = 360\Delta t_\varepsilon f_o \tag{2.2}$$

A corresponding phase angle error due to an observed time difference at each reported sample, however is dependent on the source of timing error. Thus, the instantaneous phase angle error introduced in any reported sample at time, t from the moment of error initiation is given by a generalized error propagation model,

$$\Delta\delta_\varepsilon(t) = 360\Delta t_\varepsilon(t) f_o \tag{2.3}$$

$\Delta t_\varepsilon(t)$ is the instantaneous, accumulated time drift (or time-skew) at time t.

PMUs report equal time-interval samples of data measurements in cycles, such that the number of data samples reported at any cycle is known as the report rate. The accumulated time drift at any sample point is dependent on the source of error.

1. Clock drift

Here, the internal clock of a PMU is observed to gradually drift away in time due to a delay, which then causes an uneven, accumulating time-interval between samples within a report cycle. A periodic, re-synchronization attempt with a GPS pulse per second (PPS) signal only resets the synchronization status of the first data sample in the next report cycle before the clock drift begins all over again. The error propagation model for this time error behavior is given as,

$$\Delta t_{\varepsilon,i}(t) = (i-1)\Delta t_\varepsilon, i = 1,2 \ldots n \tag{2.4}$$

where n is the reporting rate of the PMU.

2. Intermittent GPS Signal

Due to issues, such as loose wiring or incorrect placement of PMU GPS receiver, the device loses connection to the GPS reference signal. A time error, due to a delay, is observed to appear uniformly on subsequent data samples. The time error is observed to appear randomly on consecutive sets of data samples when GPS connectivity is intermittent (e.g. due to loose wiring), and an accumulating time error observed on all samples during a total GPS signal loss (e.g. due to

improper placement or malfunctioning of device). The models for the intermittent and total GPS siganal loss (GSL) time error behaviors are states respectively as,

$$\Delta t_{\varepsilon}(t) = \Delta t_{\varepsilon} \tag{2.5}$$

$$\Delta t_{\varepsilon}(t) = t\Delta t_{\varepsilon} \tag{2.6}$$

3. Spoofing of GPS receiver signal

Here, an attacker initially acts as an authentic source of correct external reference signal to the PMU, and then attacks the device by gradually leading its signal away from the authentic GPS signal mode. The attack model is given as,

$$\Delta t_{\varepsilon}(t) = \Delta t_{\varepsilon,capture} + tdt \tag{2.7}$$

$\Delta t_{\varepsilon,capture}$ is a time error at the instance when an attacker completely captures the device receiver, and dt is the rate of time signal divergence induced by the attacker.

2.2.2 Non-Time Errors

Similar to data measurements obtained from other grid-installed sensors, PMU data are prone to the effects of unwanted noisy signals, data drops due to communication issues which affect network data streaming ability and repeated measurement values.

Noise in data measurements is modeled as an additive, Gaussian distributed signal, which is parameterized by a zero-mean and finite variance (σ^2). The standard deviation (σ), associated with each of the measurement time points, is obtained from a Signal-Noise Ratio, (SNR, which is in decibels),

$$\sigma = 10^{-SNR/20} \tag{2.8}$$

Data drop is measured by a drop-out rate attribute, and defines the rate at which packets are lost in a data stream [19]. No data is reported at time points during which packets are lost or delayed, and [22] suggests the use of NaN (not a number) or 0x8000 (-32768)- corresponding to zero values - as filler data, which are not used in actual computation.

2.2.3 Updating Derived Measurements (Frequency and ROCOF)

Depending on the type of synthetic data error that is prototyped, a re-computation of the frequency and ROCOF signals is required. Currently, no specific estimation technique for these quantities has been defined by the IEEE reference documentation [22]. Based on the implicit definition of frequency as the rate of change of phasor angle, the derived measurements can be computed in the frequency domain as,

$$f = \frac{s}{1 + sT}\theta \tag{2.9}$$

$$ROCOF = \frac{s}{1 + sT} f \tag{2.10}$$

where $T \sim 0.2$ second is a time-delay used to capture a window of data samples.

2.3 Synthetic Networks

Confidentiality issues associated with obtaining actual field data poses a challenge to research activities, and thus prompts the use of artificially-generated data for study and research purposes through the design of synthetic networks.

Synthetic grids are fictitious, but realistic, models of power grids [23-26]. They are statistically similar to real power grids since they are designed with respect to publicly available data e.g. size and locations of generators, population density, etc. Thus, they do not contain any critical energy infrastructure information (CEII) and can be freely shared, used in project publications and freely provided to other researchers [27].

Fig. 2.1. shows a synthetic 2,000-bus network spread out over the geographic region of Texas, and with a system operating frequency of 60-Hz.

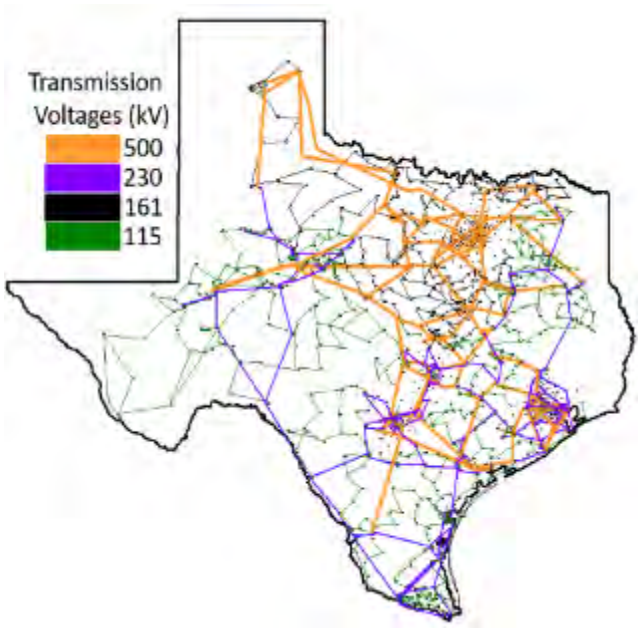

Fig. 2.1. A 2,000-bus synthetic network

Comprising of 1,250 substations, 432 generators, 3,209 transmission lines and different component dynamics set up in the system, the network is designed to simulate the operation of an actual power grid. More details on this, and a 10,000-bus system used in this work are presented in Appendix A.

2.4 PMU Data Prototypes for Time Errors

Figs. 2.2 and 2.3 illustrate voltage angle (VA) profiles based on the time propagation models in (4) – (7). Four different PMU time error prototypes were generated using original data from a test bus in the 2,000-bus network after a 30 second simulation. Error injection is initiated at the 5th second, and exists for 20 seconds. The report rate of the PMU is 30 samples per second.

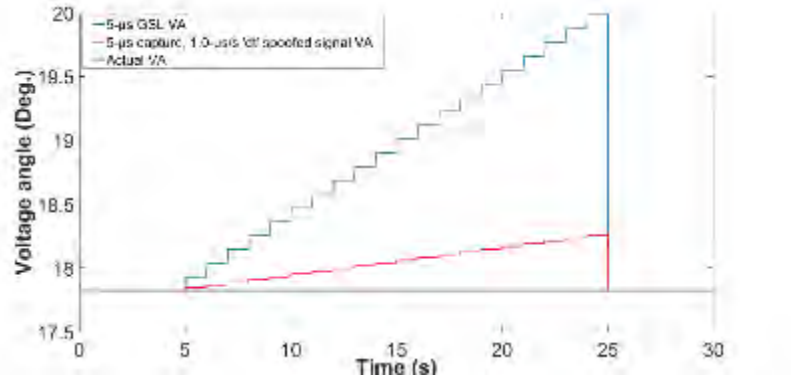

Fig.2.2. Prototype voltage angles for GSL and signal spoof

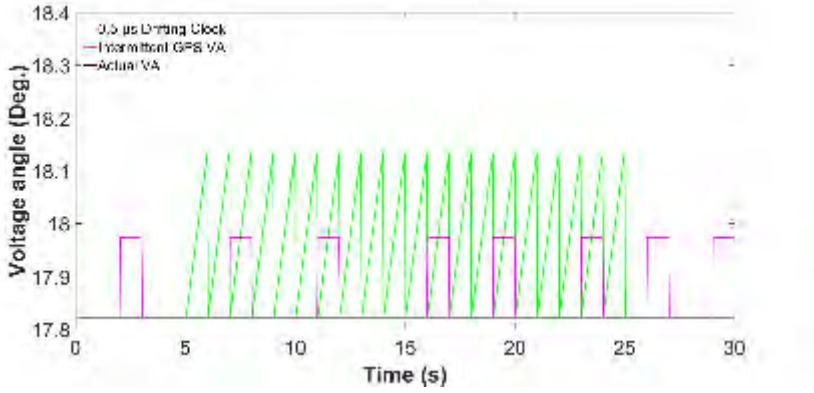

Fig.2.3. Prototype voltage angles for clock drift and intermittent GPS

In Fig. 2.2, the VA waveforms of the GPS signal loss (GSL) event and a spoofed-GPS time signal are shown. The black horizontal line is the original, steady state VA. The blue-colored GSL event has a pulse per second (PPS) time error (Δt_ε) of 5 μs, and the red-colored spoofed signal event has a time error divergence rate (dt) of 1 μs/s. For each of the events, the phase angle error $\Delta\delta_\varepsilon(t)$ is applied uniformly on all 30 samples in a one-second reporting period prior to the next set of reported samples.

Fig 2.3. illustrates VA profiles due to two different causes of PMU clock time offsets – a constant 0.5 μs time error due to a drifting internal clock, and a 1.0 μs error due to intermittent GPS clock signals received by the PMU device. The green-colored ramp for the cloc drift error is indicative of the accumulatng time error at each sample. In contrast, a uniform time error is observed for all samples in the case of intermittent GPS signal.

PMUs report ROCOF data which can also be used to monitor phasor angle changes. The derived ROCOF data for the voltage angle errors are shown in Fig. 2.4 and 2.5.

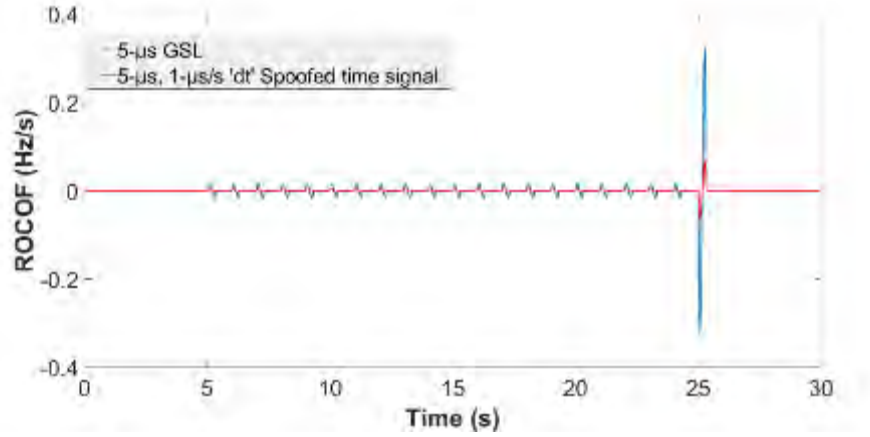

Fig.2.4. Derived ROCOF data for prototyped PMU voltage angles in Fig. (2.2)

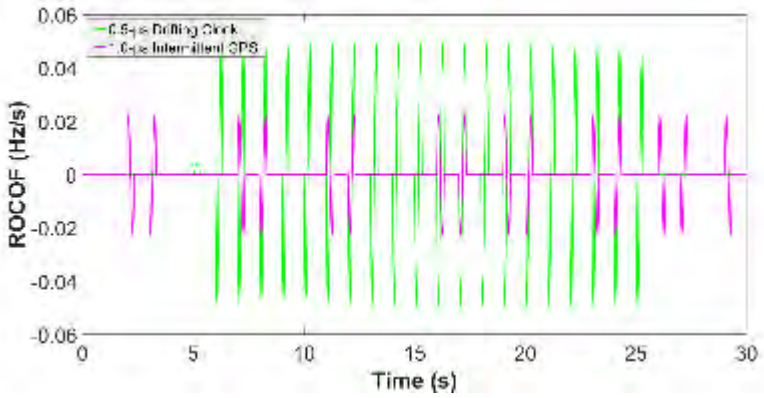

Fig.2.5. Derived ROCOF data for prototyped PMU voltage angles in Fig. (2.3)

Periodic ripples observed in Fig. 2.4 for both GSL and spoofed GPS signal are attributed to the small jumps in voltage angles due to the incremental time errors. However, at the point of error removal, the accumulated voltage angle deviation results in a sudden spike in the ROCOF. We observe that the GSL event generates a significant spike (0.33 Hz/sec) which is due to the large angle deviation as compared to the case of the spoofed time signal.

In Fig. 2.5, the observed uniform ROCOF measurements for a PMU internal clock offset is consistent with the periodic VA ramp-and-reset observed in Fig. 2.3. With an intermittent GPS signal, we observe a pairwise formation of positive and negative edges of ROCOF measurements.

3. Large-Scale System Data Error Analysis for PMU Synchrophasor Data

In this chapter, a distributed, error analysis technique is proposed to evaluate data segments of time-series measurements for errors using bus data obtained from a large-scale system. This constitutes the PMU data error analysis (PDA) block in the proposed framework of Fig. 1.1.

3.1 Distributed Application of a Local Outlier Factor Analysis Method

Given a dataset $\boldsymbol{X}$, composed of different time series measurements obtained from n number of PMU nodes, the aim is to be able to identify inconsistent data segments within any of the n measurements.

$$\boldsymbol{X} = \{\boldsymbol{x_1^t}, \boldsymbol{x_{2,}^t} \ldots \boldsymbol{x_n^t}\};\ \boldsymbol{x_i} = \{x_{i1}, x_{i2}, \ldots x_{ip}\} \tag{3.1}$$

$\boldsymbol{x_i}$ is the data time series obtained from the i^{th} PMU device, and consists of p data points.

In previous works [28, 29], a local outlier factor (LOF) method was implemented to compute degrees of correlation of all measurements relative to a PMU dataset, from which computed error metric were used to identify data measurements considered to deviate from the dataset. The LOF technique is an unsupervised outlier detection algorithm which is based on the density of the k-nearest neighborhood of each object [30]. By comparing the relative densities of each neighbor, and computing an LOF value, it is able to detect an outlying object by identifying the largest-value LOF, and which is also most distinct from other LOF values in the set. A summary of the procedures for computing LOF values are given in appendix B.

In this work, a windowing technique which searches for erroneous data segments across all time-series measurements obtained from a large-scale system is implemented. It is observed that in a large system where buses are separated by large geographical and electrical distances, wide-area variations in bus signal trends during system events can mask out bad data due to wrongly-computed LOF values. In addition, it is observed that a direct implementation of the LOF method in a large system is computationally intensive since the k-nearest neighborhood of a measurement can be very large.

Figure 3.1 shows eleven locations in the grid from which voltage measurements were obtained after the contingency outage of a 230-kV line in the 2,000-bus synthetic grid. The simulation was run for 3-seconds, and the report rate of all PMUs set to 30 samples per second.

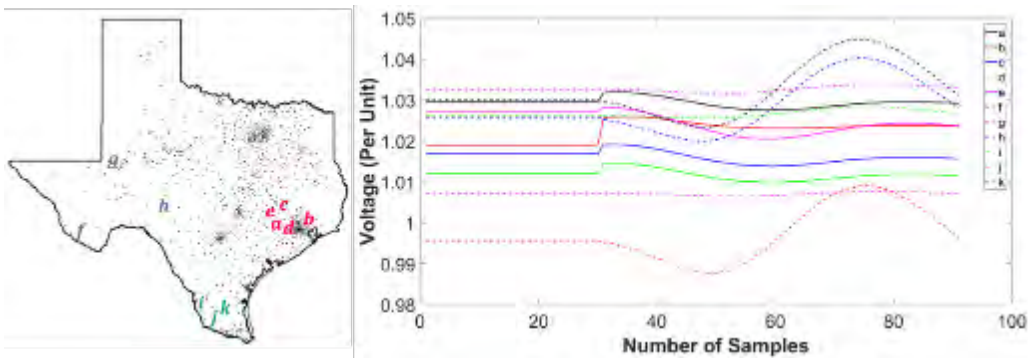

Fig. 3.1. 3-second voltage measurement

Using all signals in an LOF-based data error analysis, the computed error metrics for the eleven different bus signals are given in Table 3.1.

Table 3.1. LOF results for all 11 signals

Bus	a	b	c	d	e	f	g	h	i	j	k
LOF	1.000	4.342	1.000	1.000	4.590	4.937	5.069	4.891	1.000	1.000	1.000

The dis-similar signal trends in the selected bus measurements are adequately captured by the computed LOF values. Though the non-uniform LOF value metrics is solely caused by the grid event, this pre-existing state sets a condition that easily distorts true LOF computation and error identification in the event that actual measurement errors indeed exist in the system. In addition, considering all 2,000 input grid signals in the error analysis process, runtime for computing the LOF value for each of the bus measurement can be prohibitively high.

To address these limitations, a distributed computation method, which takes into consideration local signal variations in the wide-area network is proposed. Table 3.2 show computed LOFs when the signals are aggregated into two different, naïve clustering formations: A - $\{a, b, c, d, e\}$,$\{f, g, h\}$, $\{i, j, k\}$; and B - $\{b, e\}$, $\{a, c, d\}$, $\{f, g, h\}$, $\{i, j, k\}$ respectively.

Table 3.2. LOF results for all 11 signals using two sets of clustering

Bus	a	b	c	d	e	f	g	h	i	j	k
LOF-A	1.000	4.342	1.000	1.000	4.590	1.000	1.000	1.000	1.000	1.000	1.000
LOF-B	1.000	1.000	1.000	1.000	1.000	1.000	1.000	1.000	1.0000	1.000	1.000

A uniform set of computed error metrics observed at all bus locations for *B*-cluster formation provides a base condition for which the true presence of data errors can be detected if they exist in the system.

3.2 Procedures in a Distributed Error Analysis

The flowchart for the proposed distributed LOF error analysis for the measurements obtained from the large system is illustrated in Fig. 3.2.

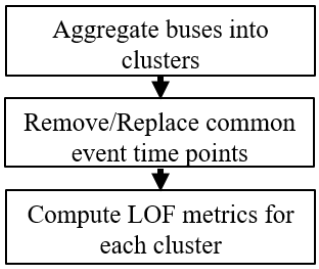

Fig. 3.2. Wide-area search for data errors

3.2.1 Bus Aggregation

The method used to partition the system into smaller and local groups is governed by the concept of voltage control areas i.e. groups of buses exhibiting strong electrical coupling among each other. Augmented local bus information – bus geographical location and derived information from bus voltage measurement – are used to determine bus clusters. Integration of bus geography with voltage information ensures that generated bus clusters are able to track the dynamic response of the system rather than a sole use of fixed, bus geography coordinates (longitude and latitude) which are devoid of any electrical information.

Principal component analysis (PCA) method is used to extract true voltage information pertaining to individual buses. The PCA technique re-expresses the data set $\boldsymbol{X}$ into its most meaningful set of basis [31], and for which an orthonormal matrix, $\boldsymbol{P}$ (the basis) is known to diagonalize a covariance matrix, $\boldsymbol{S_Y}$ $(= \frac{1}{n-1}\boldsymbol{YY^T})$, such that $\boldsymbol{Y} = \boldsymbol{P^T X}$. The eigen-decomposition of $\boldsymbol{S_Y}$ yields the ordered eigenvalues and eigenvectors,

$$\lambda = \{\lambda_1, \lambda_2, \dots \lambda_m\};\ \lambda_1 \geq \lambda_2 \dots \geq \lambda_m$$

$$\boldsymbol{P} = \{\boldsymbol{PC_1}, \boldsymbol{PC_2}, \dots \boldsymbol{PC_m}\};\ \boldsymbol{PC_i} \in \boldsymbol{R^n} \tag{3.2}$$

The order of importance of the principal component vectors in $\boldsymbol{P}$, which is given as $\boldsymbol{PC_1} > \boldsymbol{PC_2} > \cdots \boldsymbol{PC_m}$, is then based on the order of the largest to the smallest-sized eigenvalues.

Figure 3.3 shows plots of the first eight principal vector components, and the corresponding eigenvalues, after performing PCA technique on voltage data set obtained from the synthetic 2,000-bus system after a generator outage at bus 1506, however with noise signals injected at buses 1 and 2. Table 3.3 gives the variance percentage for each of the components.

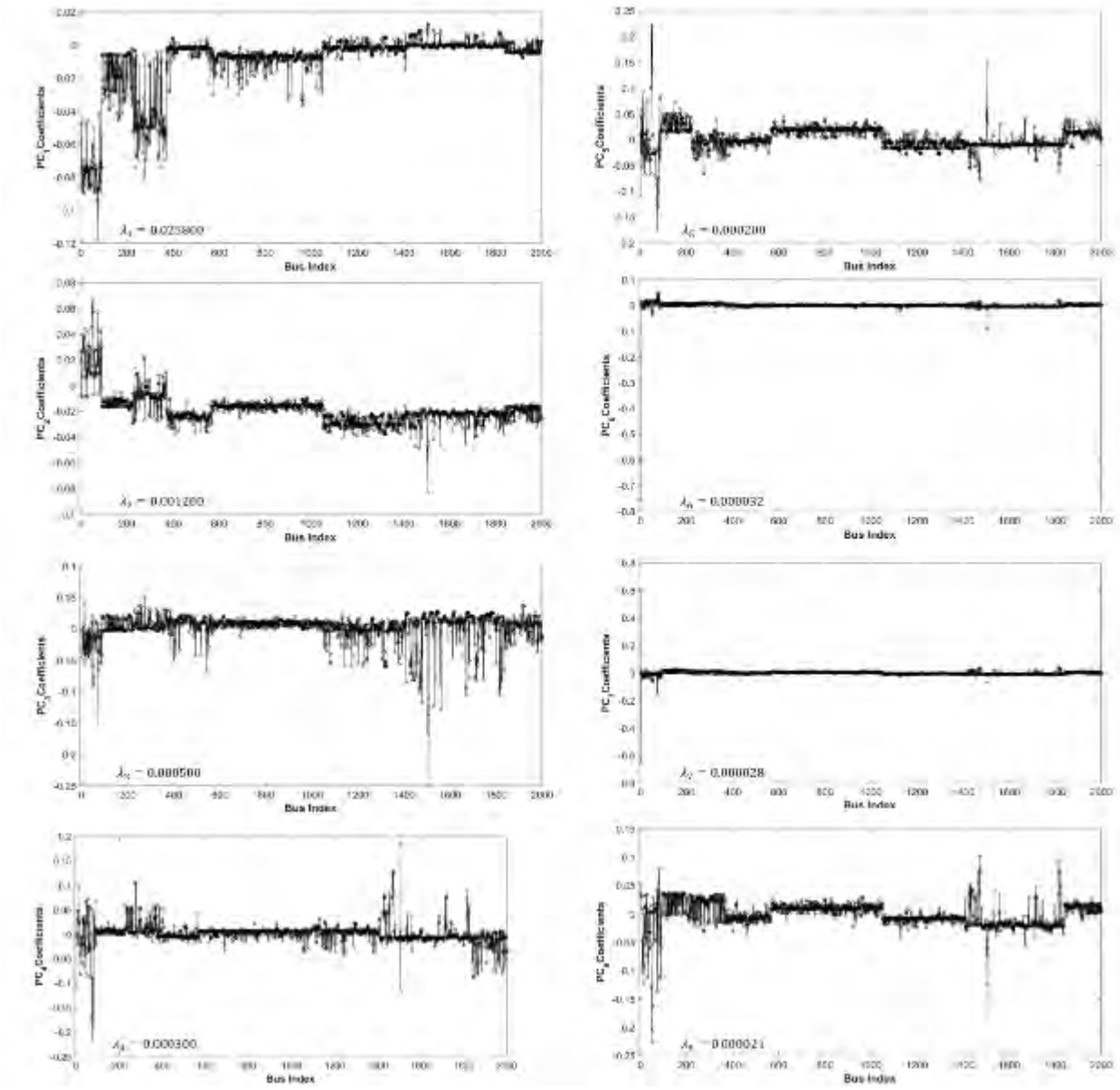

Fig. 3.3. First eight principal component vectors

Table 3.3. Variance percentage of principal components - $(PC_i/\sum PC_i) \times 100\%$

Principal Component	$\boldsymbol{PC_1}$	$\boldsymbol{PC_2}$	$\boldsymbol{PC_3}$	$\boldsymbol{PC_4}$	$\boldsymbol{PC_5}$	$\boldsymbol{PC_6}$	$\boldsymbol{PC_7}$	$\boldsymbol{PC_8}$
Variance %	91.880	4.270	1.780	1.068	0.712	0.114	0.0997	0.075

The extent of activity of any i^{th} bus is indicated by the absolute value of its coefficient in the component vector. As expected, the variance percentage for $\boldsymbol{PC_1}$ (i.e., 91.88%) is observed to be dominant since it bears most of the voltage information in the system. True system information is embedded in the first few components after which the effect of system noise and data errors become more dominant as observed by the bus coefficients in $\boldsymbol{PC_6}$ and $\boldsymbol{PC_7}$.

A hybrid, data-driven approach implemented for the purpose of clustering, thus augments every bus geography information with its principal vector coefficient(s).

$$\boldsymbol{X}_i = \left[Geo_{lat,i}, Geo_{long,i}, \boldsymbol{PC}_{1,i}, \ldots \boldsymbol{PC}_{n,i}\right] \tag{3.3}$$

$\boldsymbol{X}_i$ is an hybrid vector for the i^{th} bus, which entries are made up of latitude and longitude coordinates, $Geo_{lat,i}$ and $Geo_{long,i}$, and bus entries in the n significant principal components $\boldsymbol{PC}_{1,i}, \ldots \boldsymbol{PC}_{n,i}$.

An aggregation of the bus vectors in (3.3) is carried out using *k*-means algorithm [32] - a simple and fast clustering technique. Furthermore, a pre-processing step prior to the detection of bus or PMU locations reporting data errors is to identify and isolate actual system disturbance data.

3.2.2 Error Assessment of Bus Measurements

A distributed LOF computation is performed cluster-wise on the grid. Using a sliding window, defined by τ- width and τ_s-sliding time, the bus signals are individually assessed for errors by computing error metric for m segments in the time-series data.

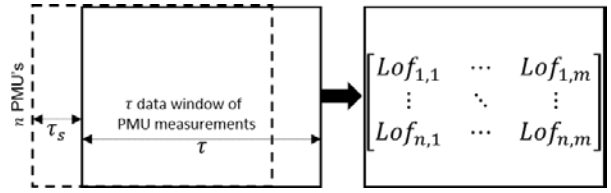

Fig. 3.4. Window technique for assessing error level in data segments

Note: A phasor measurement consists of a magnitude and angle component. Because PMU errors affect either or both components, it is important to specify the measurement component being assessed for errors. If the focus is magnitude (or angle), the input data to the LOF routine is phasor magnitude (or ROCOF). Absolute values of voltage angles do not convey much information, and cannot be used to adequately monitor PMU time errors. On the other hand, ROCOF measurements provide a good indication of voltage angle dynamics with an added ability of being able to detect small and sudden changes in voltage angles. Consequently, ROCOF qualifies as a good parameter to monitor time errors in PMU devices.

3.3 Simulation and Results

A 10-second simulation is carried out on the 2,000 bus network during which one of the 115-kV transmission lines is disconnected after 3 seconds. A data error analysis is carried out on the voltage measurements obtained from the system. Considering only the contingency event (a 115-kV line outage), Table 3.4 gives a summary of the computed error metrics for different system configurations.

Table 3.4. Summary of computed phasor magnitude LOFs (event only)

# Control areas /clusters	Event points removed?	Highest LOF(s)	Bus Index
1	Y	[16.69,8.355,8.358,8.355]	[6276,4174,6128,6015]
	N	[16.69,8.355,8.358,8.355]	[6276,4174,6128,6015]
5	Y	8.360	6015, 6128
	N	8.360	6015, 6128
20	Y	1.000	ALL
	N	8.360	6128
1	Y *	5.060	6276

* Event time points removed separately for individual bus measurements

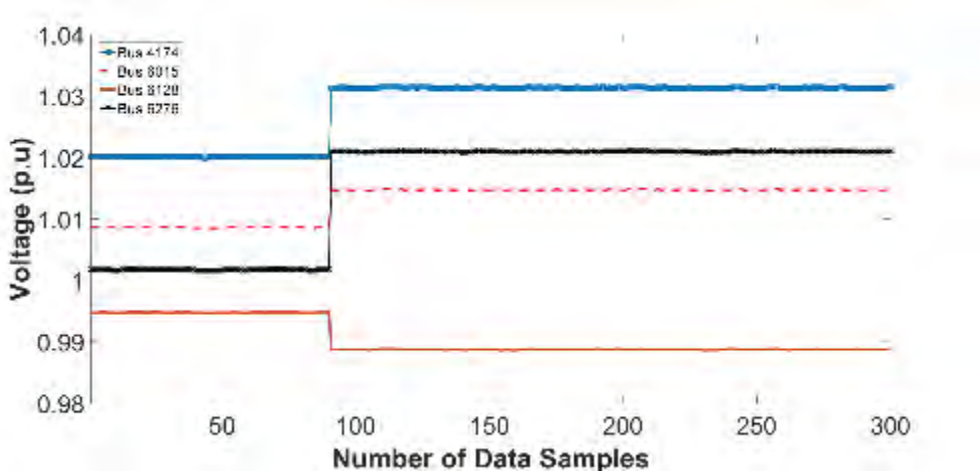

Fig. 3.5. Voltage magnitude measurements at event bus locations

According to the direct LOF computation method, false data error notifications are observed at buses (IDs: 6276, 4174, 6128, 6015) where the event is most significant, even though the disturbance has little impact on the system. Regardless of the removal of event points, LOF analysis is not able to distinguish the event from instances of data errors, and thus mis-identifies event buses as locations with the largest system LOFs. The proposed distributed method applied to a 5-cluster system aggregates bus IDs 4174 and 6276 into a cluster where a high voltage correlation results in smaller LOF values. However, a false identification of bus IDs 6015 and 6128 with LOF values 8.36 is due to both buses belonging to separate clusters with disparities in their voltage patterns.

Using a 20-cluster system, more groups containing buses with similar, dynamic voltage response are generated. Fig. 3.6 shows re-allocation of the event buses to cluster 2, 5 and 17 such that computed LOF value is 1.0 at all buses, thus isolating the impact of the event.

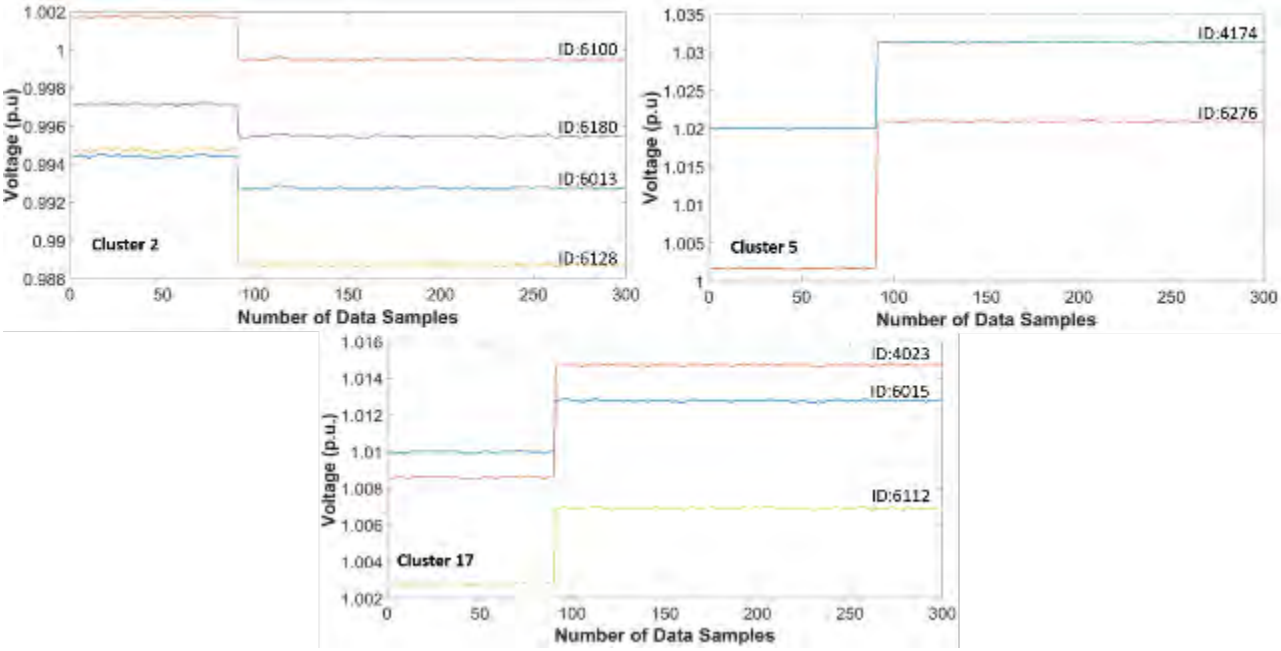

Fig. 3.6. Event buses re-distributed to three clusters

Error 1: In this scenario, 45-dB of noise signal is injected in the phasor voltage measurements reported by the PMU located at substation ID 1250. Table 3.5 provides a summary of the computed LOFs.

Table 3.5. Summary of computed phasor magnitude LOFs (event and noise error)

# Control areas /clusters	Event points removed?	Highest LOF(s)	Bus Index
1	Y	[16.69,8.355,8.358,8.355]	[6276,4174,6128,6015]
	N	[16.69,8.355,8.358,8.355]	[6276,4174,6128,6015]
5	Y	[8.358,8.358,2.941,3.263,2.941]	[6015,6128,8158,8159,8160]
	N	[8.358,8.358,2.941,3.263,2.941]	[6015,6128,8158,8159,8160]
20	Y	[2.941,3.263,2.941]	[8158,8159,8160]**
	N	[8.360,2.941,3.263,2.941]	[6128,8158,8159,8160]
1	Y *	5.060	6276

* Event time points removed for individual bus measurements, ** PMU 1250 reports measurements for buses 8158-8160

Based on the large LOF values observed at the event buses, the direct LOF computation mis-identifies these locations as sources of erroneous measurements even though data errors are reported by another PMU set of phasor measurements. A distributed error analysis on the 5-cluster system identifies all three erroneous measurements, with LOF values 2.941, 3.263 and 2.941, in

addition to two event bus measurements (bus IDs 6015 and 6128). Finally, with a 20-cluster system, all event buses are isolated, and thus correctly identifying only the measurements with true data errors. Table 3.6 shows bus allocations in four groups within the 20-cluster system.

Table 3.6. Cluster formation

Cluster 2	[6013,6100,6128,6180]
Cluster 5	[4174,6276]
Cluster 16	[8158,8159,8160, …]
Cluster 17	[4023, 6015, 6112]

Error 2: In addition to the actual system event and scenario of Error 1, time errors were incorporated into the phasor measurements reported by the PMUs located at substation IDs 4, 538 and 764. Time error details and the voltage angles for the affected measurements are shown in Table 3.7 and Fig. 3.7 respectively.

Table 3.7. Simulated time errors

SS/PMU ID	**# buses**	**Error Type (T)**	**Error**	**Parameters**	**Duration**
4	2	T-2	Clock drift	Skew: 1-µs	7-sec
538	1	T-2	Clock drift	Skew: 0.5-µs	10-sec
764	1	T-1	Int. GPS	Skew: 10-µs, 5 instances	1-sec/instance

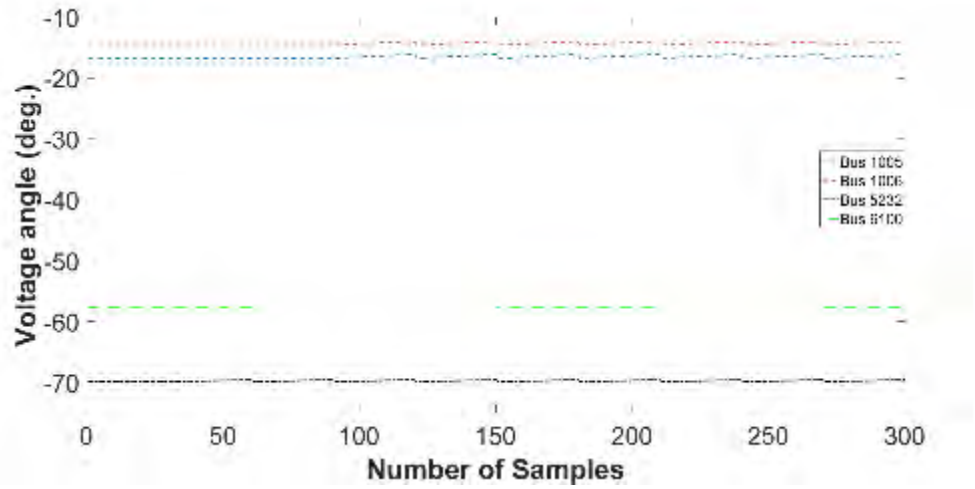

Fig. 3.7. Voltage angle measurements at time-error bus locations

The effects of both data errors are observed in the ROCOF data, and thus used as the input data source in the error analysis. Table 3.8 summarizes the results.

Table 3.8. Summary of computed phasor angle LOFs (event, noise and time errors)

# Control areas /clusters	**Event points removed?**	**Highest LOF(s)**	**Bus Index**
1	Y	[522,522,325,200,58,248,253,291]	[1005,1006,5232,6100,6276,8158,8159,8160]
	N	[522,522,325,200,58,248,253,291]	[1005,1006,5232,6100,6276,8158,8159,8160]
20	Y	[297,192,192,41,248,253,132]	[5232,1005,1006,6100,8158,8159,8160]

Similar to the previous scenario, the distributed method is able to detect all bus/PMU locations where data errors were reported while isolating the event bus locations.

Table 3.9 shows error analysis computation times for the single area, 5-cluster, and 20-cluster system configuration which was carried out on 10-second data on a 3.6 GHz processor, windows-based system.

Table 3.9. LOF execution time for different system configurations

# Control areas /clusters	1	5	20
Time (sec)	284	70	21

A notable processing time for the single area can be attributed largely to the several executions of some of the LOF analysis steps carried out within the large *k*-neighborhood of each of the 2,000 measurements. This is not the case with the clustered configurations, and it is assumed that with parallel computation, the running time for clustered systems can be much reduced.

Windowing Scheme

A distributed LOF computation for the windowing scheme in Fig. 3.4 is applied on the 10-sec data obtained for error cases 1 and 2, using time window and time step of 1-sec and 0.5-sec respectively. The derived error values for each segment in all 2,000 measurements for both data error cases is shown in Fig. 3.8 and 3.9.

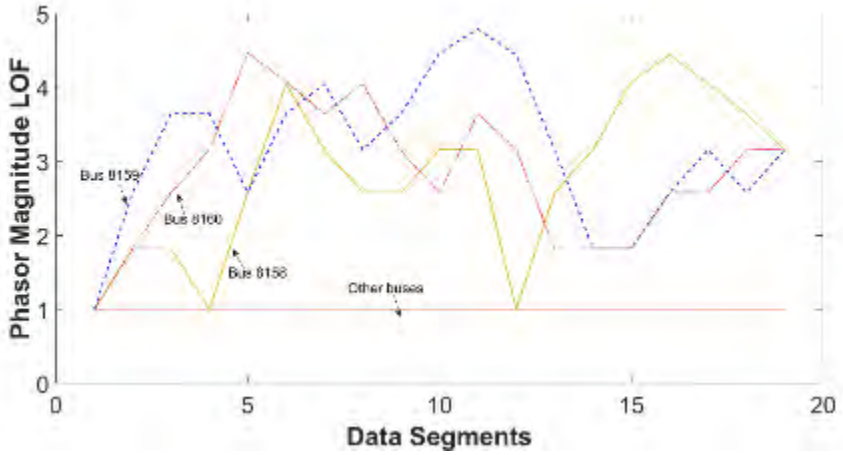

Fig. 3.8. Data segment errors in all 2,000 voltage magnitude measurements for error case #1

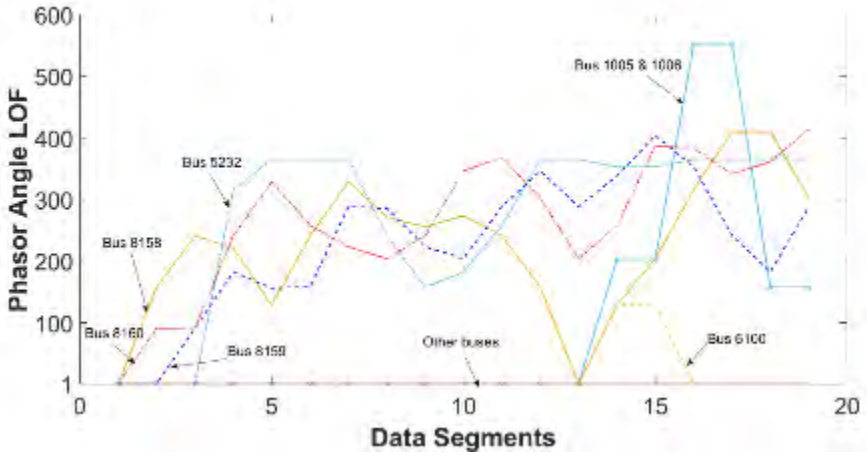

Fig. 3.9. Data segment errors in all 2,000 voltage angle measurements for error case #2

4. Presenting Computed Data Error Results of Large-Scale System through Multidimensional Scaling Visualization

In this chapter, error metrics computed for the different measurements in a large-scale system (here, the 2000-bus synthetic network) and PMU device information about the synchronization status of each data sample are presented in visual form. This constitutes the PMU data visualization (PDV) block in the proposed framework of Fig. 1.1. An overview of the multidimensional scaling technique, and how it was applied in this work to the error cases in the previous chapter are presented.

4.1 Data Error Visualization Using Multidimensional Scaling

Depending on the number of data segments assessed for errors, the computed time-series, LOF values for each PMU measurement can generate vectors of high dimensions. The method which has been adopted for visualizing errors in this work relies on observing correlations among different bus measurements for any given data error type, and visually displaying them as dis-similarities in a two dimension chart. The different charts generated are based on the use of the multidimensional scaling (MDS) which can be a useful method for representing power system information [33, 34].

MDS is used to represent measurements of similarity or dissimilarity among pairs of objects as distances between points of a low-dimensional, multidimensional space [35]. Given the time-series error values ($\boldsymbol{LOF_{orig}}$) computed at m different data segments for n PMU measurements, and a pairwise, proximity matrix ($\boldsymbol{\delta}$) between them in (1) and (2) respectively.

$$\boldsymbol{LOF_{orig}} = \begin{bmatrix} Lof_{1,1} & \dots & Lof_{1,m} \\ \vdots & \ddots & \vdots \\ Lof_{n,1} & \dots & Lof_{n,m} \end{bmatrix} \tag{4.1}$$

$$\boldsymbol{\delta} = \begin{bmatrix} \delta_{11} & \dots & \delta_{1n} \\ \vdots & \ddots & \vdots \\ \delta_{n1} & \dots & \delta_{nn} \end{bmatrix}, \delta_{ij} = \begin{cases} dissim\left(Lof_i, Lof_j\right); & i \neq j \\ 0; & i = j \\ i, j = 1,2, \dots n \end{cases} \tag{4.2}$$

The output of the MDS algorithm is a set of n coordinates, $\boldsymbol{LOF_{coord}}$ in two dimensions, which re-re-represents $\boldsymbol{LOF_{orig}}$, and preserves or approximates the pairwise proximities in $\boldsymbol{\delta}$. That is,

$$\boldsymbol{LOF_{coord}} = \begin{bmatrix} l_{1,1} & l_{1,2} \\ \vdots & \vdots \\ l_{n,1} & l_{n,2} \end{bmatrix} \tag{4.3}$$

$$\boldsymbol{d} = \begin{bmatrix} d_{11} & \dots & d_{1n} \\ \vdots & \ddots & \vdots \\ d_{n1} & \dots & d_{nn} \end{bmatrix}, d_{i\square} = \begin{cases} dissim(i,j); & i \neq j \\ 0; & i = j \end{cases} \tag{4.4}$$

The MDS optimization problem is then to identify the optimal set of coordinates in $\boldsymbol{LOF_{coord}}$ which minimizes a stress function which corresponds to a sum of squared errors.

$$\sigma = \underset{(l_{1,1},l_{1,2}),\ldots,(l_{n,1},l_{n,2})}{arg\,min} \sum_{i=1}^{n-1} \sum_{j=i+1}^{n} (d_{ij} - \delta_{ij})^2 \tag{4.5}$$

Computation of $\boldsymbol{LOF_{coord}}$

The choice of classical MDS [36] for this work is due to it being a non-iterative technique, and generating analytical solutions within a fast computation time. Classical MDS assumes the proximity matrix, $\boldsymbol{\delta}$ as a distance matrix, and finds the coordinate matrix, $\boldsymbol{LOF_{coord}}$ comprising of the two leading eigenvectors obtained from the eigen-decomposition of the normalized proximity matrix.

4.2 Generating Data Error, Hybrid Correlation Charts

For this work, the MDS is used to facilitate the display of the system structure by observing all PMU similarities using smaller LOF dimensions. It is used to transform the dissimilarities observed within a given dataset into a 2-D graphical representation. The benefit lies in visually displaying the dynamic electrical parameters (e.g. voltage magnitude and angle, frequency and ROCOF), and providing a better means of conveying the measurement errors.

Proximity Matrices

The multidimensional matrix, $\boldsymbol{LOF_{orig}}$ is used to compute the entries in the proximity matrix, $\boldsymbol{\delta}$ in (4.2), which are defined as Euclidean distances i.e.,

$$dissim(Lof_i, Lof_j) = \sqrt[2]{\sum_{p=1}^{m} (Lof_{i,p} - Lof_{j,p})^2} \tag{4.6}$$

When the choice is on visualization of the similarities among the synchronization status of all PMUs, which is based on their sync bits, the pairwise, binary-based distances, in the proximity matrix, $\boldsymbol{\delta_{sync}}$ are computed using the Rogers & Tanimoto binary similarity measure [35, 37], given as,

$$dissim(Pmu_i, Pmu_j) = \frac{a+d}{a+d+2(b+c)} \tag{4.7}$$

Each of Pmu_i, Pmu_j is a binary string formed by cascading all data frame sync bits in a given PMU measurement; a, b, c and d are obtained from Table 4.1.

Table 4.1. Expression of binary instances

		Object B	
		1	0
Object A	1	a	b
	0	c	d

a is the number of times elements in Object A and B are simultaneous bit-1;
d is the number of times elements in Object A and B are simultaneous bit-0
b is the number of times elements in Object A are bit-1, and elements in B are bit-0; and
c is the number of times elements in Object A are bit-0, and elements in B are bit-1

The choice of selection of this binary similarity measure is based on the need to emphasize bit differences and similarities between PMUs. In addition, computed dis-similarity values always lies between 0 and 1.

Selecting MDS axis for plotting

Time-series phasor measurements, obtained from PMUs, comprise of two aspects – magnitude and angle – which are both affected differently depending on the type of error. Therefore, we propose to visualize the wide-area similarity in all measurements using the relevant aspect when an error type is specified.

1. Noise Errors: Noisy signals are observed in both aspects of phasor measurements. As a result, significant noise levels are identified by visualizing the coordinate matrices of both magnitude-based and angle-based $\boldsymbol{LOF}$ matrices.

   Input: Proximity matrix ($\boldsymbol{\delta_{M,LOF}}$) corresponding to magnitude-based $\boldsymbol{LOF}$; and proximity matrix ($\boldsymbol{\delta_{R,LOF}}$) corresponding to angle-based $\boldsymbol{LOF}$.
   Output: First dimension of coordinate matrix, $\boldsymbol{X_M}$; and first dimension of coordinate matrix, $\boldsymbol{X_R}$

2. Timing Errors (GPS vs Clock drift): Timing errors reflect in the phasor angles. In addition, the PMU Sync bit (bit 13 in the STAT field) is flagged to '1' once time-issues are observed to have occurred. Thus, we visualize the coordinate matrices of both angle-based $\boldsymbol{LOF}$ and sync status.

   Input: Proximity matrix ($\boldsymbol{\delta_{R,LOF}}$) corresponding to angle-based $\boldsymbol{LOF}$; and proximity matrix ($\boldsymbol{\delta_{sync}}$)
   Output: First dimension of coordinate matrix, $\boldsymbol{X_R}$; and first dimension of coordinate matrix, $\boldsymbol{X_{sync}}$

4.3 Simulation and Results

The simulation case involves the outage of one of the 115-kV lines during a 10-second simulation, and the information being used are obtained from the error injection case which was previously described in chapter 3 i.e. an integration of the original event measurements with noisy signals at PMU 1250 and time errors signals at PMUs 4,538 and 764. Based on these different types of errors (noise and time errors) which are present in the data, two different MDS visualization options are used for this purpose.

Bit Adjustments for Time Synchronization Issues [22]

Given the occurrence of clock drift and intermittent GPS time errors as described in Table 4.4, the flag bit values indicating the status of each sample synchronization (PMU Sync bit 13) are demonstrated in Fig. 4.1 and 4.2. A bit value of zero (or OFF) indicates a synchronized sample, and a bit value of one (or ON) is a sample that is out of sync.

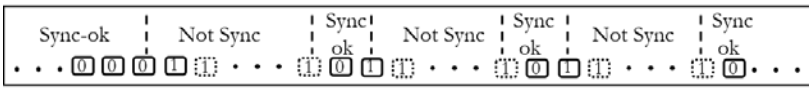

Fig. 4.1. Bit flag updates for clock drift error

The clock drift is an alternating sequence of bit changes. Prior to time issues, bit 13 is 0 (Sync ok) until the moment the drifting begins with the first data sample, when bit 13 changes to 1 (Not Sync). For a reporting period, it remains out of sync, and all sample bit status is preserved as value 1. An attempt at re-synchronizing first sample in the next report cycle sets bit 13 to 0 momentarily, after which drifting continues with the second sample. Bit 13 is set back to 1 for the reporting period. The cycle is repeated for as long as the PMU clock issue exists.

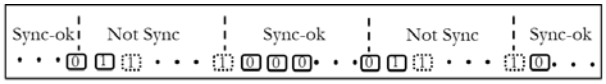

Fig. 4.2. Bit flag updates for intermittent GPS error

Sequencing of bit changes in the case of intermittent GPS is to a lesser degree than the clock drift, and depends on the frequency and duration of signal loss. Hence, the non-periodic sequencing of bit changes in Fig. 4.2. A period of bit-OFF (Sync-ok, and bit value is 0), followed by another equal- or non-equal duration of bit-ON (Not Sync, and bit value is 1).

Generation of MDS Correlation Graphs

Based on figures 4.1 and 4.2, bit adjustments due to clock drifts and intermittent GPS signal reception are performed on the bus measurements of PMUs 4, 538, and PMU 764 respectively. Execution of MDS procedures on the proximity matrices – $\boldsymbol{\delta_{M,LOF}}$, $\boldsymbol{\delta_{R,LOF}}$ and $\boldsymbol{\delta_{sync}}$ – across all 2,000 buses generates the reduced two-dimension coordinate matrices, $\boldsymbol{X_M}$, $\boldsymbol{X_R}$ and $\boldsymbol{X_{sync}}$ respectively. Table 4.2 shows the normalized coordinates for each bus in the $\boldsymbol{X_M}$, $\boldsymbol{X_R}$ and $\boldsymbol{X_{sync}}$ matrices

Table. 4.2 MDS coordinates for PMU bit-13 status flag and phasor angle error

PMU ID	Bus IDs	$X_{M,1}$	$X_{M,2}$	$X_{R,1}$	$X_{R,2}$	$X_{sync,1}$	$X_{sync,2}$
4	1005	0.001	0.000	-0.251	0.657	-0.512	-0.323
	1006	0.001	0.000	-0.251	0.657	-0.512	-0.323
538	5232	0.001	0.000	-0.517	-0.240	-0.591	0.031
764	6100	0.001	0.000	-0.028	0.012	-0.352	0.889
1250	8158	-0.526	0.864	-0.414	-0.070	0.001	0.000
	8159	-0.639	-0.495	-0.428	-0.190	0.001	0.000
	8160	-0.560	-0.225	-0.499	-0.193	0.001	0.000
Others	Others	0.001	0.000	0.001	0.000	0.001	0.000

In the absence of errors, the coordinates of all buses in either of the three coordinate matrices should approximately lie close to an origin i.e. (0, 0). However, isolated bus coordinates exhibiting significant deviations from this point is an indication of the presence of anomaly in the reported measurement. The hybrid-MDS graph in Fig. 4.3 is obtained by plotting $X_{R,1}$ and $X_{sync,1}$, and provides a method to visualize the correlations among PMU measurements when time errors are present.

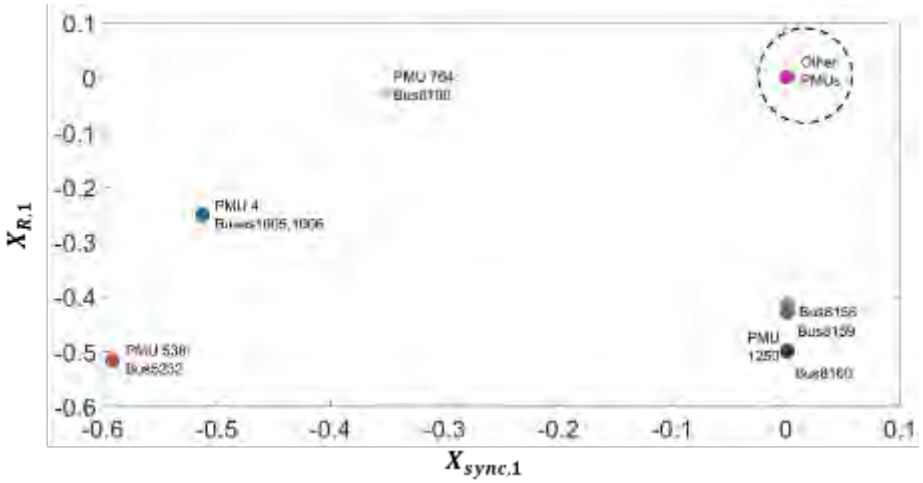

Fig. 4.3. Hybrid-MDS spatial representation of noise and time errors in PMU data

The diagonal distances spanned across both sync and phasor angle correlation axis from majority of other PMU measurements is indicative of actual time errors present in some of the reported measurements. The most severe cases are observed to occur in measurements obtained from PMUs 4 and 538 where the clock drift error had occurred for the most part of the simulation (i.e. 7 and 9 seconds respectively) followed by the five instances of intermittent, external time synchronization in PMU device 764. The vertical distance between PMU ID 1250 and 'other PMUs', however does not necessarily indicate a time error as the device is correlated in the sync axis with 'other PMUs'. Further investigations, by updating the graph to a plot of $X_{R,1}$ and $X_{M,1}$ in Fig. 4.4, reveal the large deviation of PMU 1250 with respect to the other PMUs along the phasor magnitude correlation axis. The data error can be attributed to other causes which simultaneously impact on both components of phasor measurements, and in this case, the effect of noisy signals.

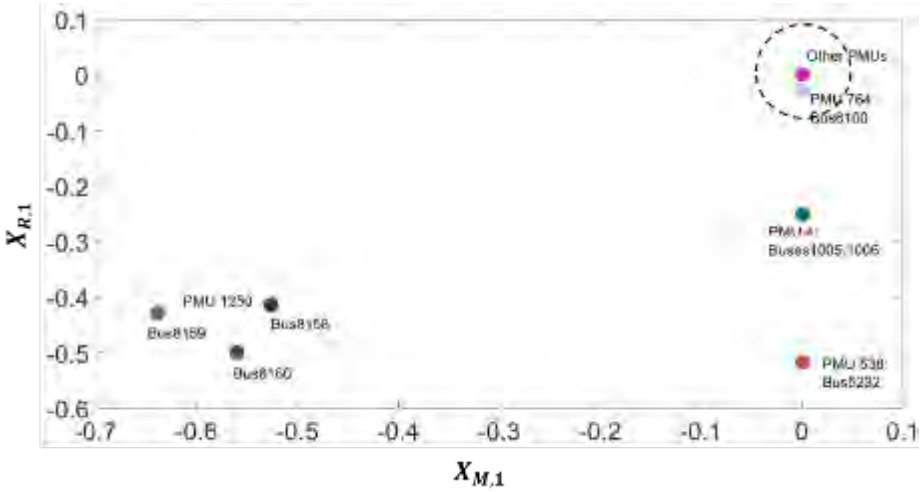

Fig. 4.4. Hybrid-MDS spatial representation of errors in PMU magnitude and angle data

5. Wide-Area Visualization of Large-Scale, Grid Oscillation Results Obtained from the Analysis of Synchrophasor Data

In this chapter, wide-area visualization methods are used to present results of low-frequency disturbance modes obtained from the analysis of synchrophasor data obtained from large-scale grids. Information pertaining to mode estimation quality, oscillation mode activities and source of oscillations are presented in a wide-area perspective in order to capture the holistic, underlying state of the system.

5.1 Oscillation Monitoring

A critical activity in preserving the safe operation of the power grid, the objective of oscillation analysis, monitoring and control is to search for sources of low-frequency oscillation disturbances that may threaten the stability of the system in order to eliminate them [15, 38]. This is achieved through the technique of modal analysis whose goal is to obtain a re-constructed signal , $\hat{y}(t)$ that is a sum of un(damped) sinusoids and considered to be a close approximate of an original signal $y(t)$. The observations not fully captured by the reconstructed signal often constitutes an error signal, $e(t)$.

$$\hat{y}(t) = \sum_{j=1}^{q} A_j e^{\sigma_j t} \cos(\omega_j t + \phi_j) \tag{5.1}$$

$$e(t) = \sum_{j=1}^{q} \left\| y(t_j) - \hat{y}(t_j) \right\|_2^2 \tag{5.2}$$

An identified j^{th} low-frequency signal (or mode) is characterized by its modal parameters: damping factor (σ_j), frequency (ω_j) and mode shape consisting of amplitude (A_j) and phase (ϕ_j). q is the number of dominant low-frequency modes captured by the analysis.

Different modal analysis techniques are used in power systems to reveal underlying low frequency signals intrinsic to power system measurements [39-43]. The traditional Prony analysis computes the roots of a polynomial to determine the modal frequencies of a signal. These characteristic polynomials are associated with a discrete linear prediction model (LPM) which are used to fit the observed measurements. In the matrix pencil technique, a singular value decomposition is performed on a Hankel matrix, after which the eigenvalues and other modal parameters are obtained. One of the advantages of this method is its tolerance to the presence of noise in the observed measurements. A nonlinear least squares optimization method, which encapsulates the linear variables into nonlinear variables, is used by the variable projection method (VPM) to simultaneously estimate all the modal parameters. However, [44] showed that the initial modes provided by the matrix pencil method are usually sufficient. Also, a fast method of dynamic mode decomposition was proposed in [43] for off-line and on-line simultaneous processing of multiple time-series signals.

Though the above-mentioned modal techniques are able to estimate the modal contents of power system oscillatory disturbance data, the focus of this work is not to dwell on the chosen method used to identify these low frequency signals in power system measurements. Rather, the objective of this work is to demonstrate how wide-area visualizations, different from other visualization techniques [45-49], can be used to convey holistic system dynamics to control center personnel. A power systems simulation software, PowerWorld simulator, is used to demonstrate the proposed wide area visualization techniques.

5.2 Wide-Area Visualization of Modal Information

Synthetic networks on which oscillation results are presented are based on pre-existing, one-line diagrams which have been over laid on a geographical map of the United States. In addition to the use of contour plots, dynamic data are visualized using geographical data views (GDVs), which are implemented as part of an information layering technique to present large amounts of data [50-52].

5.2.1 Quality Estimation of Modal Analysis Technique

The desire is to approximate as closely as possible each original signal using the signals from (5.1). However, the few dominant system modes are not sufficient to fully represent the original signal and other dynamics in the system. The quality of the mode estimation process is thus measured in terms of the difference between the original and reconstructed signal.

Fig. 5.1 shows the actual (blue), reproduced (red) frequency signals and the CFs (cost functions or mismatch errors, ε) at nine different buses in a 2,000-bus network. Here, the case involves a 10-second transient stability simulation of the system during which two generators are disconnected after one second.

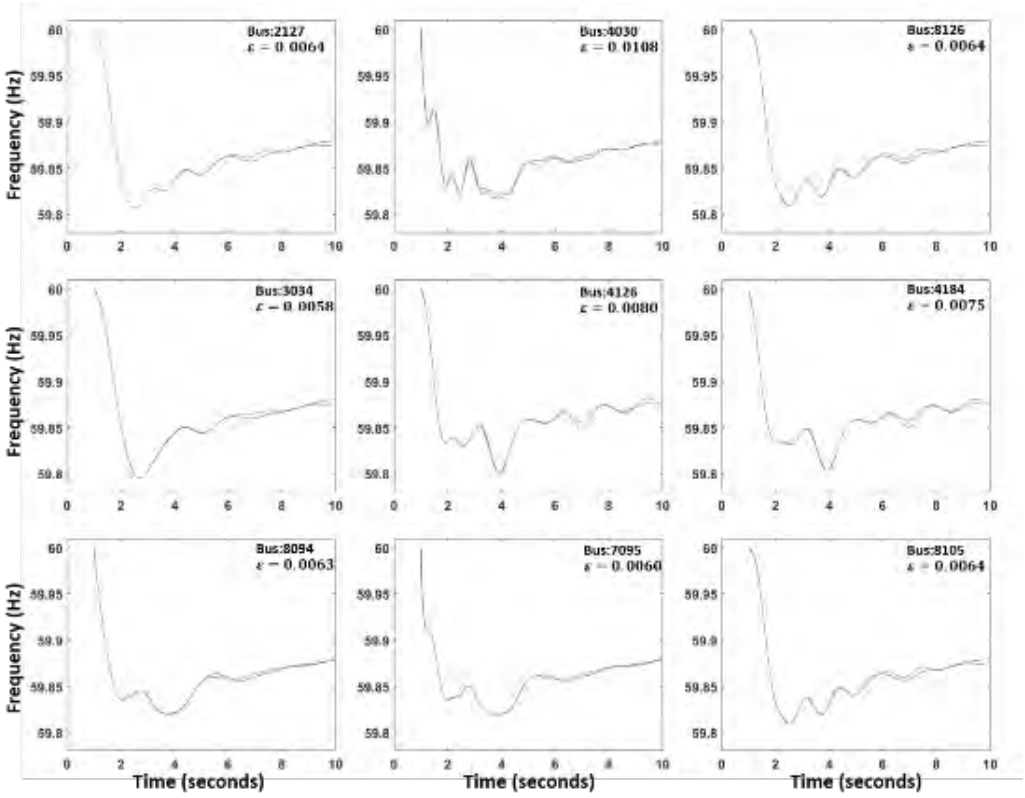

Fig. 5.1. The cost functions, actual and reproduced frequency signals at 9 locations

Using the definition in (5.2), the computed best and worst case cost functions are 0.0058 and 0.0108 respectively, and which were observed at bus IDs, 3034 and 4030, respectively. However, relatively low values of the extreme CF quantities indicate the good matching ability of the proposed technique. The wide-area trend of the CF is shown in Fig. 5.2.

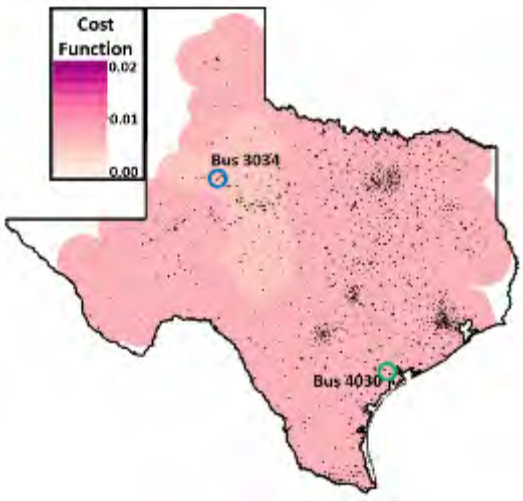

Fig. 5.2. Wide-area system cost function

A color scale has been set arbitrarily [0, 0.02] to indicate the best and worst case matching errors while the signal buses 3034 and 4030 are enclosed by blue and green circles respectively. The uniform variation of the cost function is largely indicative of the global pattern of system frequency, and good quality of the modal technique used for this purpose.

Fig. 5.3 (a) shows the wide-area trend of the CF when modal decomposition was applied on the voltage measurements.

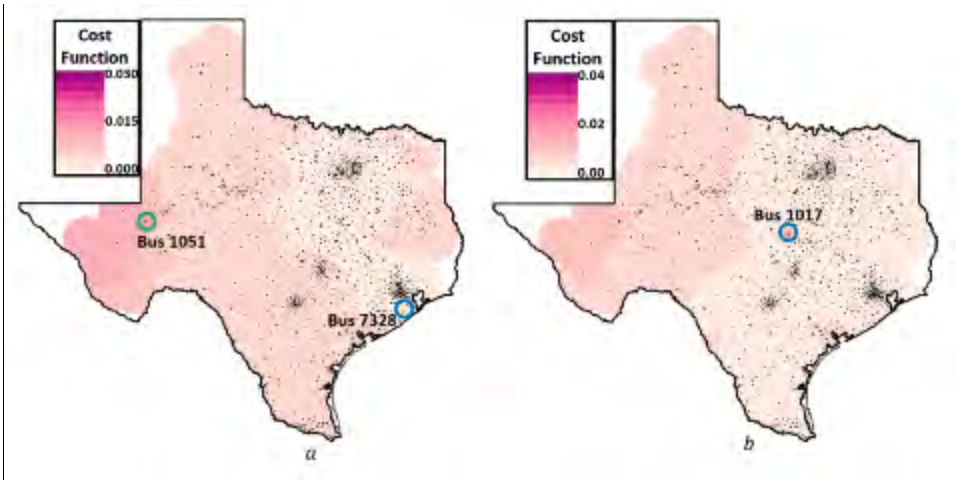

Fig. 5.3. (a)Wide-area cost function using voltage measurements; (b) with noise signal at bus 1017

A wider CF range, [0.0014 0.028] at bus IDs 7328 and 1051 respectively, and more variation in all bus CFs are indicative of the local action of voltage trends observed in the system after the contingent generator outage. This can be attributed to the fact that fewer frequency modes could be prevalent at different bus locations, however they remain invisible to the system. Hence, they are not captured during signal reconstruction.

Another unique case of CF variation that could point to an event, and thus assist operators in understanding the system is when locations report erroneous data deemed to be inconsistent with the actual system trend. Fig. 5.3(b) is the wide-area CF when noisy data is reported by a PMU device at bus location 1017. High CF at an isolated bus location indicates a prevailing, anomaly condition, and especially when nearby buses have much lower CF values.

5.2.2 Oscillation Modes

The mode shape describes the relative activity of the state within an oscillation mode. Comprising of both magnitude and angle information, this vectoral attribute can be a distraction source when visualizing individual signal mode shape information in a wide area network.

Fig. 5.4 shows the current phasor technique used to view mode shapes in different sections of the power system [15, 49, 53]. Mode shapes at twenty different bus locations (a to t) are currently being displayed.

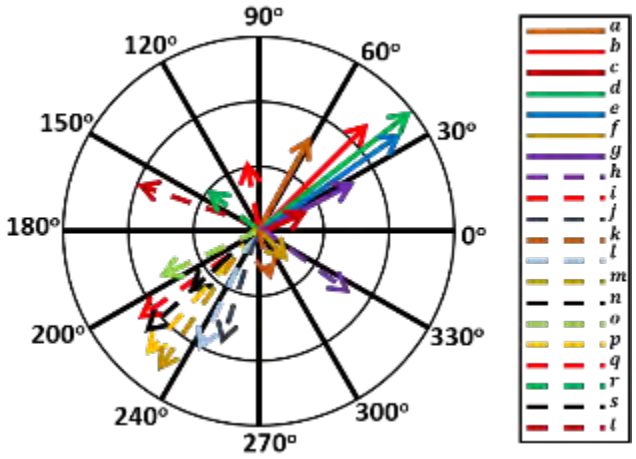

Fig. 5.4 Phasor vector plot of mode shapes at 20 bus locations

Using this method, the figure is able to capture the relative magnitudes and angles at the different buses. However, as mode vectors align in the same direction, and vector magnitudes become equal, the occurrence of significant vector overlaps result in the inability to distinguish among the mode shapes at the different buses. Most importantly, extracting the underlying system dynamics information from the phasor diagram is challenging without the use of an actual geographic map.

Vector Field Visualization

The vectoral characteristics of all bus mode shape information makes them amenable to being represented as two-dimension (2D) vector fields on geographical-based, one-line diagram of the system [50, 54, 55]. Among the different forms for vector field visualization in 2D surfaces, the choice of using arrow icons on a rectangular grid (GRID) vector field visualization is predicated on its ability to convey a sense of bus swing direction at any of the grid regions. This information is more critical to an operator rather than, for example, the short time it may take an operator to identify a critical point on the vector field if line-integral convolution (LIC) were used [55]. In addition, the GRID method has the ability to help users identify critical points within local neighborhoods on the vector field, which could indicate locations in need of attention. For example, the arrows forming the boundary of the green-colored, contour region of the grid indicates the extent of bus inclusions in the two-area swing of the system.

Based on the highlighted benefits of using 2D vector fields, a more effective, wide-area visualization is implemented to address the challenges faced by the phasor plot. This technique makes use of the attributes of glyph objects (phasor arrows) which are geographically-distributed on the one-line diagram to capture mode activities at all the individual buses. As a layering option, contour plots which encode other bus or area information (e.g. the direction of swing) are set in the background to provide more system dynamics that might not be fully captured by the mode vectors. Fig. 5.5(a) and (b) show mode shape information for an inter-area mode (0.541 Hz) and a local mode (3.576 Hz) using the frequency measurements obtained from the 2,000-bus case during two different simulations. All signal amplitudes have been scaled by their standard deviation values.

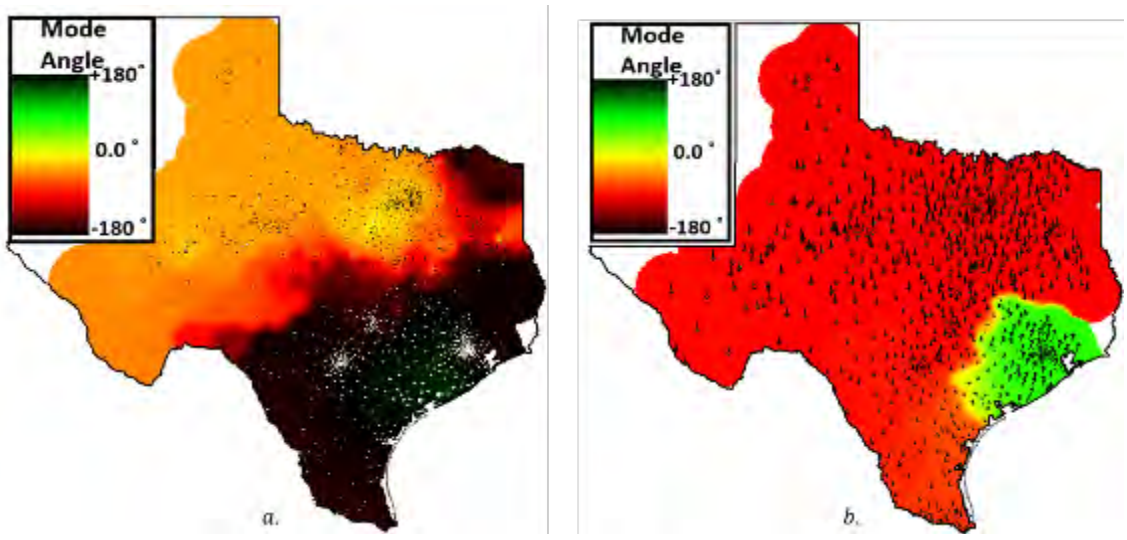

Fig. 5.5. Frequency mode shape for (a) local, and (b) inter-area modes

Abrupt change in colored contours between angle limits, -180˚ and 180˚, are often misleading since in actual geometry both angles are exact. To avoid this sudden color change, a circular (or cyclic) color map, which assigns the same or similar colors to angular values close to these limits, has been used. The color map used to highlight the mode angles at different signal bus locations provides a user with a wide-area summary of the swing direction at the different buses. Individual bus signal amplitude and angle are encoded in the size and orientation of the phasor arrow relative to the positive x-axis respectively. The geographical information of each bus is used to set the location of its GDV-based arrow. The inter-area oscillation in Fig. 5.5(b) shows two marked distinct areas, such that buses in these regions have a similar direction of swing for the oscillation mode. A comparison of the arrow lengths indicates the lower level of mode activity in the local mode of Fig. 5.5(a) than the inter-area oscillation in Fig. 5.5(b).

5.3 Visualization of Oscillation Sources

Sustained oscillations pose a threat to the safe and secure state of the system, and it is important to identify oscillation sources in order to eliminate them. An energy-based method [56, 57] is used for locating the source of oscillation by computing several dissipating energy (DE) coefficients associated with oscillation energy flowing across different transmission lines in the network. In large, inter-connected systems, a wide-area visualization of branch energy flows becomes critical for users to reliably point to disturbance sources by tracking the directions and magnitudes of DE flow arrows. The derivations of the DE_{ij} factor for any transmission line connecting bus i and j, are given in [56, 57].

The direction of oscillation is dictated by the sign of DE_{ij} – negative sign indicating energy production from a source to the network element dissipating the energy. In a wide-area visualization sense, computed DE coefficients can then be aggregated at each bus to show the net contribution to oscillation energy in the network.

A demonstration of the oscillation energy flow in the detection of an oscillation source is carried out for a 2,000-bus case, whereby one of the system generators is set to negative damping and a 500-kV line is outaged. A 3.576 Hz local mode, with a negative damping of -0.06, is identified in the system, and indicative of a sustained system oscillation. Using the measurements (frequency and voltage at all buses, and real and imaginary power flows across all transmission lines) obtained for this mode, the energy-based approach is used to track the source of disturbance in the system.

Fig. 5.6 shows the time-evolution oscillation energy and computed DE coefficient for all branches in the network.

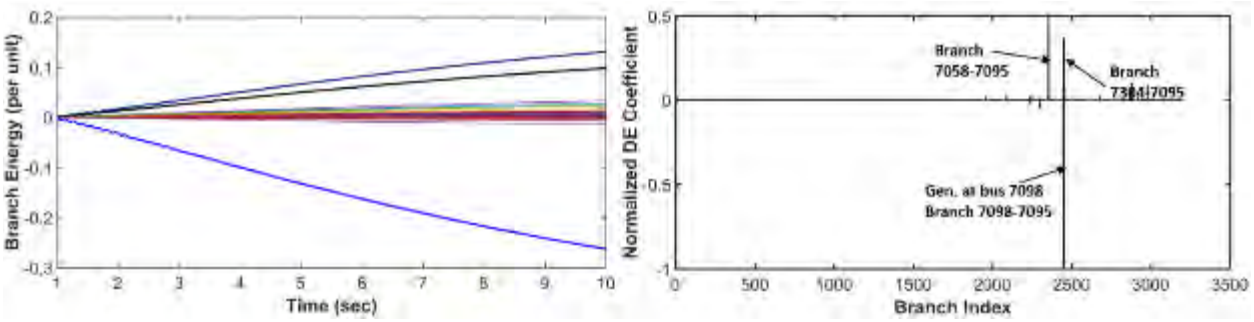

Fig. 5.6. Local oscillation - All branch oscillation energies and dissipating energy (DE) coefficients

The increasing, outward flow of oscillation energy on the branch connected to bus 7098 is due to the negative damped response of the generator at the node, which is supported by the computed DE value. Relatively few transmission lines are involved in the flow of oscillation energy. Using size and color attributes of GDV-based, ovals to encode bus DE magnitude and direction of flow of the oscillation energy respectively, Fig. 5.7 is able to quickly convey to a user the source of oscillation. Constant generation of oscillation energy is a result of the negative damping which was set on the generator machine. An informed, control decision (e.g. disconnect the generator from the system) can then be taken.

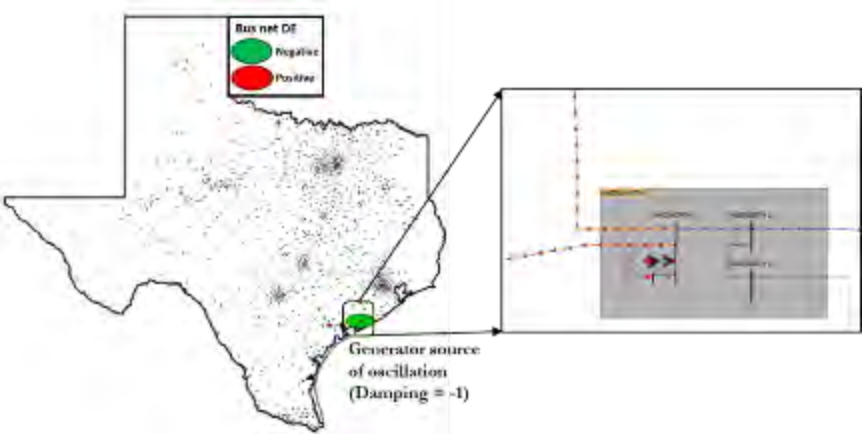

Fig. 5.7. Local oscillation - Oscillation source and branch DE flow

Inter-area oscillations are more complex than local oscillations, as it involves a higher participation of majority of the system transmission lines, buses and substations. Several research works are still being performed to understand this type of oscillation. An example wide-area visualization of an inter-area mode is shown in Fig. 5.8, and is based on the computed oscillation energies and branch DE values in Fig. 5.9.

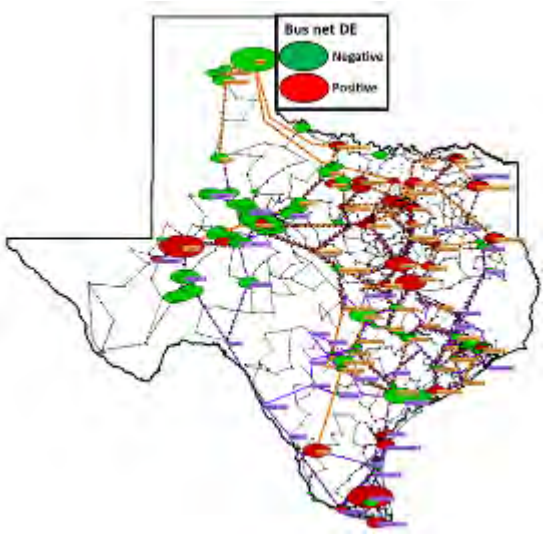

Fig. 5.8. Inter-area oscillation - Oscillation source and branch DE flow

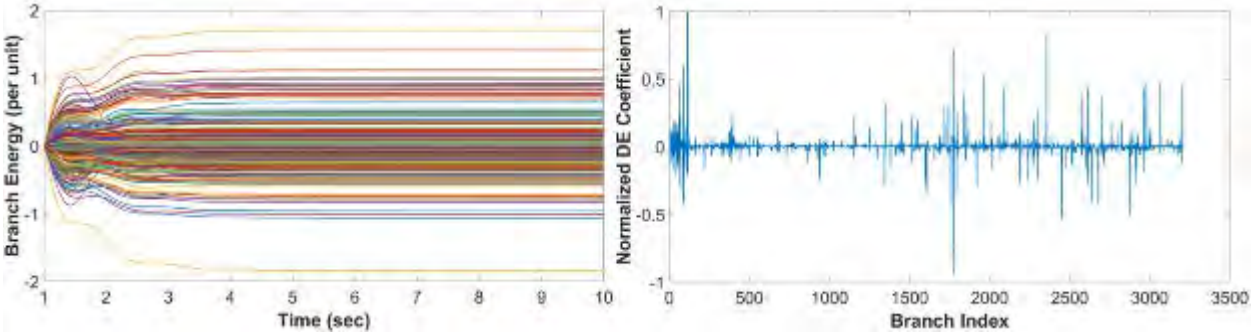

Fig. 5.9. Inter-area oscillation - All branch oscillation energies and dissipating energy (DE) coefficients

6. Conclusions

In this report, data errors in PMU and other synchrophasor devices which cause some of the data quality issues associated with synchrophasor data are discussed. Error mechanisms pertaining to the unique time stamping and synchronization operation of the devices are presented as time error propagation models in order to understand the evolution of different time errors. Furthermore, prototype data errors which manifest these timing inconsistencies are then synthesized.

As power systems increase in scale and components, spatio-temporal correlations among bus measurements become more complex. A distributed analysis technique, supported by density-based clustering technique, is proposed for use in the error assessment of phasor data measurements obtained from buses in a 2,000-bus, large-scale synthetic network. Generated results are observed to better reflect the true quality state of grid phasor measurements than when a central error analysis, which considers all the measurements, is performed.

Given that large amounts of data are generated and transmitted to control centers, a method to present computed error metrics information for a large-scale system using multidimensional analysis scaling visualization is proposed. The method provides a visual, comparative assessment of measurement errors at different buses in the system.

Finally, as a demonstration of some of the new techniques that are currently being implemented in PowerWorld simulator, wide area visualization methods are used to show how system-based, large-scale grid oscillation results can be presented to Engineers in a holistic manner. These methods are used to capture overall system state and dynamics for improved decision making.

Appendix A

Synthetic 2000-bus Texas Network

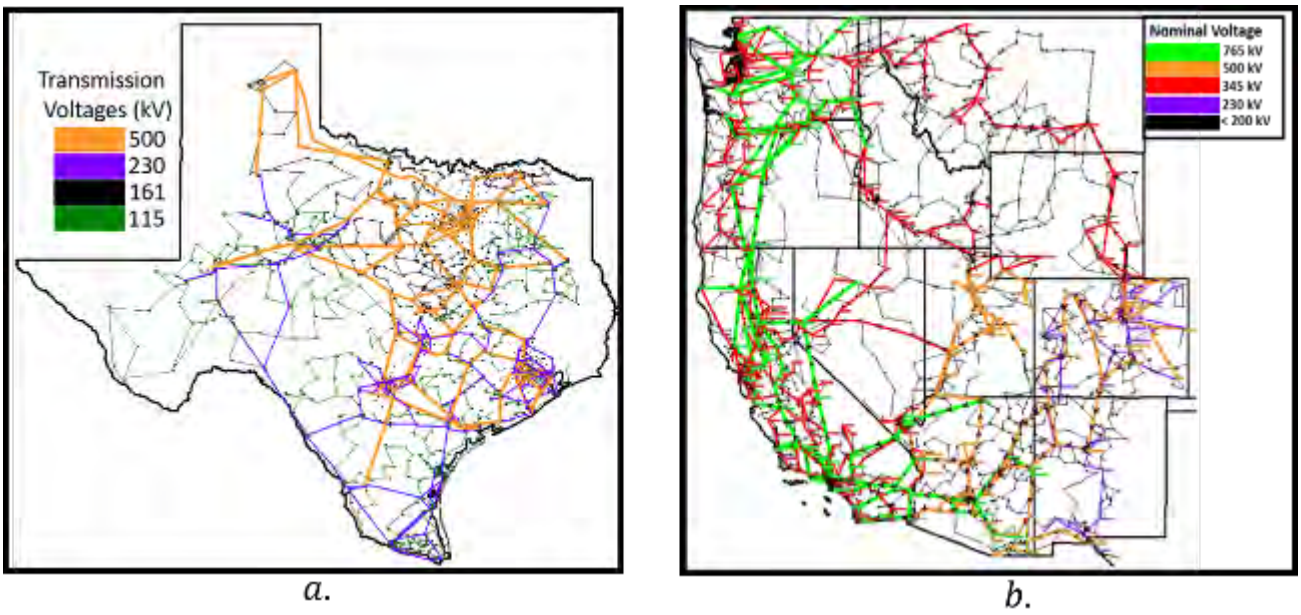

Fig. A-1. (a) 2,000-bus network (b) 10,000-bus network

The 2,000- and 10,000-bus networks are artificially-created grids covering the geographical space of the state of Texas, and the interconnected grid of Western U.S. respectively. Relevant details used for this work are shown in Table A-1.

Table A-1. Network Information

	2,000-bus	10,000-bus
# of substations	1,250	4,762
# of generators	432	1,937
# of transmission lines	3,209	12,706
Operating frequency	60 Hz	
PMU report rate	30 samples/ second	

Appendix B

Computing Local Outlier Factor (LOF)

Given objects $p, o \in D, o' \in D\backslash\{p\}$; D= Total space; p = Object of interest ; $k, MinPts > 0$

Step 1. Compute k-distance, $k\text{-}dist(p)$

$$k\text{-}dist(p) = d(p,o); \begin{cases} d(p,o') \leq d(p,o); for\ at\ least\ k\ objects \\ d(p,o') \leq d(p,o);\ for\ at\ most\ (k-1)\ objects \end{cases}$$

Step 2. Compile k-nearest neighbors, $N_{k-dist}(p)$

$$N_{k-dist}(p) = o \in D\backslash\{p\}; d(p,o) \leq k\text{-}dist(p)$$

Step 3. Compute reachability distance, $reach\text{-}dist_k(p,o)$

$$reach\text{-}dist_k(p,o) = \max(k - dist(o), d(p,o))$$

Step 4. Compute reachability density , $lrd_{MinPts}(p)$

$$lrd_{MinPts}(p) = 1 \Big/ \left[\frac{\sum_{o \in N_{MinPts(p)}} reach - dist_{MinPts}(p,o)}{|N_{MinPts}(p)|} \right]$$

Step 5. Compute local outlier factor, $LOF_{MinPts}(p)$

$$lrd_{MinPts}(p) = 1 \Big/ \left[\frac{\sum_{o \in N_{MinPts(p)}} reach - dist_{MinPts}(p,o)}{|N_{MinPts}(p)|} \right]$$

A small LOF value (~ 1.0) is indicative of a high density neighborhood around an object. Large LOF values are associated with a sparse neighborhood, and typical of an outlier object [10]. For this work, k and $MinPts$ parameters are set to both equal 50% of the total measurements (or objects) in the dataset being considered.

References

[1] A. Silverstein. Synchrophasors and the grid [Online]. Available: https://www.energy.gov/sites/prod/files/2017/09/f36/2_Modern%20Grid-networked%20Measurement%20and%20Monitoring%20Panel%20-%20Alison%20Silverstein%2C%20NASPI.pdf

[2] A. G. Phadke, "Synchronized phasor measurements in power systems," *IEEE Computer Applications in Power,* vol. 6, no. 2, pp. 10-15, 1993.

[3] J. Zhao, L. Zhan, Y. Liu, H. Qi, J. R. Garcia, and P. D. Ewing, "Measurement accuracy limitation analysis on synchrophasors," in *2015 IEEE Power & Energy Society General Meeting*, 2015, pp. 1-5.

[4] M. Brown, M. Biswal, S. Brahma, S. J. Ranade, and H. Cao, "Characterizing and quantifying noise in PMU data," in *2016 IEEE Power and Energy Society General Meeting (PESGM)*, 2016, pp. 1-5.

[5] D. Macii, D. Fontanelli, G. Barchi, and D. Petri, "Impact of Acquisition Wideband Noise on Synchrophasor Measurements: A Design Perspective," *IEEE Transactions on Instrumentation and Measurement,* vol. 65, no. 10, pp. 2244-2253, 2016.

[6] Q. Zhang, V. Vittal, G. Heydt, Y. Chakhchoukh, N. Logic, and S. Sturgill, "The time skew problem in PMU measurements," in *2012 IEEE Power and Energy Society General Meeting*, 2012, pp. 1-6.

[7] T. Bi, J. Guo, K. Xu, L. Zhang, and Q. Yang, "The Impact of Time Synchronization Deviation on the Performance of Synchrophasor Measurements and Wide Area Damping Control," *IEEE Transactions on Smart Grid,* vol. 8, no. 4, pp. 1545-1552, 2017.

[8] D. P. Shepard, T. E. Humphreys, and A. A. Fansler, "Evaluation of the vulnerability of phasor measurement units to GPS spoofing attacks," *International Journal of Critical Infrastructure Protection,* vol. 5, no. 3-4, pp. 146-153, 2012.

[9] X. Jiang, J. Zhang, B. J. Harding, J. J. Makela, and A. D. Domı´nguez-Garcı´a, "Spoofing GPS Receiver Clock Offset of Phasor Measurement Units," *IEEE Transactions on Power Systems,* vol. 28, no. 3, pp. 3253-3262, 2013.

[10] C. Huang *et al.*, "Data quality issues for synchrophasor applications Part I: a review," *Journal of Modern Power Systems and Clean Energy,* vol. 4, no. 3, pp. 342-352, 2016.

[11] P. Kansal and A. Bose, "Bandwidth and latency requirements for smart transmission grid applications," in *2013 IEEE Power & Energy Society General Meeting*, 2013, pp. 1-1.

[12] M. Asprou and E. Kyriakides, "The effect of time-delayed measurements on a PMU-based state estimator," in *2015 IEEE Eindhoven PowerTech*, 2015, pp. 1-6.

[13] J. D. Taft, "Grid architecture 2," Pacific Northwest National Laboratory (PNNL), Richland, WA (United States)2016.

[14] D. Novosel, V. Madani, B. Bhargave, K. Vu, and J. Cole, "Dawn of the grid synchronization," *IEEE Power and Energy Magazine,* vol. 6, no. 1, pp. 49-60, 2008.

[15] D. Trudnowski. Properties of the Dominant Inter-Area Modes in the WECC Interconnect [Online]. Available: https://www.wecc.biz/Reliability/WECCmodesPaper130113Trudnowski.pdf

[16] NERC, "Reliability guideline - forced oscillation monitoring & mitigation," 2017.

[17] E. National Academies of Sciences and Medicine, *Enhancing the Resilience of the Nation's Electricity System*. National Academies Press, 2017.

[18] P. Simulator, "PowerWorld Corporation," ed: October, 2005.

[19] P. NASPI, "PMU Data Quality: A Framework for the Attributes of PMU Data Quality and Quality Impacts to Synchrophasor Applications," 2017.
[20] I. Idehen, Z. Mao, and T. Overbye, "An emulation environment for prototyping PMU data errors," in *2016 North American Power Symposium (NAPS)*, 2016, pp. 1-6.
[21] Q. F. Zhang and V. M. Venkatasubramanian, "Synchrophasor time skew: Formulation, detection and correction," in *2014 North American Power Symposium (NAPS)*, 2014, pp. 1-6.
[22] "IEEE Standard for Synchrophasor Data Transfer for Power Systems," *IEEE Std C37.118.2-2011 (Revision of IEEE Std C37.118-2005),* pp. 1-53, 2011.
[23] A. B. Birchfield, T. Xu, and T. J. Overbye, "Power Flow Convergence and Reactive Power Planning in the Creation of Large Synthetic Grids," *IEEE Transactions on Power Systems,* pp. 1-1, 2018.
[24] Z. Wang, A. Scaglione, and R. J. Thomas, "Generating Statistically Correct Random Topologies for Testing Smart Grid Communication and Control Networks," *IEEE Transactions on Smart Grid,* vol. 1, no. 1, pp. 28-39, 2010.
[25] E. Cotilla-Sanchez, P. D. H. Hines, C. Barrows, and S. Blumsack, "Comparing the Topological and Electrical Structure of the North American Electric Power Infrastructure," *IEEE Systems Journal,* vol. 6, no. 4, pp. 616-626, 2012.
[26] G. A. Pagani and M. Aiello, "The power grid as a complex network: a survey," *Physica A: Statistical Mechanics and its Applications,* vol. 392, no. 11, pp. 2688-2700, 2013.
[27] ECEN. Electric Grid Test Case Repository [Online]. Available: https://electricgrids.engr.tamu.edu/electric-grid-test-cases/
[28] M. Wu and L. Xie, "Online Detection of Low-Quality Synchrophasor Measurements: A Data-Driven Approach," *IEEE Transactions on Power Systems,* vol. 32, no. 4, pp. 2817-2827, 2017.
[29] I. Idehen and T. Overbye, "A similarity-based PMU error detection technique," in *2017 19th International Conference on Intelligent System Application to Power Systems (ISAP)*, 2017, pp. 1-6.
[30] M. M. Breunig, H.-P. Kriegel, R. T. Ng, and J. Sander, "LOF: identifying density-based local outliers," in *ACM sigmod record*, 2000, vol. 29, no. 2, pp. 93-104: ACM.
[31] J. Shlens, "A tutorial on principal component analysis," *arXiv preprint arXiv:1404.1100,* 2014.
[32] J. MacQueen, "Some methods for classification and analysis of multivariate observations," in *Proceedings of the fifth Berkeley symposium on mathematical statistics and probability*, 1967, vol. 1, no. 14, pp. 281-297: Oakland, CA, USA.
[33] F. Belmudes, D. Ernst, and L. Wehenkel, "Pseudo-Geographical Representations of Power System Buses by Multidimensional Scaling," in *2009 15th International Conference on Intelligent System Applications to Power Systems*, 2009, pp. 1-6.
[34] P. Cuffe and A. Keane, "Visualizing the Electrical Structure of Power Systems," *IEEE Systems Journal,* vol. 11, no. 3, pp. 1810-1821, 2017.
[35] C.-h. Chen, W. K. Härdle, and A. Unwin, *Handbook of data visualization*. Springer Science & Business Media, 2007.
[36] Togerson's Classical MDS Derivation [Online]. Available: http://forrest.psych.unc.edu/teaching/p230/Torgerson.pdf

[37] S.-S. Choi, S.-H. Cha, and C. C. Tappert, "A survey of binary similarity and distance measures," *Journal of Systemics, Cybernetics and Informatics,* vol. 8, no. 1, pp. 43-48, 2010.
[38] NERC. 1996 System Disturbances [Online]. Available: https://www.nerc.com/pa/rrm/ea/System%20Disturbance%20Reports%20DL/1996SystemDisturbance.pdf
[39] J. F. Hauer, "Application of Prony analysis to the determination of modal content and equivalent models for measured power system response," *IEEE Transactions on Power Systems,* vol. 6, no. 3, pp. 1062-1068, 1991.
[40] Y. Hua and T. K. Sarkar, "Matrix pencil method for estimating parameters of exponentially damped/undamped sinusoids in noise," *IEEE Transactions on Acoustics, Speech, and Signal Processing,* vol. 38, no. 5, pp. 814-824, 1990.
[41] L. L. Grant and M. L. Crow, "Comparison of Matrix Pencil and Prony methods for power system modal analysis of noisy signals," in *2011 North American Power Symposium*, 2011, pp. 1-7.
[42] A. R. Borden and B. C. Lesieutre, "Variable Projection Method for Power System Modal Identification," *IEEE Transactions on Power Systems,* vol. 29, no. 6, pp. 2613-2620, 2014.
[43] S. Mohapatra and T. J. Overbye, "Fast modal identification, monitoring, and visualization for large-scale power systems using Dynamic Mode Decomposition," in *2016 Power Systems Computation Conference (PSCC)*, 2016, pp. 1-7.
[44] A. B. Birchfield and T. J. Overbye, "Convergence characteristics of the variable projection method for mode extraction," in *2017 IEEE Texas Power and Energy Conference (TPEC)*, 2017, pp. 1-6.
[45] R. A. Becker, S. G. Eick, and A. R. Wilks, "Visualizing network data," *IEEE Transactions on Visualization and Computer Graphics,* vol. 1, no. 1, pp. 16-28, 1995.
[46] M. J. Laufenberg, "Visualization approaches integrating real-time market data," in *IEEE PES Power Systems Conference and Exposition, 2004.*, 2004, pp. 1550-1555 vol.3.
[47] S. Yan and T. J. Overbye, "Visualizations for power system contingency analysis data," *IEEE Transactions on Power Systems,* vol. 19, no. 4, pp. 1859-1866, 2004.
[48] Y. Zhang *et al.*, "Visualization of wide area measurement information from the FNET system," in *2011 IEEE Power and Energy Society General Meeting*, 2011, pp. 1-8.
[49] J. N. Bank, O. A. Omitaomu, S. J. Fernandez, and Y. Liu, "Extraction and visualization of power system interarea oscillatory modes," in *IEEE PES General Meeting*, 2010, pp. 1-7.
[50] C. Ware, *Information visualization: perception for design*. Elsevier, 2012.
[51] E. R. Tufte, *Envisioning information*. Graphics Press, 1990.
[52] T. J. Overbye, E. M. Rantanen, and S. Judd, "Electric power control center visualization using Geographic Data Views," in *2007 iREP Symposium - Bulk Power System Dynamics and Control - VII. Revitalizing Operational Reliability*, 2007, pp. 1-8.
[53] R. M. Gardner, G. B. Jordan, and Y. Liu, "Wide-Area mode visualization strategy based on FNET measurements," in *2009 IEEE Power & Energy Society General Meeting*, 2009, pp. 1-6.
[54] D. Weiskopf, *Vector Field Visualization*. Springer, 2007.
[55] D. H. Laidlaw *et al.*, "Comparing 2D vector field visualization methods: a user study," *IEEE Transactions on Visualization and Computer Graphics,* vol. 11, no. 1, pp. 59-70, 2005.

[56] L. Chen, Y. Min, and W. Hu, "An energy-based method for location of power system oscillation source," *IEEE Transactions on Power Systems,* vol. 28, no. 2, pp. 828-836, 2013.
[57] S. Maslennikov, B. Wang, and E. Litvinov, "Locating the source of sustained oscillations by using PMU measurements," in *2017 IEEE Power & Energy Society General Meeting*, 2017, pp. 1-5.

Leveraging Conservation Voltage Reduction for Energy Efficiency, Demand Side Control and Voltage Stability Enhancement in Integrated Transmission and Distribution Systems (S-70)

<table>
<tr><td>Summary</td><td>We propose a comprehensive framework that assesses energy saving, demand reduction and stability enhancement potential of conservation voltage reduction (CVR). A new algorithm based on load modeling is developed to assess real-time real/reactive load-reduction effects of CVR. A co-simulation framework for transmission and distribution systems is proposed to investigate the impacts of CVR on voltage stability margins of transmission systems. The identified time-varying load models are integrated into the co-simulation framework to capture CVR effects. The coordination between energy-oriented and stability-oriented CVR will be studied. The mutual impacts between voltage reduction and voltage control of DGs will also be investigated. The combination of these approaches will assist utilities to select feeders to implement voltage reduction, perform cost/benefit analyses, reduce the stress of transmission systems, and improve the operation of integrated transmission and distribution systems.</td></tr>
<tr><td>Research Stem</td><td>System Stem</td></tr>
<tr><td>Academic Team Members</td><td>Project Leader:
Zhaoyu Wang (Iowa State University, wzy@iastate.edu, 515-294-6305)
Team members: Hao Zhu (University of Illinois, haozhu@illinois.edu)
Venkataramana Ajjarapu (Iowa State University, vajjarap@iastate.edu)</td></tr>
<tr><td>Industry Team Members</td><td>Xiaoming Feng (ABB)
Baj Agrawal (APS)
Evangelos Farantatos (EPRI), Parag Mitra (EPRI)
Chaitanya Baone (GE), Suresh Gautam (GE), Santosh Veda (GE)
Liang Min (LLNL)
Edin Habibovic (MISO)
Eduard Muljadi (NREL)
Cuong Nguyen (NYISO)
George Stefopoulos (NYPA)
Jianzhong Tong (PJM)</td></tr>
<tr><td>Project Period</td><td>July 1, 2016 to August 31, 2018</td></tr>
<tr><td>Requested Funding from <u>Base</u> PSERC Budget</td><td>
<table>
<tr><th><u>Budget by Researcher:</u></th><th><u>CY 2016</u></th><th><u>CY 2017</u></th><th><u>Total</u></th></tr>
<tr><td>Zhaoyu Wang</td><td>$40K</td><td>$40K</td><td>$80K</td></tr>
<tr><td>Hao Zhu</td><td>$35K</td><td>$35K</td><td>$70K</td></tr>
<tr><td>Venkataramana Ajjarapu</td><td>$35K</td><td>$35K</td><td>$70K</td></tr>
<tr><td>Total</td><td>$110K</td><td>$110K</td><td>$220K</td></tr>
</table>
</td></tr>
<tr><td>Additional Membership Funding</td><td>N/A</td></tr>
</table>

Project Description: Conservation voltage reduction (CVR) is to lower voltage levels in distribution systems in a controlled manner so as to achieve energy saving and demand reduction. Previous studies show that the cumulative CVR revenue will amount to nearly $1.9 billion between 2013 and 2020 [1-2]. In addition to energy saving and demand reduction, another possible benefit of CVR is the voltage stability enhancement in integrated transmission and distribution systems since reactive load consumption is directly related with voltage. By implementing voltage reduction in distribution systems, the stress of the connected transmission systems can be relaxed, thereby improving the stability of transmission systems. CVR can be considered as a noninvasive approach to provide real power and VAr support to

transmission systems. Utilities have yet to take full advantage of CVR benefits, because of the challenges in quantifying CVR effects and the integration of DGs and new-type loads. The *objective* of this project is to develop a comprehensive CVR assessment framework to assist utilities to identify, validate and exploit the *economical* and *operational* benefits of CVR. The specific goals are listed as follows:

- To assess the real-time CVR effects for both peak-time and permanent voltage reduction, and provide guidance to assist utilities to select feeders to implement CVR;
- To establish a co-simulation framework for integrated transmission and distribution systems, and evaluate the impacts of CVR on voltage stability margins of transmission systems, i.e., degree of voltage reduction vs. reduction of reactive power demand;
- To study the impacts of DGs on CVR through simulations.

We propose a time-varying load modeling method to identify load-to-voltage sensitivities based on robust extended Kalman filter. Real-time load-reduction effects of CVR can be calculated using the identified load models at the feeder level using substation SCADA data. By applying the proposed method, utilities can assess load-reduction effects without performing long-term day on/day off tests. The proposed method can also assess the VAr effects of CVR which are difficult to estimate using existing methods, yet important for maintaining voltage stability. To investigate the voltage stability enhancement in transmission systems by applying CVR to distribution systems, we propose a co-simulation framework that incorporates PSS/E (for power flow calculation of transmission systems) and OpenDSS (for three-phase unbalanced power flow of distribution systems). The identified time-varying load models will be integrated into the simulation framework to capture CVR effects. Sensitivity analysis will be performed to resolve the following questions: (*(1) how CVR can reduce the reactive power demand and improve voltage stability margins in transmission systems, (2) which substations have more influence on CVR-based stability enhancement, and (3) are there any conflicts between load reduction-oriented and stability enhancement-oriented CVR, and how to coordinate the two objectives*. The increasing penetration of DGs has been one of major challenges facing utilities. We will also simulate the impacts of DGs (especially photovoltaic generators) on voltage reduction effects in OpenDSS. The proposed methods will be validated with practical utility data of CVR tests on a variety of feeders available in our previous work [3-4, 10] and/or provided by PSERC industry members.

Potential Benefits: This research will bring about major benefits to utilities, ISOs/RTOs, electricity consumers, and vendors/consultants. Assessing the benefits of CVR has always been a critical issue in strategizing its implementation and performing cost/benefit analyses. Previous CVR assessment methods rely on long-term day on/day off tests that are time consuming, costly, and inaccurate. Using the proposed load modeling-based assessment method, utilities will be able to assess real-time CVR effects without changing substation regulation schemes, greatly facilitating the location of feeders with best CVR benefits. Effects of CVR on transmission systems have not been fully investigated before. Utilities and ISOs/RTOs can use the proposed co-simulation framework to study CVR's impacts on voltage stability margins and take full advantage of both economical and operational benefits. This research will also provide analysis of impacts of DGs on CVR. Electricity consumers can benefit from the reduced energy consumption from CVR. Vendors/consultants may be able to justify the deployment of new technologies for voltage/VAr control (VVC) and CVR.

Expected Outcomes:

- Software algorithms for real-time assessment of CVR effects based on load modeling
- Validations of CVR assessment method based on OpenDSS simulations and real CVR testing data
- Case studies of practical CVR tests for a variety of feeders
- A co-simulation framework for analyzing integrated transmission and distribution systems with voltage reduction at the distribution level

- Analyses and validation of CVR effects on voltage stability enhancement of transmission systems
- Case studies to facilitate better understandings of DGs' impacts on CVR
- Progress reports, and posters and presentations at PSERC IAB meetings to summarize key developments and findings; and a final report that provides detailed descriptions of the proposed methodologies, results and findings of case studies, and conclusions drawn from the project work
- Journal and conference publications based on results of this project

Potential Applications: The potential for future commercialization of real-time CVR benefit assessment and co-simulation of transmission and distribution framework is high. The utilities and regulatory agencies are seeking accurate, reliable and fast techniques to assess economical and operational benefits of CVR. Successful completion of this project will provide great opportunities to allow real-time and overhead-free assessment of load-reduction effects and voltage stability enhancement potential of CVR. This information can be used to assist utilities to select feeders to implement voltage reduction, perform cost/benefit analyses of VVC/CVR programs, reduce the stress of transmission systems, and improve the operation of integrated transmission and distribution systems.

Technical Approach: We propose a comprehensive framework to investigate load-reduction and voltage stability enhancement effects of CVR as well as DGs' impacts on CVR.

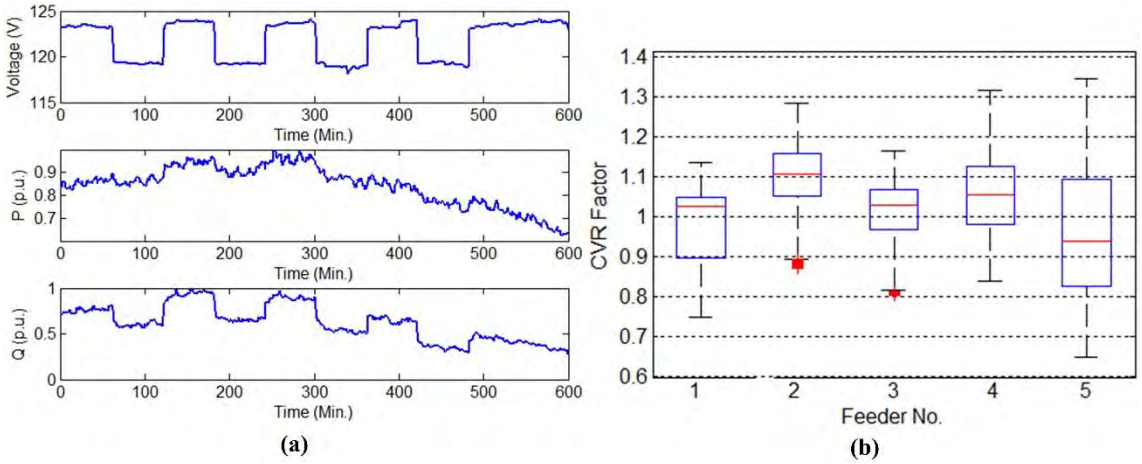

Figure 1: (a) Practical CVR test data, (b) Preliminary results of CVR factors

1. Real-time assessment of load reduction effects.

We propose a load modeling-based method to assess load reduction effects of CVR. The load-reduction effects are evaluated by the conservation voltage reduction factor (*CVRf*), which is the percentage change in load consumptions to 1% change in voltage. Fig. 1 (a) shows a practical hourly on/off test of voltage reduction. We model the load as a function of voltage, i.e., a ZIP (constant impedance, constant current and constant power) model. The ZIP model is selected because it is a widely applied static model to represent load-to-voltage sensitivities (LTI), and can capture the characteristics of many new-type loads which are constant-current or constant-power. Another reason is that ZIP model has been integrated into most distribution analysis software used by industry members. The *CVRf* can be calculated by identifying parameters of the ZIP model in a real-time manner. For example, CVR effects decrease when LTI changes from a constant-impedance type load to a constant-power type. Assume that $a_{1p,t}$, $a_{2p,t}$ and $a_{3p,t}$ represent compositions of constant impedance, constant current, and constant power loads, respectably, and $\hat{a}_{1p,t}$, $\hat{a}_{2p,t}$ and $\hat{a}_{3p,t}$ represent the identified values, we have

$$\begin{aligned} P_{L,t} &= f_p(a_{1p,t}, a_{2p,t}, a_{3p,t}, V_t) = a_{1p,t}V_t^2 + a_{2p,t}V_t + a_{3p,t} \\ Q_{L,t} &= f_q(a_{1q,t}, a_{2q,t}, a_{3q,t}, V_t) = a_{1q,t}V_t^2 + a_{2q,t}V_t + a_{3q,t} \end{aligned} \quad (1)$$

Hence, the *CVRf* can be calculated as (only the active power is shown)

$$CVR_{fp} = \frac{(P_{cvroff} - P_{cvron})/P_{cvroff}}{(V_{cvroff} - V_{cvron})/V_{cvroff}} = \frac{[f_p(\hat{a}_{1p,t}, \hat{a}_{2p,t}, \hat{a}_{3p,t}, V_{cvroff}) - f_p(\hat{a}_{1p,t}, \hat{a}_{2p,t}, \hat{a}_{3p,t}, V_{cvron})]/f_p(\hat{a}_{1p,t}, \hat{a}_{2p,t}, \hat{a}_{3p,t}, V_{cvroff})}{(V_{cvroff} - V_{cvron})/V_{cvroff}} \quad (2)$$

Fig. 1 (b) shows preliminary results of real-power CVR factors of five utility feeders in our previous research. It can be seen from the figure that for 1% voltage reduction, the real power reduction of the five feeders is 0.65-1.35%. To increase parameter identification accuracy and better deal with measurement noises and bad data, we propose to perform the real-time identification by using a robust extended Kalman filter to improve our previous work. Since different load characteristics may exist in different phases of a distribution system, we will perform the load modeling on a per-phase basis. The proposed assessment method will be applied to investigate CVR effects for various types of loads, e.g., residential, commercial, industrial and motor-type loads.

2. Co-simulation of transmission and distribution systems with CVR.

The active and reactive load consumption of a power distribution system can be reduced through CVR, which can serve as a support to the voltage stability of a transmission system. It can be seen from Fig. 1 (a) that reactive power consumption is normally directly related with voltage levels, and CVR is expected to reduce the VAr drawn from transmission systems, which can improve the voltage stability margin. To investigate and quantify the stability enhancement potential of CVR, we propose a co-simulation framework as shown in Fig. 2. The integrated transmission and distribution network is divided into three systems: transmission system, boundary system, and distribution systems. X_T, X_B, and X_D represent states of transmission, boundary and distribution systems, respectively. S_T, S_B, and S_D represent the power flow in transmission, boundary and distribution systems, respectively. The basic idea is to make the boundary variables converged through iterations. After the power flow is converged, we can evaluate the loadability margin by continuous power flow or coupled single-port method where the PIs have made significant contributions [6-8]. The voltage stability enhancement potential of CVR is heavily dependent on load characteristics. Since the load behaviors are time-varying, we will evaluate the loadability margin for each time stamp. A transmission system is connected by multiple distribution systems. The load characteristics and locations of distribution systems affect the voltage stability enhancement potential of CVR. A substation with the highest *CVRf* may not make the most contribution to the voltage enhancement. We will perform sensitivity analyses to investigate the voltage stability enhancement potential of each substation and the relationship between the load reduction-oriented and the stability enhancement-oriented CVR. A multi-objective optimization formulation can be developed to find the optimal voltage reduction levels at substations to coordinate these two key aspects of CVR.

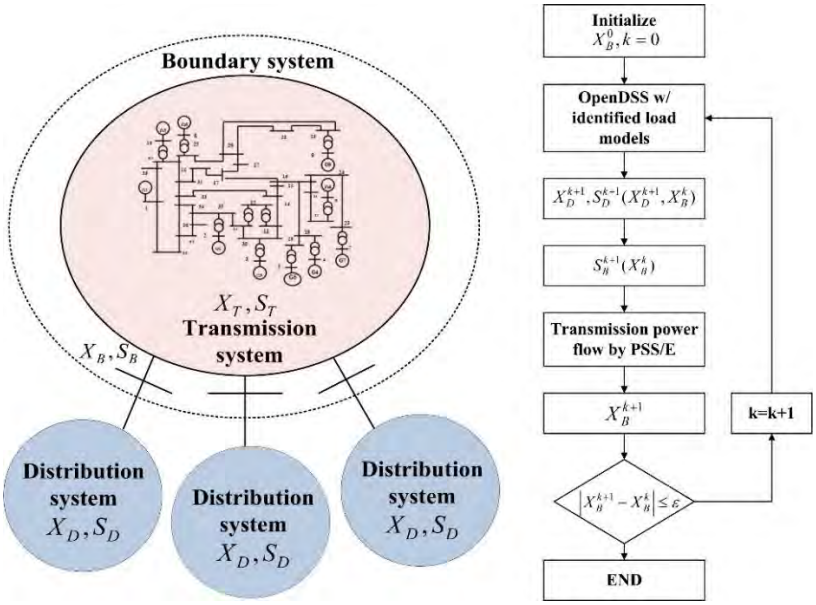

Figure 2: Co-simulation framework of transmission and distribution systems

3. Impacts of DGs on CVR.

The implementation of CVR requires a relatively flat voltage profile along the feeder. However, the power injection of renewable DGs can lead to voltage fluctuations. By lowering feeder voltage, CVR may be in conflict with DG's voltage regulation control. This research will investigate the impacts of photovoltaic generators (PVs) on voltage reduction. We plan to perform the following case studies to better understand how the volatile outputs of PVs could affect CVR implementations and how to coordinate inverter-based VVC and voltage reduction: 1) Different levels of PV penetration, e.g., 10% to 100%, 2) Different locations of PVs, 3) Different power factors of PV inverters, 4) Transient cloud movement over PV panels, and 5) mutual impacts of CVR and DG's voltage regulation control. The PIs have contributed to one of the pioneering work on this topic [9], by investigating the effects of DG placement on CVR. Motivated by this work, we propose to integrate the identified real-time load model in Thrust 1 into OpenDSS, in order to study the effects of stochastic PV outputs using e.g., Monte-Carlo simulations and/or dynamic system reliability analysis tools.

Work Plan:

Task 1: Literature search and survey of the state of the art and industry practice. (Wang; Zhu; Ajjarapu)
Task 2: Development of load modeling-based real-time CVR assessment method. (Wang; Zhu)
Task 3: Development of co-optimization framework using PSS/E, PSLF, and OpenDSS. (Wang; Ajjarapu)
Task 4: Validating assessment algorithms on simulation data and real CVR testing data. (Wang; Zhu)
Task 5: Sensitivity analysis to investigate the impacts of CVR on voltage stability margin and the coordination between energy-oriented and stability-oriented CVR. (Ajjarapu)
Task 6: Investigation of DGs effects on CVR in OpenDSS. (Zhu)
Task 7: Reporting, computer demonstrations and publications. (Wang; Zhu; Ajjarapu)

Tasks	06/16-09/16	10/16-12/16	01/17-03/17	04/17-06/17	07/17-09/17	10/17-12/17	01/18-03/18	04/18-08/18
T1								
T2								
T3								
T4								
T5								

T6								
T7								

Work Supported by Additional Membership Funds: N/A

Related Work: Previous CVR assessment methodologies can be mainly classified into two categories: comparison-based methods [5] and regression-based methods [3]. Both methods estimate what the load would be if there was no CVR and require long-term day on/day off tests. The concept of use of load modeling for assessing CVR effects in real time is relatively new and PIs have made substantial contributions in this area [4]. This project is an extension of our previous work with more accurate load models and robust identification algorithms. Therefore, the proposed project will benefit from the prior work, which was tested on realistic utility data. The proposed work will be validated on a number of PSERC industry members test systems. Investigating CVR's impacts on transmission system voltage stability is a new topic that will further justify benefits of CVR. PIs are actively working in voltage stability area [6-8] and this knowledge can be applied to study the impact of CVR on voltage stability. The study of DG's impacts on CVR is also a new topic. PIs have investigated the coordination of DG planning and CVR [9], which is helpful to this project.

How this Work Differs from Related Work: Unique contributions of the proposed work are:

- It proposes a comprehensive framework to investigate both the load reduction and voltage stability enhancement potential of CVR. To best of our knowledge, leveraging CVR implementations to improve transmission system operation has not been fully studied before.
- It provides utilities the ability to assess real-time CVR effects without performing day on/day off tests. Compared to existing comparison-based assessment methods which require long-term tests on one or more feeders, the proposed load modeling-based assessment method is more accurate and economical. Compared to our previous work on load modeling-based CVR assessment, the proposed method utilizes ZIP model to better capture load characteristics, does not require model linearization, and is robust to measurement noises and bad data.
- It develops a co-simulation framework to investigate the impacts of CVR on the voltage stability of transmission systems. This framework is able to capture the interactions of transmission and distribution systems.
- It investigates the impacts of DGs on CVR, which has not been thoroughly studied in existing work.

Relationship of this Work to the Research Plan and Topic Areas for this Solicitation: The proposed work addresses critical and timely issues within the topics of "Load modeling" and "System performance-voltage and Vars" among the core areas of the System stem. It also directly responds to the topics of interest indicated by PSERC industry members, including "Conservation voltage reduction: Hardware implementation and quantification of impact," and "Distributed resources and new load effects on conservation voltage reduction." We are not aware of any ongoing PSERC project that addresses similar topics as this proposal.

Collaboration Plan: The project team plans to work seamlessly throughout the project. We will conduct monthly teleconferences among the faculty and student teams. Quarterly teleconferences will be organized for the research team and industry advisors to solicit inputs from industry members and provide them with periodic status reports. The team will maintain day-to-day contact through Skype and emails. We will meet in person at PSERC meetings and PES GM whenever feasible. The lead PI will develop and maintain a website to report project progress. We will work closely and take advantage of the judgment and expertise of the industrial advisors in conducting the case studies of CVR effects.

Potential Conflict of Interest: None

References

[1] Wang, Z.; and J. Wang. “Review on Implementation and Assessment of Conservation Voltage Reduction,” *IEEE Trans. Power Systems*, vol. 29, no. 3, pp. 1306-1315, May 2014.

[2] Navigant Research, “Conservation Voltage Reduction. Available: https://www.navigantresearch.com/research/conservation-voltage-reduction.

[3] Wang, Z.; M. Begovic, and J. Wang. Analysis of Conservation Voltage Reduction Effects Based on Multistage SVR and Stochastic Process. *IEEE Trans. Smart Grid*, vol. 5, no. 1, pp. 431-439, January 2014.

[4] Wang, Z.; and J. Wang. "Time-Varying Stochastic Assessment of Conservation Voltage Reduction Based on Load Modeling," *IEEE Trans. Power Syst*., vol. 29, no. 5, pp. 2321-2328, September 2014.

[5] Krupa, T. J.; and H. Asgeirsson. “The effects of reduced voltage on distribution circuit loads,” *IEEE Trans. Power Syst*., vol. PAS-101, no. 7, pp. 1013-1018, 1987.

[6] Juan, Y.; L. Wenyuan, V. Ajjarapu, Y. Wei, and Z. Xia. "Identification and location of long-term voltage instability based on branch equivalent," *IET Gener. Transm. Distrib*., vol. 8, no. 1, 2014.

[7] Ajjarapu, V.; and C. Christy. "The continuation power flow: a tool for steady state voltage stability analysis," *IEEE Trans. Power Syst*., vol. 7, no. 1, pp. 416-423, February 1992.

[8] Konopinski, R. J.; P. Vijayan, and V. Ajjarapu. "Extended Reactive Capability of DFIG Wind Parks for Enhanced System Performance," *IEEE Trans. Power Syst*., vol. 24, no. 3, pp. 1346-1355, 2009.

[9] Wang, Z.; B. Chen, J. Wang, and M. Begovic. "Stochastic DG Placement for Conservation Voltage Reduction based on M*ultiple* Replications Procedure," *IEEE Trans. Power Deli*., vol. 30, no. 3, pp. 1039-1047, June 2015.

[10] Liu, H. J.; R. Macwan, N. Alexander, and H. Zhu. "A methodology to analyze conservation voltage reduction performance using field test data," *IEEE Intl. Conf. on SmartGridComm*, pp. 529-534, 2014.

Project Status (Status Reports in Reverse Chronological Order)

Project proposed and recommended on December 2015. Project begins in July 2016.

Work progress since Dec 2017

(1) The T&D co-simulation framework is completely developed for steady-state analysis and has been used to investigate the impact of conservation voltage reduction (CVR) on long-term voltage stability margin (VSM). This includes various simulation studies on small and large distribution netowrks with and without distributed generation (DG). It is concluded that the presence of DG does not affect CVR’s effects on the long-term VSM. The conclusions are that considering the detailed modeling of the distribution system for overall system studies is essential, and CVR negatively impacts the VSM of the system.

(2) A fully decentralized method is developed to optimally coordinate the fast-dispatch of photovoltaic (PV) inverters with the slow-dispatch of on-load tap changer (OLTC) and capacitor banks (CBs) for conservation voltage reduction in three-phase unbalanced distribution systems. The trade-off relationship between CVR and power losses is analyzed by the developed multi-weight, multi-objective optimization formulation. The conclusions are that the load reduction due to CVR is dominating for voltage-dependent loads. CVR will lead to less loss reduction compared to the case where loss reduction is optimized. But optimizing power losses only have less aggregate demand reduction at the substation than optimization CVR.

(3) In order to address the challenges of varying dynamics in operating conditions and communication rate in current distribution systems, the dynamics for local voltage/var control (VVC) and hybrid VVC are studied. The impact of droop coefficient and level of dynamics on the performance of local VVC mechanisms is studied. A hybrid VVC scheme is developed which adapts to varying rates of communications and dynamic operating conditions.

Description of work activities and anticipated project outcomes/deliverables by each project team member during next reporting period.

The project is ending in August 2018. The team will prepare a final project report with technical details, results and major findings.

Description of and reasons for any revisions to the current work plan

NA

Conference calls with industry advisors since Dec 2017

We had a conference call with the industry advisors on April 12th, 3 PM CST, to share the results and seek feedback.

Describe other interactions with industry advisors since Dec 2017

There were interactions with PJM regarding the T&D co-simulation interface and the project team will be delivering the co-simulation interface soon to PJM.

Students working on the project

Name	Email Address
Alok Kumar Bharati	alok@iastate.edu
Qianzhi Zhang	qianzhi@iastate.edu
Hao Jan Liu	haoliu6@illiones.edu

New project-related documents or presentations (peer-reviewed papers, conference papers, conference presentations, etc.)

Since Dec 2017, the project team is developing the following papers:

[1] A.K. Bharati et al., "CVR Impact on Transmission System Voltage Stability Margin using T&D Co-Simulation," paper in progress

[2] Q. Zhang et al., "Fully Decentralized Control of PV Inverters with Conventional Voltage Control Devices in a Three-Phase Unbalanced Distribution System," paper in progress

Project Website (if any)

NA

Status Report for the Dec 2017 IAB Meeting

Work progress since May 2017

(1) The team has developed a co-simulation framework using a Python platform with PSSE and GridLAB-D. Case studies have demonstrated the need for using T&D co-simulation to analyze CVR's effects on transmission load margin. The validation of this newly developed co-simulation framework is in progress.

(2) The team has formulated the PV inverters' reactive power control as a distributed optimization problem with parallel computing. The coordination between conventional voltage/Var control devices and inveters is under study.
(3) The team has developed a robust recursive algorithm to identify real-time parameters of composite load models, which could be used to increase the accuracy of CVR effect assessment.
(4) The team has developed a communication-free voltage/Var control algorithm for distributed energy resources (DERs), which can achieve the network-wide optimal voltage regulation performance while relying on only local measurements of voltage magnitude.
(5) The team has proposed a game-theoretic characterization of voltage/Var control with only locally connected communication networks. Existence and uniqueness conditions for the Nash equilibrium of the game are analyzed, followed by the design of a fully distributed equilibrium-learning algorithm with provable convergence guarantees.
(6) The team has proposed a general distribution system management (DSM) framework for dynamic coordination of DERs with a locally connected communication network. Also based on a game-theoretic characterization, the team developed an online projected-gradient-based distributed algorithm to track the Nash equilibrium under dynamic settings.

Description of work activities and anticipated project outcomes/deliverables by each project team member during next reporting period.

(1) Validate the co-Simulation framework with inclusion of DGs in the distribution network and coordinating all distribution system devices that control voltage. Based on the co-simulation framework to investigate the optimal implementation of CVR to achieve benefits for both distribution and transmission sytems.
(2) Invetigate how the CVR effects overall voltage stability of the integrated system
(3) Investigate DGs' impacts on CVR, and coordinate DGs, LTCs, VRs, CAPs, to achieve optimal performance of CVR.
(4) Apply distributed optimization to control DGs to facilitate CVR implementation.
(5) Explore the application of high-performance computing technologies such parallel-computing into distribution voltage/Var optimization to reduce the computational burden.
(6) Perform dynamic temporal distribution system analysis using the developed communication-cognizant DSM schemes to understand the impacts of communication link availability
(7) Investigage the dynamic impacts of DERs and loads on distribution system voltage/Var control

Description of and reasons for any revisions to the current work plan

No revision is anticipated at this stage.

Conference calls with industry advisors since May 2017

We plan to meet advisors at the IAB meeting in December.

Describe other interactions with industry advisors since May 2017

N/A

Students working on the project

Name	Email Address
ALOK KUMAR BHARATI	alok@iastate.edu
QIANZHI ZHANG	qianzhi@iastate.edu
Kaiqing Zhang	kzhang66@illinois.edu

New project-related documents or presentations (peer-reviewed papers, conference papers, conference presentations, etc.)

[1] C. Wang, Z. Wang, J. Wang, and D. Zhao, "Robust Time-Varying Parameter Identification for Composite Load Modeling," IEEE Transactions on Smart Grid, accepted for publication.
[2] S. Madani, Z. Wang, and V. Ajjarapu, "Participation Factor Based CVR for Enhanced Voltage Stability Using Integrated Transmission and Distribution Systems," The 49the North American Power Symposium, Morgantown, WV, September 17-19, 2017.
[3] Bharati, S. Ankit, V. Ajjarapu, and Z. Wang, "Comparison of CVR Impact on Transmission System Load Margin with Aggregated and De-Aggregated Distribution System," The 49the North American Power Symposium, Morgantown, WV, September 17-19, 2017.
[4] K. Zhang and H. Zhu, "A game-theoretic approach for communication-free voltage-var optimization," in *the 5th IEEE Global Conference on Signal and Information Processing (GlobalSIP),* Montréal, CA, Nov. 2017.
[5] K. Zhang, Wei Shi, Hao Zhu, and Tamer Basar, "Distributed equilibrium-learning for power network voltage control with a locally connected communication Network", submitted to 2018 *IEEE American Control Conference (ACC).*
[6] K. Zhang, Wei Shi, Hao Zhu, Emiliano Dall'Anese, and Tamer Basar, "Dynamic power distribution system management with a locally connected communication network", submitted to *IEEE Journal of Selected Topics in Signal Processing.*

Project Website (if any)
N/A

Status Report for the May 2017 IAB Meeting

Work progress since December 2016

1) Development of practical integrated transmission and distribution co-simulation framework by means of providing an interface between transmission and distribution simulators which will be capable of handling co-simulation effectively. Efforts are in progress to build the co-simulation framework with PSSE and GridLAB-D for validation of the findings on the transmission network with aggregated distribution system. The distribution system power flow with CVR was extended to be included into the transmission network (IEEE 9-bus network) to study the impact of CVR on the transmission system voltage stability margin (VSM). Preliminary results are available with aggregated distribution system modeled as ZIP load.
2) Development of a framework in which CVR will be applied aiming at voltage stability improvement. In this framework, a two-stage optimization will be used in order to determine the set point of voltage controllers. In the first stage, the relative share of each distribution system in load change will be determined. Based on the outcome of the first stage, the second stage will calculate the set-point of voltage controllers. The second stage is performed in two timely separated phases based on response-time of voltage controllers with the purpose of reducing switching actions of ULTC/cap banks using fast-response inverters.
3) Assessment of performance and control of inverters as one the fast-response voltage control actuators. In this area, researches have been focused on two topics: i) investigating the effects of system transients on the design of smart inverter control for distribution system voltage regulation; and ii) studying the fundamental performance limits of inverter-based voltage control depending on the communication network topology. Numerical studies have been performed on the first topic and study the choice of droop control slope based on how fast the input dynamics evolves. As well, some theoretical results to characterize the best solutions for given communication topology has been obtained.

Description of work activities and anticipated project outcomes/deliverables by each project team member during next reporting period.

1) Study of impact of CVR with various levels of DG penetration on the load margin (VSM) modeled as an aggregated distribution system.
2) Development of the co-simulation framework for integration of PSSE and GridLAB-D to validate the observations with the aggregated distribution system.
3) Development of two-stage optimization scheme for CVR implementation considering voltage stability of transmission systems.
4) Study of the interactions among various voltage control mechanisms (CVR, LTC transformer, and smart inverter control) under different levels of DG penetration.

Description of and reasons for any revisions to the current work plan
The current work plan is to use the PSSE software or transmission network studies in place of Matpower due to PSSE's scalability to large transmission systems. This plan is being evaluated for complexity and integrity of the timescales while co-simulation. It is ideal to consider a more realistic transmission and distribution grid for accurate results, but there is a need to build an interfacing software between the tools to implement the same whose architecture is developed.

Conference calls with industry advisors since December 2016
We plan to meet advisors at the IAB meeting in May.

Describe other interactions with industry advisors since December 2016
N/A

Students working on the project

Name	Email Address
Alok Kumar Bharati	alok@iastate.edu
Kaiqing Zhang	kzhang6@illinois.edu
Seyed Sohail Madani	madani@iastate.edu

New project-related documents or presentations (peer-reviewed papers, conference papers, conference presentations, etc.)

[1] J. Zhao, Z. Wang, and J. Wang, "Robust Time-Varying Load Modeling for Conservation Voltage Reduction Assessment," IEEE Transactions on Smart Grid, accepted for publication.
[2] Z. Wang, B. Cui, and J. Wang, "A Necessary Condition for Power Flow Insolvability in Power Distribution Systems with Distributed Generators," IEEE Transactions on Power Systems, accepted for publication.
[3] H. Zhu, "Communication-cognizant hybrid voltage control for power distribution systems," presented at the INFORMS Computing Society (ICS) Conference, Jan 2017.
[4] H. Zhu, "Communication-cognizant distribution system management," presented at *the Intl. Conference on Future Electric Power Systems and the Energy Transition*, Feb 2017.

Project Website
None.

S-70 Status Report for the December 2016 IAB Meeting

Work progress since July 2016
Time-varying ZIP models are used to assess CVR effects. A robust recursive least square-based algorithm has been developed to identify ZIP models and quantify CVR factors in real-time using both simulated and practical data. Simulations and sensitivity analyses on CVR's potential in improving voltage stability margin have been conducted using IEEE 34-node test feeders.

List of Work Plan tasks completed:
T1: Literature search and survey of the state of the art and industry practice.
T2: Development of load modeling-based real-time CVR assessment method.
T4: Validating assessment algorithms on simulation data and real CVR testing data.
Partial T7: A transaction paper is under second round review.

Description of work activities and anticipated project outcomes/deliverables by each project team member during next reporting period

1) Z.Wang will continue to refine the developed load modeling-based real-time CVR assessment method, and characterize the statistics of CVR factors.
2) V. Ajjarapu and Z. Wang will investigate CVR's impacts on voltage stability margin and develop a T&D co-simulation framework.
3) H. Zhu will investigate DGs' effects on CVR.

It is expected that more simulation results and two more papers will be delivered in next reporting period.

Description of and reasons for any revisions to the current work project
N/A

Conference calls with industry advisors since July 2016
One conference call with industry advisors.

Please describe any other interactions with industry advisors since July 2016
On 10/06/16, visited with MidAmerican Energy (ISU EPRC member and local utility) to discuss ongoing research within our department. This PSERC project is one they are interested in the outcomes.

Students working on the project
Ankit Singhal, Yanda Jiang, and Max Liu

New project-related documents or presentations (peer-reviewed papers, conference papers, conference presentations, etc.)
One paper on IEEE Transactions on Smart Grid is under the second round review.

Project website (if any)
N/A

Monitoring and Maintaining Limits of Area Transfers with PMUs

Final Project Report

S-64

Power Systems Engineering Research Center
Empowering Minds to Engineer
the Future Electric Energy System

Monitoring and Maintaining Limits of Area Transfers with PMUs

Final Project Report

Project Team
Ian Dobson, Project Leader
Iowa State University

Marija Ilic
Carnegie Mellon University

Graduate Student
Vikram Kumar Reddy Chiluka
Iowa State University

Stefanos Baros
Nipun Popli
Carnegie Mellon University

PSERC Publication 19-1

January 2019

For information about this project, contact
Ian Dobson
Iowa State University
ECpE Department
Ames IA 50011 USA
dobson@iastate.edu

Power Systems Engineering Research Center

The Power Systems Engineering Research Center (PSERC) is a multi-university Center conducting research on challenges facing the electric power industry and educating the next generation of power engineers. More information about PSERC can be found at the Center's website: http://www.pserc.org.

For additional information, contact:

Power Systems Engineering Research Center
Arizona State University
527 Engineering Research Center
Tempe, Arizona 85287-5706
Phone: 480-965-1643
Fax: 480-727-2052

Notice Concerning Copyright Material

Acknowledgements

For the area angle work, we thank the industry advisors for help with formulating the areas and providing industry context for the work and particularly Slava Maslennikov for perspectives in section 4.6 and Milorad Papic for advice about power flow patterns in Idaho, and Atena Darvishi for providing expert advice. We gratefully acknowledge access to the WECC power flow data that enabled this research. The analysis and conclusions are strictly those of the authors and not of PSerc, NSF, WECC, BPA, NYPA, Idaho Power, DOE, or SCE.

For the structural approach to operations and planning work, we thank the industry advisors for help with providing industry context for the work and particularly Slava Maslennikov for serving as a PhD committee member for Stefanos Baros' thesis. Stefanos Baros was in part supported by this project. We also appreciate the input provided by Patrick Panciatici from RTE and George Stefopoulos from NYPA. Feedback on the ideas were also provided at the early stages of the project by CAISO personnel.

Executive Summary

The report is presented in two parts. Part 1 extends area angle monitoring with PMUs to get actionable information in emergencies. Part 2 describes structural modeling and performance metrics needed for monitoring and control of the changing electric power system.

Part 1: Monitoring and Maintaining Limits of Area Transfers with PMUs

Phasor Measurement Units, or PMUs, also known as synchrophasors, can quickly measure voltage phasor angles with respect to a common reference at multiple locations spread across the power grid. When these measured PMU angle data are made available at a control center, the challenge is to turn the data into actionable information about the power grid.

Most of the current methods have the easier objective of detecting system conditions that are anomalies or outliers. Indeed, if we subtract measured PMU angles to get angle differences, then unusually large angle differences generally correspond to stressed conditions, and these stressed conditions can be distinguished from normal operating conditions. While it is of some use to be able to detect and report that the conditions are stressed, the problem underlying the stress, whether action needs to be taken, and which action to take are not specified. That is, the PMU data processed in this unstructured way can detect a generally stressed condition, but does not provide actionable information to solve a specific problem.

To get actionable information from PMUs we need to formulate a more specific problem, and this project addresses the effect of line outages inside a particular area when there is a particular overall pattern of power flow through the area. The PMU angle measurements are made around the border of the area. We use circuit theory to combine the measured angles into a scalar "area angle" that quantifies the area stress with respect to line outages inside the area. That is, the area angle measures the impact of line outages inside the area. Offline computations can set a threshold for the area angle that is related to the N-1 criterion. Then if the area angle exceeds the threshold, emergency action to reduce the power flow through the area is recommended. Equally important is that if the area angle is less than the threshold, no emergency action is needed. This actionable information is obtained essentially by restricting the problem formulation to monitor and respond to the overloading problem associated with a particular power transfer through a particular area.

The standard way to compute effect of line outages inside the area is to perform state estimation in order to get a detailed description of the outages and individual line flows inside the area so that corrective actions can be taken as needed. Using the state estimator in this way is an accurate and useful procedure when it can be performed. The advantage of the area angle computation from PMU measurements is that it is faster, and available when the state estimator does not converge. This makes the area angle particularly appropriate when there are multiple simultaneous line outages that could cause further outages in a cascade. Multiple outages are the most difficult case for state estimation, and quickly determining whether emergency action is needed with the area angle based on PMUs is particularly useful in this case of potential further cascading. Since the area angle is a single bulk measure of the complexities of power flows and outages interacting

inside the area, it is an approximation. However, it appears to be a practical approximation that can give actionable information.

The area angle is calculated online from a weighted sum of the voltage phasor angles measured around the border of the area. This is a very easy and fast calculation. The weights are calculated offline from a DC load flow of the area. There is an assumed pattern of power flow through the area and positive weights correspond to buses which have power entering the area and negative weights correspond to buses which have power leaving the area or loads. The area angle is thus a bulk angle between buses on one "side" of the area to the other "side" of the area. Since the area angle is derived from circuit theory, it behaves intuitively when conditions change. If the power flow through the area increases by 10%, then the angle across the area increases by 10%. If there are line outages inside the area, then the power flow through the area is passing through an area of higher impedance and so the area angle increases. That is, even if the power flow through the area does not change much, the rerouted power flow through the area due to the line outages encounters more impedance, and so the area angle increases. This shows how the area angle responds to line outages inside the area, and how the area angle provides information not available from the bulk power flows into the area.

Previous work (with PSerc support) tested the area angle on the north-south transfer of power through Washington and Oregon states. One side of the area in which power flows into the area largely corresponds to the Canadian border and the other side of the area in which power leaves the area largely corresponds to the California-Oregon intertie. Thresholds for emergency action were computed and tested with multiple outages inside the area. For further practical applications of overload monitoring and mitigation with area angles computed from PMUs, it is important to define power system areas and their associated patterns of power flow in meaningful ways. That is, the area angle should be set up to monitor and mitigate a particular and salient pattern of power flow stress in the power system.

This project extends the area angle monitoring and mitigation to a different sort of area in which the power flows from the border of the area into large loads inside the area. Testing these new areas in Southern Idaho and in Southern California shows that emergency thresholds for area angle developed in relation to the N-1 criterion seem effective in discriminating the triple outages that require no quick action from those that require quick emergency action to curtail the power transfer. This new demonstration and testing of area angle extends the capability to combine PMU measurements into a scalar index to monitor a specific problem and determine if emergency action needs to be taken or not. This fast action based on PMU measurements is particularly useful for multiple contingencies when it is possible that the state estimator may not converge.

In order to work with these two new areas in the WECC region, we used a more detailed 19402 bus model of the WECC, and we refined the project modeling, software and algorithms to make them efficient enough to handle this detailed system model. One of the original project objectives was to redo the previous work on the north-south transfer through Washington and Oregon states with the more detailed model to assess the advantages or limitations of the detailed model versus a reduced model in this case. However, we were unable to get good results for the detailed model for this case. We also briefly assess the performance of the area angle when the power stress

direction varies. The case we tested showed considerable robustness to variation of the power stress direction.

The online calculation of the area angle, given the weights for combining the PMU measurements at the border of the area, are very easy and trivial. The offline testing of the area angle and the offline computation of the weights was performed in Mathematica software. This code is strictly research grade, but is available to PSerc members on request.

DOE project DE-0000849 “Real Time Applications Using Linear State Estimation Project (RTA/LSE)”, led by Electric Power Group LLC and subcontracting to Iowa State University pursues a practical industry demonstration of area angle monitoring with PMUs.

Part 2: A Structural Approach to Operations and Planning in the Changing Industry

The first section of Part 2 explains the broader context to the project work of needs and opportunities emerging in the changing industry. As the industry is changing, many solutions are being proposed. It has been difficult to put the specific methods into use. To cope with this problem, a unified approach is needed for modeling which supports extensions of current operating protocols to include and use fast measurements without data overload, and at value. There is also an overall context of an emerging broader framework for supporting interactions in complex electric power grids so that each group of grid users, and the grid itself, contribute to electricity service according with well-defined interactions and with a multi-layered modeling for future electric power grids. A transformed state space lends itself naturally to answering some key questions in this project, namely determining the minimum number of sensors (PMUs) and PMU-enabled actuators so that power transfers across area boundaries are stabilized in closed loop is achieved. It has been conceptualized how, instead of modeling system dynamics as a single "flat" model, interactions between components within an area; and interactions between areas within a region can be described by interaction variables. This concept could form the basis of next generation SCADA needed for PMU-based control without excessive complexity.

Placement of PMUs for enabling the best power delivery has a basic requirement of making the system dynamics observable. The second section of Part 2 describes the methods introduced to do this. Once the system dynamics are observable, one can begin to place actuators and protection to close the loop and ensure stable operation. An analogue method can be used to place actuators for fast closed-loop control. Ultimately, next generation SCADA emerges as a carefully selected fast communications scheme supporting fast control/protection that ensures no instabilities such as voltage collapse. We worked on graph methods for placing the PMUs and controllers so that the small signal stability of an electric power system is achieved. Theoretical work was done on structural controllability and observability conditions which can be used to select minimum number of locations and types of sensors and actuators to ensure stable operation.

The third section of Part 2 uses PMUs to control wind farms so that they can in an aggregated way provide power committed to the system operator. Specific control schemes of wind farms were introduced by incorporating feedback signals from PMU measurements, to enable them to regulate their power output to system-condition-dependent dynamic references. By meeting these power

references, the wind farms can contribute to guaranteed small-signal stability of the interconnected system while its loading conditions vary. This work shows how one may use PMUs to enable integration of renewable resources.

Project Publications:

[1] Nipun Popli, Sergio Pequito, Soummya Kar, A Pedro Aguiar, and Marija Ilic. Selective strong structural minimum cost resilient co-design for regular descriptor linear systems. to appear in Automatica (arXiv preprint arXiv:1704.01157, 2017)

[2] S. Pequito, N. Popli, S. Kar, M. Ilic, and A.P Aguiar. A framework for actuator placement in large scale power systems: Minimal strong structural controllability. In Proceedings of IEEE International Workshop on Computational Advances in Multi-Sensor Adaptive Processing, December 2013.

[3] S. Baros, M. Ilic, Distributed Torque Control of Deloaded Wind DFIGs for Wind Farm Power Output Regulation, IEEE Transactions on Power Systems, Volume: 32, Issue: 6, pp. 4590 - 4599, Nov. 2017.

[4] S. Baros, M. Ilic, A Consensus Approach to Real-time Distributed Control of Energy Storage Systems in Wind Farms, IEEE Transactions on Smart Grid, vol. PP, Issue: 99, pp.1-1, Sept. 2017

Student Theses:

[1] Vikram K.R. Chiluka, *New areas for fast synchrophasor monitoring of multiple overloads with area angles*, Master's Thesis, Iowa State University, 2017.

[2] Nipun Popli, *Multi-layered Energy Conversion and Frequency Control in Complex Electric Power Systems*. PhD Dissertation, Carnegie Mellon University, 2017.

Part I

Monitoring and Maintaining Limits of Area Transfers with PMUs

Ian Dobson

Vikram Kumar Reddy Chiluka, Graduate Student

Iowa State University

For information about this project, contact

Ian Dobson
Iowa State University
ECpE Department
Ames IA 50011 USA
dobson@iastate.edu

Power Systems Engineering Research Center

The Power Systems Engineering Research Center (PSERC) is a multi-university Center conducting research on challenges facing the electric power industry and educating the next generation of power engineers. More information about PSERC can be found at the Center's website: http://www.pserc.org.

For additional information, contact:

Power Systems Engineering Research Center
Arizona State University
527 Engineering Research Center
Tempe, Arizona 85287-5706
Phone: 480-965-1643
Fax: 480-727-2052

Notice Concerning Copyright Material

Table of Contents

List of Tables

List of Figures

1. Introduction

This report shows how to combine together synchrophasor measurements into a scalar area angle that quickly indicates whether multiple line outages require emergency action to reduce a specific power flow through the area to forestall line overloads. The state of the art is extended by setting up the area and the specific power flow in practical examples in which power flows into the border of the area and is consumed by loads inside the area. The advantages of using synchrophasor measurements in this way are their speed and their independence from state estimation. That is, the synchrophasor area angle can quickly recommend emergency action when needed, even if the state estimator fails to converge, as is possible when there are multiple outages. If the state estimator converges, then the area angle gives a fast indication that can be confirmed some minutes later with the more detailed conventional analysis based on state estimation.

The angle across an area of a power system is a weighted combination of synchrophasor measurements of voltage phasor angles around the border of the area [3, 7]. The weights are calculated offline from a DC load flow model of the area in such a way that the area angle satisfies circuit laws. Area angles were first developed for the special case of areas called cutset areas that extend all the way across the power system [4, 5, 6]. This was generalized to an area with power flow in one principal direction through the area as illustrated in Figure 1.1b and demonstrated with the north-south flow from Canada to California through an area that included Washington and Oregon states [10]. There are also AC versions of area angles [3, 15]. The area angle describes the stress on the area due to the power transfer, and an increase in the angle corresponds to increasing the loading of the area lines carrying the power transfer. (Since the area angle satisfies circuit laws, the intuition for this behavior is similar to the simple special case of two parallel circuits joining two buses: If one of the circuits outages, the total power flow transfers to the remaining circuit, but the angle between the two buses increases because the remaining circuit has higher impedance than the double circuit.) The purpose of setting up a specific area stressed with a specific power transfer from one area border to another area border is so that the corresponding area angle across the area and between those borders can be a meaningful scalar measurement for which thresholds for emergency action can be set.

For the area angle defined in [10], actionable thresholds for the area angle were developed so that the north-south power transfer could be quickly curtailed on an emergency basis if the area angle exceeded its threshold. This fast indication of the need for emergency action is particularly useful for multiple outages in which there is a possibility that the state estimator will not converge, so that the methods based on state estimation of detecting and mitigating line overloads are not available.

The new areas we introduce in this report consist of one boundary M_a enclosing the entire area and another boundary M_b formed by major loads in the middle of the area as shown in Figure 1.1a. The power flow pattern of interest is the import of power into the area through boundary M_a and its flow through the area to the loads M_b inside. This pattern of power flow stresses the area by loading its lines, and the area angle between M_a and M_b measures this stress.

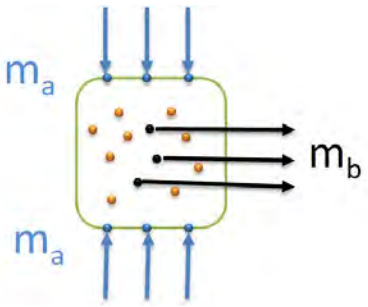

(a) Border buses for load area

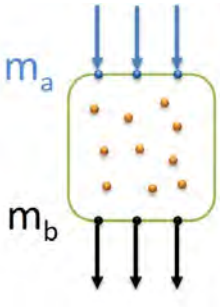

(b) Border buses for transfer path area

Figure 1.1: Border bus selection for different areas. Power enters the area in the border buses in M_a and leaves the area in border buses M_b.

All the results are based on a 19402 bus, 2024 summer base case DC load flow model of the WECC system unless otherwise stated. Throughout the report, we do not address the line outages inside the area that island the area.

1.1 Objective

The angle difference between two buses indicate a stressed power system. But an area of a power system has many buses and looking at the angle difference between any two buses does not give actionable information of the stress in the system. We reduce the area to a single line and combine the synchrophasor measurements at the border buses of an area to form an area angle. The area angle is the angle difference between the two buses of the reduced network and gives the stress across the system. Thresholds can be set for the area angle to monitor multiple line outages inside the area.

The specific objectives of this report are the following:

1. Test the area angle for new types of areas
2. Check the robustness for different patterns of stress while setting up actionable thresholds.
3. Study the effects the detailed model has on the offline computation process and develop efficient algorithms for better computation.
4. Explore calculating the area angle and setting up the thresholds in a twenty thousand bus WECC system model.

1.2 Organization of report

The first chapter gives a brief introduction on the intuition behind area angle and the objectives of the report. Chapter 2 gives a detailed description of the calculation of area angles and setting up actionable thresholds for them for monitoring. Chapter 3 describes the detailed WECC model. Chapter 4 gives the simulation results for new areas, robustness to stress patterns, effects of exceptional outages and the effect of model detail. Chapter 5 concludes the report. The appendix describes improvements in modeling and computation.

2. Review of area angle

2.1 Calculation of area angle and power across the area

Area angle is a scalar quantity obtained from angle measurements from the Phasor Measurement Units (PMUs or synchrophasors) at the border buses of an area. These angle measurements from PMUs are combined in a linear combination with weights to give one area angle. (The detail description and calculation of the area angle is found in [1, 7]). This can be thought of as in effect reducing the area to a single transmission line and finding the angle across the line which gives us the stress across it.

After choosing the area of interest, the border buses of an area must be identifed. The selection of border buses depends on the type of area and is described in section 2.2. The power entering into the area is the power flowing across the tie lines (tie lines which are outside the area), P_{tie}^{m} and the power injections at the border buses P^{m}. All the buses inside the area are reduced by the Kron reduction process. The power injections across the interior buses are also reduced by Kron reduction and replaced as power injections at the border buses P_{int}. Hence the total power into the reduced area is the sum of internal and external powers:

$$P = P_{tie}^{m} + P^{m} + P_{int} \tag{2.1}$$

Now the reduced area consists of border buses and the lines connecting them as shown in figure 2.1. This network can be further reduced to a single transmission line. The power injections across its nodes P_{ab} is the sum of power injections across the border buses. The susceptance of the reduced line depends on the susceptances of the lines inside the network. Thus the value of susceptances changes whenever there is a change inside the network (For example outages of the lines inside changes the configuration of the network and changes susceptance of the reduced line). The angles at the border buses M_a have positive weights and angles at border buses M_b have negative weights. We assume angle measurements from synchrophasors are available at the chosen border buses of

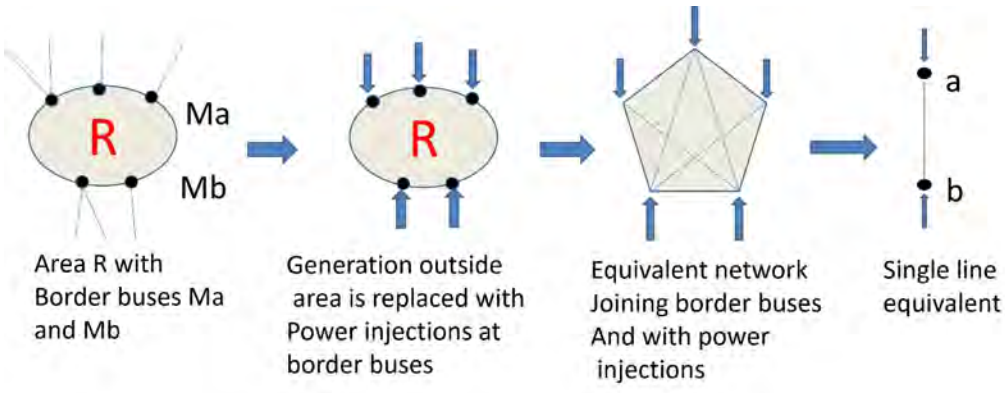

Figure 2.1: Area angle representation

an area. Area angle is computed as a weighted combination of angles across the border buses of an

area. If the border buses are ordered as 1,2,3,...,m and angles across these buses are $\theta_1, \theta_2, ..., \theta_m$ then the area angle is computed as

$$\theta_{area} = \sum_{j=1}^{m} w_j \theta_j \tag{2.2}$$

$$w_j = \frac{\sigma_a B_{eq}}{b_{area}} \tag{2.3}$$

$$b_{area} = \sigma_a B_{eq} \sigma_a^T \tag{2.4}$$

$$\sum_{j=1}^{m} w_j = 0 \tag{2.5}$$

Here σ_a is the row vector of length m with entries of 1 at positions where there are M_a buses and the rest are zero. B_{eq} is the equivalent susceptance matrix of the border buses and b_{ab} is the bulk susceptance of the area. The power flow across an area is then

$$P_{ab} = b_{ab} \theta_{area} \tag{2.6}$$

2.2 Selection of border buses

The area angle calculation and maximum power that can enter the area depends on the susceptance of the area, which in turn depends on the configuration of the area chosen. Different configurations of the area can be obtained by choosing a different set of border buses and for each of these configurations, area angle will be different since the susceptances change. For the area angle to be calculated, the border buses of an area must be chosen in such a way that isolating the border buses disconnects the area from the rest of the network. In other words, the tie lines connecting the border buses must form a cutset.

The border buses of an area can be categorized into two sets. The first set of border buses must be chosen such that power entering into those buses along the tie lines must be positive. The second set must be chosen such that power entering those buses is negative. For example consider the BPA area (Figure 1.1b) which acts as a transmission corridor transferring power from northwest Canada to northern California. In this case northern border buses are named as M_a border buses and southern border buses are named as M_b border buses. For the load areas such as the southern California area (Figure 1.1a), the power is entering across all its outer border buses. In this case, all the outer border buses are selected to be M_a border buses and some load buses inside the area are selected to be M_b border buses. The choice of the M_b load buses depends on the availability of PMU measurements. Generally, electric utilities install PMUs at the largest load buses to monitor various parameters and hence we can select these buses to be M_b border buses.

2.3 The maximum power that can enter an area under single contingencies

Previous work uses area angle to define thresholds to monitor stress across the area under various contingencies [10] and showed that area angle is a good indicator of stress. The strategy is to define thresholds based on the line limits in terms of maximum power transfer through the area and convert the maximum power transfer threshold to an equivalent area angle threshold to monitor stress across the area. Then data from PMU are combined to measure the area angle and this area

angle is compared to the threshold. If the measured area angle is greater than the threshold, then it is an indication that the system is under stress and action is required.

To evaluate the maximum power that can enter the area it is necessary to stress the area with additional power injections [10]. These additional power injections can be made at border buses in proportion to the tie line flows entering or leaving at the border buses and in proportion to the net injection at the buses inside the area. That is, to find out the maximum power injection at the border buses we can inject the additional power at the border buses M_a and M_b.

To calculate the additional power injections, we first apply any contingencies by removing lines inside the area and then the DC power flow is calculated and the power flows through all the lines is determined. We need to calculate the amount of power that needs to be injected at the border buses such that line k reaches its limit in case of contingency i. The power injection is calculated from the generation shift factor as

$$\Delta P^{ab(i)kmax} = \frac{\Delta P_k^{limit(i)}}{\rho_k^{ab(i)}} \tag{2.7}$$

$$\rho_k^{ab(i)} = b_k(e_u^T - e_v^T)((B^i)^{-1})(e_a - e_b) \tag{2.8}$$

where $\Delta P_k^{limit(i)}$ is the difference between the power flow and its rated power flow in line k after contingency i. $\rho_k^{ab(i)}$ is the generation shift factor of the line k with respect to the power at border buses M_a. B_i is the susceptance matrix after line i is outaged, b_k is the admittance of the line i. u and v are the sending and receiving end buses of line k. For e_a, we can choose its entries corresponding to the M_a buses according to weights $\alpha_j, j \in M_a$ that are the fraction of power flows along the tie lines connecting the border buses:

$$\alpha_j = \frac{P_{intoj}}{P_{intoa}} \tag{2.9}$$

Similarly for e_b, we can choose $\alpha_j = \frac{P_{intoj}}{P_{intob}}, j \in M_b$. Alternatively, the weights can be chosen as the weights w_j used to define the area angle. These alternatives are discussed further in Chapter 4 of this report.

The maximum possible extra power injection into the border buses when line i is out such that the system satisfies the N-1 contingency criteria is the minimum of all additional power injection that satisfies all the line limits.

$$\Delta P^{inj} = Min\left\{\Delta P^{ab(1)kmax}, \Delta P^{ab(2)kmax}, ...\Delta P^{ab(n)kmax}\right\} \tag{2.10}$$

If the power is injected at border buses M_a then the share of power injection at each border bus is

$$\Delta P_j = \alpha_j \Delta P^{inj} \tag{2.11}$$

Then the maximum power that can enter the area at border buses M_a is the sum of power across the cutset of lines joining the M_a border buses to the network outside the area and additional power calculated from equation 2.10 and the power injections at border M_a buses.

$$P_{ma}^{max(i)} = \Delta P^{injout} + \sigma_a P^{minto(i)} + P_{ma} \tag{2.12}$$

where $P^{minto(i)}$ is the sum of power flows through the M_a border buses when line i is outaged.

While calculating the area angle for different line outages, we do not consider the line outages which isolate the system when removed such as the radial distribution lines.

A threshold is set to be the area angle that occurs when the worst case single line outage happened. When area angle computed after other line outages is less than this area angle, then emergency measures should be taken to curtail the power transfer through the area.

2.4 Monitoring multiple outages

2.4.1 Simple example

Suppose the area is a transfer path area and power is transferred from north to south buses. Whenever a contingency happens, the power flow and voltage angles get redistributed. Whenever there is no path parallel to and outside the area, the tie flow into the area does not change. Whenever there is a high impedance path parallel to the area, the tie flow into the area does not change much. Hence, in these cases, the power entering the area is the same or approximately the same in both base case and in case of contingencies.

Consider the simple example of the case of three parallel lines connecting two buses as shown in Figure 2.2. The power entering the area is the same in all cases (base case and contingency

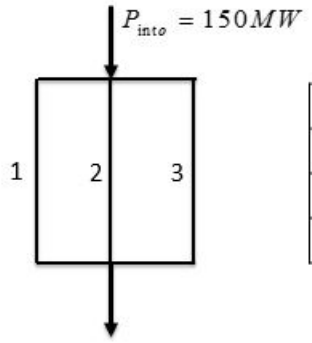

Lines	b	Limits(MW)
1	500	125
2	300	90
3	200	60

Figure 2.2: Simple example on monitoring multiple outages

cases).

Here we show in this simple example, the procedure to set up angle threshold to monitor multiple contingency cases.

Consider the case where line 3 is out. The powers flowing in lines 1 and 2 are 93.75 MW and 56.25 MW respectively. The maximum power that can enter into the area depends on the line limits and power flows. The additional power that should be injected at the north bus such that line 2 reaches its limit is 90MW ($\Delta P_{inj}\frac{300}{800} = 90 - 56.25$). Therefore for line 2 to reach its limit, the maximum power that should be injected at the north bus is $P_{inj} = 150 + 90$. Similarly, for line 1 to reach its limit, the power that should be injected is $P_{inj} = 150 + 50$. Therefore, the maximum power that can enter into the area without violating the N-1 contingency criteria is minimum of the above maximum powers which is 200 MW. The area angle in this case is 10.74^{o}. We can compute the maximum power that can enter the area and the area angle for the cases when lines 1, 2, $1\&2$, $1\&3$,$2\&3$ each outage and these cases are given in table 2.1

Table 2.1: Simple example demonstrating that area angle tracks severity

	Base case			line 1 out			line 2 out			line 3 out		
Lines	P	θ_{ab}	P_{max}	P	θ_{ab}	P_{max}	P	θ_{ab}	P_{max}	P	θ_{ab}	P_{max}
1	75		250	0		-	107.14		175	93.75		200
2	45	8.59°	300	90	17.18°	150	0	12.27°	-	56.25	10.74°	240
3	30		300	60		150	42.86		210	0		-
		8.59°	$P_{max}^{min} = 250$		17.18°	$P_{max}^{min} = 150$		12.27°	$P_{max}^{min} = 175$		10.74°	$P_{max}^{min} = 200$

	lines 1 & 2 out			lines 1 & 3 out			lines 2 & 3 out		
Lines	P	θ_{ab}	P_{max}	P	θ_{ab}	P_{max}	P	θ_{ab}	P_{max}
1	0		-	0		-	150		-25
2	0	42.97°	-	150	28.64°	-60	0	17.18°	-
3	150		-90	0		-	0		-
		42.97°	$P_{max}^{min} = -90$		28.64°	$P_{max}^{min} = -60$		17.18°	$P_{max}^{min} = -25$

From table 2.1, we can see that in the case of single line outages, as the maximum power that can enter the area decreases from 250 MW to 150 MW, the area angle increases from 8.59° to 17.18°. Similarly, for double line outages, the maximum power that can enter the area decreases from –25 MW to –90 MW, thus effectively violating the N-1 contingency criteria. The area angle in this case increases from 17.18° to 42.97°.

The area (Figure 2.2) is designed such that it follows N-1 criteria. Now, we set the maximum power entering the area in the worst case single contingency to be the emergency power threshold. Since the maximum power is a hypothetical quantity and cannot be monitored, we convert the maximum power emergency threshold to emergency area angle threshold. The area angle can be computed from the measurements of synchrophasor data available at border buses.

Following the procedure, we set the emergency power threshold in the simple example (2.2) to be 150 MW i.e., the worst case single contingency happens when line 1 is out and the corresponding area angle is 17.18°. We choose this area angle to be emergency area angle threshold. We can see that, in case of multiple outages, the area angle is always above the emergency area angle threshold, thus effectively indicating that multiple outages inside the area are worse than the worst case N-1 case, and require emergency action to reduce the transfer through the area.

2.4.2 Algorithm

We now summarize the area angle algorithm from [10].

Offline calculations

1. Choose the border buses of an area such that the border buses form a cutset (section 2.2).

2. For each single outage inside the area, after the outage, calculate the maximum power that can enter the area before the first line limit is encountered. The maximum power that can enter the area for the worst case single outage is the emergency threshold for the maximum power entering the area. Also define the alarm threshold on the maximum power entering the area.

3. Set the base case power entering the area to the emergency threshold of the maximum power. Then for all single outages inside the area, calculate the area angle after the outage.

4. After eliminating the exceptional outages, choose the minimum of all the maximum powers from step 2 as the emergency power threshold (This is because this is the maximum amount of power that can enter into the area under worst case single contingency without violating N-1 contingency criteria). The corresponding area angle will be emergency area angle threshold.

Online implementation

1. Continuously observe the system using synchrophasors at the border buses. Get the values of voltage angles from the synchrophasors in real time.

2. Calculate the area angle using the weights computed offline.

3. If outages which are causing local power redistribution problems have not occurred, then compare the area angle to its thresholds to take no action or to take proper action with the appropriate urgency.

4. If the area angle is above the emergency area angle threshold (it implies that the multiple outages are worse than worst case single line contingency and not following the N-1 criteria), then take emergency actions to reduce the power in the tie lines of the area.

2.5 Exceptional outages

It is not always the case that the area angle is inversely related to the maximum power that can enter the area. In our experience we encountered some cases in which there are exceptional outages for which the area angle does not necessarily track the maximum power that can enter into the area. In [10], Darvishi explained one illustrative example of an exceptional outage where the area angle increases but the maximum power entering the area remains the same for the simple network of Figure 2.3. Here we show additional cases by changing the susceptance and line limit values for the same illustrative example.

The various possibilities of exceptional outages are given in table 2.2. In order to explain all

Table 2.2: The possibilities of exceptional outages

P_{into}^{max}	θ_{ab}
Decreases	Constant
Increases	Constant
Constant	Decreases
Constant	Increases
Decreases	Decreases
Increases	Increases
Constant	Constant

the possibilities of exceptional outages in table 2.2, consider the following network in Figure 2.3.

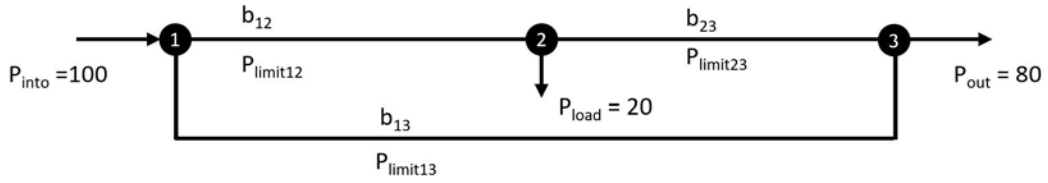

Figure 2.3: Simple network for illustrating exceptional outages

The line limits are chosen such that the network satisfies the N-1 criteria. In this network the power entering into the area (bus 1) is 100 pu and is always the same in base case and in case of contingencies. However, the maximum power that can enter into the area changes. The power out is 80 pu and load is 20 pu in all the cases. By changing the limits and susceptances of the lines inside the area, we can demonstrate all the possible exceptional cases as shown in table 2.3. The single line outages which are not following the inverse relation are exceptional outages. This more general analysis of exceptional outages should be useful in understanding cases in which the area angle does not work as expected.

Table 2.3: Exceptional outages in simple network

$P_{limit12}$	b_{12}	$P_{limit13}$	b_{13}	$P_{limit23}$	b_{23}	line 1-2 out		line 1-3 out		P_{into}^{max}	θ_{13}
						P_{into}^{max}	θ_{13}	P_{into}^{max}	θ_{13}		
100	40	100	30	80	20	100	3.3	100	6.5	constant	increase
100	50	120	30	80	60	120	3.3	100	3.3	decrease	constant
100	50	120	20	80	60	120	5	100	3.3	decrease	decrease
100	50	100	20	80	60	100	5	100	3.3	constant	decrease
120	50	100	30	100	60	100	3.3	120	3.3	increase	constant
120	40	100	30	100	20	100	3.3	120	6.5	increase	increase
100	50	100	30	80	60	100	3.3	100	3.3	constant	constant

3. Description of power system network model

The data used for modeling and simulation is the North American Western interconnection (WECC) system. The details and the difference between reduced and detailed model are given in table 3.1. The network formed is given in Figure 3.1. The top part of the graph corresponds to those buses

Table 3.1: Difference between the detailed and reduced models

	Detailed model	Reduced model
Number of buses	20194	1553
Number of loads	10951	898
Number of transmission lines	16912	2115
Number of generators	4254	493
Number of two winding transformers	7654	243
Number of three winding transformers	561	0
Number of HVDC lines	3	0
Number of areas	239	64

which are in Canada followed by those buses which are in Washington, Montana, Oregon, Idaho, Nevada, Utah, Colorado and the bottom part of graph corresponds to buses which are in southern California, Arizona. The DC load flow voltage angle is computed for all the buses in the network and these are shown by the colors in Figure 3.1. It can be seen that angle is higher at northern buses and tends to reduce as one progresses towards the south, indicating that power is transferred from northern part of Washington state (where there is generation available) to load parts such as south western part of California (where there are major load centers) with some power consumed in between. In this report, we explain the area angle concepts on Southern California region and Southern Idaho region that are essentially load areas, and the BPA area which covers the states of Washington, Oregon and part of Idaho. The BPA area acts as transmission corridor transferring power from Canada to California.

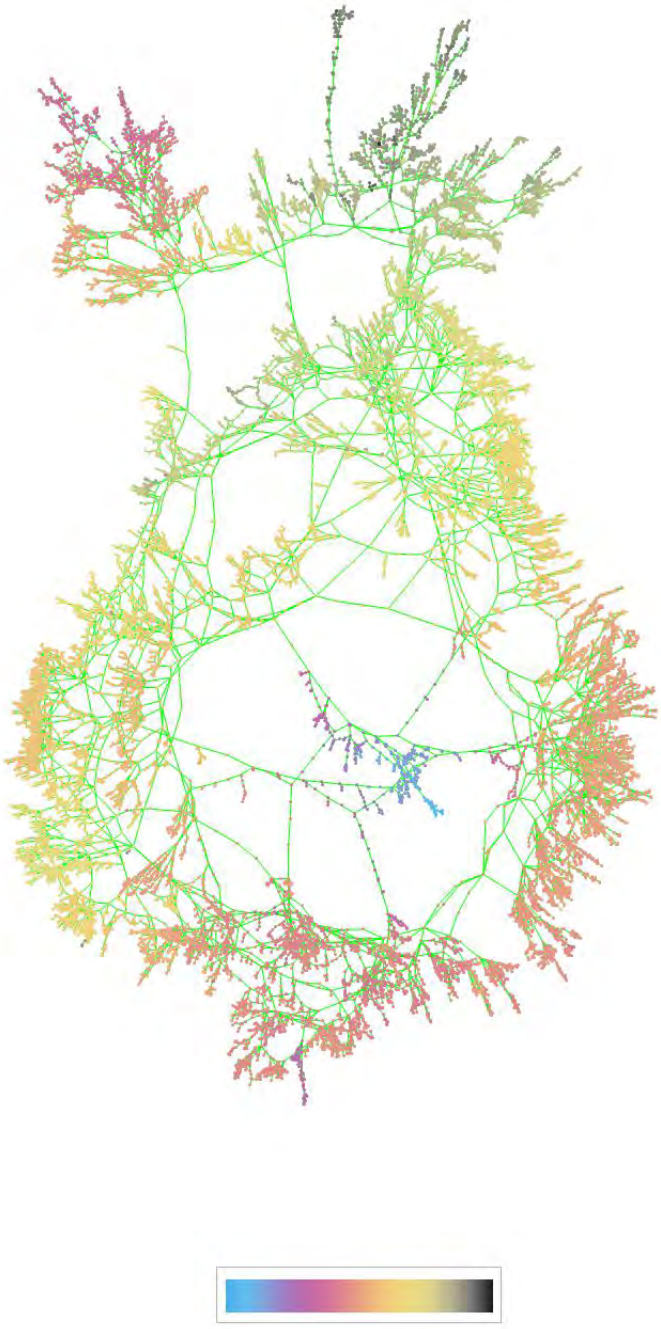

Figure 3.1: Angles at the buses plotted on a 19402 bus WECC model. The black color represents a higher value and blue color represents a lower value. Layout is not geographic.

4. Areas, area angles and thresholds

We calculated the area angle and set the thresholds on area angles for three different areas. Two areas in Idaho and in Southern California are load areas. The third area is a transmission corridor through the states of Washington and Oregon supplying power from Canada down to California.

4.1 Southern Idaho area

The Southern Idaho area is a load area, where the power is consumed inside the area. According to the model, it has about 271 buses and 312 transmission lines. The Idaho area is given below with the M_a border buses colored in red and M_b border buses colored in blue and all the other buses inside the area are colored in black. The numbers across the border buses represents the weights at those buses.

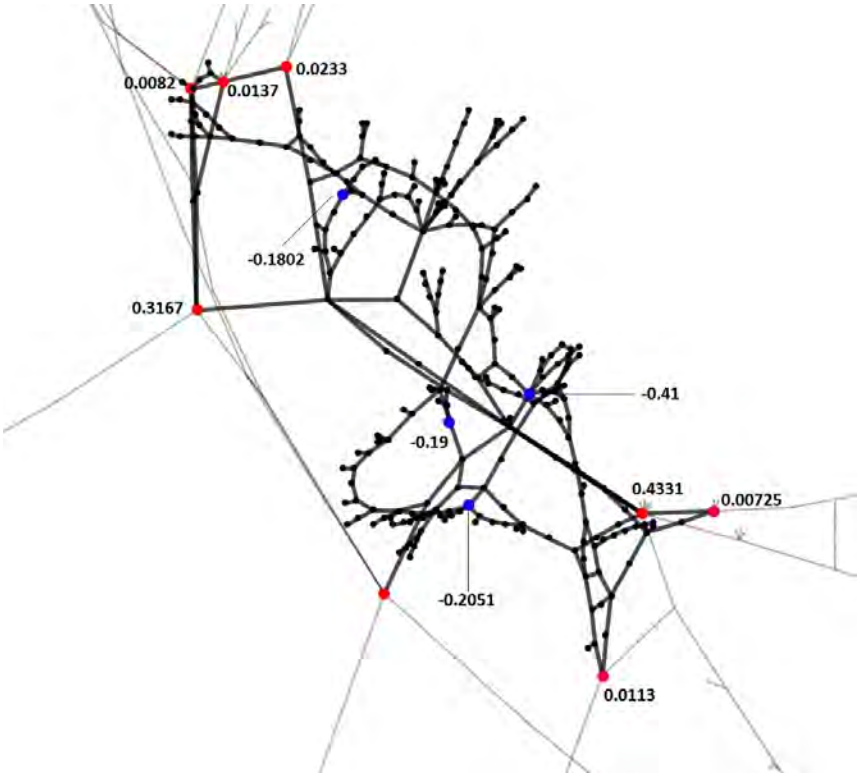

Figure 4.1: Southern Idaho area: Border M_a buses are colored in red and border M_b buses area colored in blue. Numbers represent the weights

4.1.1 Outages and the calculation of thresholds for area angle

All the lines inside the area are simulated to be outaged one at a time and after removing the exceptional outages, the results are plotted below. The minimum of the maximum powers that can enter the area is 33.2 pu with corresponding area angle 9.93 deg. So, the emergency threshold in this case will be 9.93 deg. (We do not set any alarm thresholds in this case as in [10] as the slope

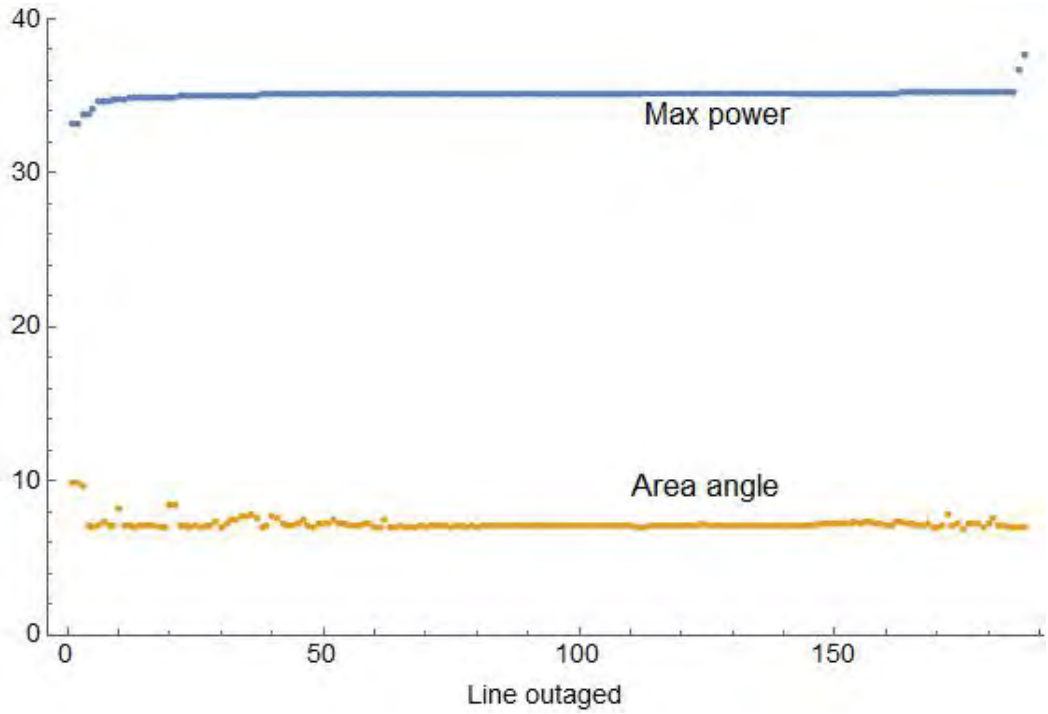

Figure 4.2: Single line non-exceptional outages for Southern Idaho area. Outages are ordered so the maximum power increases.

of the maximum power is not clear.) The double and triple outages are given below after excluding the exceptional outages. We can see that the area angle emergency threshold discriminates the double and triple outages that have powers less than the emergency power threshold.

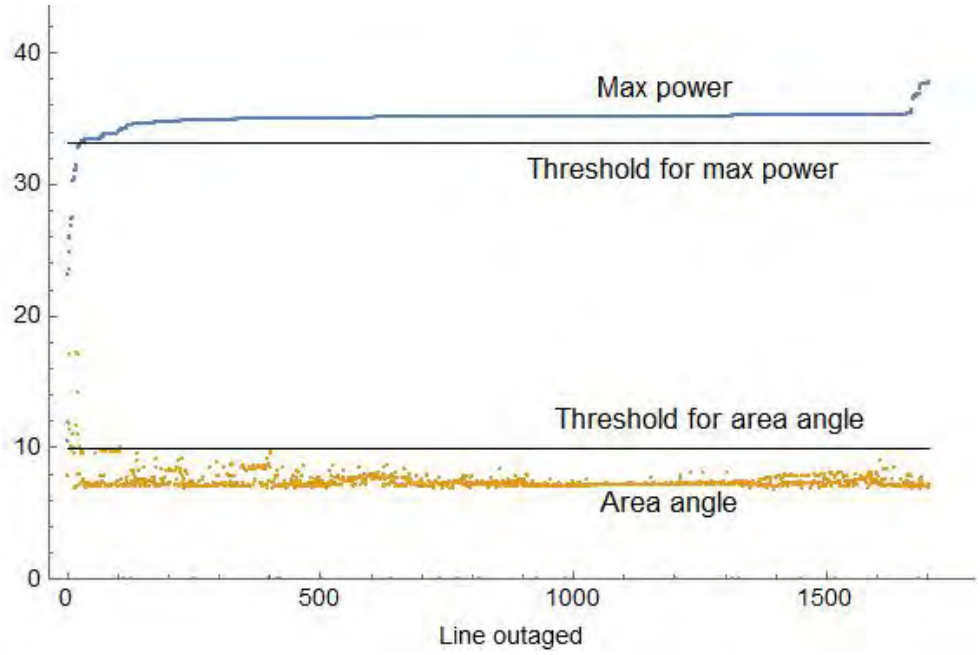

Figure 4.3: Random sample of 1700 double line non-exceptional outages for Southern Idaho area

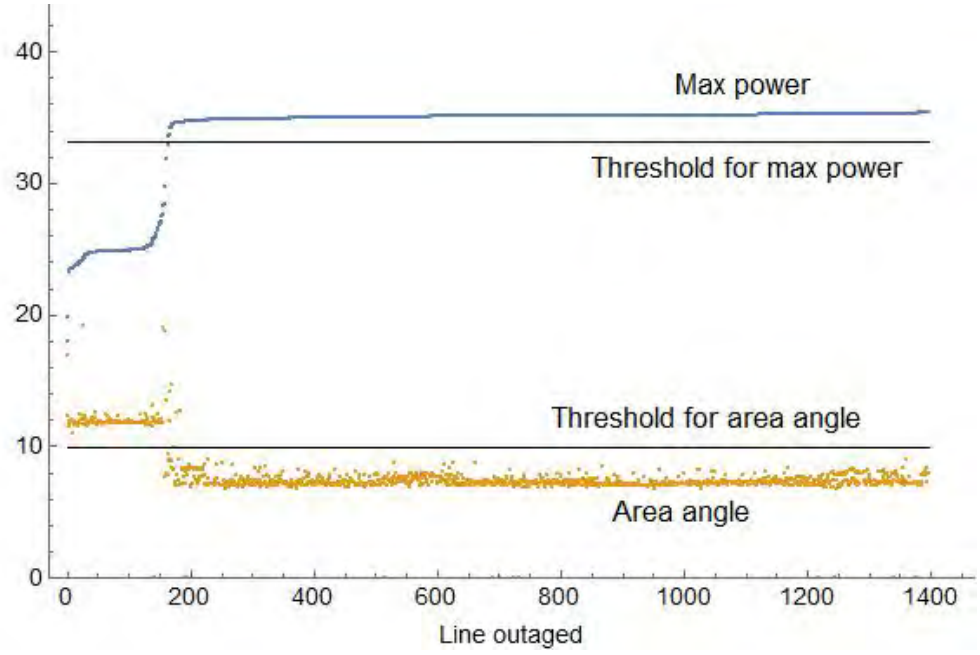

Figure 4.4: Random sample of 1396 triple line non-exceptional outages for Southern Idaho area.

4.2 Southern California area

The Southern California is a load area with power transferred through an outer border and consumed inside the area. The Southern California area network buses and transmission lines are shown in Figure 4.5.

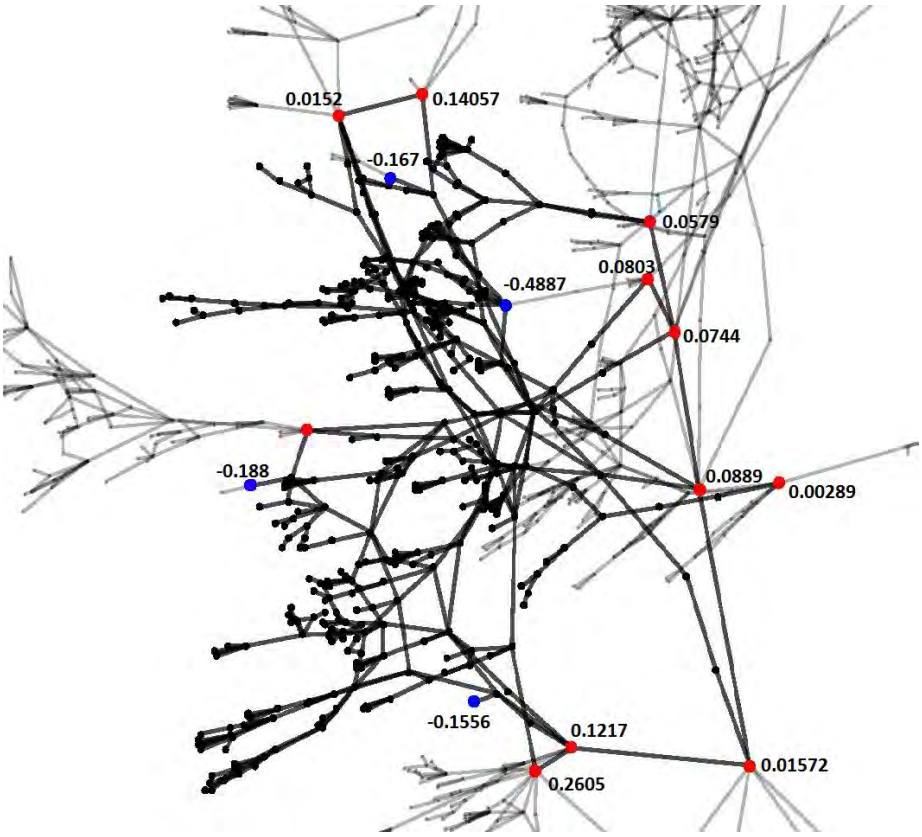

Figure 4.5: Southern California area

One pattern of bulk power flow through the Southern California area transfers power from the outer border of the area to Los Angeles. This bulk power flow is limited by maximum power flow limits on the transmission lines. Under normal operation, there is considerable margin available for this power transfer. Single contingencies reduce but do not eliminate this margin, and in this case state estimation can generally identify the contingency and converge to give the flows on all the remaining lines and identify any corrective actions necessary. In rare but consequential cases, there can be multiple outages, and in this case the state estimator may or may not converge, but there is always a need to quickly discriminate whether fast emergency action to reduce the power transfer is necessary or not.

The Southern California area consists of Los Angeles and regions surrounding Los Angeles and is shown by the darker buses and lines in Figure 4.5. The Southern California area network has 418 buses and 501 lines. Red buses in Figure 4.5 represent the outer border buses and blue buses are major loads in Los Angeles. The weights used to compute the area angle are shown in Figure 4.5 and are calculated offline and updated occasionally. Given the weights and the availability of

the synchrophasor measurements at the specified buses, the online calculation of the area angle from the synchrophasor measurements using the weights is trivial. In practical application, we can expect some simplification and reduction in the measurements required. It may be possible and desirable to omit measurements with small weights, or to approximate a lower voltage bus measurement by a constant angle difference from the higher voltage bus in the same substation or close by.

Here we are assuming synchrophasor measurements are available at the specified buses. As of 2010, synchrophasors were installed or proposed at all the border buses except for one of the load buses. The trend is for synchrophasor measurements to become more widespread, particularly as modern relays can include synchrophasor measurements. We note in computing the area angle that border buses with very small weights can be omitted from the calculation so that synchrophasor measurement at those buses is not required.

4.2.1 Outages and area angle thresholds

The single line outages are given below.

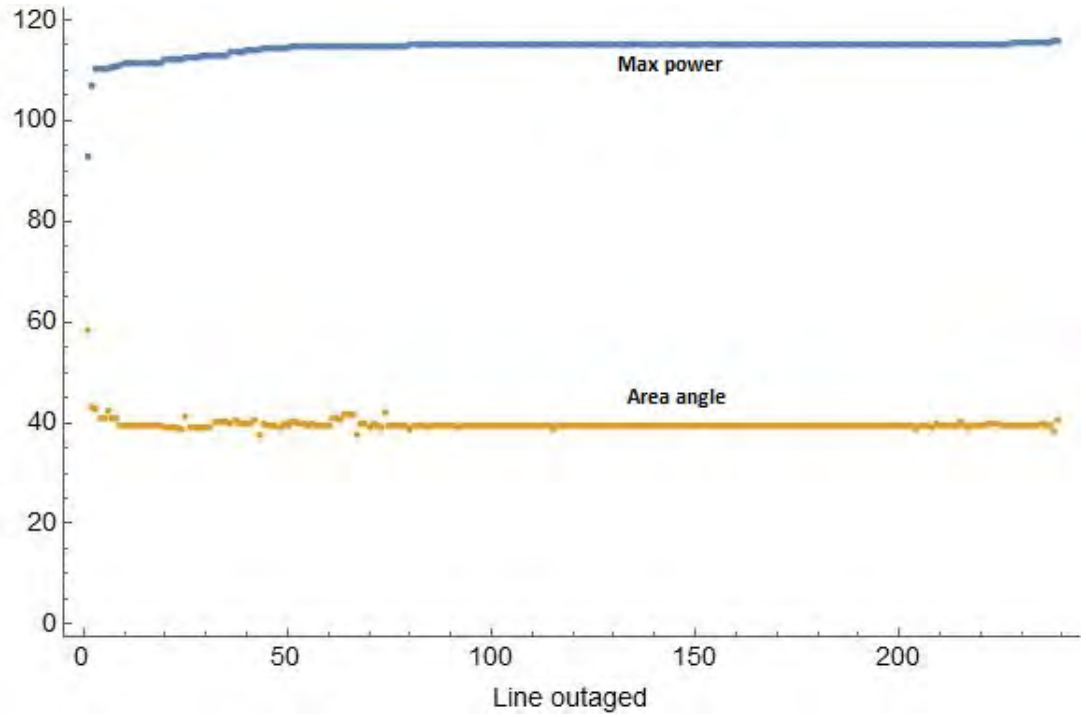

Figure 4.6: Single line non-exceptional outages for Southern California area. Outages are ordered so that maximum power increases

The power entering the area during the worst case single contingency is approximately 93 pu and the corresponding area angle is 58 pu (approximately). The double and triple outages are given below with the emergency thresholds for area angle and max power and it can be seen that the thresholds clearly detect the double and triple outages which are worse than worst case single contingency.

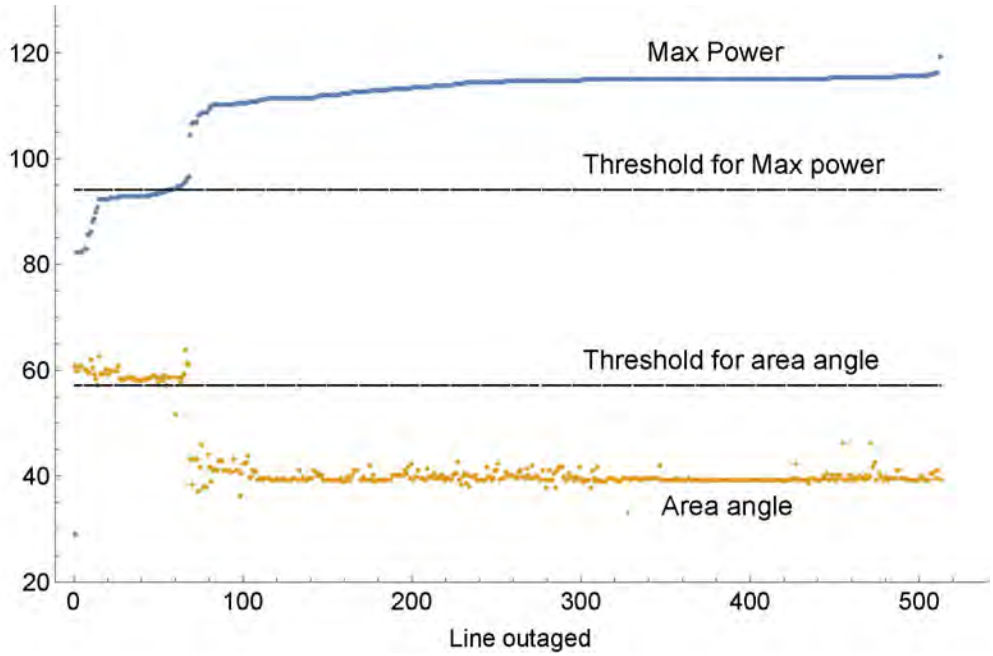

Figure 4.7: Random sample of 512 double line non-exceptional outages for Southern California area.

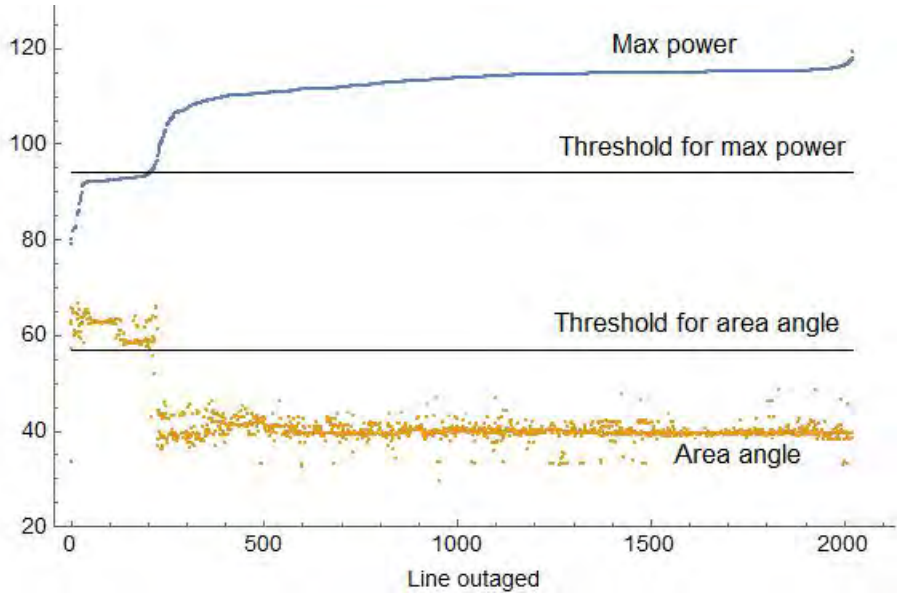

Figure 4.8: Random sample of 2020 triple line non-exceptional outages for Southern California area.

4.3 BPA area

Unlike Idaho and Southern California areas, which are load areas, the BPA area acts as a transmission corridor sending power from Canada in the north to California in the south. The border

buses form a minimal cutset of the network and are shown in Figure 4.9. This BPA network has 407 buses and is formed from a reduced 1553 bus WECC network and is the same area studied in [10],

We also worked on a much more detailed model of the BPA area consisting of 3737 buses and 4271 lines, but were unable to get satisfactory results.

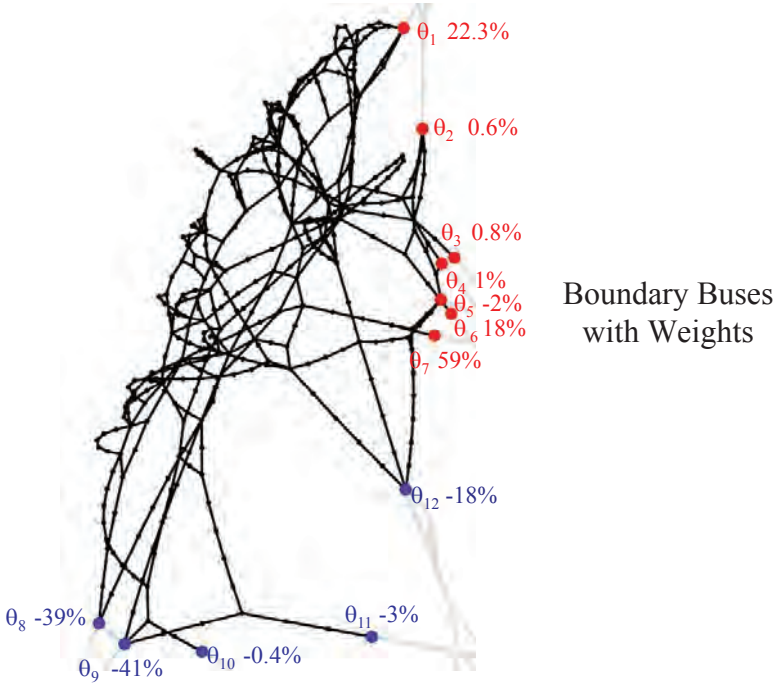

Figure 4.9: BPA area in reduced WECC network

4.4 Robustness to changing stress direction

When determining the area angle thresholds, it is necessary to choose a pattern of stress by which the power transfer is increased. When a line is out, the participation factors for all the remaining lines are calculated with respect to power injections at the border buses. The maximum power that can be injected across the border buses such that line k inside the area reaches its limit is obtained by dividing the limit of that line by its participation factor according to equation (4) in [10]. Then the amount of power to be injected into the border buses is the minimum of injections across all the lines. The amount of power to be injected at the border bus such that line k reaches its maximum power limit depends on the generation shift factor of line k. According to equation (8) in [10] the generation shift factor for line k with respect to injections at border buses is given by

$$\rho_k^{ab(i)} = b_k(e_u^T - e_v^T)((B^i)^{-1})(e_a - e_b)$$

Here e_a and e_b are $n \times 1$ vectors (n is the number of buses) with values only at the positions of border buses and the rest are zero. We choose the values in these column vectors to specify the pattern of stress. The first method is to choose e_a and e_b according to the weights at the buses. The second method chooses e_a and e_b according to $\alpha = P_{intoj}/P_{intom}$. The pattern of stress is defined by how the border buses participate in changes in the power transfer.

We compare these two different methods of stressing each area to assess the robustness of the thresholds when the power stress pattern is changed.

1. The first method increases the power at border bus i proportional to the power injected at border bus i from outside the area.

2. The second method increases the power at border bus number i proportional to the area angle weight w_i.

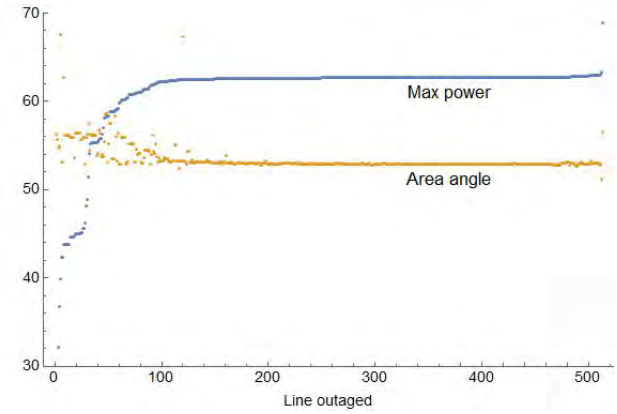

Figure 4.10: Single line outages for reduced BPA network. Pattern of stress used here is according to weights at the buses

Here we compare the single line outages of BPA network in a reduced network. Single line outages for the reduced BPA area from [10] is reproduced here for easy reference in Figure 4.10.

The outages are ordered according to increasing amount of maximum power transfer into the area. The results in [10] for the north-south transfer of power through the BPA area are obtained with the second method, so here we give the results for the first method[1]. The weights at the border buses used for stressing the system in [10] are

$$w = \{0.23, 0.0057, 0.0078, 0.1, 0.18, 0.017, 0.6, \\ -0.03, -0.4, -0.38, -0.18, -0.004\} \tag{4.1}$$

The weights at the border buses which are proportional to tie line flows are

$$\alpha = \{0.68, 0.0111, 0.002, 0.056, 0.019, 0.042, 0.18, \\ -0.002, -0.4, -0.35, -0.23, -0.029\} \tag{4.2}$$

We note the substantial difference in the weights in (4.1) and (4.2).

The single outages of the system stressed according to α are given in Figure 4.11. Comparing Figure 4.11 with Figure 4.10 we can see that the results are similar and the thresholds do not depend on the method of stress.

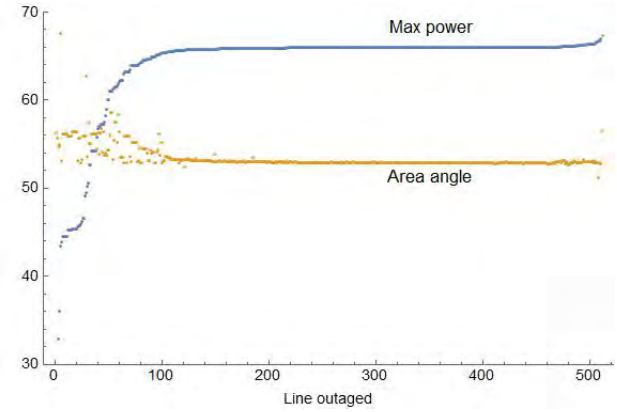

Figure 4.11: Single line outages for reduced BPA network. Pattern of stress used here is proportional to the tie line power flows into the buses.

4.5 Effect of exceptional outages

The formulation of the areas is such that power enters into the area through one set of border buses and transfers or get consumed at the other set of border buses. The radial lines inside the area do not participate in the power transfer. The meshed lines in the area can participate in the power transfer. There is a general tendency for an outage of one the meshed lines to decrease the maximum power that can be transferred through the area, since the outage tends to transfer more power to the parallel paths. Moreover, the outage tends to increase the impedance across the area while the power transfer remains constant. Since the area angle obeys circuit laws, it follows that the area angle generally increases. Thus there is generally an inverse relationship between area angle and

[1]The first method is described by equation (8) of [10]. However the results presented in [10] tacitly use the second method.

maximum power transfer that we exploit in the monitoring. However, there are some exceptional cases in which the area angle does not respond inversely to the maximum power transfer. These exceptional cases usually correspond to local power redistribution problems as explained in [10] and further in Chapter 3 of this report. Depending on the nature of the lack of response, some of the lines giving exceptional outages need to be independently monitored to improve the accuracy of the interpretation of the area angle changes. Figure 4.12 shows all the single line outages for the Idaho area, including the exceptional outages shown as red dots. Figure 4.13 shows all the triple line outages for the Idaho area that include at least one exceptional outage.

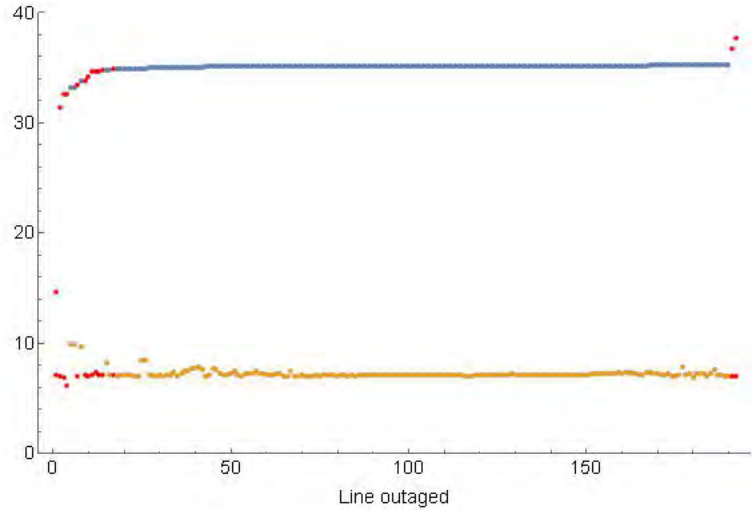

Figure 4.12: All single line outages for Idaho area with exceptional outages colored in red

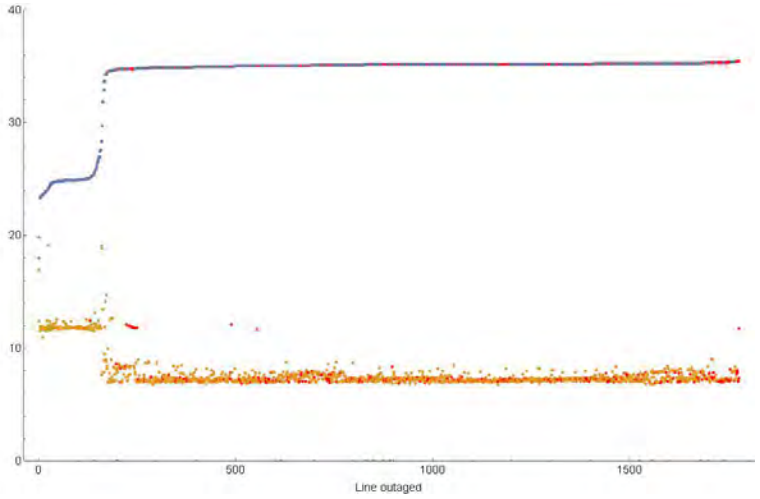

Figure 4.13: Random sample of triple line outages for Idaho area with exceptional outages colored in red

4.6 A perspective from interface power flow limits

Area angle is an approach to monitoring and mitigating overload limits with a scalar bulk measurement. It provides a fast but approximate PMU-based alternative to detailed methods of monitoring each line via state estimation that can function for multiple contingencies when the state estimator does not converge.

A conventional scalar bulk measurement approach to system limits uses interface power flow limits. Interface definition is created by using offline studies and "engineering experiences". That approach works reasonably well for stable power flow patterns. Today, the interfaces defined in this static way become less efficient and there are good chances that the interface-based approach could be too optimistic or/and too conservative. Thus as power flow patterns become more varied, interface limits need to be computed more dynamically.

Similar considerations should apply for area angles. Several different area angles (for different patterns of flow across the same area or for different areas) may need to be developed, one for each pattern of power flow. While it seems that a choice of several relevant area angles could be made using the approach of this report and engineering judgment, it seems that we do not yet understand forming meaningful areas well enough to make feasible automatically and dynamically forming areas and their angles. This could be considered in future work. However, while dynamically varying limits are useful from a operations/security prospective, they are less desirable from a market perspective because the market needs a long term "monetary feedback" and a dynamic interface cannot provide that.

It is also interesting to compare interface power flow limits with area angles. There is a fundamental difference between a flow variable such as power through an interface and a voltage difference variable such as an area angle. (They are of course related via Ohm's law.) Area angles react to contingencies differently than interface power flows, since line outages often just redirect the same power flows to parallel paths, whereas the angle responds to the increased impedance the power is flowing through. The power industry probably developed using interface power flow limits because the power could be readily measured. Now that PMUs are becoming widespread, the different possibilities of area angles can be also be pursued.

One of the interesting heuristics for forming meaningful areas is to assemble the approximate border of the area from key interfaces already established in the power system. Either the interface has to be a closed interface already surrounding the area or it has to be assembled from open interfaces so that they completely surround the area. This type of area can help to show how the concept of interface power flows relates to the concept of area angles.

In future practical applications, the strict requirement that the border buses of the area form a nodal cutset entirely separating the area from the rest of the network may need to be relaxed a bit, mainly because of PMU availability. While the relevant PMUs are often available at medium and high voltage buses, in order to strictly form a cutset, it is sometimes necessary to choose lower voltage buses as border buses. Some of these low voltage border buses will tend to be connected to high impedance lines that can cause their weights to be small or negligible, and approximations can be made with little error in the area angle response. For example, one can either use nearby PMU measurements (which can be further adjusted with the typical average difference between their angles if needed) or one could use more elaborate statistical methods to estimate the voltage angle at the missing PMU buses. These approaches should be explored in future work.

5. Conclusion

Our overall philosophy to extract actionable information from synchrophasor data is to restrict the problem to one pattern of stress for one phenomenon, and suitably combine data from multiple synchrophasors into a meaningful scalar to be monitored. This restriction of the problem then allows not only detection of emergency conditions when the scalar exceeds a threshold, but specific mitigation actions to correct the problem. In particular, we use an area angle to monitor a specific power transfer through a specific area with respect to thermal limits.

To advance and make workable this philosophy for area angles monitoring thermal limits inside an area, it is necessary to develop the art of choosing areas and power transfers stressing these areas, and show that meaningful thresholds can be developed. In this report, we extend the area angle monitoring to a different sort of area in which the power flows from the border of the area into large loads well inside the area. The emergency thresholds for area angle developed in relation to the N-1 criterion seem effective in discriminating the triple outages that require no quick action from those that require quick emergency action to curtail the power transfer.

We also briefly assess the performance of the area angle with respect to power stress direction. We have a choice of stressing the system either according to the weights or according the proportional tie line power flows. The maximum power that can enter the area remained the same irrespective of the type of the stress and the emergency thresholds that are setup discriminates the multiple outages.

The time required to run the offline algorithm of calculating and setting up the thresholds will be in the magnitude of days if computed by brute force methods. The techniques introduced helped achieve computational efficiency. After employing these techniques, the time required for offline algorithm varies from hours to days depending on the size of the area. The offline calculations that calculate the weighting for the angles were improved to be practical for large system models, but there is room for further improvement in calculation efficiency. Online algorithm calculations are very fast since the computation is trivial and they use phasor voltage angle measurements from the synchrophasors at the border buses of the area.

Our testing of area angle extends the capability to combine synchrophasor measurements into a scalar index to monitor a specific problem and determine if emergency action needs to be taken or not. This fast action based on synchrophasor measurements is particularly useful for multiple contingencies when it is possible that the state estimator may not converge. In particular, we have shown that an area angle that suitably combines synchrophasor measurements can monitor a specific power flow through a power system area, and that a threshold on the area angle for emergency action to reduce the power flow can be set so that multiple line outages that are more severe than the worst case single line outage can be quickly distinguished. The area angle leads to actionable advice because it is associated with a particular pattern of power flow, and that is the power flow that would be curtailed if the area angle exceeds its threshold. The online calculations combining the synchrophasor measurements are fast and the monitoring and actions would be independent of the state estimator. The area angle is based on circuit theory and reacts intuitively in a way that is analogous with the angle difference across a transmission line. The area angle

is not perfect (there are some exceptional cases of line outages for which the area angle does not suitable respond), but it is one of the few methods that goes beyond monitoring to yield actionable information based on synchrophasor measurements.

A. System modeling and computation

As described in the previous chapters, all the simulations are run on a twenty thousand bus Western Interconnection (WECC) system and all the calculations are done using Mathematica software. This chapter describes the modeling and steps to improve the computational efficiency. The data available for simulation is in the PSLF epc format. We have the choice of running DC load flow either in PSLF or PSSE software and export the necessary details for further calculations in any format supported by Mathematica. Since we have the framework set up to read PSSE .raw file format in Mathematica, we exported the .epc file as a .raw file.

A detailed system is always challenging in terms of modeling, computational efficiency, data analysis etc. Techniques are employed to reduce the computational time and memory required for computations. In the offline calculations testing area angle and setting thresholds, line outages have to be simulated. Whenever a line is out, the network topology changes and the susceptance matrix changes. In the calculation of participation factor, inverse of susceptance matrix is used as shown in equation 2.8. The network has 20000 buses, so the susceptance of network is a matrix with 20000 rows and 20000 columns. Inverse calculation of such a matrix involves huge computational time and memory. We use the matrix inversion lemma to calculate the inverse of such a huge matrix and this is further explained in section A.5. We achieved better computational time efficiency by utilizing many of the inbuilt functions in Mathematica. The computational time and memory required to simulate the area depends on the size of the area.

A.1 Branches

The DC power flow is given by the equation

$$P = B\theta \tag{A.1}$$

where $P_{n\times 1}$ is the column vector of power injections at the n buses, $\theta_{n\times 1}$ is a column vector of voltage angle at the buses, and $B_{n\times n}$ is the admittance matrix where

$$B_{ii} = -\sum_{n=1}^{k} b_{in} \tag{A.2}$$

$$B_{ik} = -b_{ik} \tag{A.3}$$

and b_{ik} is the susceptance of the line joining bus i and bus k. In the DC load flow, all the branches are considered lossless. Therefore all the two winding transformers and transmission lines are represented with series impedance $z = r + jx, b = \frac{-1}{x}$.

A.2 Three winding transformers

A three winding transformer modeling is different from a two winding transformer. While modeling a three winding transformer, we have the choice of a three bus equivalent model or a four bus equivalent model as shown in Figure A.1. In the three bus model, the three winding transformer is split into two transformers. It does not consider the impedance of primary winding. In the four bus equivalent, it is split into three two-winding transformers. For the DC load flow calculation,

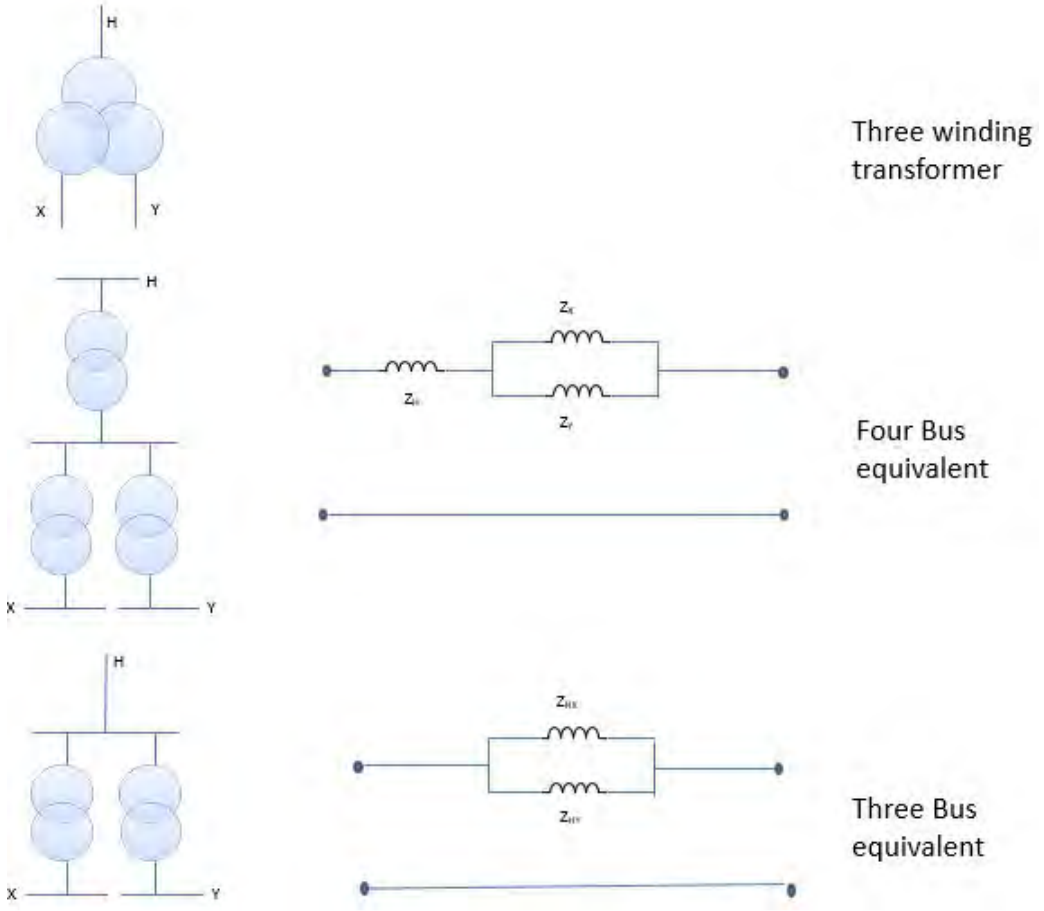

Figure A.1: Modeling of three winding transformer

the primary impedance can be ignored. Therefore, for the DC load flow calculations, the three bus equivalent is used to model the three winding transformer.

A.3 HVDC lines

In the western interconnection, there are three HVDC connections

1. Eastern Alberta Transmission line, which is 485 km long interconnecting Newell HVDC static inverter plant near Brooks, Alberta with Heathfield static inverter plant near Gibbons, Alberta.

2. Pacific DC Intertie, also called Path 65, is 846 miles long interconnecting Celilo converter station in Oregon to Sylmar converter station north of Los Angeles.

3. Intermountain HVDC power line, also called Path 27, is 488 miles long interconnecting Adelanto converter station in Adelanto, California to Intermountain converter station in Delta, Utah.

In order to model the HVDC lines, we remove power from those buses where HVDC power is injected and add power to those buses where HVDC power is extracted. In other words, if P_{dc} is

the amount of power that is transferred through the HVDC line from bus a to bus b, then at bus a, the injection will be $-P_{dc}$ and at bus b, the injection will be P_{dc}.

A.4 Participation factor calculation

The area angle computation and the setting of area angle threshold helps us discriminate the double and triple line outages which are comparable to worst case single line outage. The shift factor of each line inside the area with respect to the border buses of the area is given by equation (2.8), which is copied here as

$$\rho_k^{ab(i)} \quad = \quad b_k(e_u^T - e_v^T)((B^i)^{-1})(e_a - e_b) \tag{A.4}$$

Here e_a and e_b have nonzero entries corresponding to buses M_a and M_b. e_u and e_v have entry 1 at the starting bus position and ending bus position of line k respectively.

After choosing a particular area, the values and positions of elements in the column matrices e_a and e_b do not change since they are ratios of base power injections at the border buses. The values of row matrices e_u^T and e_v^T do not change but the positions change according to the starting and ending buses of line k. However, these positions are within range of buses in the area since the area angle is computed only for the chosen area and all the values at the positions outside the range of area buses are zero. The structure of the matrices is given below

$$e_u^T - e_v^T = \begin{bmatrix} 0 & 0 & \cdots & 0 & v_1 & v_2 & \cdots & v_k & 0 & \cdots & 0 & 0 \end{bmatrix}$$

$$((B^i)^{-1})(e_a - e_b) = \begin{bmatrix} x_1 \\ x_2 \\ \vdots \\ x_n \end{bmatrix}$$

$$(e_u^T - e_v^T)((B^i)^{-1})(e_a - e_b) = 0 * x_1 + 0 * x_2 + \cdots + v_1 * x_{b1} + v_2 * x_{b2} + \cdots + v_k * x_{bk} + \cdots + 0 * x_n$$

From the above equations, we can see that in the participation factor calculation, only the elements of the *Binverse* matrix whose positions are within the range of area buses are required. Hence we can form a sparse *Binverse* matrix which has elements only in the range of buses of the chosen area and all other elements allowed to be zero. This not only reduces the memory to store the *Binverse* matrix but also increases efficiency in calculation of participation factor.

A.5 B inverse matrix calculation

To calculate the participation factor during single, double, and triple outages, it is necessary to calculate B_{out}^{-1} matrix for each outage i. We calculate the B_{out}^{-1} matrix from the matrix inverse

lemma.

$$e_{ij} = \begin{bmatrix} 0 \\ \vdots \\ 1 \\ \vdots \\ -1 \\ \vdots \\ 0 \end{bmatrix}$$

$$B_{out} = B + b_{ij} e_{ij} e_{ij}^T \tag{A.5}$$

Here B_{out} is the B matrix after line k is out. e_{ij} has 1 at the starting bus position of line k and -1 at the ending bus position. b_{ij} is the susceptance of the line k with starting and ending bus positions at i and j respectively.
From the matrix inversion lemma

$$(B + cd^T)^{-1} = B^{-1} - B^{-1}c(I^M + d^T B^{-1} c)^{-1} d^T B^{-1} \tag{A.6}$$

where B is an $n \times n$ matrix, c and d are $n \times m$ matrices and I is an $m \times m$ Identity matrix.
Applying the Matrix inversion lemma to our problem results in the calculation of B_{out}^{-1} from base case B^{-1} matrix:

$$B_{out}^{-1} = B^{-1} - \frac{B^{-1} b_{ij} e_{ij} e_{ij}^T B^{-1}}{1 + b_{ij} e_{ij}^T B^{-1} e_{ij}} \tag{A.7}$$

Here B^{-1} is the base case pseudoinverse of the B matrix with elements only in the positions which are in the range of area buses.

References

[1] I. Dobson, M. Parashar, A cutset area concept for phasor monitoring, *IEEE PES General Meeting*, Minneapolis, MN USA, July 2010.

[2] A. Darvishi, I. Dobson, A. Oi, C. Nakazawa, Area angles monitor area stress by responding to line outages, *North American Power Symposium*, Manhattan KS, Sept. 2013.

[3] I. Dobson, Voltages across an area of a network, *IEEE Transactions on Power Systems*, vol. 27, no. 2, May 2012, pp. 993-1002.

[4] I. Dobson, M. Parashar, C. Carter, Combining phasor measurements to monitor cutset angles, Forty-third Hawaii International Conference on System Sciences, Kauai, Hawaii, January 2010.

[5] I. Dobson, M. Parashar, A cutset area concept for phasor monitoring, IEEE PES General Meeting, Minneapolis, MN USA, July 2010.

[6] G.J. Lopez, J.W. Gonzalez, R.A. Leon, H.M. Sanchez, I.A. Isaac, H.A. Cardona, Proposals based on cutset area and cutset angles and possibilities for PMU deployment, IEEE PES Gen. Meeting, San Diego CA, July 2012.

[7] I. Dobson, New angles for monitoring areas, IREP Symposium, *Bulk Power System Dynamics and Control*- VIII, Buzios, Brazil, Aug. 2010.

[8] A. Darvishi, I. Dobson, Synchrophasor monitoring of single line outages via area angle and susceptance, *North American Power Symposium,* Pullman WA USA, September 2014.

[9] 2013 WECC Path Reports, WECC staff, September 2013

[10] A. Darvishi, I. Dobson, Threshold-based monitoring of multiple outages with PMU measurements of area angle, *IEEE Transactions on Power Systems*, vol.31, no.3, May 2016, pp. 2116-2124.

[11] Mathew P. Oommen, J.L. Kohler, Effect of three winding transformer models on the analysis and protection of mine power systems. *IEEE Transactions on Industry applications*, vol. 35, Issue 3, pp. 670-674.

[12] H. Sehwail, I. Dobson, Locating line outages in a specific area of a power system with synchrophasors, North American Power Symposium (NAPS), Urbana-Champaign IL, Sept. 2012.

[13] H.Sehwail, I.Dobson, Applying synchrophasor computations to a specific area, *IEEE Trans. Power Systems*, vol 28, no 3, Aug 2013, pp. 3503-3504.

[14] J.E. Tate, T.J. Overbye, Line outage detection using phasor angle measurements, *IEEE Trans. Power Syst.*,vol.23, no.4, Nov.2008, pp.1644-1652.

[15] L. Ramirez, I. Dobson, Monitoring voltage collapse margin with synchrophasors across transmission corridors with multiple lines and multiple contingencies, IEEE Power and Energy Society General Meeting, Denver CO, July 2015.

Part II

A Structural Approach to Operations and Planning in the Changing Industry

Marija Ilic

Stefanos Baros, Graduate Student
Nipun Popli, Graduate Student

Carnegie Mellon University

For information about this project, contact

Marija Ilic
Senior Research Scientist
LIDS 32-D726
77 Mass Avenue
Cambridge, MA 02139
ilic@mit.edu

Power Systems Engineering Research Center

The Power Systems Engineering Research Center (PSERC) is a multi-university Center conducting research on challenges facing the electric power industry and educating the next generation of power engineers. More information about PSERC can be found at the Center's website: http://www.pserc.org.

For additional information, contact:

Power Systems Engineering Research Center
Arizona State University
527 Engineering Research Center
Tempe, Arizona 85287-5706
Phone: 480-965-1643
Fax: 480-727-2052

Notice Concerning Copyright Material

Table of Contents

List of Tables

List of Figures

1. Introduction

Section 2 of Part 2 in this report is contributed by Prof. Marija Ilic, as part of her broader research efforts, and describes a general structural approach to modeling and control of the changing electric power systems. The problem of aggregated information exchange and its implementation using PMUs and other sensors is considered in the context of next generation SCADA, referred to as Dynamic Monitoring and Decision Systems (DyMoNDS). This contribution is summarized for its relevance to ensuring reliable electricity service by the changing electric power system that is characterized by dynamic actions not fully under the control of utility operators. Specific methods reported in sections 3 and 4 are put in the context of broader framework for supporting interactions in complex electric power grids so that each group of grid users, and the grid itself, contribute to electricity service according to well-defined interactions within a multi-layered modeling for future electric power grids. A transformed state space lends itself naturally to answering some key questions in this project, namely determining the minimum number of sensors (PMUs) and PMU-enabled actuators so that power transfers across area boundaries are stabilized in closed loop is achieved. The transformed state space is fully formalized in a major recently completed publication [R3]. It has been conceptualized how, instead of modeling system dynamics as a single "flat" model, interactions between components within an area and interactions between areas within a region can be captured by utilizing the notion of so-called interaction variables. This concept could form the basis of next generation SCADA needed for PMU-based control without excessive complexity.

Specific contributions in Section 3 are made in collaboration with graduate student Nipun Popli, who is currently a postdoctoral fellow at the MIT Energy initiative. Early on in this project he CMU team worked on graph methods for placing the PMUs and controllers so that the small signal stability of an electric power system is achieved. Theoretical work was done on structural controllability and observability conditions which can be used to select minimum number of locations and types of sensors and actuators to ensure stable operation. This resulted in the following publications:

- Nipun Popli, Sergio Pequito, Soummya Kar, A Pedro Aguiar, and Marija Ilic. Selective strong structural minimum cost resilient co-design for regular descriptor linear systems. to appear in Automatica (arXiv preprint arXiv:1704.01157, 2017)

- S. Pequito, N. Popli, S. Kar, M. Ilic, and A.P Aguiar. A framework for actuator placement in large scale power systems: Minimal strong structural controllability. In Proceedings of IEEE International Workshop on Computational Advances in Multi-Sensor Adaptive Processing, December 2013.

- Nipun Popli. Multi-layered Energy Conversion and Frequency Control in Complex Electric Power Systems. PhD thesis, Department of Electrical and Computer Engineering, Carnegie Mellon University, USA, 2017.

Dr. Nipun Popli continued working at CMU after his doctoral thesis defense. Dr. Slava Maslennikov (ISO-NE) served as an industry advisor on his PhD thesis committee. This has ensured direct collaboration with our industry member who provided us with most feedback throughout this project.

Specific contribution to this project was made by the CMU graduate student Stefanos Baros, currently also a postdoctoral fellow at the MIT Energy Initiative. Under this effort specific control schemes of wind farms were introduced by incorporating feedback signals from PMU measurements, to enable them to regulate their power output to system-conditions-dependent dynamic references. By meeting these power references the WFs can contribute to guaranteed small-signal stability of the interconnected system while its loading conditions vary. As a follow up to our earlier work, we have further enhanced the methods for distributed control of wind power plants, and two technical papers have been published:

- S. Baros, M. Ilic, Distributed Torque Control of Deloaded Wind DFIGs for Wind Farm Power Output Regulation, IEEE Transactions on Power Systems, Volume: 32, Issue: 6, pp. 4590 - 4599, Nov. 2017.

- S. Baros, M. Ilic, A Consensus Approach to Real-time Distributed Control of Energy Storage Systems in Wind Farms, IEEE Transactions on Smart Grid, vol. PP, Issue: 99, pp.1-1, Sept. 2017 This work represents an illustration of how one may use PMUs to enable integration of renewable resources.

Part 2 of this report is organized as follows. In Section 2, the efforts and specific contributions are put in the context of broader needs and opportunities emerging in the changing industry. As the industry is changing, many solutions are being proposed. It has been difficult to put the specific methods into use. To cope with this problem, a unified approach is needed for modeling which supports extensions of current operating protocols to include and use fast measurements without data overload, and at value. In particular, placement of PMUs for enabling best power delivery requires in start that these make the system dynamics observable. Section 3 provides results on specific methods introduced to do this. Similarly, once the system dynamics is observable, one can begin to place actuators and protection to close the loop and ensure stable operation. Analogue method can be used to place actuators for fast closed-loop control. Ultimately, next generation SCADA begins to emerge into carefully selected fast communications scheme supporting fast control/protection that ensures no instabilities, such as voltage collapse. Finally, Section 4 concerns specific uses of PMUs for controlling wind farms so that they can in an aggregated way provide power committed to the system operator. The specific contributions and publications are examples of how this can be done, assuming PMU measurements are available and utilized.

2. A structural approach to operations in the changing industry

2.1 Overview

The overall approach we take is based on the structural modeling and performance metrics needed for monitoring and control of the changing electric power systems. An important objective has been to establish a foundation for multi-layered modeling so that:

- A systematic information structure is established between different industry layers, starting from EHV balancing authorities (BAs), through transmission providers, load serving entities (LSEs), distribution companies, down to very small clusters of end users.
- This information structure forms the basis for future general end-to-end multi-layered SCADA with well-defined functionalities.
- The next generation SCADA builds on the existing information exchange supporting economic dispatch and automatic generation control (AGC).
- An interaction variable (intVar) is an aggregate measure of multi-rate multi-spatial power imbalance between an intelligent Balancing Authority (iBA) and the rest of the system to which it is interconnected.
- Different sensors and communication channels are needed for different level of temporal and spatial granularity. For the first time even the very fast intVar relevant for monitoring fast transient instabilities and, even electromagnetic interactions between different parts of power electronically controlled parts of the system can be used. PMUs are one particular example of such fast sensors.

We provide the contextual rationale for extending today's SCADA and NERC criteria to multi-temporal and multi-spatial information exchange protocols in support of highly distributed and highly dynamic industry in which resources, demand and grid which potentially can cause reliability problems and can also contribute to enabling more reliable electricity services.

This section is based on the invited presentation made by Prof Marija Ilic to PSERC Systems Stem, December 2016 in Atlanta, Georgia. The work is motivated by the general observation that as the industry moves forward to adopt new technologies, and to integrate new non-utility stakeholders into the electric power grid, many non-unique/methods-dependent solutions become possible. In particular, key to the PSERC project S-64, it is clear that there exists the need for next generation controllers using PMUs to avoid system stress, such as congestion of thermal limits, voltage collapse, loss of synchronism, inter-area oscillations and many other complex grid problems. Potentially powerful methods are generally hard to utilize for variety of reasons. To start with, it is hard to explain to map potential benefits from these methods into binding information protocols and reliability requirements. As a result, there exists a disconnect between what PMUs and new smarter controllers/protection can do, on one hand, and the regulatory and financial incentives for their deployments. In this section we propose a possible way forward by which all entities

connected to the grid are required to become or belong to an intelligent Balancing Authority iBA [Stefanos Baros, and Marija Ili. "Intelligent balancing authorities (IBAS) for transient stabilization of large power systems." PES General Meeting— Conference & Exposition, 2014 IEEE. IEEE, 2014.] responsible for either operating in an islanded disconnected way or, if connected, exchanging minimum information at the pre-agreed rates. This minimum information exchange basically needs to be such that iBAs meet their own internal sub-objectives subject to ensuring that commitment made through the required information exchange are met. This approach is intended to both eliminate "free riders" and to manage otherwise overwhelming complexity which can result from the need for a single system operator to model and control very detailed spatial and temporal interconnected system dynamics. At the same time, it is a natural outgrowth of today's balancing authorities. Notably, the emergence of "mini-control areas" closer to the end users was foreseen some time ago by both early visionaries in our field [Lester Fink in Ilic, Marija, Francisco Galiana, and Lester Fink, eds. Power systems restructuring: engineering and economics. Springer Science & Business Media, 2013]. Also, we observe that early in industry deregulation some major non-utility players, including Enron [Free, Clinton, and Norman Macintosh. "Management control practice and culture at Enron: The untold story." (2006)], wanted to become their own control areas, but this idea was not approved by the industry. More recently, it has become practically impossible to manage highly unconventional intermittent resources as well as price responsive demand according to reliability rules in place.

Notably, managing uncertainties is difficult since most of the rules rely on (N-1)/(N-2) deterministic criteria. The technologies and methods capable of managing these uncertainties are therefore hard to justify and pay for. Speaking more generally, anything that is not viewed as a deterministic disturbance is managed by setting margins just in case these uncertainties occur. There are no specific end users which are identified as sources of disturbances nor specific control/protection technologies dedicated to managing these disturbances. Section 2 is written with an intent to suggest a possible extension of today's balancing authorities (BAs) into iBAs with carefully defined binding information exchange. The main R&D challenge then becomes the one of physics-based modeling for setting specifications to be met by all groups of system users. These must be basis for straightforward to understand/enforce industry protocols. Prof. Marija Ilic proposed such approach for industry consideration in context of an invited testimony to FERC; FERC recommended to further discuss this proposal with industry. In this report we re-iterate principles of this proposal and attach as an appendix to the report the FERC testimony. In light of project S-64 methods monitoring and control methods introduced here are some examples of technologies needed to be used by the future iBAs so they implement methods for meeting iBA specifications proposed. Effectively, the proposed iBAs as the basis for next generation SCADA are an outgrowth of today's BAs which are more granular spatially and temporally. Because of fast intermittent disturbances it is no longer possible to only set criteria for quasi-static area-control-error (ACE), but iBAs must be responsible for small signal stability and transient stability. Similarly, spatial aggregation and granularity are an end-to-end concept which includes distribution systems, microgrids, non-utility owned distributed energy resources (DERs), demand response participation and alike. Finally, and possibly most critical, are extensions for enabling risk management related to wide range of disturbances and topology changes. If congestion occurs on the high voltage grid, it can be managed by the large generators as well as by the smaller clusters of grid users [Ilic, M., Joo,

J. Y., Carvalho, P. M., Ferreira, L. A., & Almeida, B. (2013, August). Dynamic monitoring and decision systems (DYMONDS) framework for reliable and efficient congestion management in smart distribution grids. In Bulk Power System Dynamics and Control-IX Optimization, Security and Control of the Emerging Power Grid (IREP), 2013 IREP Symposium (pp. 1-9). IEEE].

2.2 Main industry challenge

The above concerns comprise several major technical challenges:

1. Establishment of quantifiable performance criteria/metrics/protocols needed to support automated control of hard-to-predict (uncertain) deviations from scheduled conditions (power profiles and/or equipment status).

2. These are needed to avoid:

    - operational problems (short-term instabilities)
    - long-term instabilities (resource adequacy, financial instabilities, not discussed in this project).

The basic principles of the existing standards, notably AGC principles are summarized in an earlier PSERC report [Ilic, Marija. "Toward Plug-and-Play Standards for Dynamics in the Changing Electric Energy Systems." (2015)]. In the same report principles of new standards for the changing industry by evolving from the existing standards (based on similar high-level principles) are proposed.

The innovation challenges to deployment of methods proposed in project S-64 are as follows:

- There is no single entity charging the entire design, possibly different for micro-grids
- The power network spreads over vast geographical areas, creating challenges for sensing, communication and estimation.

Key issues that must be overcome are:

- Establishing a new information structure supported by future SCADA. The proposed structural approach is one possible way forward [Ilic, Marija D. "Toward a unified multi-layered modeling and simulation paradigm for electric energy systems." Power Symposium (NAPS), 2017 North American. IEEE, 2017.]
- What needs to be controlled
- Where to place sensors and why
- What needs to be communicated

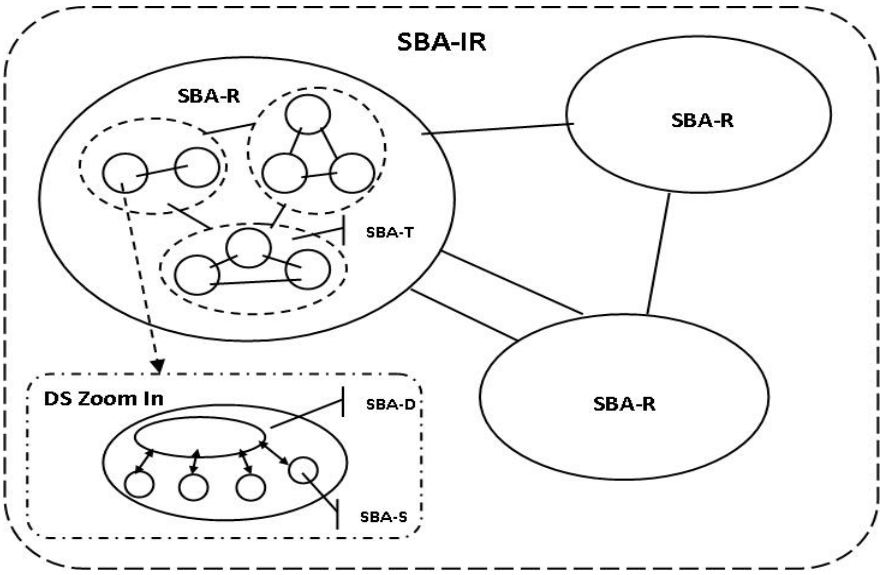

-SBA: Smart Balancing Authorities
(Generalization of Control Area)
-IR: Inter-Region
-R: Region
-T: Tertiary
-D: Distribution
-S: Smart Component

Figure 2.1: General structure of the emerging electric energy systems

2.3 General structure of the changing electric energy systems

Shown in Figure 1 is a sketch of the emerging electric energy system in which smart (intelligent) Balancing Authorities are interacting [Ilic, M., "Dynamic Monitoring and Decision Systems for Enabling Sustainable Energy Services", Network Engineering for Meeting the Energy and Environmental Dream, Scanning the Issue, Proc. of the IEEE, 2011.] Major observations:

- All about balancing power at the right temporal and spatial granularity (makes it simple)
- But, the models used are not explicitly posed this way
- New structural modeling to overcome this problem [Ilic, Marija D. "Toward a unified modeling and control for sustainable and resilient electric energy systems." Foundations and Trends in Electric Energy Systems 1.1-2 (2016): 1-141.]
- Use to support interactive Dynamic Monitoring and Decision Systems- DyMonDS
- Much room for generalizing today's hierarchical control
- Much room for making use of nonlinear control; use of PMUs to manage fast transient and small signal oscillations in real time.

2.4 Fundamental modeling contribution

Arriving at a physics-based structural modeling required using transformed state space for representing interactions between sub-systems/iBAs. Much the same way as today's specifications for automated generation control (AGC) are in terms of energy/power measured as area control error (ACE), we propose to model the high level interactions between iBAs using power and rate of change of power for a stratum of temporal horizons relevant for ensuring stable and reliable operation. In [Ilic, Marija D., and Rupamathi Jaddivada. "Multi-layered interactive energy space modeling for near-optimal electrification of terrestrial, shipboard and aircraft systems." Annual Reviews in Control (2018).] the fundamental underpinnings of this transformed state space modeling are derived. For purposes of this project and possible industry consideration it is relevant to summarize that interaction variables are a triple of data, representing power, rate of change of power and energy (time) specified for each temporal horizon of interest. This means that for very fast transient processes one must have technologies which are extremely flexible and are capable of delivering power at the rate specified over an extremely short time interval relevant for transient stability. This is followed by the slower specifications using the same common interaction variables. For example scheduling in energy markets will require specifications by the iBAs about power, rate of power produced (consumed) ("ramp rate") and time interval (hour, 15 minutes). The same way, frequency regulation will require the same variable specifications over the time interval relevant for this power balancing. If this is done, the system frequency, as a consequence, will remain within the tolerance specified by the industry [Ilic, M., Skantze, P., Yu, C. N., Fink, L., & Cardell, J. (1999, February). Power exchange for frequency control (PXFC). In Power Engineering Society 1999 Winter Meeting, IEEE (Vol. 2, pp. 809-819). IEEE.]

2.5 The role of PMUs and methods described in Sections 3 and 4

Assume now that a set of protocols/standards based on these interaction variable specifications is in place and the next generation SCADA communicates these variables for coordinated management at the system level. Meeting these requirements at the very fast rates (for transient and/or small signal stability) will prompt the iBAs to deploy and use methods which are capable of ensuring that the specifications communicated in terms of fast interaction variables are implementable. Methods introduced in Section 3 can be used to decide placement of PMUs, controllers and their communications (iBA-level SCADA) to ensure that the specifications about the net interaction of each iBA with the rest of the system are met. This is then utilized by the clusters of wind farms (Section 4) for their contribution to IBA meeting the specified performance. The entities utilizing more effective technologies will be capable of meeting these specifications at lower cost and serve their end users better. At the same time, they can participate in system-level management and electricity markets more competitively.

3. PMU-enabled small-signal voltage and frequency stabilization via decentralized control laws

We summarize CMU's proposed approach to co-design PMU-communication-Storage to guarantee voltage or frequency stabilization with decentralized control laws. The overall objective of the proposed co-design architecture is to guarantee observability, controllability and stable eigenmodes, in closed-loop, for both voltages and frequencies across the network.

3.1 Voltage and frequency stabilization: A strong structural approach

A large-scale power system's dynamics, for a wide range of operating conditions, is represented by a set of nonlinear differential algebraic equations as:

$$\dot{x}(t) = f(x(t), y(t), u(t), p(t)), \tag{3.1}$$

$$0 = g(x(t), y(t), u(t), p(t)). \tag{3.2}$$

where $x \in \mathbb{R}^n$, $u \in \mathbb{R}^m$, $y \in \mathbb{R}^p$ are the states, inputs and outputs, and $p \in \mathbb{R}^q$ the system parameters. Typically, for a small-signal stability analysis, the set (3.1)-(3.2) is linearized around the nominal operating point of the grid, to obtain a linear system:

$$\Delta\dot{x} = A\Delta x + B\Delta u, \tag{3.3}$$

$$\Delta y = C\Delta x. \tag{3.4}$$

The sets of equations (3.3)-(3.4) represent a standard state-space form. Subsequently, critical system properties such as observability, controllability, and stability of open-loop eigenmodes are assessed. Nevertheless, these assessments are based on following strong assumptions:

1. System Identification: The machine parameters $p \in \mathbb{R}^q$ are known accurately.
2. Time-invariance: The linearized representation is assumed to be fixed over time.

Now, it must be noted that observability, controllability, and stability properties are numerics-dependent. In other words, these properties are highly susceptible to (in)accuracies of the parameters and the time-invariance assumption for the linear representation. Besides, for large systems, the properties are also influenced by the accuracy of the computational algorithms. In this project we invoke the theory of selective strong structural systems to address such challenges. We assume that only the structure of the system matrix A is given. Specifically, the sparsity of the matrix A is categorized in the form of *strictly zero entry* (0), *strictly non-zero entry* ($\times$), or *arbitrary real-value entry* ($\otimes$) which can take zero or non-zero value. Furthermore, we assume that sparsities of the control input matrix B and output matrix C are unknown. In other words, the input and the output matrices are to be designed. For the given sparsity, the matrix A can take multiple numerical forms. Therefore, given the system matrix structure, the goal is to determine:

1. Best locations for placing PMUs, which measure only one state variable each, to ensure system observability for all nominal operating conditions.

2. Best locations for placing ideal controllers, for instance, capacitor banks for voltage stabilization or fast storage for frequency stabilization, which control only one state variable each, to ensure system controllability for all nominal operating conditions.

3. Best communication channels between the PMUs selected in 1), and the controllers selected in 2), such that eigenmodes, in closed-loop, are stabilizable for all nominal operating conditions. Specifically, there are no fixed modes in closed-loop.

The aforementioned objectives translate in to the following subproblems:

1. Design sparsity of the output matrix C, with each row having exactly one *strictly non-zero entry* ($\times$), so that (A, C) are observable for all numerical realizations.

2. Design sparsity of the input matrix B, with each column having exactly one *strictly non-zero entry* ($\times$), so that (A, B) are controllable for all numerical realizations.

3. Design sparsity of the gain matrix K, coupling each *strictly non-zero entry* ($\times$) in output matrix C to exactly one *strictly non-zero entry* ($\times$) in input matrix B, so that the eigenmodes of the closed-loop matrix $(A - BKC)$ are stabilizable for all numerical realizations.

Motivated by the need for a formal framework to deploy storage-based technologies to ensure system-wide dynamic controllability, the concept of strong structural theory was utilized in [1]. More precisely, the storage-based technologies such as batteries, electric vehicle charging stations, cluster of flywheels, fast demand response, etc actuate the most critical state variables in the form of power injections and bus frequencies, to guarantee system-wide dynamic controllability across wide range of operating conditions. For instance, in [1], it was illustrated that careful selection of candidate load for frequency-based demand response precludes the requirement of expensive grid-scale storage. For example, in support of frequency stabilization, the matrix A of the linearized system in (3.3) is inherently singular due to power conservation laws captured by the algebraic equations in (3.2). Therefore, the controllability for the pair (A, B) cannot be ensured. So, the issue of an interconnected system's singularity, or loss of controllability, due to power conservation laws, can be addressed by placing either a fast storage device or automating controllable demand technologies [1, 2]. Effectively, by placing of fast or ideal balancing resources, the matrix B is designed so that the pair (A, B) is controllable. In addition, by invoking the concept of duality, our proposed notion of system-wide dynamic controllability can be extended to ensure system-wide dynamic observability [1]. Particularly, the framework allows for the selection of state variables to be measured with fast PMU-based sensors. For instance, in case of voltage stabilization, it is difficult to guarantee observability for pair (A, C) under certain numerical scenarios resulting from some of the operating conditions. To overcome this problem, the matrix C can be designed for a provably observable pair (A, C) over a wide range of operating condition. Now, in the context of large-scale power systems, we often require decentralized control schemes due to limited data sharing between the sensors and the controllable resources. The information pattern captures the information accessibility to controllable resources and implicitly represents the communication/cyber requirements associated with the decentralized control scheme, and its design is crucial to attain feasible decentralized control solutions. Subsequently, it is imperative to design communication channels to close the loop between the sensors and the actuators without fixed modes [3].

We propose that the guarantee of closed-loop stability, achieved by co-design approach to PMU-communication-storage architecture, is robust to parametric uncertainties as well as the assumption of time-invariance of the linearized system [4]. The proposed approach can be adopted to address small-signal stability of voltage/frequency around different operating points. In summary, conventional analysis only tests if instability may occur with the existing primary controllers, however, we propose a co-design of co-design approach to PMU-communication-storage architecture for obtaining decentralized control laws that would ensure the stability properties. Next, a proof-of-concept example is provided in support of the proposed approach.

3.2 Proof-of-concept: 5-bus power system

Consider in Fig. 3.1 a 5-bus power system with five dynamical components interconnected through transmission lines. These are two coal-fired steam turbines C_1, C_2, one gas-fired combustion turbine G_3 and the aggregate loads D_4, D_5. The generators C_1, C_2 and G_3 are modeled as linearized

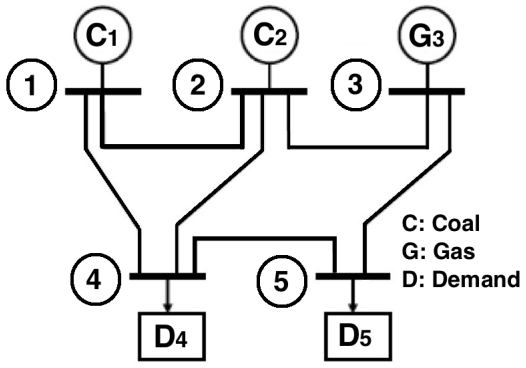

Figure 3.1: IEEE 5-bus test system (*1,2,3,4,5* are the bus numbers)

governor control. The aggregate loads D_4, D_5, modeled as dynamic components, are represented by swing equations. Subsequently, the generators and the loads are electrically coupled through the differentiated linearized real-power flow equations[1]. The 5-bus power system is represented as a 16^{th} order LTI system (3.3), and the structural representation of the matrix $A_{5_{\text{bus}}}$ is of the form:

where, the state variables are described in Table 3.1.

The first step is to ensure controllability of the 5-bus system over wide range of operating conditions, particularly for a given or a known sparsity of the structural matrix $A_{5_{\text{bus}}}$. Therefore, we determine the minimal number of storage-based devices to be placed in the system, along with their locations. Now, let there be a 16^{th} order structural identity matrix I_{16}, with diagonal entries as strictly nonzero $(\times)$ and off-diagonal entires as strictly zero (0). Therefore, for each $\lambda \in \mathbb{C}$, the sparsity of the matrix $A^{\lambda}_{5_{\text{bus}}} = A_{5_{\text{bus}}} - \lambda I_{16}$ is of the form: Next, the rows and columns of the structural matrix $A^{\lambda}_{5_{\text{bus}}} = A_{5_{\text{bus}}} - \lambda I_{16}$ are permuted to obtain a lower-triangular form $M^{\lambda}_{5_{\text{bus}}}$ (see [1] for details on algorithm):

where the row and the column indices labelled in $M^{\lambda}_{5_{\text{bus}}}$ correspond to the row and the column indices in $A^{\lambda}_{5_{\text{bus}}}$, i.e., before permutations, respectively. Simply speaking, they correspond to

[1]The coupling constraints are the linearized power flow equations. For the purpose of real-power balancing, decoupling between real and reactive power flow is assumed.

$$A_{5_{\text{bus}}} = \begin{bmatrix}
\times & \times & \times & 0 & 0 & 0 & 0 & 0 & 0 & 0 & 0 & \times & 0 & 0 & 0 & 0 \\
0 & \times & \times & 0 & 0 & 0 & 0 & 0 & 0 & 0 & 0 & 0 & 0 & 0 & 0 & 0 \\
\times & 0 & \times & 0 & 0 & 0 & 0 & 0 & 0 & 0 & 0 & 0 & 0 & 0 & 0 & 0 \\
0 & 0 & 0 & \times & \times & \times & 0 & 0 & 0 & 0 & 0 & 0 & \times & 0 & 0 & 0 \\
0 & 0 & 0 & 0 & \times & \times & 0 & 0 & 0 & 0 & 0 & 0 & 0 & 0 & 0 & 0 \\
0 & 0 & 0 & \times & 0 & \times & 0 & 0 & 0 & 0 & 0 & 0 & 0 & 0 & 0 & 0 \\
0 & 0 & 0 & 0 & 0 & 0 & \times & \times & 0 & 0 & 0 & 0 & 0 & \times & 0 & 0 \\
0 & 0 & 0 & 0 & 0 & 0 & 0 & \times & \times & 0 & 0 & 0 & 0 & 0 & 0 & 0 \\
0 & 0 & 0 & 0 & 0 & 0 & \times & 0 & \times & 0 & 0 & 0 & 0 & 0 & 0 & 0 \\
0 & 0 & 0 & 0 & 0 & 0 & 0 & 0 & 0 & \times & 0 & 0 & 0 & 0 & \times & 0 \\
0 & 0 & 0 & 0 & 0 & 0 & 0 & 0 & 0 & 0 & \times & 0 & 0 & 0 & 0 & \times \\
\times & 0 & 0 & \times & 0 & 0 & 0 & 0 & 0 & \times & 0 & \times & 0 & 0 & 0 & 0 \\
\times & 0 & 0 & \times & 0 & 0 & \times & 0 & 0 & \times & 0 & 0 & \times & 0 & 0 & 0 \\
0 & 0 & 0 & \times & 0 & 0 & \times & 0 & 0 & 0 & \times & 0 & 0 & \times & 0 & 0 \\
\times & 0 & 0 & \times & 0 & 0 & 0 & 0 & 0 & \times & \times & 0 & 0 & 0 & \times & 0 \\
0 & 0 & 0 & 0 & 0 & 0 & \times & 0 & 0 & \times & \times & 0 & 0 & 0 & 0 & \times
\end{bmatrix},$$

$$A^{\lambda}_{5_{\text{bus}}} = \begin{bmatrix}
\otimes & \times & \times & 0 & 0 & 0 & 0 & 0 & 0 & 0 & 0 & \times & 0 & 0 & 0 & 0 \\
0 & \otimes & \times & 0 & 0 & 0 & 0 & 0 & 0 & 0 & 0 & 0 & 0 & 0 & 0 & 0 \\
\times & 0 & \otimes & 0 & 0 & 0 & 0 & 0 & 0 & 0 & 0 & 0 & 0 & 0 & 0 & 0 \\
0 & 0 & 0 & \otimes & \times & \times & 0 & 0 & 0 & 0 & 0 & 0 & \times & 0 & 0 & 0 \\
0 & 0 & 0 & 0 & \otimes & \times & 0 & 0 & 0 & 0 & 0 & 0 & 0 & 0 & 0 & 0 \\
0 & 0 & 0 & \times & 0 & \otimes & 0 & 0 & 0 & 0 & 0 & 0 & 0 & 0 & 0 & 0 \\
0 & 0 & 0 & 0 & 0 & 0 & \otimes & \times & 0 & 0 & 0 & 0 & 0 & \times & 0 & 0 \\
0 & 0 & 0 & 0 & 0 & 0 & 0 & \otimes & \times & 0 & 0 & 0 & 0 & 0 & 0 & 0 \\
0 & 0 & 0 & 0 & 0 & 0 & \times & 0 & \otimes & 0 & 0 & 0 & 0 & 0 & 0 & 0 \\
0 & 0 & 0 & 0 & 0 & 0 & 0 & 0 & 0 & \otimes & 0 & 0 & 0 & 0 & \times & 0 \\
0 & 0 & 0 & 0 & 0 & 0 & 0 & 0 & 0 & 0 & \otimes & 0 & 0 & 0 & 0 & \times \\
\times & 0 & 0 & \times & 0 & 0 & 0 & 0 & 0 & \times & 0 & \otimes & 0 & 0 & 0 & 0 \\
\times & 0 & 0 & \times & 0 & 0 & \times & 0 & 0 & \times & 0 & 0 & \otimes & 0 & 0 & 0 \\
0 & 0 & 0 & \times & 0 & 0 & \times & 0 & 0 & 0 & \times & 0 & 0 & \otimes & 0 & 0 \\
\times & 0 & 0 & \times & 0 & 0 & 0 & 0 & 0 & \times & \times & 0 & 0 & 0 & \otimes & 0 \\
0 & 0 & 0 & 0 & 0 & 0 & \times & 0 & 0 & \times & \times & 0 & 0 & 0 & 0 & \otimes
\end{bmatrix}$$

$$M^{\lambda}_{5_{\text{bus}}} = \begin{bmatrix}
 & \textit{3} & \textit{2} & \textit{1} & \textit{12} & \textit{6} & \textit{5} & \textit{4} & \textit{13} & \textit{9} & \textit{8} & \textit{7} & \textit{10} & \textit{14} & \textit{15} & \textit{11} & \textit{16} \\
\textit{2} & \times & \otimes & & & & & & & & & & & & & & \\
\textit{3} & \otimes & 0 & \times & & & & & & & & & & & & & \\
\textit{1} & \times & \times & \otimes & \times & & & & & & & & & & & & \\
\textit{5} & 0 & 0 & 0 & 0 & \times & \otimes & & & & & & & & & & \\
\textit{6} & 0 & 0 & 0 & 0 & \otimes & 0 & \times & & & & & & & & & \\
\textit{4} & 0 & 0 & 0 & 0 & \times & \times & \otimes & \times & & & & & & & & \\
\textit{8} & 0 & 0 & 0 & 0 & 0 & 0 & 0 & 0 & \times & \otimes & & & & & & \\
\textit{9} & 0 & 0 & 0 & 0 & 0 & 0 & 0 & 0 & \otimes & 0 & \times & & & & & \\
\textit{12} & 0 & 0 & \times & \otimes & 0 & 0 & \times & 0 & 0 & 0 & 0 & \times & & & & \\
\textit{13} & 0 & 0 & \times & 0 & 0 & 0 & \times & \otimes & 0 & 0 & \times & \times & & & & \\
\textit{7} & 0 & 0 & 0 & 0 & 0 & 0 & 0 & 0 & 0 & \times & \otimes & 0 & \times & & & \\
\textit{10} & 0 & 0 & 0 & 0 & 0 & 0 & 0 & 0 & 0 & 0 & 0 & \otimes & 0 & \times & & \\
\textit{14} & 0 & 0 & 0 & 0 & 0 & 0 & \times & 0 & 0 & 0 & \times & 0 & \otimes & 0 & \times & \\
\textit{15} & 0 & 0 & \times & 0 & 0 & 0 & \times & 0 & 0 & 0 & 0 & \times & 0 & \otimes & \times & \\
\textit{11} & 0 & 0 & 0 & 0 & 0 & 0 & 0 & 0 & 0 & 0 & 0 & 0 & 0 & 0 & \otimes & \times \\
\textit{16} & 0 & 0 & 0 & 0 & 0 & 0 & 0 & 0 & 0 & 0 & \times & \times & 0 & 0 & \times & \otimes
\end{bmatrix}$$

Table 3.1: 5-bus power system state variables

States	Description
x_1	C_1's prime mover frequency
x_2	C_1's turbine mechanical power output
x_3	C_1's governor valve position
x_4	C_2's prime mover frequency
x_5	C_2's turbine mechanical power output
x_6	C_2's governor valve position
x_7	G_3's turbine fuel flow
x_8	G_3's prime mover frequency
x_9	G_3's governor valve position
x_{10}	frequency at bus-4
x_{11}	frequency at bus-5
x_{12}	power injection by C_1
x_{13}	power injection by C_2
x_{14}	power injection by G_3
x_{15}	power consumption by D_4
x_{16}	power consumption by D_5

$$M^{\lambda}_{5_{\text{bus}}} = \begin{array}{c} \\ 2 \\ 3 \\ 1 \\ 5 \\ 6 \\ 4 \\ 8 \\ 9 \\ 12 \\ 13 \\ 7 \\ 10 \\ 14 \\ 15 \\ 11 \\ 16 \end{array} \begin{bmatrix} 3 & 2 & 1 & 12 & 6 & 5 & 4 & 13 & 9 & 8 & 7 & 10 & 14 & 15 & 11 & 16 \\ \times & \otimes & & & & & & & & & & & & & & \\ \otimes & 0 & \times & & & & & & & & & & & & & \\ \times & \times & \otimes & \times & & & & & & & & & & & & \\ 0 & 0 & 0 & 0 & \times & \otimes & & & & & & & & & & \\ 0 & 0 & 0 & 0 & \otimes & 0 & \times & & & & & & & & & \\ 0 & 0 & 0 & 0 & \times & \times & \otimes & \times & & & & & & & & \\ 0 & 0 & 0 & 0 & 0 & 0 & 0 & 0 & \times & \otimes & & & & & & \\ 0 & 0 & 0 & 0 & 0 & 0 & 0 & 0 & \otimes & 0 & \times & & & & & \\ 0 & 0 & \times & \otimes & 0 & 0 & \times & 0 & 0 & 0 & 0 & \times & & & & \\ 0 & 0 & \times & 0 & 0 & 0 & \times & \otimes & 0 & 0 & \times & \times & & & & \\ 0 & 0 & 0 & 0 & 0 & 0 & 0 & 0 & 0 & \times & \otimes & 0 & \times & & & \\ 0 & 0 & 0 & 0 & 0 & 0 & 0 & 0 & 0 & 0 & 0 & \otimes & 0 & \times & & \\ 0 & 0 & 0 & 0 & 0 & 0 & \times & 0 & 0 & 0 & \times & 0 & \otimes & 0 & \times & \\ 0 & 0 & \times & 0 & 0 & 0 & \times & 0 & 0 & 0 & 0 & \times & 0 & \otimes & \times & \\ 0 & 0 & 0 & 0 & 0 & 0 & 0 & 0 & 0 & 0 & 0 & 0 & 0 & 0 & \otimes & \times \\ 0 & 0 & 0 & 0 & 0 & 0 & 0 & 0 & 0 & 0 & \times & \times & 0 & 0 & \times & \otimes \end{bmatrix}$$

the state variables indices to be considered for the storage-PMU-communicaton channel design. Notice that $M^{\lambda}_{5_{\text{bus}}}$ contains 13 strictly non-zero entries, marked as $\times$:

It must be noted that there exist no non-zero entries in rows labeled as $13, 15, 16$. In addition, the rows with labels $12, 13$ in $M^{\lambda}_{5_{\text{bus}}}$ can be permuted so that there are no non-zero entries in rows labeled as $12, 15, 16$. Similar argument holds for the rows with labels $14, 15$. Therefore, it requires three dedicated storage-devices, and the possible collection of state variables that can be controlled by dedicated actuators are indexed by $\mathscr{I}_1 = \{12, 14, 16\}$, $\mathscr{I}_2 = \{13, 14, 16\}$, $\mathscr{I}_3 = \{12, 15, 16\}$, or $\mathscr{I}_4 = \{13, 15, 16\}$ (notice the row indices highlighted in red). Corresponding to these solutions, there are three possible ways to construct the input matrix $B_{5_{\text{bus}}}$, so that the row-column permutation of the concatenated matrix $\left[A^{\lambda}_{5_{\text{bus}}}, B_{5_{\text{bus}}}\right]$ will fulfill Popov controllability test for all possible realization of the structural matrix $A_{5_{\text{bus}}}$. To summarize, at least three dedicated storage devices

$$M^{\lambda}_{5_{\text{bus}}} = \begin{bmatrix}
 & 3 & 2 & 1 & 12 & 6 & 5 & 4 & 13 & 9 & 8 & 7 & 10 & 14 & 15 & 11 & 16 \\
2 & \times & \otimes & & & & & & & & & & & & & & \\
3 & \otimes & 0 & \times & & & & & & & & & & & & & \\
1 & \times & \times & \otimes & \times & & & & & & & & & & & & \\
5 & 0 & 0 & 0 & 0 & \times & \otimes & & & & & & & & & & \\
6 & 0 & 0 & 0 & 0 & \otimes & 0 & \times & & & & & & & & & \\
4 & 0 & 0 & 0 & 0 & \times & \times & \otimes & \times & & & & & & & & \\
8 & 0 & 0 & 0 & 0 & 0 & 0 & 0 & 0 & \times & \otimes & & & & & & \\
9 & 0 & 0 & 0 & 0 & 0 & 0 & 0 & 0 & \otimes & 0 & \times & & & & & \\
12 & 0 & 0 & \times & \otimes & 0 & 0 & \times & 0 & 0 & 0 & 0 & \times & & & & \\
13 & 0 & 0 & \times & 0 & 0 & 0 & \times & \otimes & 0 & 0 & \times & \times & & & & \\
7 & 0 & 0 & 0 & 0 & 0 & 0 & 0 & 0 & 0 & \times & \otimes & 0 & \times & & & \\
10 & 0 & 0 & 0 & 0 & 0 & 0 & 0 & 0 & 0 & 0 & 0 & \otimes & 0 & \times & & \\
14 & 0 & 0 & 0 & 0 & 0 & 0 & \times & 0 & 0 & 0 & \times & 0 & \otimes & 0 & \times & \\
15 & 0 & 0 & \times & 0 & 0 & 0 & \times & 0 & 0 & 0 & 0 & \times & 0 & \otimes & \times & \\
11 & 0 & 0 & 0 & 0 & 0 & 0 & 0 & 0 & 0 & 0 & 0 & 0 & 0 & 0 & \otimes & \times \\
16 & 0 & 0 & 0 & 0 & 0 & 0 & 0 & 0 & 0 & 0 & \times & \times & 0 & 0 & \times & \otimes
\end{bmatrix}$$

are required to achieve the condition of controllability over wide range of operating condition, and their placement in the 5-bus system is non unique. Nevertheless, as per the four alternative input matrices achieving the minimal design, the state variables to be controlled are subsets of the nodal power injections/consumptions. The states x_{16} always require a dedicated storage, i.e., the power consumption by the aggregate load D_5. For example, instead of placing a storage device at D_5 to actuate x_{16}, a possible alternative is to actuate the aggregate load by embedding local automation. The second storage device can be placed at bus-4 (x_{15}), or, at bus-3 (x_{14}). The third can be placed at bus-4 (x_{15}), or, at bus-3 (x_{14}). All possible input matrices are physically feasible. However, based on performance objective, for example cost or location of storage, some of the input matrices may be more suitable. But, all possible input matrix constructions are physically feasible. Similarly, for observability across wide range of operating of operating conditions, three dedicated PMU-based sensors are required. However, in contrast to the non unique solutions to guarantee controllability, the solution to ensure observability condition is unique, and consists in measuring with three dedicated sensors, the state variables indexed by $\mathscr{J} = \{2, 5, 8\}$. The output matrix $C_{5_{\text{bus}}}$ can be constructed in a unique way. The state variables that need to be measured are turbine mechanical power outputs of C_1 (bus-1) and C_2 (bus-2), and the prime mover frequency deviations of G_3 (bus-3), marked as $\otimes$: Next, minimum three communication links are required to relay the data from the PMU-based sensors measuring the state variables indexed by $\mathscr{J} = \{2, 5, 8\}$, to the three storage-based devices. The objective is to ensure, in closed-loop, the system is stabilizable for all realizations of the matrices. In other words, for the given sparsity of the system matrix $A_{5_{\text{bus}}}$, each sensor-measurement (represented by one row in $C_{5_{\text{bus}}}$), is fed to each storage-based controller (represented by one column in $B_{5_{\text{bus}}}$), so that the output-based feedback ensures stability of the system for all possible realization of $A_{5_{\text{bus}}}$, $B_{5_{\text{bus}}}$, and $C_{5_{\text{bus}}}$. In other words, the exist no fixed modes for any of the operating condition. More precisely, the stabilizability of the system is guaranteed is the sensors and the storage are paired based on the approach proposed in [4]. In case of the given 5-bus system, non unique pairing exists between the three PMUs and three storage devices. Therefore, suppose that the cost associated with the possible storage placement schemes is uniform, i.e., the placing of storage-based energy resources at $\mathscr{I}_1 = \{12, 14, 16\}$, $\mathscr{I}_2 = \{13, 14, 16\}$, $\mathscr{I}_3 = \{12, 15, 16\}$, or $\mathscr{I}_4 = \{13, 15, 16\}$ require same capital investment. In addition, assume that the cost associated with communication channels are nonuniform, and are based on the distance between the buses. Assuming a homogenous cost of control by battery storage, and a homogenous

cost of sensing by PMUs, the cost of communication links is determined by the pairings between the PMUs and the storages devices. If the PMU-based measurements of the state variables indexed by $\mathscr{J} = \{2, 5, 8\}$ are fed to the dedicated storage devices actuating the state variables indexed by $\mathscr{I}_2 = \{13, 14, 16\}$, based on the pairings $(13, 5)$, $(14, 8)$ and $(16, 2)$, minimum communication cost is incurred. Notice that the pairing between PMUs and storage devices. The pairings $(13, 5)$ and $(14, 8)$ are placed at the same geographical location, i.e., bus-2 and bus-3, respectively. In addition, the proposed stabilizability property can be made robust with respect failure of dedicated storage device(s), dedicated PMU-based sensor(s), or a communication channel(s) (see [4] for details).

4. Distributed control of wind farms for power output regulation

In our work we developed distributed control methods for power output regulation of wind farms comprised of state-of-the-art (SoA) wind generators (WGs). Since wind farms produce high amount of power in current power systems, we can leverage their power regulation capability together with the advanced measurement capabilities of PMUs to ensure small signal stability and effective power control in certain areas of power systems. In the first thrust which we analyze below, we developed a distributed control design which can be adopted by SoA WGs with integrated storage devices to continuously, dynamically and distributively self-organize and control their power outputs by exploiting limited peer-to-peer communication. With the proposed scheme a wind farm can ensure that its total power output tracks a total power reference under highly dynamical conditions. This reference can be fast-varying depending on the overall system conditions. In the second thrust which we analyze below, we developed a distributed method for torque control of deloaded wind double-fed induction generators (DFIGs), the most common type of WGs deployed today. With this control scheme deloaded DFIGs can dynamically, distributively and fairly self-dispatch and adjust the power they generate so that their total power closely tracks a dynamic reference. By designing these advanced control methods, our goal was to enable WFs to effectively regulate their power outputs fast and dynamically in order to meet system-level stability requirements as well as to ensure that power transferred through specific transmission lines in the vicinity of the WFs respects certain thermal limits. Implementation of our proposed advanced feedback control schemes that we analyze below requires that several state-variables are measured using PMUs.

4.1 A consensus approach to real-time distributed control of energy storage systems in wind farms

According to a U.S. DOE study envisions that the wind integration level in the coming years (by 2050) is going to be such that 35% of the U.S. annual electricity demand will be generated by wind generators. Although high wind integration levels are desirable, there are some obstacles that need to be circumvented before they become realizable. The most important challenges related to high wind integration are balancing wind intermittency by enabling WGs to provide short-term predictable power and to provide frequency/inertial control. Because of wind intermittency, power quality deteriorates and the cost of electricity increases since expensive generators are called to generate the mismatch between scheduled/predicted and real wind power. At the same time, having WGs replacing SGs without providing frequency/inertial control decreases the overall inertia of the grid. As a result, power imbalances cause a more pronounced effect on the system frequency. Fortunately, nowadays, General Electric (GE) is commercializing state-of-the-art (SoA) WGs that have energy storage incorporated into their design, which provides a promising technology for overcoming the above issues. Nevertheless, in both industry and academia, no systematic control methods for this WG technology have been proposed that reveal and take full advantage of its capabilities. In our research, we established several novel distributed control architectures for the SoA WGs that have, among others, the following attributes: 1) they are based on ideas from multi-agent systems theory (e.g consensus), enabling eets of SoA WGs to accomplish mul-

tiple complex capabilities that require coordination; 2) they integrate and leverage the available advanced sensing, communication technologies into the control scheme of the SoA WGs; 3) have theoretical guarantees for the stability and performance they attain.

In our paper "A Consensus Approach to Real-time Distributed Control of Energy Storage Systems in Wind Farms", we established a novel distributed control architecture for SoA WGs that enables them to balance the wind intermittency and provide short-term predictable power at the wind farm level, using the storage devices in a load-sharing fashion (i.e all storage devices provide the same amount of power). Lastly, we developed Control Lyapunov Function-based power electronics controllers for SoA WGs that implement the proposed protocol. The distributed power-electronics control architecture: 1) will contribute to the total generation cost reduction (especially in large-scale applications) since it uses stored wind energy, which eliminates the need for fast ramping-up SGs; 2) is practically realizable, requiring WGs to exchange feedback signals that can be easily measured locally; 3) has stability and performance that are guaranteed with or without communication delays.

On the practical side, regarding SoA WGs, our work is the rst work that introduces a distributed power-electronics control architecture that exploits and reveals their full potential and enables them to accomplish complex objectives through self-organization and coordination. Further, we emphasize that since these WGs will be main energy generating units in the coming years, systematic control methods that are both practical and mathe-matically rigorous are needed before their large-scale application. Below we present the main ideas and results obtained in this research thrust.

4.2 Modeling

Here we are concerned with wind DFIGs as they are the most popular and commonly deployed WGs today. Wind DFIGs are characterized by high operational efficiency as they can vary the speed of their rotors in a wide range extracting maximum power from the wind for a large span of wind speed conditions. Interestingly, General Electric (GE) is now commercializing DFIGs with storage devices with the additional flexibility (over standard DFIGs) of being capable of meeting power commitments even when the wind conditions are poor. A typical DFIG with a storage device is depicted in Fig. 4.1. In what follows, we use the following notation convention. We denote the set of SoA DFIGs by $\mathscr{G}$ and index each WG by i such that $i \in \mathscr{G}$. The relevant models for our analysis are the models of the GSC, the interfacing capacitor, and the supercapacitor which we present next.

Grid-side Converter Model

The GSC model captures the dynamics of its output current in a $d-q$ coordinate system and it can be stated as follows.

$$\frac{dI_{dg,i}}{dt} = -\omega_s\Big(\frac{R_{g,i}}{L_{g,i}}\Big)I_{dg,i}+\omega_s I_{qg,i}+\omega_s\Big(\frac{V_{dg,i}-V_{s,i}}{L_{g,i}}\Big) \tag{4.1a}$$

$$\frac{dI_{qg,i}}{dt} = -\omega_s\Big(\frac{R_{g,i}}{L_{g,i}}\Big)I_{qg,i}-\omega_s I_{dg,i}+\omega_s\Big(\frac{V_{qg,i}}{L_{g,i}}\Big), i \in \mathscr{G} \tag{4.1b}$$

The constants $R_{g,i}, L_{g,i} \in \mathbb{R}_+$ denote the resistance and inductance of the GSC, $V_{s,i} \in \mathbb{R}$ the terminal voltage and $V_{dg,i}, V_{qg,i} \in \mathbb{R}$ the GSC's controllable voltage components.

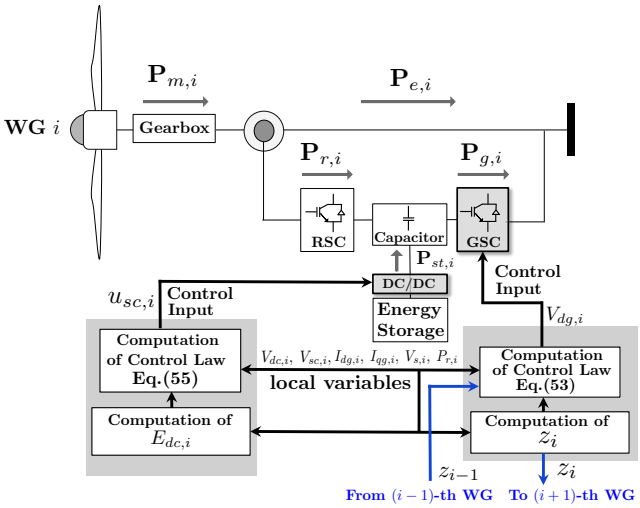

Figure 4.1: Distributed control of SoA wind DFIG with integrated energy storage

Interfacing capacitor model

An interfacing capacitor can be modeled through the dynamics of its DC voltage as:

$$(C_{dc,i}V_{dc,i})\frac{dV_{dc,i}}{dt} = (P_{r,i}+P_{st,i}-P_{g,i}), \quad \forall i \in \mathscr{G} \tag{4.2}$$

The constants $C_{dc,i}, V_{dc,i} \in \mathbb{R}$ represent the capacitance and DC voltage of the capacitor. Further, the variables $P_{g,i}$, $P_{r,i}$ and $P_{st,i}$ denote the power outputs of the GSC, the RSC, and the storage, respectively.

Supercapacitor (energy storage) model

We have particularly chosen supercapacitors as they have high efficiency and small reaction time-constant. Supercapacitors can be modeled as follows.

$$(C_{sc,i}V_{sc,i})\frac{dV_{sc,i}}{dt} = V_{sc,i}\frac{(u_{sc,i}-V_{sc,i})}{R_{sc,i}}, \quad \forall i \in \mathscr{G} \tag{4.3}$$

The variable $u_{sc,i} \in \mathbb{R}$ denotes the voltage input which is controlled by the DC-DC converter, and $C_{sc,i}, V_{sc,i}, R_{sc,i} \in \mathbb{R}_+$ denote the supercapacitor's capacitance, DC voltage and resistance, respectively. The storage power output in terms of $u_{sc,i}$ can be expressed as:

$$P_{st,i} = \frac{V_{sc,i}}{R_{sc,i}}(V_{sc,i}-u_{sc,i}) \ , \qquad \forall i \in \mathscr{G} \tag{4.4}$$

One can easily see that, this power output can be modified solely by the DC-DC converter.

4.3 Problem formulation

Consider the following setting. A WF with n WGs that incorporate supercapacitors is committed to the ISO for the provision of total power P_d. This schedule is issued by the ISO through the deployment of a wind forecasting method and an economic dispatch (ED) process. Sufficient

stored energy in the supercapacitors is ensured at the planning phase as part of the ED process which is repeated every 5 mins. Specifically, the planning ensures sufficient stored energy in the devices for effectively attaining real-time WF power output regulation, by taking into account the uncertainty about the expected wind power realization over the next look-ahead 5-min time window. Presuming sufficient energy reserves in the supercapacitors, our main problem can be formulated as follows: *To design an algorithm to control the storage devices in a distributed and coordinated way so that they collectively ensure real-time regulation of the WF's power output to a given reference P_d while the contribution of each device's power output is equal.* Below, we analyze several cases to provide more insight on the mechanics involved in attaining real-time WF power output regulation with the assistance of storage devices. First, we analyze the case where the storage devices are inactive and their power output is zero, i.e $P_{st,i} = 0,\ \forall i$ (Fig. 4.1). In this case, enforcing power balance at interfacing capacitor depicted in Fig. 4.1 leads to:

$$P_{g,i} = P_{r,i} + P_{st,i} \overset{P_{st,i}=0}{\Rightarrow} P_{g,i} = P_{r,i},\quad i \in \mathscr{G} \tag{4.5}$$

This is translated to the GSC power output being equal to the RSC power output. Moreover, the sum of the stator and rotor power outputs $P_{e,i}$ and $P_{r,i}$ approximately equals the mechanical power extracted from the wind $P_{m,i}$, i.e $P_{e,i}+P_{r,i} \approx P_{m,i}$. It follows immediately that, the total electrical power output of the WF is approximately equal to the total mechanical power:

$$\sum_{i\in\mathscr{G}} (P_{e,i}+P_{r,i}) \approx \sum_{i\in\mathscr{G}} P_{m,i} \tag{4.6}$$

Bearing in mind that the latter is highly volatile, one can realize that the WF's total power output will also be highly volatile. This constitutes the primary reason that can render the WF unable to meet its power commitment. Another reason is that there exists a significant time-delay between the moment the ISO issues the schedule P_d and the moment that it is physically implemented by the WF. This delay, together with the minute-to-minute variability of the wind speed, might in fact result in having:

$$\sum_{i\in\mathscr{G}} (P_{e,i}+P_{r,i}) < P_d \tag{4.7}$$

On the contrary, in the case where the storage devices participate in the WF power output regulation, the WF will be able to meet its power commitment even when the power emanating from the wind is insufficient. In this case, we will have:

$$\sum_{i\in\mathscr{G}} (P_{e,i}+P_{r,i}+P_{st,i}) = P_d \tag{4.8}$$

This can be realized by having each storage device generating (or drawing) power, in steady-state, equal to:

$$P_{st,i} = (P_{g,i}-P_{r,i}),\quad i \in \mathscr{G} \tag{4.9}$$

Hence, the storage devices can act both as sources and sinks of energy with the ultimate goal of driving the total power to the reference P_d. The total power commitment will be met when the aggregate storage power satisfies the equation:

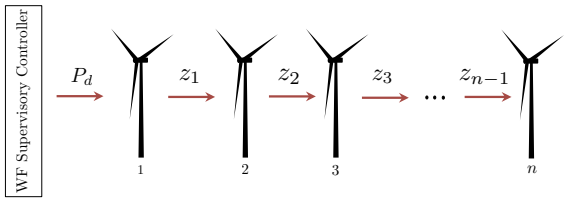

Figure 4.2: Allowable communication between WGs

Condition 1 (Total storage power reference tracking).

$$\sum_{i\in\mathscr{G}} P_{st,i} = P_d - \sum_{i\in\mathscr{G}} (P_{e,i} + P_{r,i}) \tag{4.10}$$

Beyond meeting the WF's power commitment P_d, another requirement that we impose on the storage devices is that they contribute equally to this goal. The reason behind imposing such a constraint is to accommodate fair utilization of the storage devices. This is of practical importance as the amount of power that these devices are generating determines the electrical loading experienced by their power electronics. In fact, the above requirement appears very often when dealing with power electronics because it guarantees that the total electrical loading is evenly distributed among them and that the endured wear and tear is comparable. Very commonly, this requirement appears as a control objective for photovoltaic generators. In our case, the load-sharing requirement can be translated into the following condition.

Condition 2 (Load-sharing (consensus) among storage devices).

$$P_{st,i} = P_{st,j}\ , \quad \forall i,j \in \mathscr{G} \tag{4.11}$$

With the two primary control objectives (meeting Conditions 1, 2) having been analyzed, the main problem can be stated as follows.

Problem 1. *Coordinate and control the energy storage devices and GSCs of a fleet of SoA WGs in a distributed way so that they attain real-time WF power output regulation with load-sharing.*

4.4 A consensus approach to distributed control

Our proposed control approach for solving Problem 1 is outlined below, partitioned into five main steps.

- **Step 1**: We pose Problem 1 as a twofold control problem, a constrained consensus problem for the GSCs with variables of interest $z_i \triangleq (P_{g,i} - P_{r,i})$, i.e the mismatch between the GSCs' and RSCs' power outputs, and a tracking control problem for the DC-DC converters where variables of interest are the storage power outputs $P_{st,i}$ with objective $\lim_{t\to\infty} P_{st,i}(t) = z_i,\ \forall i$.

- **Step 2**: We introduce a leader-follower consensus protocol that GSCs can implement through their control systems to drive their z_i to a common value (consensus), and a closed-loop form for the interfacing capacitor dynamics that DC-DC converters can implement through their control system to enable the variables $P_{st,i}$ to attain reference tracking.

- **Step 3**: We perform timescale separation analysis of the coupled closed-loop dynamics of the consensus protocol and the interfacing capacitor, deriving explicit conditions that the control gains of the GSCs and DC-DC converters have to satisfy in order for these dynamics to manifest three distinct timescales.

- **Step 4**: We let the control gains of all the converters fulfill the Conditions in Step 3. Given that, we establish asymptotic stability of the closed-loop dynamics by leveraging temporal decomposition and compositional stability analysis tools.

- **Step 5**: We design a distributed controller for the GSC which leads to the closed-loop dynamics of z_i matching the consensus protocol dynamics and a CLF-based controller for the DC-DC converter which ensures that the closed-loop dynamics of the capacitor take the desired form stated in Step 2.

4.5 Reducing the control problem to equivalent subproblems

Real-time WF power output regulation with load-sharing is formulated in Section 4.3 as a control problem for the storage devices with objective to meet *Conditions* 1 and 2. Here, we propose the following approach for meeting these conditions: dynamically regulate each power output $P_{st,i}$ to z_i, i.e ensure that $P_{st,i} \to (P_{g,i} - P_{r,i})$, and coordinate the GSCs so that their controlled-variables z_i satisfy the next two conditions.

Condition 3 (**Total power reference tracking**).

$$\sum_{i \in \mathscr{G}} z_i = \Big(P_d - \sum_{i \in \mathscr{G}} (P_{e,i} + P_{r,i}) \Big) \tag{4.12}$$

Condition 4 (**Consensus among** z_i).

$$z_i = z_j, \quad \forall i, j \in \mathscr{G} \tag{4.13}$$

Using these two conditions, our main problem can be reduced to two equivalent control subproblems; the first one is for the GSCs to attain restricted consensus among all z_i and the second one for the DC-DC converters to regulate the storage power outputs $P_{st,i}$ to their respective z_i.

Problem 2 (**Constrained Consensus among** z_i). *Coordinate and control the GSCs so that the variables z_i asymptotically converge to a common value (consensus), i.e fulfill Condition 4, while the constraint given in Condition 3 is met.*

Problem 3 (**Storage Power Outputs Reference Tracking**). *Control each storage device $i \in \mathscr{G}$ so that its power output $P_{st,i}$ is regulated to its respective z_i, i.e* $\lim_{t \to \infty} P_{st,i}(t) = z_i$.

4.6 Consensus protocol and proposed closed-loop form of capacitor's dynamics

Next, a consensus protocol is presented, that the GSCs can adopt to self-organize and drive their z_i to consensus, and a proposed closed-loop form for the capacitors' dynamics that can enable the power outputs of the storage devices $P_{st,i}$ to attain reference tracking.

Leader-Follower Consensus Protocol

Without loss of generality we choose WG l, where $l \triangleq 1$, as the leader, and describe the followers with the set $\overline{\mathscr{G}} \triangleq \mathscr{G} \backslash l$. Our proposed leader-follower consensus protocol is described through the dynamical equations below.

Consensus Protocol $\mathscr{P}_1$

$Leader$

$$\frac{d\xi_h}{dt} = \Big(P_d - \sum_{i \in \mathscr{G}} (P_{e,i} + P_{r,i} + z_i)\Big) \qquad \xi_h \in \mathbb{R} \tag{4.14a}$$

$$\frac{dz_l}{dt} = -k_{\alpha,l}(z_l - \xi_h) \ , \qquad z_l \in \mathbb{R}, \ z_l \triangleq z_1 \tag{4.14b}$$

$Followers$

$$\frac{dz_i}{dt} = -k_{\alpha,i}(z_i - z_{i-1}) \ , \qquad z_i \in \mathbb{R}, \ \forall i \in \overline{\mathscr{G}} \tag{4.14c}$$

The protocol's states are the variables z_i and the auxiliary variable of the leader ξ_h. The variable ξ_h is the one that "drives" the protocol dynamics and guarantees regulation of the total WF power to the reference P_d. Notice that every WG is allowed to communicate with a single neighboring WG.

The protocol $\mathscr{P}_1$ is executed through the following mechanism. The leader WG receives information about the reference P_d from the WF supervisory controller while, at the same time, it communicates to its neighbor (WG 2) the variable z_1. Synchronized with the leader, each follower i receives from its neighbor $(i-1)$ the variable z_{i-1} and communicates to its neighbor $(i+1)$ the variable z_i. Upon receiving P_d, the leader combines that with the information $\sum_{i \in \mathscr{G}} (P_{e,i} + P_{g,i})$ that can be retrieved locally and updates both the state-variables ξ_h and z_1 through equations (4.14a) and (4.14b). Similarly, each follower i, upon receiving z_{i-1}, updates its corresponding z_i through equation (4.14c). Next, the performance on Protocol $\mathscr{P}_1$ under communication link and agent failures is discussed.

Performance under communication link or agent failures

The proposed consensus protocol relies on a row-connected communication network topology which offers low levels of robustness with respect to communication link and agent failures. Specifically, if one communication link or an agent is compromised the protocol cannot reach convergence with the total number of agents participating even when the failure is detected and the control logic of several agents is modified. This can happen because the agents that are connected after the receiving node of the affected link (or agent) will be left uncoordinated after the failure. On the other hand, communication networks with redundant number of links can offer higher levels of robustness to such failures and can yield convergence of the protocol with the total number of agents participating, in the case of a link failure, and with all but the affected agent participating, in the case of an agent failure. However, this can be realized presuming that the failures can be detected and the control logic of several affected agents can be modified accordingly. Our control

approach can be easily adapted to accommodate such communication network topologies. Regarding the requirement for modifying the control logic of several agents after a link or agent failure, we underline that this is a general limitation present in most, if not in all, distributed control algorithms. Its presence is due to the fact that the performance of these algorithms relies heavily on the ability of all agents to update/control certain state-variables and exchange information reliably.

Proposed closed-loop form of capacitor's dynamics

Our proposed closed-loop form for the interfacing capacitor's dynamics, stated in terms of the variable $\Delta E_{dc,i} \triangleq (E_{dc,i} - E_{dc0,i})$ that denotes deviation of the capacitor's stored energy level from its equilibrium, can be written as:

$$\frac{d(\Delta E_{dc,i})}{dt} = -k_{2,i}(\Delta E_{dc,i}), \qquad \forall i \in \mathscr{G} \tag{4.15}$$

The DC-DC converters can shape the closed-loop capacitors' dynamics so that they acquire this form, enabling the storage power output $P_{st,i}$ to track the variable z_i. To see that, consider the open-loop dynamics of the stored energy as:

$$\frac{d(\Delta E_{dc,i})}{dt} = (P_{r,i} + P_{st,i} - P_{g,i}), \qquad \forall i \in \mathscr{G} \tag{4.16}$$

With the closed-loop dynamics of the capacitor taking the form (4.15), the dynamics of the storage device's power output $x_i \triangleq P_{st,i}$ can be derived as follows. First, let (4.15) be equal to (4.16), differentiate both sides of the resulting equation and substitute dz_i/dt from (4.14c). This will eventually yield:

Storage Power Dynamics

$$\frac{dx_i}{dt} = -k_{\alpha,i}(z_i - z_{i-1}) - k_{2,i}(x_i - z_i), \qquad \forall i \in \mathscr{G} \tag{4.17}$$

Observe that, when the protocol is at equilibrium, the above equation yields $x_i = z_i$ which means the storage device's power output equals z_i. The protocol dynamics in (4.14b) and (4.14c) serve as the desired closed-loop dynamics for z_i and can be realized by the GSCs, while the dynamics in (4.17) serve as the desired closed-loop dynamics for x_i and can be realized by the DC-DC converters. The overall system comprised of the coupled protocol dynamics and the closed-loop storage power dynamics, can be described by equations (4.14a)-(4.14c) and (4.17).

4.7 Numerical results

In this section, we evaluate the performance of the controllers and the effectiveness of the consensus protocol and closed-loop form of capacitor dynamics in resulting in WF power output regulation with load-sharing. For this scope, a modified version of the IEEE 24-bus reliability test system is used, where, at bus 22, a row-connected WF comprised of 10 SoA WGs with supercapacitors is placed. The network topology that characterizes the communication links among the WGs is depicted in Fig. 4.8b. The GSCs and DC-DC converters of all WGs adopt respectively, the proposed distributed control law and the CLF-based control law. Numerical simulations are conducted under the following representative scenarios.

- *Scenario 1*: The WF power reference P_d is constant (see Fig. 4.3a).
- *Scenario 2*: The WF power reference P_d varies in a step-wise manner (see Fig. 4.5a).

The results under Scenario 1 are discussed first. Observe from Fig. 4.3a that the total WF power output is tightly confined around P_d. This is accomplished through the rapid convergence of the GSC-controlled variables $\mathbf{z}$ and storage power outputs $\mathbf{x}$ to ξ_h (consensus) which, on a slower timescale, converges to ξ_{h0}, as depicted in Fig. 4.3b and Fig. 4.4a, respectively. The variations of the stored energy levels in the supercapacitors are depicted in Fig. 4.4b. Altogether, the results verify that WF power output regulation with load-sharing of the storage devices is carried out effectively in this Scenario.

Moving forward, the results under Scenario 2 are discussed. From Fig. 4.5a, one can observe that the proposed distributed controllers attain WF power reference tracking with good performance as the total WF power rapidly and closely tracks the fast-varying reference P_d.

In Fig. 4.5b, observe the dynamic responses of the variables z_i which are driven by the regulation of the GSCs' power outputs through the proposed protocol in response to changes in the reference. These variables manifest indistinguishable trajectories (see Fig. 4.5b) as they all reach consensus rapidly and converge to the variable ξ_h which varies on a slower timescale. On this slow timescale, ξ_h converges to the equilibrium ξ_{h0} (which depends on P_d) driving the variables $\mathbf{z}$ to the equilibrium ξ_{h0} as depicted in Fig. 4.5b. In particular, observe that the variables $\mathbf{z}$ and ξ_h are concurrently driven to the quasistatic equilibrium ξ_{h0} while consensus among them is already attained. Finally, the variations of the stored energy levels in the supercapacitors under this Scenario are depicted in Fig. 4.7.

The responses of the variables $\mathbf{x}$ match one-to-one the responses of the variables $\mathbf{z}$, manifesting indistinguishable trajectories, as seen in Fig. 4.6a. This is explained as follows. The DC-DC converters, through their controllers, regulate the storage power outputs $\mathbf{x}$ to their corresponding $\mathbf{z}$ in order to provide the power demanded by the GSCs to attain WF power output regulation. This action indirectly leads to the storage power outputs $\mathbf{x}$ reaching consensus as well, achieving that way the load-sharing objective.

In conclusion, the distributed controllers, by realizing the proposed consensus protocol and closed-loop capacitor's dynamics, effectively carried out WF power output regulation with power-sharing among storage devices.

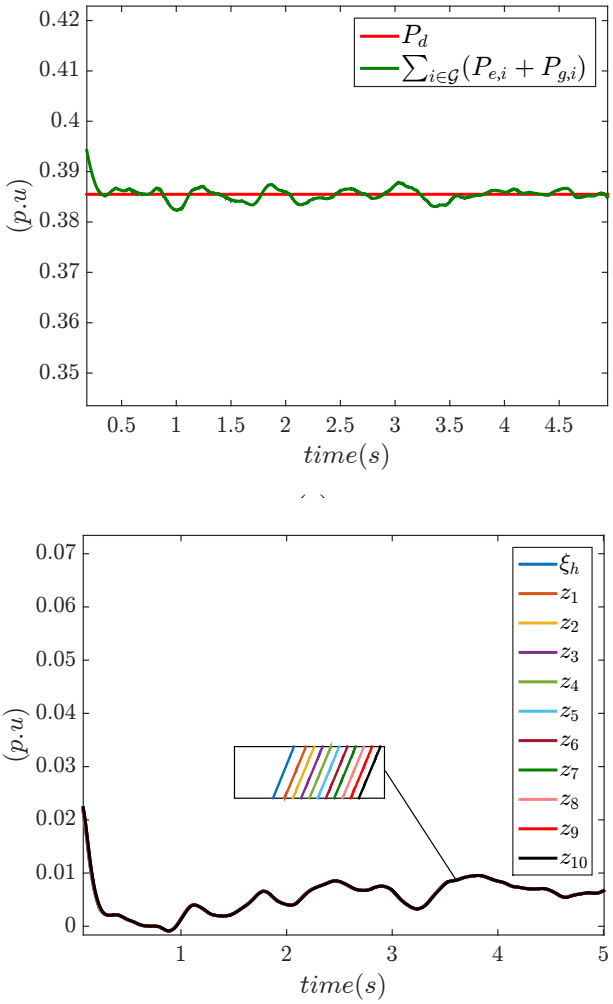

(b)

Figure 4.3: *Scenario 1* a) WF total power output, b) State-variables z_i

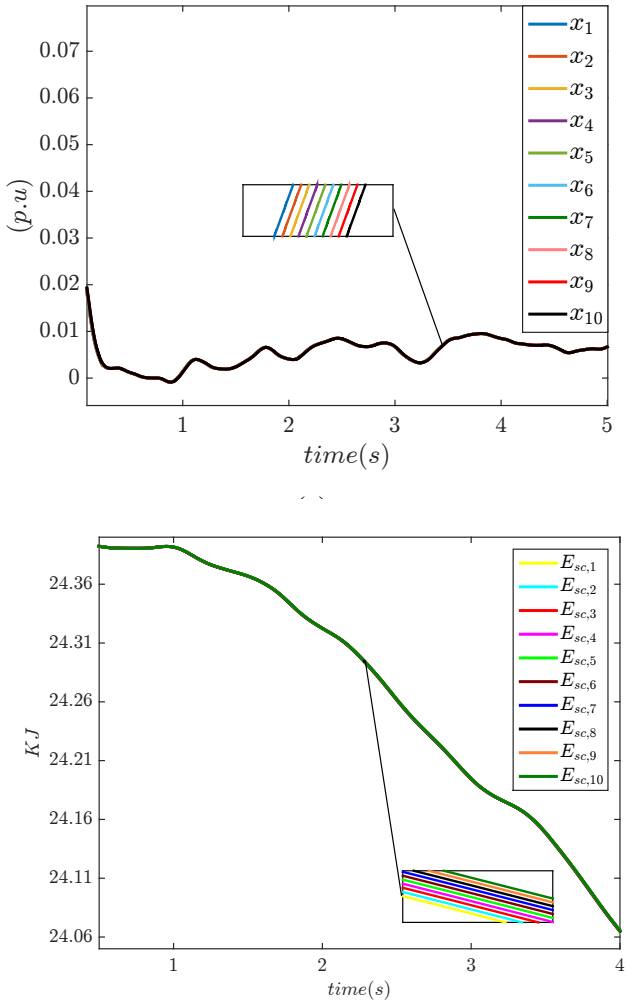

(b)

Figure 4.4: *Scenario 1* a) Storage power outputs x_i, b) Energy levels $E_{sc,i}$ with $V_{sc,i} = 1kV,\ C_{sc,i} = 50mF,\ i = 1, ..., 10$

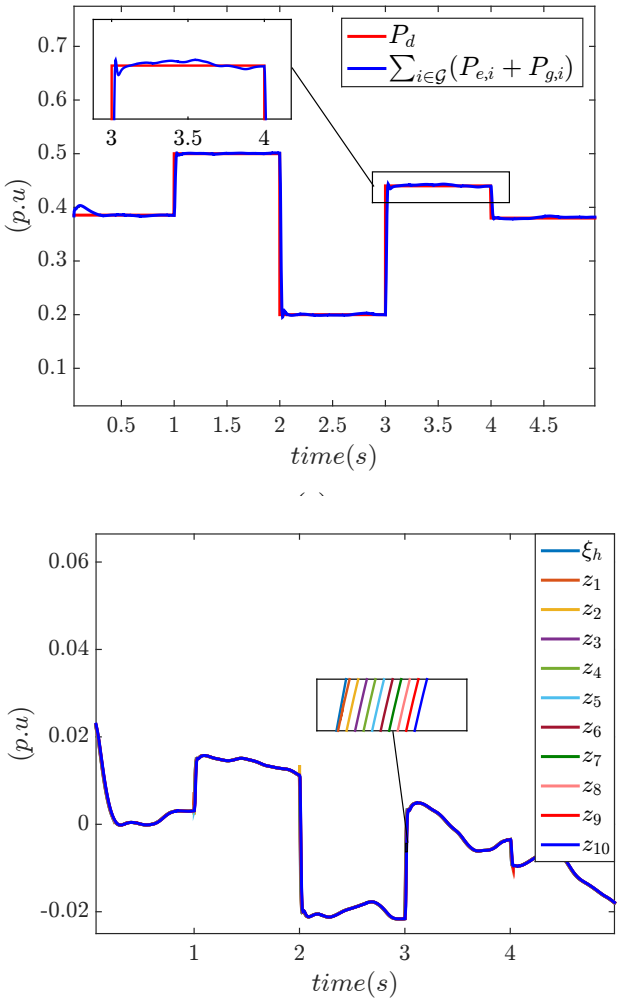

(b)

Figure 4.5: *Scenario 2* a) WF power output (*blue*) and reference (*red*), b) z_i

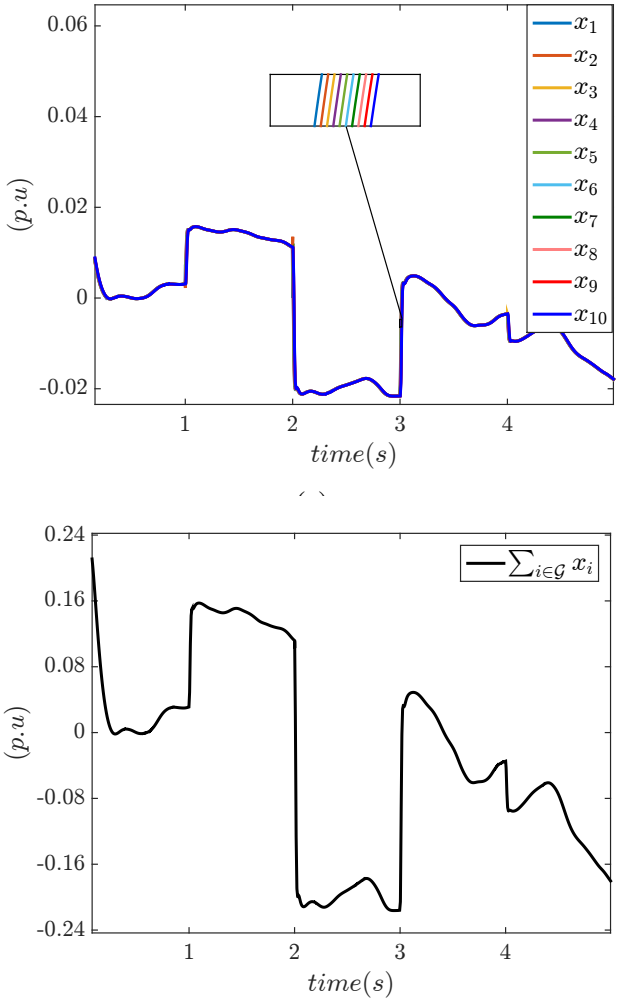

(b)

Figure 4.6: *Scenario 2* a) Storage power outputs x_i, b) Total storage power

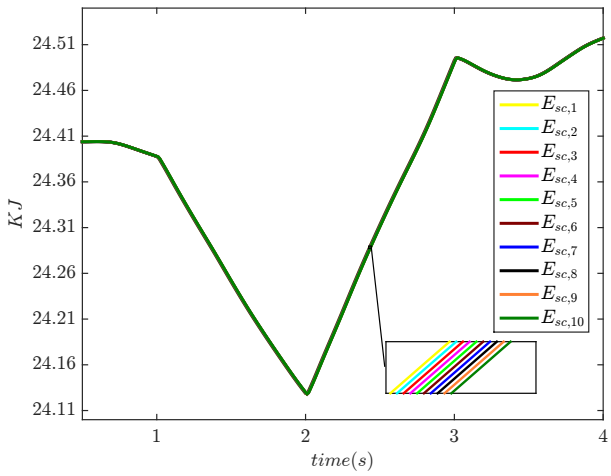

Figure 4.7: *Scenario 2* Energy levels $E_{sc,i}$ with $V_{sc,i} = 1kV,\ C_{sc,i} = 50mF,\ i = 1, ..., 10$

4.8 Distributed torque control of deloaded wind DFIGs for wind farm power output regulation

In today's power systems, WGs are often operated in a deloaded regime, extracting less power than the maximum available from the wind. When WGs are being operated in such regime, they are able to increase their power output when needed in order to provide frequency regulation for example. In the operation of large wind farms (WFs) comprised of numerous WGs being operated in a deloaded regime, a challenge that arises is to dene the set-points of these WGs. In other words, to dispatch a group of WGs based on the required total WF power and according to the local wind speed conditions (to each WG), in a timely, robust and computation-ally efficient fashion: timely, since in the future, WFs will have to respond faster to maintain supply-demand balance, especially in microgrid settings; robust, such that the performance of WFs is also reliable and computation-ally efficient to support timely and cost-effective operation (especially when the number of WGs is very large). Current approaches that address the above problem are centralized, meaning that information from each WG is communicated to a central WF controller. These approaches are prone to single-point failures, require high computational effort, extensive communication infrastructure and might not be able to respond timely. In our work, we effectively addressed the above problem by developing a novel distributed control architecture for deloaded WGs, elaborated below.

In our paper "Distributed Torque Control of Deloaded Wind DFIGs for Wind Farm Power Output Regulation", whose main ideas and results we present below, we introduced a novel distributed control architecture that WGs can adopt to dynamically self-dispatch themselves, ensuring that: their total extracted power from the wind matches a given reference and their utilization levels are the same (i.e load-sharing). More specifically, we developed a Control Lyapunov Function-based torque controller for the rotor-side power electronics of WGs that implements the proposed protocol. The proposed control architecture: 1) can dispatch a group of WGs based on local wind-speed conditions eliminating the need for a central wind farm controller and leading to low computational cost; 2) requires minimum peer-to-peer communication among neighboring WGs; 3) enables WGs to be dispatched timely which is critical since dispatching is performed under fast-varying dy-

namical wind and loading conditions to balance supply-demand (especially in autonomous power systems such as microgrids); 4) has guaranteed stability and performance.

Our work is the first work to systematically and effectively solve the problem of dispatching a group of deloaded WGs in a distributed, dynamic and efficient manner. In contrast with previous work, our method is dynamic in the sense that the proposed power electronics WG controllers reach consensus dynamically according to a given reference. We emphasize that the problem of dispatching WGs efficiently and distributively is as critical as solving the Economic Dispatch (ED) problem of SGs in a distributed fashion, which has already attracted a lot of attention in the power systems and control communities. Therefore, our work provides the first steps in this direction. Below, we outline the main ideas and results obtained in this direction.

4.9 Dynamical modeling

We consider control of the rotor-side dynamics, therefore, we only present the dynamical models associated with the rotor. These can be fully described by three ordinary differential equations (ODEs) which represent the internal rotor-voltages dynamical model with the RSC control input and the rotor-speed dynamical model of each DFIG. The set of deloaded WGs is denoted by $\mathscr{G} \triangleq \{1, ..., n\}$ and each WG is indexed by i so that $i \in \mathscr{G}$.

4.9.1 Internal rotor voltages dynamical model

The first two equations describe the dynamics of the internal rotor-voltages and can be stated as:

$$\dot{E}'_{d,i} = \frac{1}{T'_{0,i}}\Big[-(E'_{d,i}-(X_{s,i}-X'_{s,i})I_{qs,i})+T'_{0,i}(-\omega_s\frac{X_{m,i}}{X_{r,i}}V_{qr,i} +(\omega_s-\omega_{r,i})E'_{q,i})\Big],\ i \in \mathscr{G} \tag{4.18a}$$

$$\dot{E}'_{q,i} = \frac{1}{T'_{0,i}}\Big[-(E'_{q,i}+(X_{s,i}-X'_{s,i})I_{ds,i})+T'_{0,i}(\omega_s\frac{X_{m,i}}{X_{r,i}}V_{dr,i} -(\omega_s-\omega_{r,i})E'_{d,i})\Big],\ i \in \mathscr{G} \tag{4.18b}$$

We underline that the rotor-voltage dynamics are given in a $d-q$ coordinate system, where d is the axis that is aligned with the terminal voltage phasor vector, and q is the axis that is orthogonal to d.

4.9.2 Rotor speed dynamical model

The rotor speed dynamics can be described by:

$$\dot{\omega}_{r,i} = \frac{\omega_s}{2H_i}(T_{m,i}-T_{e,i}),\quad i \in \mathscr{G} \tag{4.18c}$$

where the mechanical torque can be expressed analytically as:

$$T_{m,i} \triangleq \frac{1}{2}\frac{\rho\pi R_i^2\omega_s}{S_{b,i}\omega_{r,i}}C_p(\lambda_i,\theta_i)v_{w,i}^3\ ,\quad i \in \mathscr{G} \tag{4.18d}$$

The power coefficient $C_{p,i}$ can be expressed in terms of the pitch angle θ_i and tip-speed λ_i as:

$$C_{p,i} \triangleq 25.52\Big[(\frac{1}{\lambda_i+0.08\theta_i}-\frac{0.035}{\theta_i^3+1})\Big]\cdot \mathrm{e}^{-12.5(\frac{1}{\lambda_i+0.08\theta_i}-\frac{0.035}{\theta_i^3+1})} \tag{4.18e}$$

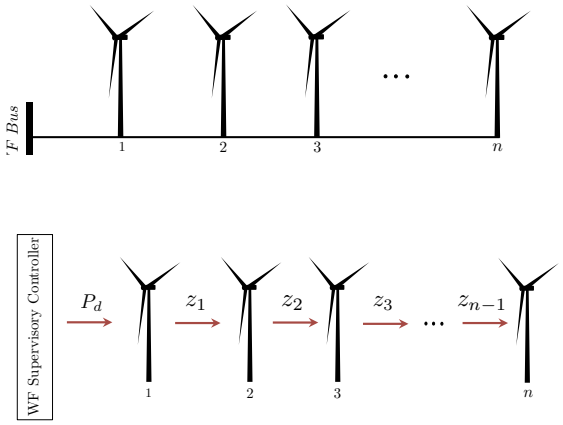

(b)

Figure 4.8: a) Physical topology b) Communication topology of WF

Finally, in terms of rotor speed and wind speed, the tip-speed can be expressed as:

$$\lambda_i \triangleq \frac{2k_i}{p_i}\frac{\omega_{r,i}R_i}{v_{w,i}} \ , \quad i \in \mathscr{G} \tag{4.18f}$$

The mechanism through which the RSC adjusts the mechanical power can be explained by focusing on the last three equations. Concretely, the RSC regulates the rotor speed $\omega_{r,i}$ through which it adjusts the power coefficient $C_{p,i}$, and eventually the mechanical torque $T_{m,i}$.

4.10 Problem formulation

Here, we study a wind farm comprised of n wind generators operating in a deloaded mode. The mechanical power extracted from the wind by each WG i is determined by equation:

$$P_{m,i} \triangleq \frac{1}{2}\rho C_{p,i} A_i v_{w,i}^3 \ , \qquad i \in \mathscr{G} \tag{4.19}$$

where $C_{p,i} \in \mathbb{R}_+$ is the power coefficient, $\rho \in \mathbb{R}_{++}$ the air density (kg/m^3), $v_{w,i} \in \mathbb{R}_{++}$ the wind speed in (m/s) and $A_i = \pi R_i^2 \in \mathbb{R}_{++}$ the area swept by the blades with $R_i \in \mathbb{R}_+$ being the blade radius. Notice that, the only controllable variable in (4.19) is $C_{p,i}$, which can be regulated by the WG through variation of the rotor speed $\omega_{r,i}$. When the wind speed is low, DFIGs are usually operated under a Maximum Power Point Tracking (MPPT) strategy. Under this strategy, a wind DFIG is controlled so that $C_{p,i} = \overline{C}_{p,i}$, where $\overline{C}_{p,i} = \max_{\lambda_i}\{C_{p,i}(\lambda_i, \theta_i^*)\}$ and so that $P_{m,i}$ in (4.19) equals:

$$\overline{P}_{m,i} \triangleq \frac{1}{2}\rho \overline{C}_{p,i} A_i v_{w,i}^3 \ , \qquad i \in \mathscr{G} \tag{4.20}$$

The constant $\overline{C}_{p,i}$ denotes the maximum value of the power coefficient, so it holds that $C_{p,i} \in [0, \overline{C}_{p,i}]$. In our case, the DFIGs operate in a deloaded mode so that $C_{p,i} < \overline{C}_{p,i},\ P_{m,i} < \overline{P}_{m,i},\ \forall i \in \mathscr{G}$. Thus, they can be controlled through their RSCs so that they vary their power coefficients in the above range and their corresponding mechanical power $P_{m,i}$ takes values in the continuous set

$[0, \overline{P}_{m,i}]$. The only requirement is that the total mechanical power has to be equal to the total power reference P_d which corresponds to the power that the WF is committed to supply to the grid in a 5-minute time-window. This reference comes from the system operator (SO) and is the outcome of a wind forecasting and an economic dispatch (ED) process conducted every several minutes. Here, we assume that the reference satisfies $P_d \leq \sum_{i\in\mathscr{G}} \overline{P}_{m,i}$, i.e that it is realizable by the WGs, considering the current prevalent local wind-speed conditions. We note that the deloaded DFIGs can meet any total power request P_d as long as $P_d \in [0, \sum_{i\in\mathscr{G}} \overline{P}_{m,i}]$. Nevertheless, extensive wear and tear on the shafts of the WGs can be avoided when the reference P_d is sufficiently slow-varying so that the WGs are not called to regulate their power outputs very fast.

For our setting, the general power dispatch and regulation problem can be formulated as: *given* $v_{w,i},\ \forall i \in \mathscr{G}$ *and* P_d*, compute the set-points* $P^*_{m,i} \in [0, \overline{P}_{m,i}],\ C^*_{p,i} \in [0, \overline{C}_{p,i}]$ *for all WGs and regulate their mechanical power outputs such that* $\lim_{t\to\infty} \sum_{i\in\mathscr{G}} P_{m,i}(t) = \sum_{i\in\mathscr{G}} P^*_{m,i} = P_d$. Observe that there exist multiple combinations of set-points that satisfy the above constraints, in fact, any power dispatch $(P^*_{m,1}, ..., P^*_{m,n})$ that respects the above conditions is realizable. On the other side, when the set-points are required to also satisfy $(P^*_{m,1}/\overline{P}_{m,1}) = ... = (P^*_{m,n}/\overline{P}_{m,n})$ this combination becomes unique. Note that the latter requirement is common when dispatching WGs, since it guarantees more efficient operation. In particular, each WG will contribute to the total power output analogously to the available wind speed potential at its location. Often, the same requirement is imposed when dispatching photovoltaic generators. A dispatch that satisfies this requirement is known as *"fair dispatch"* since the power outputs of the WGs are proportional to their maximum values which depend on the local wind speed conditions i.e WGs operate under the same loading levels (fair load-sharing). In summary, the conditions power outputs of WGs have to meet to realize a fair dispatching scenario can be formally stated as follows.

Condition 5 (**Total power output regulation**).

$$\sum_{i\in\mathscr{G}} P^*_{m,i} = P_d \tag{4.21a}$$

Condition 6 (**Fair load-sharing**).

$$\frac{P^*_{m,i}}{\overline{P}_{m,i}} = \frac{P^*_{m,j}}{\overline{P}_{m,j}}, \qquad i, j \in \mathscr{G} \tag{4.21b}$$

The following definition can now be stated.

Definition 1. A power dispatch $\mathbf{P}^*_m = [P^*_{m,1}, ..., P^*_{m,n}]^\top$ that satisfies both Conditions 5 and 6, is called a *fair dispatch.*

At this point, we state the following remark.

Remark 1.

$$\frac{P^*_{m,i}}{\overline{P}_{m,i}} = \frac{C^*_{p,i}}{\overline{C}_{p,i}}, \qquad i \in \mathscr{G} \tag{4.22}$$

The ratio $(C^*_{p,i}/\overline{C}_{p,i})$ corresponds to the utilization (or loading level) of each WG. By employing Remark 1, which is directly obtained by taking the ratio of (4.19) and (4.20), Condition 6 can be substituted by the new and equivalent condition below.

Condition 7 (Fair load-sharing).

$$\frac{C^*_{p,i}}{\overline{C}_{p,i}} = \frac{C^*_{p,j}}{\overline{C}_{p,j}}, \qquad i,j \in \mathscr{G}$$

Using the above conditions, we formulate the main problem as follows.
Problem formulation (*WF Power Output Regulation via Distributed Fair Dynamic Dispatching and Regulation of WGs' Power Outputs*). Develop a distributed control design for the RSCs which leverages limited communication to dynamically dispatch and regulate the power outputs of WGs such that these meet Conditions 5 and 7.

Traditionally, this problem is addressed through centralized control approaches. In these approaches, WGs first communicate their wind-speed measurements to a central WF controller which then computes the power set-points for the individual WGs so that these meet the above two conditions. Finally, the WF controller communicates the computed set-points to the WGs. This paper provides a distributed solution to this problem with the control methodology introduced next.

4.11 Distributed control approach

To solve the main problem, WGs have to guarantee in a distributed manner (using peer-to-peer communication) that their utilization levels $C_{p,i}/\overline{C}_{p,i}$ asymptotically converge to a common value, while their total power tracks the reference P_d, i.e that Conditions 5 and 7 are fulfilled. This problem can be naturally posed as a *constrained consensus problem* among WGs, where they have to reach consensus on their utilization levels $C_{p,i}/\overline{C}_{p,i}$ under the constraint that their total power matches the reference P_d. WGs can accomplish these objectives by deploying a properly designed consensus protocol with limited peer-to-peer communication.

4.11.1 Leader-follower consensus protocol

We propose the following *leader-follower consensus protocol* for the coordination of WGs that can be implemented by their RSCs to realize dynamic, distributed dispatch and regulation of their power outputs, leading to the Conditions 5 and 7 being satisfied asymptotically.

Consensus Protocol $\mathscr{P}_1$ Dynamics

Leader WG

$$\frac{d\xi_h}{dt} = (P_d - \sum_{i\in\mathscr{G}} P_{m,i}) \qquad \xi_h \in \mathbb{R} \tag{4.23a}$$

$$\frac{dz_l}{dt} = -k_{\alpha,l}(z_l - \xi_h)\ , \quad z_l \triangleq z_1 \qquad z_l \in \mathbb{R} \tag{4.23b}$$

WG i

$$\frac{dz_i}{dt} = -k_{\alpha,i}(z_i - z_{i-1}) \ , \quad i \in \overline{\mathscr{G}} \qquad\qquad z_i \in \mathbb{R} \tag{4.23c}$$

Without loss of generality, WG 1 is assigned as the leader, i.e $l \triangleq 1$, and the set of followers is denoted by $\overline{\mathscr{G}} \triangleq \mathscr{G} \backslash \{l\} \triangleq \{2, ..., n\}$. The consensus protocol's state-variables are the utilization levels $z_i \triangleq C_{p,i}/\overline{C}_{p,i}$ and the auxiliary variable ξ_h of the leader. Each WG is allowed to communicate with two other (physically) neighboring WGs, as shown in Figure 4.8.

The protocol is executed through the following mechanism. The supervisory WF controller obtains a total power set-point P_d from the SO and communicates it to the leader WG. Subsequently, the leader WG controls the dynamics of its state-variables z_l and ξ_h, using the reference P_d and information (retrieved distributively via indirect information passing) from all WGs, and communicates only its power coefficient z_l and the derivative of its power coefficient, $\dot{z}_l$, to its neighbors. In synchrony with the leader, all the followers control the dynamics of their state-variables z_i, and communicate their respective z_i and $\dot{z}_i$ to their $(i{+}1)$ neighbors. The leader has to retrieve the information $\sum_{i \in \overline{\mathscr{G}}} P_{m,i}$ as well, which is required in (4.23a). This can be done either through indirect information passing between WGs or through a much faster average consensus protocol involving the mechanical power.

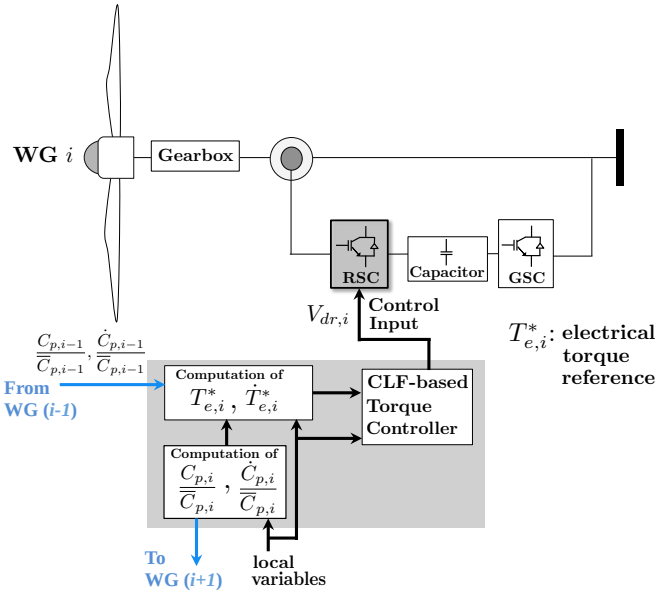

Figure 4.9: Distributed CLF-based torque controller

4.12 Case studies

We present numerical simulations under several critical scenarios in order to validate our theoretical results. The simulations are conducted in MATLAB. In particular, the simulations are performed on the modified IEEE 24-bus RT system with all the synchronous generators modeled in detail using the one-axis model and each wind DFIG modeled using the models stated in Section 4.9. The 24-bus system is modified such that, on bus 22, a WF is placed, comprised of 10 WGs (the physical and communication topologies shown in Fig. 4.8). We emphasize that all WGs are assumed to share the same technical characteristics. The initial local wind-speed conditions are assumed to be $v_{w,i} = 13.17m/s$ and homogeneous throughout the WF. In this set-up, the simulations are conducted with the RSC of each WG implementing the distributed CLF-based torque controller under the following critical scenarios and with the WGs initiated with non-identical $C_p/\overline{C}_p$ ratios. The goal is to comprehensively evaluate the stability and performance of the proposed protocol and corresponding distributed CLF-based torque controller.

- **Scenario 1** (WF power Reference P_d varies with constant wind speed $v_w = 13.17\ m/s$)
  - $t = 0s$: The reference is constant at $P_d = 0.38\ p.u.$
  - $t = 3s$: The reference decreases to $P_d = 0.36\ p.u.$
  - $t = 9s$: The reference increases to $P_d = 0.40\ p.u.$
- **Scenario 2** (Wind speed v_w varies with constant reference $P_d = 0.38$)
  - $t = 0s$: Wind speed is constant at $v_w = 13.17\ m/s$.
  - $t = 2s$: Wind speed decreases to $v_w = 12\ m/s$.
- **Scenario 3** (Both the WF power reference P_d and wind speed v_w vary)
  - $t = 0s$: Reference and wind speed are constant, $P_d = 0.38\ p.u,\ v_w = 13.17m/s$.
  - $t = 3s$: Reference increases to $P_d = 0.40\ p.u.$
  - $t = 9s$: Wind speed increases to $v_w = 14.17\ m/s$.
  - $t = 15s$: Reference decreases to $P_d = 0.36\ p.u$ and wind speed decreases to $v_w = 12.17\ m/s$.

At first, we elaborate on the results under *Scenario 1*. By observing Fig. 4.10b we can conclude that the WF total power output of the WF is able to effectively track the reference P_d as it varies, with good dynamic performance e.g short response time, and small overshoot. Hence, the distributed CLF-based torque controllers succeed in providing total WF power output regulation. In fact, they achieve that by dynamically redispatching and readjusting the corresponding power outputs of their WGs indirectly, through regulation of the loading levels (i.e consensus states) to their new equilibria. These equilibria depend on the reference P_d and the wind speed conditions. In our case, two new equilibria arise, one at $t = 3s$, and one at $t = 9s$, computed as:

$$t = 3s:\ \xi_{h0} = \frac{0.36{\cdot}100{\cdot}10^6}{10{\cdot}(0.5{\cdot}1.225{\cdot}0.438{\cdot}\pi{\cdot}52^2{\cdot}13.17^3)} = 0.6915$$

$$t = 9s:\ \xi_{h0} = \frac{0.40{\cdot}100{\cdot}10^6}{10{\cdot}(0.5{\cdot}1.225{\cdot}0.438{\cdot}\pi{\cdot}52^2{\cdot}13.17^3)} = 0.7684$$

The "fair dispatch" or equivalently, the "fair load-sharing" among the WGs can be seen in Fig. 4.10a, where the loading levels (ratios $C_{p,i}/\overline{C}_{p,i}$) converge to a common value soon after each perturbation. This is accomplished through the following mechanism. In the fast time-scale, the ratios $C_{p,i}/\overline{C}_{p,i}$ reach consensus and rapidly converge to the auxiliary state-variable ξ_h of the leader, where ξ_h can be thought of as a quasistatic equilibrium for the fast state-variables $C_{p,i}/\overline{C}_{p,i}$. On the other hand, in the slow time-scale, the state-variable ξ_h converges to its equilibrium ξ_{h0}, which depends on the new reference P_d, as depicted in Fig. 4.10a. The convergence of ξ_h drives the state-variables $C_{p,i}/\overline{C}_{p,i}$ to eventually converge to the equilibrium of ξ_h, ξ_{h0}.

The intuition driving the execution of the protocol and the numerical simulations under *Scenario 1* can be explained as follows. First, the leader WG senses the variations of P_d through its auxililiary state-variable ξ_h which decreases and increases at $t = 3s$ and at $t = 9s$, respectively. Correspondingly, the leader's consensus state-variable z_l, by tracking ξ_h, decreases at $t = 3s$ and increases at $t = 9s$. In a concurrent and synchronized manner, the followers decrease and then increase their utilization levels (consensus states) in order to reach consensus with the leader. Combined, these actions lead to the loading levels converging to 0.6915 after $3s$ and to 0.7684 after $9s$, while their initial value is 0.73 (Fig. 4.10a). Practically, the distributed CLF-based torque controllers regulated the loading levels by initially accelerating and then decelerating their turbines as shown in Fig. 4.10c. These adjustments of the rotor speeds enable the WGs to reduce and then increase their mechanical power outputs so that their total power output tracks the desired power reference in both cases (Fig. 4.10b).

Moving to the simulation results under *Scenario 2*, we can observe from Fig. 4.11b that the total mechanical power $\sum_{i\in\mathcal{G}} P_{m,i}$ is initially constant, while after the sudden drop in the wind-speed it dives to a lower value. The equilibrium of the WGs' loading levels and the auxiliary state-variable ξ_h, before the wind-speed disturbance (i.e in $t \in [0, 2s]$), is:

$$\xi_{h0} = \frac{P_d}{\sum_{i=1}^{10} \alpha_i} = \frac{0.38{\cdot}100{\cdot}10^6}{10{\cdot}(0.5{\cdot}1.225{\cdot}0.438{\cdot}\pi{\cdot}52^2{\cdot}13.17^3)} = 0.729$$

The loading levels starting from non-equal values converge to this equilibrium asymptotically during the first 2 seconds, as can be seen in Fig. 4.11a. Subsequently, the leader senses the wind-speed drop through the dynamics of the auxiliary variable ξ_h whose equilibrium, also that of the loading levels, changes to:

$$\xi_{h0} = \frac{P_d}{\sum_{i=1}^{10} \alpha_i} = \frac{0.38{\cdot}100{\cdot}10^6}{10{\cdot}(0.5{\cdot}1.225{\cdot}0.438{\cdot}\pi{\cdot}52^2{\cdot}12^3)} = 0.965$$

This change signifies that the WGs' loading levels have to increase in order for the WGs to be able to generate the same power P_d but now with lower wind-speed, $v_w = 12\ (m/s)$ instead of $v_w = 13.17\ (m/s)$. The auxiliary state-variable of the leader is the first to move toward the new equilibrium. Concurrently and in synchrony with the leader, each of the followers exploit the peer-to-peer communication to regulate their loading levels to the loading levels of their respective neighbors. Ultimately, these actions cause all loading levels to converge to the new equilibrium ξ_{h0} as seen in Fig. 4.11a, leading to fair load-sharing among the WGs.

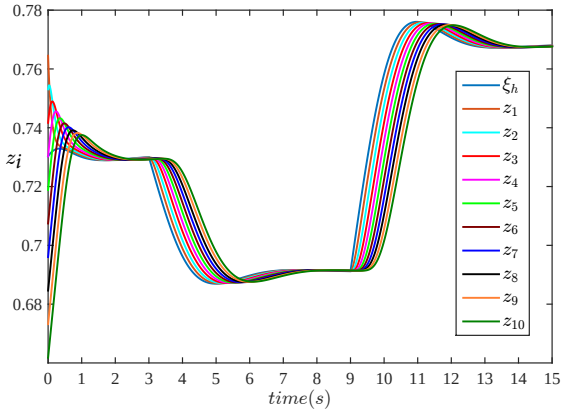

(a) Loading levels

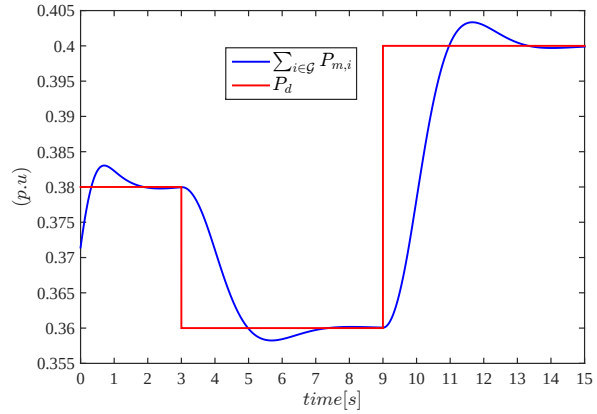

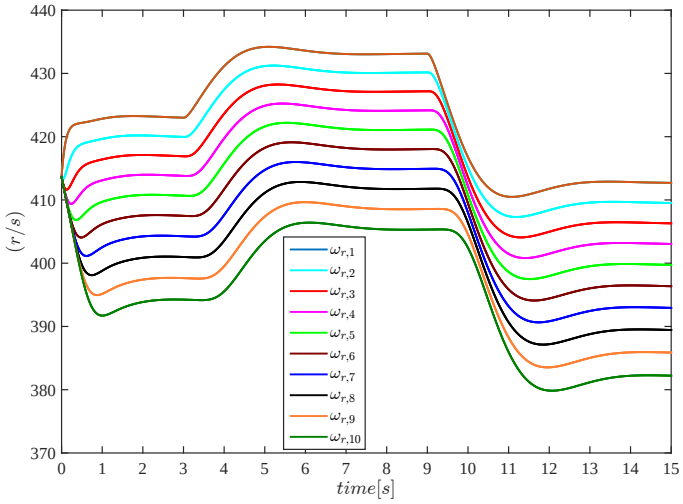

(c) Rotor speeds

Figure 4.10: Simulation results under *Scenario 1*

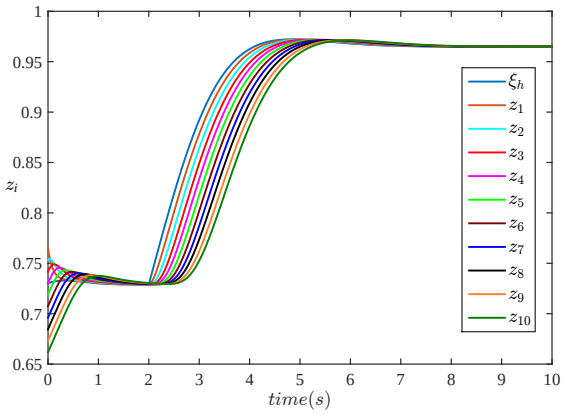

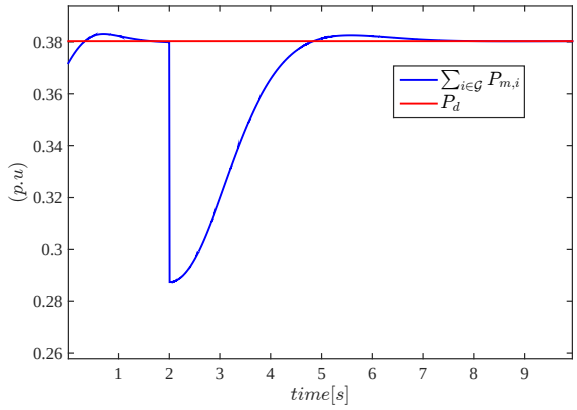

(b) Total mechanical power

Figure 4.11: Simulation results under *Scenario 2*

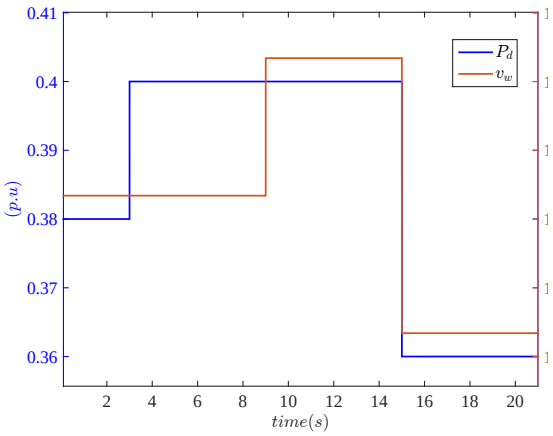

(a) Wind speed (v_w)

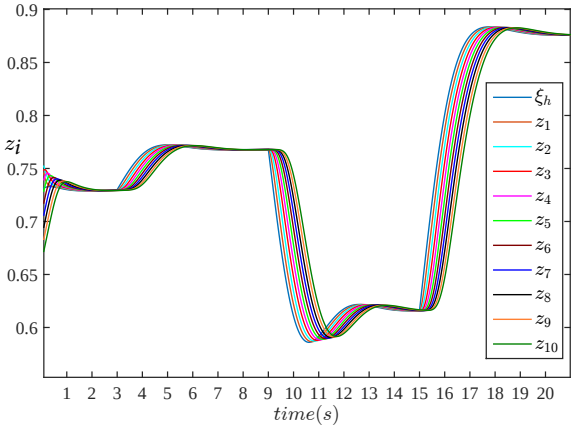

(b) Local voltage levels

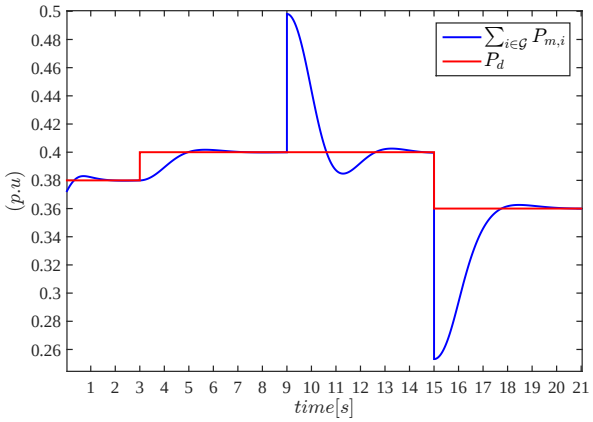

(c) Total mechanical power

Figure 4.12: Simulation results under *Scenario 3*

In *Scenario 3*, the WF experiences both variations on the reference P_d and the wind speed v_w as can be seen in Fig. 4.12a. First, at $t = 3s$ the WF power reference increases from $0.38\ p.u$ to $0.4\ p.u$, causing both the loading levels of WGs, and correspondingly the total mechanical power, to increase, with the latter tracking the new value of the reference. These responses are depicted in Fig. 4.12b and Fig. 4.12c, respectively. At $t = 9s$, the wind speed increases from $13.17m/s$ to $14.17\ m/s$ (Fig. 4.12a). That leads the controllers to decrease the WGs' loading levels (Fig. 4.12b) such that they still generate total power equal to $0.4\ p.u$ but now with higher wind speed. The abrupt rise of the wind speed causes a spike in the response of the total mechanical power, and at $t = 15s$, the sudden drop of the wind speed causes the mechanical power to dive as depicted in Fig. 4.12c. In the latter case, the loading levels increase in order to track their new equilibrium value that depends on both the reference P_d and the wind speed v_w. The reason is that the drop of P_d alone would cause the loading levels to decrease while the drop of the wind speed v_w alone, would cause the loading levels to increase. In our case, these variations combined eventually cause the loading levels to increase (Fig. 4.12b) which means that the effect of the wind speed variation is more pronounced on the new equilibrium of the loading levels.

In summary, the above numerical simulations verify that the proposed protocol and the corresponding distributed CLF-based torque controllers are able to distributively and dynamically self-organize and control a group of deloaded WGs in a fair load-sharing fashion so that WF power output regulation is attained under fast-varying conditions.

5. Discussion and conclusion

5.1 Open questions – future work

A big open question still remains in our work: how to appropriately integrate several PMUs in the developed control systems so the variables that are needed in the feedback control loop are readily available to the controllers. Given that, WFs can then better regulate their power output to given references and contribute to small-signal stability of large-scale systems under highly dynamical conditions. Our future work will focus on the practical implementation aspects of the developed wind farm control schemes with integrated PMUs.

5.2 Interactions with industry advisors

We interacted extensively with industry advisors and discussed the results and outcomes of our research in the annual PSERC Industry-University Members Meeting in 2015 and 2016. The questions raised by the industry people were mostly related to the practical applicability of the developed wind farm control methods and the corresponding technical requirements. We took the industry advisors' feedback into account and in the final journal papers that we published we also discussed how the proposed wind farm control methods can be applied in practice and the PMU-related requirements for the control methods.

5.3 Conclusions and proposed next steps

In summary, Part 2 of this report offers an extension of today's modeling in support of next generation SCADA first. This is needed to implement protocols for ensuring stable and reliable operation in the changing electric power industry which has become very complex as unconventional technologies and non-utility owned stakeholders connect to the power grid. It is proposed that today's Balancing Authorities (BAs) further evolve into end-to-end intelligent Balancing Authorities (iBAs). All end users connected to the electric power grid must belong to one of the iBAs and cooperate with the iBAs coordinators for communicating their needs and abilities to participate in power balancing and delivery. Similarly, all the iBAs must exchange minimal information to be coordinated by the utility system operators to ensure stable and reliable operation at value. The basic information exchange proposed is in terms of power, rate of change of power for each specific time horizon of interest. Similar to AGC requiring ACE information for quasi-static frequency regulation, iBAs must either communicate needs or provide specifications of power, rate of change of power and time horizon over which they are capable of meeting their commitments. The time horizons are a stratum of times ranging from milliseconds to hours. Once such specifications are set, all end users and IBAs will begin to consider their technological options for meeting these specifications and their value, if/when participating in markets for these services. The specific methods reported in Sections 3 and 4 now become options for consideration by the iBAs to meet their operating requirements. In Section 3 methods for placing the PMUs and controllers so that each iBA is observable and controllable so that it meets the specifications in terms of power, rate of change of power and time horizon over which the specifications can be met are implementable. In Section 4 specific examples of control for wind power farms and their coordination into an

iBA are introduced. The main recommendation to PSERC members is to consider the proposed extension of today's SCADA and its required information exchange for possible adoption. Prof. Marija Ilic is willing to volunteer her time to move this concept further. As the first step, she gave a PSERC seminar on September 26, 2018. Notably, this relatively low cost project has helped fund partially 15 publications and provide partial support for two doctoral theses at CMU. This support by PSERC is greatly appreciated.

Bibliography

[1] S. Pequito, N. Popli, S. Kar, M. Ilić, and A.P Aguiar. A framework for actuator placement in large scale power systems: Minimal strong structural controllability. In *Proceedings of IEEE International Workshop on Computational Advances in Multi-Sensor Adaptive Processing*, December 2013.

[2] Nipun Popli and Marija Ilić. Storage devices for automated frequency regulation and stabilization. In *Proceedings of the IEEE Power and Energy Society General Meeting*, 2014.

[3] Nipun Popli. *Multi-layered Energy Conversion and Frequency Control in Complex Electric Power Systems*. PhD thesis, Department of Electrical and Computer Engineering, Carnegie Mellon University, USA, 2017.

[4] Nipun Popli, Sergio Pequito, Soummya Kar, A Pedro Aguiar, and Marija Ilic. Selective strong structural minimum cost resilient co-design for regular descriptor linear systems. In *to appear in Automatica (arXiv preprint arXiv:1704.01157˙*, 2017.

[5] Stefanos Baros. *Distributed Control for Wind Farm Power Output Stabilization and Regulation*. PhD thesis, Carnegie Mellon University, May 2016.

[6] Stefanos Baros. intelligent balancing authorities (ibas) for transient stabilization of large power systems. In *Proceedings of the IEEE Power and Energy Society General Meeting*, 2014.

[7] Stefanos Baros. A novel ectropy-based control scheme for a dfig driven by a wind turbine with an integrated energy storage. In *Proceedings of the American Control Conference*, 2015.

[8] Stefanos Baros and Marija Ilić. Robust ectropy-based control of a wind dfig with an integrated energy storage for transient stabilization and mppt. In *Proceedings of the IEEE Power and Energy Society General Meeting*, 2015.

[9] Stefanos Baros and Marija Ilić. Distributed control of wind dfigs with integrated storage for predictable power output. In *Proceedings of the IEEE Power and Energy Society General Meeting*, 2016.

[10] Stefano Baros and Marija Ilić. Distributed dynamic dispatching of deloaded wind dfigs via consensus torque control. In *Proceedings of the IEEE Power and Energy Society General Meeting*, 2016.

[11] Stefanos Baros and Marija Ilić. Distributed torque control of deloaded wind dfigs for wind farm power output regulation. *IEEE Transactions on Power Systems*, 32(6):4590–4599, November 2017.

[12] Stefanos Baros and Marija Ilić. A consensus approach to real-time distributed control of energy storage systems in wind farms. *IEEE Transactions on Smart Grid*, PP(99), September 2017.

[13] Marija Ilić and Rupamathi Jaddivada. Multi-layered interactive energy space modeling for near-optimal electrification of terrestrial, shipboard and aircraft systems. *Annual Reviews in Control*, 2018.

[14] Marija Ilić. Panel i: 2016 state of reliability, remarks of marija ilic. In *Proceedings of FERC Reliability Technical Conference*, June 2016.

[15] Marija Ilić. Toward a Unified Approach to Sustainable and Resilient Electric Energy Systems: Modeling and Control. *Journal on Fundamentals and Trends in Electric Energy Systems*, 1(1), 2016.

6. Appendix

FERC Reliability Technical Conference
Panel I: 2016 State of Reliability

Remarks of Marija Ilic, Professor
Carnegie Mellon University

June 1, 2016

It is my great privilege and honor to respond to specific questions raised by this panel. Thank you for this opportunity. The comments provided are strictly mine and do not represent positions taken by any other parties. However, they are result of many R&D years with my collaborators, and their direct or indirect input is greatly appreciated.

I first make several general comments, and then respond to specific questions raised by the Commission in light of these comments.

General comments

Need to relate mandatory standards with their quantifiable relevance to reliable and efficient BPS operation**--**Given a very complex nature of operating BPS, it is often difficult for non-utility industry participants to appreciate the need for mandatory standards of one kind or the other. Because they are viewed as additional cost to the basic electric energy services, it is necessary to have a way to directly interpret their relevance for reliable and efficient operation. We suggest that it is, therefore, necessary to work on evolving mandatory standards so that this becomes possible.

One way forward would be to establish general, relatively simple, framework based on common transparent and quantifiable metrics and protocols. The framework should be based on straightforward physical and economic principles. To achieve this, it is necessary to base today's standards on unifying principles of electric power system operations subject to end users' quality of service (QoS) specifications. This is a tall order, given that today's system operation is a complex mix of various methods under various assumptions.

For the basic framework to work (ensure reliable service at well-understood value to all) it must be designed to account for complex spatial and temporal interdependencies within a multi-layered multi-temporal architecture of the emerging electric energy systems. The complex multi-layered spatial boundaries create well-known "seams" problems; these problems are not only between Balancing Authorities (BAs), they exist within a BA between Transmission System Owners (TSOs), Distribution System Owners (DSOs); between utility-owned and non-utility-owned parts of the system. To overcome this problem, all components must provide information about their ability to contribute and their needs for reliable service using common interaction variables between themselves and the rest of the system. Second, in order to manage highly dynamic system reliably, a family of well-organized temporal standards is necessary. These needs are described next. We identify key open problems which require solutions. Finally, we take the liberty to propose possible solutions based on our long-term R&D findings.

Need for distributed, multi-layered standards**--** Technological and organizational industry changes have led to BPS architecture with "nested" Balancing Authorities (BAs) [Ref. 1]. Each group of components responsible for participating in reliable service at value is called an intelligent Balancing Authority (iBA) [Ref. 2]. For example, non-utility-owned parts of the system with their own sub-objectives are often embedded inside today's BAs and are hard to align with the utility objectives. To account for their effects, more granular standards for all BPS members must be established. Clear characterization of their roles in balancing the system during both normal and abnormal conditions is required. NERC reliability standards recognize this emerging architecture evolution, and have been geared toward setting mandatory rules for both utility-owned and non-utility-owned generators. These should be extended to all groups of components within BPS in accordance with well-defined principles.

Key open technical problem comes from lacking technical foundations for relating certain BPS operating problem (loss of synchronism, for example) to the mandatory requirements on specific equipment and its physical controllers (primary frequency reserve in the case of loss of synchronism); much serious industry effort is under way to solve this problem [Ref.3]. However, since it is fundamentally impossible to uniquely map a specific BPS reliability problem to the technical requirements which must be met by the components themselves, many such on-going industry efforts will still face the fundamental problem of how to justify the technical requirement set by the mandatory standard.

This problem can be overcome by requiring all components to provide information themselves about their ability to participate in reliable service, and the system operators to use this information to minimally coordinate them on-line so there is no system-level problem. Moreover, if components also provide the cost associated with their participation in reliable service, it also becomes possible for system operators to manage the system efficiently without deteriorating system-level reliability.

To do this systematically, without biasing certain technologies and participants, we propose that common variables and metrics must be used and that these must be replicable and quantifiable. Higher-level iBA entities must be responsible for meeting standards expressed in terms of the same types of variables and metrics. The key role of higher level iBA is to minimally coordinate its member iBAs so that their own metrics are met.

Need for dynamic, multi-temporal standards— The well-established approach to power balancing in the past has been "horizontal", namely the slowest generators are scheduled first, and the faster ones are scheduled closer to real time to supply system-level demand. This has been possible because the system demand has been quite stationary and predictable. Feed-forward (ahead of time) scheduling of generation is done so that the only feedback (automation) needed is to regulate frequency in response to hard-to-predict imbalances in between scheduling intervals (AGC, by the BAs) and primary stabilization in response to fast small deviations in near real time (primary control, by the governors, AVRs and PSSs primary controllers of generators).

Key new challenge —These historically practiced temporal hierarchies underlying power balancing are currently challenged as both net load and new technologies connected to the system often exhibit previously unseen temporal fluctuations.

Proposed technical solution-In order to bring some order to balancing power over time by the most effective technologies, it is essential to think of standards as "dynamic" standards [Ref. 4,Ref. 5]. All components connected to BPS are responsible for providing specifications about their ability to participate in balancing power at certain rate and over certain time horizon. If this information is provided, it becomes then the responsibility of system operators to request the right amount of power at the right rate from technologically very diverse components. For technical details on such dynamic standards, see [Ref.4, Ref.5].

Possible Dynamic Monitoring and Decision Systems (DyMoNDS) framework for Reliable, Efficient and Clean Electricity Service

The idea of having common metrics and protocols within a consistent general framework raises the key technical question regarding the existence and nature of such common variables and metrics.

To account for complex multi-layered BPS spatial architecture, we first must think of a BPS as comprising many electrically interconnected heterogeneous iBAs [Ref.1, Ref.2,Ref.6]. Each BPS member (component, or group of components, physically connected to the grid) must belong to an intelligent Balancing Authority (iBA).

To account for complex multi-temporal dynamics, the required information must be in terms of temporally-organized metrics relevant for the entire range of operating problems.

Definition of intelligent Balancing Authority (iBA) –A group of cooperative components within the BPS freely bundled according to its own objectives and subject to its own technical constraints. In order to be part of BPS it must: (a) provide information about its ability and needs in terms of variables and metrics common to all other iBAs; and, (b) must participate in protocols determined by the higher-level iBAs, ultimately responsible for reliable service at today's BA levels and higher.

The proposed general framework is named Dynamic Monitoring and Decision Systems (DyMonDS) framework. It is based on straightforward on-line information exchange between iBAs according to a simple protocol that lower level iBAs must provide information to the higher level iBAs to which they are electrically connected. The higher-level iBAs, in turn, have the responsibility and authority to minimally coordinate their iBA members. Each IBA has its own "DyMonDS" defined as follows:

Definition of DyMonDS—Information processing unit responsible for providing information about its common metrics and QoS. The unit is equipped with sensors, automation, computer applications in support of their own decision making so that it is capable of meeting its own specifications. These are characterized in terms of common interaction variables (intV) and Quality of Service (QoS).

Definition of Common Interaction Variable (intV)-- An interaction variable z_i(t,T) between component i and the rest of the system is characterized as a set of physical variables comprising incremental stored energy E_i(t,T), power p_i(t,T) and rate of change of power dp/dt_i(t,T) which an iBA can produce or which it needs.

Definition of Common Metrics-- The general metric represents *bounds on common variable intV*.

Definition of Quality of Service (QoS)--- Each iBA specifies limits on voltage delta v_i(t,T) and delta f_i(t,T) frequency deviations acceptable.

Shown in Figure 1 is a sketch of DyMonDS-based SCADA. It can be seen that DyMonDS framework is basically next generation SCADA system required to implement protocols for on-line information exchange in support of reliable and efficient service at specified QoS. It can also be seen that multi-layered, multi-directional and multi-temporal information exchange becomes key to systematic operations and control.

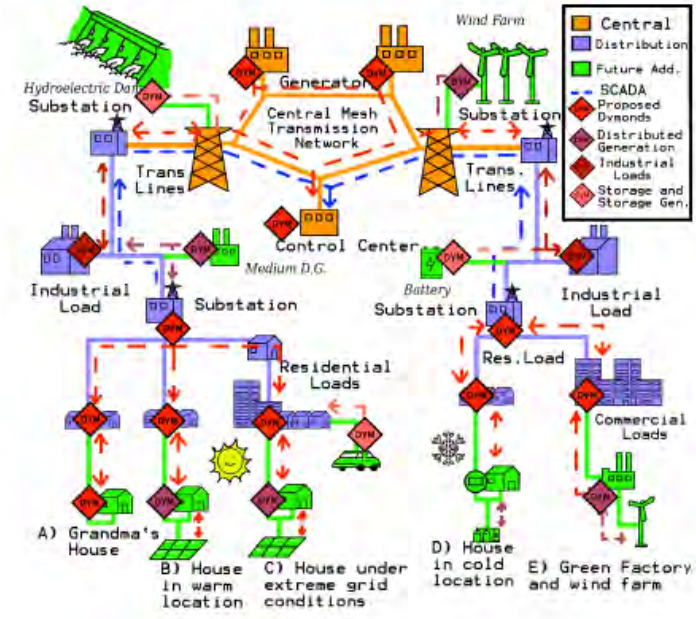

Figure 1 DyMonDS-based next generation SCADA [Ref.2, Ref.6]

Several important observations regarding proposed DyMonDS framework

Natural outgrowth of today's operations --- Proposed metrics and protocols underlying DyMonDS are direct extensions of well-known Area Control Error (ACE) used in Automatic Generation Control (AGC). The extensions are two-fold: An ACE-like interaction variable is introduced to characterize any given component connected to a BPS and intV must be defined over carefully-organized temporal horizons T so that all operating problems are managed using these variables [Ref. 6]. The basic technical idea is that the instantaneous power must balance at several rates and that users must have desired QoS. In AGC power balances

every 10 minutes by responding to ACE (incremental energy, average power over this period) and frequency at the BA level is specified QoS. Very similar extensions can be introduced for specific dynamic problems of concern to NERC. In our answers to specific questions we illustrate this under Part b.

Possible to interpret all NERC requirements in terms of common variables and metrics—This fact is critical. Recent CMU provisional patent [Ref. 6] offers unified modeling by transforming current dynamic modeling into multi-layered modeling. Original variables of any dynamic component can be represented in this new space as comprising its intV and the remaining internal states. It is shown that components must know their internal states to design their sensing and control so that they can operate within the specified metrics. On the other hand, higher-level inter-area dynamical model does not have to know internal technological details nor models. Higher-level iBA can minimally coordinate its interconnected components so that no reliability problems of any sort occur. This model is fundamentally critical for moving forward in this vastly multi-layered industry.

No requirement on one size fits all -- Reliability problems of concern to engineers can be managed by the smallest iBAs themselves, or by the higher-level iBAs. How is this done depends on the available control at different level iBAs, as well as on their interest to explore new solutions. Even the boundaries of iBAs can be created in a bottom up way as long as each iBA follows the proposed protocol.

Implications of using DyMonDS framework on innovation

Explicit incentives to select right technology-Assuming a general framework as proposed, it becomes possible to innovate at well-understood value to those doing it. The BPS members have clear options between implementing technologies to meet the metrics/standards themselves, or in cooperation with other iBA members. Higher level iBA can coordinate its members by either allocating technical responsibilities or by having market incentives in an IT-enabled DyMonDS environment. A quantifiable binding burden of proof is set on all BPS members to meet their metrics measured in terms of interaction variables or pay to iBA for doing it on their behalf. The incentives shift to the level of granularity needed to assess what may be the most effective technology (software and hardware) to which BPS members. In particular, iBAs quickly recognize that for them to meet their metrics it is essential to operate in a much more flexible way than it is currently done. We point out that for this to be implemented much innovation is needed in software for enabling on-line reliable operation. Instead of ERO mandating provision of, say, specific primary frequency reserve, or voltage control, or deployment of FACTS, iBAs will utilize these so that their performance metrics are met in the most effective ways.

Recommended software innovations— For DyMonDS framework to become reality, it is necessary to enhance both automation embedded into components/iBAs and computer applications currently used by the system operators. Decisions on how to operate BPS on-line as conditions vary are currently based on system operators' knowledge about the specifics of their part of the system and on the off-line analyses under different assumptions. In particular, today system operators base their decisions on the worst-case contingency

studies. We recommend that NERC and Commission would do well to move toward corrective reliability management with minimal required reserve for non-time critical contingencies. This means that, instead of operating during normal operations conservatively so that in case contingency happens no system-level problems occur, it is necessary to have software which, after a contingency occurs, quickly decides on what are the best adjustments on the remaining functional equipment. This mode of operation is likely to become unavoidable because of higher presence of hard-to-predict worst-case scenarios created by larger variations in net demand as seen by the BPS operators. In our Part b. response we illustrate potential value of an extended AC OPF, for example, when determining rule on reactive power support.

Also, to avoid time-critical problems, it is essential to ensure that iBAs have sufficient embedded automation to transiently stabilize equipment in response to large sudden changes, including faults. Humans can only act at limited speed. Theoretical state of the art designs are known for designing nonlinear controllers of several types so that closed-loop primary dynamics are stable within the specified bounds on interaction variable (metrics). Manufacturers need to implement such controllers. Otherwise, the system will experience previously unseen oscillations such as sub-synchronous control instabilities (SSCI) [Ref. 7,Ref.8]. NERC should require testing of equipment automation prior to deploying to the system so that the dynamic standards are met as measured in terms of metrics set on interaction variables.

Minimal information exchange and internal privacy- Relevant for availability requirement of certain databases, the model used by an iBA to ensure that the specified metrics are feasible by means of their own primary control design is a very detailed model of specific technologies. The higher-level model is only in terms of interaction variables of all iBAs within the BPS; it is, therefore, sufficient to coordinate actual power outputs for stabilizing system-level performance without knowing full detail of internal models and parameters. The bounds on interaction variables (metrics) can vary in operations, the higher level iBA simply selects the actual value of the interaction variable for all of its iBA members so that no system-wide operating problems occur. For reliable service to be implemented at the BPS level, it is necessary to only exchange information about interaction variables between the iBAs and their higher level iBA. It is not essential for the highest BPS level operating entity to know much detail about the specifics of technologies embedded within the lower-level iBAs. This observation sets the basis for a new multi-layered approach to ensuring reliability by:

- Requiring non-uniform specifications of all iBAs in terms of their own interaction variables; these variables are common to all iBAs. Achievable bounds on interaction variables (metrics) must be guaranteed and tested by the iBA itself at each rate of response of interest. This requires full knowledge of local iBA only.
- Requiring higher-level iBAs to minimally coordinate the actual values of interaction variables so that bounds on interaction variable at their level are also met. This does not require full knowledge if local iBAs comprising the higher-level iBA. Only bounds on their interaction variables are needed.

Much the same way as AGC of each BA (formerly control area) is characterized in terms of its own Area Control Error (ACE), each iBA is characterized in terms of its own interaction

variable with the rest of the system; and has much autonomy to decide on technologies and means of meeting the AGC standard.

Potential effects on economics for reliable service- We suggest that DyMonDS framework gives lots of flexibility to save while observing reliability. Members within each iBA are free to decide on how to implement their specified metrics and to cooperate to make the most out of their resources. Savings within any given iBA happen through cooperation. Savings across same-level iBAs are achieved either through minimal coordination or through competition depending on the tradeoffs of potential gains and complexity of communications implementation. Notably, iBAs compete within the BPS for their members. A well-designed electricity market is ultimately DyMonDS framework in which technical and economic signals are communicated and aligned [Ref. 9]. For this to happen, common IntV and metrics must also have the cost specified.

In closing-- We humbly suggest to the Commission and NERC to further consider the proposed DyMonDS framework. It is not too late to re-think principles of mandatory standards for reliability and establish a general framework according to such principles. Such an approach is likely to make the overall process systematic and easy to quantify and monitor. We have developed at CMU a Smart Grid in a Room Simulator (SGRS) in collaboration with NIST which can be used as a means of demonstrating DyMoNDS-enabled BPS performance and for comparing it with the effects of today's mandated standards [Ref. 10]. We point out that the proposed framework is not suggested lightly; we have simulated many of its aspects using real-world models of electric grids in two Azores Islands. This work started in response to the challenging question of how would one minimize the use of expensive fossil fuel without increasing long-term electricity service cost and without affecting QoS [Ref. 11]. I strongly believe that we could extend these concepts to enable BPS reliable operations at reasonable long-term cost.

Response to Specific Questions Raised by the Commission Panel 1

a. Primary accomplishments and new future issues

Planners, operators and transmission owners have continued to work hard to ensure no major loss of service at the BPS levels. They are to be congratulated for this. As pointed out by all participating in this panel, the system has performed well; this has been mainly accomplished by a heavy reliance on a combination of mandatory standards for reliability and the engineering expert knowledge. However, the industry has remained short of having a unifying framework in support of systematic transitioning from voluntary to mandatory standards; as a result the process has been extremely time consuming and hard to follow. Perhaps the main challenge has been the lack of simple transparent metrics and protocols underlying evolution of standards. In our General Comments we provide a detailed discussion of this issue and propose a possible framework for moving forward. Our basic recommendation is that a systematic approach to innovating today's engineering tools and computer applications should be given major attention when defining reliability standards in such complex systems. It is well-known that the complexities are not only technical, but economic, organizational and societal. Aligning all of this requires systematic framework.

Furthermore, ensuring reliable service by strictly planning more equipment (transmission, generation) and not changing the way the infrastructure is used in the actual operations will fall short of ensuring reliable service at any reasonable cost as uncertainties seen by the BPS operators increase. In particular, relying on off-line analyses and putting the burden of proof on operators to make on-line decisions will result in many situations previously unseen by them and in hard-to-foresee wide-spread blackouts. We strongly recommend that Commission and NERC consider enhanced decision-making tools beyond the ones currently used. Improvements are needed to facilitate on-line decisions by system operators; computer applications capable of managing events on-line as they occur, instead of relying solely on the worst-case reserves are critical. Similarly, fast automation capable of avoiding time critical events (fast control and protection) must be deployed; humans can only act at certain speed.

b. Assessment of the effectiveness of NERC's reliability activities and related industry efforts

The Commission and NERC have issued several dockets related to reliability services. They all share common challenges described in my General Comments. In particular, various activities have been concerned with various specific technical requirements and have not addressed these requirements in direct relation to their impact on reliable system operations. We have seen a sequence of dockets which are hard to interpret by those who are not intimately familiar with the power system operations. This situation begs questions regarding the need for these services and the amounts mandated. As explained in our General Comments above, this is simply because at present the industry does not have general model-based framework which in a transparent way explains how the BPS operates and why are certain standards needed.

The proposed Dynamic Monitoring and Decision Systems (DyMonDS) framework offers a relatively straightforward thinking about how is very complex BPS operated. It is as simple as having to balance power (deliver produced power to the locations needed) at the fast rate. The faster the rate at which the power balances, the less deviations in system frequency and voltages. So, the natural common variables for defining metrics are in terms of integrals of power (incremental energy), power and rate of change of power. Everyone can understand this. Moreover, the Quality of Service (QoS) is courtesy to the BPS end users, and should not be explicit in determining system-level requirements. It is these two observations, together with lots of theoretical foundations work, which should begin to set the basis for common metrics and protocols. Once this is understood, one begins to avoid all together difficult details regarding exact protection standard settings, or specifications for frequency reserves (primary and secondary) and voltage/reactive power support complications. These should be internal to those operating the system on-line as information about common metrics is made available and updated on line. It is no longer possible to operate the system reliably for the worst-case scenario which is probably never to happen. What is needed are methods for resilient on-line operation.

To illustrate, we briefly discuss some recent activities by the Commission in light of our general comments:

The debate regarding essential reliability services --the first Docket No. RM16-1, November 2015 about exemption for wind generators from providing reactive power--- It does not appear plausible to provide meaningful incentives for this support without having interactive protocols in place to select out of many different options the ones which are most effective as seen by the higher level iBAs. For example, given metrics, AC OPF obtains the most effective reactive power support [Ref.12]. As a rule, the result of AC OPF based voltage dispatch is never for all iBAs to provide the same reactive power support. The question of reactive power support is particularly thorny one for several reasons. To start with, based on the discussion in general comments, no common metrics are needed in terms of reactive power. Instead, only QoS measured in terms of acceptable voltage deviations explicitly enter the proposed protocol. Also, a closer look into controllers for generators and other equipment (including power converters) shows that none of these control directly reactive power, they control voltage. Therefore, it is needed that BPS members provide information on common metric specifications as well as ranges of acceptable voltage deviations and not worry about reactive power support specifications. Some of the BPS members would require higher level voltage dispatch coordination if they are not capable of supporting their own voltage, and other iBAs will be capable and willing to adjust their voltages within relatively large ranges, and, therefore, help out other parts of the system.

We stress that requiring each iBA to provide unity power factor is pointless for variety of reasons as we have documented in the past studies for industry [Ref.13]. Instead, much the same way as with other on-line corrective actions, as conditions vary the available resources are adjusted by the coordinating entities to ensure that a BPS as a whole does not experience voltage "collapse" problems. We have documented in excruciating details how this can be done for the case of NYCA [Ref. 13]. It was shown, for example, that on a hot summer day approximately 1GW power can be delivered beyond what is being delivered from Niagara to NYC by implementing voltage dispatch [Ref. 14]. Similar studies have shown that in PJM even after retiring major power plants the system can be operated reliably if on-line systematic voltage dispatch is practiced when dispatching real power [Ref. 15]. The infamous PV curve can become much more forgiving (allow for larger transfers) when voltage dispatch is implemented, as shown for the case of ERCOT [Ref.16].

Unfortunately, my discussions over the past decade with many leading engineers have clearly demonstrated that deployment of any new software creates a risk in its own right and, moreover, no direct incentives exist to do so. As a result, sub-optimal utilization of available resources takes place and, at the same time, the threat of voltage collapse is not eliminated; at least a dozen major blackouts worldwide have been caused by poor management of available reactive power resources, and not by their shortage. It was shown that the blackout of 2003 could have easily been avoided by on-line corrective actions despite the specific triggering event [Ref.17].

However, if there are no bids in terms of financial incentives this is hard to do since higher level iBAs won't have a quantifiable way of allocating cost of meeting reliability performance by diverse smaller iBAs. Of particular importance are incentives to lower level iBAs and transmission and distribution owners to help support voltage by their higher level iBAs. Adjusting tap changer setting and AVR settings in NYCA BPS (and/or) the neighboring systems would be a major means of directing more power from clean hydro to NYC. Serious economic studies must be done to compare the effects and cost of such BPS solutions (dominated by economies of scale) to the solutions envisioned by NY REV (deployment of many small-scale DERs).

Provision and Compensation of Primary Frequency Response, Docket No. RM16-6, February 2016 is particularly straightforward to discuss in light of our proposed reliability metrics. To start with, we highlight that frequency deviation is a rather poor indicator of power imbalance-related instabilities. Recall that even in steady state AGC is in response to power imbalance known as ACE, and not in

response to frequency deviation. Long ago adjusting frequency bias was a major job for at least one engineer. A single frequency bias in iBAs comprising highly heterogeneous technologies (with large and smaller, or no, inertia) is a non-starter and therefore an impossible job for designers of mandatory standards. Instead, we propose to specify metrics in terms of feasible ranges of power and rates of change of power. Determining the amount of primary frequency response can only be done if protocol is in place to specify which components are likely to cause how much sudden power change (either because they fail to operate or they have insufficient means of responding fast to follow desired rate of power changes).

Finally, selecting sources of primary frequency control should be revisited in somewhat serious way. It is our understanding that current industry effort is putting all its thinking into determining the bandwidth of governor response needed to have adequate primary frequency response [Ref. 3]. We stress that governor would quickly break if it were to serve the purpose of saving a generator from loss of synchronism following sudden rate of change of power output and being required to respond to it. Instead, AVR, PSS, SVC,FACTS, fast storage, such as flywheels and batteries (as the last resource because of their excessive cost) can all contribute in major ways to transiently stabilizing BPS response and preventing loss of synchronism. For this to be implemented, these potential suppliers of primary frequency response should make their metric known to the higher level iBA, which, in turn would assess which disturbances can the system withstand. Instead of reducing power transfers and making ranges of operating conditions more conservative prior to these disturbances, the higher level iBAs should solicit sufficient supply for stabilization across all these newly emerging technologies. While they may appear too costly to implement, it is possible to asses an optimal level of investment in fast power-electronically switched controllers whose cost pays off by operating the system efficiently during normal operations [Ref. 18]. It is at this critical time scale that PMU-based monitoring and wide-area control schemes may become essential, this is to be determined by the higher-levels iBAs. We stress that there exists fundamental difference between special protection schemes (SPS) on one side, and wide-area fast control schemes. The objective of protection is to disconnect the equipment, and the objective of fast control is to support the system operation even when protection would have had to disconnect it otherwise. A recommended case study is to take the case of SSR controller proposed in [Ref. 19] and compare to SPS in AEP for protecting the system against SSR [Ref. 20].

As a side note, principles for secondary frequency reserve are straightforward to determine, following the same general metrics. As an illustration of possible standards for ensuring small signal stable frequency response and frequency regulation within the pre-specified threshold is just an example of the more general principle proposed [Ref. 21].

In short, we strongly recommend taking a step back and setting up systematic principles for primary frequency support protocols according to the general proposed metrics, instead of struggling with tightening up the requirement for governor response.

Please notice that sufficient flexibility ought to be given to both existing and new resources when attempting to implement consistent protocols and standards. The response given to me during a recent presentation at CA-ISO is very supportive of the proposed metrics and protocols [Ref. 22]. Two basic takeaways from that meeting are: Both engineers and market folks understand power, rate of change of power, and incremental stored energy. Our findings so far are that it is sufficient to have multi-temporal metrics in terms of these variables only without being too concerned about the type of technology and its details.

All the other Commission events (Ride-Through Requirements for Small Generators, Docket No. RM16-8, March 2016; NERC Reliability Standard for Geomagnetic Disturbances, TPL-007-1; FERC Docket No. RM15-11, May 2015; FERC proposed directive for new requirements Docket No. RM15-14, July 2015)

should be assessed in light of common general framework for reliable services proposed here.

FERC proposed non-public access for Commission staff
Docket No. RM15-25, September 2015

Relevant for availability requirements of certain databases, the model used by an iBA to ensure that the bounds on interaction variable are feasible by means of their own primary control design is a very detailed model of specific technologies. The higher-level model is only in terms of interaction variables of all iBAs within the BPS; it is, therefore, sufficient to coordinate actual power outputs for stabilizing system-level performance without knowing full detail of internal models and parameters. The bounds on interaction variables can vary in operations, the higher level iBA simply selects the actual value of the interaction variable for all of its iBA members so that no system-wide operating problems occur. For reliable service to be implemented at the BPS level, it is necessary to only exchange information about interaction variables between the iBAs and their higher level iBA. It is not essential for the highest BPS level operating entity to know much detail about the specifics of technologies embedded within the lower-level iBAs. This observation sets the basis for a qualitatively different multi-layered approach to ensuring reliability by:

- Requiring non-uniform specifications of all iBAs in terms of their own interaction variables; these variables are common to all iBAs. Achievable bounds on interaction variables (metrics) must be guaranteed and tested by the iBA itself at each rate of response of interest. This requires full knowledge of local iBA only.
- Requiring higher-level iBAs to minimally coordinate the actual values of interaction variables so that bounds on interaction variable at their level are also met. This does not require full knowledge if local iBAs comprising the higher-level iBA. Only bounds on their interaction variables are needed.

c. What metrics have been, or should be, developed to define whether reliability, in whole or in part, is improving? How can we assess if the risk of blackouts is increasing or decreasing and, if increasing, due to what causes? Can a quantitative risk analysis be used?

Reliability is not a single number! It should be measured in terms of how are specified metrics and QoS met by BPS members and by the higher-level iBAs. If BPS members specify their common metrics (bounds on stored energy, power and rate of power change) they are capable of providing or needing, as well as their own QoS acceptable, it is up to higher-level iBAs to implement these according to their least cost metric (a combination of fuel cost, environmental impact and risk of not serving); here, again, iBAs metrics are measured using the same variables as for their members. A quantitative risk analyses depends on how is the system operated, and the effects of operating practices should be looked into very carefully. Proactive protocols should be put in place to enable implementation of desired reliable service within the multi-layered BPS.

Coordinating protocol for ensuring reliable service becomes the one of computing the actual value within the ranges specified by the metrics of BPS members and sending the commands to them to implement at different rates relevant for specific technical problems. Dynamic standards are fundamentally families of multi-temporal requirements as follows:

To avoid sub-synchronous electromagnetic and electromechanical oscillations –each iBA must specify range of power needing/producing at the rate relevant for this dynamic phenomenon, say specifications must be set for response within the split second time intervals[Ref. 23].

To avoid loss of synchronism --each iBA must specify range of power needing/producing at the rate relevant for this phenomenon. These are typically rates relevant for ensuring critical clearing time following major loss or major sudden dip in power generated or consumed [Ref. 24]. For example, an iBA could be a wind power with storage and conventional generator jointly managing loss of synchronism when a fault occurs in their part of the grid [Ref. 25].

To avoid small signal instabilities specifications of the proposed metric must be made for the time responses so that they do not trigger under-/over-frequency and voltage [Ref. 26].

To ensure frequency and voltage regulation the existing ACE metric must be specified for minutes to 10 minutes [Ref. 4,Ref.5]; in systems with continuously fluctuating DERs the existing ACE must be enhanced and it becomes a dynamic metric [Ref. 26].

To ensure that ramping rates important for balancing power when dispatch is performed it is important to specify the proposed metric for time intervals over which dispatch is being done [Ref. 27].

The more granular metrics over time, the smoother system-level response is achievable. Adding to currently observed time scales the new shortest time scale which brings about the assurance that no power electronics-related electromagnetic instabilities would be created in response to extremely sudden changes, could be an excellent starting point for ensuring reliable service at value by all entities.

Specific recommendations for transparent regulatory rules in support of effective reliability standards

When/if iBAs fail to meet their specifications by not responding to the coordinating entities the reasons may be multiple. They could range from having failures in their own hardware components and/or failures in their embedded DyMonDS implementation. Part of the protocol is that they must notify higher level coordinating iBA and this entity should have stand-by ready methods to modify the commands to the remaining iBAs according to the well defined performance objective at the aggregate level. Similar interactive protocol must exist between all layers.

Monitoring whether the metric are implemented becomes the objective of enforcing reliability standards. An important technical detail is that if all (groups of) component(s) are required to participate in enabling reliability than one could consider enriching the protocols to specify two types of metrics: The first metric is to operate according to the best possible specified metrics, and the second metric is to be specified for abnormal conditions when some components fail to meet the specified metric for normal operation.

We observe that the specifications of iBAs multi-temporal metrics must be made prior to the iBA connecting to a BPS. The on-line commands, on the other hand, are issued in a

feed-forward way at the rate determined by the higher level iBAs. The committed/required metric is implemented by the lower level iBA.

We point out that the technical problem of higher level iBA coordination so that the system as a whole does not experience instability problems at particular rate and to also ensure that system frequency and voltage remain within pre-specified bounds requires serious attention by both industry and academia. It is truly a solvable problem. As an example of control area computing how much power (secondary frequency reserve) and at which rate so that the system frequency settles to within the pre-specified threshold epsilon can be found in [Ref. 21]. It is extremely important to observe that this is not possible to answer unless all BPS members and iBAs specify their demand for frequency reserve to compensate likely deviations from dispatched power and all iBAs providing frequency reserve specify their ability to do so in terms of above proposed metrics. Similar extension is needed to all metrics within the multi-temporal family for each iBA, independent from the specific technology or ownership.

Specific recommendations for transparent electricity market designs in support of reliability service at value

Parts of the large complex bulk electric power systems which are operated as electricity markets naturally lend themselves to participating in reliable service at value by being required to specify the same technical metric. In addition to specifying the technical metric they would be required to participate in a family of multi-temporally clearing markets by providing supply and demand bid curves for [E_i(t,T)^min; E_i(t,T)^max]; range of power [p_i(t,T)^min; p_i(t,T)^max] and rate of change of power [dp_i(t,T)/dt^min; d p_i(t,T)/dt^max] capable of either producing or needing during the time T of interest. The role of higher level iBAs then becomes the one of not only ensuring that the technical metric is implemented according to their coordinating commands, but also that the cost of ensuring reliability is optimized. For transactive energy control to work such specifications will become essential.

Specific recommendations for combining technical standards and market design rules

Notably, the proposed reliability metrics are expressed in terms of common variables [E_i(t,T)^min; E_i(t,T)^max]; range of power [p_i(t,T)^min; p_i(t,T)^max] and rate of change of power [dp_i(t,T)/dt^min; dp_i(t,T)/dt^max] capable of either producing or needing during the time T of interest for both reliability and for defining market derivatives hybrid solutions are possible. Given this important fact, hybrid solutions are possible in which existing iBAs may meet technical standards while the newly deployed technologies can be selected by the electricity markets to best align the cost and technical performance.

References:

[Ref. 1] Ilić, M.D. and S.X. Liu, *Hierarchical Power Systems Control: Its Value in a Changing ElectricPower Industry,* Springer-Verlag London Limited Series, Advances in Industrial Control,1996.

[Ref. 2] Ilić, M., "Dynamic Monitoring and Decision Systems for Enabling Sustainable Energy Services", " Network Engineering for Meeting the Energy and Environmental Dream", Scanning the Issue, Proc. of the IEEE, pp. 58-79.

[Ref. 3] http://www.nerc.com/pa/stand/Pages/default.aspx.

[REF. 4] ILIC, M., BAROS, S. , "Standards and Protocols for Stable Dynamics
in the Electric Power Systems, PSERC Final Report S-55, 2016.

[Ref. 5] Ilic, M., "Tooward Standards for Dynamics in Future Electric Energy Systems"< PSERC White paper, 2012.

[Ref. 6] Ilic, Marija, " A Unified Approach to Dynamic Monitoring and Decision Systems (DyMonDS) for Complex Electric Energy Systems", Disclosure of invention No. No. 2016-061, Carnegie Mellon University, 2012 (refiled 2016).

[Ref. 7] Shun-Hsien (Fred) Huang, "Wind Integration: ERCOT Experience", 8th CARNEGIE MELLON CONFERENCE ON THE ELECTRICITY INDUSTRY, March 13-14,2012.

[Ref. 8] http://www.nrel.gov/pv/performance_reliability/pdfs/2015_pvmrw_130_berdner.pdf

[Ref. 9] Ilić, Marija, "3Rs for Power and Demand", Public Utilities Fortnightly Magazine, December 2009.

[Ref.10] Kevin Bachovchin, Martin Wagner, Marija Ilic, "Multi-Layered Simulation using the SGRS Simulator; Interaction of TE and Flywheel Controlled Dynamic System", 10th CMU Electricity Conference Pre-conference Workshop March 30, 2015.

[Ref. 11] Ilić, M. D, Le, X., Liu, Q. (co-Eds) Engineering IT-Enabled Sustainable Electricity Services: The Tale of Two Low-Cost Green Azores Islands, Springer August 2013.

[Ref. 12] Marija D. Ilic, Jeffrey H. Lang, Eugene Litvinov and Xiaochuan Luo, "The Critical Role of Computationally Robust AC Optimal Power Flow in Reliable and Efficient Reactive Power/Voltage Dispatch ",

[Ref. 13] NETSS Final Report to NYSERDA on ``Voltage Dispatch and Pricing in Support of Efficient Real Power Dispatch'', Contract No. 10476,2012.

[Ref.14] Ilic, M., Lang, J., Litvinov, E., Luo, X., Tong, J., Fardanesh, B., Stefopoulos, Toward the Coordinated Voltage Control (CVC) Enabled Smart Grids, IEEE PES Innovative Smart Grid Technologies (ISGT), Dec. 5 7, 2011, Manchester, UK.

[Ref. 15] Marija Ilic, Sanja Cvijic, Jeffrey H. Lang, Jiangzhong Tong, " Optimal resource management for enhancing electricity market efficiency", IEEE PES General Meeting, 2015.

[Ref. 16] Marija Ilic, Sanja Cvijic, Jeffrey H. Lang, Jiangzhong Tong, and Diran Obadina, *Member IEEE,"* Operating Beyond Today's PV Curves: Challenges and Potential Benefits, IEEE PES General Meeting, 2015.

[Ref. 17] Ilić, M., E. Allen, J. Chapman, C. King, J. Lang, and E. Litvinov. "Preventing Future Blackouts by Means of Enhanced Electric Power Systems Control: From Complexity to Order.", Proc. of the IEEE, vol. 93, no. 11, pp. 1920-1941, November 2005.

[Ref. 18] Elizondo, Marcelo, Marija Ilic, and Pedro Marcado. "Determining the Cost of Dynamic Control Capacity for Improving System Efficiency." Proceedings of the IEEE General Power Meeting, Montreal CA, June 2006, paper # 06GM0839.

[Ref. 19] Allen, E. H., J. W. Chapman, and M. Ilic, "Effects of Torsional Dynamics on Nonlinear Generator Control, Parts I & II," Proceedings of the 34th IEEE Conference on Decision and Control, New Orleans, LA, December 1995, pp. 3479-3485 and pp. 3887-3894

[Ref. 20] American Electric Power, Special SSR Protection Scheme (private correspondence with Pasternak, circa 1990)

[Ref. 21] Ilic, M., P. Skantze, C-N. Yu, L. H. Fink, and J. Cardell, "Power Exchange for Frequency Control (PXFC)," Proceedings of the International Symposium on Bulk Power Systems Dynamics and Control-IV: Restructuring, Santorini, Greece, August 23-28, 1998.

[Ref. 22] Ilic, Marija, CA-ISO, invited talk, January 2016.

[Ref. 23] Cvetkovic, M. and Ilic, M. "A two-level approach to tuning FACTS for transient stabilization." Proceedings of the 2014 IEEE PES General Meeting, pp. 1-5.

[Ref. 24] M. D. Ilić, M. Cvetković, K. Bachovchin, A. Hsu, "Toward a Systems Approach to Power-Electronically Switched T&D Equipment at Value", *Invited paper at IEEE PES General Meeting*, Detroit, USA, July 2011.

[Ref. 25] Baros, Ilic, PES General Meeting, Boston, MA, 2016.

[Ref. 26] Marija D. Ilić and Qixing Liu, "Toward Standards for Model-Based Control of Dynamic Interactions in Large Electric Power Grids," Asia Pacific Signal and Information Processing Association Annual Summit and Conference 2012, Dec 2012, Hollywood, California, USA

[Ref. 27] Popli, N., Ilic, M., IFAC 2016, India.

Real Time Synchrophasor Measurements Based Voltage Stability Monitoring and Control

Final Project Report

S-65

Power Systems Engineering Research Center
Empowering Minds to Engineer
the Future Electric Energy System

Real Time Synchrophasor Measurements Based Voltage Stability Monitoring and Control

Final Project Report

Project Team
Venkataramana Ajjarapu
Umesh Vaidya
Iowa State University

Chen-Ching Liu
Washington State University

Graduate Students
Amarsagar Reddy
Subhrajit Sinha
Iowa State University

Ruoxi Zhu
Washington State University

PSERC Publication 17-08

September 2017

For information about this project, contact

Venkataramana Ajjarapu
Iowa State University
Department of Electrical and Computer Engineering
Ames, Iowa, USA 50011-3060
Phone: 515-294-7687
Fax: 515-294-4263
Email: vajjarap@iastate.edu

Power Systems Engineering Research Center

The Power Systems Engineering Research Center (PSERC) is a multi-university Center conducting research on challenges facing the electric power industry and educating the next generation of power engineers. More information about PSERC can be found at the Center's website: http://www.pserc.org.

For additional information, contact:

Power Systems Engineering Research Center
Arizona State University
Engineering Research Center #527
551 E. Tyler Mall
Tempe, Arizona 85287-5706
Phone: 480-965-1643
Fax: 480-727-2052

Notice Concerning Copyright Material

Acknowledgments

We express our appreciation for the support provided by PSERC's industry members and thank the industry advisors for this project:

- Aftab Alam (CAISO)
- Mahendra Patel, Navin Bhatt and Evangelos Farantatos (EPRI)
- Jianzhong Tong (PJM)
- Jay Giri (GE Grid Solutions)
- George Stefopoulos (NYPA)
- Di Shi and Jidong Chai (GEIRINA)
- Orlando Ciniglio (Idaho Power)
- Liang Min (LLNL)
- Alan Englemann and David Schooley (Exelon/ComEd)
- Eduard Muljadi (NREL)
- Reynaldo Nuqui (ABB)
- Prasant Kansal (AEP)
- Devin Vanzandt (GE Energy Consulting)
- Mutmainna Tania (Dominion Power)
- Florent Xavier (RTE)
- Kevin Harrison (ITC)

Executive Summary

There is increasing pressure on power system operators and on electric utilities to utilize the existing grid infrastructure to the maximum extent possible. This mode of operation leads to the system to operate close to its limits and this mode of operation can lead to instability problems. There are several forms of voltage instability [1] and each type of instability requires different techniques to monitor and control. To overcome this change in system operation, adopting real-time tools using Wide-Area measurements and Phasor Measurement Units (PMUs), that provide operators with better situational awareness are necessary. Various methodologies have been developed to monitor and control instability utilizing the PMU infrastructure that can analyze the data from the PMU in a real-time manner and can provide the operator with better awareness of the grid behavior. In this project, Iowa State University looked at analyzing short term voltage instability while Washington State University concentrated on long term voltage instability.

Part I: Real Time Synchrophasor Measurements Based Short Term Voltage Stability Monitoring and Control

As the bulk electric system operation is moving in to an operation regime where the economics are more important than in the past, the system is operating close to the operating points with more chance of voltage instability. An important type of voltage instability is the short term large disturbance voltage instability that is caused due to increasing penetration of the induction motor and electronic loads.

In Part I, the problem of monitoring and mitigating Fault Induced Delayed Voltage Recovery (FIDVR) is addressed by utilizing the high sampling rate of PMU's and understanding the physics underlying the FIDVR problem to issue control signals to smart thermostats and shunt devices in real-time.

Initially, the voltage measured by the PMU is used to quantify the amount of FIDVR. To ensure the robustness of the proposed methodology, the voltage waveform is converted into a time varying probability distributions that is compared to another time varying probability distributions derived from a predefined reference voltage waveform. The comparison between the probability distributions is performed using the Wasserstein metric that has the appealing properties of continuity and a limited output. These methods are implemented for real-time validation in OpenPDC to verify that they can indeed operate in the real-time environment and that they can handle noise introduced by measurement error and delays in the communication network. OpenPDC is chosen as it is in use by the utilities and so the code developed can be directly ported into the utilities' operations with minimal effort.

To determine the control, just utilizing the voltage did not provide sufficient information as several varying parameters of the load can lead to similar voltages. To overcome this, the composite load model is studied in detail and is simplified based on engineering judgment and it is shown that an admittance approach is well suited for this purpose. Analytical relations were derived by approximations of expressions and the time to recovery in terms of the measured admittance is derived. This is verified on PSSE simulations on the IEEE 162-bus system and the error between the expected times and the measured times to recovery were less than 1 second.

The low error provides confidence on utilizing this method for control to ensure that the FIDVR recovery can occur within a pre-specified time. The only control schemes that can mitigate FIDVR are shown to be the tripping of Air Conditioners or the injection of reactive power via Shunt devices. An analytical expression for the magnitude of control action as a function of trip time is derived and this is also tested in PSSE. The expression is shown to be accurate to within 1 second with control actions up to 30% Air conditioner load tripping and provides a use case for the utilities to implement smart thermostats in their distribution network.

The main take away here is that utilizing PMU measurements and a few offline simulations will enable the utilities to detect FIDVR phenomenon and estimate the time to recover from FIDVR in less than 3 seconds. This capability combined with Air conditioner control utilizing smart thermostats can ensure that the FIDVR recovery meets the transient voltage criteria set by reliability coordinators.

Part II: Real Time Synchrophasor Measurements Based Long Term Voltage Stability Monitoring and Control

With the increasing scale and complexity, power systems are being operated closer to voltage stability limits. Therefore, long term voltage stability is a focus area for power system research. Numerous measurements are available on a power system, e.g., Supervisory Control and Data Acquisition (SCADA) and Phasor Measurement Units (PMUs). Therefore, it is critical to utilize these measurements, particularly the large amount of PMU data, to assess the voltage stability in a timely manner. The main objective of the work in Part II is to develop a methodology for long term voltage stability assessment using a reduced network given a limited number of phasor measurements.

The Voltage Stability Assessment Index (VSAI) has been proposed in previous WSU work to calculate voltage stability indices at a load bus. This Thevenin Equivalent based method utilizes PMU data and the network information to estimate the voltage stability margin. Based on the work of VSAI, this project proposes an extension, called VSAI-II, that incorporates voltage dynamic mechanisms. The model improves the accuracy of the voltage stability index. A 179-bus system is used as the test system to demonstrate the effectiveness of VSAI-II. The results show that VSAI-II can not only provide the indices for the overall system but also the critical locations for voltage stability.

A major load center is usually supplied by multiple generation and transmission facilities through several boundary buses. To investigate voltage stability of a load center, a new method, OPF-LI, is developed to extend the voltage stability index based on an enhanced model of the generation and transmission systems. OPF-LI is demonstrated on the 179-bus system. The computation of the algorithms is performed by MATLAB. The commercially available tool, TSAT, is used to determine the loading limits of the load center with the dynamic model of the 179-bus system. The results comparing with TSAT simulation show that the results of OPF-LI are good approximations of the loading margin.

To incorporate the proposed OPF-LI with limited PMU data, a computational tool called the State Calculator (SC), developed in previous WSU work in an EPRI sponsored project, is used to

approximate the trajectory of state variables from the available PMU measurements. By using the SC, the loading limit are approximated as time progresses. The OPF-LI with SC is demonstrated on the 179-bus system.

Based on the dynamic mechanisms of OLTCs, an OTLC blocking control is proposed. The OTLC blocking control can prevent the critical buses from entering unstable operating states. OPF-LI is modified to incorporate the proposed OLTC blocking control. the simulation results with the 179-bus system indicate that the loading limit has been improved.

Project Publications:

[1] A. Reddy and V. Ajjarapu, "PMU based real-time monitoring for delayed voltage response," *2015 North American Power Symposium (NAPS)*, Charlotte, NC, 2015, pp. 1-6.

[2] A. R. R. Matavalam and V. Ajjarapu, "Implementation of user defined models in a real-time cyber physical test-bed," *2016 National Power Systems Conference (NPSC)*, Bhubaneswar, 2016, pp. 1-6.

[3] S. Sinha, P. Sharma, U. Vaidya and V. Ajjarapu, “Identifying Causal Interaction in Power System: Information-Based Approach”, accepted for publication in Conference in Decision and Control, 2017

[4] A. R. R. Matavalam and V. Ajjarapu, “ Synchrophasor based Mitigation methods for Delayed Voltage Recovery”, To be submitted for publication.

[5] R. Zhu and C. C. Liu, "Assessment of Voltage Stability Limit Using an Extended Ward-PV Network Model," To be submitted for publication.

Student Theses:

[1] A. R. R. Matavalam, *Real Time Synchrophasor Measurements Based Voltage Stability Applications*, PhD dissertation, Iowa State University, Ames IA, (In Progress).

[2] S. Sinha, *Information Transfer in Dynamical Systems*, PhD dissertation, Iowa State University, Ames IA, (In Progress).

[3] Ph.D. Dissertation, Ruoxi Zhu (In Progress).

Part I

Real Time Synchrophasor Measurements Based Short Term Voltage Stability Monitoring and Control

Venkataramana Ajjarapu
Umesh Vaidya

Amarsagar Reddy, Graduate Student
Subhrajit Sinha, Graduate Student

Iowa State University

For information about this project, contact

Venkataramana Ajjarapu
Iowa State University
Department of Electrical and Computer Engineering
Ames, Iowa, USA 50011-3060
Phone: 515-294-7687
Fax: 515-294-4263
Email: vajjarap@iastate.edu

Power Systems Engineering Research Center

The Power Systems Engineering Research Center (PSERC) is a multi-university Center conducting research on challenges facing the electric power industry and educating the next generation of power engineers. More information about PSERC can be found at the Center's website: http://www.pserc.org.

For additional information, contact:

Power Systems Engineering Research Center
Arizona State University
Engineering Research Center #527
551 E. Tyler Mall
Tempe, Arizona 85287-5706
Phone: 480-965-1643
Fax: 480-727-2052

Notice Concerning Copyright Material

Table of Contents

List of Figures

List of Tables

1. Introduction

1.1 Background

As the bulk electric system operation is moving in to an operation regime where the economics are more important than in the past, the system is operating close to the operating points with more chance of instability. Figure 1.1 provides the classification of power system stability as defined by the IEEE and CIGRE task force.

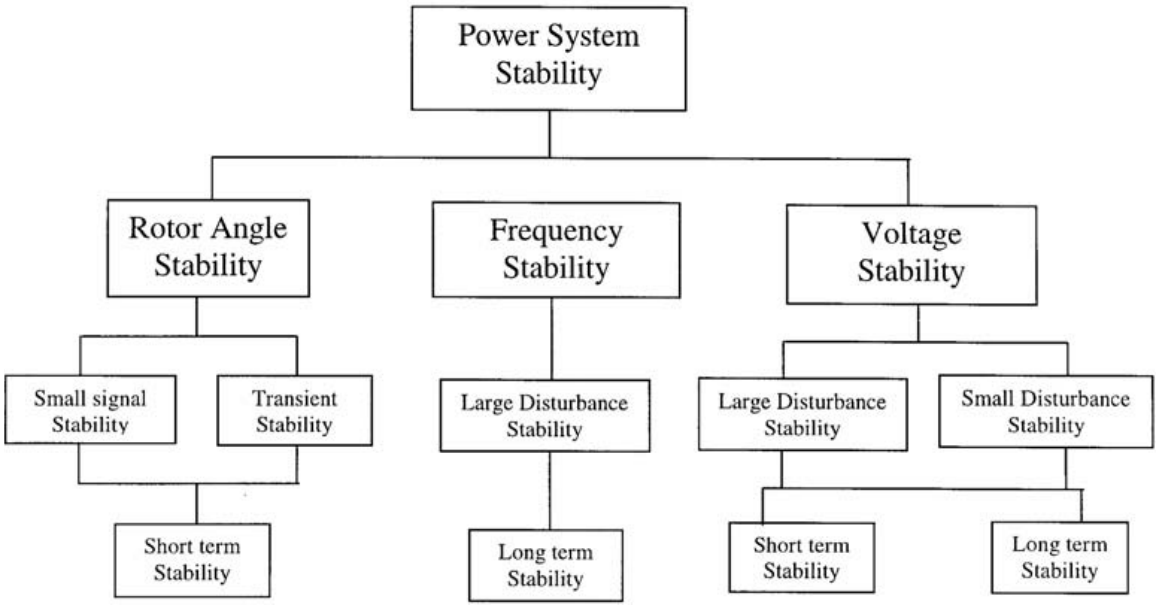

Figure 1.1 Classification of the various stability phenomenon in power systems [1]

An important type of instability is the short term large disturbance voltage instability that is caused due to increasing penetration of the induction motor and electronic loads. A specific type of short term large disturbance voltage instability is the Fault Induced Delayed Voltage Recovery (FIDVR) and is the main focus of this project.

In the FIDVR phenomena, the recovery of the voltage after a disturbance is delayed, resulting in sustained low voltages for several seconds (~15 sec). FIDVR is mainly caused in systems with a moderate amount of single phase induction motor loads (25% ~ 30%). After a large disturbance (fault, etc.), these motors, that are connected to mechanical loads with constant torque, stall and typically draw 5-6 times their nominal current and this leads to the depression of the system voltage for a significant amount of time. The low voltages in the system inherently lead to some load being tripped by protection devices close to the fault. However, even after this, the concern is that the sustained low voltages (>10 s) can lead to cascading events in the system steering towards a blackout.

Various methods have been proposed in literature that try to mitigate the FIDVR by ensuring that sufficient VAR resources are present in the system during the planning phase in the system[2, 3, 4]. However, these methods cannot take all the scenarios into account and so a methodology based on the measurements is preferred. This approach is also facilitated by the increasing penetration

of the Phasor Measurement Units (PMU) in the transmission system. The PMU can sample the voltage and current phasors at high rates and so the PMU can capture the transition of the system into FIDVR and determine an amount of local control if possible or communicate the control requirements to a control center.

1.2 Report Organization

The report is organized as follows

1. Section 2 describes the Fault Induced Delayed Voltage Recovery phenomenon in detail and illustrates the various requirements by the reliability coordinators to ensure that this phenomenon is not seen in practice. The load model that can demonstrate FIDVR in software simulations (composite load model) is discussed in detail to illustrate the various components involved in the phenomenon.
2. Section 3 describes the various methods to detect and quantify FIDVR in real time utilizing the PMU voltage measurements at the transmission substation. These methods utilize a reference waveform to quantify the deviation from expected behavior. Several methods with differing properties are introduced and results comparing and contrasting the methods are presented
3. Section 4 presents an analytical framework to analyze the FIDVR phenomenon in terms of the load admittance measures at the transmission substation PMU. The admittance of various components of the composite load model are examined in detail and an analytical expression for the time to recovery from FIDVR in terms of the measured quantities and a few basic properties of the composite load model is derived. Similarly, an expression for the control of air conditioners is also derived in terms of measurements. These expressions are validated on simulation results and are shown to have good agreement with the theoretical expressions.
4. Section 5 describes briefly the OpenPDC methods and presents results from OpenPDC.

2. Fault Induced Delayed Voltage Recovery

Short term large disturbance voltage stability is an increasing concern for industry because of the increasing penetration of induction motor and electronically controlled loads. While it is not analytically proven which power system components cause angle and voltage instability, recent work based on an information transfer metric in dynamical systems [5] seems to suggest that the induction motor loads are very much related to voltage instability. The short-term voltage instability is mainly caused by stalling of induction motor loads, and can manifest in the form of fast voltage collapse or delayed voltage recovery. One form of voltage stability is Fault Induced Delayed Voltage Recovery (FIDVR) is the phenomena in which the recovery of the voltage after a disturbance is delayed, resulting in sustained low voltages for several seconds (~15 sec).

2.1 Phenomenon in Power Systems

FIDVR is mainly caused in systems with a moderate amount of single phase induction motor loads (25% ~ 30%). After a large disturbance (fault, etc.), these motors, that are connected to mechanical loads with constant torque, stall and typically draw 5-6 times their nominal current and this leads to the depression of the system voltage for a significant amount of time. The low voltages in the system inherently lead to some load being tripped by protection devices close to the fault. However, even after this, the concern is that the sustained low voltages (>10 s) can lead to cascading events in the system steering towards a blackout. A typical delayed voltage response after a fault along with the various features is shown in Figure 2.1.

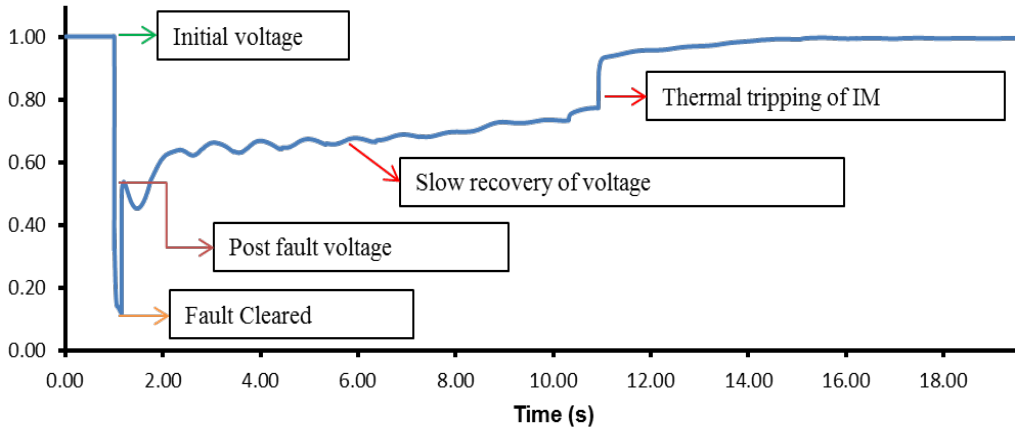

Figure 2.1 Conceptual delayed voltage recovery waveform at a bus.

Most single phase induction motor are used in residential air-conditioners and so the FIDVR phenomenon has been historically observed in systems where a large number of residential AC's are operational at the same time (e.g. summer in California or Arizona). Most of these devices do not use Under Voltage protection schemes and are only equipped with the thermal protection with an inverse time-overcurrent feature, delaying the tripping up to 20s.

Description of several FIDVR events observed in the field are listed in [6] and almost all of the occur in high residential load areas during a period of high temperature. As an example, Figure 2.2 shows an FIDVR event on a 115kV bus in Southern California on July 24, 2004. The sustained

low voltage is likely caused by stalled AC IM's and the voltage finally recovered to pre-contingency voltage around 25s after the fault. Out of the substation load of 960 MW, 400 MW of load was tripped by protection devices in residential and commercial units to recover the voltage.

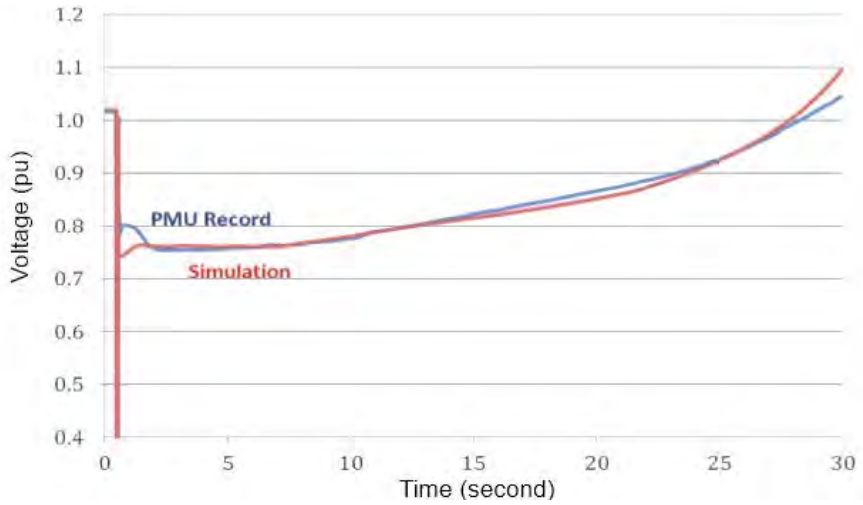

Figure 2.2 Recorded delayed voltage recovery waveform at a 115kV bus in Southern California on July 24, 2004 [6].

2.1.1 Transient Voltage Criteria

To prevent uncontrolled loss of load in the bulk electric system, NERC, WECC and other regulatory bodies have specified transient voltage criteria that utilities and system operators need to satisfy after a fault has been cleared. Figure 2.3 provides a pictorial representation of the WECC criteria and the PJM criteria.

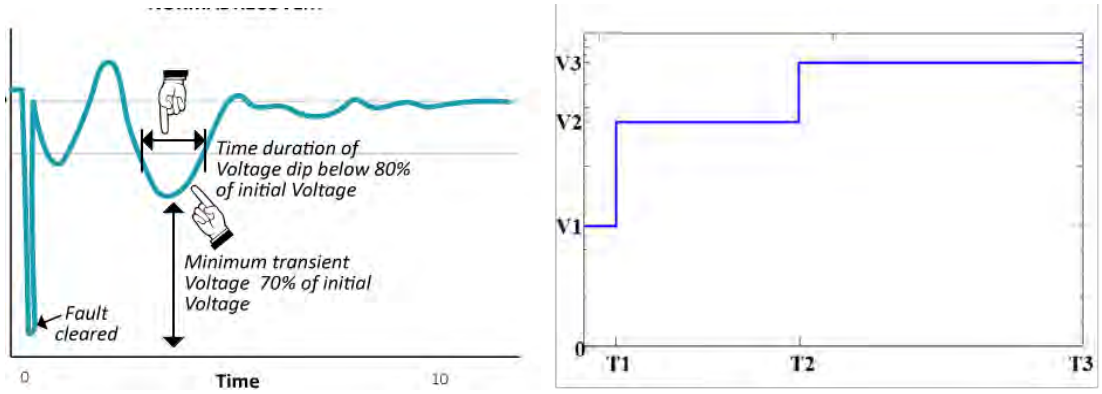

(a) (b)

Figure 2.3 (a) WECC transient voltage criteria [7] (b) Simplified voltage criteria [3].

The WECC transient criteria is defined as the following two requirements [7]

1. Following fault clearing, the voltage shall recover to 80% of the pre-contingency voltage within 20 seconds of the initiating event.

2. Following fault clearing and voltage recovery above 80%, voltage at each applicable bulk electric bus serving load shall neither dip below 70% of pre-contingency voltage for more than 30 cycles nor remain below 80% of pre-contingency voltage for more than two seconds.

A simplified voltage criteria is used generally by utilities and the trajectory of the recovering voltage must be above the curve in Figure 2.3(b) where $V_1 = 0.5, V_2 = 0.7$ & $V_3 = 0.95$ and $T_1 = 1\ s, T_2 = 5\ s$ & $T_3 = 10\ s$. The ERCOT criteria for transient voltage response requires that voltages recover to 0.90 p.u. within 10 seconds of clearing the fault [8].

The utilities ensure that the voltage recovery satisfies the guidelines specified by their regulatory authority during their planning phase and operational phase by either installing VAR devices (STATCOM, SVC, etc.) in critical regions and by ensuring that sufficient dynamic VARS are available during operation.

2.2 Modelling for Simulation – WECC Composite Load Model

In order to enable the utilities and system operators to simulate the FIDVR phenomenon to estimate the amount of VAR support required, a dynamic load model has been developed recently by WECC called as the Dynamic Composite Load Model. The composite model essentially aggregates the various kinds of dynamic loads in the sub-transmission network into several 3-ϕ IM (representing high, medium and low inertias) and an aggregate 1-ϕ IM (representing the AC loads). Furthermore, the protection schemes that trip a proportion of the loads are also implemented for each of the motor representing the Under Voltage and Under Frequency protections policies. An equivalent feeder is also present that tries to emulate the impact of voltage drop in the distribution system when a large current is drawn. The overall structure of the composite load model is shown in Figure 2.4.

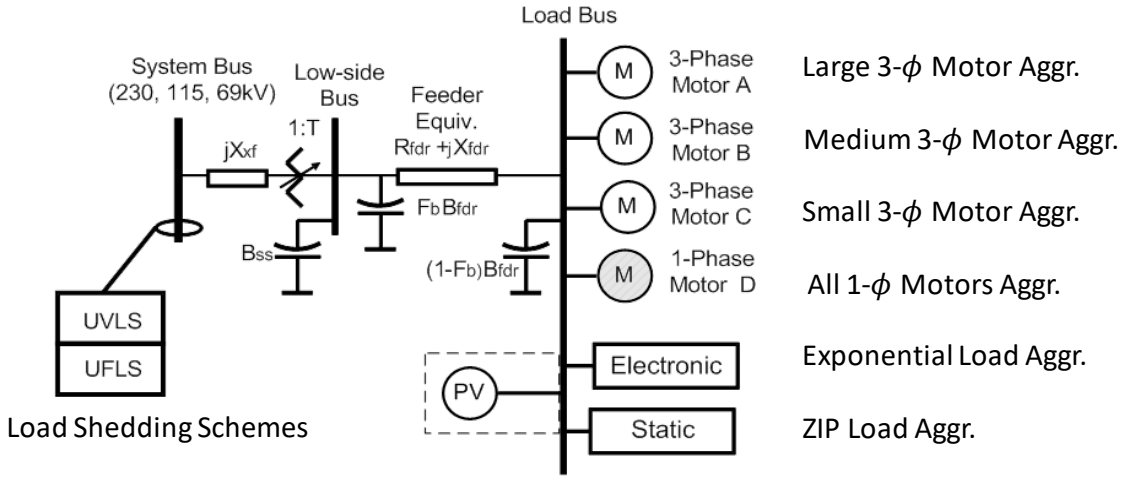

Figure 2.4 Structure of the composite load model [9]

This model has 132 parameters and has been implemented by vendors in commercial software such as PSSE, PSLF and PowerWorld. More details along with descriptions of the various parameters can be found in [9]. As part of this project, the CMLD model is studied in detail in

order to understand the behavior and simplify the model for control schemes to mitigate FIDVR or to ensure that the FIDVR phenomenon is taken care within the time as specified by the corresponding operator (ERCOT/PJM/WECC)

2.3 Examination of the WECC Composite Load Model

As the composite load model has comparatively large number of parameters and discrete controls compared to a conventional load model, understanding the model and how the various parameters impact the voltage performance is important. Moreover, the model specifications [9] only mention the behavior of most of the components and do not specify the actual equations used. Thus, engineering judgement needs to be made with regards to developing equations for analysis. For this purpose, understanding the 3-phase IM model and the 1-phase IM model along with their protection components are key. These are detailed in the following sub-section.

2.3.1 3-Phase Motor Modelling

A standard way to model, referred to here as the Krauss model, the 3-ϕ IM is by an equivalent circuit [10] where the stator and rotor impedances along with the mutual inductances are specified (R_A, X_A, X_m, R_1 & X_1). The equations are well studied and it is intuitively understandable as the current in the equivalent circuit directly enables the user to estimate the electric torque. However, as per WECC model specifications, the 3-ϕ IM is specified by the transient and sub-transient parameters (Lp, Lpp, Tp0 & Tpp0). The equations for this are not so easily analyzable as they are in the dq frame of reference and so it becomes hard to estimate the impact of load on the electric torque.
One way to get around this issue is to convert the sub-transient quantities into corresponding resistance and reactance and analyze the resulting induction motor characteristics (see Appendix 1). To ensure that the dynamics of the load models are comparable, a motor starting study is conducted on the WECC model and the corresponding Krauss model and the resulting speed and torque are plotted in Figure 2.5.

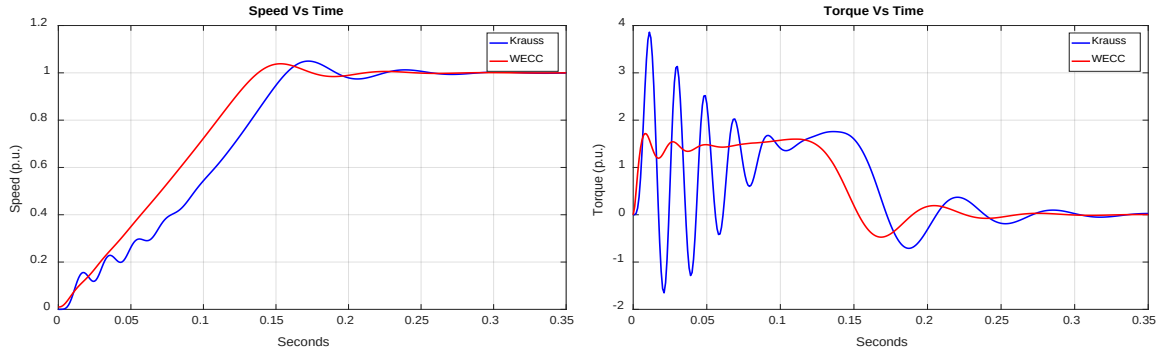

Figure 2.5 Comparison of speed and torque between the Krauss and the WECC model for motor starting.

It can be observed from Figure 2.5 that the WECC model is indeed able to capture the overall dynamics after 0.17s. However, the large oscillations in the torque in the Krauss model till 0.1s are not captured, showing the deficiency of the model. This discrepancy only occurs at low motor

speed which is not the normal operation of the motor. Even after a fault, the UV relays ensure that the motor operates at a speed close to the rated speed. Thus, this WECC 3-ϕ model can replace the Krauss model, assuming that the motor operates close to the rated speed.

Another important test is how the variation between the Krauss model and the WECC model changes with the motor inertia. Figure 2.6 plots the steady-state torque-speed curves for the Krauss and the WECC model for high inertia (H=0.5) and low inertia (H=0.1) machines. From the plots, is observed that the maximum torque of the Krauss model is around 10% higher than the WECC model and the difference between the curves is higher for smaller machines.

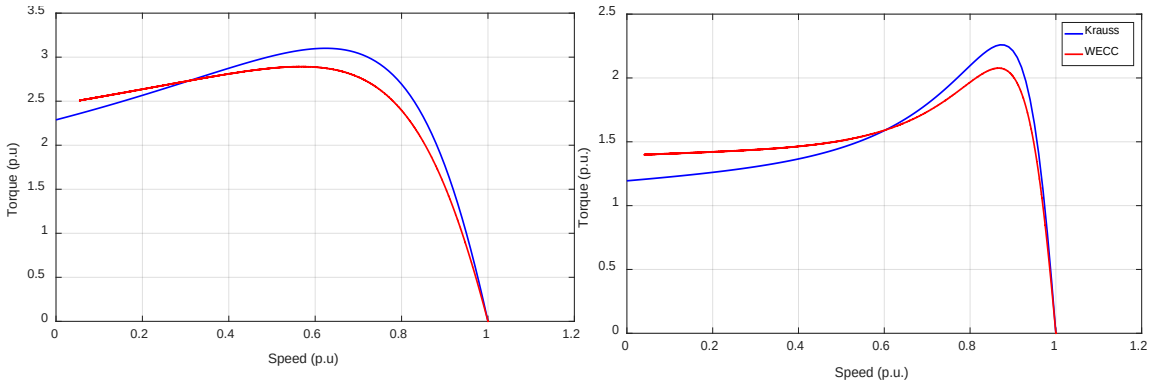

Figure 2.6 Steady-state torque-speed comparison between the Krauss and the WECC model for low inertia (left) and high inertia machines (right).

Another detail that is often overlooked is the behavior of the motor when a percentage of load is tripped by UV relays. An intuitive method to achieve this is by reducing the mechanical torque by the same percentage to reflect this loss of load. While this indeed reduces, the active power demanded, it does not reduce the reactive power demand. In reality, some of the 3-ϕ motors are disconnected and to properly reflect this physical scenario, the resistances of the equivalent circuit must be proportionally increased along with the reduction in the load torque. This ensures a reduction in both the active and reactive power demand.

2.3.2 1-Phase Motor Modelling

The 1-ϕ induction motor is the main reason why the FIDVR is observed. The 1-ϕ IM model has representations of the AC compressor motor, compressor motor thermal relay, under-voltage relays and contactors. Depending upon the input voltage, the motor operates either in 'running' or 'stalled' state. The behavior of the motor as a function of the voltage can is understood based on the power consumption of the motor and Figure 2.7 plots the active and reactive power demand as a function of the voltage for the normal operation and stalled operation.

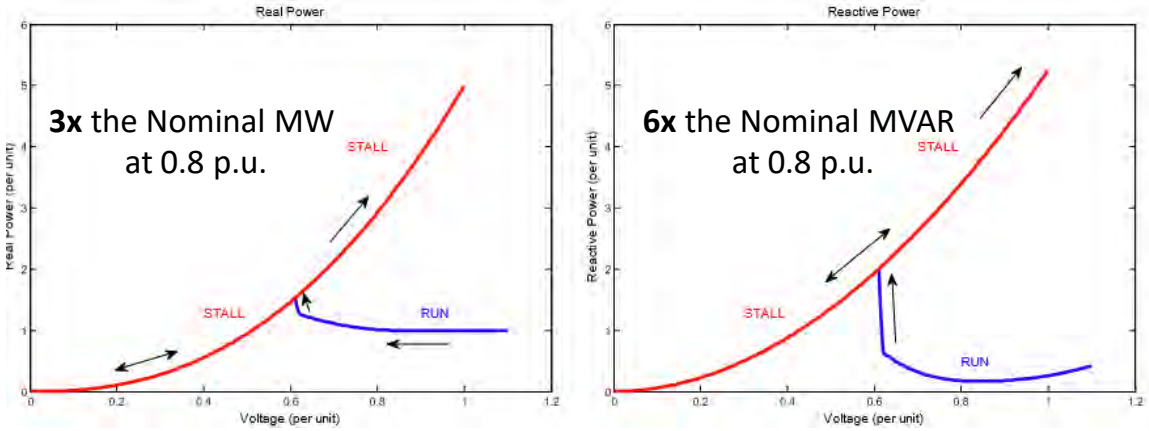

Figure 2.7 Active power (left) and Reactive power (right) versus the voltage for the normal operation and stalled operation for the $1-\phi$ induction motor [9].

From Figure 2.7, it can be seen that in the stalled state, the active power demand is 3 times the nominal amount and the reactive demand is 6 times the nominal amount compared to the normal 'running' state. This large demand is the reason why the voltage reduces at the substation causing FIDVR. This demand naturally is reduced via thermal protection that takes around 10-15 seconds. More details regarding the 1-phase motor are present in Section 4.1.

3. Local Voltage Based FIDVR Monitoring

To characterize the performance of the voltage response, WECC has provided guidelines to analyze the voltage performance following a fault. However, the criterion is a pass/fail criterion and do not give any means to quantify the deviation from a normal voltage recovery waveform.

3.1 Lyapunov Exponent

The Lyapunov exponent (LE) is an idea that is adapted from the Ergodic theory of dynamical systems. The maximum Lyapunov exponent is a measure of rate of separation of two trajectories in the system and is used to ascertain the system stability. If the maximum Lyapunov exponent is negative, the trajectories of the system converge to a stable equilibrium. However, if the maximum Lyapunov exponent is positive, the trajectories of the system diverge this suggests a possibly unstable and chaotic system. The equation to compute the Lyapunov exponent of individual buses to estimate the contribution of individual buses to the system stability/instability by using the voltage from a single bus is shown below.

$$\lambda_i(k\Delta t) = \frac{1}{Nk\Delta t}\sum_{m=1}^{N} log\frac{||V_i((k+m)\Delta t) - V_i\big((k+m-1)\Delta t\big)||}{||V_i((m)\Delta t) - V_i\big((m-1)\Delta t\big)||} \tag{3.1}$$

Where $V_i((m)\Delta t)$ is the m^{th} sample of voltage measurement at the i^{th} bus and λ_i is the Lyapunov exponent at the i^{th} bus. Further details about the LE calculation methodology are in [11]. The bus where the exponent is largest is the main contributor to the instability and control actions taken at this bus will have a large stabilizing impact on the system.

The existing formulation of the Lyapunov exponent does not detect FIDVR due to the slow recovery. In order to detect this type of waveforms, a virtual voltage reference is generated at the PMU and the difference between the actual and the reference voltage is used for the calculation of the Lyapunov exponent [12]. The virtual reference is designed such that any voltage waveform above it will be fast recovery and any voltage waveform below it will be delayed recovery. A generic voltage reference which satisfies the above property is shown in 0 with the various parameters whose values can be set depending on the system response. The parameters that decide the waveform can be determined for a given system by doing offline studies. The virtual reference can also be looked as a continuous approximation of the WECC box criterion. The expression for the reference voltage can be written as follows

$$V_{ref}(t) = \begin{cases} V_0 & t < T_0 \\ V_0 + V_1 \cdot (1 - e^{(3(T_0 - t))/T_1}) & t \geq T_0 \end{cases} \tag{3.2}$$

The reference voltage for time T_0 is flat and is at a low voltage V_0. This is to allow other protection and control schemes to correct the delayed voltage recovery. Then, the reference voltage rises as an exponential response to settle at $(V_0 + V_1)$ in a few seconds depending on T_0. The reference voltage rises very quickly in the beginning and then the voltage becomes almost flat. The input to the Lyapunov exponent calculation V_{eff} is zero, when reference voltage is below the bus voltage,

and is equal to the difference between the reference voltage and the actual voltage response, when the reference voltage is above the actual voltage.

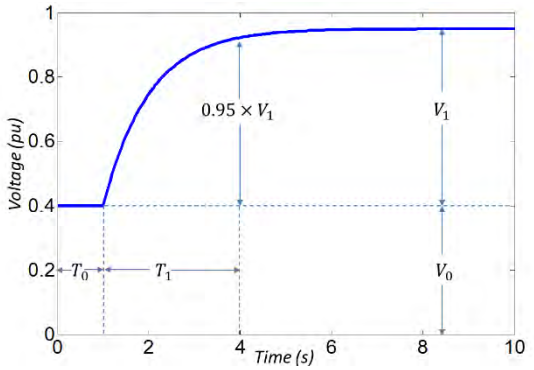

Figure 3.1 A generic voltage reference for applying the Lyapunov exponent to delayed voltage recovery.

This methodology is applied to response of the IEEE 162 system after a fault of 0.1s. 12 loads are represented by the composite load model in IEEE 162 system with a moderate percentage (30%) of induction motor loads. Fig. 7 shows the voltage response, which is a typical delayed voltage response. The parameter values of the reference voltage waveform are $V_0 = 0.4, T_0 = 1, V_1 = 0.55$ & $T_1 = 3$. The Lyapunov exponents are calculated using both the conventional method and by using the difference between the reference and actual waveform. Results for the case of IEEE 162 bus system with 30% IM load are shown in Fig. 8. It can be seen that the Lyapunov exponent without using the reference is always negative which implies that there is no problem in the system. But there is clearly a delayed voltage recovery problem in the system. This is captured by the Lyapunov exponent going positive by using the reference waveform.

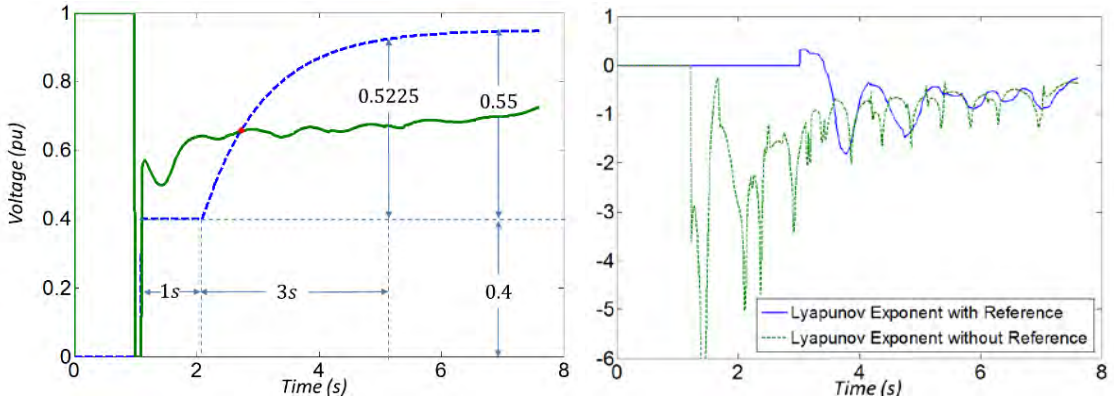

Figure 3.2 The bus voltage (blue) and the voltage reference (green) at a bus in the IEEE 162 system. The LE with and without the reference are plotted on the right.

The Lyapunov exponent without using the reference is always negative while it is positive initially by using the reference waveform. The Lyapunov exponent calculated using the reference goes negative after some time. This is due to the fact that the reference has become constant while the actual voltage is slowly recovering. Hence the difference between the two signals will decrease continuously with time – leading to a negative exponent. Thus, utilizing the voltage for determining FIDVR has to be improved.

3.2 Kullback- Leibler Divergence

To improve over the LE methodology, instead of using the difference between voltages in a window and comparing them to the initial difference, we will be using the divergence of the voltage waveforms in a time-window. This was inspired on the KL distance proposed to quantify FIDVR for planning of reactive reserves [13]. The divergence is the statistical distance between the probability distribution of the original voltage waveform and the probability distribution of the reference. A pictorial representation of the PDF's is shown in figure 3.3. This specific probability density function is for the time after the fault (1.1 sec) to the end (5 sec). We use the idea in smaller time-windows to get a real-time implementation.

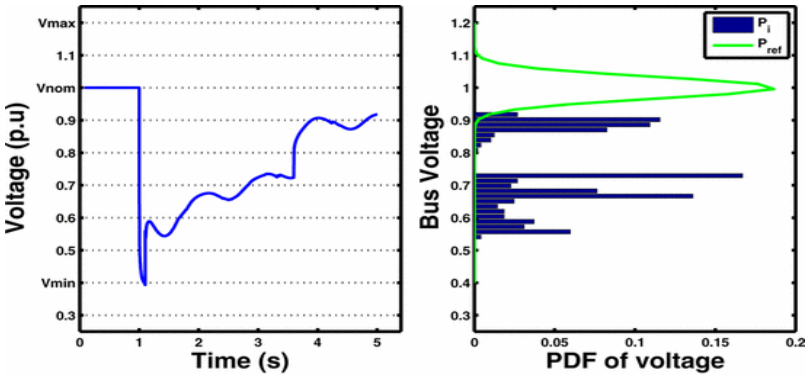

Figure 3.3 The Voltage time series and the PDF for the voltage series in along with a voltage reference PDF [13].

The distance between two probability distributions is a well-studied topic in statistics and has been defined so that a positive distance implies a violation of the FIDVR criteria. The KL divergence metric between a probability p and a reference probability p_{ref} is given by equation 3.3, where p_i & $p_{ref,i}$ is the probability in the ith bin of the measured waveform and the reference waveform respectively.

$$KL = \sum_{i=1}^{n} p_i \ln\left(\frac{p_i}{p_{ref,i}}\right) \tag{3.3}$$

The 'log' function in the KL expression is a nonlinear term and can cause the divergence to go very high. Also, the division of two probability densities can be impacted by sudden switching actions and unexpected behavior, especially when $p_i > 0$ and $p_{ref,i} \sim 0$. This scenario causes the KL index to be negative with a high value due to the division and logarithm function. Thus, the KL index gives a large weight to the bins where the p_{ref} is close to zero but the p is not close zero. Despite these drawbacks, it can be slightly modified to have a reasonable behavior[4] to analyze the FIDVR event and Figure 3.4 plots the KL index versus time for curves with increasing percentage of IM.

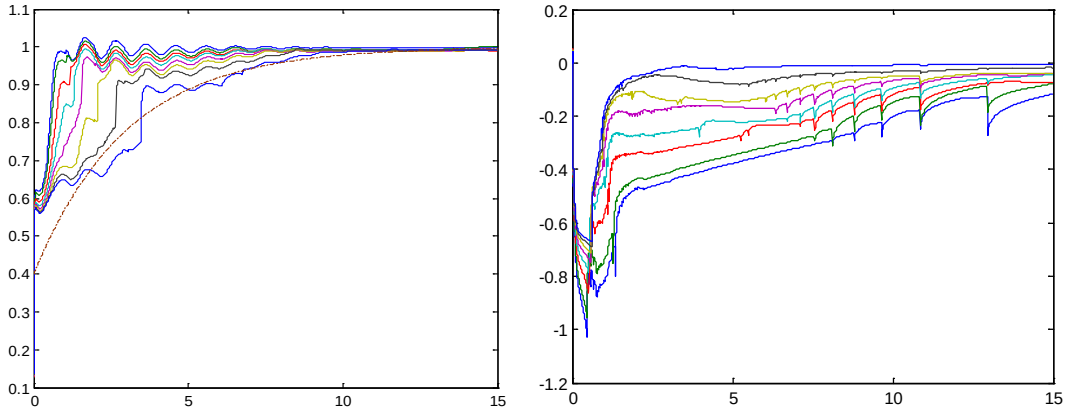

Figure 3.4 The voltage at the bus with increasing percentage of induction motor load. The Moving Divergence based Index of the delayed voltage waveforms.

It can be seen from Figure 3.4 that the KL waveforms are well separated and can be used to distinguish between the various responses while it is not so clear just by looking at the voltages. The higher the IM percent, the longer they take to recover to their pre-fault voltage. Also, the response with the least amount of IM has the most negative KL while the response with the largest amount of IM is the least Negative and goes positive for a small amount of time. The slope of the KL index can be used to estimate the time required for the FIDVR to recover, this cannot be done directly on the voltages due to the oscillations. However, there are sharp transitions in the KL index due to the logarithm function and this needs to be improved as well for predictive capabilities.

3.3 Wasserstein Metric

To overcome the challenges with the KL divergence, a smoother metric is needed and for this purpose, the Wasserstein metric is chosen. The Wasserstein metric [14], also called as the earth movers distance, can be understood as the minimal amount of work done to transform a shape of PDF_1 into PDF_2. To determine this distance, an optimization problem needs to be solved and this is not appropriate for real-time applications. However, for 1-D probability density distributions, which is the case we are interested in, the optimal solution has been analytically solved and is shown in Equation 3.4, where $F_{1,i}$ and $F_{2,i}$ are the cumulative probability functions of PDF_1 & PDF_2 in bin i respectively.

$$W - index = \sum_{i=1}^{n} \left| F_{1,i} - F_{2,i} \right| \tag{3.4}$$

Comparing the formulations of the KL divergence and the W-index in equations 3.3 & 3.4, we can make the following observations.

1. The W-index is symmetric as the absolute function is symmetric. The KL index is not symmetric and so is harder to intuitively interpret.

2. The W-index is incrementally linear, i.e. a small variation in the inputs causes a comparable change in the output value as the absolute function is incrementally linear. This is not the case for the KL divergence due to the logarithm function and the division. A small variation in the inputs can cause an unbounded change in the KL divergence. This property ensures that the W-index is a continuous function with no sudden changes.
3. The W-index is bounded. This is because the cumulative probability functions always lie between 0 and 1, the distance between them can be a maximum of 2. The KL divergence is not bounded again due to the logarithm function. The bounded nature is particularly useful in case of implementation where large results can lead to overflow problems.

To verify that the W-index can indeed be more appropriate in quantifying FIDVR from the voltage waveforms, Figures 3.5 – 3.8 plot the FIDVR response and the W-index.

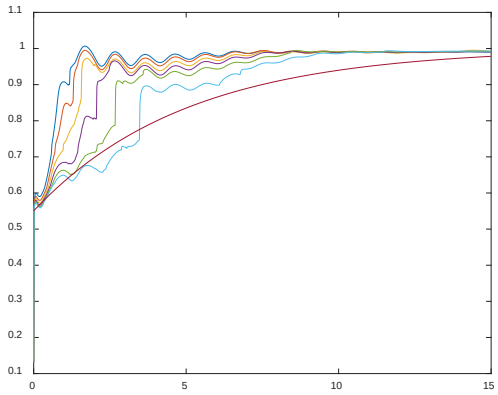

Figure 3.5 The voltage at the bus with increasing percentage of IM load.

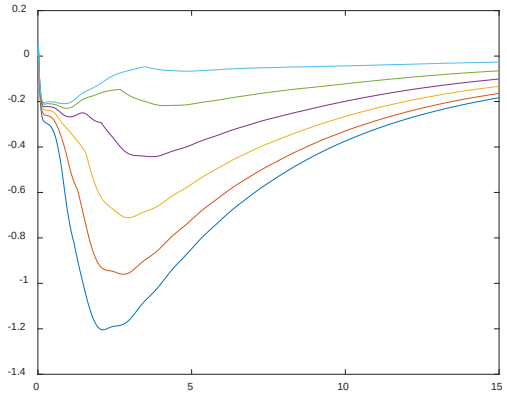

Figure 3.6 The Wasserstein metric based Index of the FIDVR waveforms

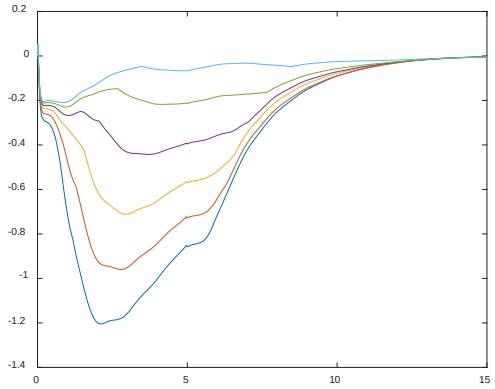

Figure 3.7 The Wasserstein metric based Index of the FIDVR waveforms using a moving time windows of 5s.

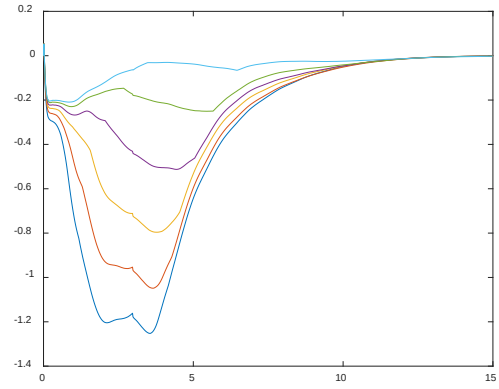

Figure 3.8 The Wasserstein metric based Index of the FIDVR waveforms using a moving time windows of 3s.

Similar to the KL plot, it can be seen from Figure 3.6 that the voltages with the least FIDVR have the most negative value of the W-index while the voltages with the FIDVR violating the reference waveform have a W-index that goes to 0 quickly and also becomes positive in the most severe cases. A key difference is that the W-index can differentiate between the waveforms almost from

the start while the KL plot only showed the waveforms moving apart after around 2 seconds. The other key difference is that the W-index waveform is much smoother than the KL plot and is due to the continuity property. This enables us to reduce the time window to improve speed of calculations and the memory requirements.

Comparing Figure 3.6 with Figures 3.7 and 3.8, the essential information of the deviation from the reference is captured with minimal changes to the waveform. This is not possible with the KL divergence as it is far more non-linear. Thus, the W-index is the best metric to use to quantify FIDVR in real time at a PMU. One of the drawbacks of this approach is that the control mechanisms cannot directly use this information as no information of the reason for the FIDVR is present in the voltage waveforms. To overcome this drawback, we analyzed the admittance of the load during FIDVR and realized that the admittance of the load under FIDVR can have important information that can be used for control. Thus, we propose to utilize the load admittance calculated at the PMU which is observing FIDVR and this is described in the next section.

4. Load Admittance Based FIDVR Control

In the previous section, the voltage at the load bus is used to estimate whether the load is experiencing FIDVR and quantify the FIDVR response. This is natural as the WECC and the NERC criteria is in terms of the voltage recovery. However, utilizing the voltage waveform has two issues

1. The voltage waveform has oscillations that are mainly caused due to the behavior of the generator controls and cause problems in the monitoring methods
2. The amount of variation in the voltage between FIDVR waveforms with different amount of IM's is comparatively small – making it hard to effectively quantify FIDVR

Thus, a quantity that that is comparatively smoother than the voltage and which varies more than the voltage is preferable. This quantity should also be closely related to the FIDVR phenomenon as an analytical relation can lead us to predictions on time to recovery. The next sections demonstrate that the load admittance that can be measured using PMU's satisfies the properties we need and can be very closely linked to the FIDVR phenomenon

4.1 Simplification of the Composite Load Model After Stalling

To understand how the admittance of the composite load can be useful, it is better to represent each load component as an admittance that varies with time. Figure 4.1 represents the structure of the various components of the CMLD model as admittances.

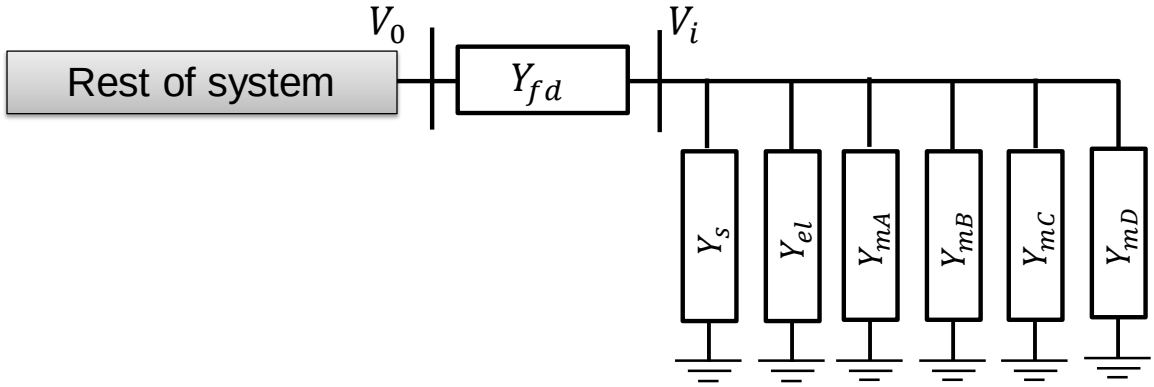

Figure 4.1 Structure of the composite load model with load components as admittances

The voltage at the internal load bus is given by Eq 4.1.

$$V_i = V_0 \cdot \frac{Y_{fd}}{Y_{fd} + Y_L}; Y_L = Y_{mA} + Y_{mB} + Y_{mC} + Y_{mD} + Y_s + Y_{el} \quad (4.1)$$

It is observed that after stalling, the variation in the admittance of static loads (Y_s) and the admittance of electronic loads (Y_{el}) do not very much as they are directly reduced as the voltage drops. The admittances of the motors do change significantly during the FIDVR phenomenon and these admittances are analyzed in the sub-sections below.

4.1.1 3-Phase Motor Admittance Analysis

The equivalent circuit of the 3-phase motor is shown in Figure 4.2 and is used to analyze how the motor admittance varies during the stalling condition. The equivalent impedance of the motor is a function of the slip (s) and is shown in equation 4.2.

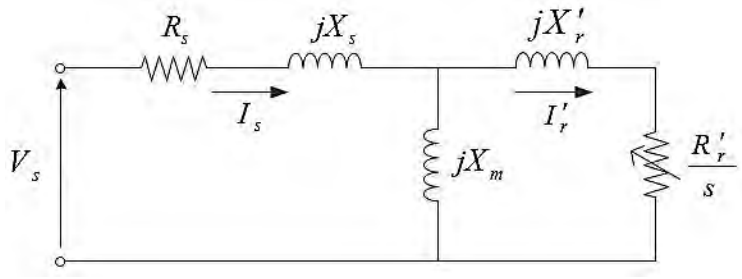

Figure 4.2 Simplified equivalent circuit of a 3-phase induction motor [10]

$$Z_m = R_s + j \cdot X_s + \frac{\left(\frac{R_r}{s} + j \cdot X_r\right)(j \cdot X_m)}{\left(\frac{R_r}{s} + j(X_r + X_m)\right)} \tag{4.2}$$

As per the WECC CMLD document [9], the 3-Phase motors are all equipped with appropriate UV relays that ensure that load is reduced as the voltage drops. This is pictorially represented in Figure 4.3 with the load torque proportional to the square of the rotation speed.

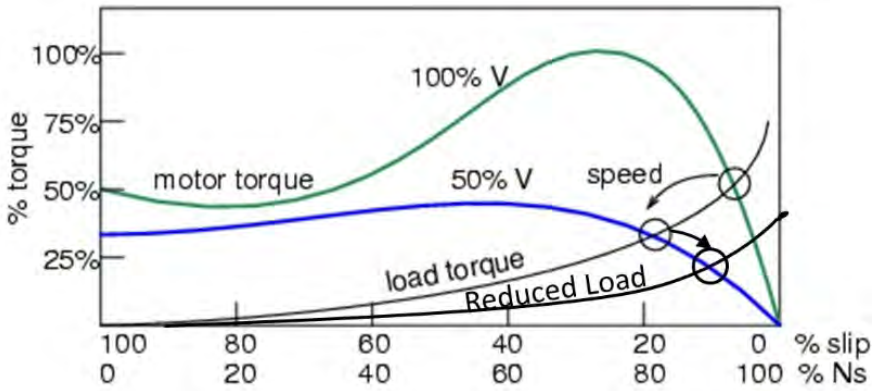

Figure 4.3 The variation in motor speed when the voltage and the load are reduced

These features ensure that the rotor speed of the 3-Phase motors is close to the rated speed and so the slip (s) varies in a tight range (around 0.04 at nominal operation to an extreme of 0.1 at the low voltage condition). Utilizing this range of slip, the admittance of the load motors is now analyzed below in equations 4.3 to 4.11.

$$Y_m(s) = \frac{R_r/s + j(X_r + X_m)}{(R_r/s + j \cdot X_r)(j \cdot X_m) + \big(R_r/s + j(X_m + X_r)\big)(R_s + j \cdot X_s)} \tag{4.3}$$

Using the fact that for practical motors, $X_m \gg X_r$ & $X_s \gg R_s$, it is simplified to

$$Y_m(s) \approx \frac{R_r + j \cdot X_m \cdot s}{(R_r + j \cdot X_r \cdot s)(j \cdot X_m) + (R_r + j \cdot X_m \cdot s)(j \cdot X_s)} \tag{4.4}$$

$$Y_m(s) \approx \frac{R_r + j \cdot X_m \cdot s}{\left(R_r \cdot (j \cdot X_m + j \cdot X_s)\right) + (j \cdot X_m \cdot s)(j \cdot X_s + j \cdot X_r)} \tag{4.5}$$

Using the fact that for practical motors, $X_m \gg X_s$, it is simplified to

$$Y_m(s) \approx \left(\frac{1}{j \cdot X_m}\right)\left(1 + \frac{j(X_m - X_s - X_r)}{R_r/s + (j \cdot X_s + j \cdot X_r)}\right) \tag{4.6}$$

Suppose only a fraction ($f_{uv} < 1$) of the motors are operating during FIDVR (i.e. $(1 - f_{uv})$ fraction is tripped), then the admittance is also scaled by f_{uv}. Thus, the expression for the admittance during FIDVR is given by

$$Y_m(s) = \left(\frac{f_{uv}}{j \cdot X_m}\right)\left(1 + \frac{j(X_m - X_s - X_r)}{R_r/s + (j \cdot X_s + j \cdot X_r)}\right) \tag{4.7}$$

Suppose the slip of the motor is s_0 at nominal operating point and it is s_1 during the FIDVR, then the ratio between the two admittances is given by Eq 4.8.

$$\frac{Y_m(s_1)}{Y_m(s_0)} = f_{uv} \cdot \frac{R_r + j \cdot X_m \cdot s_1}{R_r + (j \cdot X_s + j \cdot X_r) \cdot s_1} \cdot \frac{R_r + (j \cdot X_s + j \cdot X_r) \cdot s_0}{R_r + j \cdot X_m \cdot s_0} \tag{4.8}$$

$$\frac{Y_m(s_1)}{Y_m(s_0)} = f_{uv} \cdot \frac{R_r^2 - X_m(X_s + X_r) \cdot s_1 \cdot s_0 + j \cdot R_r \cdot (X_m \cdot s_1 + (X_s + X_r) \cdot s_0)}{R_r^2 - X_m(X_s + X_r) \cdot s_1 \cdot s_0 + j \cdot R_r \cdot (X_m \cdot s_0 + (X_s + X_r) \cdot s_1)} \tag{4.9}$$

Let $R_r = \eta_1 \cdot s_0$ & $s_1 = \eta_2 \cdot s_0$. Utilizing the fact that $X_m \gg (X_s + X_r)$, Eq 4.9 can be simplified as

$$\frac{Y_m(s_1)}{Y_m(s_0)} \approx f_{uv}\left(1 + \frac{j(\eta_2 - \eta_1) \cdot (X_m)}{1 - X_m(X_s + X_r) \cdot \eta_2 \cdot \eta_1 + j(X_m \cdot \eta_1 + (X_s + X_r) \cdot \eta_2)}\right) \tag{4.10}$$

As it was discussed from Figure 4.3 , $1.5 < \eta_2 < 3$. Also, in practical motors, $1/3 < \eta_1 < 2$ & $f_{uv} \approx 0.6$. For the default motor parameters in WECC, the ratio satisfies equation 4.11.

$$1 < \left|\frac{Y_m(s_1)}{Y_m(s_0)}\right| < 3.5 \tag{4.11}$$

Thus, the admittance of the 3-Phase motors during the FIDVR phenomenon can be at most around 3.5 times the nominal admittance.

4.1.2 1-Phase Motor Admittance Analysis

The stalling of the 1-phase motors is the main cause of the FIDVR phenomenon. Due to this, the 1-phase motors that remain connected during the FIDVR phenomenon are represented by a constant impedance. This impedance is much smaller than the nominal impedance of the 1-phase motor in normal operation. Since we are inspecting at all the elements in the CMLD model as admittances, we can conclude that the FIDVR admittance of the 1-phase motor is several times the nominal admittance. From Figure 2.7, it can be deduced that for the WECC default parameters, the FIDVR conductance is 5 times the nominal conductance and the FIDVR susceptance is 10 times the nominal susceptance. This large increase in the conductance and susceptance can be used to characterize the 1-phase motor.

Another important characteristic of the 1-phase motor are the various control schemes. Just as the 3-phase motor has UV protection devices to reduce the load when the voltage drops, the 1-phase motor also has UV protection, but the percentage of load that has this protection is very small (~5%-10% of the 1-phase motors). On top of the UV relays, there are also contactors that reduce the load below 0.65 p.u. voltage. However, the main protection device is the thermal protection logic that is present in *all* the 1-phase motors. The thermal tripping logic is shown in Figure 4.4, where f_{TH} is the fraction of 1-phase motors connected, θ is the internal motor temperature, T_{th} is the thermal delay time constant in the protection logic with the thermal power dissipated in the motor given by $V^2 \cdot G_{stall}$.

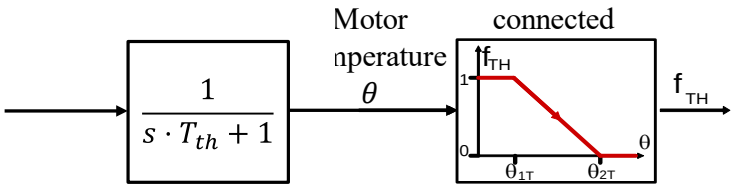

Figure 4.4 The thermal protection logic implemented in the composite load model

The admittance of the 1-phase motor during FIDVR is given by equation 4.12.

$$Y_{mD} = f_{UV} \cdot f_{TH}(G_{stall} + j \cdot B_{stall}) \tag{4.12}$$

As the admittance of the 1-phase motor is dependent on f_{th}, it is important to analyse the behavior of the thermal trip logic. After a fault that initiates the FIDVR event, the thermal loss in the motor increases suddenly and the thermal trip logic is initiated. The thermal delay block simulates the time delay of the rise in the temperature of the motor coil. This estimated motor coil temperature

is what determines the fraction of 1-phase motor connected to the grid. The fraction of 1-phase motors connected is determined by the θ_1 & θ_2 parameters. A temperature that is lesser than θ_1 does not change the admittance and keeps the fraction connected (f_{TH}) as 1. When the motor temperature is between θ_1 and θ_2, the f_{TH} is reduced linearly from 1 to 0. And when the temperature is reaches θ_2, there are no more 1-phase motors connected to the grid. The parameters θ_1 and θ_2 are key in determining the time that the FIDVR event persists and analytically deriving the time taken for the temperature to reach θ_2 is a way to estimate this time.

4.1.2.1 Derivation of time for thermal tripping to initiate (t_1)

Since the behavior of the system is different before and after θ_1, we first determine the time taken for the motor temperature to rise to θ_1. Since θ is the output of a time delayed block with a delay T_{TH} and the thermal power rises suddenly at stalling, we can use the step input formula to determine the variation of θ as a function of time. Let the thermal power be denoted by P_{th} and let t_1 be the time taken to reach a temperature of θ_1. Equations 4.13 to 4.16 follow from the definitions and using the first term in the power series expansion $\ln(1-x) \approx -x$.

$$P_{th} = V_i^2 \cdot G_{stall} = V_0^2 \cdot \frac{\left(Y_{fd}\right)^2}{\left(Y_{fd} + Y_L\right)^2} \cdot G_{stall} \tag{4.13}$$

$$\theta_1 = P_{th}\left(1 - e^{(-t_1/T_{th})}\right) \tag{4.14}$$

$$t_1 = -T_{th} \cdot \ln(1 - \theta_1/P_{th}) \approx T_{th} \cdot \theta_1/P_{th} \tag{4.15}$$

$$t_1 \approx \frac{T_{th} \cdot \theta_1}{V_0^2 \cdot G_{stall}} \cdot \left(1 + \frac{Y_L}{Y_{fd}}\right)^2 \tag{4.16}$$

Using the fact that the Y_L is mostly made up of the admittance of $Y_{mD} = B_{stall} + j \cdot G_{stall}$, with $B_{stall} = G_{stall}$, we can simplify the expression to

$$t_1 \approx \frac{T_{th} \cdot \theta_1}{V_0^2} \cdot \left(\frac{1}{G_{stall}} + \frac{2}{Y_{fd}} + \frac{2 \cdot B_{stall}}{Y_{fd}^2}\right) \approx \frac{2 \cdot T_{th} \cdot \theta_1 \cdot B_0}{V_0^2 \cdot Y_{fd}^2} \tag{4.17}$$

Here B_0 is the susceptance seen by the high voltage transmission bus before the feeder. Hence, the time taken for the thermal tripping to begin is proportional to the initial susceptance B_0, Thermal time constant T_{TH}, Temperature setting θ_1 and is inversely proportional to the initial post-contingency high voltage transmission voltage V_0 square and the feeder impedance squared.

4.1.2.2 Derivation of time for thermal tripping to terminate (t_2)

Now that the behavior of the system is understood before θ_1, we can determine the time taken for the motor temperature to rise to θ_2 from θ_1 by understanding the linear reduction in the thermal trip fraction f_{TH}. Equations 4.18 to 4.22 follow from the definitions and by utilizing the first order differential equation relation between the thermal power (P_{TH}) and the motor temperature (θ).

$$\dot{\theta} = \frac{1}{T_{Th}}(P_{TH} - \theta) \tag{4.18}$$

$$f_{TH} = 1 - \left(\frac{\theta - \theta_1}{\theta_2 - \theta_1}\right) \Rightarrow \theta = (\theta_2 - \theta_1) \cdot (1 - f_{TH}) + \theta_1 \tag{4.19}$$

$$P_{TH} = V_i^2 \cdot G_{stall} = V_0^2 \cdot \frac{\left|Y_{fd}\right|^2}{\left|Y_{fd} + f_{TH} \cdot Y_L\right|^2} \cdot G_{stall} \tag{4.20}$$

Utilizing the above expressions, a differential equation in terms of the fraction

$$\dot{f_{TH}} = -\frac{\dot{\theta}}{(\theta_2 - \theta_1)} \tag{4.21}$$

$$\dot{f_{TH}} = \frac{1}{T_{TH}(\theta_2 - \theta_1)}\left(\theta_2 - (\theta_2 - \theta_1) \cdot f_{TH} - \frac{V_0^2 \cdot G_{stall}}{\left|1 + f_{TH} \cdot (Y_L/Y_{fd})\right|^2}\right) \tag{4.22}$$

The power series expansion for $\frac{1}{(1+x)^2}$ is $\Sigma(n+1)x^n$. This is valid as $f_{TH} \leq 1$ and in practice the ratio $Y_L/Y_{fd} < 0.5$. Let $\gamma = 1/T_{TH}(\theta_2 - \theta_1)$. Considering only the first 2 terms in the power series expansion, the equation can be simplified as follows.

$$\dot{f_{TH}} = \gamma\left(\theta_2 - (\theta_2 - \theta_1) \cdot f_{TH} - V_0^2 \cdot G_{stall} \cdot \left(1 - 2 \cdot \left(\frac{f_{TH} \cdot Y_L}{Y_{fd}}\right)\right)\right) \tag{4.23}$$

$$\dot{f_{TH}} = \gamma\left((\theta_2 - V_0^2 \cdot G_{stall}) - \left((\theta_2 - \theta_1) - \frac{2 \cdot V_0^2 \cdot G_{stall} \cdot Y_L}{Y_{fd}}\right) \cdot f_{TH}\right) \tag{4.24}$$

Using the fact that $V_0^2 \cdot G_{stall} > \theta_2$, $(\theta_2 - \theta_1) > 0$ and $\frac{Y_L}{Y_{fd}} < 0.5$, we get

$$\dot{f_{TH}} = \alpha + \beta \cdot f_{TH} \tag{4.25}$$

$$\alpha = \frac{(\theta_2 - V_0^2 \cdot G_{stall})}{T_{TH}(\theta_2 - \theta_1)} < 0 \tag{4.26}$$

$$\beta = -\left((\theta_2 - \theta_1) - \frac{2 \cdot V_0^2 \cdot G_{stall} \cdot Y_L}{Y_{fd}}\right) < 0 \tag{4.27}$$

Since both the coefficients are negative, the fraction f_{TH} monotonically decreases. The initial value of f_{TH} is 1 and as f_{TH} is decreasing, the fraction reaches 0 at which time the equations do not valid anymore. Since this is a small range, an approximation that the slope of f_{Th} is constant is reasonable. To determine this slope, the average value of $\dot{f_{TH}}$ at $f_{TH} = 1$ and $f_{Th} = 0$ can be used. In the derivation above, we have assumed that V_0 is constant. However, the voltage at the transmission bus rises to around 1.0 p.u. when the fraction $f_{Th} = 0$. Hence the average slope is given by equation 4.28.

$$\dot{f}_{TH-mean} = \frac{1}{2 \cdot T_{TH}(\theta_2 - \theta_1)}\left(\theta_1 - V_0^2 \cdot G_{stall}\left(1 - 2 \cdot \frac{Y_L}{Y_{fd}}\right) + \theta_2 - G_{stall}\right) \tag{4.28}$$

$$\dot{f}_{TH-mean} = \frac{1}{2 \cdot T_{TH}(\theta_2 - \theta_1)}\left(\theta_1 + \theta_2 - G_{stall}\left(1 + V_0^2 - \frac{2 \cdot V_0^2 \cdot Y_L}{Y_{fd}}\right)\right) \tag{4.29}$$

Utilizing the identity $\Sigma(n+1)x^n = \frac{1}{(1+x)^2}$, the mean slope can be written as

$$\dot{f}_{TH-mean} = \frac{1}{2 \cdot T_{TH}(\theta_2 - \theta_1)}\left(\theta_1 + \theta_2 - G_{stall}\left(1 + \frac{V_0^2}{\left|1 + (Y_L/Y_{fd})\right|^2}\right)\right) \tag{4.30}$$

In practice, the $G_{stall} \gg (\theta_1 + \theta_2)$ and so we can approximate the slope as

$$\dot{f}_{TH-mean} = \frac{-G_{stall}}{2 \cdot T_{TH}(\theta_2 - \theta_1)}\left(1 + \frac{V_0^2}{\left|1 + (Y_L/Y_{fd})\right|^2}\right) \tag{4.31}$$

Since G_{stall} and B_{stall} are same and it is more valid to approximate B_{stall} with B_0, we arrive at the final expression for the mean slope of the thermal trip fraction.

$$\dot{f}_{TH-mean} = \frac{-B_0}{2 \cdot T_{TH}(\theta_2 - \theta_1)}\left(1 + \frac{V_0^2}{\left|1 + (Y_L/Y_{fd})\right|^2}\right) \tag{4.32}$$

Thus, from expression above, the slope of the susceptance during the FIDVR event is inversely proportional to the Thermal delay (T_{TH}), the difference $(\theta_2 - \theta_1)$ and directly proportional to the initial observed susceptance during the FIDVR event (B_0).

In the above derivations for $t_1 \& t_2$, several approximations and simplifying assumptions were made. It is important to validate that $t_1 \& t_2$ do indeed vary as simple functions of the measured susceptance B_0. The validation of the variation of $t_1 \& t_2$ as a function of $T_{TH}, \theta_1, \theta_2$ & B_0 is done on PSSE simulations in the next sub-section.

4.2 Validation Results from PSSE Simulations

The IEEE 162 bus system is used to test the claims from the previous section regarding the variation of the time to recover from FIDVR utilizing the effective susceptance of the composite load. A fault is applied at 1 sec lasting 3 cycles and is cleared by opening a line. The information of the location of the composite load model and other system details are in [3]. The simulation outputs the voltage and the active and reactive powers observed at the transmission substation and the following equations are used to determine the susceptance and the conductance at every time step. These calculations are straightforward and can be implemented easily at the PMU in real-time when the FIDVR occurs.

$$Y_0 = G_0 + jB_0 \tag{4.33}$$

$$P_{trans} = V_0^2 \cdot G_0 \Rightarrow G_0 = P_{trans}/V_0^2 \tag{4.34}$$

$$Q_{trans} = V_0^2 \cdot B_0 \Rightarrow B_0 = Q_{trans}/V_0^2 \tag{4.35}$$

The stall impedance is kept constant at 0.1+j0.1for all the results in this section. The load fractions of the various components and the parameters of the thermal trip logic are varied to see how they match up to the expectations. Figures 4.5 and 4.6 plot the voltage and susceptance for a normal voltage recovery and a delayed voltage recovery after a fault.

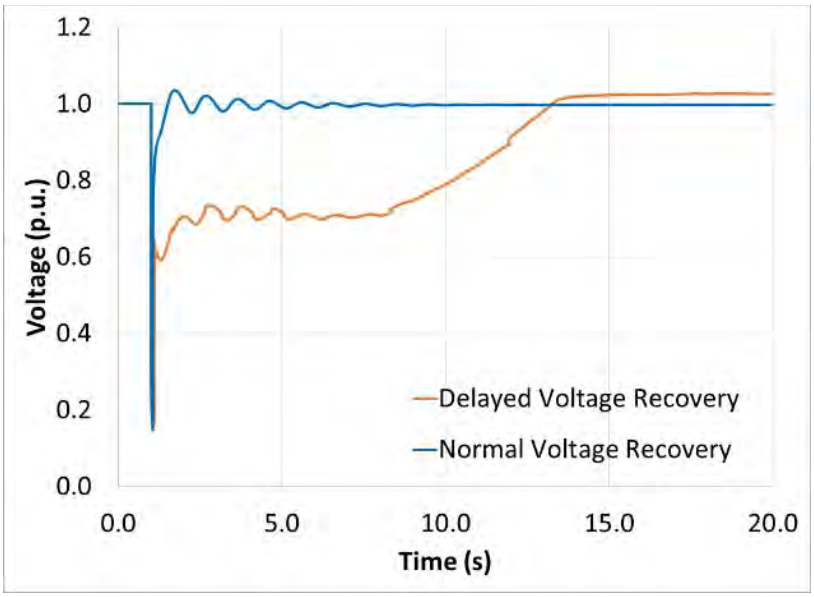

Figure 4.5 Voltage plots of the normal and delayed voltage recovery after fault clearing

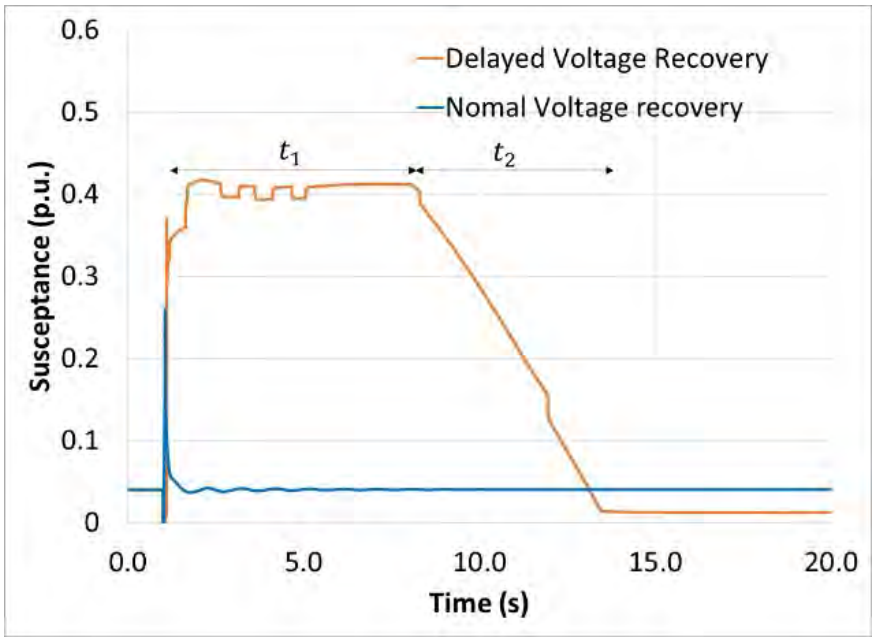

Figure 4.6 Susceptance plot of the normal and delayed voltage recovery scenarios

It can be observed from the plots that the oscillations present in the voltage wave form are not present in the susceptance plot. In case of a normal recovery, the susceptance very quickly returns to the pre-contingency susceptance while in case of the delayed recovery, there is large delay for the susceptance to return to the pre-contingency levels and it actually settles to a lower value as some of the load is tripped by protection logic during the FIDVR event. The voltage has oscillations after the clearing of the fault while the oscillations in the susceptance are comparatively smaller. The susceptance remains almost flat for t_1 seconds and then reduces linearly to the pre-contingency level in t_2 seconds. This behavior is what was modelled in the

previous section and the results seem to validate the analysis. There are small deviations from what is ideally expected in the susceptance waveform

1. Small step variations in the susceptance around 4 seconds
2. Small drop in the susceptance around 12 seconds

Both variations are due to the switching of the UV trip circuit of the 3-phase motors and the electronic loads. Notice that their impact on the overall behavior of the susceptance is negligible. To verify the claims made in section 4.1, several simulation runs in PSSE are conducted with varying the fractions of motors A, B, C, D, Static Load and Electronic load. In the interest of space, results of the following cases are discussed further.

1. Case-0: $f_{mA} = 0.1, f_{mB} = 0.1, f_{mD} = 0.0$
2. Case-1: $f_{mA} = 0.1, f_{mB} = 0.1, f_{mD} = 0.2$
3. Case-2: $f_{mA} = 0.1, f_{mB} = 0.1, f_{mD} = 0.35$
4. Case-3: $f_{mA} = 0.1, f_{mB} = 0.2, f_{mD} = 0.35$
5. Case-4: $f_{mA} = 0.2, f_{mB} = 0.2, f_{mD} = 0.35$

The voltage and the susceptance for these cases after a fault is plotted in Figures 4.6 & 4.7.

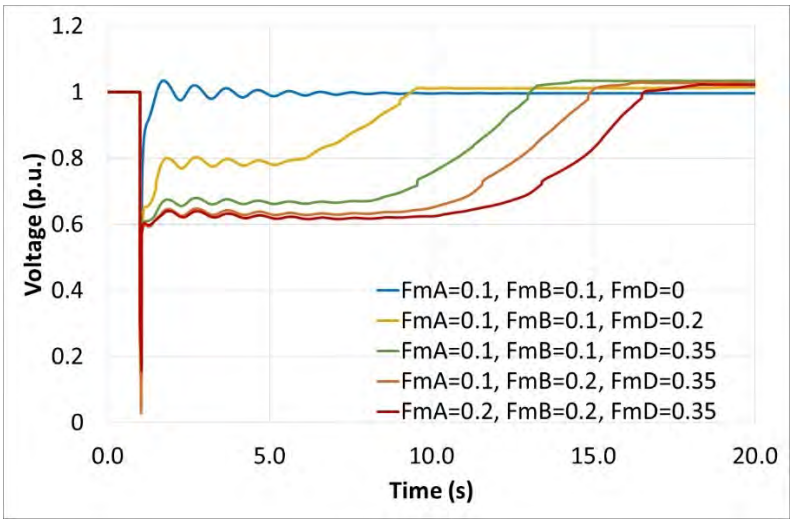

Figure 4.7 Voltage plot for different proportions of motors A, B &D

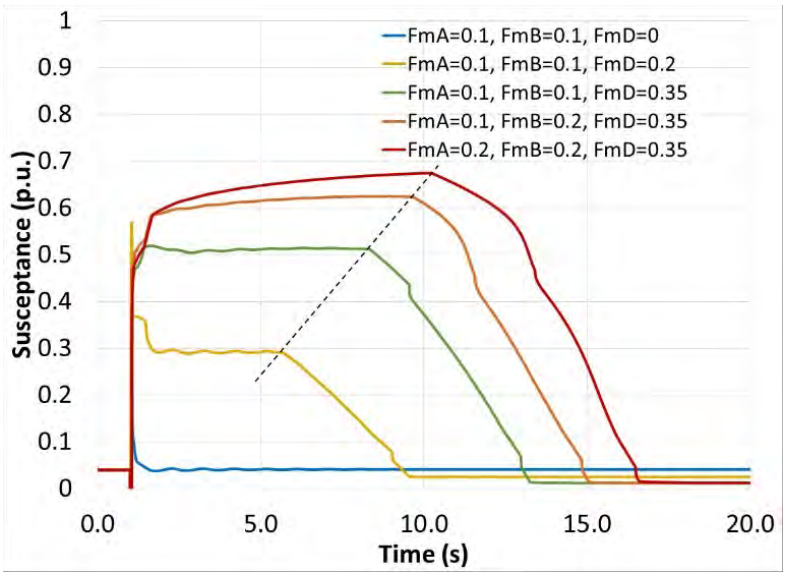

Figure 4.8 Susceptance plot for different proportions of motors A, B &D

The following important observations can be made from the voltage and susceptance plots for the various scenarios

1. The voltage recovery in Case-0 is very fast while the voltage recovery in all the other cases is delayed.
2. The susceptance in FIDVR cases suddenly rises after the fault ($>$ 5 times) and this sudden rise be used as an indicator of FIDVR.
3. The susceptance plot can be divided into region where the susceptance is nearly constant and another where the susceptance decreases to pre-contingency level in a nearly linear manner.
4. The time before the thermal protection begins tripping devices almost varies linearly to the susceptance. The straight line in the figure passes through the point where the thermal tripping begins.
5. The slope of the linear region is different for the different scenarios and seems to be related to the post-contingency susceptance. i.e. higher the susceptance, the steeper the slope. This provides evidence for equation 4.32.
6. As the fraction of motor A and motor B increase, the susceptance curve during the stalled state changes from being a flat line to a sloped curve. This is due to the increasing slip of the 3-phase motors during the low voltage state and this causes deviations from the expected behavior as derived in section 4.1.
7. The increased fraction of the 3-phase motors also causes the curvature when the thermal tripping starts and leads to more deviation from the behavior modelled in section 4.1.

The susceptance diagram provides all this information which enables us to deduce that the recovery time for case-4 will be larger than case-3. It is not possible to realize this from just the voltage plots as the voltage waveforms of case-3 and case-4 are very similar for almost 7 seconds after the fault is cleared. This provides more reason to use the susceptance for analyzing the FIDVR

phenomenon in real-time. Furthermore, the linear behavior of the susceptance with time makes it a much easier quantity to project forward in time rather than the voltage as used in [15].

4.2.1 Validation of linear relation of total time to recovery to B_0

To determine precisely how the times for voltage recovery depend on the susceptance, a linear fitting problem is solved with the data shown in Table 4.1. Since case-4 seems to be not exactly following the expected linear curve, we do not use it for the curve fitting.

Table 4.1 Variation of t_1 and t_2 with the various load parameters

Load parameters	Susceptance (B_0)	t_1	t_2
$f_{mA} = 0.1, f_{mB} = 0.1, f_{mD} = 0.2$	0.3 p.u.	4.76 sec	4.79 sec
$f_{mA} = 0.1, f_{mB} = 0.1, f_{mD} = 0.35$	0.5 p.u.	7.42 sec	5.87 sec
$f_{mA} = 0.1, f_{mB} = 0.2, f_{mD} = 0.35$	0.6 p.u.	8.73 sec	6.27 sec
$f_{mA} = 0.2, f_{mB} = 0.2, f_{mD} = 0.35$	0.65 p.u.	9.28 sec	7.22 sec

The equations for t_1 and t_2 along with their R^2 value are shown in equations 4.33 and 4.34.

$$t_1 = 13.2 \cdot B_0 + 0.8; R^2 = 1 \tag{4.33}$$

$$t_2 = 5 \cdot B_0 + 3.3; R^2 = 1 \tag{4.34}$$

The R^2 value of 1 suggests that the fit is very good. If we set a constraint that the intercept is 0, i.e. the linear fit should not have a constant term, then we get the following equations for t_1 and t_2 along with their R^2 value

$$t_1 = 14.8 \cdot B_0;\ R^2 = 0.98 \tag{4.35}$$

$$t_2 = 11.6 \cdot B_0;\ R^2 = 0.88 \tag{4.36}$$

The R^2 values have now reduced to 0.98 and 0.88 for t_1 and t_2 respectively. This is still a reasonable approximation and Table 4.2 lists the error in the estimation of t_1&t_2 using equations 4.35 & 4.36.

Table 4.2 Error in prediction of t_1 & t_2 with change in load composition

Load parameters	Error in t_1	Error in t_2
$f_{mA} = 0.1, f_{mB} = 0.1, f_{mD} = 0.2$	-0.3 sec	-1.3 sec
$f_{mA} = 0.1, f_{mB} = 0.1, f_{mD} = 0.35$	-0.01 sec	0.06 sec
$f_{mA} = 0.1, f_{mB} = 0.2, f_{mD} = 0.35$	0.16 sec	0.7 sec
$f_{mA} = 0.2, f_{mB} = 0.2, f_{mD} = 0.35$	0.35 sec	0.33 sec

The errors are comparatively small considering that this time is the time taken to completely recover to pre-contingency conditions. Usually, the operator/utility are interested in ensuring that they reach to 0.9 p.u. voltage within a certain time (e.g. 10s). The time t_2 listed in Table 4.1 is the time taken to recover to 1 p.u. Thus, ensuring that $t_1 + t_2 < 10$ ensures that the voltage recovers to 0.9 p.u. in 10s. Thus, the total time for recovery is given by

$$T_{total} = 26.4 \cdot B_0 \tag{4.37}$$

In practice, the coefficients of the linear relation among B_0 and t_1& t_2 is determined by offline studies depending on the utilities models of the composite model parameters specific to their distribution feeders. Once these offline simulations are analyzed, the derived coefficients can be used for a wide range of operating conditions. Recent research in composite load parameter estimation also can provide more hints on how to update these parameters based on changes in the distribution system such as feeder reconfiguration, etc.

4.2.2 Validation of the linear relation of total time to recovery to θ_2

To verify the dependence of t_2 on the θ_2, simulations are performed keeping everything constant and only varying θ_2. Figure 4.9 plots the variation of the susceptance for case-3 above as the θ_2 changes, keeping θ_1 constant and Table 4.3 lists the load parameters and the corresponding t_2. The following observations can be made from Figure 4.9 regarding the time to recovery.

1. The susceptance is same for the 3 values of θ_2 till the start of the tripping of the 1-Phase IM. This is because θ_1 is kept constant for the 3 scenarios.
2. The slope decreases as the θ_2 increases and this increases t_2. This is consistent with the equation 4.32.

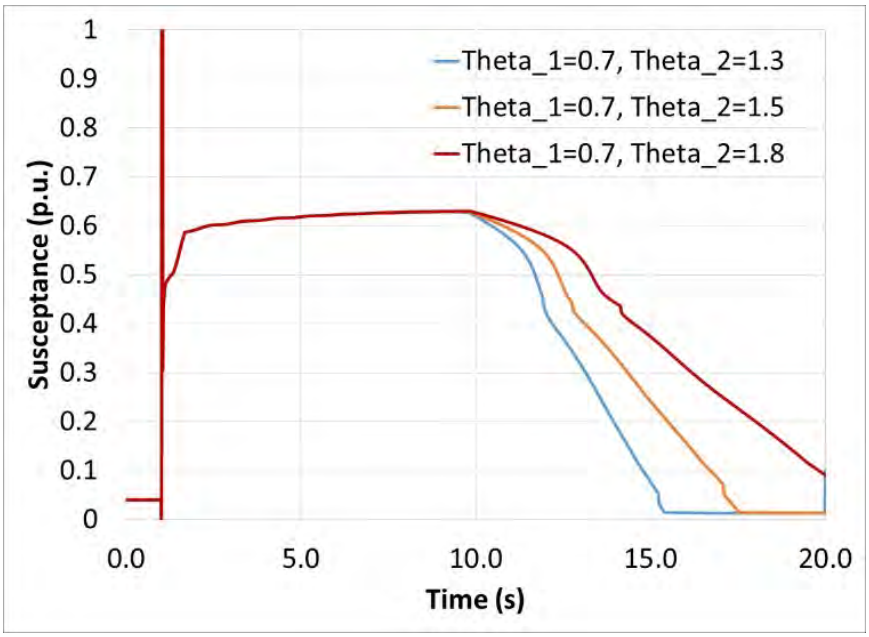

Figure 4.9 Susceptance plot for various values of θ_2

Table 4.3 Variation of t_2 with various values of θ_2

Load parameters	t_2
$\theta_1 = 0.7, \theta_2 = 1.3$	5.27 sec
$\theta_1 = 0.7, \theta_2 = 1.5$	7.62 sec
$\theta_1 = 0.7, \theta_2 = 1.8$	10.49 sec

The linear function that fits this data without fixing the intercept and with fixing the intercept to 0 are presented below. The high R^2 value for the no intercept function is an indication that the purely linear fit is a good estimate of t_2. To verify this, the error in t_2 utilizing equation 4.39 is listed in Table 4.4.

$$t_2 = 10.3 \cdot (\theta_2 - \theta_1) - 0.85;\ R^2 = 1 \tag{4.38}$$

$$t_2 = 9.4 \cdot (\theta_2 - \theta_1);\ R^2 = 0.99 \tag{4.39}$$

Table 4.4 Error in t_2 with change in θ_2 using equation 4.39

Load parameters	Error in t_2
$\theta_1 = 0.7, \theta_2 = 1.3$	0.37 sec
$\theta_1 = 0.7, \theta_2 = 1.5$	-0.1 sec
$\theta_1 = 0.7, \theta_2 = 1.8$	-0.15 sec

4.2.3 Effect of other parameters on the total time to recovery

While these are the main parameters that impact the voltage recovery time significantly, the variation of other parameters does have an impact on the recovery time. As an example, Figure 4.10 plots the susceptance as the V_{stall} is changed from 0.55 to 0.5 and θ_2 is changed between 1.3 and 1.8.

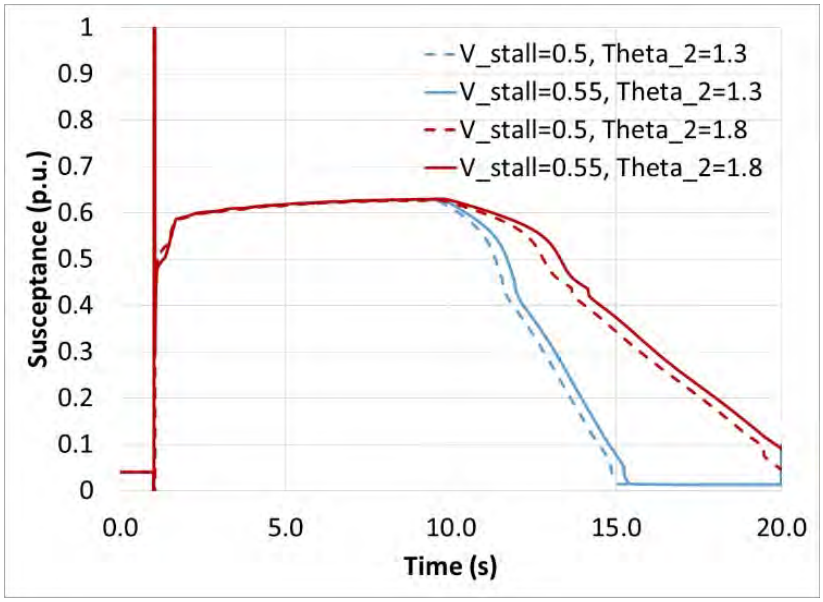

Figure 4.10 Susceptance plot with variation of V_{stall} and θ_2

4.3 Control Schemes Utilizing Admittance

The final simplified model of the composite load model during the FIDVR event is given by Figure 4.11. The admittance of the 1-ϕ motor dominates the other load admittances and so the admittance of the load can be reasonably approximated to be that of the 1-ϕ motor. The figure also contains a switched shunt located at the transmission level that can be used to mitigate the FIDVR phenomenon.

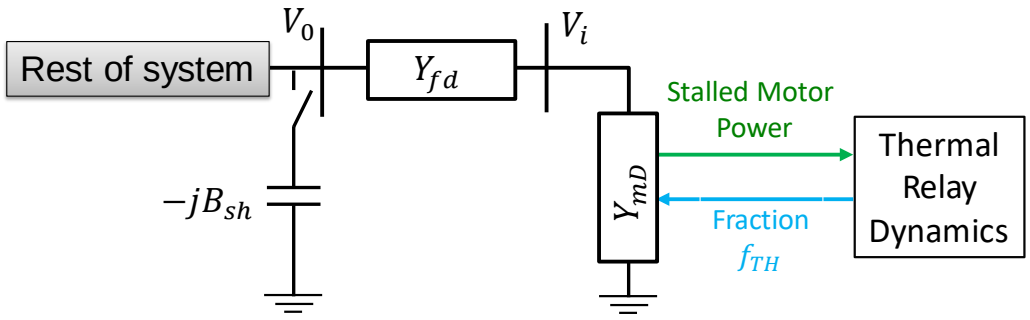

Figure 4.11 Final simplified model of the composite load model during FIDVR

As an example, a load of 20 MW and 13 MVAR is converted to a composite load model with $F_{mA} = 20\%, F_{mB} = 20\%, F_{mC} = 10\%, F_{mD} = 25\%$. The power demand of each of the components before and after fault (during FIDVR) is listed in Table 4.5. The power demanded by the Motor-D significantly rises during FIDVR and dominates the behavior of the load during this phenomenon.

Table 4.5 Power distribution between the various components of the composite load model before and after the fault

Type	Power Before Fault	Power After Fault (V=0.7)
Motor-A	4MW + 3 MVAR	2MW + 1.4 MVAR
Motor-B	4MW + 3.3 MVAR	1.3MW + 0.7 MVAR
Motor-C	2MW + 1.7 MVAR	1MW + 0.5 MVAR
Motor-D	5MW + 2.3 MVAR	25MW + 25 MVAR
Static Load	5MW + 2.5 MVAR	1MW + 0.5 MVAR

The simplified structure also allows us to deduce that the only method to control the FIDVR recovery time is to either control the 1-ϕ motor load by disconnecting AC's utilizing smart thermostats or by adding a shunt at the transmission bus that effectively reduces the admittance at the FIDVR bus. Figure 4.12 pictorially explains the relation between connecting the shunts and disconnecting the AC's to the rise in voltage during FIDVR.

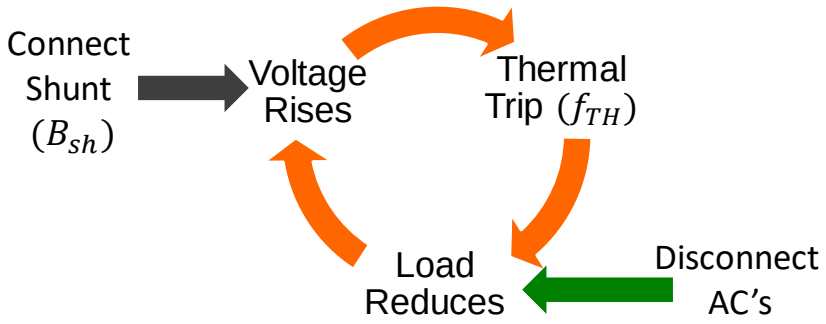

Figure 4.12 Pictorial representation of relation between connecting the shunts and disconnecting the AC's to rise in voltage

The scenario to be controlled is selected to be the case-2 in the previous section that exhibits the FIDVR phenomenon. To determine that the FIDVR phenomenon is occurring and that control is necessary, either the voltage based indices described in chapter 3 can be used or the sudden rise in the susceptance value can be used. The control schemes described in this section are purely local, i.e. the control action occurs at the bus where the FIDVR is observed and no information is sent to a centralized location to determine this control. This has the advantage of not requiring any communications and ensuring that the control can occur quickly. However, a wide area control mechanism can lead to less amount of load being dropped or a different shunt element being switched on that can alleviate the FIDVR phenomenon on a group of buses instead of a single bus, which is more practical. This trade-off between the local and wide-area control is out of the scope of this project and will be studied in the future.

4.3.1 Utilizing Smart Thermostats for Controlling Air-Conditioners

The increasing use of smart thermostats in modern residences enables the utility to utilize the thermal capacity of the residences to improve the overall system. The smart thermostats can turn the AC's off very quickly when they receive a signal from the utility [17]. The ideal behavior of the susceptance is assumed to be as shown in Figure 4.13.

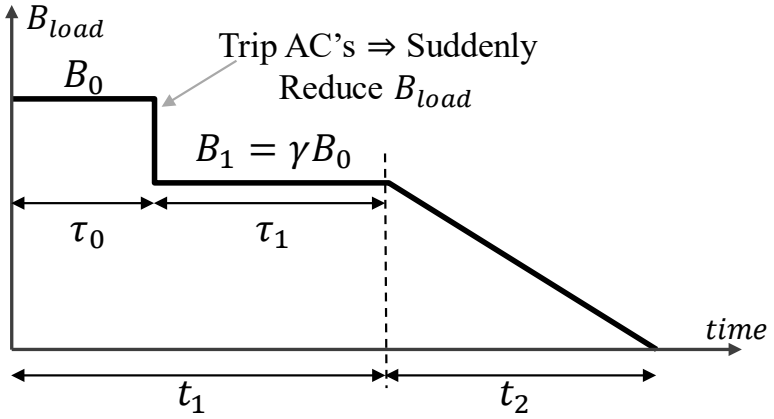

Figure 4.13 Idealized behavior of the susceptance during FIDVR with AC disconnection

The time t_1 is determined by the weighted average susceptance of B_0 and B_1 weighted by τ_0 and τ_1 and the time t_2 is determined by B_1. Assume that after tripping, γ fraction of the AC load remains connected, thus $B_1 = \gamma B_0$. The utility would like to estimate the amount of AC's to trip at a particular time τ_0 so that the total time to recovery is equal to a specified time, t_{sp} (usually 10 s). The following equations are derived from their definitions.
z

$$B_{avg} = \frac{\tau_0 B_0 + \tau_1 B_1}{\tau_0 + \tau_1} = \frac{\tau_0 + \gamma\tau_1}{\tau_0 + \tau_1} B_0 \tag{4.40}$$

$$t_1 + t_2 = t_{sp} \tag{4.41}$$

$$\tau_0 + \tau_1 = t_1 \tag{4.42}$$

As demonstrated in previous section, t_1 and t_2 are reasonable approximated as linear functions of the susceptance. Equations 4.43 and 4.44 can be written with this assumption.

$$t_1 = \alpha \cdot B_{avg} = \alpha \cdot \frac{\tau_0 + \gamma\tau_1}{\tau_0 + \tau_1} B_0 \tag{4.43}$$

$$t_2 = \beta \cdot B_1 = \beta \cdot \gamma \cdot B_0 \tag{4.44}$$

Combining the above equations, the following set of equations 4.45 can be obtained. This set of equations has 2 unknowns (γ & τ_1) and can be solved. Since the system of equations are quadratic, we get 2 solutions and only the solution with $\gamma > 0$ is physically realizable. Also, if the resulting γ is greater than 1, it implies that the FIDVR phenomenon will naturally recover by the specified time with no control being necessary.

$$(\tau_0 + \tau_1)^2 = \alpha(\tau_0 + \gamma\tau_1)B_0 \tag{4.45a}$$

$$\tau_0 + \tau_1 + \beta \cdot \gamma \cdot B_0 = t_{sp} \tag{4.45b}$$

The resulting γ implies that $(1 - \gamma)$ fraction of the AC load has to be tripped at τ_0 time instant to ensure that the FIDVR event is resolved within the specified time. This is tested in PSSE on various values of t_{sp} and τ_0 for case-3 detailed in section 4.2. For this case, $\alpha = 14.8$ and $\beta = 11.6$ and Table 4.6 lists the actual values of time to recover from the FIDVR event with a fraction of AC load tripped as determined by solving equation 4.45.

Table 4.6 Time to recover from FIDVR event in the PSSE simulations by tripping fraction of AC's

Time to recover from FIDVR (t_{sp})	Time to trip AC's (τ_0)	AC tripped calculated by Eq (4.45)	Actual time to recover from PSSE simulations
10 sec	2 sec	30 %	9.8 sec
10 sec	3 sec	33 %	9.9 sec
11 sec	2 sec	20 %	10.5 sec
11 sec	3 sec	23 %	10.5 sec

It can be seen from Table 4.6 that the time to recover from PSSE simulations is very close to the estimated time of recovery t_{sp}. Further, the actual time is less than the necessary time and this ensures that the control action is conservative. The variation of the susceptance is plotted in Figure 4.14 And it can be seen that the tripping of the AC's causes the susceptance to behave in a manner similar to the ideal curve in Figure 4.13. `

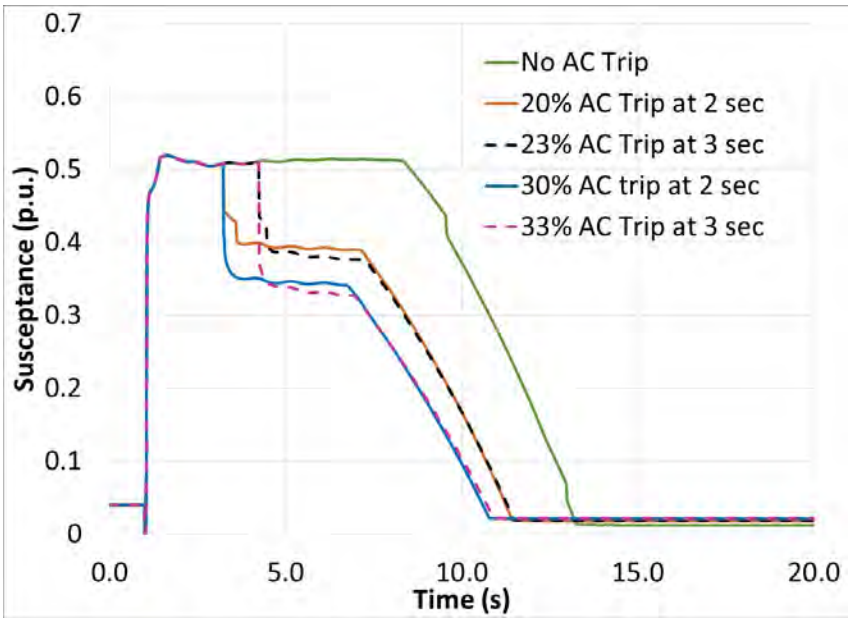

Figure 4.14 Susceptance plot during FIDVR with AC disconnection as control

The voltage at the transmission bus is plotted in Figure 4.15 for the various control amounts and times. It can be seen that the scenarios with coincident voltage waveforms also have coincident susceptance curves in Figure 4.14.

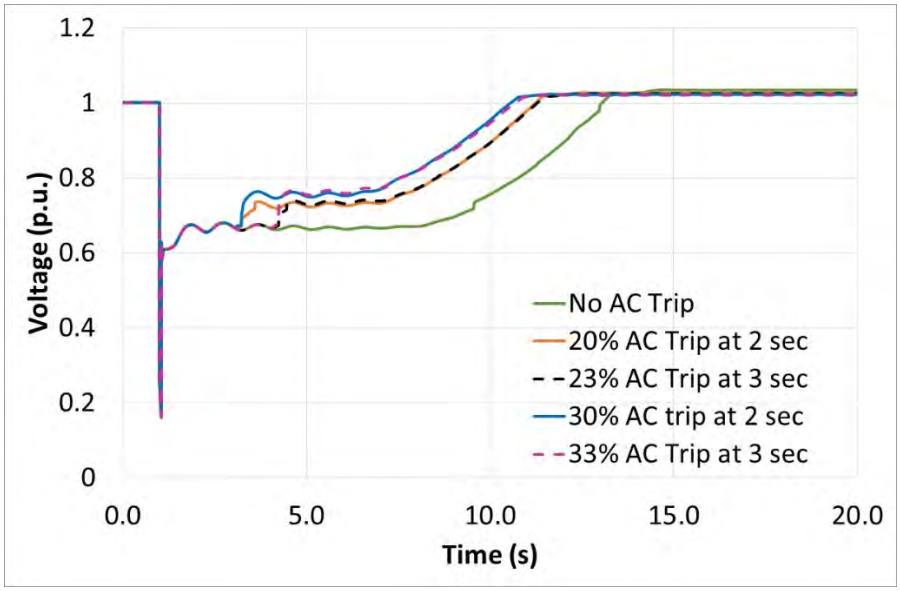

Figure 4.15 Voltage plot of FIDVR with AC disconnection as control

Hence, the expressions for the time to recovery can be used to determine the percentage of AC's to trip to ensure that the FIDVR event is over within a pre specified amount of time.

4.3.2 Switching Shunt Devices

Another option is to switch shunt devices close to the load bus to supply reactive power to enable the voltages to rise faster and reduce the time of FIDVR. This also can be analyzed utilizing the methodology for the AC tripping as the equivalent susceptance reduction can be modelled as an addition of an equivalent shunt. However, there is key difference between switching a shunt device and disconnecting AC's. Disconnecting the AC's leads to a reduction in the conductance also which is not the case while connecting a shunt device. This implies that a larger shunt device must be connected to achieve the same effect to compensate for the fixed conductance. A thumb rule is to connect 50% more shunt compensation than the reduction in AC disconnection required.

Table 4.7 Time to recover from FIDVR event by switching the shunt device

Time to recover from FIDVR (t_{sp})	Time to connect shunt (τ_0)	B_{sh} calculated by Eq (4.44) + 50%	Actual time to recover from PSSE simulations
10 sec	3 sec	0.20 p.u.	9.9 sec
11 sec	3 sec	0.15 p.u.	10.6 sec

Figure 4.16 plots the voltage for variations in the switched shunt amount at 3 seconds after the fault has been cleared. As per equation 4.44, a shunt of 0.1 p.u. needs to be connected at 3 seconds to recover from FIDVR in 11 seconds. However, only connecting 0.1 p.u. will not be sufficient as the conductance is not changing. This is reflected in the recovery time being equal to 12 seconds. Adding 50% more resolves this issue and this also why we connect 0.2 p.u. than 0.15 p.u. to recover from FIDVR in 10 seconds.

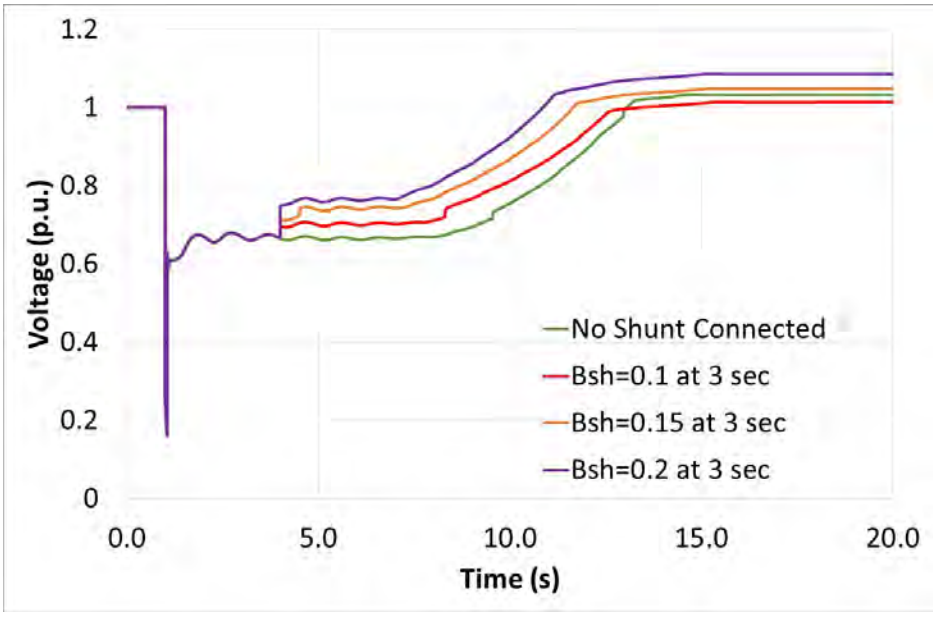

Figure 4.16 Voltage plot of FIDVR with shunt switching as control

5. Real Time Test Bed Implementation of Algorithms in OpenPDC

An important deliverable in this project is the implementation of the methodologies in a real time test bed and an evaluation of their applicability in real-time operations. As we are dealing with phasor data, we need to use a Phasor Data Concentrator (PDC) to implement our techniques to run in real-time. For this project, we use the OpenPDC, an open-source PDC as it is open-source and is used by utilities to analyze data from PMU's in the field.

We have implemented the following real-time phasor analytics in OpenPDC

1. W-Index Calculation for quantifying FIDVR for Voltage waveform (CSV output along with Visualization)
2. Lyapunov Exponent to determine the short-term voltage stability (CSV output along with Visualization)

These methods have been compiled into dll files that the utilities can directly use in their OpenPDC instance. The output of the method is either a CSV output file for analyzing any data after the event has happened or it can be visualized as a plot in real-time giving the operators at the utilities a real-time indication of the system stability. Figures 8 & 9 plot the W-Index and the Lyapunov Exponent for two voltage waveforms (on the top) that demonstrate short term voltage stability and FIDVR respectively.

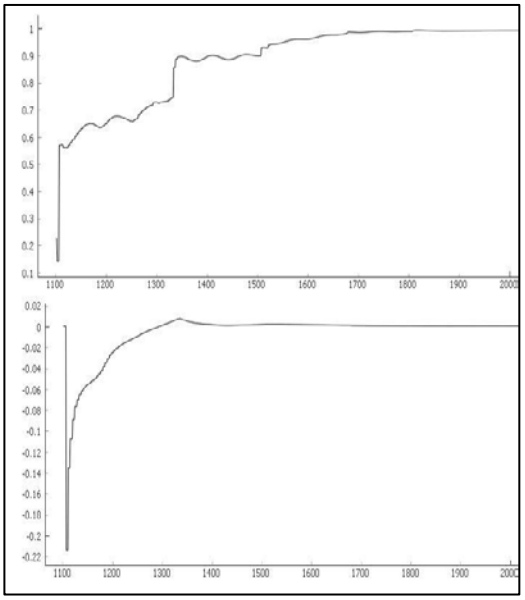

Figure 5.1 Delayed voltage response (top) and the corresponding W-index (bottom) vs the time in samples (60 samples per sec).

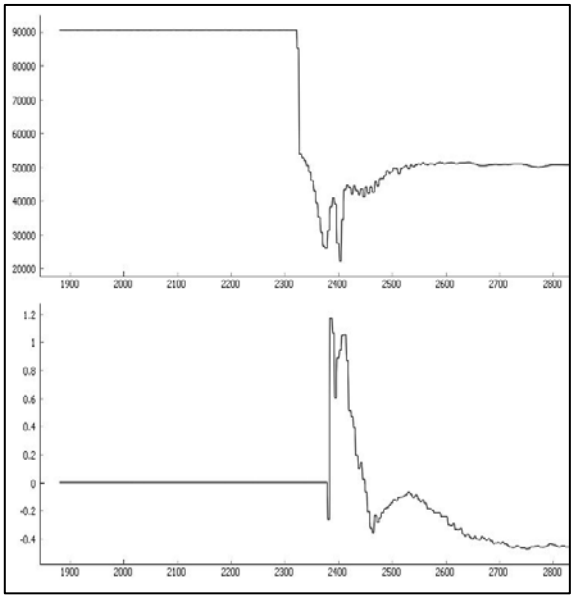

Figure 5.2 Voltage instability event (top) and the corresponding Lyapunov Exponent (bottom) vs the time in sample (60 samples per sec).

The W-index stays near 0 and even goes positive around 3 seconds after the event. This low value will enable us to conclude a severe FIDVR event and initiate mitigation schemes. The Lyapunov

Exponent goes positive very quickly after the event, implying a severe voltage stability problem and enables us to initiate mitigation schemes.

The C# code for calculating the W-index in OpenPDC is present in Appendix 2 with various comments enabling readers to implement the methodology. At present, it outputs the data as an output adapter into a csv file that is prespecified by the user for a set of voltages.

6. Conclusion

In this project, the problem of monitoring and mitigating FIDVR is addressed by utilizing the high sampling rate of PMU's and understanding the physics underlying the FIDVR problem to issue control signals to smart thermostats and shunt devices in real-time.

The initial methodology to understand and monitor is based on the voltage measurements being made at the transmission substation where the FIDVR is manifested. To ensure the robustness of the proposed methodology, the voltage waveform measured at the PMU is converted into a time varying probability distributions that is compared to another time varying probability distributions derived from a predefined voltage waveform that is determined by the reliability coordinator. The comparison between the probability distributions is performed using the Wasserstein metric that has the appealing properties of continuity and a limited output. This ensures that the measure calculated at the PMU is robust and reliable.

The methods are implemented for real-time validation in OpenPDC to verify that they can indeed operate in the real-time environment and that they can handle noise introduced by measurement error and delays in the communication network. OpenPDC is chosen as it is in use by the utilities and so the code developed can be directly ported into the utilities' operations with minimal effort.

To determine the control, just utilizing the voltage did not provide sufficient information as several varying parameters of the load can lead to similar voltages. To overcome this, the composite load model is studied in detail and is simplified based on engineering judgment and it is shown that an admittance approach is well suited for this purpose. Analytical relations were derived by approximations of expressions and the time to recovery in terms of the measured admittance is derived. This is verified on PSSE simulations and the error between the expected times and the measured times to recovery were less than 1 second.

The low error provides confidence on utilizing this method for control to ensure that the FIDVR recovery can occur within a pre-specified time. The only control schemes that can mitigate FIDVR are shown to be the tripping of Air Conditioners or the injection of reactive power via Shunt devices. An analytical expression for the magnitude of control action as a function of trip time is derived and this is also tested in PSSE. The expression is shown to be accurate to within 1 second with control actions upto 30% Air conditioner load tripping and provides a use case for the utilities to implement smart thermostats in their distribution network.

Appendix 1: 3-Phase IM Models

The circuits for the conventional 3-phase IM models and the block diagram of the equations in the dq frame of reference are shown in Figure A1.1.

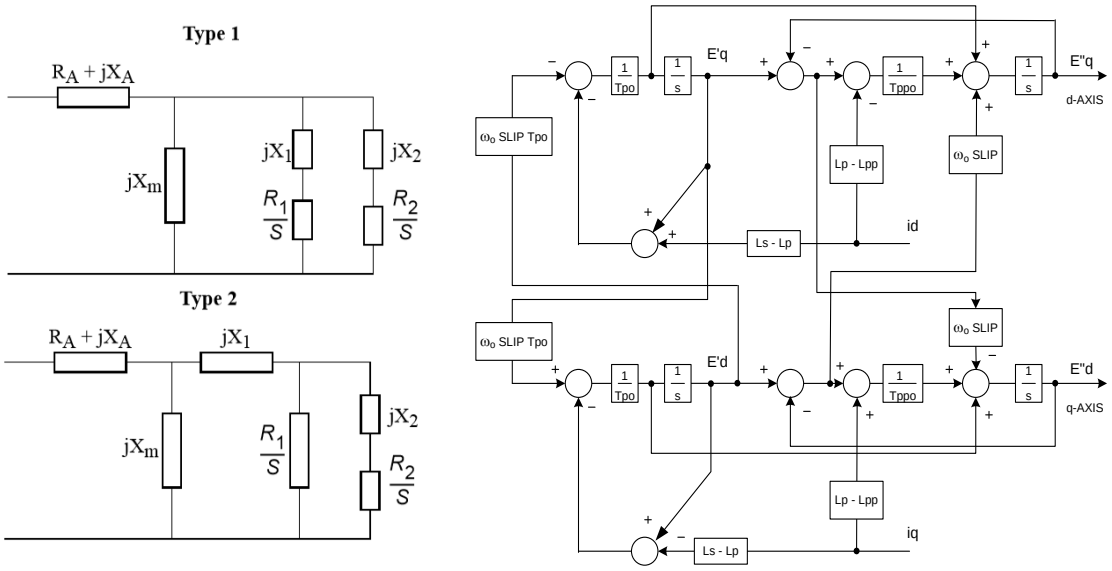

Figure A1.1 circuits for the conventional 3-phase IM models (left) and the block diagram of the equations in the dq frame of reference (right)

The conversion between the WECC model parameters into the Krauss model [17] are listed below for reference.

$$L_s = (X_A + X_m)/\omega_{base}$$

$$L_p = \left(X_A + (X_1 \cdot X_m)\ /(X_1 + X_m)\right)/\omega_{base}$$

$$L_{pp} = \left(X_A + (X_1 \cdot X_2 \cdot X_m)\ /(X_1 \cdot X_2 + X_2 \cdot X_m + X_m \cdot X_1)\right)/\omega_{base}$$

$$T_{p0} = (X_1 + X_m)/(\omega_{base} \cdot R_1)$$

$$T_{ppo} = \left(X_2 + (X_1 \cdot X_m)\ /(X_1 + X_m)\right)/(\omega_{base} \cdot R_2)$$

Utilizing these equations, we can estimate the parameters of the Krauss model given the WECC motor parameters with the additional condition that $X_1 = X_A$.

Appendix 2: C# Code implementing KL-index & W-Index in OpenPDC

```
//For more information contact Amar (amar@iastate.edu)

using GSF;
using GSF.TimeSeries;
using GSF.TimeSeries.Adapters;
using System;
using System.Collections.Generic;
using System.ComponentModel;
using System.Diagnostics;
using System.IO;
using System.Linq;
using System.Text;
using System.Threading.Tasks;

namespace KLWOutputAdapater
{
[Description("KLWOutputAdapater : Writes KLW average into a CSV file")]
public class KLWAdapter : OutputAdapterBase
{
#region [ Members ]

//Fields - Part of OutputAdapterBase
private string m_fileName; // The file name to write into
private StreamWriter m_outStream; // Output File name
private int m_measurementCount; // Measurement Count

//Useful for custom implementation

// To write header into the CSV File
private bool header_written = false;

// Threshold Value to trigger action
private double ThresholdTriggerValue;

// Parameters to be passed as values for the custom action
private double ChangingParameter1, ChangingParameter2;

//A set of dictionaries to keep track of the measurements

//Key : Measurement ID , Value : A queue of measurement values
private Dictionary<Guid, Queue<double>> measurement_dictionary;

//Key : Measurement ID , Value : Dictionary of <Value of Voltage bin ,
Histogram count> pairs
private Dictionary<Guid, SortedDictionary<double, int>>
measurement_Histogram_dictionary;

//Key : Measurement ID , Value : Dictionary of <Value of Voltage bin ,
Histogram count> pairs
private Dictionary<Guid, SortedDictionary<double, int>>
KL_W_Reference_Histogram_dictionary;

//Key : Measurement ID , Value : KLW iteration count
private Dictionary<Guid, int> KL_W_iteration_dictionary;
```

```
//Key : Measurement ID , Value : start flag
private Dictionary<Guid, bool> KL_W_start_flag_dictionary;

//Key : Measurement ID , Value : window over flag
private Dictionary<Guid, bool> KL_W_window_over_flag_dictionary;

//Key : Measurement ID , Value : KLW values
private Dictionary<Guid, double> KL_W_dictionary;

//Time between two measurement samples
private double delta_time;

//Initial reference voltage
private double V1;

//rise time
private double Tc;

//should be 180 for KL and 45 for LE
private int window_length;

//Percentage trigger
private double percentage_trigger;

// First Measurement Key
private MeasurementKey FirstMeasurementKey;

//Value of first window average
private double first_average;

#endregion

#region [ Overridden Methods ]
/// <summary>
/// Gets or sets the name of the CSV file.
/// </summary>
[ConnectionStringParameter,
Description("Define the name of the CSV file to which measurements will be
archived."),
DefaultValue("measurements_test.csv"),
CustomConfigurationEditor("GSF.TimeSeries.UI.WPF.dll",
"GSF.TimeSeries.UI.Editors.FileDialogEditor", "type=save; defaultExt=.csv;
filter=CSV files|*.csv|All files|*.*")]

public string FileName
{
get
{
return m_fileName;
}
set
{
m_fileName = value;
}
}
```

```
/// <summary>
/// Returns a flag that determines if measurements sent to this
/// <see cref="CustomCSVOutputAdapter"/> are destined for archival.
/// </summary>

public override bool OutputIsForArchive
{
get
{
return true;
}
}

/// <summary>
/// Gets a flag that determines if this <see cref="CustomCSVOutputAdapter"/>
/// uses an asynchronous connection.
/// </summary>
protected override bool UseAsyncConnect
{
get
{
return false;
}
}


/// <summary>
/// Gets a short one-line status of this <see cref="CSVOutputAdapter"/>.
/// </summary>
/// <param name="maxLength">Maximum length of the status message.</param>
/// <returns>Text of the status message.</returns>
public override string GetShortStatus(int maxLength)
{
return string.Format("Archived {0} measurements to File : {1} in the custom
format", m_measurementCount, m_fileName).CenterText(maxLength);
}


/// <summary>
/// Attempts to connect to this <see cref="CustomCSVOutputAdapter"/>.
/// </summary>

protected override void AttemptConnection()
{
m_outStream = new StreamWriter(m_fileName);
}

// <summary>
/// Attempts to disconnect from this <see cref="CustomCSVOutputAdapter"/>.
/// </summary>
protected override void AttemptDisconnection()
{
m_outStream.Close();
}
```

```
/// <summary>
/// Initializes this <see cref="CustomCSVOutputAdapter"/>.
/// </summary>
public override void Initialize()
{
base.Initialize();

Dictionary<string, string> settings = Settings;
string setting;
string Temporary;

// Load optional parameters

if (settings.TryGetValue("FileName", out setting))
m_fileName = setting;

if (settings.TryGetValue("TriggerValue", out Temporary))
//If the TriggerValue is not given b the user, it is null and will throw an
exception when converitng to double.
ThresholdTriggerValue = (Temporary.Equals("") || Temporary == null) ? 0 :
Convert.ToDouble(Temporary);

if (settings.TryGetValue("ChangingParameter1Value", out Temporary))
//If the TriggerValue is not given b the user, it is null and will throw an
exception when converitng to double.
ChangingParameter1 = (Temporary.Equals("") || Temporary == null) ? 0 :
Convert.ToDouble(Temporary);

if (settings.TryGetValue("ChangingParameter2Value", out Temporary))
//If the TriggerValue is not given b the user, it is null and will throw an
exception when converitng to double.
ChangingParameter2 = (Temporary.Equals("") || Temporary == null) ? 0 :
Convert.ToDouble(Temporary);


if (settings.TryGetValue("DeltaTime", out Temporary))
//If the Delta Time is not given by the user, it is zero and will throw a
divide by zero exception
delta_time = (Temporary.Equals("") || Temporary == null) ? 1.0/60 :
Convert.ToDouble(Temporary);
if (settings.TryGetValue("InitialReferenceVoltage", out Temporary))
//If the Initial Reference Voltage is not given by the user, it is zero and
will throw a divide by zero exception
V1 = (Temporary.Equals("") || Temporary == null) ? 0.55 :
Convert.ToDouble(Temporary);
if (settings.TryGetValue("RiseTime", out Temporary))
//If the rise time is not given by the user, it is zero and will throw a
divide by zero exception
Tc = (Temporary.Equals("") || Temporary == null) ? 5.0 :
Convert.ToDouble(Temporary);
if (settings.TryGetValue("WindowLength", out Temporary))
//If the window length is not given by the user, it is zero and will throw a
divide by zero exception
window_length = (Temporary.Equals("") || Temporary == null) ? 0 :
Convert.ToInt32(Temporary);

//SetPythonProcessInfo();
```

```
/* Inputs from User :
FileName=E:\testing_csv_trial43b.csv;
InputMeasurementKeys=069c5e29-f78a-46f6-9dff-c92cb4f69371;
RequeueOnException=False;
TriggerValue=400000;
ChangingParameter1Value=100;
ChangingParameter2Value=200;
InitialReferenceVoltage = 0.55;
RiseTime = 5.0;
window_length = 180;
percentage_trigger = 0.02
*/



//Intializing the dictionaries
measurement_dictionary = new Dictionary<Guid, Queue<double>>(2 *
window_length);
measurement_Histogram_dictionary = new Dictionary<Guid,
SortedDictionary<double, int>>();
KL_W_Reference_Histogram_dictionary = new Dictionary<Guid,
SortedDictionary<double, int>>();
KL_W_iteration_dictionary = new Dictionary<Guid, int>(2 * window_length);
KL_W_start_flag_dictionary = new Dictionary<Guid, bool>();
KL_W_window_over_flag_dictionary = new Dictionary<Guid, bool>();
KL_W_dictionary = new Dictionary<Guid, double>();

}



// <summary>
/// Used to process the measurements that come in.
/// <param name="measurements">List of Measurements at this moment</param>
/// </summary>

protected override void ProcessMeasurements(IMeasurement[] measurements)
{
if ((object)measurements != null)
{
StringBuilder builder = new StringBuilder();
StringBuilder manipulated_builder = new StringBuilder();
if (!header_written)
builder.Append(WriteHeader(measurements));

FirstMeasurementKey = measurements[0].Key; // Get the first measurement key

int number_of_measurement_keys = measurements.MeasurementKeys().Length;
for (int i = 0; i < measurements.Length; i = i + number_of_measurement_keys)
{
builder.Append((long)measurements[i].Timestamp);
for (int j = 0; j < measurements.Select(m =>
m.Key).Distinct().ToArray().Length; j++)
{
builder.Append(',').Append(measurements[i + j].AdjustedValue);
```

```
//Append the output of the moving average
string KL_W_value = Calculate_KL_W_InMeasurement(measurements[i + j].ID,
window_length, delta_time);
manipulated_builder.Append(KL_W_value);

}
builder.Append(manipulated_builder.ToString()); // append the string received
from the calculate average method

builder.Append(Environment.NewLine);
}

m_outStream.Write(builder.ToString()); // Write to the stream
m_measurementCount += measurements.Length;
}
}

#endregion

#region [ Custom Methods]
/// <summary>
/// Calculate the first average of the current measurement
/// </summary>
/// <param name="dictionary">Dictionary of Timestamp and values</param>
public void CalculateFirstAverage(Dictionary<long, double> dictionary)
{
first_average = dictionary.Take(window_length).ToDictionary(pair => pair.Key,
pair => pair.Value).Values.Average();
}

/// <summary>
/// Initialize Histogram
/// </summary>
/// <param name="NBins">Number of bins in the histogram</param>
/// <returns></returns>
public SortedDictionary<double, int> InitializeHistogram(int NBins)
{
double range = 1.05 * first_average;
SortedDictionary<double, int> HistogramDictionary = new
SortedDictionary<double, int>();
double increment = range / NBins;
double start = 0;
while (start <= range)
{
HistogramDictionary.Add(start, 0); // Amar - Can we do this once instead of
every time??
start += increment;
}

return HistogramDictionary;
}

/// <summary>
/// Add the
/// </summary>
/// <param name="measurement_id">current measurment ID</param>
/// <param name="value">value</param>
```

```
/// <param name="type">reference/measurement</param>
/// <returns></returns>

public SortedDictionary<double, int> AddToHistogram(Guid measurement_id,
double value, string type)
{
SortedDictionary<double, int> HistogramDictionary = new
SortedDictionary<double, int>();
if (type == "reference")
{
HistogramDictionary = KL_W_Reference_Histogram_dictionary[measurement_id];
}
else if (type == "measurement")
{
HistogramDictionary = measurement_Histogram_dictionary[measurement_id];
}
/*else
{
int x;// For testing
}*/

double valueRange = HistogramDictionary.Keys.Where(key => value >=
key).Last();
HistogramDictionary[valueRange]++;

return HistogramDictionary;
}

public SortedDictionary<double, int> RemoveFromHistogram(Guid measurement_id,
double value, string type)
{
SortedDictionary<double, int> HistogramDictionary = new
SortedDictionary<double, int>();
if (type == "reference")
{
HistogramDictionary = KL_W_Reference_Histogram_dictionary[measurement_id];
}
else if (type == "measurement")
{
HistogramDictionary = measurement_Histogram_dictionary[measurement_id];
}
else
{
int x;// For testing
}

double valueRange = HistogramDictionary.Keys.Where(key => value >=
key).Last();
HistogramDictionary[valueRange]--;

return HistogramDictionary;
}


public double SumAbsCum(SortedDictionary<double, int> dictionary)
{
double sum = 0, sum2 = 0, sum3 = 0, n = 0;
```

```
foreach (double key in dictionary.Keys)
{

sum += dictionary[key]; // getting the cumulative sum
sum2 += Math.Abs(sum); // sum of abs cumulative sums
sum3 += n * dictionary[key];//difference of the means of the 2 distributions
n++;

}
return 2 * sum2 * sum3 / Math.Sqrt(dictionary.Keys.Count) / n;// divide by is
to normalise the sum3
}

public SortedDictionary<double, int>
SubtractDictionary(SortedDictionary<double, int> first,
SortedDictionary<double, int> second)
{
SortedDictionary<double, int> SubtractedDictionary = new
SortedDictionary<double, int>();
if (first.Count == second.Count)
{
foreach (double key in first.Keys)
SubtractedDictionary.Add(key, first[key] - second[key]);
}
return SubtractedDictionary;
}

public string Calculate_KL_W_InMeasurement(Guid measurement_id, int
window_length, double delta_time)
{

StringBuilder builder = new StringBuilder();
Queue<double> measurement_queue;
SortedDictionary<double, int> measurement_Histogram;
SortedDictionary<double, int> KL_W_Reference_Histogram;
double Appending_term_reference;
double KL_W_value;
int KL_W_iteration_value = 0;
bool KL_W_start_flag_value = false;
bool KL_W_window_over_flag_value = false;

if (!measurement_dictionary.TryGetValue(measurement_id, out
measurement_queue))
{
measurement_queue = new Queue<double>();
measurement_dictionary.Add(measurement_id, measurement_queue);
}
if (!measurement_Histogram_dictionary.TryGetValue(measurement_id, out
measurement_Histogram))
{
measurement_Histogram = new SortedDictionary<double, int>();
measurement_Histogram_dictionary.Add(measurement_id, measurement_Histogram);
}
if (!KL_W_Reference_Histogram_dictionary.TryGetValue(measurement_id, out
KL_W_Reference_Histogram))
{
KL_W_Reference_Histogram = new SortedDictionary<double, int>();
```

```
KL_W_Reference_Histogram_dictionary.Add(measurement_id,
KL_W_Reference_Histogram);
}
if (!KL_W_dictionary.TryGetValue(measurement_id, out KL_W_value))
{
KL_W_dictionary.Add(measurement_id, KL_W_value);
}
if (!KL_W_iteration_dictionary.TryGetValue(measurement_id, out
KL_W_iteration_value))
{
KL_W_iteration_dictionary.Add(measurement_id, KL_W_iteration_value);
}
if (!KL_W_start_flag_dictionary.TryGetValue(measurement_id, out
KL_W_start_flag_value))
{
KL_W_start_flag_dictionary.Add(measurement_id, KL_W_start_flag_value);
}
if (!KL_W_window_over_flag_dictionary.TryGetValue(measurement_id, out
KL_W_window_over_flag_value))
{
KL_W_window_over_flag_dictionary.Add(measurement_id,
KL_W_window_over_flag_value);
}
if (measurement_queue.Count == window_length)
{
//measurement_log_voltage_diff_queue.Enqueue((Math.Log(Math.Abs(measurement_q
ueue.Peek()-measurement_queue.ElementAt(2))/10000+0.001)));
double a = measurement_queue.ElementAt(window_length - 1);
double b = measurement_queue.ElementAt(window_length - 2);
if (a < 60000)
{
int x = 0;
}
if (KL_W_start_flag_dictionary[measurement_id] == false)
{
if (((measurement_queue.ElementAt(window_length - 1) -
measurement_queue.ElementAt(window_length - 2)) > first_average *
percentage_trigger))
//if( (a-b))
{
KL_W_start_flag_dictionary[measurement_id] = true;
KL_W_Reference_Histogram_dictionary[measurement_id] =
InitializeHistogram(108); //InitializeHistogram(measurement_id, 108);
measurement_Histogram_dictionary[measurement_id] = InitializeHistogram(108);
//InitializeHistogram(measurement_id, 108);
}
else
{
KL_W_start_flag_dictionary[measurement_id] = false;

}
}
else // this implies KL_W_start_flag_dictionary[measurement_id] = true;
{
KL_W_start_flag_dictionary[measurement_id] = true;
}
```

```
if (measurement_queue.Count == window_length &&
KL_W_start_flag_dictionary[measurement_id] == true)
{

if (KL_W_window_over_flag_dictionary[measurement_id] == false)
{
if (((measurement_queue.ElementAt(1) - measurement_queue.ElementAt(0)) >
first_average * percentage_trigger))
{
      KL_W_window_over_flag_dictionary[measurement_id] = true;
}
else
{
      KL_W_window_over_flag_dictionary[measurement_id] = false;

}
}
else // automatically implies
KL_W_window_over_flag_dictionary[measurement_id] = true;
{
KL_W_window_over_flag_dictionary[measurement_id] = true;
}
if ((KL_W_Reference_Histogram.Values.ToArray().Sum()) < window_length - 2)
{
//builder.Append(",");
//builder.Append("KL Window - Small");
Appending_term_reference = first_average * (V1 + (1 - V1) * (1 - Math.Exp(-
delta_time * KL_W_iteration_dictionary[measurement_id] / Tc))); // this 0.45
& 3 can be changed
KL_W_Reference_Histogram_dictionary[measurement_id] =
AddToHistogram(measurement_id, Appending_term_reference, "reference");
measurement_Histogram_dictionary[measurement_id] =
AddToHistogram(measurement_id, measurement_queue.ElementAt(window_length -
1), "measurement");
KL_W_dictionary[measurement_id] =
SumAbsCum(SubtractDictionary(KL_W_Reference_Histogram_dictionary[measurement_
id], measurement_Histogram_dictionary[measurement_id]));
//builder.Append(",");
builder.Append(KL_W_dictionary[measurement_id] / (1 +
KL_W_iteration_dictionary[measurement_id]) / (1 +
KL_W_iteration_dictionary[measurement_id]));
KL_W_iteration_dictionary[measurement_id]++;
}
else if ((KL_W_Reference_Histogram.Values.ToArray().Sum()) >= window_length -
2) // should coincide with KL_W_window_over_flag_dictionary[measurement_id] =
true;
{
if (KL_W_window_over_flag_dictionary[measurement_id] == true)
{
      Appending_term_reference = first_average * (V1 + (1 - V1) * (1 -
Math.Exp(-delta_time * KL_W_iteration_dictionary[measurement_id] / Tc))); //
this 0.45 & 3 can be changed
      KL_W_Reference_Histogram_dictionary[measurement_id] =
AddToHistogram(measurement_id, Appending_term_reference, "reference");
      measurement_Histogram_dictionary[measurement_id] =
AddToHistogram(measurement_id, measurement_queue.ElementAt(window_length -
1), "measurement");
```

```
      KL_W_dictionary[measurement_id] =
SumAbsCum(SubtractDictionary(KL_W_Reference_Histogram_dictionary[measurement_
id], measurement_Histogram_dictionary[measurement_id]));
      //builder.Append(",");
      builder.Append(KL_W_dictionary[measurement_id] / (1 +
KL_W_iteration_dictionary[measurement_id]) / (1 +
KL_W_iteration_dictionary[measurement_id]));
      //Removing_term_reference = first_average * (V1 + (1 - V1) * (1 -
Math.Exp(-delta_time * (KL_W_iteration_dictionary[measurement_id] -
(window_length - 2))/Tc))); // this 0.45 & 3 can be changed
      //KL_W_Reference_Histogram_dictionary[measurement_id] =
RemoveFromHistogram(measurement_id, Removing_term_reference, "reference");
      //measurement_Histogram_dictionary[measurement_id] =
RemoveFromHistogram(measurement_id, measurement_queue.Peek(), "measurement");
      KL_W_iteration_dictionary[measurement_id]++;
}
else// should not come here
{
      builder.Append(",");
      builder.Append("Check indices");
}
}
}
}
if (KL_W_iteration_dictionary[measurement_id] > 2000)
{
//measurement_log_voltage_diff_queue.Clear();
KL_W_start_flag_dictionary[measurement_id] = false;
KL_W_window_over_flag_dictionary[measurement_id] = false;
KL_W_iteration_dictionary[measurement_id] = 0;
KL_W_dictionary[measurement_id] = 0;
KL_W_Reference_Histogram_dictionary[measurement_id].Clear();
measurement_Histogram_dictionary[measurement_id].Clear();
//measurement_LE_initial_dictionary[measurement_id] = 0;
}
return builder.ToString();
}

/// <summary>
///
/// </summary>
/// <param name="measurements"></param>
/// <returns></returns>
private string WriteHeader(IMeasurement[] measurements)
{
StringBuilder builder = new StringBuilder();
builder.Append("Timestamp");

MeasurementKey[] unique_measurement_keys = measurements.Select(m =>
m.Key).Distinct().ToArray();

foreach (MeasurementKey key in unique_measurement_keys)
builder.Append(",").Append(key);

//To be included-

foreach (MeasurementKey key in unique_measurement_keys)
```

```
builder.Append(",").Append(key).Append("-").Append("Moving
Average").Append(",").Append(key).Append("-").Append("LE Calculated");


builder.Append(Environment.NewLine);
header_written = true;

return builder.ToString();

}


#endregion


}
}
```

References

[1] P. Kundur, J. Paserba, V. Ajjarapu, G. Andersson, A. Bose, C. Canizares, N. Hatziar-gyriou, D. Hill, A. Stankovic, C. Taylor, T. Van Cutsem, and V. Vittal, "Definition and classification of power system stability IEEE/CIGRE joint task force on stability terms and definitions," Power Systems, IEEE Transactions on, vol. 19, no. 3, pp. 1387–1401, 2004.

[2] M. Paramasivam, A. Salloum, V. Ajjarapu, V. Vittal, N. B. Bhatt and S. Liu, "Dynamic Optimization Based Reactive Power Planning to Mitigate Slow Voltage Recovery and Short Term Voltage Instability," in IEEE Transactions on Power Systems, vol. 28, no. 4, pp. 3865-3873, Nov. 2013.

[3] M. Paramasivam," Dynamic optimization based reactive power planning for improving short-term voltage performance", PhD Dissertation, Iowa State University.

[4] M. Paramasivam, S. Dasgupta, V. Ajjarapu and U. Vaidya, "Contingency Analysis and Identification of Dynamic Voltage Control Areas," in *IEEE Transactions on Power Systems*, vol. 30, no. 6, pp. 2974-2983, Nov. 2015.

[5] S. Sinha, P. Sharma, U. Vaidya and V. Ajjarapu, "Identifying Causal Interaction in Power System: Information-Based Approach", accepted for publication in Conference in Decision and Control, 2017.

[6] Modeling and validation work group, "White paper on modeling and studying FIDVR events," Western Electricity Coordinating Council, Technical Report, October 20, 2011.

[7] North American Electric Reliability Corporation, Reliability Standard TPL-001-4, Transmission System Planning Performance Requirements.

[8] North American Transmission Forum, Transient voltage criteria reference document, September 2016.

[9] Modeling and validation work group, "WECC Dynamic Composite Load Model Specifications," Western Electricity Coordinating Council, Technical Report, January 25, 2015.

[10] Paul Krauss, "Analysis of Electric Machinery and Drive Systems", 2nd Edition.

[11] S. Dasgupta, M. Paramasivam, U. Vaidya and V. Ajjarapu, "Real-Time Monitoring of Short-Term Voltage Stability Using PMU Data," in *IEEE Transactions on Power Systems*, vol. 28, no. 4, pp. 3702-3711, Nov. 2013.

[12] A. Reddy and V. Ajjarapu, "PMU based real-time monitoring for delayed voltage response," *2015 North American Power Symposium (NAPS)*, Charlotte, NC, 2015, pp. 1-6.

[13] S. Dasgupta, M. Paramasivam, U. Vaidya and V. Ajjarapu, "Entropy-Based Metric for Characterization of Delayed Voltage Recovery," in *IEEE Transactions on Power Systems*, vol. 30, no. 5, pp. 2460-2468, Sept. 2015.

[14] Olkin, I. and Pukelsheim, F. (1982). "The distance between two random vectors with given dispersion matrices". Linear Algebra Appl. 48: 257–263.

[15] S. Halpin, K. Harley, R. Jones, and L. Taylor, "Slope-permissive under-voltage load shed relay for delayed voltage recovery mitigation," Power Systems, IEEE Transactions on, vol. 23, no. 3, pp. 1211 –1216, Aug. 2008

[16] A. Radaideh, U. Vaidya and V. Ajjarapu, "Sequential Set-point Control for Heterogeneous Thermostatically Controlled Loads Through an Extended Markov Chain Abstraction," in IEEE Transactions on Smart Grid, vol. PP, no. 99, pp. 1-1.

[17] Siemens PTI Power Technologies Inc., PSS/E 33, Program Application Guide, Vol. II, May 2011

Part II

Real Time Synchrophasor Measurements Based Long Term Voltage Stability Monitoring and Control

Chen-Ching Liu

Ruoxi Zhu, Graduate Student

Washington State University

For information about Part II, contact

Dr. Chen-Ching Liu
School of Electrical Engineering and Computer Science
Washington State University
Pullman, WA, 99164-2752
Email: liu@wsu.edu
Phone: 509-335-1150

Power Systems Engineering Research Center

The Power Systems Engineering Research Center (PSERC) is a multi-university Center conducting research on challenges facing the electric power industry and educating the next generation of power engineers. More information about PSERC can be found at the Center's website: http://www.pserc.org.

For additional information, contact:

Power Systems Engineering Research Center
Arizona State University
Engineering Research Center #527
551 E. Tyler Mall
Tempe, Arizona 85287-5706
Phone: 480-965-1643
Fax: 480-727-2052

Notice Concerning Copyright Material

Table of Contents

List of Figures

List of Tables

1. Introduction

1.1 Background

As the scale and complexity of an interconnected power grid has increased significantly, major blackouts in power systems have occurred due to system instability. Long term voltage stability is a focus area for power system research.

Since power systems can be operated close to the verge of voltage instability, it is necessary for dispatchers to monitor voltage stability in an on-line operating environment. A voltage collapse is characterized by the fact that the voltage magnitude of some buses declines over time. Many algorithms have been proposed to estimate the margin to voltage instability at an operation point.

The mechanisms of voltage instability are reported in [1][2]. These papers introduce the nonlinear aspects of voltage dynamics. Based on the dynamic behavior, Thevenin equivalent based methods are developed. According to Thevenin equivalent, the voltage stability or reactive-power reserve indices can be obtained [3][4].The VIP method [3] is intended to use local measurements to track the Thevenin equivalent. In recent years there are also measurement-based methods to assess voltage stability from the available measurements [5][6].

The main objective of this work is to develop a methodology for long term voltage stability assessment using a reduced network given a limited number of phasor measurements.

1.2 Overview of the problem

Long term voltage stability refers to the stability problem that occurs over a relatively long time frame, such as several minutes. These stability problem usually involves slow acting devices such as thermostatically controlled loads, LTC transformers, and distribution voltage regulators.

To assess the long term voltage stability for a power system, two classes of methods have been developed. One is a model based method. Base on the system topology and operation condition, several indices can be extracted from power flow equations. Using the Jacobian matrix, several modes can be derived from the eigenvalues. Once the critical mode becomes zero, the system is considered to be unstable [7]. For the detection of the unstable condition, continuous power flow method, bifurcation theory, and sensitivity methods are proposed [8],[9],[10].

The other class, which is also popular is the measurements based method. Since numerous measurements are installed on a power system, e.g., SCADA and PMU. It is critical to utilize these measurements, particularly the large amount of PMU data. Many methods are based on Thevenin Equivalent (TE), such as the methods proposed in [3], [11]. The computational simplicity makes Thevenin equivalent based approaches suitable for real time applications. Since Thevenin equivalent simplifies the system to a two-node system, the results obtained by comparing the equivalent impedance and load impedance may not be accurate, Researchers propose to extend the TE model to an n-node model [6].

This research addresses the critical issues by proposing two different methods. One is the Voltage Stability Assessment Index (VSAI) and the other is Optimal Power Flow-Loading Limit (OPF-LI). Both methods are intended for long-term voltage stability assessment. VSAI is a TE based method, which is used to calculate the indices in a non-iterative manner. Due to the shortcomings of TE model, OPF-LI is developed to assess the voltage stability margin for a load area. To utilize available PMU measurements, State Calculator (SC) is included in the algorithm to approximate the system states at the buses where PMU measurements are not available. The methods proposed in this research have been validated by test systems.

1.3 Report organization

The organization of the remaining chapters is as follows: Chapter 2 is a summary of the formulation of VSAI method. The improved approach, OPF-LI, for monitoring voltage stability of a load area is described in Chapter 3. In Chapter 4, OPF-LI with PMU measurements including estimates states calculated by SC is described. Then, OPF-LI incorporating OLTC operating control is discussed in Chapter 5. The conclusion of this report is provided in Chapter 6.

2. Voltage Stability Assessment Index

Long-term voltage stability involves slow acting equipment for which the time scale of the phenomena can be several minutes. The existing centralized model based approaches often use multiple power flows to compute the voltage stability margin of a system. Hence it is computationally burdensome and not suitable for real time applications.

The VSAI algorithm is a hybrid approach using the PMU data and the network information to calculate voltage stability indices at a load bus. It computes the distance to the point of voltage collapse (PoC) in a non-iterative manner by making use of wide area phasor measurements and system topological information.

2.1 Formulation of VSAI

To calculate VSAI-I, the first version of VSAI, a linearized Jacobian matrix of the power system is obtained based on the topological data and the system parameters. Then, one derives one or more sets of additional system characteristics (e.g., estimated voltages and currents for all buses) based on the specified perturbations. Finally, the TE impedance is estimated based on the actual system parameters and the derived system parameters. An index called 'Voltage Stability Assessment Index (VSAI)' is computed at every load bus, i.e.,

$$VSAI_k = \frac{\left| Average\left\{ \left(\frac{x_k - x_{k\,\widehat{(+ve)}}}{w_{k\,\widehat{(+ve)}} - w_k} \right) , \left(\frac{x_{k\,\widehat{(-ve)}} - x_k}{w_k - w_{k\,\widehat{(-ve)}}} \right) \right\} \right|}{\left| \frac{x_k}{w_k} \right|} \quad (1)$$

where ‘k’ means the load bus k, the average value is the equivalent impedance, and $|x_k / w_k|$ represents the load impedance based on the actual system parameters [3]. Note that the index is a value between 0 and 1, i.e., $0 \leq VSAI_k \leq 1$ for any bus 'k', where k ϵ load bus. A $VSAI_k$ value near “0” indicates that the bus ‘k’ is highly stable while a $VSAI_k$ value near "1" indicates that the bus 'k' is on the verge of voltage instability. The original work of VSAI is reported in [12].

2.2 Simulation for VSAI-I

VSAI-I is a version of VSAI based on the steady state model of VSAI in Sec. 2.1. The performance of VSAI-I is validated by simulation with the IEEE 30-bus system test under different scenarios of deteriorating voltage stability conditions. Figure 2.1 shows the VSAI indices of all load buses in the system along with important system metrics for the base case. It can be observed that for the base case system with no contingency, the VSAI of all the load buses are low. The VSAI of the weakest bus in the system is that of Bus 19, for which $VSAI_{19} = 0.1251$.

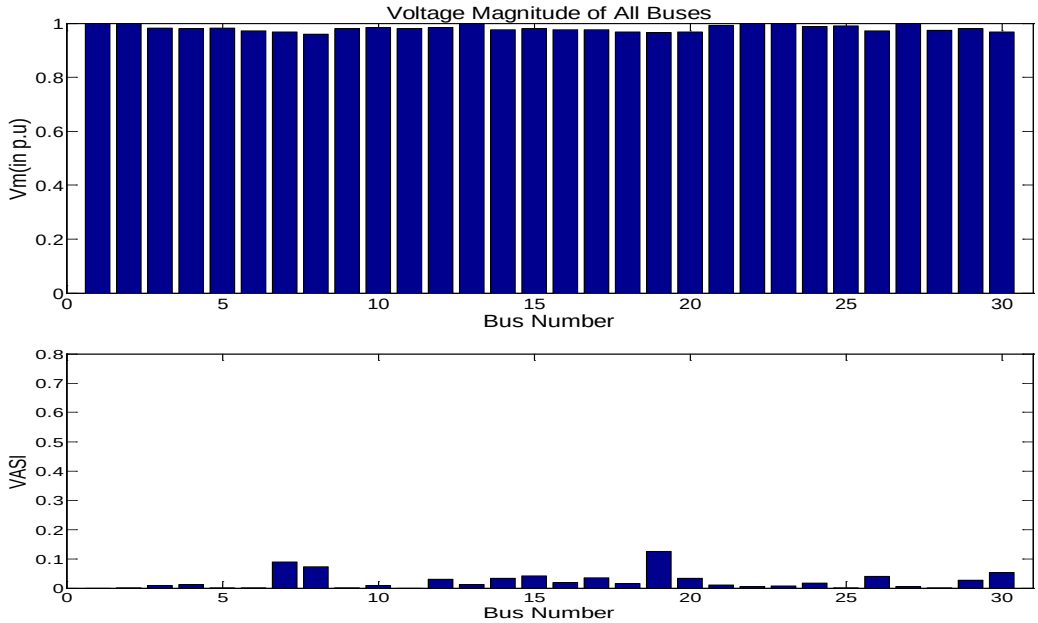

Figure 2.1 VSAI and voltage magnitudes for IEEE-30 bus system at the base case

In contrast, as shown in Figure 2.2, when the contingencies take place (i.e. when the transmission lines between Buses 6 & 8 and 6 & 28 are taken out of the system), the voltage magnitudes at the buses decreased, particularly at Bus 8. This is due to the fact that there is only one generator feeding Bus 8 after two lines are de-energized. This is indicated by a significantly increased VSAI (VSAI8=0.7159) of the affected load bus (Bus 8). Hence the system instability index is high.

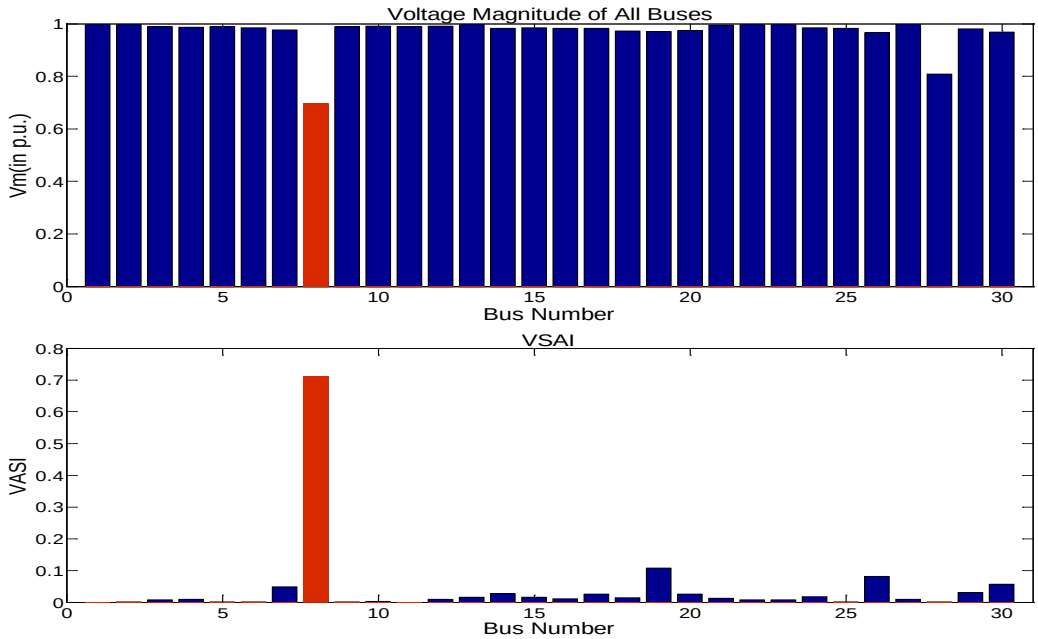

Figure 2.2 VSAI and voltage magnitudes of IEEE 30-bus system after a contingency

This information is visualized at the control center giving the operator the critical locations for voltage stability, allowing the operator to take appropriate actions based on control actions suggested by the tool.

2.3 VSAI with voltage dynamic mechanisms (VSAI-II)

Here the second version of VSAI, VSAI-II, refers to the enhanced version of VSAI-I incorporating voltage dynamic mechanisms. The model improves the accuracy of the voltage stability index for the real-time environment. It is proposed in this study to incorporate the voltage dynamic mechanisms, including generator excitation capability, stator current limit, and on-load tap changers.

The generator is modeled by a voltage source E behind a reactance X_d, where E varies in order to maintain the terminal voltage V at a constant V_0 during a normal operating condition. The excitation voltage is limited, and the stator current I also has an upper limit I_{lim}. The main strategies are as follows.

1) Normal operation: $V=V_0$, $E< E_{lim}$, $I< I_{\lim}$;
2) Operation at the excitation voltage limit: When $P^2+\left[Q+\frac{V^2}{X_d}\right]=\frac{E^2V^2}{{X_d}^2}\geq\frac{{E_{\lim}}^2V^2}{{X_d}^2}$, add a virtual node n+1 at this PV bus, convert the original generator i to a PQ bus (P, Q are specified by the bus load) and the voltage magnitude of the new bus is specified as E_{lim}. Update the admittance matrix and the power flow equations as follows:
   New generator bus (PV bus):
   $$P_{n+1}=E_{n+1}V_i(G_{(n+1)i}\cos\delta_{(n+1)i}+B_{(n+1)i}\sin\delta_{(n+1)i})+(E_{n+1})^2G_{n+1} \tag{2}$$
   Original generator bus (PQ bus):
   $$\begin{aligned}P_i&=V_i\sum_{j=1}^{n+1}V_j(G_{ij}\cos\delta_{ij}+B_{ij}\sin\delta_{ij})\\Q_i&=V_i\sum_{j=1}^{n+1}V_j(G_{ij}\sin\delta_{ij}-B_{ij}\cos\delta_{ij})\end{aligned} \tag{3}$$
   where n+1 means that the number of buses increases considering the virtual bus, and the number of the virtual bus is n+1.
3) Operation at the stator current limit: When $\frac{P^2+Q^2}{V^2}=I^2\geq{I_{\lim}}^2$, convert this PV bus to a constant current generator. By doing so, the following equation can be used to modify power flow equation for this generator i.
   $$\begin{aligned}&|S_i|^2=|V_i|^2*|I_i|^2=P_i^2+Q_i^2\\&=V_i^2\left[\left(\sum_{j=1}^{n}V_j(G_{ij}\cos\delta_{ij}+B_{ij}\sin\delta_{ij})\right)^2+\left(\sum_{j=1}^{n}V_j(G_{ij}\sin\delta_{ij}-B_{ij}\cos\delta_{ij})\right)^2\right]\end{aligned} \tag{4}$$

On-Load Tap Changers (OLTCs) are used to maintain constant load voltages. An OLTC has a reference voltage value V_0, which is the target value of automatic control. The tap movements are discrete and modeled by:

$$n_{k+1} = n_k - d \cdot f(V_k - V_0)$$
$$f(x) = \begin{cases} -1 & if\ x < -\Delta v, \\ 0 & if\ |x| < \Delta v, \\ 1 & if\ x > \Delta v, \end{cases} \tag{5}$$

Then update the tap-ratio of this load bus and, at the same time, the admittance matrix should be modified.

Incorporating the voltage dynamic mechanism, the results of the state variables would be modified, hence the method is more accurate in representing the voltage behaviors in the real-time environment.

2.4 Simulation results: VSAI-I and VSAI-II

The WECC 179 bus system is used as the test system for comparison of the results obtained from VSAI-I and VSAI-II.

Contingency: Increase load in Area1 to 1.1 times of base case loading

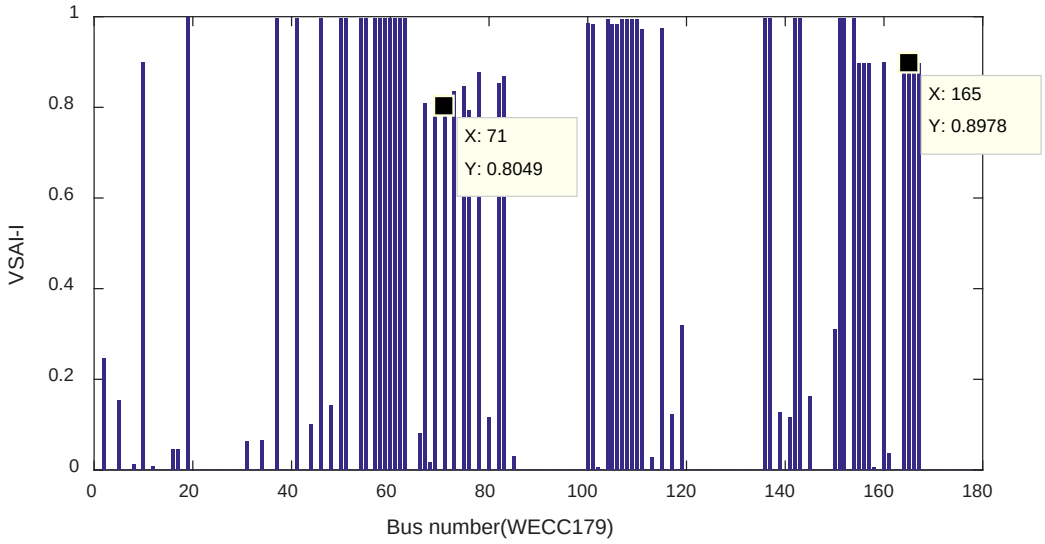

Figure 2.3 VSAI-I of the load buses

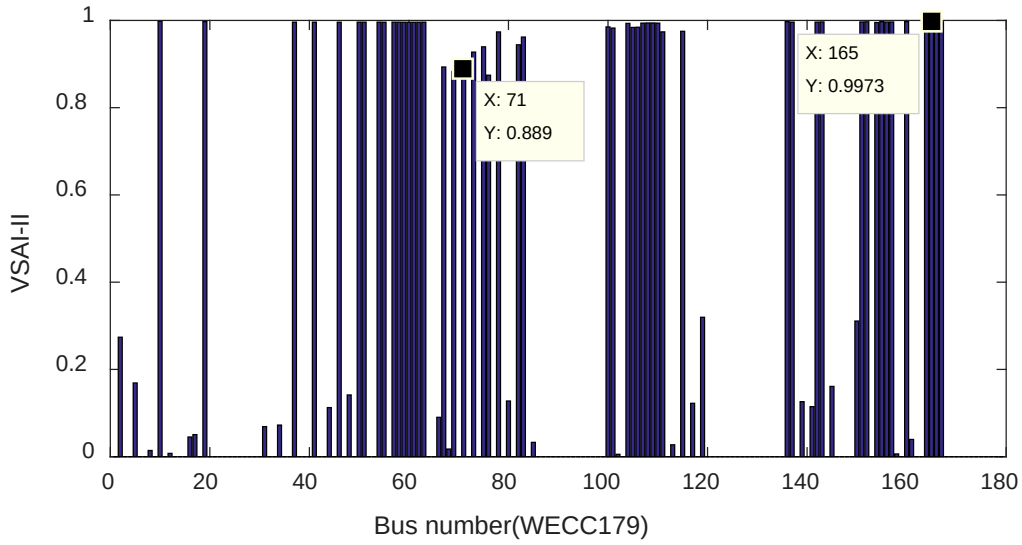

Figure 2.4 VSAI-II of the load buses

As shown in Figure 2.3, some values of the VSAI-I are equal to 1, indicating the system is close to instability. However, for VSAI-II, most values are equal to 1 indicating that the stability margin is small. For both cases, the results show the system is on the verge of voltage instability. Since no dynamic mechanism is modeled in the VSAI-I index, the system condition reflected by the upper diagram is more stable than that of VSAI-II. That is, VSAI-II is a more realistic indicator of the system operating condition. Note that the base case has a heavy loading condition and, therefore, the stability margin is expected to be small.

2.5 Summary

VSAI, which is a Thevenin Equivalent based indictor, models the entire system by two nodes, a generation and a load as shown in Figure 2.5.

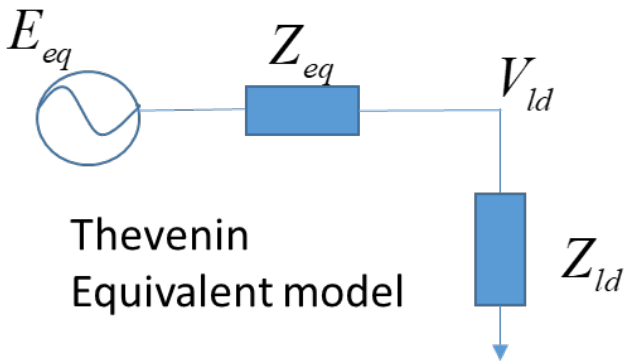

Figure 2.5 Thevenin equivalent model

By using a voltage source connected through a Thevenin impedance to approximate the rest of the system, most details of the system are eliminated. Therefore, it may not be accurate when one uses the Thevenin impedance and the magnitude of the load impedance to determine the maximum power transfer. Although the VSAI method can indicate voltage stability of the system, the margin between the operation point and voltage collapse cannot be estimated accurately.

3. OPF-LI

Many load centers exist in interconnected power systems. A major load center is usually supplied by multiple generation and transmission facilities through several boundary buses. The growth in electric energy consumption in a load center leads to heavy power transfer between the external system and the load area. Based on these properties load centers are likely to experience voltage instability. Monitoring voltage stability at a load center area is an important part of power system voltage stability assessment.

VSAI-I and VSAI-II indices are derived for a load bus based on a Thevenin equivalent (TE) approximating the rest of the power system, i.e., a voltage source connected through a Thevenin impedance. In this project, a new method, OPF-LI, is developed to extend the voltage stability index based on an enhanced model of the generation and transmission systems.

3.1 Formulation of OPF-LI

3.1.1 Ward-PV model

To investigate voltage stability of a load area, details of the load area and generation sources need to modelled. In this project, an extension is proposed to enhance the model using the Ward-PV equivalent system model [13]. In the Ward-PV model shown in Figure 3.1, the entire set of buses can be partitioned into three subsets: external, boundary, and internal buses. External buses are further partitioned into PQ buses and PV buses. External PQ buses are eliminated while the PV buses are retained. Therefore, the external system is modeled by a set of external generators and their (equivalent) transmission lines connecting to the load area through the boundary buses. The topology of the load center is preserved in this equivalent model. Then the reactive power response of the external generators is calculated based on decoupled reactive power flow [13].

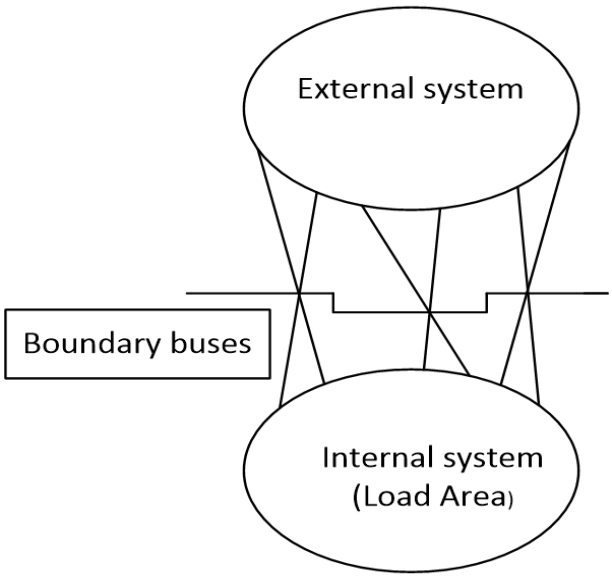

Figure 3.1 Ward-PV model

The proposed model has the following advantages:

1) Modeling a load area fed by several external generators. The effect of external PV buses as well as the detailed model of the load area is preserved.
2)The Ward-PV equivalent gives reasonably accurate results for both real and reactive power flow.
3)The large scale of the external system is reduced to a number of tie lines with the generation sources. Hence, it is feasible to compute the voltage stability margin in an on-line environment.

3.1.2 OPF based algorithm

Based on the Ward-PV equivalent system, the maximum allowable loading for the entire load area is given by the optimal solution of a new OPF based model. That is,

1) The objective of optimization is the load ratio by which the loads is uniformly modified by one parameter λ.The $n_b \times 1$ vectors are voltage angles θ and magnitudes *v*. The $n_g \times 1$ vectors are generator real and reactive power injections P_g, Q_g.
2) Objective function: Max λ.
3) Constraints:
   The updated equality constraints:

$$\begin{cases} P(v,\theta) + \lambda P_l - P_g = 0 \\ Q(v,\theta) + \lambda Q_l - Q_g = 0 \end{cases} \tag{6}$$

   The inequality constraints:

$$\begin{cases} 0 \le \lambda \le 10 \\ \left|S_b(\theta, v)\right| - S_{\max} \le 0 \\ v_{\min} \le v \le v_{\max} \\ P_{g\min}, Q_{g\min} \le P_g, Q_g \le P_{g\max}, Q_{g\max} \end{cases} \tag{7}$$

All constraints of the system are associated with characteristics of the base case. Hence, the inequality constraints of external generator injections are identical with those of the base case. The line flow constraints of the fictitious equivalent external lines are approximated based on the power flow results of the equivalent system.

3.2 Simulation results for OPF-LI

This section demonstrates the calculation of three indices on a 179-bus model resembling the structure of WECC. The analysis is focused on Area 1 of the system as the load area, as shown in Figure 3.2. The base case load for Area1 is:

$$P_L^{Area1} = 3.64 \times 10^4 MW$$
$$Q_L^{Area1} = 6.66 \times 10^3 MVAR \quad (8)$$

The computation involved in the algorithms is performed by MATLAB. The commercially available tool, TSAT, is used to determine the loading limits of Area1 with the dynamic model of the 179-bus system.

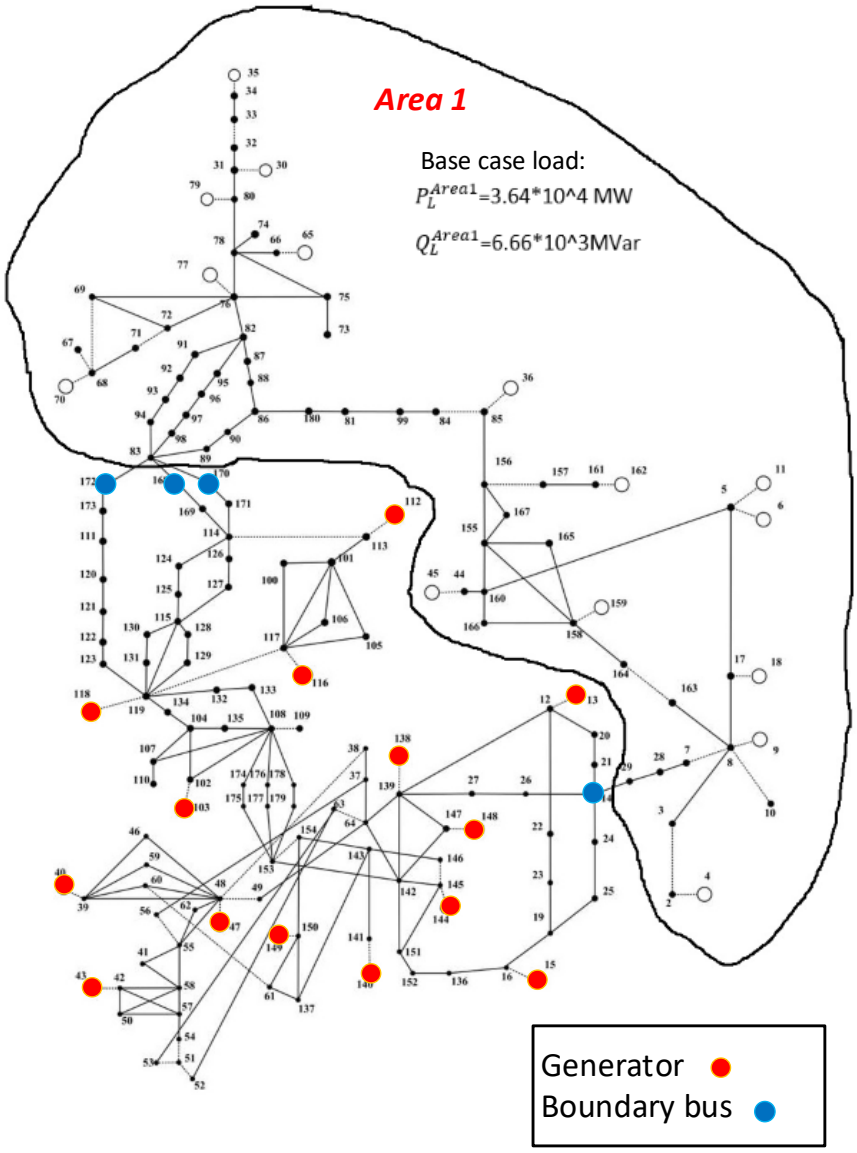

Figure 3.2 Area1 of WECC 179 bus system

3.2.1 Constructing the Ward- PV equivalent

Table 3-1 provides a comparison of the Ward-PV equivalent and the original system model

Table 3-1 Comparison of the equivalent system and the original system

Model	No. PQ Buses of External System	No. PV Buses of External System	No. Boundary Buses	No. Buses of Area 1	No. Buses of Entire System
WECC 179 Bus	89	14	4 (Bus 14,168,170,172)	72	179
Ward-PV equivalent system	None	14	4 (Bus 15,16 17,18)	72	90

3.2.2 Estimate the voltage stability margin

Use the proposed OPF model on the Ward-PV equivalent system to estimate the maximum allowable load of Area 1, represented by the optimal value of λ. In order to eliminate the impact of the tie lines connected to the WECC 179 system, load levels at the buses in Area 1 that are connected to large power import/export through tie lines are fixed. The initial λ is 1 and simulation results of this case based on the steady state OPF are shown in Table 3-2 and Table 3-3.

Table 3-2 System state at loading limits

λ_{max} (maximum of load)	$\lambda - 1$ (voltage stability margin)	System Status of the estimated point		
		P_g,Q_g constraints	*Voltage magnitude* constraints	S_b constraints
1.30	0.30	None	None	Bus26~28, 79~80, 80~84

The optimal solution provides the loading limit of area 1, i.e., 30% increase of the load in Area 1 from the base case loading. All constraints must be met.

3.2.3 TSAT validation

During the simulation, the load in Area 1 ramps up from 10 seconds and stays flat after 30 seconds. Loading at the buses connected to tie lines are fixed. The simulation time is 170 seconds. Some of the simulation results are given in Figure 3.3. It shows that the voltage profiles are declining and generators begin to lose synchronism once the load in Area 1 is increased to 1.26 times of the base case.

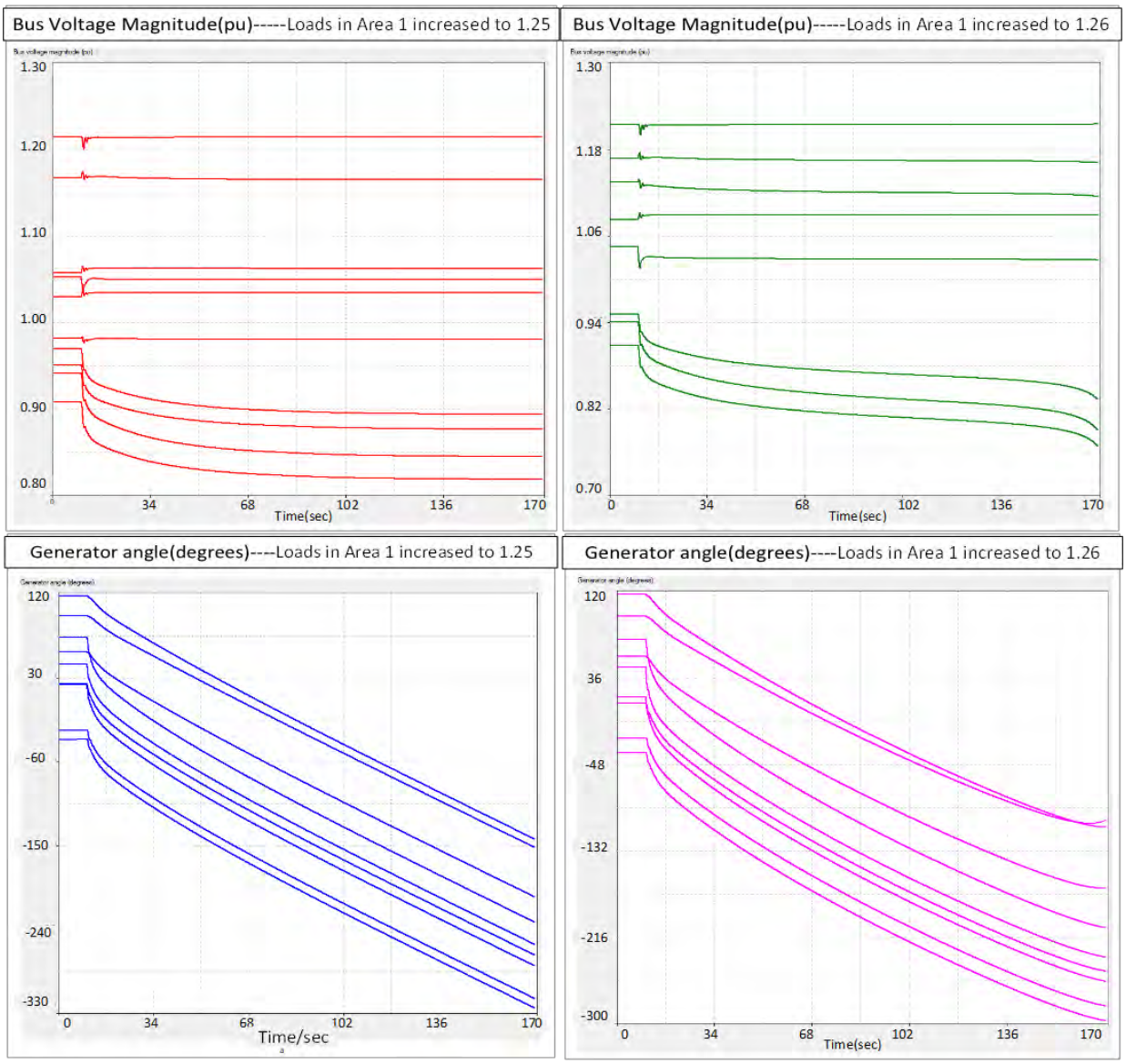

Figure 3.3 System states for loads in area1increased to1.25 or 1.26

To incorporate the control of exciters in TSAT into OPF-LI, the voltage magnitudes at PV buses in OPF-LI model are fixed. The results are compared in Table 3-3.

Table 3-3 Comparison of OPF-LI and TSAT

Indices name	**OPF-LI**	**TSAT**	**OPF-LI (fixing V of PV buses)**
Index value	1.30	1.25	1.18
Computation Time	11s	-	11s

Compare TSAT with OPF_LI : the simulation results of TSAT is a bit lower than that of OPF-LI. Since TSAT utilizes the system dynamic models to perform time domain simulation, the collapse point may be different from the maximum point of OPF-LI, which is based on a steady state model with system constraints.

Compare TSAT with OPF-LI (Fixing V of PV bus): The voltages at PV buses in OPF-LI model are fixed, similar to the function of exciters in the TSAT dynamic model. Since there is no power flow constraint in TSAT, the results of OPF-LI with constant V are lower than those of TSAT.

3.3 Summary

A new method to estimate the loading limit for load area is developed which includes the Ward-PV equivalent and OPF based algorithm. By the Ward-PV equivalent, the network reduction can be obtained, so that the computational speed for the optimization will be higher. OPF-LI approximates the loading margin directly, which represents the stability margin for the load area.

4. OPF-LI with state calculator

4.1 PMU measurement-based state calculator

A computational tool called the State Calculator (SC) is developed to approximate the trajectory of state variables from the available PMU measurements. The SC was proposed in [14]. For a N-dimensional dynamic system:

$$\dot{X} = f(x) \tag{9}$$

Assume that state variables $x_1, x_2, \dots, x_k$ in $x(t)$, denoted by x_M, are monitored by PMUs, while the remaining variables $x_{k+1}, \dots, x_n$, denoted by x_{UM}, are not. According to the differential equations of $x_M(t)$, the states at buses where PMUs are not available can be represented in terms of the known values in $x`_M(t)$. Therefore, x_{UM} is described by

$$\begin{cases} x_{UM}(t) = f_{UM}\big(x_{UM}(t), x`_M(t)\big) \\ x_{UM}(t_0) = x_{UM0} \end{cases} \tag{10}$$

The State Calculator estimates the unknown state variables x_{UM}at instant *l*+1 based on estimated values of x_{UM}at instant *l* and measured values of x_M at instant *l* and *l* +1. The predictor-corrector method of numerical integration is used to estimate the unmonitored states, i.e.,

$$\begin{aligned} \bar{x}_{UM}(t_0 + \Delta t) &= x_{UM}(t_O) + f_{UM}\big(x_{UM}(t_0), x`_M(t_0)\big)\Delta t \\ x_{UM}(t_0 + \Delta t) &= x_{UM}(t_O) + \frac{\Delta t}{2}\big[f_{UM}\big(x_{UM}(t_0), x`_M(t_0)\big) \\ &\quad + f_{UM}(\bar{x}_{UM}(t_0 + \Delta t), x`_M(t_0 + \Delta t))\big] \end{aligned} \tag{11}$$

Therefore, the state variables are approximated even though there are only limited PMU measurements. According to [14], an observability index can be used to determine the accuracy of the SC for a placement of the PMU units.

4.2 OPF-LI with SC

The proposed algorithm OPF-LI in this work is a hybrid method that uses PMU data and the network information. By using SC, the system dynamic states are approximated as time progresses. The generator electrical power P_e is calculated using rotor angle δ, generator dynamic states $E`_q, E`_d$, generator terminal voltage V_i . Since $x`_d = x`_q$:

$$\begin{aligned} I_i &= YV_i \\ I_i &= (I_{di} + jI_{di})e^{-j\left(\delta_i - \frac{\pi}{2}\right)} \\ P_{ei} &= E`_d I_{di} + E`_q I_{qi} \end{aligned} \tag{12}$$

Also, the system topology may change during the contingency, the equivalent system calculated by Ward-PV should be updated according to the updated Y bus. In order to utilize limited PMU measurements, the generator states P_e, V can be estimated by State Calculator, then the initial

value for OPF-LI are updated as the time step of simulation advances. Therefore, by incorporating the SC, the loading limit for the current transient state is estimated based on the limited PMU measurements.

4.3 Simulation results

The WECC 179-bus system is used to validate the proposed OPF-LI with SC. According to the observability index [8], the placement of PMU measurements for WECC 179 bus system is determined as shown Table 4-1.

Table 4-1 PMU placement

Numbers of PMUs	Generators with PMU measurements
15	1, 2, 5, 6, 7, 8, 9, 10, 11, 12, 15, 16, 17, 19, 24

The system has 29 generators, it is assumed that PMUs are available at generators shown in Table 4-1. Two fault scenarios are used as examples for analysis:

Case 1: A three-phase fault at generator bus 18 is applied at t=1second. The fault is cleared in 4 cycles and generator 18 is tripped. The simulation lasts for 100 seconds.

Case 2: A three-phase faults at line 114-124 is applied at t=1second. The fault is cleared in 4 cycles, and the line is de-energized. The simulation lasts for 100 seconds.

4.3.1 Simulation results: Case 1

Using TSAT time domain simulation results as the synthesized PMU data of the 15 generator buses, the states of other generators can be estimated by the SC for every cycle. The SC results are shown in Figure 4.1. It is observed that the system tends to be stable after tripping generator bus 18.

Incorporating the results of SC, OPF-LI for Area1 is calculated for every 5 seconds, and the results are shown in Figure 4.2.

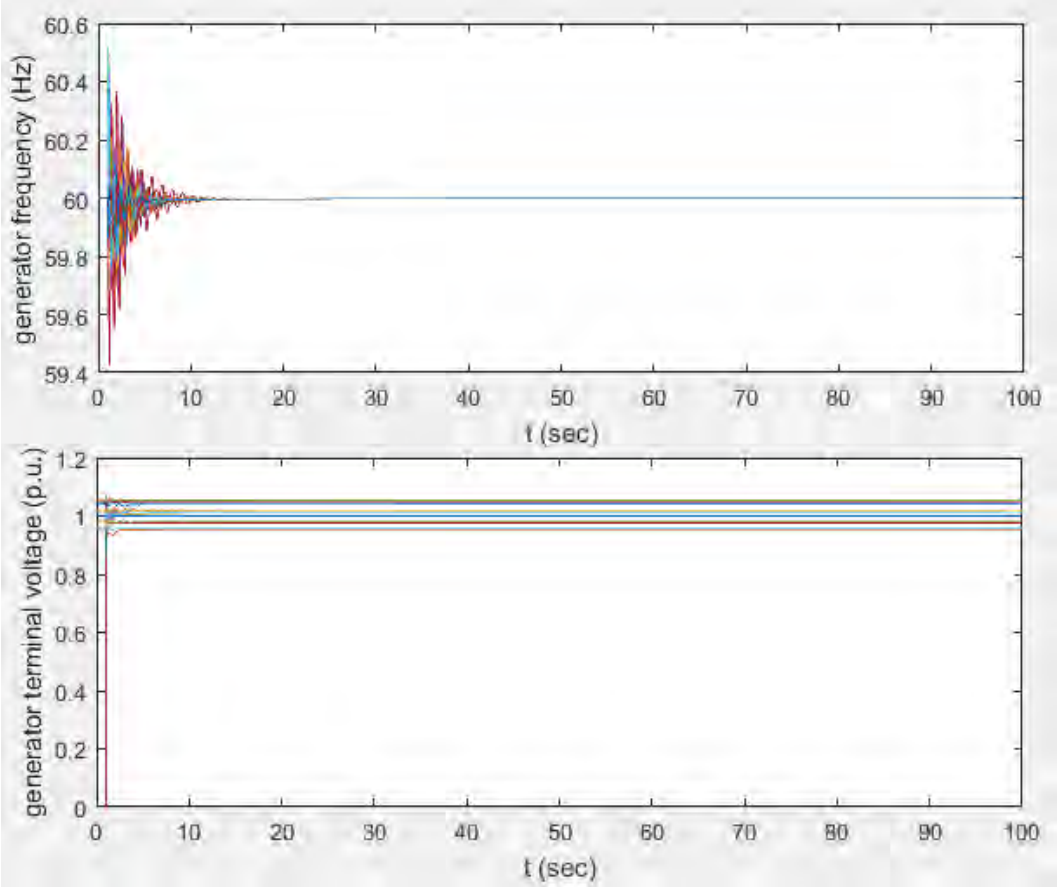

Figure 4.1 State calculator results—Case1

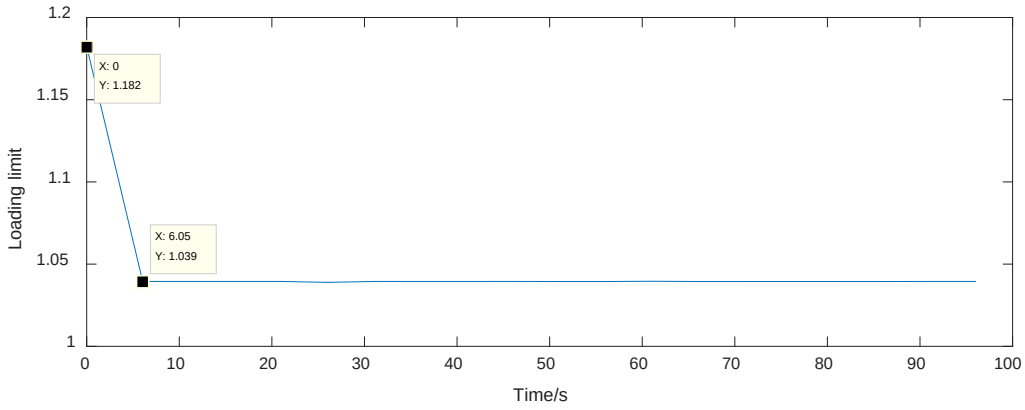

Figure 4.2 Loading limit following the contingency--Case 1

It is observed that the loading limit goes down to 1.039 due to generator tripping. Since the generator at bus 18, located in Area1, is tripped after the fault, the remaining generators, mostly from the external area, increased their output to make up for the lost generation causing the available transmission capacity to be reduced. Thus, the loading limit for Area1 decreased after the line fault.

4.3.2 Simulation results of Case 2

The SC results are shown in Figure 4.3. It is observed that the system tends to be stable after tripping the line 82-95. Incorporating the results of SC, the OPF-LI for Area1 is calculated every 5 seconds, and the results are shown in Figure 4.4.

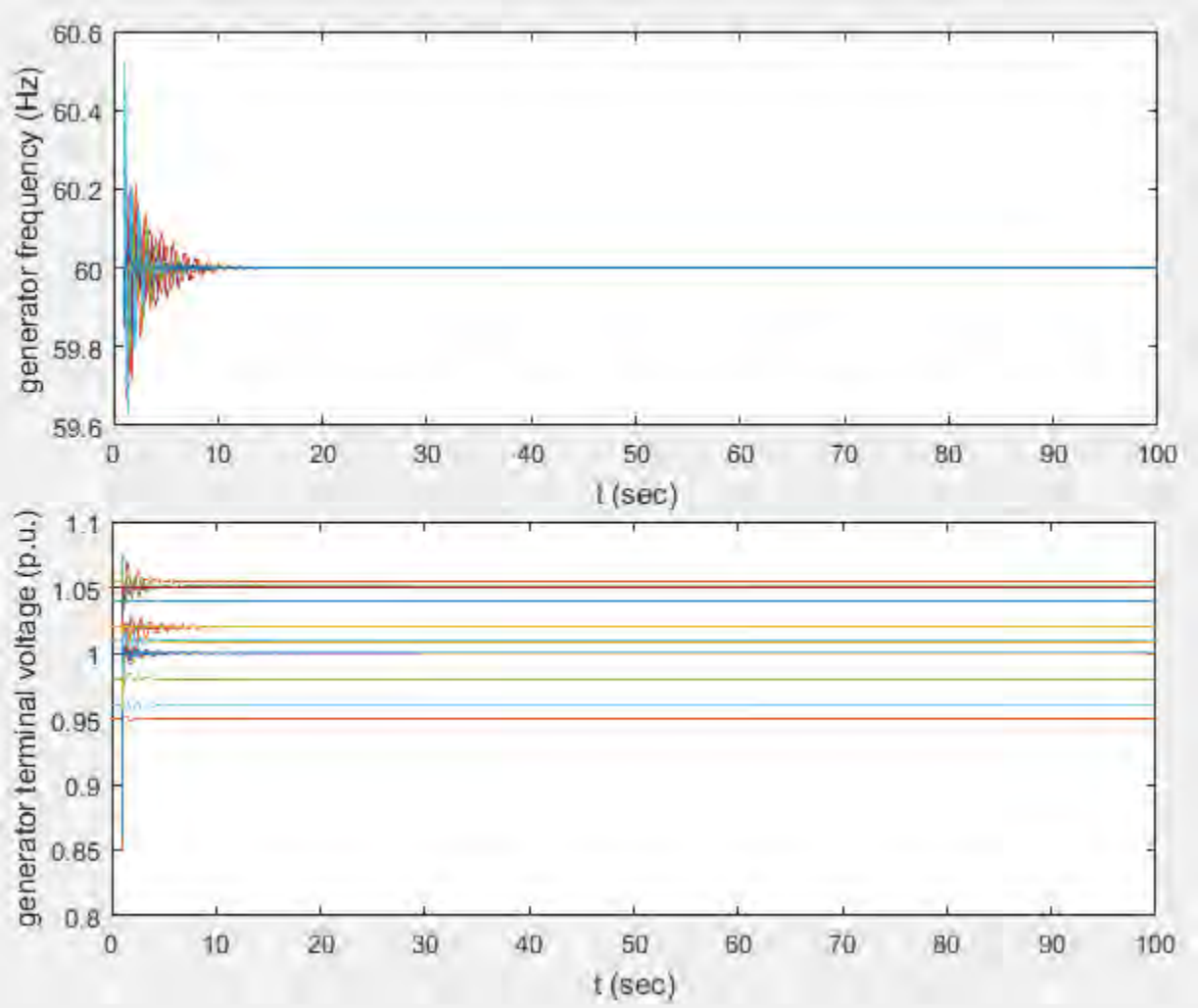

Figure 4.3 State calculator results—Case 2

As shown in Figure 4.4, the load margin of Area1 decreases to 1.011 after the line fault on Line 82-95. Line 82-95 inside Area1. The Ward-PV equivalent system is updated based on the change of system topology. Since a line is tripped, the line flow constraint of Line 82-95 no longer applies, furthermore the line flow for other lines will increase, causing the loading limit to be reduced. Although the system is stable, the reduced loading limit obtained by OPF-LI indicates that the system is stressed after the fault.

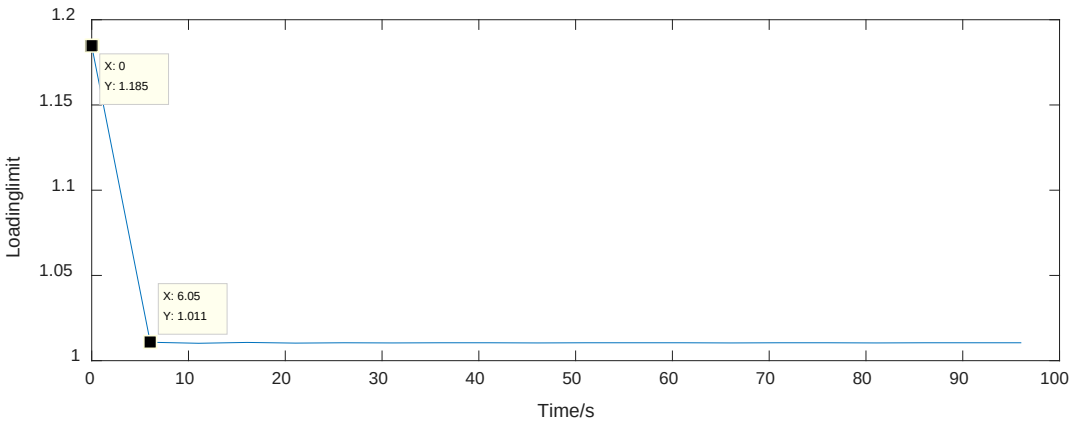

Figure 4.4 Loading limit during the contigency--Case 2

4.4 4.4 Summary

Utilizing the PMU measurements and the SC, the loading limit can be estimated based on limited PMU data from only a few buses. The predictor-corrector method of SC does not require iterations. Thus, it is faster than the implicit integration method. Also, the network reduction algorithm Ward-PV is included in the process for estimation of the load margin. Hence the proposed approach is a promising tool to meet the requirement of an on-line application.

5. OPF-LI with OLTC control

5.1 5.1 OLTC dynamic mechanism

5.1.1 OLTC model

One of the key mechanisms in load restoration is the voltage regulation performed automatically by the tap changing devices of power transformers. The tap changer controls the voltage magnitude of the secondary side V_2 by changing the transformer ratio r, as Figure 5.1 shows.

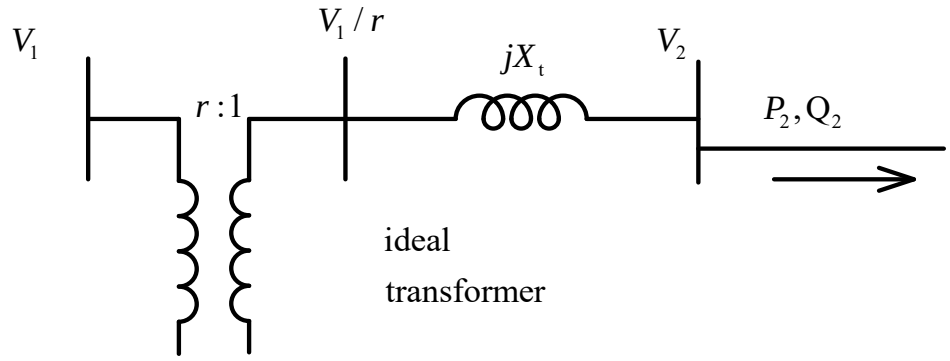

Figure 5.1 Equivalent circuit of a tap transformer

Practically, the tap positions are discrete and the OLTC is acting slowly because of the mechanical time delay and intentional time delay. A discrete model is [9]:

The LTC can operate at discrete time instants denoted by $t_k, k = 0,1, ...$

$$t_{k+1} = t_k + \Delta T_k \tag{13}$$

ΔT_k is not necessarily constant

$$\Delta T_k = T_d \frac{d}{|V_2 - V_2^0|} + T_f + T_m \tag{14}$$

T_d is the maximum time delay of the inverse-time characteristic; T_f"is the fixed intentional time delay, T_M is the mechanical time.

$$r_{k+1} = \begin{cases} r_k + \Delta r & if \quad V_2 > V_2^o + d \; and \; r_k < r^m \\ r_k - \Delta r & if \quad V_2 < V_2^o + d \; and \; r_k > r^m \\ r_k & otherwise \end{cases} \tag{15}$$

For an analytical study, the following continuous model is adopted.

The continuous OLTC model is based on the assumption of a continuously changing tap (t), which can take all real values between $r^{min}\ an\ r^{max}$.

$$\frac{dr}{dt} = \frac{1}{T}(V_2 - V_2^0) \qquad r^{min} \le r \le r^{max} \tag{16}$$

r is the tap ratio, T is time constant. The continuous LTC model is less accurate than discrete ones, but it is useful approximation, particularly convenient for analytical purposes.

5.1.2 OLTC dynamic mechanism for a simple system

By utilizing the continuous OLTC model presented before, the stability analysis for a simple power system is investigated in [16], as Figure 5.2 shows.

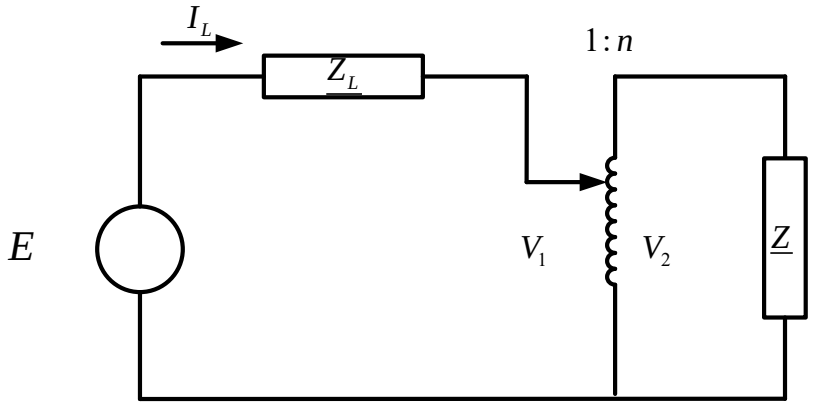

Figure 5.2 A simple power system with an OLTC

For this system, the load voltage is described by

$$V_2 = \frac{E}{Z_L + Z/n^2} * \frac{Z}{n} = \frac{nEZ}{n^2 Z_l + Z} \tag{17}$$

Based on the load voltage and tap changer continuous model, the dynamic system equation can be obtained as

$$\frac{dn}{dt} = \frac{1}{T}(V_o - \frac{nEZ}{[n^4 Z_l^2 + 2n^2 Z Z_l \cos(\theta_l - \theta) + Z^2]^{0.5}}) \tag{18}$$

Based on the two equations, the relationship between dn/dt and n can be determined, also V_2 and n. As shown in Figure 5.3, the equilibrium points n_{10}, n_{20} divide the tap positions into three intervals. Based on the sign of dn/dt in the intervals $(0, n_{10})$, (n_{10}, n_{20}), (n_{20}, ∞), the dynamic behavior of the tap changer can be illustrated in 5.3 (c).

Hence the region of attraction is $(0,n_{20})$, the stable equilibrium is n_{10}. In case the tap position is beyond n_{20}, n will increase since $\frac{dn}{dt} > 0,$ however load voltage V_2 falls down, which will serve as a cause for voltage collapse. Figure 5.3(d) shows the dynamic behavior for an OLTC in a discrete model, similar with the continuous model in Figure 5.3(c).

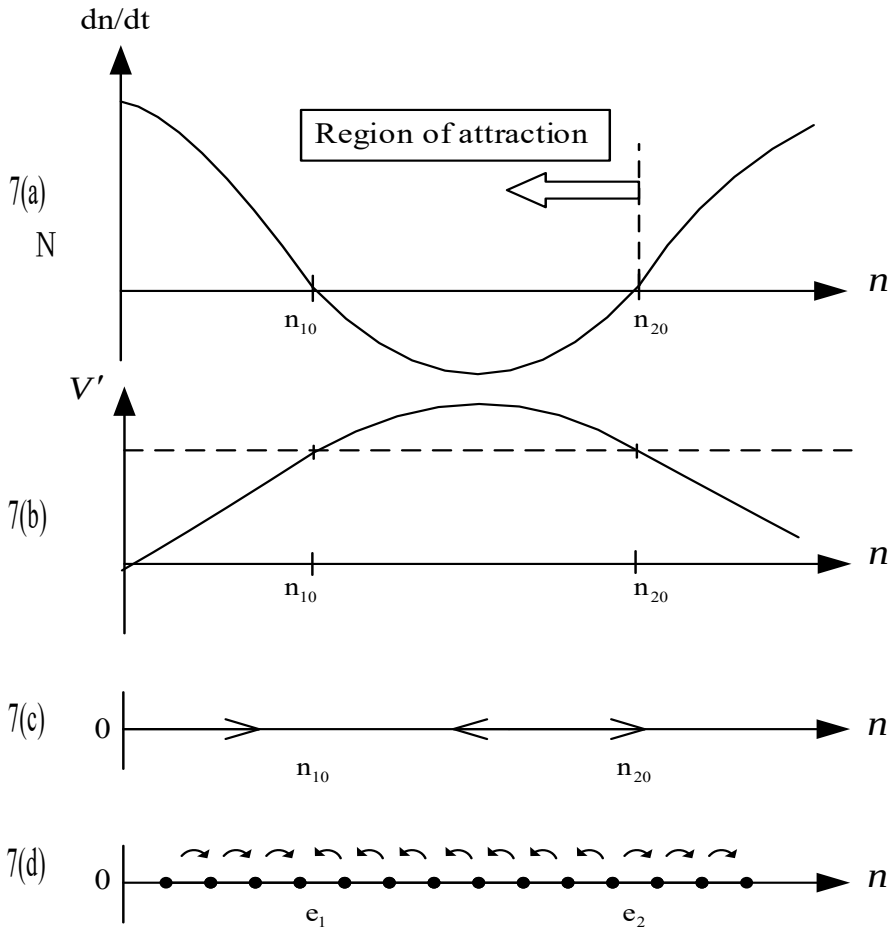

Figure 5.3 Dynamic mechanism for one OLTC system

5.1.3 OLTC dynamic mechanism for power system with M OLTCs

Generalizing the stability analysis presented before to a power system with M OLTCs, the system can be modeled by a differential-algebraic system as follows:

$$\begin{aligned} \dot{x} &= f(x,y,p) \\ 0 &= g(x,y,p) \end{aligned} \tag{19}$$

where $x \in X^n$ represents the dynamic state variables, i.e., generator voltages and rotor phases, $y \in Y^m$ are the other variables, i.e., bus voltages and other rotor flow variables. The parameter space P is composed of system parameters, e.g., the system topology, and transformer ratios. Focusing

on tap changer dynamics, the time scale is longer than that corresponding to generator dynamics, therefore it is acceptable to neglect the transient dynamics $\dot{x}$, by

$$0 = f(x, y, p) \tag{20}$$

Incorporating the continuous model for OLTC, the equilibrium points for the system model will be found by solving

$$\begin{cases} \dfrac{dr}{dt} = \dfrac{\Delta V}{T} = 0 \\ f(x, y) = 0 \\ g(x, y, r) = 0 \end{cases} \tag{21}$$

For a nonlinear system, linearization is performed around each equilibrium. Then Jacobian A will be used to determine whether this equilibrium is stable or not. However, since the system model is much more complex for a system with M OLTCs, there should be multiple equilibrium points. It will be difficult to calculate the regions of attraction. Therefore, a direct way is to describe the voltage recovery region. The voltage recovery region [15] is an area in which all bus voltages will go up with respect to time when there is a low voltage condition.

5.2 OLTC operating control

In order to improve the power system operating condition, the proposed OLTC operating control is presented blow, where k denotes the time step.

OLTC Operation:

$$\text{tap(k)-tap(k-1)} = 0/\text{-}1/1 \qquad \text{tap}^{-} \le \text{tap}(k) \le \text{tap}^{+} \tag{22}$$

If $V(k) - V_{ref} \geq \Delta V_{ref}$

$$tap(k+1) - tap(k) = 1 \tag{23}$$

Else if $V(k) - V_{ref} \leq -\Delta v_{ref}$

$$tap(k+1) - tap(k) = -1 \tag{24}$$

Else if $\left|V(k) - V_{ref}\right| < \Delta v_{ref}$

$$tap(k+1) - tap(k) = 0 \tag{25}$$

OLTC blocking:

If $tap(k) - tap(k-1) = -1 \quad AND \;\; V(k) - V(k-1) \leq 0$

$$tap(k+1) = tap(k) \tag{26}$$

The principle for OLTC Operation is based on the discrete model of the OLTC. Furthermore, it is noted that the tap changer will be blocked as soon as $\Delta tap < 0 \; and \; \Delta V < 0$. In other words, although the tap changer tries to raise the load side voltage to correct the deviation of load voltage from the set point, the voltage magnitude can still decreases due to the limitation of the OLTC control principle. Based on the analysis for the voltage recovery region, the criteria of OLTC blocking is developed. By utilizing the relation between Δtap and ΔV, OLTC blocking control is implemented.

5.3 OPF-LI with OLTC control

The proposed approach OPF-LI is used to estimate the loading limit for a load area by the OPF based algorithm. The optimization is subject to the network constraint and some inequality constraints. Base on the proposed OLTC control strategies, the dynamics of OLTC are incorporated to modify the loading limit. The flowchart is shown in Figure 5.4.

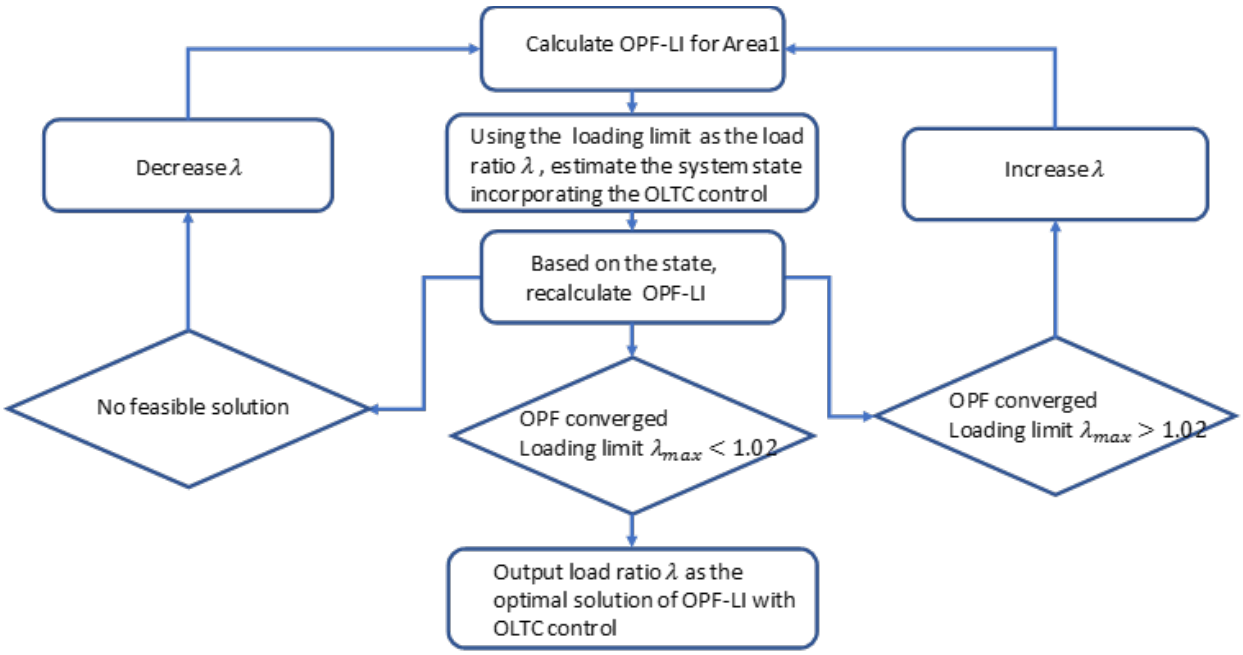

Figure 5.4 OPF-LI with OLTC operating control

The flowchart in Figure 5.4 illustrates the procedure to estimate the loading limit with the effect of OLTC operating control introduced in Section 5.2. The WECC 179 bus system is used for testing. The detailed procedure is given below:

Step1: Calculate the loading limit λ_{max} for the base case loading.
Step2: Using λ_{max} as the initial load ratio λ_0 to update the loading, the operation of OLTC is triggered.
Step3: Calculate the OPF-LI with the updated system states after the OLTC operation.

Step4: Compare OPF-LI solution with the criteria. If loading margin is still available, λ should go up for the next iteration. On the other hand, if the loading margin is close to 0 so that the OPF algorithm cannot converge, λ will decrease for the next iteration. It is indicated that the loading limit is not final once λ is modified.

Step5: Back to Step1 and recalculate the OPF-LI.

Step6: Determine the loading limit incorporating the OLTC control. Once OPF-LI solution falls below the setting limit 1.02, the load ratio λ_n will be the value which is the actual loading limit.

5.4 Simulation results

The WECC 179 bus system is used to implement the proposed OLTC operating control. Assume that the load of Area1 increases to 1.18 times from the base case loading. Because of the load increase, OLTCs are triggered by the voltage deviation. The simulation results are shown Figure 5.5, Figure 5.6.

Blue curve: voltage profile of the voltage reference;

Red cure: voltage profile at the beginning of tap operation;

Green cure: voltage profile with OLTC blocking control.

X axis: Bus number of 179 bus system

Y axis: Voltage magnitude

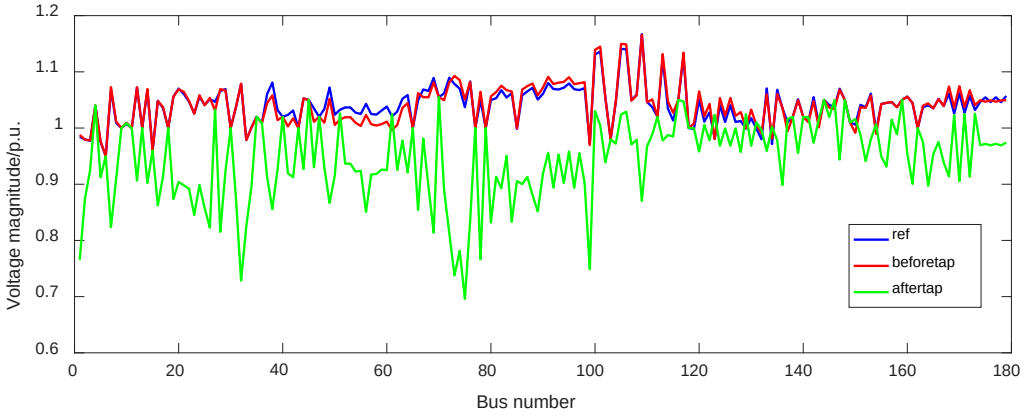

Figure 5.5 Comparison of voltage profiles—without OLTC blocking control

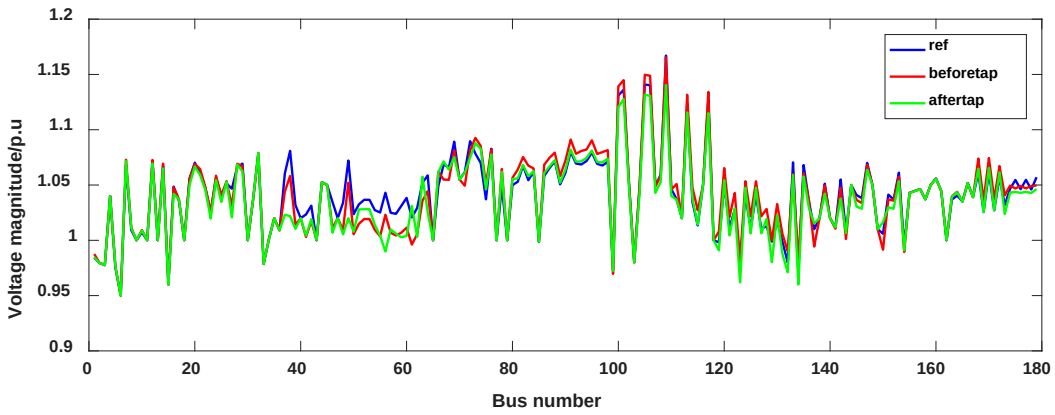

Figure 5.6 Comparison of voltage profiles—with OLTC blocking control

Table 5-1 Comparison of voltage magnitude for blocked bus

Bus number	V before tap operation	V after tap operation (without OLTC blocking)	V after tap operation (with OLTC blocking)	Voltage change (without OLTC blocking)	Voltage change (with OLTC blocking)
46	1.0348	0.9301	1.0069	-0.1047	-0.0279
47	1.0200	1.0200	1.0200	0	0
48	1.0340	0.9295	1.0054	-0.1045	-0.0286
50	1.0236	0.9153	1.0079	-0.1083	-0.0157
53	1.0366	0.9367	1.0281	-0.0999	-0.0085

Figure 5.5 illustrates that the voltage profile for the 179-bus system, represented by the green curve, is not improved after the tap operation. It is observed that the voltage of most buses drops comparing with the red curve. Without OLTC blocking, the tap changing cause the voltage drops when the operating point falls out of the recovery region. In this case, some tap changers are blocked at the maximal position when the tap ratio reaches the upper or lower limits, so that the system condition does not collapse deteriorate.

As shown in the green curve in Figure 5.6, the voltage profile is improved due to OLTC blocking control. Along with the operation, OLTCs located at transformer buses 46, 47, 48 ,50, 53 are blocked based on the criteria discussed in the previous section. By doing so, the dynamic behavior of OLTC is improved and the system condition is restored without having a voltage collapse.

It is observed from Table 5-1 that the voltages at the blocked buses (46, 47, 48 ,50, 53) decrease by 0.1 p.u. after the OLTC operation since no blocking control is adopted. The voltage change for the case with OLTC blocking shows that the blocking strategy prevents these critical buses from a collapse.

Table 5-2 Comparison of base case load case and light load case

	Base case load case	Light load case (Reduce heavy load for 10%)
OPF-LI without OLTC blocking control	1.1742	1.5090
OPF-LI after OLTC blocking control	1.2742	1.7890
The number of blocked taps	5	1

As shown in Table 5-2 shows, for the base case loading, the loading limit estimated by the original OPF-LI is 1.1742. Then the loading limit increases to 1.2742 with the OLTC blocking. OLTC as a critical device can regulate the load voltage efficiently, hence the loading margin will increase. However, the base case loading of the WECC system is heavy. Some of the taps changers are blocked to prevent instability during the operation. That is why the loading limit can only increase by 0.1 with respect to the line flow constraints and the generation constraints.

To investigate the performance of the proposed OLTC blocking control, a heavy load scenario with more than 2000 MVA in the 179 bus system is reduced by 10%. In this case, the loading limit before tap is 1.5090. However, the loading limit is modified to 1.7890 after the OLTC blocking control. Since the system is not as stressed as the base case, only one tap changer is blocked when the load is increased to 1.789.

5.5 Summary

Based on the dynamic mechanism of OLTCs, an OTLC blocking control is proposed. The OTLC blocking control can prevent these critical buses from unstable operating conditions. OPF-LI is modified to incorporate the proposed OLTC control and, as a result, the loading limit has been improved. By utilizing the relation between Δtap and ΔV, the proposed OLTC blocking strategy prevents the undesirable tap changes once the position falls within an unstable condition.

6. Conclusions

In this project, two methods VSAI and OPF-LI are proposed for the assessment of long-term voltage stability for power systems. This work includes four parts:

1) VSAI is a Thevenin Equivalent based indictor. By estimating the Thevenin impedance at a load bus, the index can indicate whether the system at this operation point is stable or not. However, it may not be accurate as the system model is radically simplified into a two-node system.
2) To extend the TE-based model from a 2-node model to a multiple bus model, a new method to estimate the loading limit for a load center is developed which includes the Ward-PV equivalent and an OPF based algorithm. By the Ward-PV equivalent, the network reduction can be obtained so that the computational speed for the optimization will be high. OPF-LI approximates the loading margin for the load area.
3) In order to utilize the limited number of available PMUs, the State Calculator is used to approximate the system states in an on-line environment. OPF-LI with SC can estimate the loading limit based on the limited PMU data. The predictor-corrector method of SC does not require iterations. Thus, it is faster than the implicit integration method. Also, the network reduction algorithm Ward-PV is included in the process estimating the load margin. Hence, the proposed approach is efficient.
4) Since the solution of OPF-LI is derived from power flow constraints, the dynamic mechanism of OLTC should be incorporated to obtain a realistic optimal solution. A novel OTLC blocking control is proposed. The OTLC blocking control can prevent these critical buses from unstable operating conditions. The loading limit incorporating the proposed OLTC blocking control is an improved index. Utilizing the relation between $\Delta \mathrm{tap}$ and ΔV, the new OLTC blocking strategy can prevent undesirable tap operations once the position falls under unstable conditions.

References

[1] K. T. Vu, C. C. Liu, C. W. Taylor and K. M. Jimma, "Voltage instability: mechanisms and control strategies [power systems]," *Proceedings of the IEEE*, vol. 83, no. 11, pp. 1442-1455, Nov 1995.

[2] T. Cutsem and C. Vournas, *Voltage stability of electric power systems*. New York: Springer, 2008.

[3] K. Vu, M. M. Begovic, D. Novosel and M. M. Saha, "Use of local measurements to estimate voltage-stability margin," in *IEEE Transactions on Power Systems*, vol. 14, no. 3, pp. 1029-1035, Aug 1999.

[4] I. Smon, G. Verbic and F. Gubina, "Local voltage-stability index using tellegen's Theorem," in *IEEE Transactions on Power Systems*, vol. 21, no. 3, pp. 1267-1275, Aug. 2006.

[5] S. Corsi and G. N. Taranto, "A Real-Time Voltage Instability Identification Algorithm Based on Local Phasor Measurements," in *IEEE Transactions on Power Systems*, vol. 23, no. 3, pp. 1271-1279, Aug. 2008.

[6] F. Hu, K. Sun, A. Del Rosso, E. Farantatos and N. Bhatt, "Measurement-Based Real-Time Voltage Stability Monitoring for Load Areas," in *IEEE Transactions on Power Systems*, vol. 31, no. 4, pp. 2787-2798, July 2016.

[7] B. Gao, G. K. Morison and P. Kundur, "Voltage stability evaluation using modal analysis," in *IEEE Transactions on Power Systems*, vol. 7, no. 4, pp. 1529-1542, Nov 1992.

[8] V. Ajjarapu and C. Christy, "The continuation power flow: a tool for steady state voltage stability analysis," in *IEEE Transactions on Power Systems*, vol. 7, no. 1, pp. 416-423, Feb 1992.

[9] N. Flatabo, R. Ognedal and T. Carlsen, "Voltage stability condition in a power transmission system calculated by sensitivity methods," in *IEEE Transactions on Power Systems*, vol. 5, no. 4, pp. 1286-1293, Nov 1990.

[10] F. Capitanescu and T. Van Cutsem, "Unified sensitivity analysis of unstable or low voltages caused by load increases or contingencies," in *IEEE Transactions on Power Systems*, vol. 20, no. 1, pp. 321-329, Feb. 2005.

[11] R. S. Diao, K. Sun, V. Vittal, R. O'Keefe, M. Richardson, N. Bhatt, D. Stradford and S. Sarawgi, "Decision Tree-Based Online Voltage Security Assessment Using PMU Measurements", *IEEE Transactions on Power Systems*, vol. 24, no. 2, pp. 832-839, 2009.

[12] S. S. Biswas and A. K. Srivastava, "Voltage Stability Monitoring in Power Systems, " U.S. Patent, Feb. 25, 2014

[13] F. Wu and A. Monticelli, "Critical review of external network modelling for online security analysis", *International Journal of Electrical Power & Energy Systems*, vol. 5, no. 4, pp. 222-235, 1983.

[14] G. Wang, C. C. Liu, N. Bhatt, E. Farantatos and M. Patel, "Observability of nonlinear power system dynamics using synchrophasor data", *International Transactions on Electrical Energy Systems*, vol. 26, no. 5, pp. 952-967, 2015.

[15] K. Vu and C. C. Liu, "Dynamic mechanisms of voltage collapse", *Systems & Control Letters*, vol. 15, no. 4, pp. 329-338, 1990.

[16] C. C. Liu and K. Vu, "Analysis of tap-changer dynamics and construction of voltage stability regions," in *IEEE Transactions on Circuits and Systems*, vol. 36, no. 4, pp. 575-590, Apr 1989.

Appendix D.
Oregon Schedule 5—Time-of-Day Pilot Plan

This page left blank intentionally.

SCHEDULE 5
RESIDENTIAL SERVICE
TIME-OF-DAY PILOT PLAN
(OPTIONAL)

AVAILABILITY

Service under this schedule is available at points on the Company's interconnected system within the State of Oregon to residential Customers where existing facilities of adequate capacity and desired phase and voltage are adjacent to the Premises to be served, additional investment by the Company for new transmission, substation, or terminal facilities is not necessary to supply the desired service, and Advanced Metering Infrastructure (AMI) is installed. Service under this pilot schedule is limited to no more than 375 metered service points.

The Residential Service Time-of-Day Pilot Plan is an optional, voluntary service that provides residential Customers the option to take electric service with seasonal time-of-day energy rates.

If a Customer requests to participate in this pilot schedule, the Customer will be placed on the schedule effective with their next billing cycle.

A Customer may terminate their participation on this schedule at any time. However, the Customer may not subsequently elect service under this schedule for one year after the effective date of cancellation. If a Customer requests to be taken off of the schedule, the Customer will be removed from the schedule as of the last meter read date.

APPLICABILITY

Service under this schedule is applicable to Electric Service required for residential service Customers for general domestic uses, including single phase motors of 7½ horsepower rating or less, subject to the following conditions:

1. When a portion of a dwelling is used regularly for business, professional, or other gainful purposes, or when service is supplied in whole or in part for business, professional, or other gainful purposes, the Premises will be classified as non-residential and the appropriate general service schedule will apply. However, if the wiring is so arranged that the service for residential purposes can be metered separately, this schedule will be applied to such service.

2. Whenever the Customer's equipment does not conform to the Company's specifications for service under this schedule, service will be supplied under the appropriate General Service Schedule.

3. This schedule is not applicable to standby service, service for resale, or shared service.

The Company shall have the right to select and reject pilot participants at its sole discretion.

TYPE OF SERVICE

The type of service provided under this schedule is single phase, alternating current at approximately 120 or 240 volts and 60 cycles, supplied through one meter at one Point of Delivery. Upon request by the owner of multi-family dwellings, the Company may provide 120/208 volt service for multi-family dwellings when all equipment is Underwriters' Laboratories, Inc. approved to operate at 120/208 volts.

SCHEDULE 5
RESIDENTIAL SERVICE
TIME-OF-DAY PILOT PLAN
(OPTIONAL)
(Continued)

WATER HEATING

All electric water heating equipment, including water storage and tankless water heaters (hot water on demand), shall conform to specifications of the Underwriters' Laboratories, Inc. and the Company. The installation of the water heating equipment shall conform to all National, State, and Municipal Codes. No single electric water heating unit shall exceed 6 kW; and where two or more heating units are used, these units shall be so interlocked that not more than 6 kW can be connected at any one time.

Where electric water heaters not complying with these specifications are installed, the Customer will be required to pay the original installation or upgrade costs for any nonstandard facilities needed to supply the electrical capacity to meet the water heater demand. Water heating equipment must not impair or interfere with service to any other customer.

RESIDENTIAL SPACE HEATING

All space heating equipment to be served by the Company's system shall be single phase equipment approved by Underwriters' Laboratories, Inc., and the equipment and its installation shall conform to all National, State and Municipal Codes and to the following:

Individual resistance-type units for space heating larger than 1,650 watts shall be designed to operate at 240 or 208 volts, and no single unit shall be larger than 6 kW. Heating units of two kW or larger shall be controlled by approved thermostatic devices. When a group of heating units, with a total capacity of more than 6 kW, is to be actuated by a single thermostat, the controlling switch shall be so designed that not more than 6 kW can be switched on or off at any one time. Supplemental resistance-type heaters, that may be used with a heat exchanger, shall comply with the specifications listed above for such units.

SUMMER AND NON-SUMMER SEASONS

The summer season begins on June 1 of each year and ends on August 31 of each year. The non-summer season begins on September 1 of each year and ends on May 31 of each year.

TIME PERIODS

The time periods are defined as follows. All times are stated in Mountain Time.

Summer Season

Peak:	3:00 p.m. to 9:00 pm. Monday through Friday
Off-Peak:	9:00 p.m. to 3:00 p.m. Monday through Friday and all hours on weekends and holidays

Non-summer Season

Peak:	7:00 a.m. to 9:00 a.m. and 3:00 p.m. to 9:00 p.m. Monday through Friday
Off-Peak:	9:00 p.m. to 7:00 a.m. and 9:00 a.m. to 3:00 p.m. Monday through Friday and all hours on weekends and holidays

SCHEDULE 5
RESIDENTIAL SERVICE
TIME-OF-DAY PILOT PLAN
(OPTIONAL)
(Continued)

TIME PERIODS (Continued)

Holidays are New Year's Day (January 1), Memorial Day (last Monday in May), Independence Day (July 4), Labor Day (first Monday in September), Thanksgiving Day (fourth Thursday in November), and Christmas Day (December 25). If New Year's Day, Independence Day , or Christmas Day falls on Saturday, the preceding Friday will be designated a holiday. If New Year's Day, Independence Day, or Christmas Day falls on Sunday, the following Monday will be designated a holiday.

MONTHLY CHARGE

The Monthly Charge is the sum of the following charges, and may also include charges as set forth in Schedule 55 (Annual Power Cost Update), Schedule 56 (Power Cost Adjustment Mechanism), Schedule 91 (Energy Efficiency Rider), Schedule 93 (Solar Photovoltaic Pilot Program Rider), Schedule 95 (Adjustment for Municipal Exactions), and Schedule 98 (Residential and Small Farm Energy Credit).

Service Charge, per month	$8.00
Energy Charge, per kWh	
Summer	
Peak	13.1739¢
Off-Peak	13.0403¢
Non-summer	
Peak	8.0547¢
Off-Peak	7.9514¢

PAYMENT

The monthly bill rendered for service supplied hereunder is payable upon receipt, and becomes past due 15 days from the date on which rendered.

Appendix E.
Effects of Solar Intensity Variations on Distribution Feeder Load Report

This page left blank intentionally.

The Effects of Solar Intensity Variations on Distribution Feeder Load

Prepared by Delivery Planning's
Research, Development and Deployment Team
05/26/2015

Executive Summary

In late 2012 / early 2013, the discussion began by questioning how residential PV systems' intermittent inoperability during cloudy conditions would affect the loads on the distribution feeders upon which the PV panels are interconnected. That discussion led to the research project, *Effect of Solar Intensity Variations on Feeder Load* (Budget ID RDND130002, Work Order 27386761) under the supervision of RD&D's project manager, Phil Anderson.

Two questions emerged that formed the basis of the research design that followed:

1. Is there a statistical relationship (correlation) between solar intensity and load?
2. What other relationships are there between load and meteorological parameters (such as wind speed and ambient temperature)?

A project plan designed to answer those questions was drafted in April 2013. According to the plan, the scope of the research project included the following tasks:

1. Study a residential feeder to determine weather / solar monitoring locations.
2. Install weather/solar stations and gather solar, weather, and load data.
3. Study the data looking for possible correlations and understanding of the coupling.
4. Develop a report on the value of distributed solar generation on peak load matching, in general, and as a source of generation, specifically.

To meet the scope and budget of the project, and in an attempt to answer the research questions, a pilot study limited to a single distribution feeder containing three solar irradiance weather stations (SIWSs) was designed. The method for performing the study included the following four chronological steps:

1. Choose a residential feeder.
2. Design and install the model weather / solar stations.
3. Gather solar, weather, and load data.
4. Analyze the data for possible correlations / understanding of the coupling.

Locust-044 in Capital region was chosen as the residential feeder, and each of the three SIWSs located along the feeder route were designed so that they collected global horizontal irradiance (GHI), westerly and southerly point-of-array (POA) wind speed, wind direction, ambient temperature, and GPS time synchronization data.

Research Study Findings

Analysis of the data gathered from the three solar irradiance weather stations was made over the research study's time period set between June 21, 2013, and September 21, 2013. Based on that analysis, following are the study's results.

First, there seems to be a statistical relationship (correlation) between solar intensity and load.

- Solar intensity data collected from the southerly-configured sensor at the three SIWSs tends to lead load from 3.96 to 4.13 hours with a correlation of 0.94 across all three locations.
- Solar intensity data collected from the global-configured sensor at the three SIWSs tends to lead load from 4.00 to 4.02 hours with a correlation ranging from 0.95 to 0.96.
- Solar intensity data collected from the westerly-configured sensor at the three SIWSs tends to lead load from 1.76 to 1.94 hours with a correlation ranging from 0.88 to 0.91.

There also seems to be a strong correlation between ambient temperature data and load data, but at best a tepid correlation between wind speed data and load data.

- Ambient temperature measured at the three SIWSs tends to lead load from 0.70 to 0.86 hours with a correlation ranging from 0.96 to 0.97 across all three locations.
- Wind speed measured at the three SIWSs tends to lead load from 1.80 to 2.38 hours with a correlation ranging from 0.68 to 0.70 across all three locations. This tepid statistical relationship between wind speed and load also was not a surprising result, considering the low auto-correlation results applied to wind speeds.

Recommendations for Moving Forward

So far, the data has already been used within the OpenDSS software in performing generation interconnection studies of large photovoltaic systems, both at the feasibility level and at the system impact level. It has also been used in support of a report on various energy storage applications, and how energy storage can be used in collaboration with photovoltaic systems in reducing the effects of feeder summer peak loads. Other ways the data has been used is in assisting with resource planning as part of Idaho Power's integrated resource plan as well as in collaboration with Sandia National Laboratories for their variability and GHI to POA conversion studies.

A couple additional possibilities for immediately applying the research data and results would be for:

- Recommending preferred photovoltaic orientations to commercial customers for their rooftop applications that would best support reducing the effects of feeder summer peak loads. Perhaps an energy efficiency program could be developed, offering incentives to such commercial customers, to configure their systems such that Idaho Power could also benefit.
- Designing a demonstration project of photovoltaic system coupled with energy storage to extend peak load reduction at the end of a distribution feeder. In fact, such a design process has already begun.

Some potential areas for future research include:

- Analyzing the ten-second data, time shifted according to photovoltaic orientation, to see the more granular relationship between solar irradiance and distribution feeder load.
- Calculating and analyzing the solar energy density (Watt-hours/m^2) per time interval for each site at each solar intensity orientation.
- Running the irradiance statistics over a multi-day time period to see if a relationship is evident as a predictor of the seasonal peak load.
- Analyzing data from other seasons of the year to see what similarities and differences might result.
- Including cross-correlations of solar to wind to see if there are any complimentary relationships to one another.
- Collecting and analyzing data from additional feeder-types where solar might be of interest, such as the areas where there have been historical interest in large solar projects as well as areas where clusters of net metering customers are emerging.
- Including variability / volatility as part of irradiance statistical analyses.

Table of Contents

List of Figures

Introduction

Based on empirical observation, there appears to be a relationship between solar intensity and distribution system load; however, that observation had yet to be tested. Idaho Power Company's (IPC's) Research, Development, and Deployment (RD&D) team was tasked in early 2013 to research the topic via the design of a project to install solar irradiance weather stations along the path of a distribution feeder as a way to determine if the prudent use of solar panels might help to offset distribution loads during times of the feeder peak.

The premise of the research study was to analyze solar intensity data collected from May 21, 2013 through September 21, 2013. The data for the study was collected from three different sites in Boise, Idaho, which were located equidistantly along the Locust-044 feeder within 2 miles of one another.

This report documents the design process involved with the study. It provides the background including literature review and research questions, the research scope, the research methods, the results of the data collection process, an analysis of the data collected, and a discussion.

The results of the study show that there is a statistically significant relationship between solar intensity and load, but that correlation is optimally significant when the solar intensity and load variables are time-shifted.

Background

In late 2012 / early 2013, the discussion began by questioning how residential PV systems' intermittent inoperability during cloudy conditions would affect the loads on the distribution feeders upon which the PV panels are interconnected.

An idea that emerged during that discussion was that the effect of cloud cover on PV operability could be less than expected because the cloud cover might also have a similar effect on distribution feeder loading; in other words, as the solar intensity (and thus PV operability) decreases, so also might the loading on the supporting distribution feeder decrease. Similarly, and perhaps more importantly, as the solar intensity (and thus PV operability) increases, so also might the loading on the supporting distribution feeder increase. However, the PV might somewhat offset the loading.

One of the possible benefits afforded to a utility when its residential customers begin interconnecting PV systems onto its distribution system will be to balance increasing loads, thus allowing the utility to postpone future feeder upgrades necessitated by load growth. Because of that possible benefit, IPC, through its RD&D team, proposed and budgeted funds to support a research project designed to collect solar intensity and feeder loading data in 2013 in order to determine if a relationship exists.

Review of Outside Sources

The research of how photovoltaic systems affect the operations of the feeders on which they have been interconnected has been extensive. Examples of the published research results that address feeder operations include:

- Distribution feeder modeling and simulations that include PV system interconnections. Sandia National Laboratories has taken the lead in developing feeder modeling protocols, first in developing the Grid Integrated Distributed PV (GridPV) application — a combination of the OpenDSS software with support from a MatLab design [1] and then by developing an method for forming a simplified equivalent representation of distribution circuits for PV impact studies [2]. Sandia has also developed a process for determining PV interconnection risks on the distribution system through the use of feeder zones, with risk being calculated according to feeder type, feeder characteristics, and location and size of the PV [3].

  Examples outside Sandia include Kern & Russell [4] who developed transient irradiance modeling techniques based on observations of over thirty 2000 W systems spread over a 50-acre area, Schone etal. [5] who focus on challenges associated with evaluating the types of systems for which potential PV-related problems become actual problems, and Cohen & Callaway [6] who modeled eight distribution feeders in two types of California climates to compute the positive and negative effects of various sizes and types of PV system interconnections.

- Distribution feeder design that takes into account the optimal locations and sizes of interconnected PV systems. In 2012 EPRI, with support of eight different utilities across the United States, published a stochastic method to determine feeder hosting capacity for PV systems [7]. Also in 2012, NREL published simulated results for sixteen typical distribution feeders with various levels of PV penetration [8] while Sandia published results of studies of two feeders — one in Utah and one in Georgia — with a simulated 100% PV penetration, both centralized and distributed [9].

  Other published research included high-penetration PV studies for the US Department of Energy SunShot Vision project [10]; projects in the Arizona Public Service (APS) territory, including the

Flagstaff pilot project [11] and the High Penetration PV Deployment Project [12]; and a project at London Hydro in Ontario, Canada [13].

- Distribution feeder voltage regulations issues with PV system interconnection. Among the example research studies is one considering the cascading effects of disconnecting residential scale PV because of voltage rise [14] and distribution voltage control via the injection of reactive power from PV inverters [15].
- Distribution feeder voltage variability / flicker issues with PV system interconnection. Among the example research studies are those that have applied voltage flicker analysis to Hawaiian distribution feeders [16] and to future Florida transmission and distribution systems [17].
- Distribution feeder protection / coordination issues with PV system interconnection. Of particular interest has been the issue of islanding on distribution feeders. Ranade, Sagi, Mulpuri, Surabhi, and Mitra [18] researched the probability of islanding within residential and commercial distribution feeders with varying penetrations of PV systems, with load closely matching the available generation being the necessary condition for islanding to occur. They concluded that anti-islanding measures are essential for uncontrolled systems.

Additionally, research of PV systems and how their interconnection onto the distribution system might be a solution for existing feeder-related issues has also been conducted and include:

- PV systems providing economical or cost-effective non-traditional solutions to distribution feeder issues. The Electric Power Research Institute (EPRI) started working with eleven electrical utilities around the United States to identify and introduce cost-effective applications for PV systems starting in the early 1990s [19]. Their applications program included identifying cost-effective applications of PV systems, informing utility personnel of the programs' existence, assisting their partner utilities in using / revising the applications, and developing tools / methods for utilities to evaluate the applications.
- PV systems combined with energy storage as a venue for feeder load shifting / peak load smoothing. As examples, Arif, Oo, Ali, and Shafiullah found that, on a small distribution system in Australia, the addition of energy storage to a PV system that is at high penetration on the system introduces bidirectional power flow and impacts voltage regulation, phase imbalance, and harmonics [20]. Larova etal. [21] discuss the implementation of battery storage as a complement to a 0.5 MW substation-sited PV system in New Mexico to see if such an aggregate can be implemented for feeder load shifting / peak load smoothing. And, Chikh and Chandra provide a method of feeding a stand-alone DC load at cold temperatures, applied to a typical home in Canada [22].
- PV systems in combination with conservation through voltage reduction (CVR) settings on distribution feeders. An example research paper by Singh, Tuffner, Fuller, & Schneider [23] describes the effects on energy consumption, peak load reduction, and voltage profile changes on a CVR-configured distribution feeder with the addition of a PV system, particularly with regard to end-of-line voltage measurements.

There has also been research to determine how solar irradiance and cloud cover affects the operation of PV systems interconnected onto distribution feeders. As a couple examples, Chengrui and Aliprantis discuss the use of a cloud shadow model that recreates the power generated by rooftop PV systems embedded in a distribution feeder [24] while the work of Stefferud, Kleissl, & Schoene created cloud shadow maps on the ground to forecast power production ramps topographically located to individual sites on a distribution feeder [25]. Additionally, Moaveni, Click, Meeker, Reedy, & Pappalardo show how the design attributes of PV systems, whether a large central plant or small distributed plants, can change

the geographic dispersion of the variability of PV energy across a distribution system caused by passing clouds [26].

Key to these examples from the extensive on-going research is the study of PV systems that are interconnected onto a distribution system. How the proposed research project differs from the example research studies is that the proposed research will seek to find the relationship between solar intensity / cloud cover and a distribution feeder's actual loading / load profile. This research is not concerned with the integration of a PV system onto a feeder; rather, it is concerned with how sunshine or clouds may increase or decrease the amount of load created throughout the day. In other words, is there a relationship between solar intensity and feeder load?

Research Questions

At the onset of the project, two questions emerged that formed the basis of the research design that followed:

1. Is there a statistical relationship (correlation) between solar intensity and load?
2. What other relationships are there between load and meteorological parameters (such as wind speed and ambient temperature)?

From those questions, the research scope and methods could be clearly defined, the appropriate data could be collected and analyzed, and determinations could be made as to how to move forward.

Research Scope

A project plan, titled *Effect of Solar Intensity Variations on Feeder Load* (Budget ID RDND130002, Work Order 27386761, under the supervision of RD&D's project manager, Phil Anderson), was drafted in April 2013. According to the plan, the scope of the project included the following tasks:

1. Study a residential feeder to determine weather / solar monitoring locations.
2. Install weather/solar stations and gather solar, weather, and load data.
3. Study the data looking for possible correlations and understanding of the coupling.
4. Develop a report on the value of distributed solar generation on peak load matching, in general, and as a source of generation, specifically.

The project, as described in its scope, was approved with a budget amount of $20,000 for work to be performed during 2013 that included purchasing and installing potentially permanent solar intensity monitors, PV panels, and power metering and recording equipment. Studying the relationships between load and meteorological parameters other than solar intensity, wind speed, and ambient temperature were considered to be outside the scope of the project.

Additionally, the research was limited to data obtained from a single residential feeder considered to be typical for the installation of roof-top PV systems; feeders that might host larger, utility-scale installations were considered to be outside the scope of this initial investigation.

The findings of the research conducted under the limited scope of this project will help determine (1) if additional research sites may be warranted for future data collection, (2) where additional research sites may need to be located for future data collection, and (3) what additional meteorological parameters (if any) may need to be included in future data collection.

Research Methods

To meet the scope and budget of the project, and in an attempt to answer the research questions, a pilot study limited to a single distribution feeder containing three solar irradiance weather stations (SIWSs) was designed. The methods for performing the study were divided into four chronological steps:

1. Choose a residential feeder.
2. Design and install the model weather / solar stations.
3. Gather solar, weather, and load data.
4. Analyze the data for possible correlations / understanding of the coupling.

Choose a Residential Feeder

To begin the process, an appropriate distribution feeder from which to collect solar irradiance data needed to be chosen that met the following conditions:

- The feeder needed to cover a geographical distance greater than two miles in an east-to-west direction (with an ideal configuration covering more than four miles east-to-west) to be able to track the effects of cloud cover as the clouds move from one SIWS site to the next.
- The feeder needed to be comprised of mostly residential and light commercial customers since those customers would most likely seek to install photovoltaic systems on their rooftops.
- The feeder needed to be one where the installation of the SIWSs would be as easy accessible as possible, located near the operating office from where the data would be collected.

Based on these conditions, any of the distribution feeders located west of Boise and east of Meridian were applicable. The feeder that was chosen for the study, Locust (LCST) 044, is a summer-peaking 34.5kV feeder rated at 20MVA. The fact that it is a 34.5kV feeder means that it covers a greater geographical area than a typical 12.5kV feeder, thus being more likely to meet the condition set for geographical configuration. The feeder is configured such that the distance from its eastern-most location to its western-most location is approximately 3.5 miles. Figure 1 shows the geographical configuration of the LCST-044 feeder.

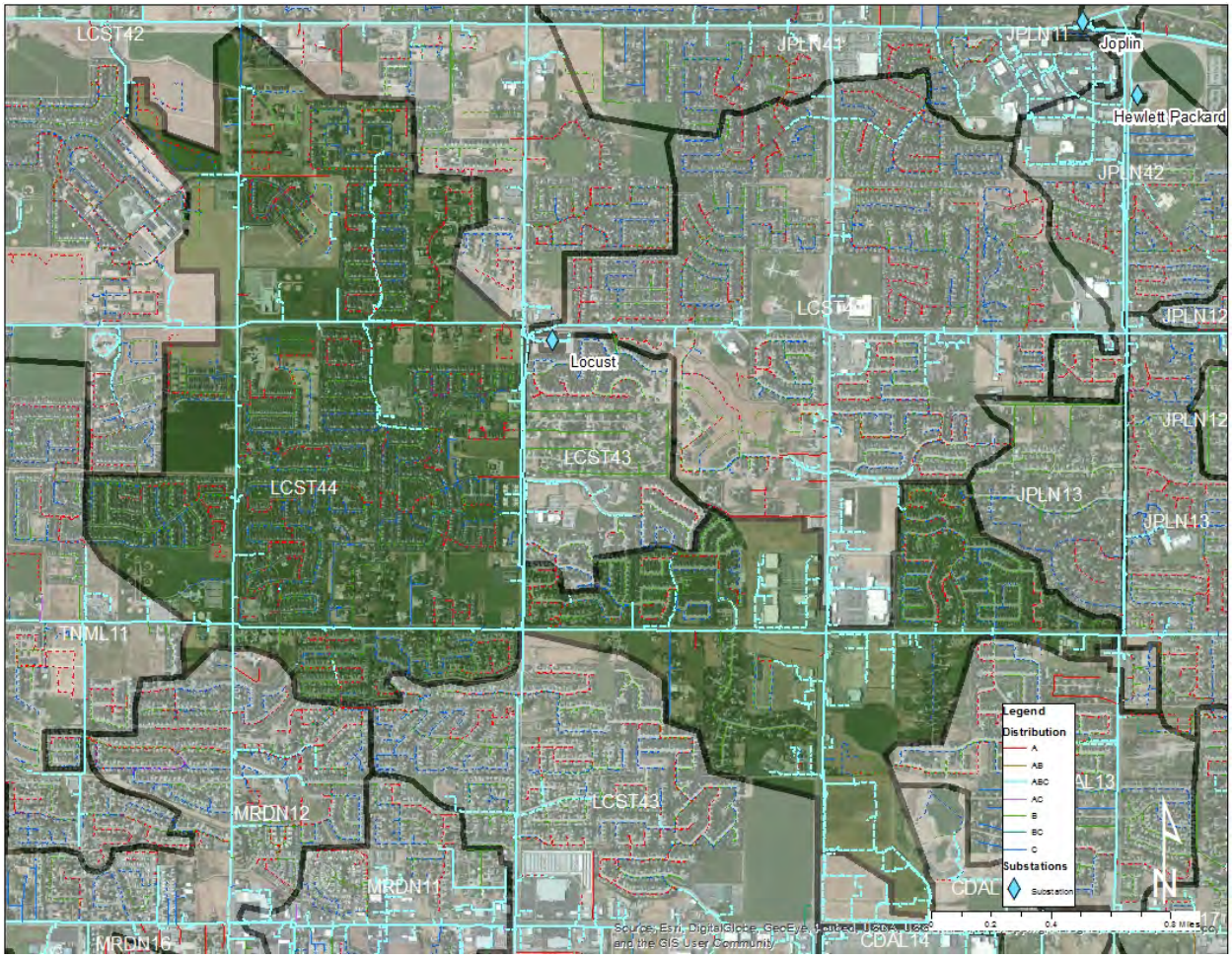

Figure 1: Locust (LCST) 044 feeder configuration

LCST-044, located in Ada County north of the City of Meridian and west of the City of Boise, serves approximately 4500 customers, most of whom are residential and small commercial, which meets the condition set for customer composition. As an aside, there is also one net metering customer on the feeder: a 4.23kW photovoltaic customer.

Finally, Locust substation is located approximately 5 miles from the nearest (Boise) operating center and approximately 10.5 miles from the Boise Plaza, where the data collected from the SIWSs will be stored and analyzed.

Design and Install the Model Weather / Solar Stations

Three SIWSs were installed on the LCST-044 feeder. Station locations were chosen so that (1) they were as geographically equidistant from one another as possible and (2) they were as free from impediments to irradiance data-gathering as possible. Figure 2 shows where on the feeder the three stations were installed.

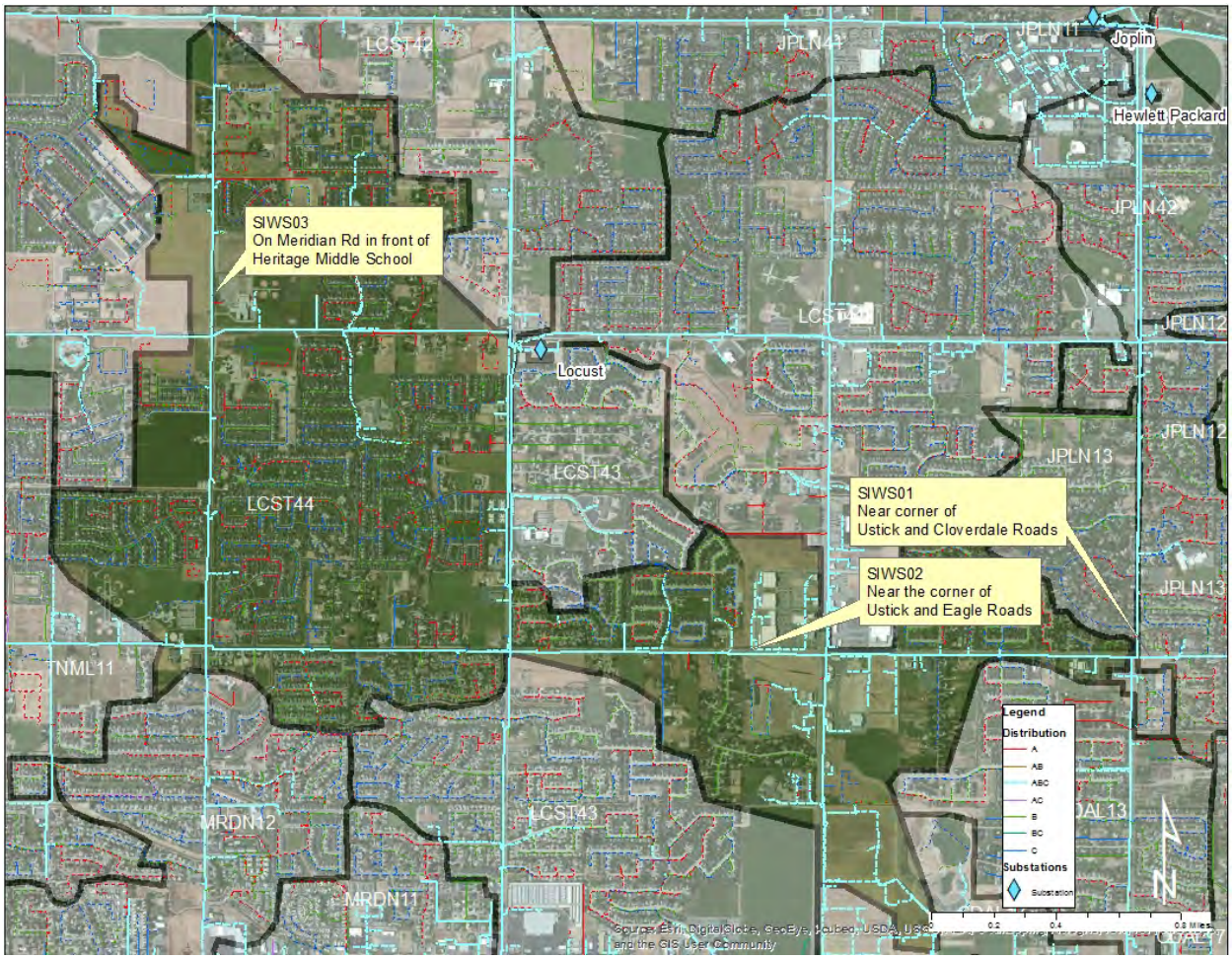

Figure 2: Locations of the 3 solar stations

Initially, each station was designed to include global horizontal irradiance (GHI) monitoring, point-of-array (POA) monitoring in the westerly direction, wind speed monitoring, wind direction monitoring, ambient temperature monitoring, and GPS time synchronization. POA monitoring in the southerly direction as well as globally was added later.

The westerly POA monitoring was chosen because of the sun's location on LCST-044 at the time of its 2012 (previous year's) peak load. Later, the southerly POA was added as part of the design of the SIWSs to emulate typical PV installations, based on discussions with a local PV installation company regarding typical design of roof-top projects.

Figures 3, 4, and 5 provide the specifications for, as well as photographs of, each of the three SIWSs as they were installed on the LCST-044 feeder.

SIWS01 (Figure 3), the eastern-most station, was located near the corner of Ustick and Cloverdale Roads.

Name			SIWS01
Location			
	Latitude		43.63377
	Longitude		W116.33405
	Elevation		2619
	Comments		Near corner of Ustick and Cloverdale
Sensors			
	Wind Speed		
		Type	APRS World #40R Anemometer
		Height	10m
	Wind Direction		
		Type	APRS World #200P Wind Vane
		Height	10m
	Ambient Temp		
		Type	APRS World Temp Sensor
		Height	approx. 3m
	Solar		
		Type	Li-Cor LI-200
		Height	approx. 5m
		Direction	Directional South 180° 35° from horizonal
		Type	Li-Cor LI-200
		Height	approx. 5m
		Direction	Directional West 269° 53° from horizonal
		Type	Li-Cor LI-200
		Height	approx. 5m
		Direction	Global South level
Logger			
	Type		APRS World
	Scan rate		10 seconds

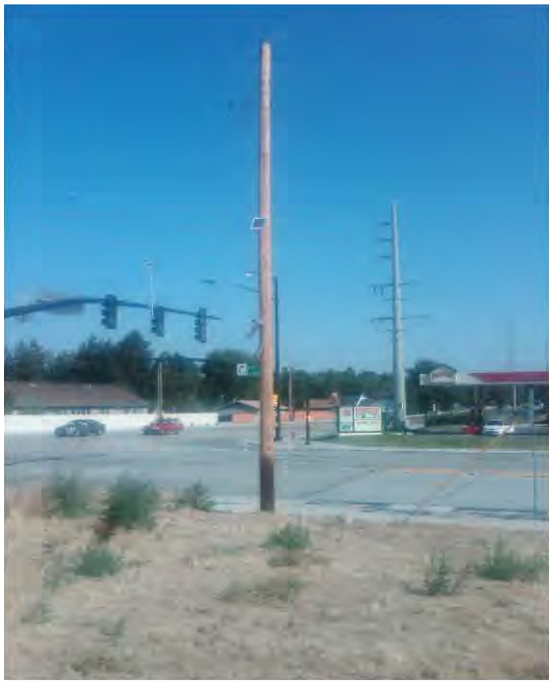

Figure 3: SIWS01 Specifications

Some possible issues to be aware of during the analysis of the data collected at the SIWS01 location include:

1. Shadows from the traffic signal shown in the Figure 3 photograph may affect the afternoon irradiance data, and
2. A building directly to the west of the SIWS01 location (not shown) contains windows, reflections from which may affect the early morning irradiance data.

SIWS02 (Figure 4) was located near the corner of Ustick and Eagle Roads.

Name		SIWS02
Location		
	Latitude	43.63395
	Longitude	W116.35944
	Elevation	2630
	Comments	Near corner of Ustick and Eagle
Sensors		
	Wind Speed	
	Type	APRS World #40R Anemometer
	Height	10m
	Wind Direction	
	Type	APRS World #200P Wind Vane
	Height	10m
	Ambient Temp	
	Type	APRS World Temp Sensor
	Height	approx. 3m
	Solar	
	Type	Li-Cor LI-200
	Height	approx. 5m
	Direction	Directional South 180° 35° from horizonal
	Type	Li-Cor LI-200
	Height	approx. 5m
	Direction	Directional West 269° 53° from horizonal
	Type	Li-Cor LI-200
	Height	approx. 5m
	Direction	Global South level
Logger		
	Type	APRS World
	Scan rate	10 seconds

Figure 4: SIWS02 Specifications

One possible issue to be aware of during analysis of the data collected at the SIWS02 location includes the effects of buildings located directly east of the weather station (not shown) that might cast shadows on the station during the morning hours.

SIWS03 (Figure 5), the northern- and western-most station, was located on Meridian Road in front of Heritage Middle School.

Name		SIWS03
Location		
	Latitude	43.65054
	Longitude	W116.39342
	Elevation	2606
	Comments	On Meridian Rd in front of Heritage Middle School
Sensors		
	Wind Speed	
	Type	APRS World #40R Anemometer
	Height	10m
	Wind Direction	
	Type	APRS World #200P Wind Vane
	Height	10m
	Ambient Temp	
	Type	APRS World Temp Sensor
	Height	approx. 3m
	Solar	
	Type	Li-Cor LI-200
	Height	approx. 5m
	Direction	Directional South 180° 35° from horizonal
	Type	Li-Cor LI-200
	Height	approx. 5m
	Direction	Directional West 269° 53° from horizonal
	Type	Li-Cor LI-200
	Height	approx. 5m
	Direction	Global South level
Logger		
	Type	APRS World
	Scan rate	10 seconds

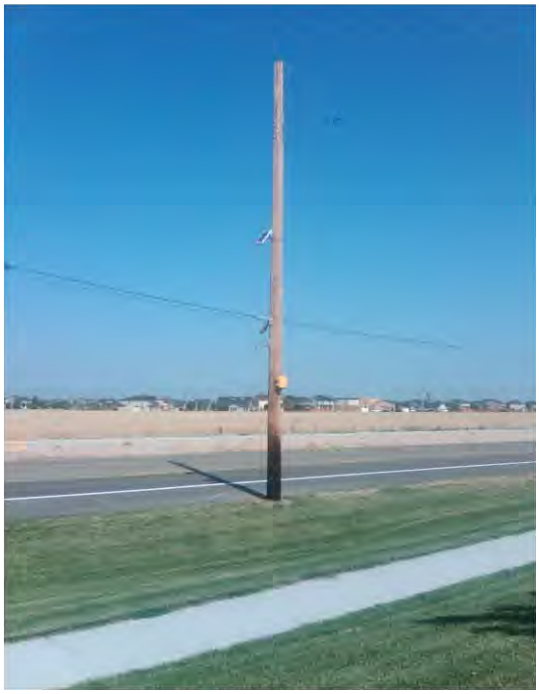

Figure 5: SIWS03 Specifications

One possible issue to be aware of during analysis of the data collected at the SIWS02 location includes the shadows cast from the distribution line located across the street from the station (as shown in the Figure 5 photograph). That shadowing could probably be considered minimal.

An issue common to each of the three station locations was the fact that their westerly-facing PV panel will always be affected by the shadow cast in the early morning hours by the stations' supporting poles.

Gather Solar, Weather, and Load Data

Solar and weather data was captured onto an SD card — at a data capacity of 2G — located in the data logger. At a set time interval, the data was collected by removing the SD card from the data logger, copying the data from the SD card to a laptop's hard drive, deleting the data from the SD card, and replacing the SD card back into the data logger.

Following is the data collected from each of the SISW sites:

- UTC time
- Wind speed (the average over a ten-second interval) in meters / second (m/s)
- Wind gust (the peak over a ten-second interval) in m/s
- Wind direction in degrees (with 0^o being North)
- Local battery voltage (over a ten-second interval)
- Ambient temperature in ^oC
- Solar irradiance POA South in watts /meter^2 (watts/m^2)
- Solar irradiance POA West in watts/m^2
- Global Horizontal irradiance in watts/m^2

At the beginning of the data gathering process, data was collected every two weeks because of (1) the uncertainty as to how much data could be stored on to the SD card and (2) the need to ensure that a minimum amount of data would be lost should a problem with the logger arise. When the logger proved itself to be dependable, the interval between data collection dates increased.

During the time of the study covered with this research report (June 21, 2013 until September 21, 2013), data was collected on the following dates:

- May 24, 2013,
- June 4, 2013,
- July 1, 2013,
- July 15, 2013,
- August 1, 2013,
- August 8, 2013,
- September 12, 2013, and
- October 2, 2013.

Because of some anomalies and corrections that occurred with the data collected early in the process, the decision was made to limit the research time frame to cover the traditional summer season, between June 21 and September 21.

As an aside, data continued to be collected from the three SIWSs after the October 2, 2013 collection date, though at greater time intervals. Data was also collected October 30, 2013, January 2, 2014, March 26, 2014, June 13, 2014, and July 7, 2014, resulting in a complete year's worth of data. The data collected after September 21, 2013, can be made available for future research.

Finally, PI load data for the LCST-044 feeder was also collected in ten-second intervals that matched the times of the collected irradiance data.

Analyze the Data for Possible Correlations / Understanding of the Coupling

Data analysis initially occurred in collaboration with the University of Idaho (U of I). Real-time solar intensity, wind speed, wind direction, and ambient temperature data, gathered from each of the SIWSs, as well as the LCST-044 real-time load data gathered from PI, were presented to the U of I in Microsoft Excel spreadsheets for the time interval between June 21, 2013, and September 21, 2013. After converting the time associated with the SISW data from UTC (Coordinated Universal Time) to MDT (Mountain Daylight Time) — to match the times of the PI loads — the U of I was asked to calculate the following correlation coefficients (daily as well as study time interval):

- Global solar intensity to load
- Southerly oriented solar intensity to load
- Westerly oriented solar intensity to load
- Ambient temperature to load
- Wind speed to load

Additionally, the U of I was asked to calculate the solar energy density (Watt-hours/m^2) per interval for each site at each orientation.

Results

The following sub-sections show the various graphs and tables that the U of I was able to create in Microsoft Excel spreadsheets from the June 21, 2013 through September 21, 2013 data they were provided.

Graphs of Solar Irradiances versus Load

The U of I provided graphs of solar irradiances versus growth sorted into categories of "max", "mid", and "min". The categories are meant to designate (1) peak load dates during the study period as "max", (2) random median load dates during the study period as "mid", and (3) the lowest load periods during the study period as "min". Solar irradiance data and load data were collected in 10-second intervals from June 21 through September 21, but graphs of solar irradiances versus load were provided only for the following days during the study period:

- 7-1-2013, 7-2-2013, 6-30-2013, 7-10-2013, and 7-15-2013 designated as "max",
- 8-31-2013, 7-12-2013, and 7-31-2013 designated as "mid", and
- 6-25-2013 and 6-21-2013 designated as "min".

July 1, 2013 was the actual peak date for the LCST-044 feeder. Figure 6 shows the graphs of solar irradiances versus load for the day of the feeder peak as an example of the information that was provided. Appendixes 1, 2, and 3 show more completely the graphs for all the designations sorted by location.

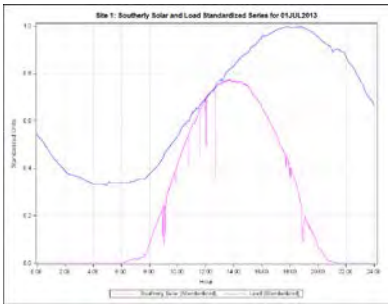

Southerly Solar & Load

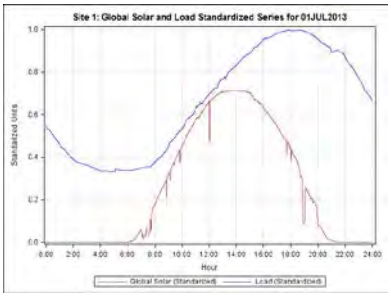

Global Solar & Load

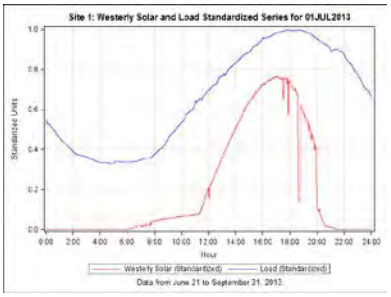

Westerly Solar & Load

SIWS01 data collected 7-1-2013

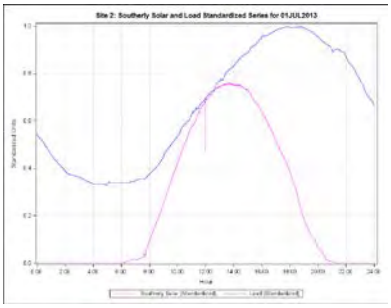

Southerly Solar & Load

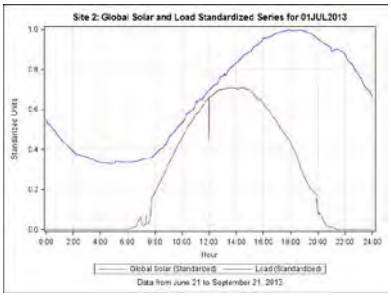

Global Solar & Load

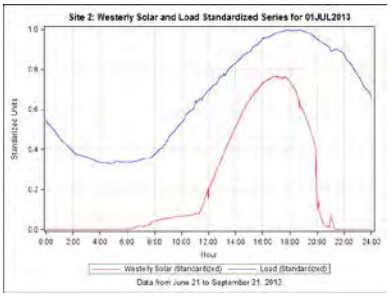

Westerly Solar & Load

SIWS02 data collected 7-1-2013

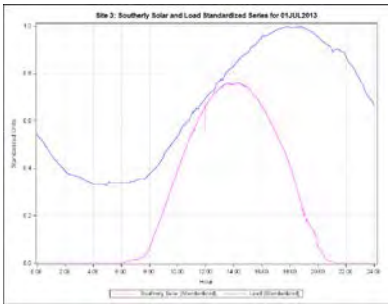

Southerly Solar & Load

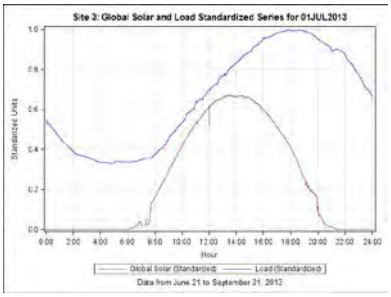

Global Solar & Load

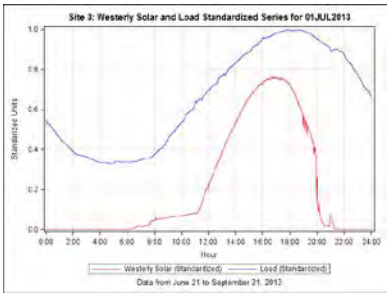

Westerly Solar & Load

SIWS03 data collected 7-1-2013

Figure 6: Graphs of Solar Irradiances versus Load, 7-1-2013

From Figure 6, relationships can be seen between irradiances and loads at all three SIWS sites on a clear, peak load day. Further analysis would need to be performed to determine actual correlations between irradiance and load, not just for the clear, hot days, but also for cloudy and cooler days. The “Analysis” section will discuss in more detail what relationships were found for the summer 2013 timeframe.

Graphs of Ambient Temperature versus Load

Since one of the research questions sought to find relationships between factors other than irradiance and load, graphs were also created for the temperature and load data for the same "max", "mid", and "min" days as created for irradiance and load. Figure 7 shows example graphs for July 1, 2013 for each of the SIWS stations.

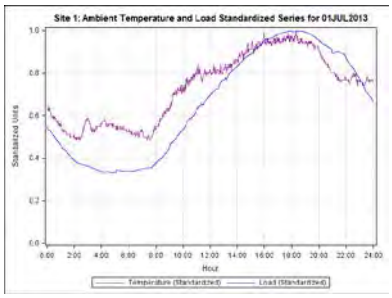

Ambient Temperature & Load

SIWS01

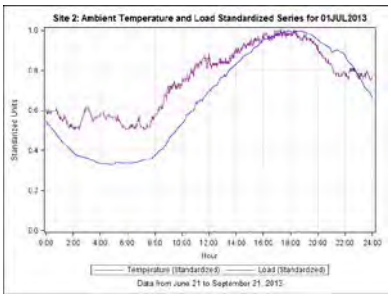

Ambient Temperature & Load

SIWS02

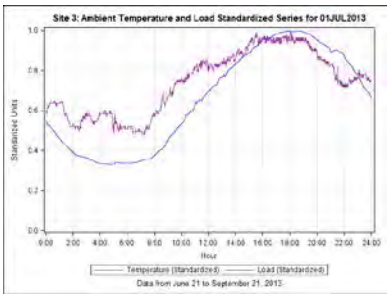

Ambient Temperature & Load

SIWS03

Figure 7: Graphs of Ambient Temperature versus Load, 7-1-2013

As with the irradiance and load graphs, the Figure 7 graphs show that there seems to be a relationship between temperature and load on a clear peak load day. Further analysis would need to be performed to determine actual correlations between temperature and load, not just for the clear, hot days, but also for cloudy and cooler days. The "Analysis" section will discuss in more detail what relationships were found for the summer 2013 timeframe.

Graphs of Wind Speed versus Load

Since one of the research questions sought to find any relationship between factors other than irradiance and load, graphs were also created for the wind speed and load data for the same "max", "mid", and "min" days as created for irradiance and load. Figure 8 shows example graphs for July 1, 2013 for each of the SIWS stations.

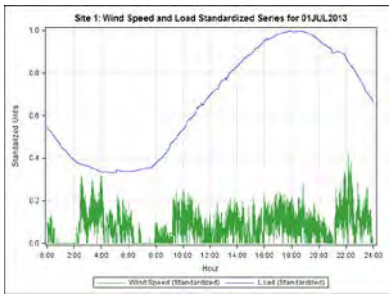

Wind Speed & Load

SIWS01

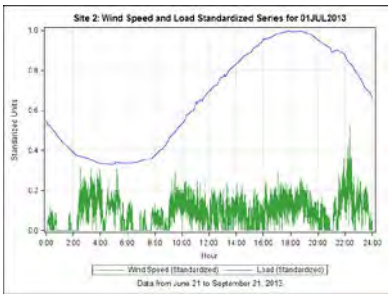

Wind Speed & Load

SIWS02

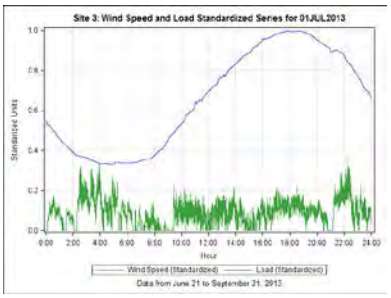

Wind Speed & Load

SIWS03

Figure 8: Graphs of Wind Speed versus Load, 7-1-2013

Unlike the irradiance / ambient temperature and load graphs, it is not obvious that the Figure 8 graphs show any relationship between wind speed and load on a clear peak load day. Further analysis would

need to be performed to determine if there is any correlation between wind speed and load, not just for the clear, hot days, but also for cloudy and cooler days. The "Analysis" section will discuss in more detail what, if any, relationships were found for the summer 2013 timeframe.

Solar Energy Density

The U of I calculated, then provided in tabular form, solar energy densities in watts per square meter for each of the SIWSs at each of the panel configurations. Figure 9 shows the July 1, 2013, portion of the table with the complete table available in Appendix 4.

Solar Energy Density (Generation per Day in w/m^2)									
	Global Solar Intensity			Southerly Solar Intensity			Westerly Solar Intensity		
Date	Site 1	Site 2	Site 3	Site 1	Site 2	Site 3	Site 1	Site 2	Site 3
7/1/2013	2899358.66	2913112.60	2917692.24	2719010.24	2707143.00	2744653.44	2194616.40	2271469.72	2282650.92
Totals 6/21/2013 to 9-21-2013	219704903.60	221463275.80	220126443.55	222963511.51	223959243.50	226517909.09	174599552.03	185305851.03	186670542.98
Average Total	220,431,540.98			224,480,221.36			182,191,982.01		

Figure 9: Solar Density information for 7-1-2013

Because of extent of analysis that was required for just the irradiance data, the decision was made to delay analysis of the solar energy density until later.

Analysis

The following sub-sections delineate, in chronological order, the process by which the collected data was analyzed and the conclusions that were drawn regarding the relationships between irradiances, load, and other meteorological variables.

Initial University of Idaho Analysis

As was requested, the U of I's initial analysis of the data was in the form of performing simple correlations between the daily peak loads and the other variables that included each SIWS site's global, southerly, and westerly configurations as well as site temperatures and wind speeds. The simple correlations spanned across the entire 93-day study period. That initial analysis yielded the graphs shown in Figure 10:

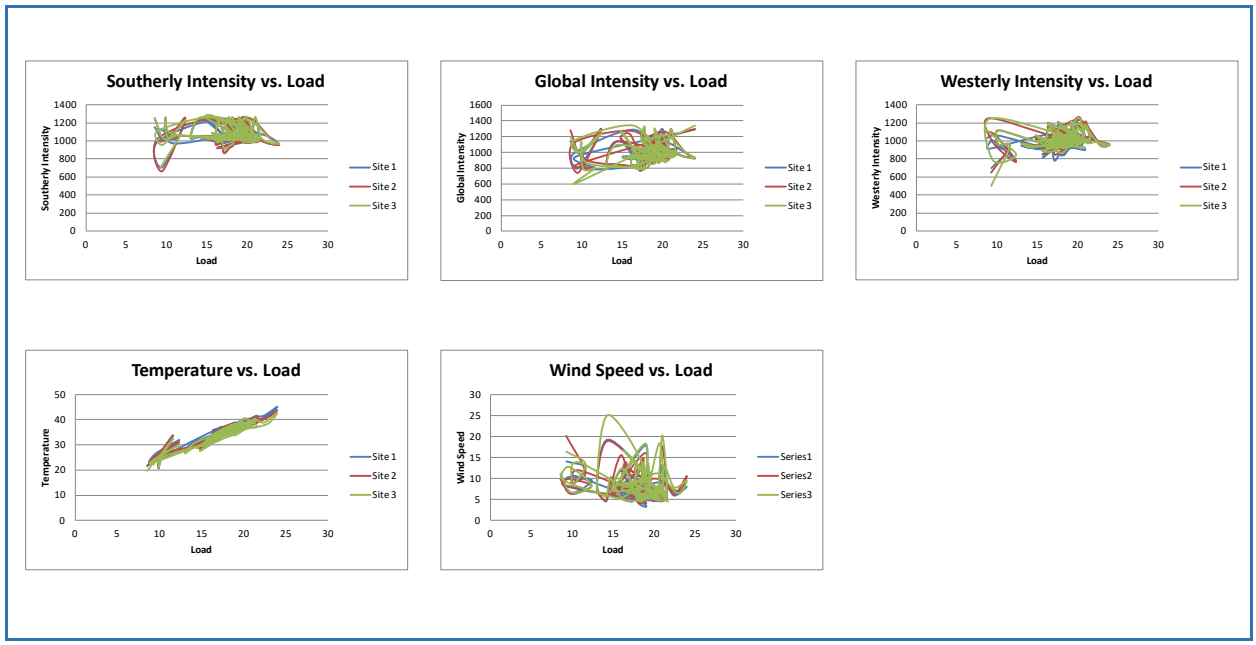

Figure 10: Initial Simple Correlations

Based upon the Figure 10 graphs, it seemed that there was no significant correlation between load and any of the variables except for temperature. However, and after some reflection, we realized that a correlation between the daily peak load and the daily peak irradiances would not have provided meaningful results, and that a comparison of the 10-second irradiance, temperature, and wind speed data to its accompanying load would be more meaningful.

Microsoft Excel's CORREL Function

As a first step, we used Microsoft Excel and applied its CORREL function to the 7-1-2013 data collected from SIWS01 to calculate simple correlations between load and each of the southerly, global, and westerly configurations. The results of the simple one-to-one correlation calculations yielded a 0.494529 correlation for the southerly configuration, a 0.494537 correlation for the global configuration, and a 0.726723 correlation for the westerly configuration, none of which were particularly significant, but all of which were more realistic than the correlations between daily peak loads and daily peak irradiances.

Figure 11 shows the LCST-044 loads compared to time graphed together with the various solar irradiance configurations compared to time on our example date of July 1, 2013.

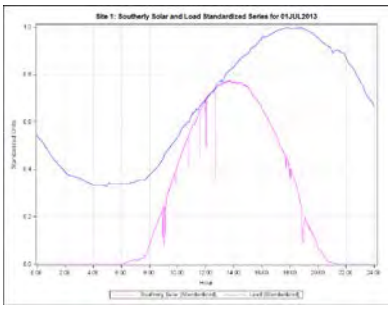

Southerly Solar & Load

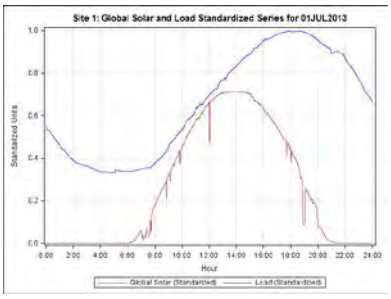

Global Solar & Load

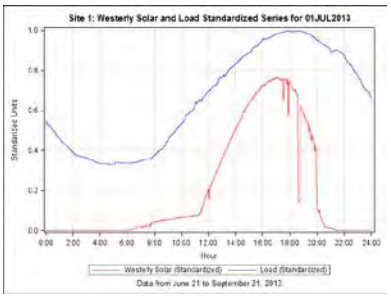

Westerly Solar & Load

Figure 11: SIWS01 data collected 7-1-2013

Just by looking at the Figure 11 graphs, it was apparent that there is a relationship between loads and each of the configurations; however, that relationship does not occur concurrently. Upon that realization, we sought to find a statistical tool that could show correlations between two variables that also accounted for time shifts.

The Auto-correlation Function

First off, the auto-correlation function, which is a correlation between the time series variable and itself, was used to determine that each time series variable was indeed non-random. The auto-correlation for the July 1, 2013, date was applied from time = 0 to a maximum lag time of 12 hours, calculating the correlations between the value at time = 0 to itself, continuing with the correlation between the value at time = 0 to time = 1, and so on. Figure 12 shows the resulting auto-correlation graphs.

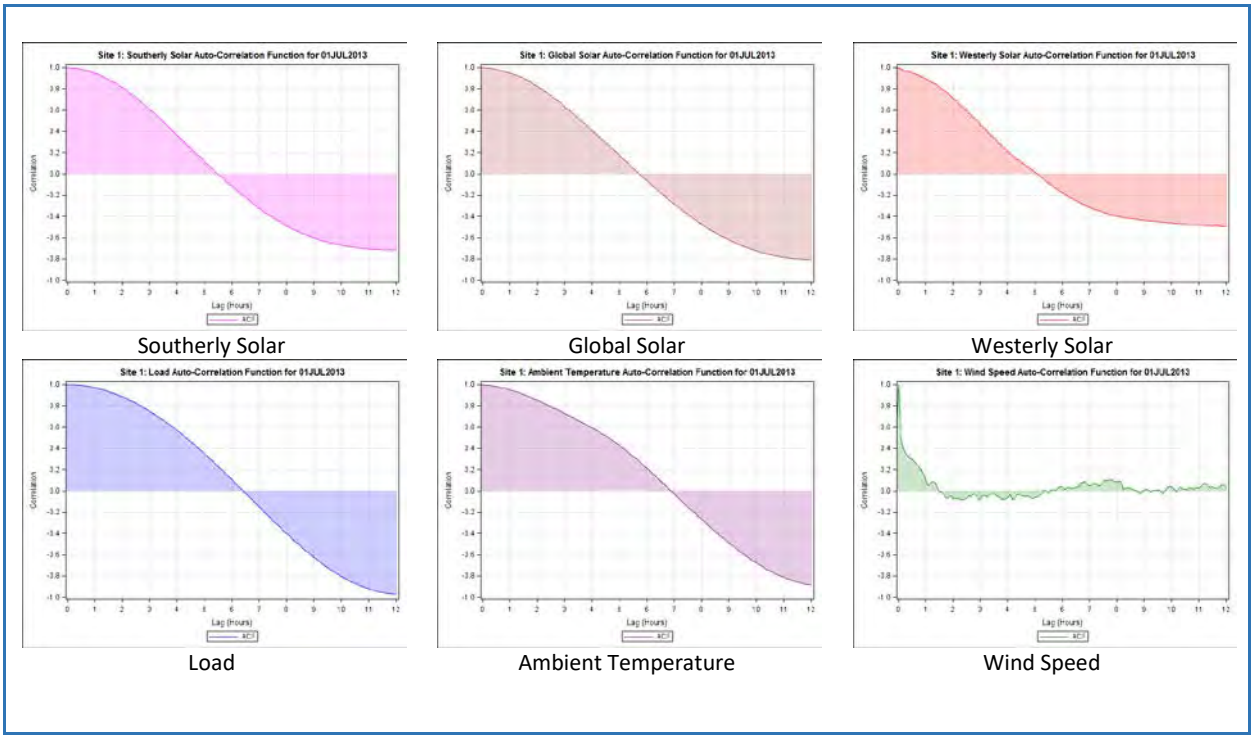

Figure 12: Auto-correlations for 7-1-2013 variables

Take, as an example, the Southerly auto-correlation graph. At time = 0, the correlation between the irradiance data and itself is 1. As time increases to time = 1, the correlation between the irradiation data at time = 0 and the data at time = 1 becomes approximately 0.9 — less certainty, but still a very good predictor of future irradiance. At a time lag of approximately 5 hours, the correlation between the irradiation data at time = 0 and the data at time = 5 hours is 0 — virtually a random predictor of future irradiance. The fact that most of the Southerly auto-correlation data is either positively or negatively correlated (in other words, the correlation data is mostly non-zero), means that it is highly unlikely that the data has occurred randomly.

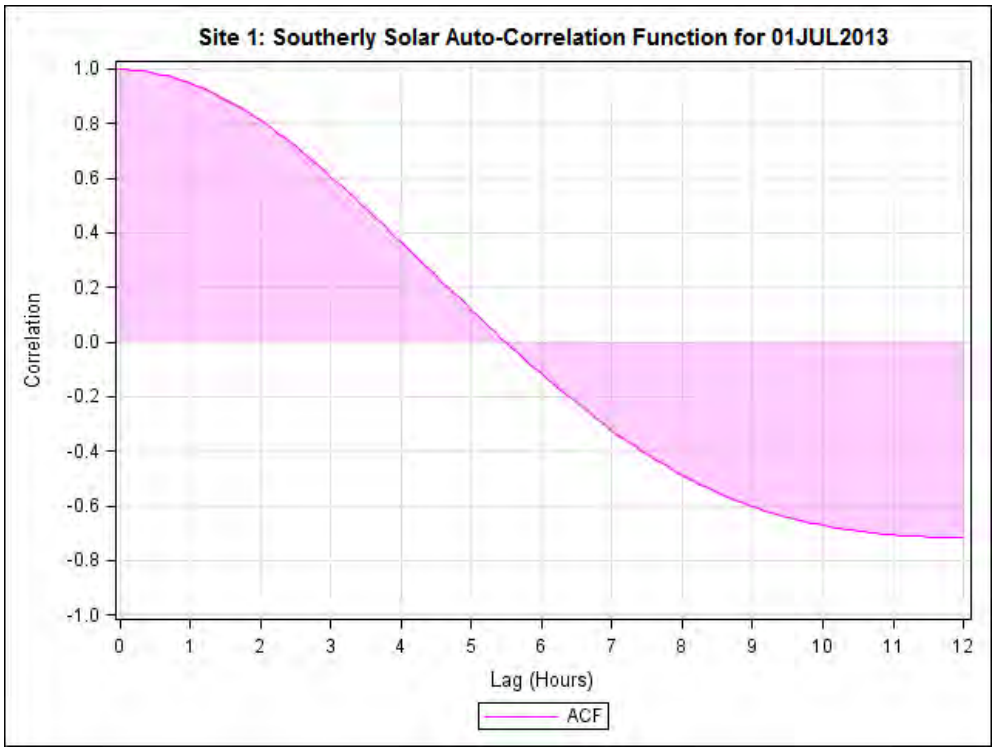

Similarly, when reviewing the wind speed data auto-correlations, both for speed and direction, the fact that most of the auto-correlations fall along the "0" line of the x-axis indicates that it is highly likely that the data could just as easily be random as not; previous wind speed data is not a good indicator of future wind speed data.

Having established the non-random nature of most of the variables allowed us to proceed with greater confidence in establishing relationships between two variables through cross-correlations.

Cross-correlation Analysis

Similar to the way the auto-correlation process compares a variable to its time-shifted self, a cross-correlation compares two variable time-series, with one time-series set as the constant and the second time-series moving through time. In order to find relationships between solar intensity and load as well as relationships between load and the other meteorological parameters (wind speed and ambient temperature), the data was nominalized so that each variable ranged between 1 (its peak) and 0 (its minimum). That was done so that the two correlated time-series would be more easily relatable when graphed as well as to provide a common axis from which to compare results for different days.

And, even though data was collected at 10 second intervals, cross-correlations were calculated at five-minute intervals to allow for quicker computations. For each correlation, the load time-series was held constant while the various other time-series — southerly, global, and westerly panel configurations; temperature; and wind speed — were shifted across a ±12-hour range. Cross-correlations were graphed for each day's worth of data for every day of the study period — June 21 through September 21, 2013 — for each of the three SIWSs. Figure 13 shows which cross-correlations were graphed for each SIWS:

Variable	Southerly	Global	Westerly	Temperature	Wind Speed
Load	Yes	Yes	Yes	Yes	Yes
Southerly				Yes	Yes
Global	Yes		Yes	Yes	Yes
Westerly	Yes			Yes	Yes
Temperature					Yes

Figure 13: List of daily cross-correlations

In Figure 13, the time-series included in the rows remained the constant that the time-series in the columns were shifted against, per site (i.e. westerly solar shifted against the global solar, or wind speed shifted against the load). These fifteen cross-correlation computations (with accompanying graphs) were made for each of the 93 days of the study period at each of the three SIWSs, resulting in the production of 4915 cross-correlation graphs.

For the July 1, 2013, SIWS01 example, Figure 14 shows the graphs of the various cross-correlation calculations at ±12 hours lag:

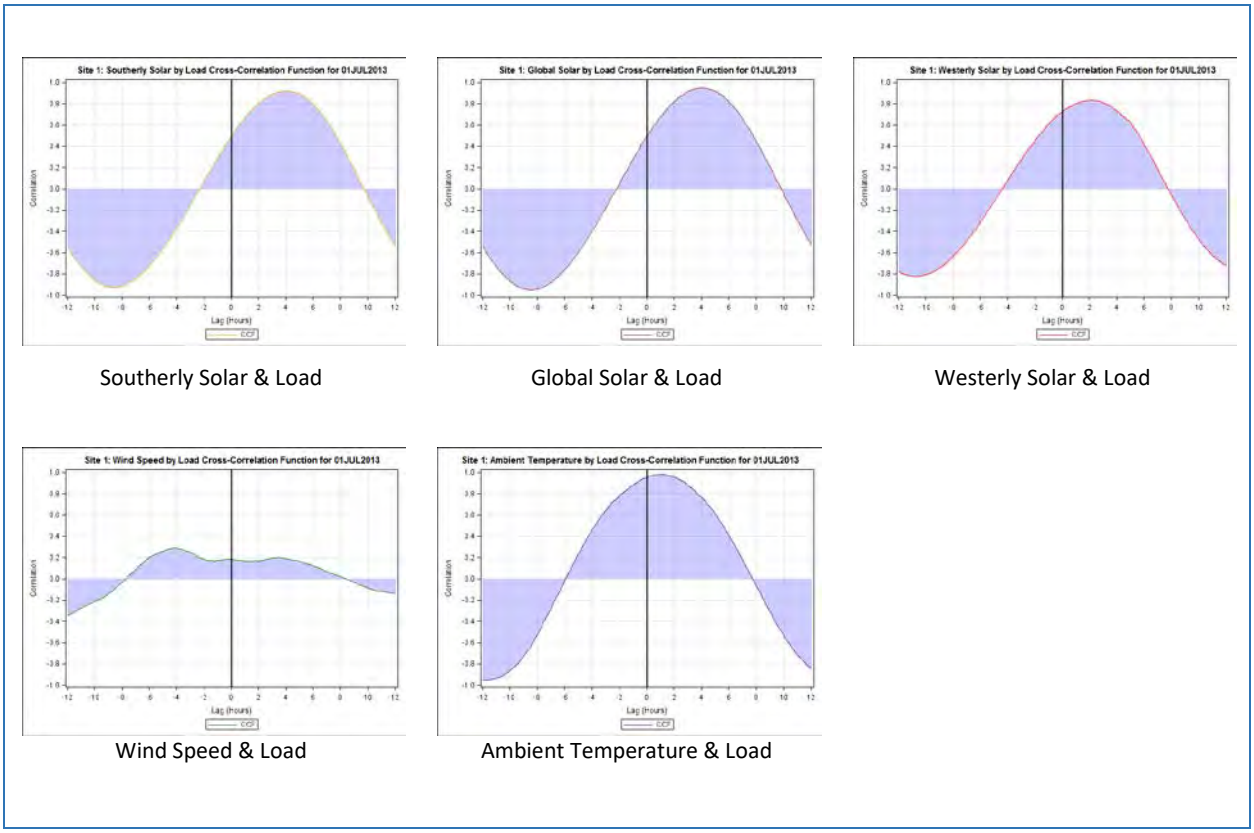

Figure 14: Cross-correlations for 7-1-2013, SIWS01

For a clear and sunny day such as July 1, 2013, when the seasonal peak on LCST-044 occurred, the correlations between the panel configuration's time series and the load's time series are fairly

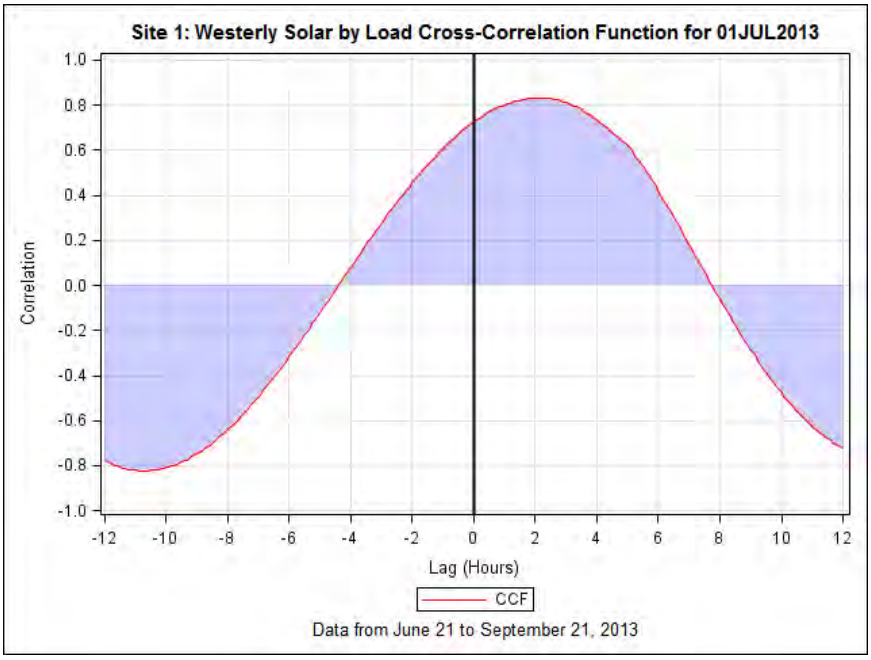

significant. For the worst case correlation —the westerly configuration versus load — the maximum correlation of approximately 0.81 occurred when the LSCT-044 load data lagged the solar intensity data by two hours. On the same day at the same SIWS, the maximum correlation is approximately 0.90 when the load data lagged the solar intensity data by four hours on the southerly-facing panel, and the maximum correlation is approximately 0.92 when the load data lagged the solar intensity data by four hours on the global panel.

Example cross-correlations for days during the 93-day study period that had smaller loads or were cloudy can be found in Appendixes 1 through 3 according to SIWS.

Maximum Cross-correlations / Kernel Densities

While the cross-correlations provided information relating to the relationships between irradiances and loads for each of the individual days of the study period, the question remained whether or not relationships over the entire 93-day study period could be identified. To attend to that question, the statistical process of using the maximum cross-correlations to create kernel densities was applied.

For each pair of time series, the maximum cross-correlation as well as the time lag when the maximum cross-correlation occurred (between ±12 hours) was identified for each of the 93 days in the study period. Next, the results from each day were used to estimate a bivariate kernel density for each pair of time series. This bivariate density estimate yielded a point which represented the most common occurrence over the course of the 93 days for the strength of the linear relationship (i.e. the correlation) and the amount of time the offset occurred at. The ranges of both the linear relationship and the offset in time were also observed from the bivariate density estimates.

For example, the density plots in Figure 15 show the estimates from SIWS01 between the load and the southerly configuration for solar intensity in a 2-dimensional view and a 3-dimensional view, respectively.

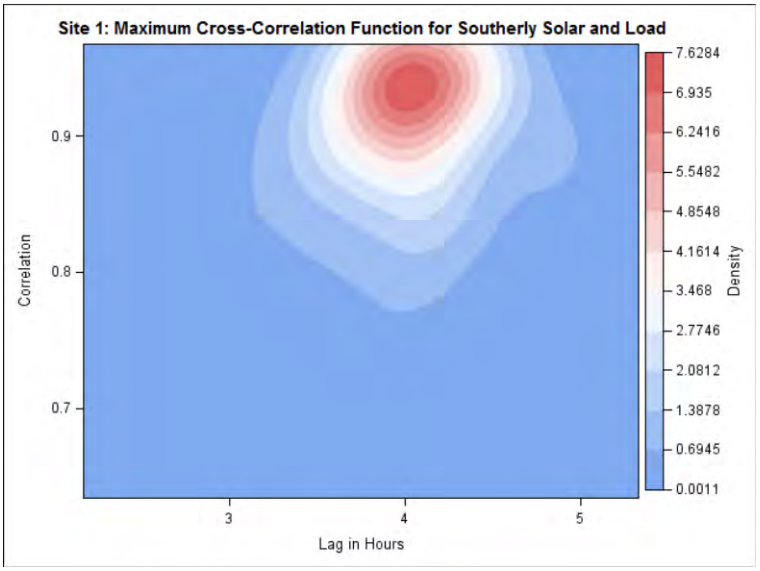

Lag	Correlation
4.045198	0.939251

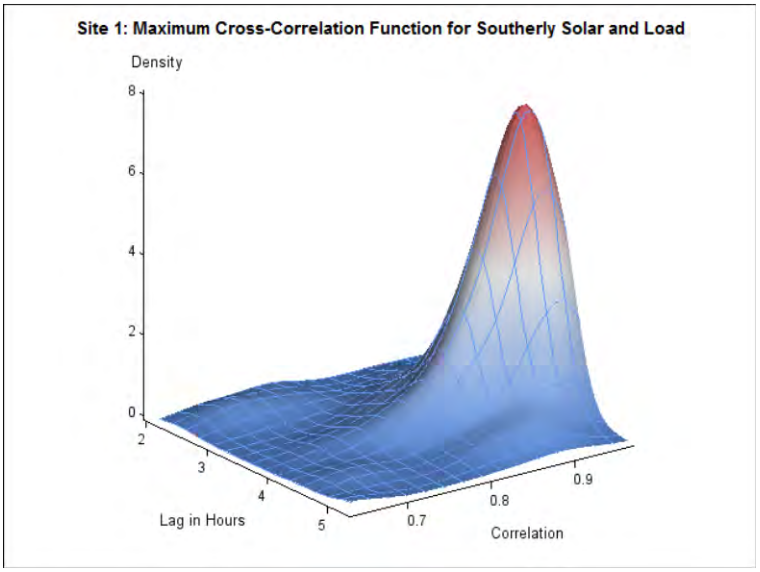

Figure 15: Example kernel density for SIWS01 southerly solar versus load over the study period

The most common daily occurrence was a strong linear relationship (approximately 0.94) between the solar intensity and load lagged by approximately four hours. Over the course of the entire summer, the range of the strength of the linear relationship was generally greater than 0.80 with the lag generally between three and five hours.

Additional kernel densities for showing the irradiances versus load relationships, the irradiances versus ambient temperature relationships, and the irradiances versus wind speed relationships at each of the three SIWS locations can be found in Appendixes 1 through 3.

Statistical Relationships

Based upon the statistical analyses of the data collected, the following generalizations can be made regarding the relationships between loads, irradiances, and other meteorological parameters.

Relationships to load

Relationship	SIWS01	SIWS02	SIWS03
Southerly Solar to load	Tends to lead load by 4.05 hours, correlation 0.94	Tends to lead load by 4.13 hours, correlation 0.94	Tends to lead load by 3.96 hours, correlation 0.94
Global Solar to load	Tends to lead load by 4.00 hours, correlation 0.95	Tends to lead load by 4.02 hours, correlation 0.96	Tends to lead load by 4.02 hours, correlation 0.96
Westerly Solar to load	Tends to lead load by 1.94 hours, correlation 0.88	Tends to lead load by 1.76 hours, correlation 0.91	Tends to lead load by 1.83 hours, correlation 0.91
Ambient temperature to load	Tends to lead load by 0.82 hours, correlation 0.96	Tends to lead load by 0.86 hours, correlation 0.97	Tends to lead load by 0.70 hours, correlation 0.96
Wind speed to load	Tends to lead load by 2.38 hours, correlation 0.68	Tends to lead load by 1.90 hours, correlation 0.70	Tends to lead load by 1.80 hours, correlation 0.69

At each of the SIWS locations, and for each of the panel configurations at those locations, it can be said that there seems to be a moderate-to-strong relationship (0.88 to 0.96 correlation) between the irradiance data and load data collected between June 21, 2013 and September 21, 2013, with the relationships of the southerly and global positions to load being stronger than the relationship of the westerly position to load. And, the relationship between westerly irradiance and load seems to be lessened because of the diversity of lead times between the three SIWS locations in comparison with the southerly and global relationships to load.

So, the answer to the research question, “Is there a statistical relationship (correlation) between solar intensity and load?”, for the time period between June 21, 2013 and September 21, 2013 seems to be yes, but with the understanding that correlation does not imply causation.

Additionally, there seems to be a strong relationship (0.97 to 0.98 correlation) between ambient temperature data and load data, but a fairly tepid yet existing relationship (0.68 to 0.70 correlation) between wind speed and load. The statistics also show much greater diversity in lead times for the correlation between wind speed and load. The fact that the auto-correlation for wind speed showed its virtually random relationship to itself made the tepid correlation between wind speed and load seem to be reasonable.

So, the answer to the other research question, “What other relationships are there between load and meteorological parameters (such as wind speed and ambient temperature?”, for the time period between June 21, 2013 and September 21, 2013, seems to be that there is a strong correlation between ambient temperature data and load data, but at best a tepid correlation between wind speed data and load data.

Even though the research questions have been answered, statistical calculations were also made for relationships to ambient temperature, relationships between panel configurations, and relationships to wind speed simply because the data was available.

Other statistical relationships

In addition to the relationships to load, the relationships that directly answered the research questions, maximum cross-correlations were also made to determine if there were any relationship of (1) the various variables to ambient temperature, (2) the various irradiances to one another, and (3) the irradiances to wind speed.

Relationships to ambient temperature

Relationship	SIWS01	SIWS02	SIWS03
Southerly Solar to temperature	Tends to lead temp. by 3.05 hours, correlation 0.89	Tends to lead temp. by 3.20 hours, correlation 0.90	Tends to lead temp. by 3.21 hours, correlation 0.90
Global Solar to temperature	Tends to lead temp. by 3.05 hours, correlation 0.91	Tends to lead temp. by 3.07 hours, correlation 0.92	Tends to lead temp. by 3.14 hours, correlation 0.92
Westerly Solar to temperature	Tends to lead temp. by 1.02 hours, correlation 0.84	Tends to lead temp. by 0.91 hours, correlation 0.87	Tends to lead temp. by 1.09 hours, correlation 0.87
Wind speed to temperature	Tends to lead temp. by 0.93 hours, correlation 0.66	Tends to lead temp. by 1.10 hours, correlation 0.66	Tends to lead temp. by 0.86 hours, correlation 0.62

At each of the SIWS locations, and for each of the panel configurations at those locations, it can be said that there seems to be a moderately-strong relationship (0.84 to 0.92 correlation) between the irradiance data and ambient temperature data collected between June 21, 2013 and September 21, 2013, that is somewhat less than the relationship between irradiance and load. The correlation between the global data to ambient temperature is the strongest of the three positions, followed by southerly data, with the correlation between the westerly irradiance data and ambient temperature being the least strong, again accounting for the greatest diversity between SIWS lead times.

While not directly answering one of the research questions, the analysis does show a statistical relationship between irradiance and temperature.

Finally, the relationship between wind speed and ambient temperature, as with the relationship between wind speed and load, is fairly tepid, with correlations ranging between 0.62 and 0.66 and the resulting lead times ranging between 0.86 hours and 1.02 hours. Again, that tepid relationship was expected due to the wind speed's relationship to itself as shown in its auto-correlation calculation.

Relationships of irradiances to one another

Relationship	SIWS01	SIWS02	SIWS03
Southerly Solar to Global Solar	Tends to lead global by 0.00 hours, correlation 1.00	Tends to lead global by 0.00 hours, correlation 1.00	Tends to lead global by 0.00 hours, correlation 1.00
Southerly Solar to Westerly Solar	Tends to lead westerly by 2.32 hours, correlation 0.95	Tends to lead westerly by 2.61 hours, correlation 0.96	Tends to lead westerly by 2.27 hours, correlation 0.97
Westerly Solar to Global Solar	Tends to lag global by 2.32 hours, correlation 0.93	Tends to lag global by 2.55 hours, correlation 0.94	Tends to lag global by 2.32 hours, correlation 0.95

At each of the SIWS locations, and for each of the panel configurations at those locations, it can be said that there seems to be a strong relationship (0.93 to 1.00 correlation) between the irradiance data gathered at one panel compared to irradiance data collected at the other two panels collected between June 21, 2013 and September 21, 2013. The irradiance data collected at the southerly panels at all three SIWSs was virtually the same as the global data collected: correlation = 1.00 with no lead or lag. The weakest correlation was between the westerly panels and the global panels, and the greatest diversity in lag times occurred in that relationship, but even so, the correlation was in the mid-0.90s.

Again, while not directly answering one of the research questions, the analysis does show a strong statistical relationship between panel irradiances.

Relationships to wind speed

Relationship	SIWS01	SIWS02	SIWS03
Southerly Solar to wind speed	Tends to lead wind by 1.87 hours, correlation 0.66	Tends to lead wind by 2.08 hours, correlation 0.68	Tends to lead wind by 1.94 hours, correlation 0.67
Global Solar to wind speed	Tends to lead wind by 1.87 hours, correlation 0.66	Tends to lead wind by 2.24 hours, correlation 0.68	Tends to lead wind by 2.32 hours, correlation 0.67
Westerly Solar to wind speed	Tends to lag wind by 0.20 hours, correlation 0.67	Tends to lag wind by 0.20 hours, correlation 0.72	Tends to lead wind by 0.20 hours, correlation 0.72

At each of the SIWS locations, and for each of the panel configurations at those locations, it can be said that there seems to be at best a tepid relationship (0.66 to 0.72 correlation) between the irradiance data and the wind speed data collected between June 21, 2013 and September 21, 2013. Interestingly, the strongest of these tepid correlations seems to occur with the westerly to wind speed data, though the lag / lead times vary from 0.20 hours lagging to 0.20 hours leading.

Disclaimers

When drawing conclusions based upon the analysis of the data, a few disclaimers need to be considered.

- The conclusions drawn by analyzing the data are limited by the study time period. The conclusions would likely have been different if data had been analyzed for seasons other than the summer.
- Additionally, the conclusions drawn by analyzing the data are limited by the locations of the study's SIWSs. The conclusions would likely have been different if data had been collected (1) from a different type of feeder, such as predominately industrial or rural rather than a residential feeder or (2) from a different geographical area, such as in the mountains / foothills rather than in a high-plains desert valley.

These disclaimers, however, can also be considered opportunities to continue the research to test the statistical methods and analysis used in this study.

Discussion

The following sub-sections will discuss what was learned during the research study and propose some possible next steps. First, the results of the study will be revisited, and then a brief reflection on the research design process with lessons learned will be made, followed by a consideration of possible applications of the results of the study, and ending with possible areas of future research.

The Study's Findings Revisited

Analysis of the data gathered from the three SIWSs over the time period between June 21, 2013 and September 21, 2013 include the following results.

First, is there a statistical relationship (correlation) between solar intensity and load? The answer seems to be yes, but with the understanding that correlation does not imply causation.

- Solar intensity data collected from the southerly-configured sensor at the three SIWSs tends to lead load from 3.96 to 4.13 hours with a correlation of 0.94 across all three locations.
- Solar intensity data collected from the global-configured sensor at the three SIWSs tends to lead load from 4.00 to 4.02 hours with a correlation ranging from 0.95 to 0.96.
- Solar intensity data collected from the westerly-configured sensor at the three SIWSs tends to lead load from 1.76 to 1.94 hours with a correlation ranging from 0.88 to 0.91. The curves of the westerly-configured irradiances tend to peak closer to the time of the load peaks, but with a somewhat lower certainty than the southerly- and global-configured irradiances.

Next, what other relationships are there between load and meteorological parameters (such as wind speed and ambient temperature)? The answers seem to be that there is a strong correlation between ambient temperature data and load data, but at best a tepid correlation between wind speed data and load data.

- Ambient temperature measured at the three SIWSs tends to lead load from 0.70 to 0.86 hours with a correlation ranging from 0.96 to 0.97 across all three locations. This was not a surprising result, as the relationship between temperature and load has long been known. What was a little surprising was the range in lead time between the three SIWSs.
- Wind speed measured at the three SIWSs tends to lead load from 1.80 to 2.38 hours with a correlation ranging from 0.68 to 0.70 across all three locations. This tepid statistical relationship between wind speed and load also was not a surprising result, considering the low auto-correlation results applied to wind speeds.

Additional analyses were also made for relationships that did not specifically answer the research questions simply because the data were available. Among the results were:

- There seems to be a moderately strong relationship between the solar intensity data and the ambient temperature data.
    - Solar intensity data collected from the southerly-configured sensor at the three SIWSs tends to lead ambient temperature from 3.05 to 3.21 hours with a correlation ranging from 0.89 to 0.90 across all three locations.
    - Solar intensity data collected from the global-configured sensor at the three SIWSs tends to lead ambient temperature from 3.05 to 4.14 hours with a correlation ranging from 0.91 to 0.92.

- Solar intensity data collected from the westerly-configured sensor at the three SIWSs tends to lead ambient temperature from 0.91 to 1.09 hours with a correlation ranging from 0.84 to 0.87.

- There seems to be, at best, a tepid relationship between the solar intensity data and the wind speed data.
  - Solar intensity data collected from the southerly-configured sensor at the three SIWSs tends to lead wind speed from 1.87 to 2.08 hours with a correlation ranging from 0.66 to 0.68 across all three locations.
  - Solar intensity data collected from the global-configured sensor at the three SIWSs tends to lead wind speed from 1.87 to 2.32 hours with a correlation ranging from 0.66 to 0.68 across all three locations.
  - Solar intensity data collected from the westerly-configured sensor at the three SIWSs tends to lag wind speed (for SIWS01 and SIWS02) by 0.20 hours with a correlation ranging from 0.67 to 0.72, and tends to lead wind speed (for SIWS03) by 0.20 with a correlation of 0.72.

Reflections on the Research Design Process with Lessons Learned

The main reason for the research was to answer the questions: (1) is there a statistical relationship (correlation) between solar intensity and load and (2) what other relationships are there between load and meteorological parameters (such as wind speed and ambient temperature). The study was designed so that data could be collected from solar irradiance weather stations (SIWSs) located along a feeder that is predominately populated with residential and commercial customers, those customers considered the most likely to install roof-top photovoltaic systems. The LCST-044 feeder was chosen because of its easterly to westerly geographical span; a typical 35kV feeder typically covers a greater geographical area than a typical 12kV feeder, and the thought when the research study was designed was that there would be comparisons also made between SIWS locations. As it turned out, to answer the research questions, the decision was made not to also study the comparisons between stations.

The three SIWSs were constructed along the feeder and spaced relatively equidistant from one another across the approximate 3.5 east-to-west mile geographical span of LCST-044 in time to begin collecting data beginning May 21, 2013. There was some discussion prior to the data-collection process regarding how to design the SIWSs sites: chiefly, if they should be comprised of panels versus sensors. The decision was made to use sensors rather than panels, and that proved to be the better choice.

The SIWSs were designed to collect data every 10 seconds, including a time stamp, wind speed, wind direction, ambient temperature, and, initially, solar intensities from two directions: westerly (269^{o} azimuth and 53^{o} from horizontal) and global upward (or horizontal to the ground). The decision to also collect solar intensity data southerly (180^{o} azimuth and 35^{o} from horizontal) was made sometime after data collection began May 21 in time for the June 21, 2013 through September 21, 2013 official study period. Future data collection would also implement a tri-directional configuration of SIWSs for collecting irradiance data rather than the initial bi-directional configuration for completeness of the data.

As with most research studies, the most difficult part of the research design process was to choose and implement the most appropriate statistical tool by which to analyze the data collected. An iterative process ensued, beginning with making a simple correlation between daily peak loads and daily peak irradiances, and realizing that comparing two variables that were clearly unrelated yielded unsatisfactory results. Making the better choice of comparing data at the same time intervals then time-

shifting the data, through the use of auto-correlations and then cross-correlations, provided analysis that was sufficient for noting relationships on a daily basis. The last step in the analysis process, applying maximum cross-correlations and plotting kernel densities, allowed the statistical relationships — over the entire 93-day span of the data gathered — to emerge. Any similar research study in the future will need to apply a cross-correlational / maximum cross-correlational / kernel density approach to analyzing the data gathered.

For future design of data-gathering research, it will be important to (1) develop specific questions that need to be answered, (2) have a good idea of the form the research will need to take to answer the questions, and (3) choose the appropriate statistical tool, upfront, that will form the data into the answers to the questions. A couple decisions made early in this research study positively affected the ability to determine the answers to the research questions: the choice to collect the data from irradiance sensors rather than from solar panels, and the choice to add a southerly-exposed sensor to the global and westerly sensors at each of the three SIWSs. The decision to collect data from three somewhat equidistant locations along the same feeder route, while not necessarily directly contributing to the answers to the research questions, did provide the opportunity to validate the data collected and will be a source of data for any research questions regarding relationships between the variables based on geography.

The weakest part of the original research design was the fact that the most appropriate statistical tool for analyzing the data had not been chosen. Frankly, at the time of design, the shape that the collected data was eventually to take remained an unknown. Once it was apparent what the various variables looked like in association with the feeder's load profile, the iterative process of choosing the appropriate statistical tool could emerge. Planning for the future analysis of irradiance data based on a certain statistical tool will begin with the knowledge obtained through the analysis of this study's data.

Possible Applications of the Research Results

So far, the data collected has already been used. For example, the data has been used within the OpenDSS software in performing generation interconnection studies of large photovoltaic systems, both at the feasibility level and at the system impact level. Additionally, it has been used in support of a report on the various energy storage applications, and how energy storage can be used in collaboration with photovoltaic systems in reducing the effects of feeder summer peak loads. Other applications of the data have been in assisting with resource planning as part of Idaho Power's integrated resource plan as well as in collaboration with Sandia National Laboratories for their variability and GHI to POA conversion studies.

Some potential areas for future research include:

- Recommending preferred photovoltaic orientations to commercial customers for their rooftop applications that would best support reducing the effects of feeder summer peak loads. Perhaps an energy efficiency program could be developed, offering incentives to such commercial customers, to configure their systems such that Idaho Power could also benefit.
- Designing a demonstration project of photovoltaic system coupled with energy storage to extend peak load reduction at the end of a distribution feeder. In fact, such a design process has already begun.

Opportunities for Further Research

One of the more difficult aspects of drafting this report has been to focus only on the material that directly supports and answers the stated research questions. Data continues to be collected from the three SIWSs beyond the June 21, 2013 to September 21, 2013 study period, resulting in more than a year's worth of data having been collected. Over the course of the many meetings that have occurred to draft this report, ideas have been generated regarding the additional studies that could be made with the study data as well as with the additional data collected post-study. Following are a few of the ideas that were generated that could be opportunities for further research.

Using this Research Study Data

Now that it is apparent that there is a time shifted correlation between solar irradiance and feeder load, the next step in the process would be to return to the ten-second data and compare solar irradiance to its time shifted load counterpart to see if, at that greater granularity, the load actually increases when irradiance increases or if load actually decreases during periods of cloud cover.

After that, the design of the layout of the SIWSs plus the initial request to the University of Idaho for data analysis leads to a couple additional opportunities for research. First off, the SIWSs were geographically configured along the LCST-044 feeder route, spaced equidistant from one another. While that fact was not particularly pertinent in answering the research questions that are the focus of this report, it could generate a follow-up research question of the form, "Is there a relationship between irradiance data collected across a geographical area?" Perhaps performing the cross-correlation analysis of the irradiance between each of the SIWS sites as follows

SIWS03	westerly southerly globally	to	SIWS02	westerly southerly globally
SIWS03	westerly southerly globally	to	SIWS01	westerly southerly globally
SIWS02	westerly southerly globally	to	SIWS01	westerly southerly globally

would catch the differences in irradiance as clouds move from east-to-west over the geographical area.

Additionally, part of the request to the University of Idaho for analyzing the data included the request to calculate the solar energy density (Watt-hours/m^2) per time interval for each site at each solar intensity orientation. This information was provided by the U of I but was not analyzed as part of this report because it did not contribute to answering the research questions.

Another possible use of the research data could be to run irradiance statistics, rather than daily, over a multiple-day time period to see if a relationship is evident as a predictor of the seasonal peak load.

Finally, the data could be used in combination (irradiance data collected from the western-oriented sensor combined with global, or western combined with southern) to determine the PV set-up for home- and business-owned systems that provide optimal benefit the utility.

Branching out from this Research Study Data

As far as other interesting areas for further research, they can be broken down by (1) using the additional data that has been collected subsequent to the study's data and (2) implementing additional types of research design protocols.

Some ideas for using the additional data that has been collected include:

1. Analyzing data from other seasons of the year in the same manner as the data collected for the study interval, to see what similarities and differences might apply. A couple time-frames that might be of particular interest might be at the time of the feeder's winter peak (for this particular set of data, the winter peak occurred 12-8-2013 at 6:05 p.m.) and at the time of the feeder's minimum peak (for this particular set of data, the minimum peak occurred 9-27-2013 at 7:55 p.m.).
2. Including cross-correlations of solar to wind to see if there are any complimentary relationships to one another (as solar irradiance increases, does the wind decrease, and vice versa).
3. Analyzing data collected in summer 2014 (a significantly cooler summer than summer 2013) using the same methods as for summer 2013, and comparing the results one with the other.

Some ideas for implementing additional design protocols include:

1. Determining what effects, if any, humidity might have on solar intensity and load.
2. Including the cross-correlations of the feeder loads going from east to west (from TNML-011 directly east of LCST-044 to LCST-044 through JPLN-013 directly west of LCST-044) to follow the effects of cloud cover.
3. Collecting and analyzing data from additional feeder-types where solar might be of interest, such as the areas where there have been historical interest in large solar projects (southeastern Oregon, the Grandview area, the desert near Mountain Home) as well as areas where clusters of net metering customers are emerging (the Wood River area, the northeast Boise foothills).
4. Including variability / volatility as part of irradiance statistical analyses.
5. Correlating wind speed to solar variability / volatility.
6. Designing a Locust-style set-up in a winter-peaking area, complete with snowy season, to see how the reflection of snow onto the sensors affects statistical relationships.

Conclusion

In analyzing the solar irradiance data collected along the path of the LCST-044 feeder in comparison with the feeder's accompanying loads during the study period of June 21, 2013 to September 21, 2013, there seems to be strong correlations between loads and solar irradiance regardless of the configuration of the irradiance sensors at the three solar irradiance weather stations. Additionally, the correlation between the ambient temperature and the feeder load seemed to be strong (as was expected), but the correlation between wind speed and feeder load seemed to be tepid, at best (also expected).

The correlations between feeder loads and solar irradiance were stronger at the southerly-facing and global-facing sensors, but the time-shift was less — by about two hours — at the westerly-facing sensors. In other words, no matter the configuration of the sensors, the curves of the measured irradiance never peaked at the same time as the feeder load. Relying on PV devices alone will have little, if any, effect on reducing the feeder load at its peak.

However, if a PV device can operate in tandem with an energy storage device, allowing the energy storage device to be charging as the PV device operates then operating as the feeder load peaks, there might be an opportunity to balance the feeder peak with energy from a renewable source.

So far, the data collected has already been used. For example, the data has been used within the OpenDSS software in performing generation interconnection studies of large photovoltaic systems, both at the feasibility level and at the system impact level. Additionally, it has been used in support of a report on the various energy storage applications, and how energy storage can be used in collaboration with photovoltaic systems in reducing the effects of feeder summer peak loads. Other applications of the data have been in assisting with resource planning as part of Idaho Power's integrated resource plan as well as in collaboration with Sandia National Laboratories for their variability and GHI to POA conversion studies.

The results of the research is also being used in support of a research demonstration project that will place a number of combination PV / energy storage systems at the end of a distribution feeder as a possible way of balancing feeder peak loads / mitigating for low end-of-line feeder voltage. The design of that research is already underway, starting with a senior design project in collaboration with Boise State University in the spring semester 2015 and scheduled to continue with an engineering intern in summer 2015.

Another possibility of applying the results of the research is to continue analyzing the data for the full year and recommending a preferred PV panel configuration for commercial customers to implement with their proposed PV systems. It may be that Idaho Power can offer some sort of incentive to its commercial customers who choose to configure their systems to best optimize IPC's requirements.

Finally, learning what still remains to be known was probably the most important part of the research and analysis of the data. Analyzing the data from the point-of-view of answering the research questions just contributed to the asking of new and different questions. Some potential areas for future research, that can begin immediately, include:

- Calculating and analyzing the solar energy density (Watt-hours/m^2) per time interval for each site at each solar intensity orientation.
- Running the irradiance statistics over a multi-day time period to see if a relationship is evident as a predictor of the seasonal feeder peak load.
- Analyzing data from other seasons of the year to see what similarities and differences might result.
- Including cross-correlations of solar to wind to see if there are any complimentary relationships to one another.
- Collecting and analyzing data from additional feeder-types where solar energy might be tapped, such as the areas where there have been historical interest in large solar projects as well as areas where clusters of net metering customers are emerging.
- Including variability / volatility as part of irradiance statistical analyses.

References

[1] M.J. Reno and K. Coogan, "Grid Integrated Distributed PV (GridPV)", Sandia National Laboratories, SAND2013-6733, August 2013.

[2] M.J. Reno, R.J. Broderick, and S. Grijalva, "Formulating a Simplified Equivalent Representation of Distribution Circuits for PV Impact Studies", Sandia National Laboratories, SAND2013-2831, April 2013.

[3] M.J. Reno, K. Coogan, S. Grijalva, R.J. Broderick, and J.E. Quiroz, "PV Interconnection Risk Analysis through Distribution System Impact Signatures and Feeder Zones", *Power and Energy Society General Meeting, 2014 IEEE,* pp. 1 – 5, 28 – 31 July 2014.

[4] E.C. Kern and M.C. Russell, "Spatial and Temporal Irradiance Variations over Large Array Fields", *Photovoltaic Specialists Conference, 1988, Conference Record of the Twentieth IEEE,* pp. 1043 – 1050, vol. 2, 1988.

[5] J. Schoene, V. Zheglov, D. Houseman, J.C. Smith, and A. Ellis, "Photovoltaics in Distribution Systems — Integration Issues and Simulation Challenges", *Power and Energy Society General Meeting (PES), 2013 IEEE,* pp. 1 – 5, 21 – 25 July 2013.

[6] M.A. Cohen and D.S. Callaway, "Modeling the Effect of Geographically Diverse PV Generation on California's Distribution System", *Smart Grid Communications (SmartGridComm), 2013 IEEE International Conference on,* pp. 702 – 707, 21 – 24 October 2013.

[7] M. Rylander and J. Smith, "Stochastic Analysis to Determine Feeder Hosting Capacity for Distributed Solar PV", Electric Power Research Institute (EPRI), Palo Alto, CA: 2012. 1026640.

[8] A. Hoke, R. Butler, J. Hambrick, and B.Kroposki, "Maximum Photovoltaic Penetration Levels on Typical Distribution Feeders", National Renewable Energy Laboratory (NREL), NREL/JA-5500-55094, July 2012.

[9] J. Quiroz and M. Reno, "Detailed Grid Integration Analysis of Distributed PV", Sandia National Laboratories, SAND report 2012-4533, 2012.

[10] H. Thomas, K. Lynn, and A. Razon, "Current Results of the US DOE High Penetration Solar Deployment Project", *Photovoltaic Specialists Conference (PVSC), 2012 38th IEEE,* pp. 731 – 736, 3 – 8 June 2012.

[11] D. Narang and J. Hambrick, "High Penetration PV Deployment in the Arizona Public Service System", *Photovoltaic Specialists Conference (PVSC), 2011 37th IEEE,* pp. 2042 – 2045, 19 – 24 June 2011.

[12] P. Gotseff, J. Cale, M. Baggu, D. Narang, and K. Caroll, "Accurate Power Prediction of Spatially Distributed PV Systems using Localized Irradiance Measurements", *Power and Energy Society General Meeting, 2014 IEEE,* pp. 1 – 5, 28 – 31 July 2014.

[13] R.K. Varma, J. Berge, I. Axente, V. Sharma, and K. Walsh, "Determination of Maximum PV Solar System Connectivity in a Utility Distribution Feeder", *Transmission & Distribution Conference and Exposition, 2012 IEEE PES,* pp. 1 – 6, 7 – 10 May 2012.

[14] A. Navarro-Espinosa and L.F. Ochoa, "On the Cascading Effects of Residential-Scale PV Disconnection Due to Voltage Rise", *Power and Energy Society General Meeting, 2014 IEEE,* pp. 1 – 5, 28 – 31 July 2014.

[15] S. Ghosh, S. Rahman, and M. Pipattanasomporn, "Local Distribution Voltage Control by Reactive Power Injection from PV Inverters Enhanced with Active Power Curtailment", *Power and Energy Society General Meeting, 2014 IEEE,* pp. 1 – 5, 28 – 31 July 2014.

[16] E.M. Steward, T.P. Aukai, S.D.J. MacPherson, B.P. Quach, D. Nakafuji, and R. Davis, "A Realistic Irradiance-based Voltage Flicker Analysis of PV Applied to Hawaii Distribution Feeders", *Power and Energy Society General Meeting, 2012 IEEE,* pp. 1 – 7, 22 – 26 July 2012.

[17] D.K. Click, H. Moaveni, K.O. Davis, R.H. Meeker Jr., R.M. Reedy, A. Pappalardo, and R. Krueger, "Effects of Solar Resource Variability on the Future Florida Transmission and Distribution System", *Transmission & Distribution Conference and Exposition, 2012 IEEE PES,* pp. 1 – 6, 7 – 10 May 2012.

[18] S.J. Ranade, D.R. Sagi, R. Mulpuri, R. Surabhi, and J. Mitra, "Likelihood of Islanding in Distribution Feeders With Photovoltaic Generation", *Power Engineering Society General Meeting, 2007 IEEE,* pp. 1 – 6, 24 – 28 June 2007.

[19] J.E. Bigger, E.C. Kern, and M.C. Russell, "Cost-effective Photovoltaic Applications for Electric Utilities", *Photovoltaic Specialists Conference, 1991, Conference Record of the Twenty Second IEEE,* pp. 486 – 492, vol. 1, 7 – 11 October 1991.

[20] M.T. Arif, A.M.T. Oo, A.S. Ali, and G. Shafiullah, "Impacts of Storage and Solar Photovoltaic on the Distribution Network", *Universities Power Engineering Conference (AUPEC), 2012 22nd Australasian,* pp. 1 – 6, 26 – 29 September 2012.

[21] O. Larova, F. Cheng, S. Abdollahy, H. Barsun, A. Mammoli, D. Dreisigmayer, S. Willard, B. Arellano, and C. van Zeyl, "Analysis of Bettery Storage Utilization for Load Shifting and Peak Smoothing on a Distribution Feeder in New Mexico", *Innovative Smart Grid Technologies (ISGT), 2012 IEEE PES,* pp. 1 – 6, 16 – 20 January 2012.

[22] A. Chikh and A. Chandra, "Sizing and Power Management for a Stand-Alone PV System in Cold Climate", *Transmission & Distribution Conference and Exposition, 2012 IEEE PES,* pp. 1 – 6, 7 – 10 May 2012.

[23] R. Singh, F. Tuffner, J. Fuller, and K. Schneider, "Effects of Distributed Energy Resources on Conservation Voltage Reduction (CVR)", *Power and Energy Society General Meeting, 2011 IEEE,* pp. 1 – 7, 24 – 29 July 2011.

[24] C. Chengrui and D.C. Aliprantis, "Cumulus Cloud Shadow Model for Analysis of Power Systems with Photovoltaics", Power Systems, IEEE Transactions on, vol. 28, no. 4, pp. 4496 – 4506, Nov. 2013.

[25] K. Stefferud, J. Kleissl, and J. Schoene, "Solar Forecasting and Variability Analyses Using Sky Camera Cloud Detection and Motion Vectors", *Power and Energy Society General Meeting, 2012 IEEE,* 22 – 26 July 2012.

[26] H. Moaveni, D.K. Click, R.H. Meeker, R.M. Reedy, and A. Pappalardo, "Quantifying Solar Power Variability for a Large Central PV Plant and Small Distributed PV Plant", *Photovoltaic Specialists Conference (PVSC),* 2013 IEEE 39th, pp. 0969 – 0972, 16 – 21 June 2013.

Appendix 1 — Graphs derived from SISW01 data

Loads and irradiances

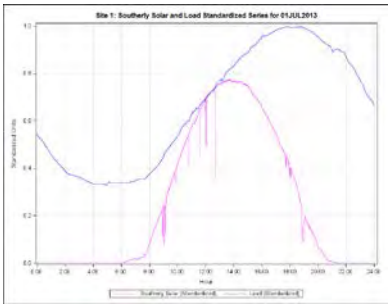

Southerly Solar & Load

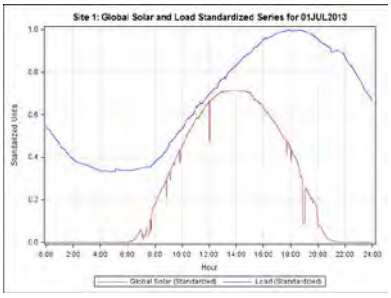

Global Solar & Load

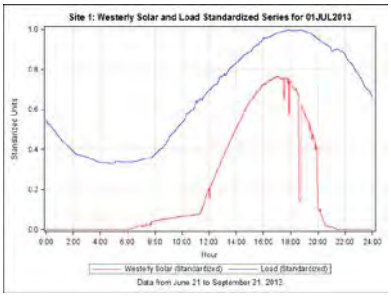

Westerly Solar & Load

07-01-2013, "max"

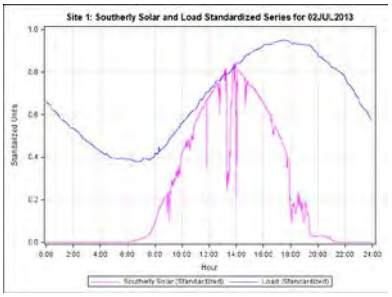

Southerly Solar & Load

Global Solar & Load

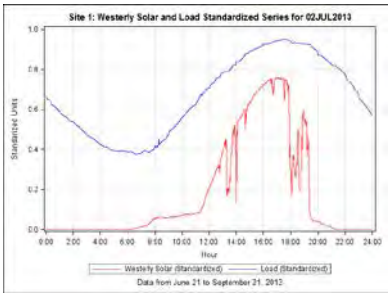

Westerly Solar & Load

07-02-2013, "max"

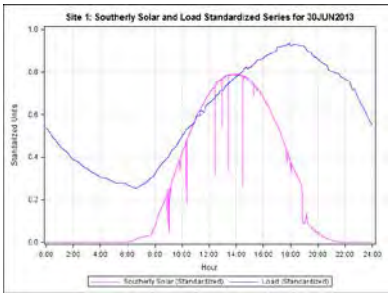

Southerly Solar & Load

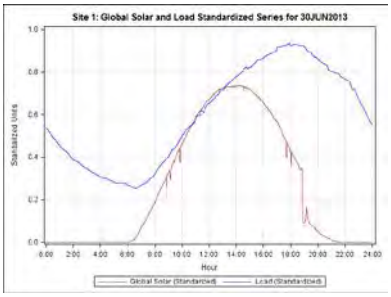

Global Solar & Load

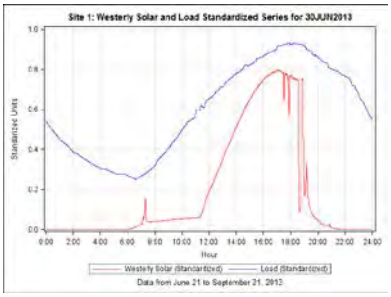

Westerly Solar & Load

6-30-2013, "max"

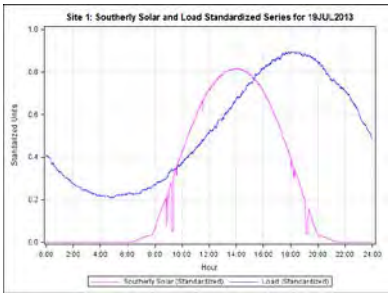

Southerly Solar & Load

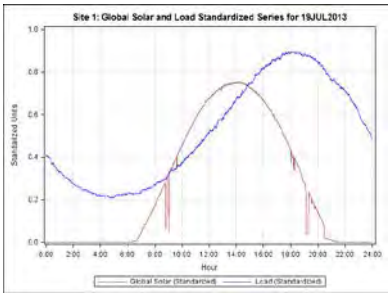

Global Solar & Load

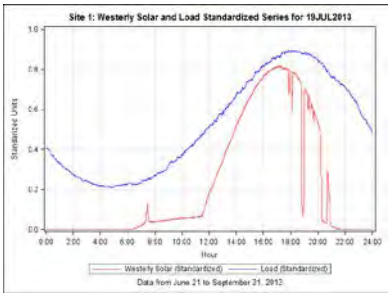

Westerly Solar & Load

7-19-2013, "max"

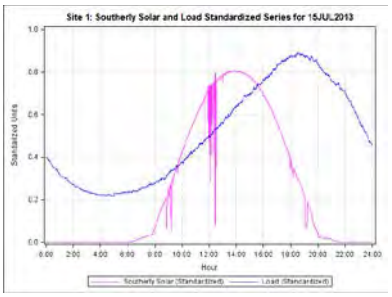

Southerly Solar & Load

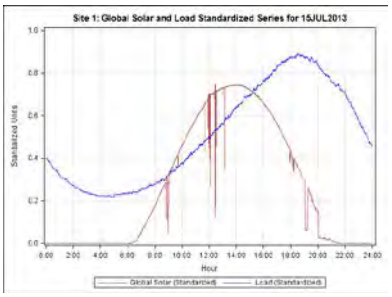

Global Solar & Load

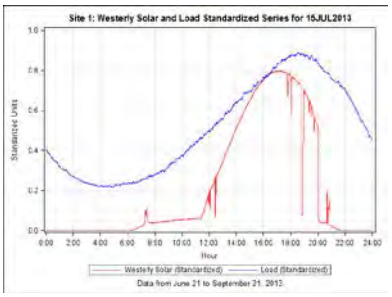

Westerly Solar & Load

7-15-2013, "max"

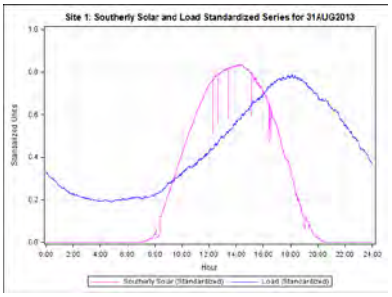

Southerly Solar & Load

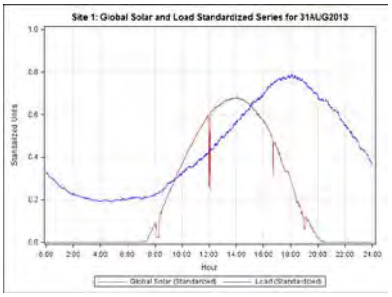

Global Solar & Load

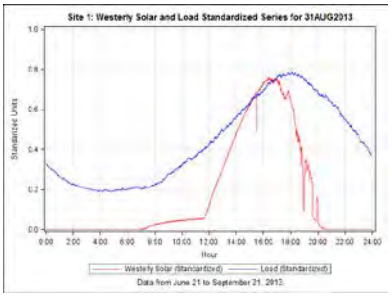

Westerly Solar & Load

8-31-2013, "mid"

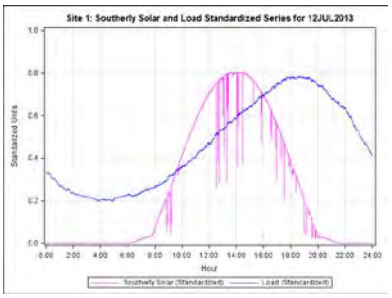

Southerly Solar & Load

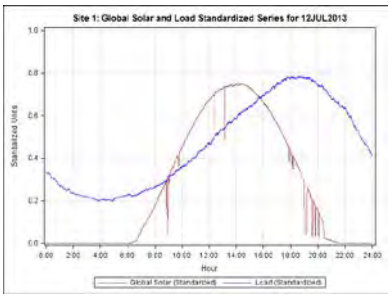

Global Solar & Load

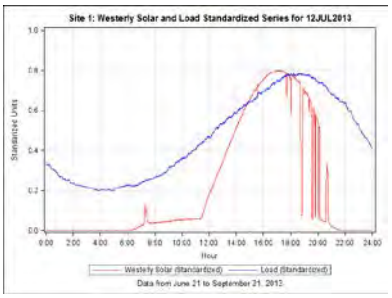

Westerly Solar & Load

7-12-2013, "mid"

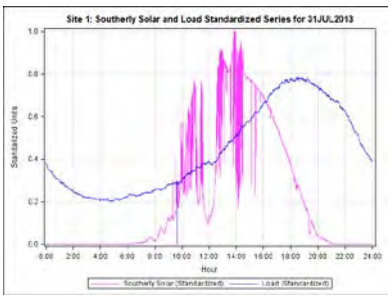

Southerly Solar & Load

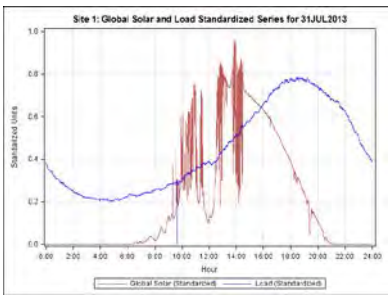

Global Solar & Load

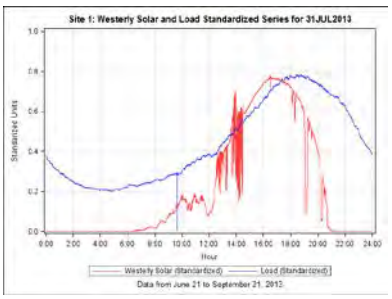

Westerly Solar & Load

07-31-2013, "mid"

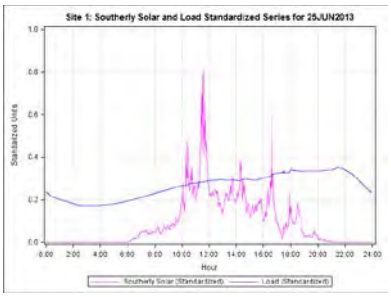

Southerly Solar & Load

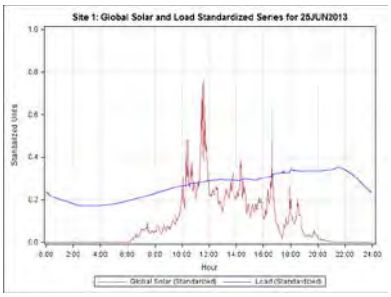

Global Solar & Load

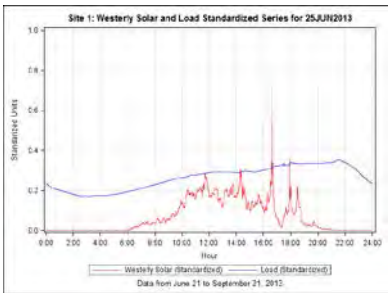

Westerly Solar & Load

06-25-2013, "min"

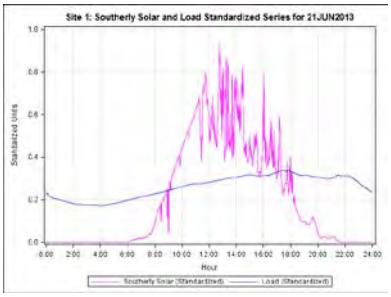

Southerly Solar & Load

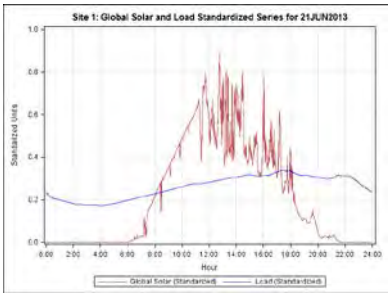

Global Solar & Load

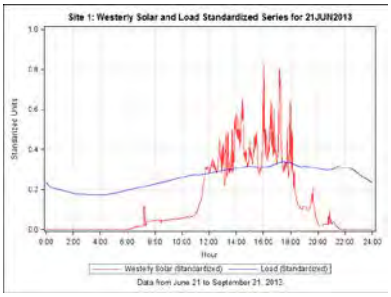

Westerly Solar & Load

6-21-2013, "min"

Auto-correlations of irradiances

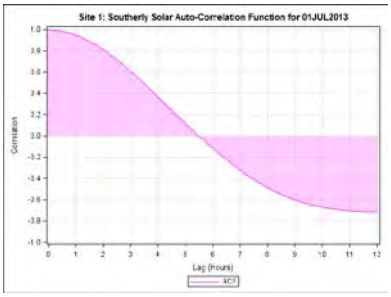

Southerly Solar

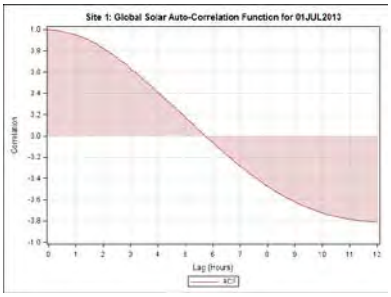

Global Solar

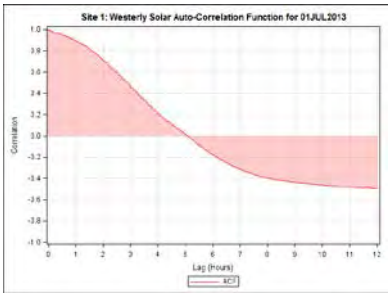

Westerly Solar

Mostly clear day: 07-01-2013

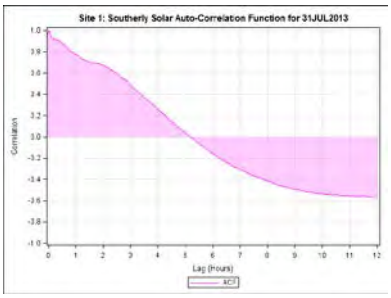

Southerly Solar

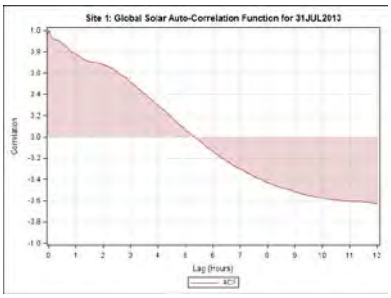

Global Solar

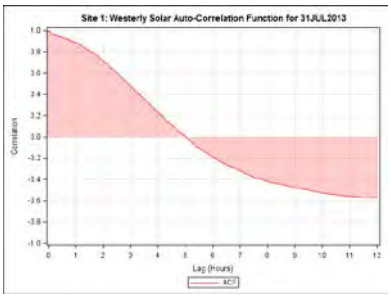

Westerly Solar

Moderately cloudy day: 07-31-2013

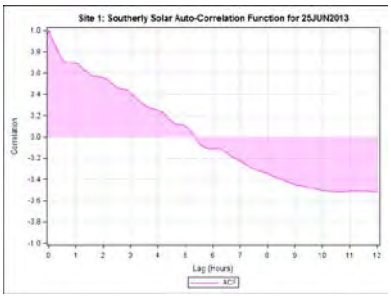

Southerly Solar

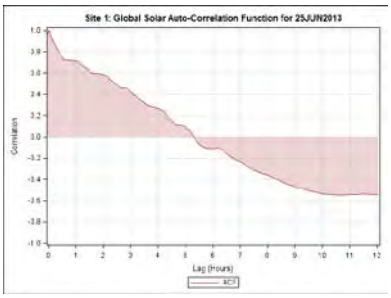

Global Solar

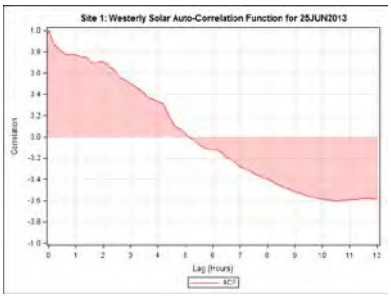

Westerly Solar

Very cloudy day: 06-25-2013

Cross-correlations of loads and irradiances

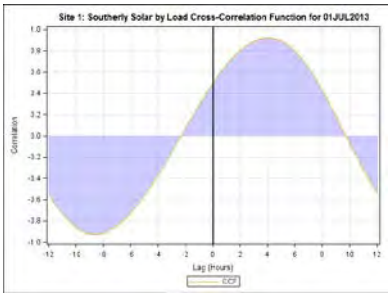

Southerly Solar & Load

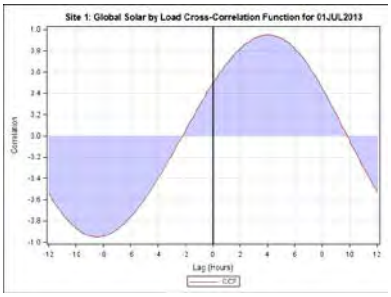

Global Solar & Load

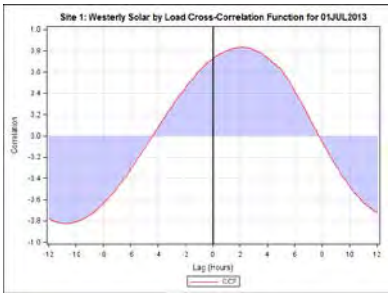

Westerly Solar & Load

Mostly clear day: 07-01-2013

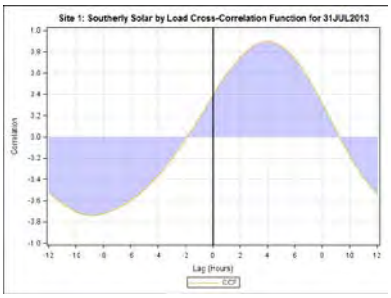

Southerly Solar & Load

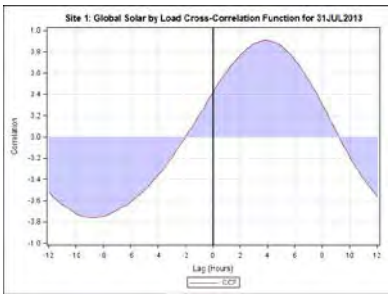

Global Solar & Load

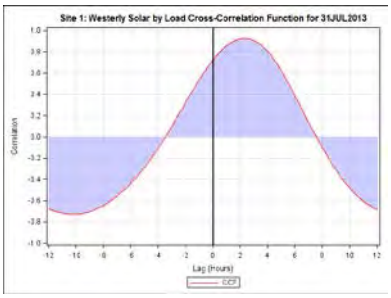

Westerly Solar & Load

Moderately cloudy day: 07-31-2013

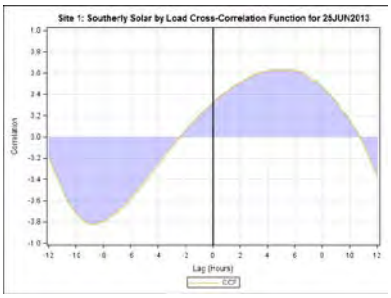

Southerly Solar & Load

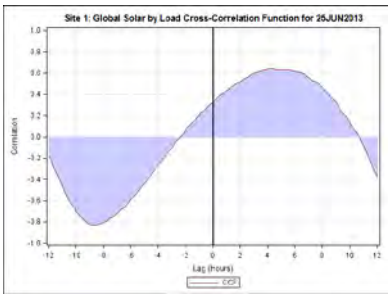

Global Solar & Load

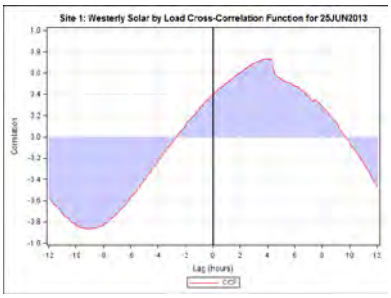

Westerly Solar & Load

Very cloudy day: 06-25-2013

Loads versus other weather factors

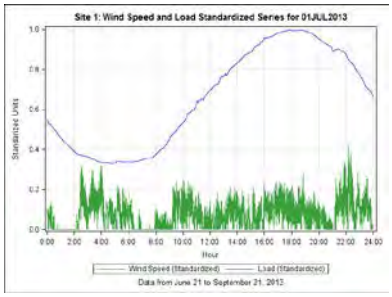

Wind Speed & Load

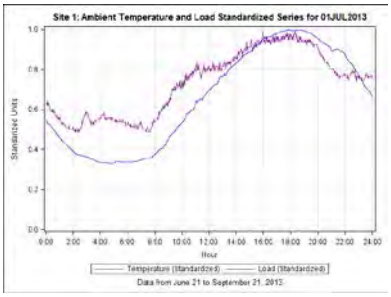

Ambient Temperature & Load

Mostly clear day: 07-01-2013

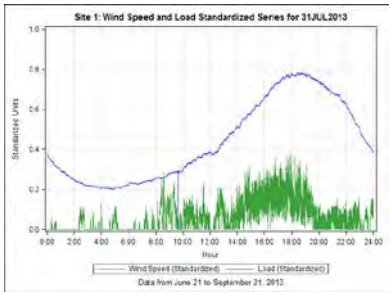

Wind Speed & Load

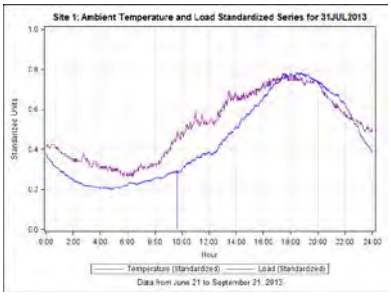

Ambient Temperature & Load

Moderately cloudy day: 07-31-2013

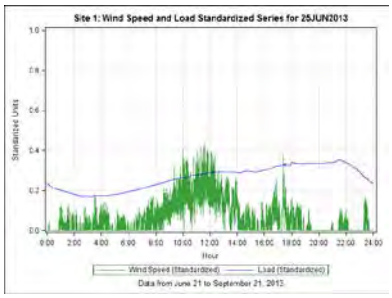

Wind Speed & Load

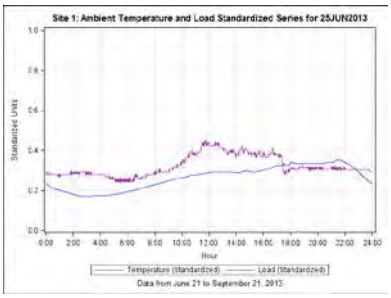

Ambient Temperature & Load

Very cloudy day: 06-25-2013

Auto-correlations of loads and other factors

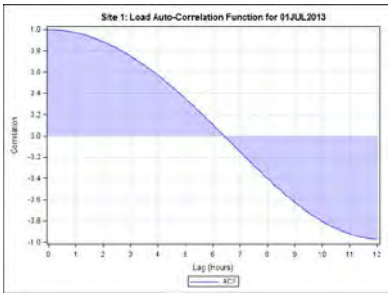

Load

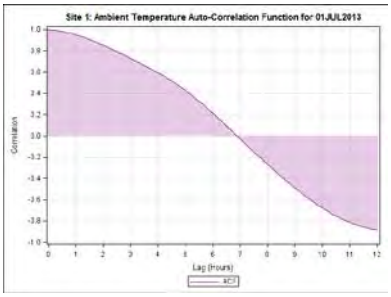

Ambient Temperature

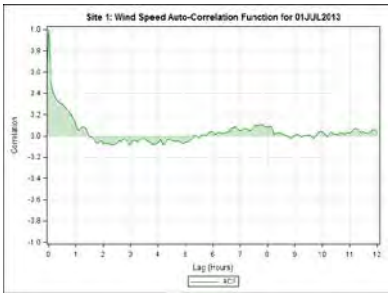

Wind Speed

Mostly clear day: 07-01-2013

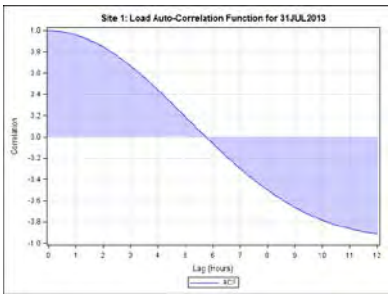

Load

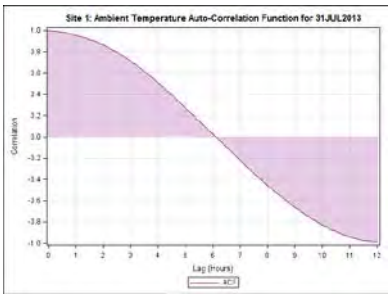

Ambient Temperature

Wind Speed

Moderately cloudy day: 07-31-2013

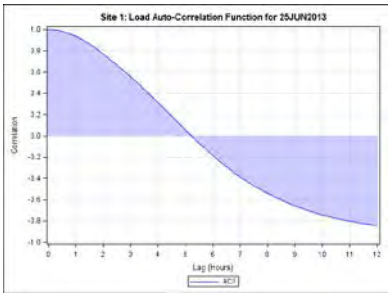

Load

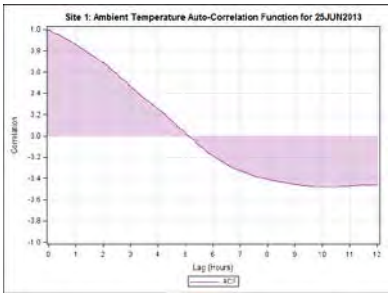

Ambient Temperature

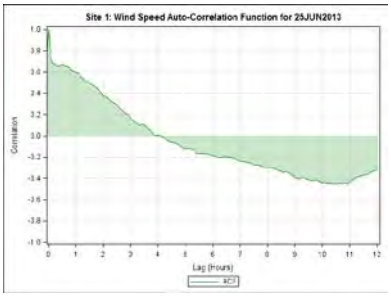

Wind Speed

Very cloudy day: 06-25-2013

Cross-correlations between loads and other weather factors

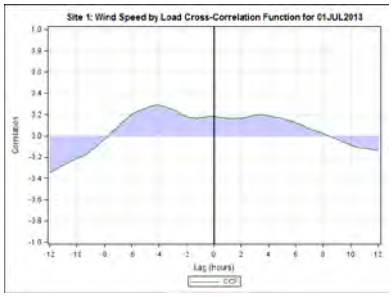

Wind Speed & Load

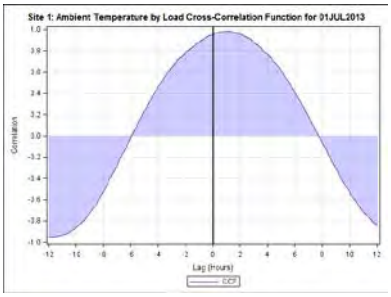

Ambient Temperature & Load

Mostly clear day: 07-01-2013

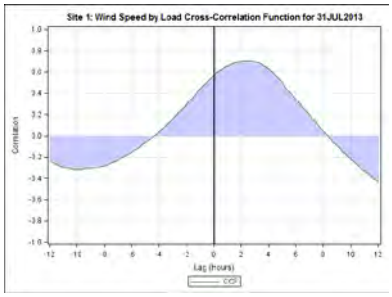

Wind Speed & Load

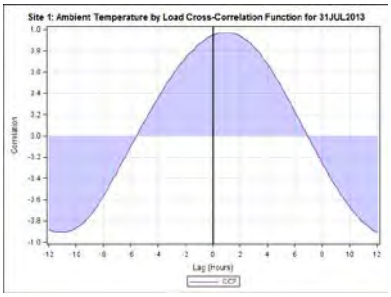

Ambient Temperature & Load

Moderately cloudy day: 07-31-2013

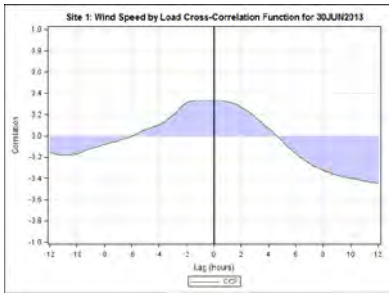

Wind Speed & Load

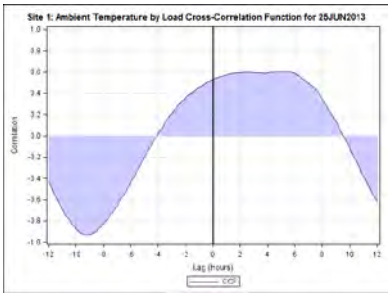

Ambient Temperature & Load

Very cloudy day: 06-25-2013

Maximum cross-correlations for the 93-day study period

Loads and irradiances

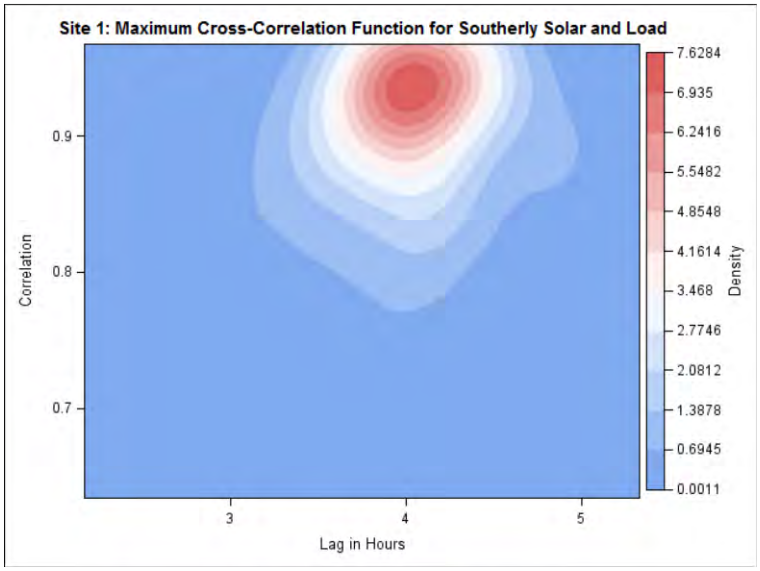

Lag	Correlation
4.045198	0.939251

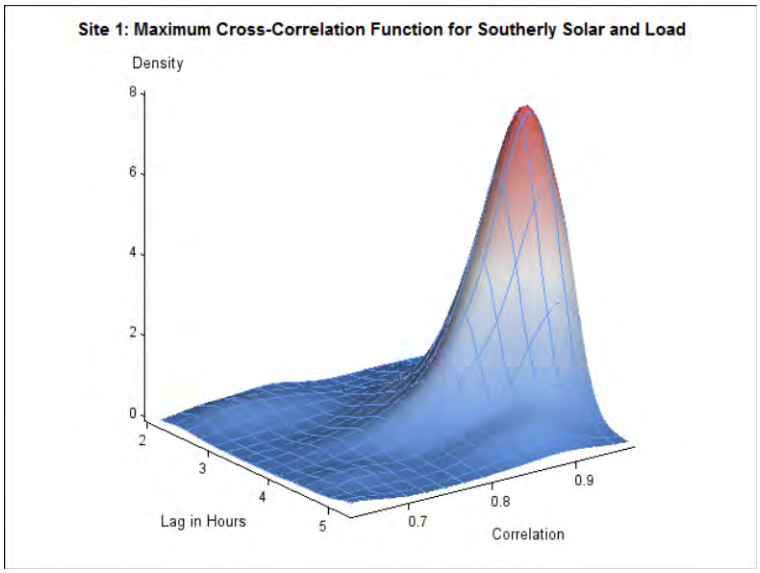

Southerly Solar & Load

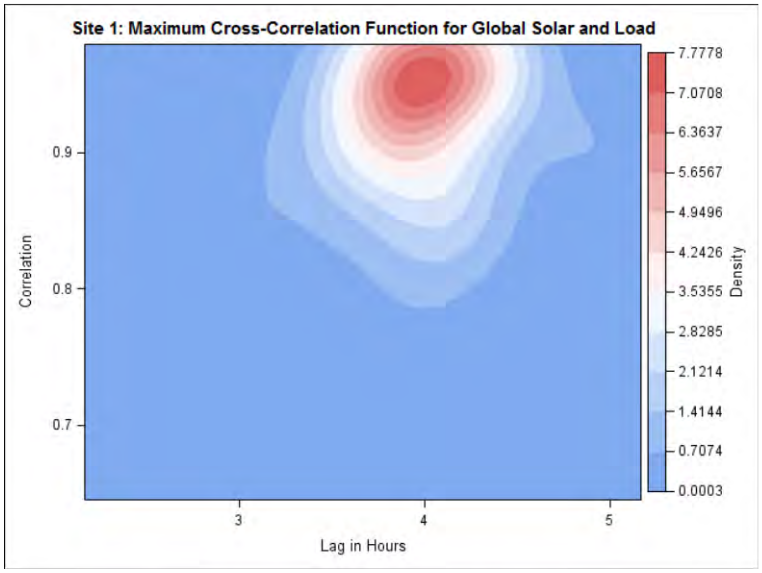

Lag	Correlation
3.997175	0.951355

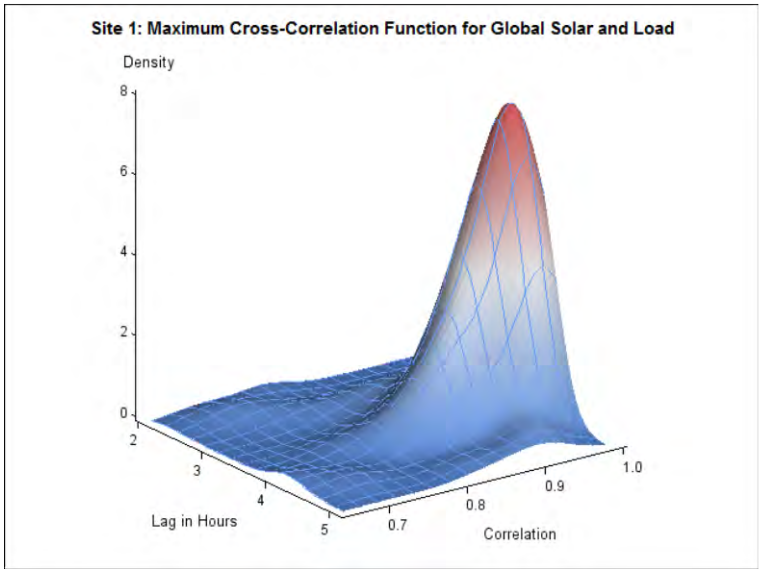

Global Solar & Load

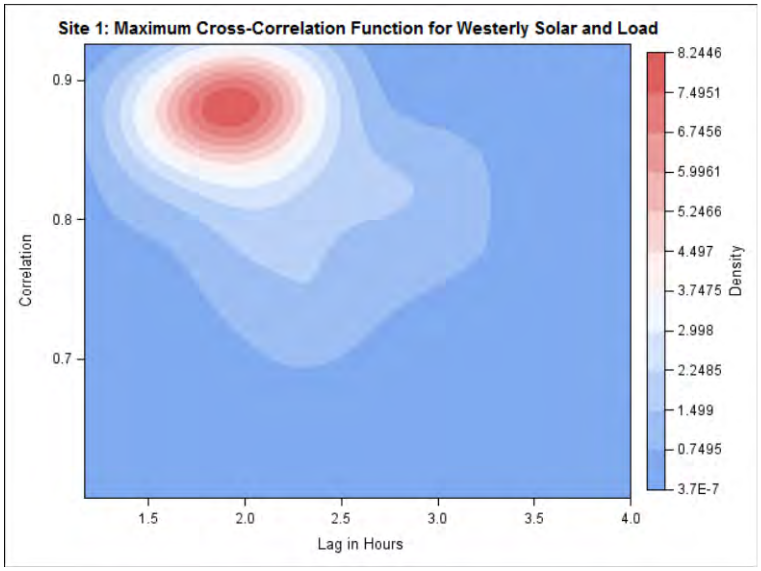

Lag	Correlation
1.935028	0.881936

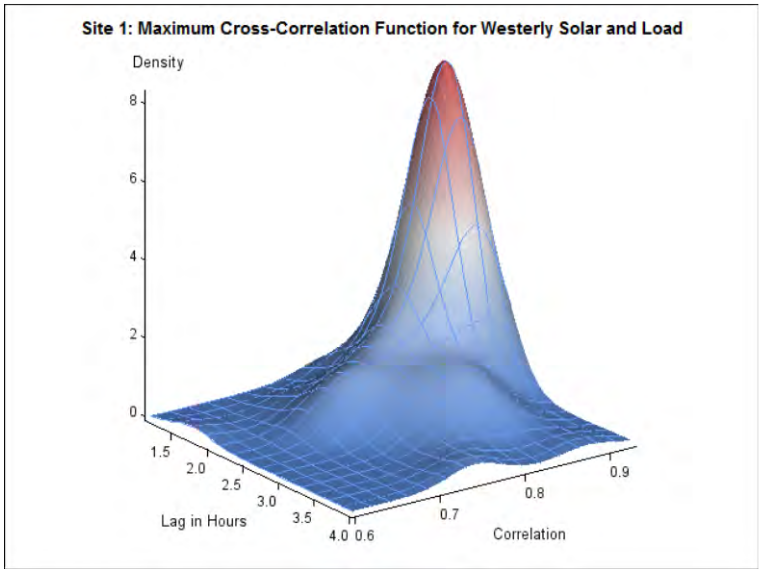

Westerly Solar & Load

Temperatures and irradiances

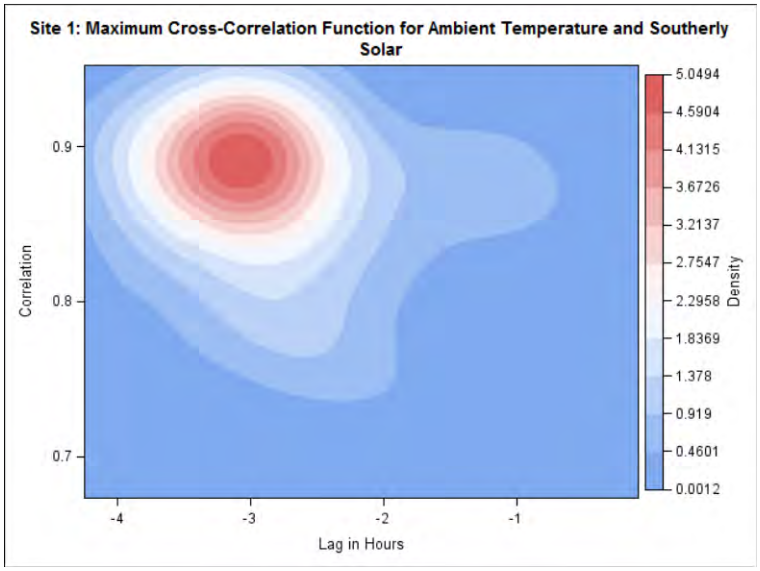

Lag	Correlation
-3.04944	0.890932

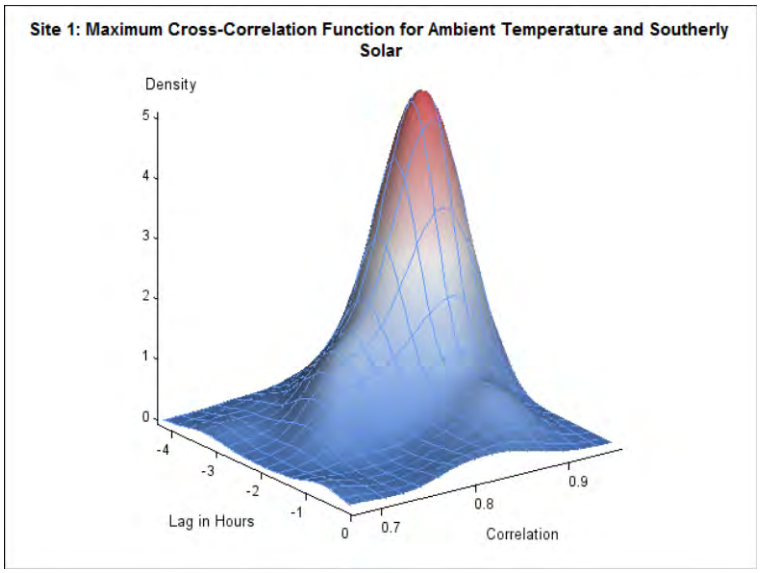

Southerly Solar & Temperature

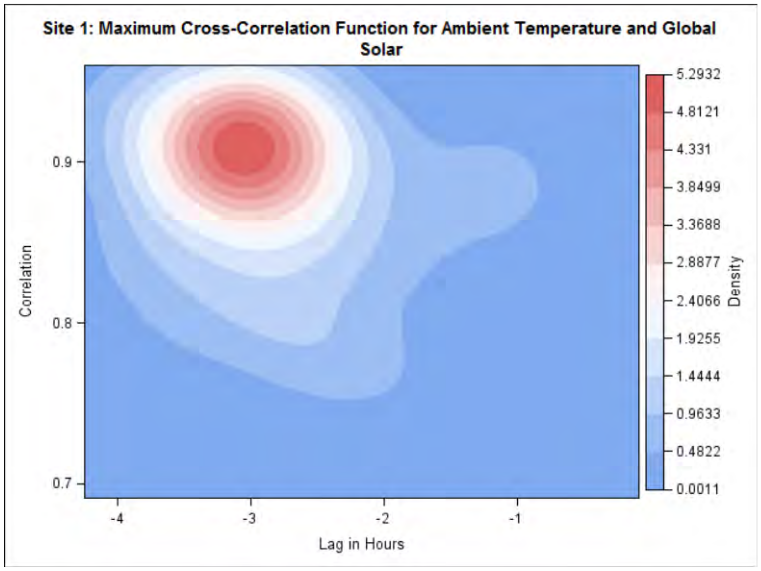

Lag	Correlation
-3.04944	0.91012

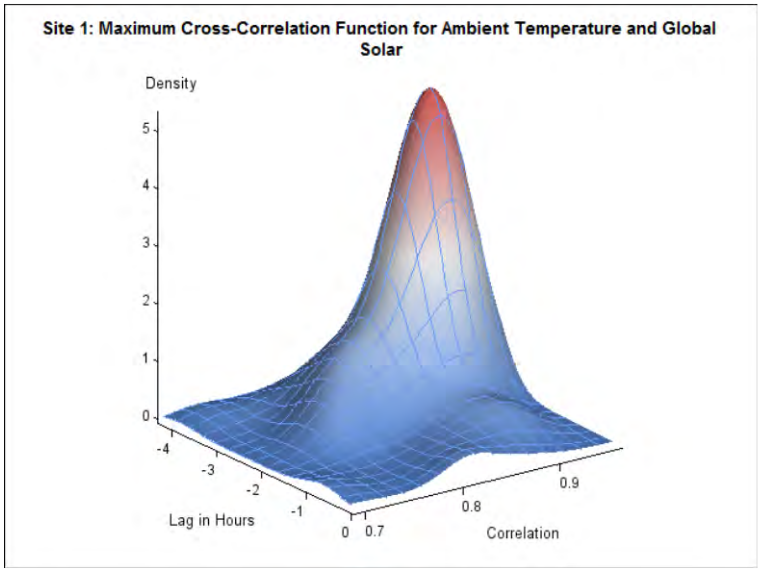

Global Solar & Temperature

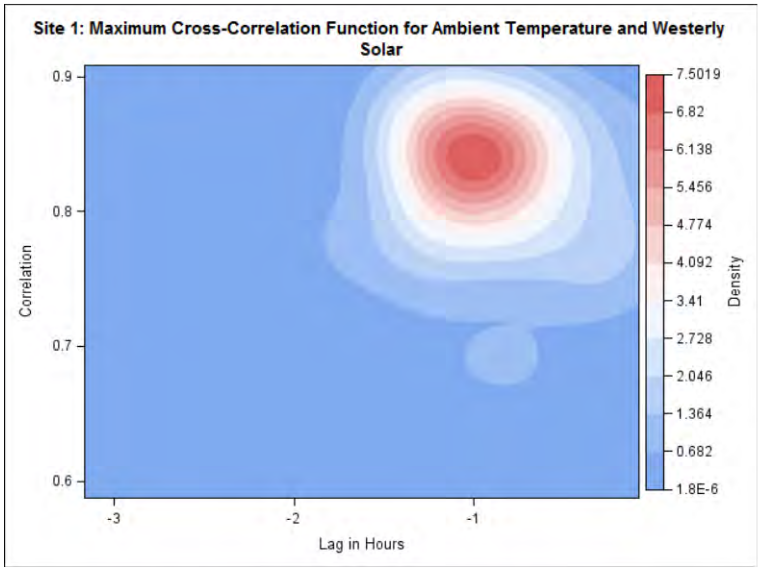

Lag	Correlation
-1.02401	0.843122

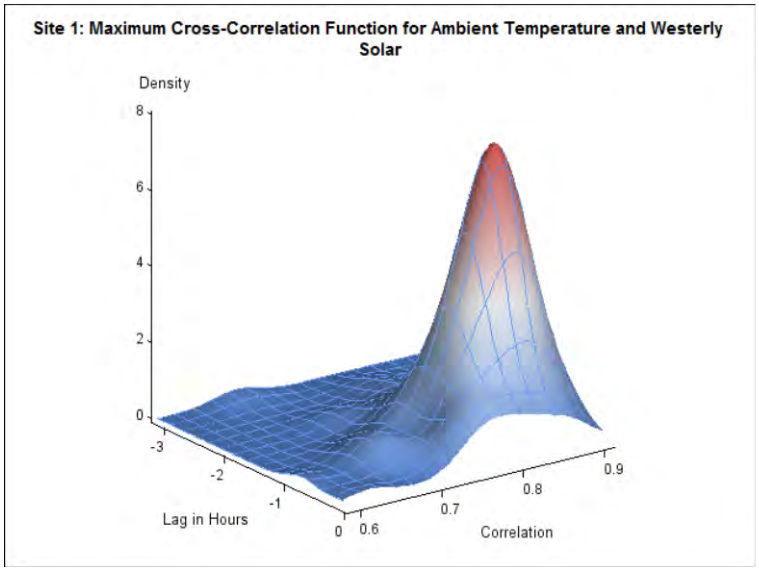

Westerly Solar & Temperature

Wind speeds and Irradiances

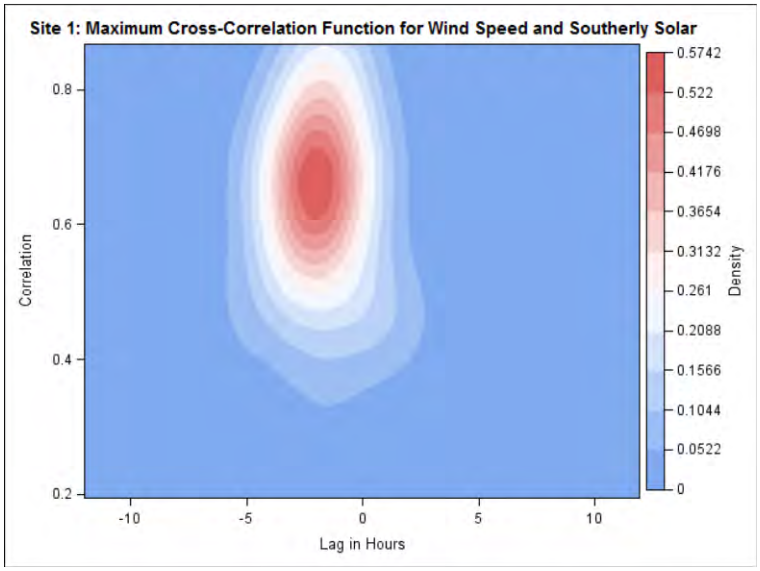

Lag	Correlation
-1.86582	0.661956

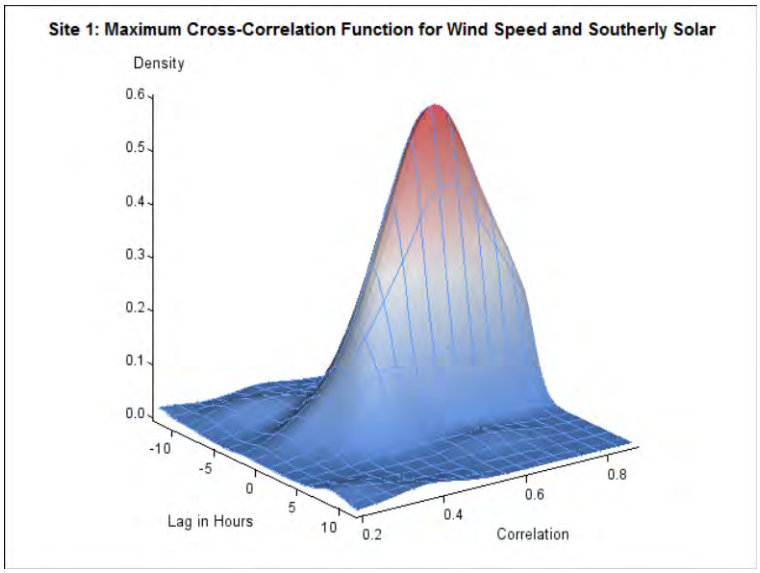

Southerly Solar & Wind Speeds

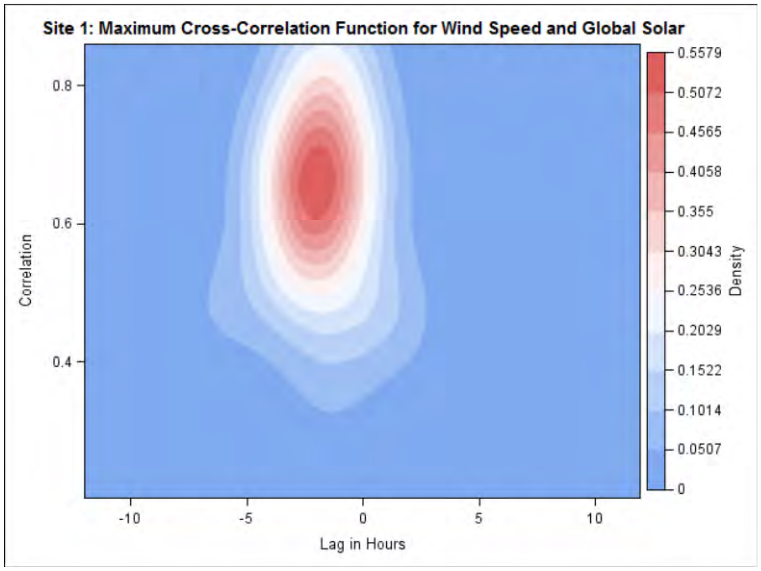

Lag	Correlation
-1.86582	0.659789

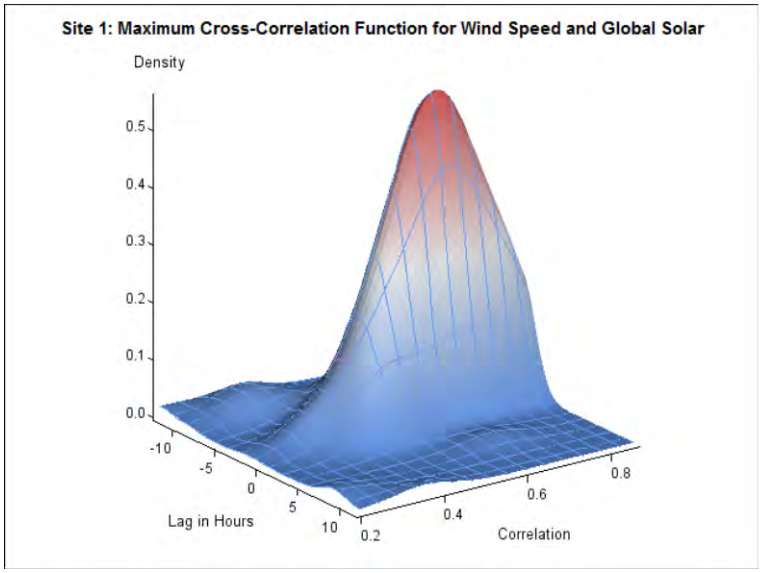

Global Solar & Wind Speeds

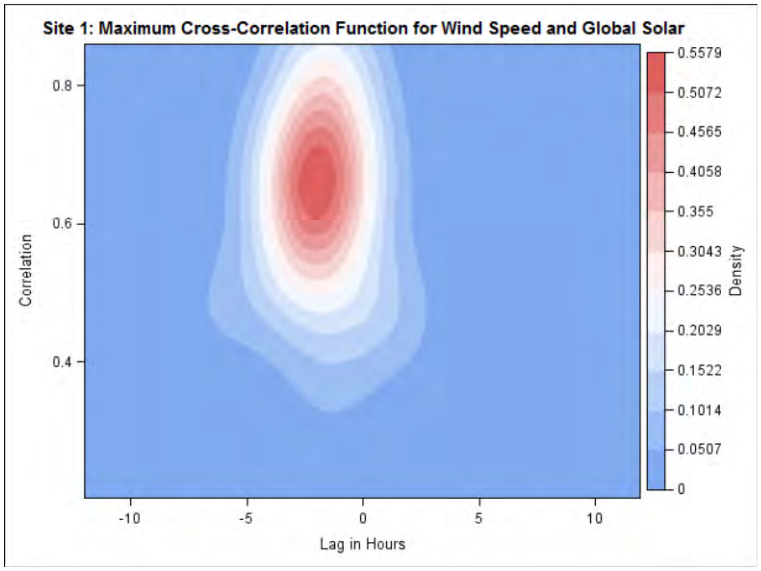

Lag	Correlation
-1.86582	0.659789

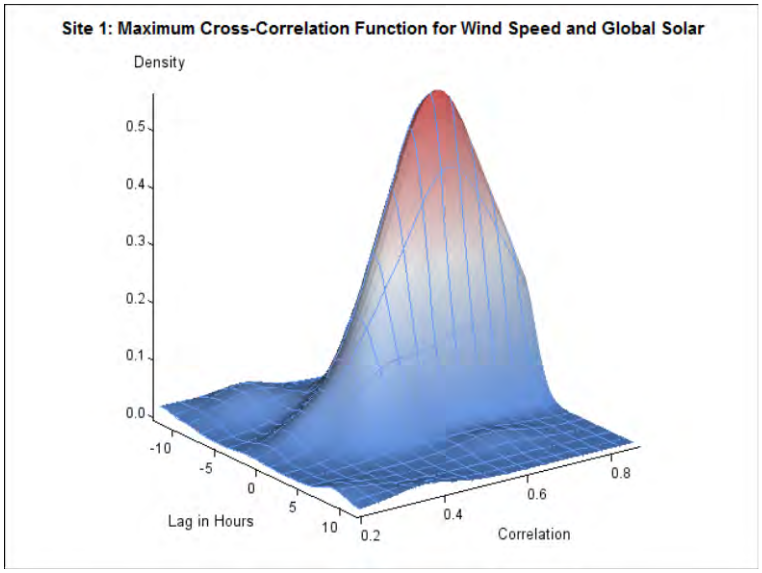

Westerly Solar & Wind Speeds

Other correlations

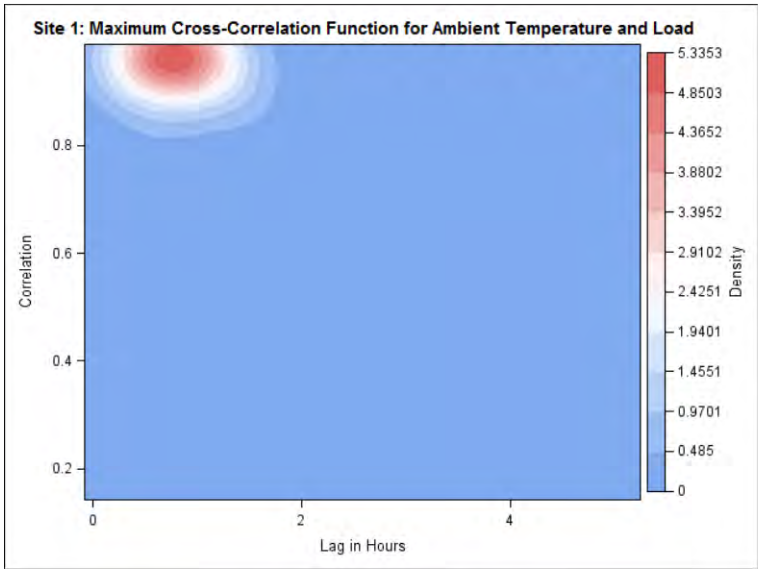

Lag	Correlation
0.820621	0.960021

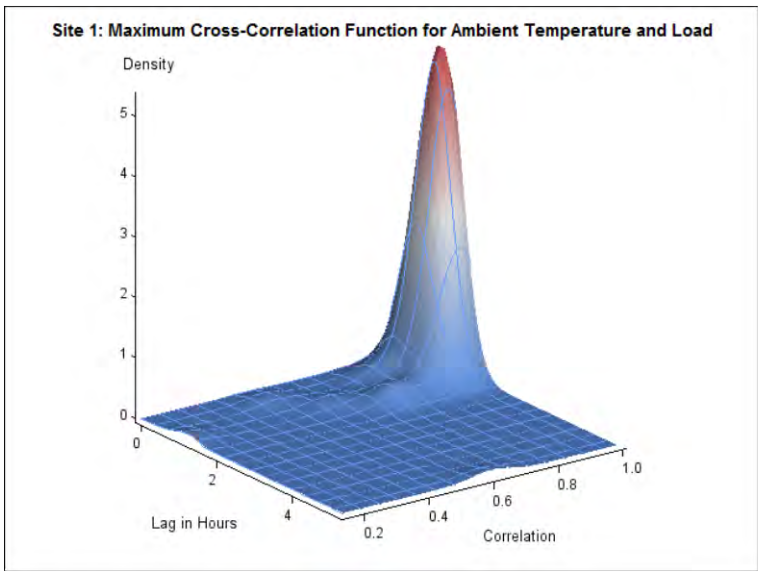

Temperature & Load

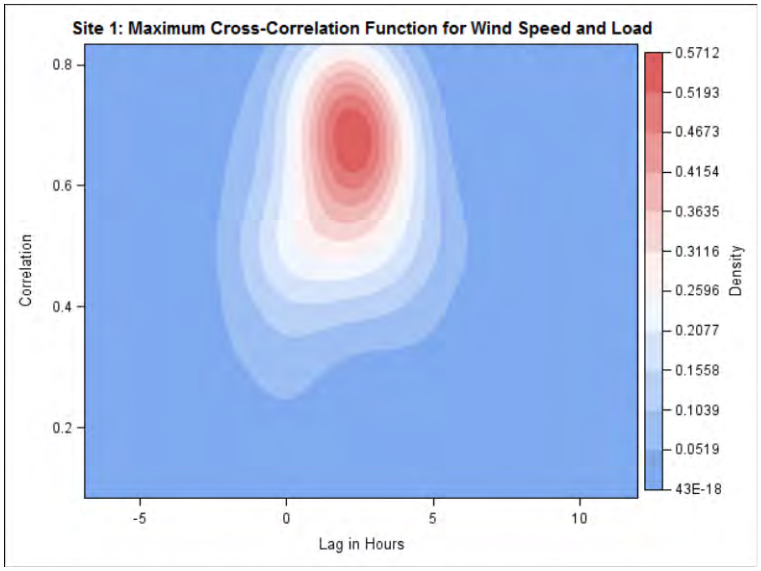

Lag	Correlation
2.381356	0.681657

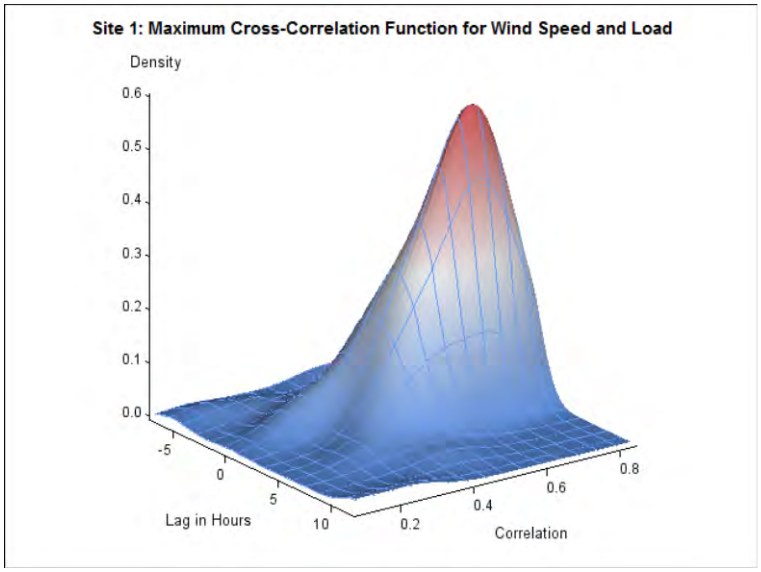

Wind Speed & Load

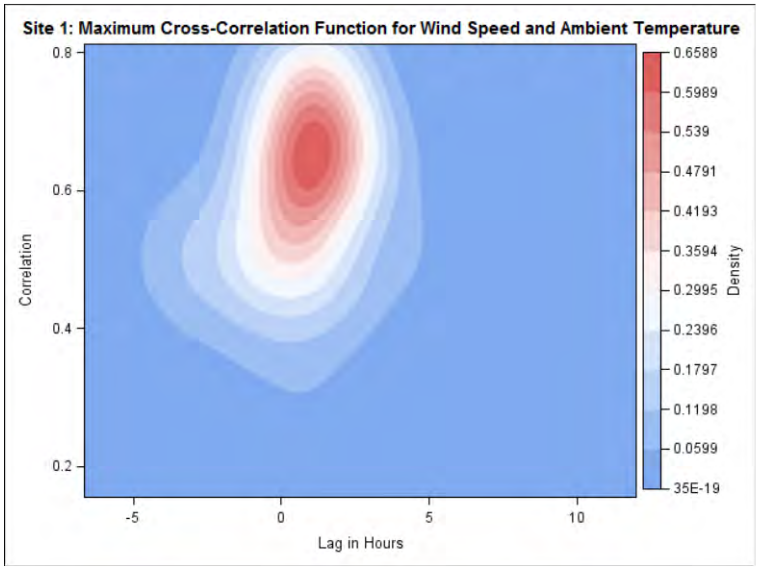

Lag	Correlation
0.926554	0.656574

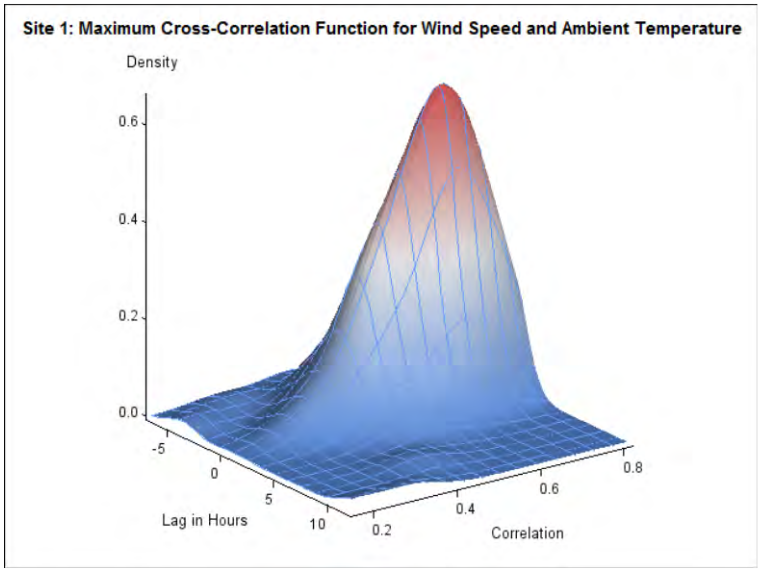

Wind Speed & Temperature

Summarized Results

SIWS01

Variable	Wind Speed	Ambient Temperature	Southerly Solar	Westerly Solar	Global Solar	Load
Wind Speed		0.66	0.66	0.67	0.66	0.68
Ambient Temperature	0.93		0.89	0.84	0.91	0.96
Southerly Solar	-1.87	-3.05		0.95	1.00	0.94
Westerly Solar	0.20	-1.02	2.32		0.93	0.88
Global Solar	-1.87	-3.05	0.00	-2.32		0.95
Load	2.38	0.82	4.05	1.94	4.00	

Wind Speed tends to lead Ambient Temperature by about 0.93 hours with a correlation of 0.66
Wind Speed tends to lag Southerly Solar by about 1.87 hours with a correlation of 0.66
Wind Speed tends to lead Westerly Solar by about 0.20 hours with a correlation of 0.67
Wind Speed tends to lag Global Solar by about 1.87 hours with a correlation of 0.66
Wind Speed tends to lead Load by about 2.38 hours with a correlation of 0.68

Ambient Temperature tends to lag Southerly Solar by about 3.05 hours with a correlation of 0.89
Ambient Temperature tends to lag Westerly Solar by about 1.02 hours with a correlation of 0.84
Ambient Temperature tends to lag Global Solar by about 3.05 hours with a correlation of 0.91
Ambient Temperature tends to lead Load by about 0.82 hours with a correlation of 0.96

Southerly Solar tends to lead Westerly Solar by about 2.32 hours with a correlation of 0.95
Southerly Solar tends to lead Global Solar by about 0.00 hours with a correlation of 1.00
Southerly Solar tends to lead Load by about 4.05 hours with a correlation of 0.94

Westerly Solar tends to lag Global Solar by about 2.32 hours with a correlation of 0.93
Westerly Solar tends to lead Load by about 1.94 hours with a correlation of 0.88

Global Solar tends to lead Load by about 4.00 hours with a correlation of 0.95

Appendix 2 — Graphs derived from SISW02 data

Loads and irradiances

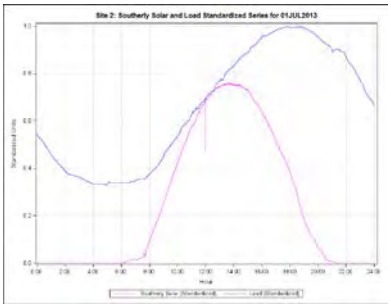

Southerly Solar & Load

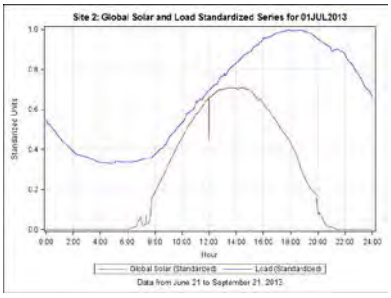

Global Solar & Load

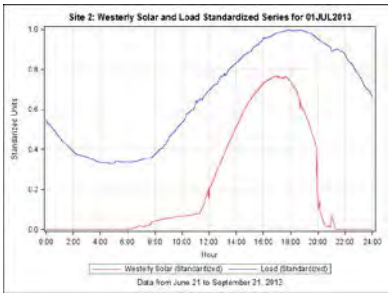

Westerly Solar & Load

07-01-2013, "max"

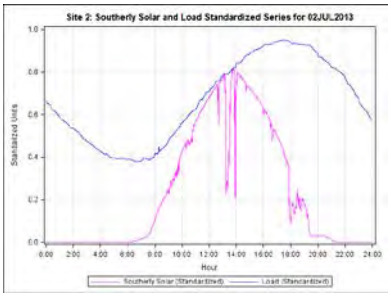

Southerly Solar & Load

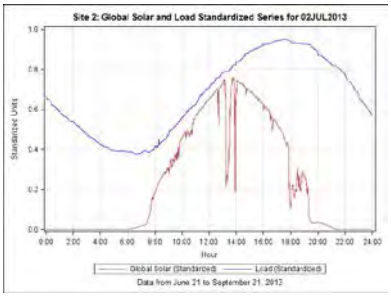

Global Solar & Load

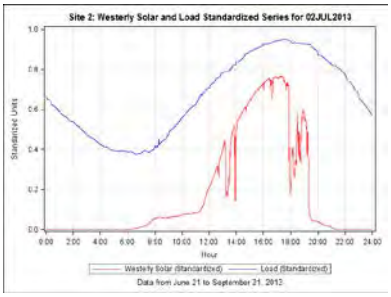

Westerly Solar & Load

07-02-2013, "max"

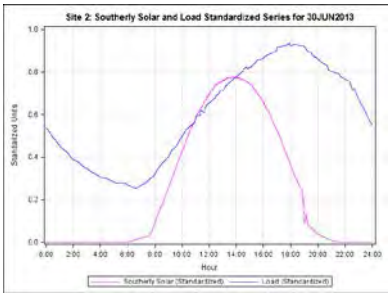

Southerly Solar & Load

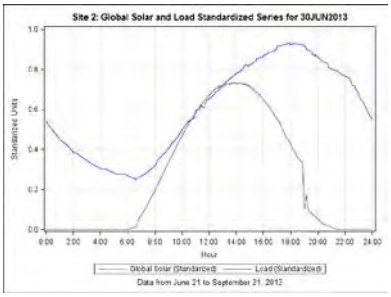

Global Solar & Load

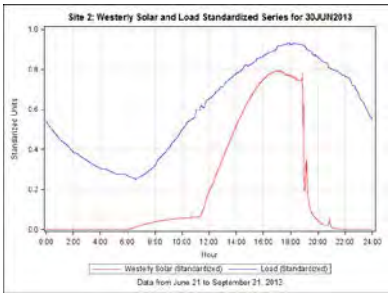

Westerly Solar & Load

6-30-2013, "max"

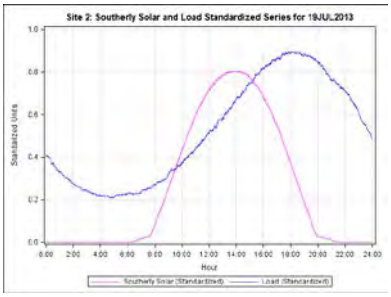

Southerly Solar & Load

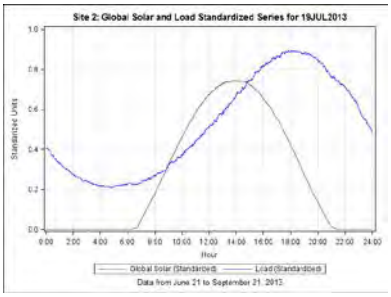

Global Solar & Load

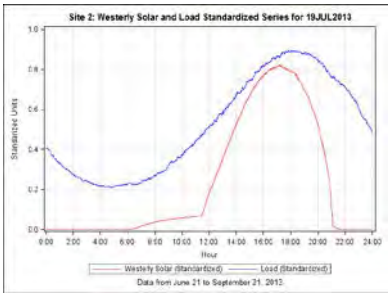

Westerly Solar & Load

7-19-2013, "max"

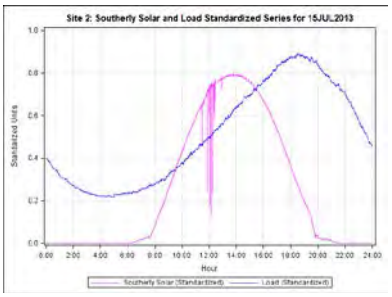

Southerly Solar & Load

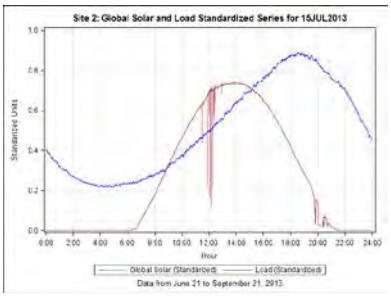

Global Solar & Load

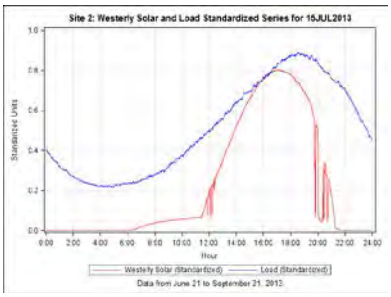

Westerly Solar & Load

7-15-2013, "max"

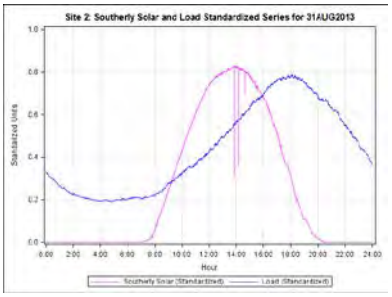

Southerly Solar & Load

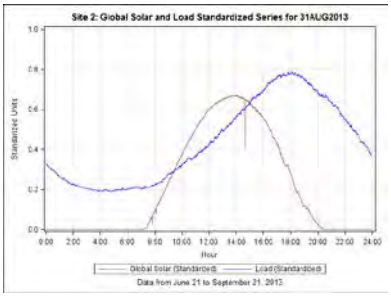

Global Solar & Load

Westerly Solar & Load

8-31-2013, "mid"

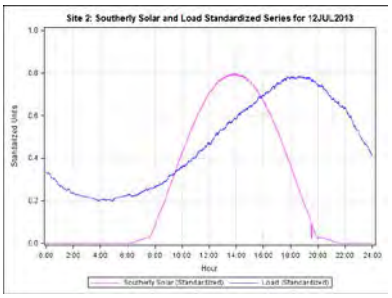

Southerly Solar & Load

Global Solar & Load

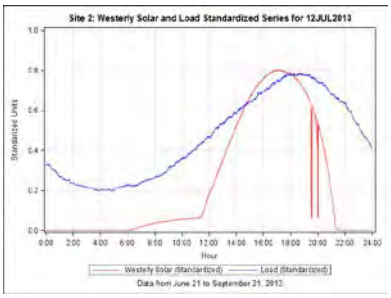

Westerly Solar & Load

7-12-2013, "mid"

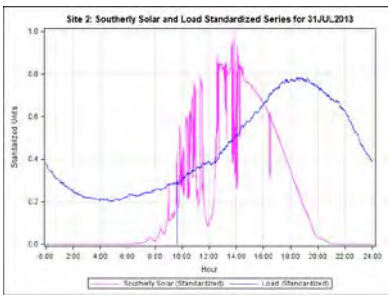

Southerly Solar & Load

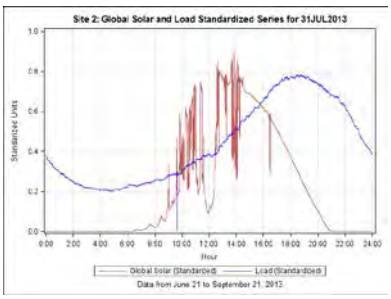

Global Solar & Load

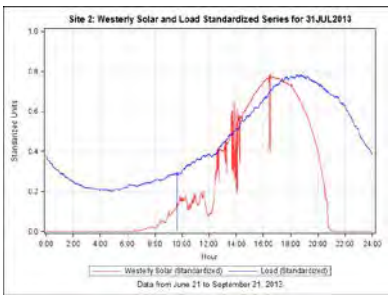

Westerly Solar & Load

07-31-2013, "mid"

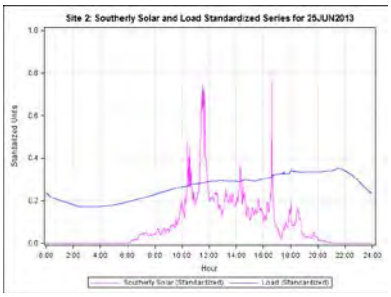

Southerly Solar & Load

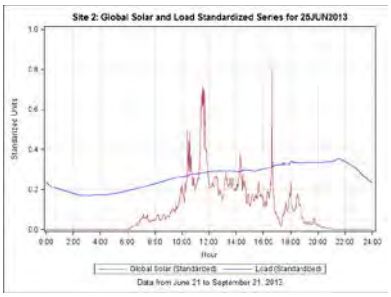

Global Solar & Load

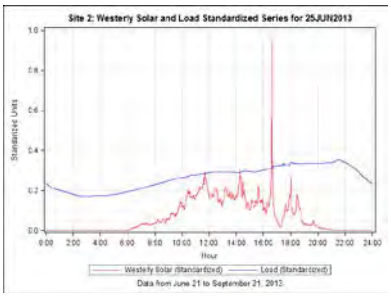

Westerly Solar & Load

06-25-2013, "min"

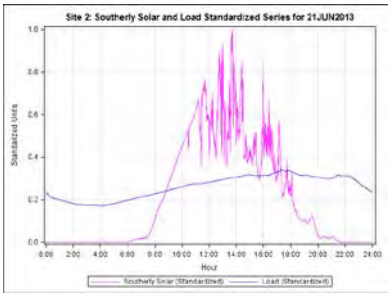

Southerly Solar & Load

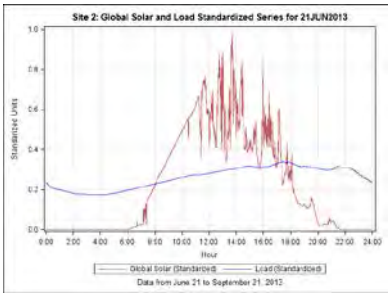

Global Solar & Load

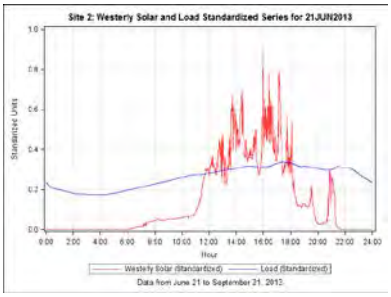

Westerly Solar & Load

6-21-2013, "min"

Auto-correlations of irradiances

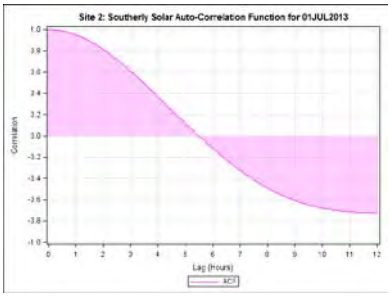

Southerly Solar

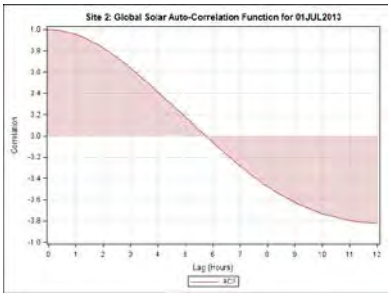

Global Solar

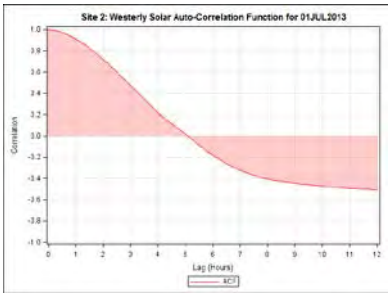

Westerly Solar

Mostly clear day: 07-01-2013

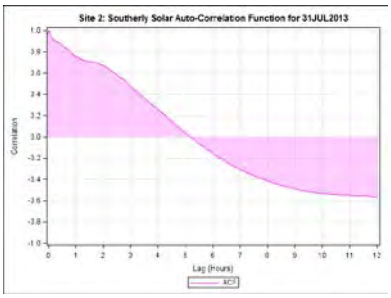

Southerly Solar

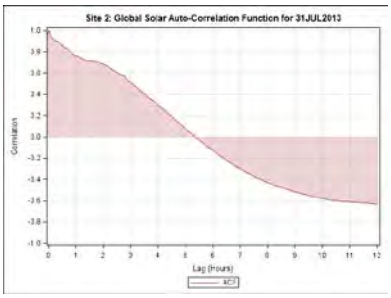

Global Solar

Westerly Solar

Moderately cloudy day: 07-31-2013

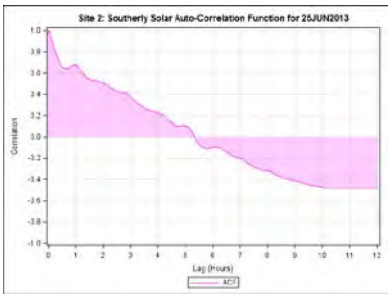

Southerly Solar

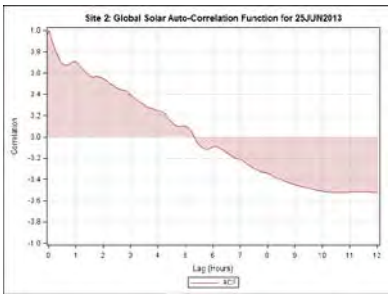

Global Solar

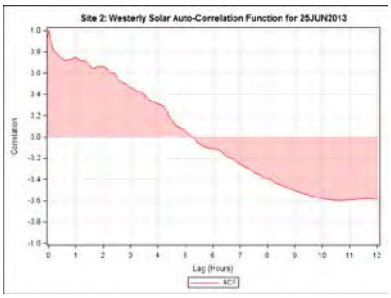

Westerly Solar

Very cloudy day: 06-25-2013

Cross-correlations between loads and irradiances

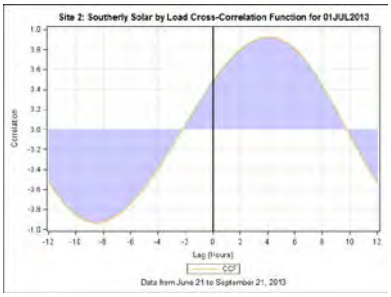

Southerly Solar & Load

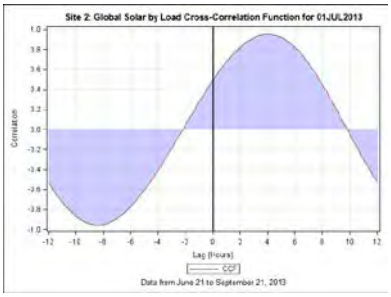

Global Solar & Load

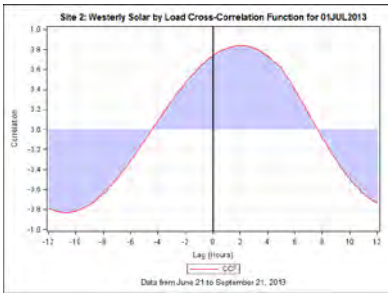

Westerly Solar & Load

Mostly clear day: 07-01-2013

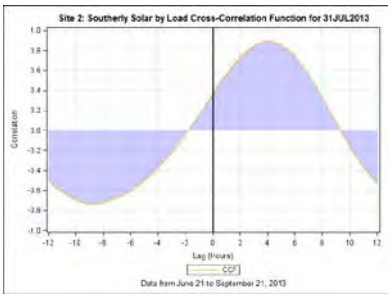

Southerly Solar & Load

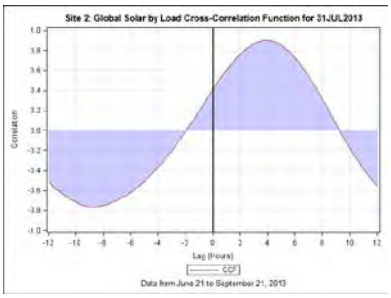

Global Solar & Load

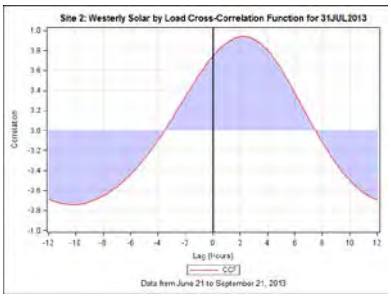

Westerly Solar & Load

Moderately cloudy day: 07-31-2013

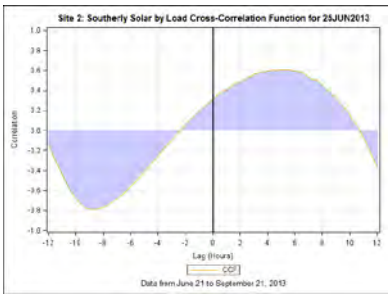

Southerly Solar & Load

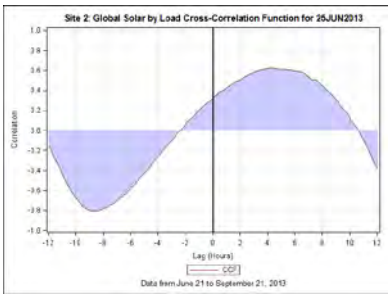

Global Solar & Load

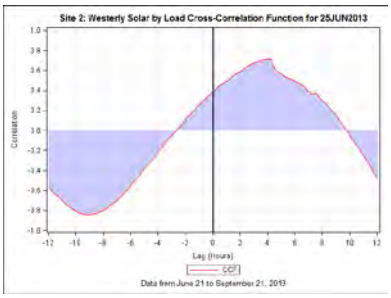

Westerly Solar & Load

Very cloudy day: 06-25-2013

Loads versus other weather factors

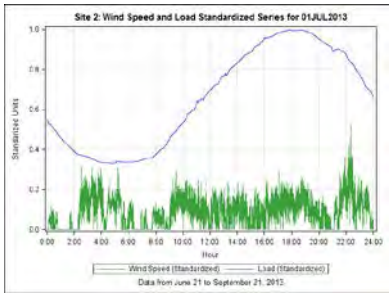

Wind Speed & Load

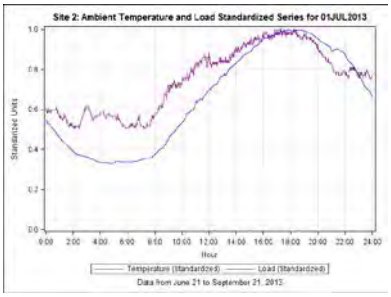

Ambient Temperature & Load

Mostly clear day: 07-01-2013

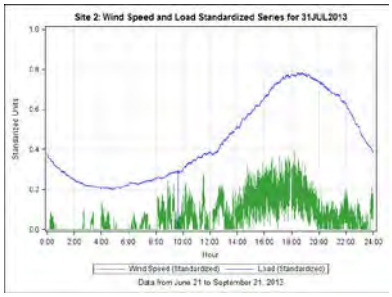

Wind Speed & Load

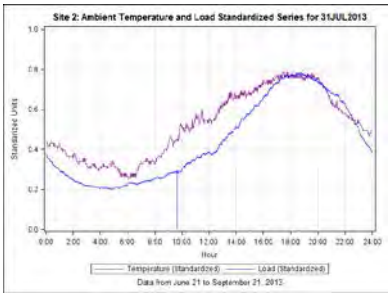

Ambient Temperature & Load

Moderately cloudy day: 07-31-2013

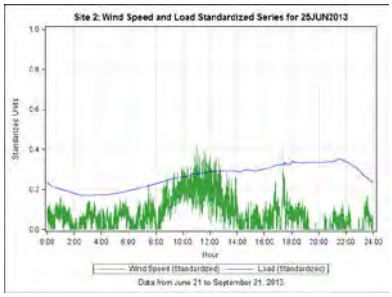

Wind Speed & Load

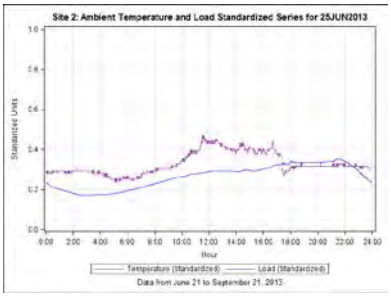

Ambient Temperature & Load

Very cloudy day: 06-25-2013

Auto-correlations of loads and other factors

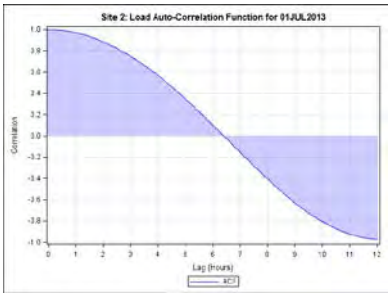

Load

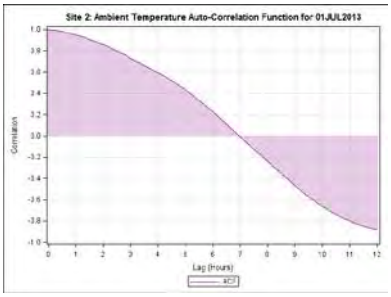

Ambient Temperature

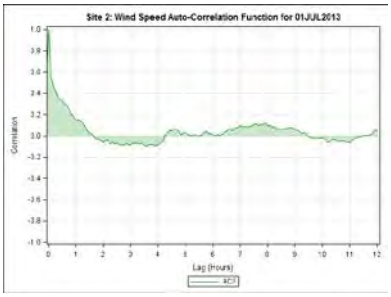

Wind Speed

Mostly clear day: 07-01-2013

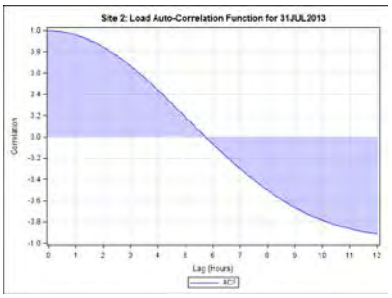

Load

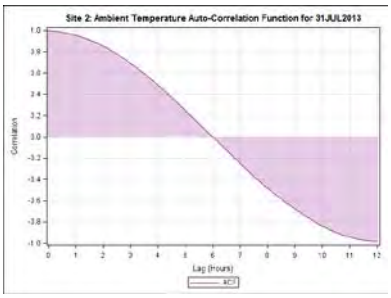

Ambient Temperature

Wind Speed

Moderately cloudy day: 07-31-2013

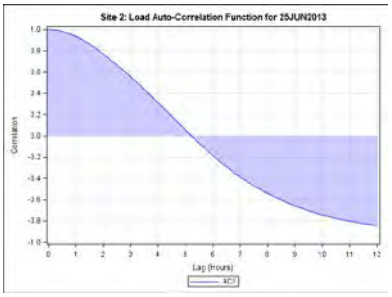

Load

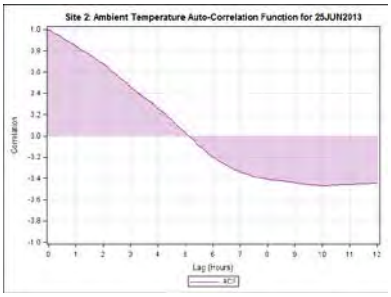

Ambient Temperature

Wind Speed

Very cloudy day: 06-25-2013

Cross-correlations between loads and other weather factors

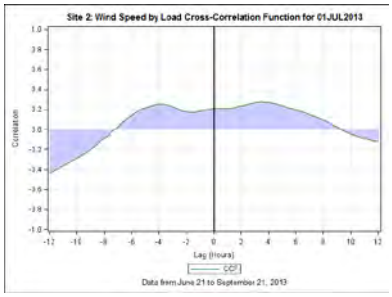

Wind Speed & Load

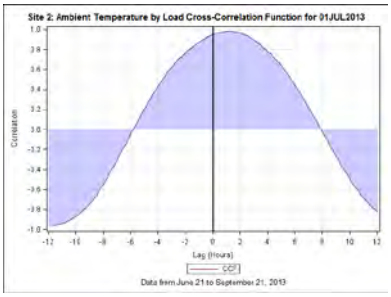

Ambient Temperature & Load

Mostly clear day: 07-01-2013

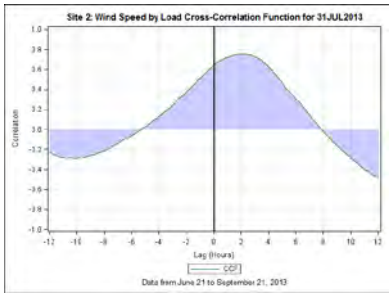

Wind Speed & Load

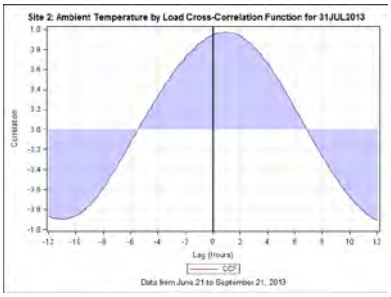

Ambient Temperature & Load

Moderately cloudy day: 07-31-2013

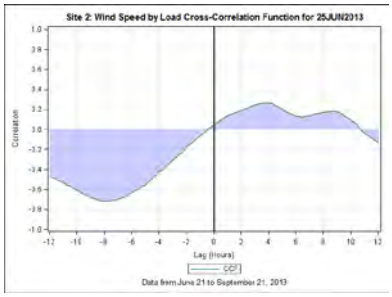

Wind Speed & Load

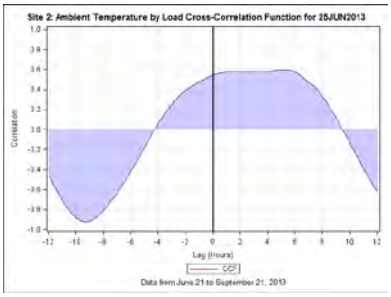

Ambient Temperature & Load

Very cloudy day: 06-25-2013

Maximum cross-correlations for the 93-day study period

Loads and irradiances

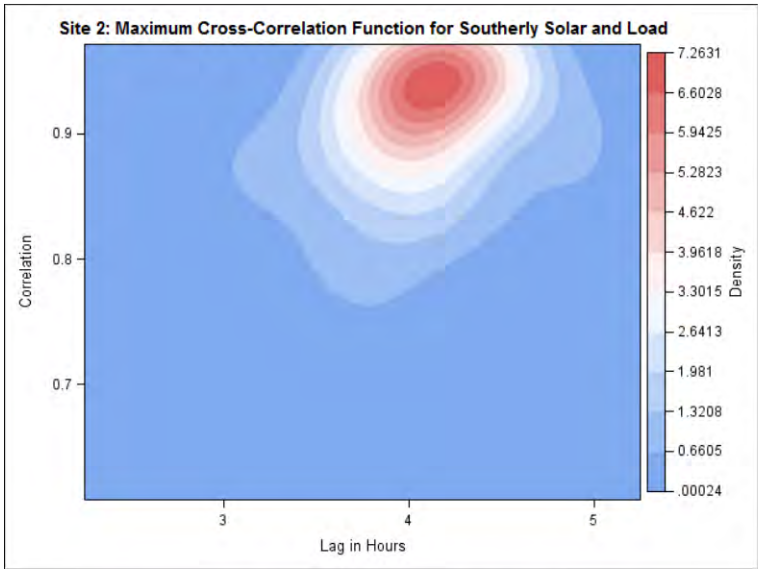

Lag	Correlation
4.131356	0.940746

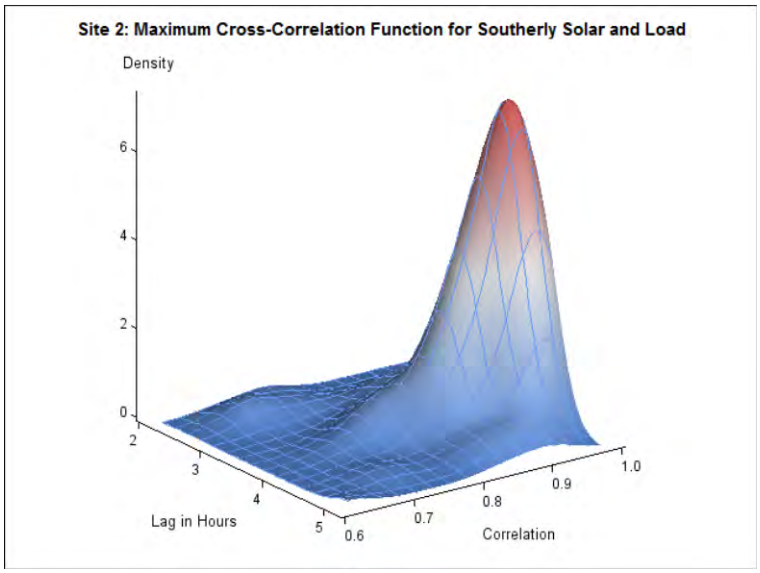

Southerly Solar & Load

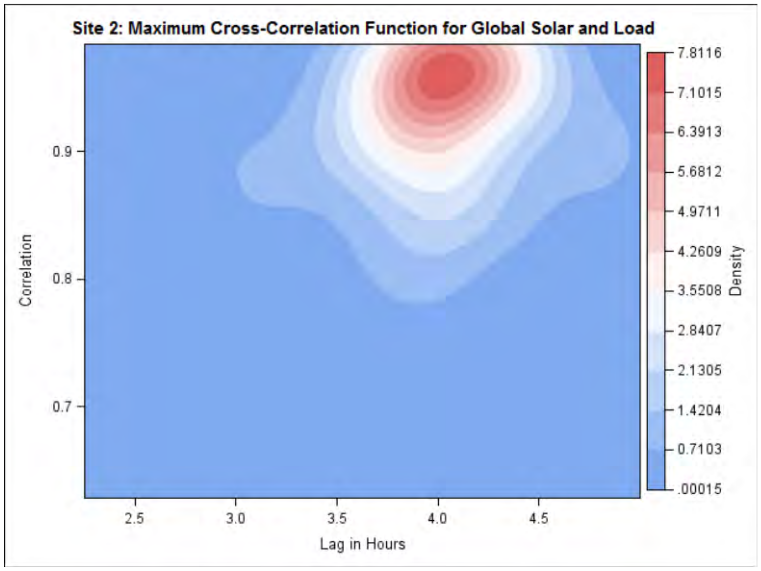

Lag	Correlation
4.021186	0.959743

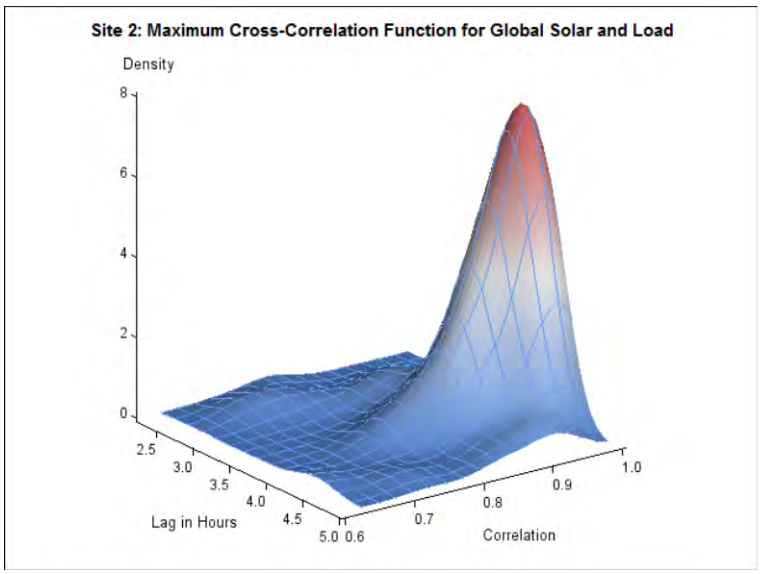

Global Solar & Load

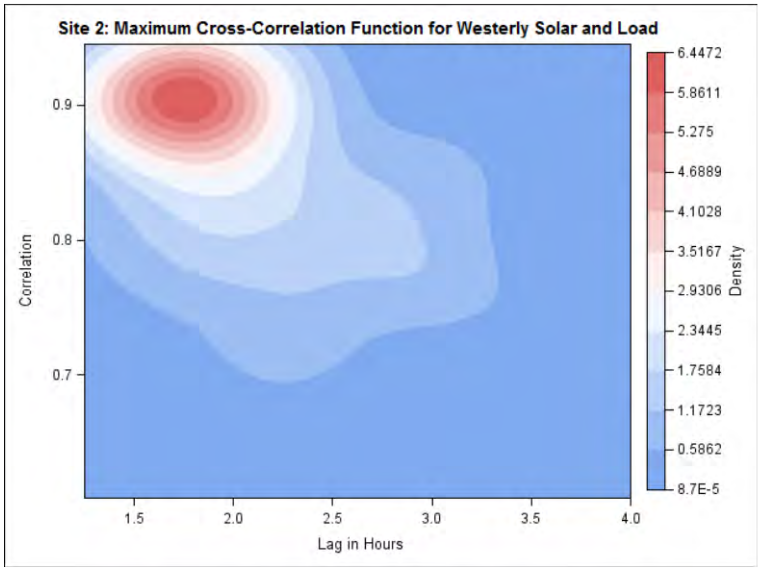

Lag	Correlation
1.762712	0.90537

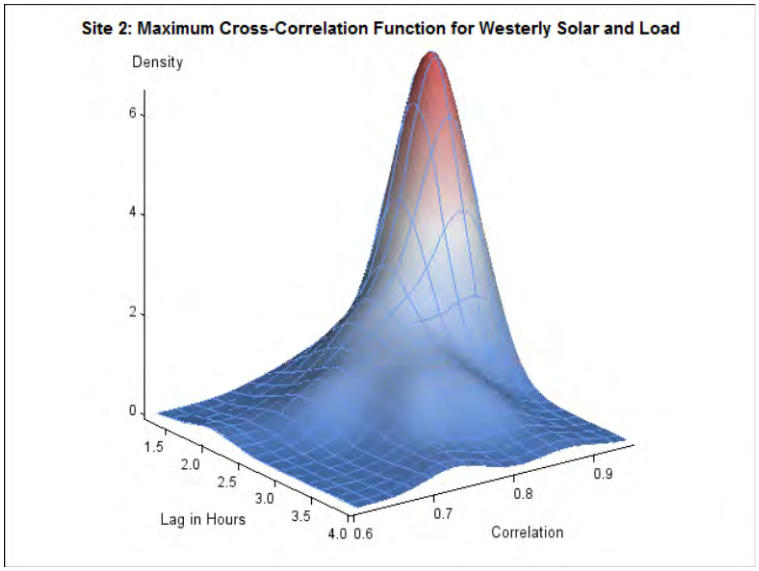

Westerly Solar & Load

Temperatures and irradiances

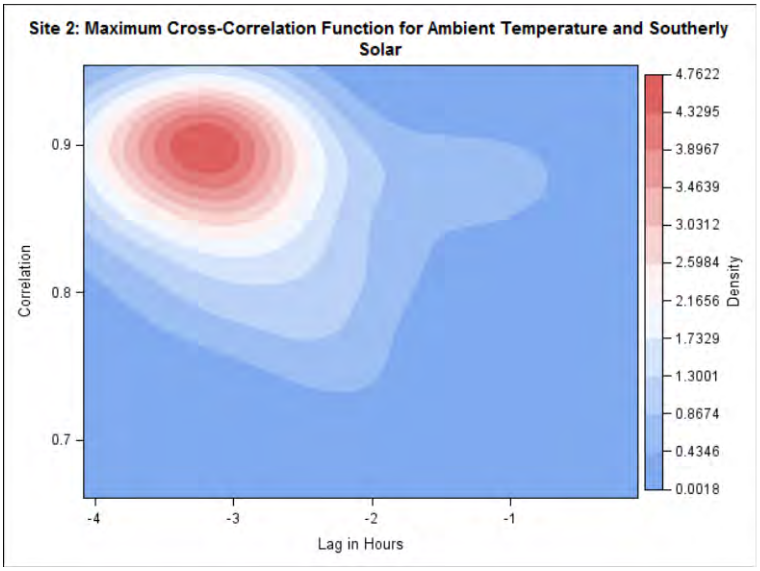

Lag	Correlation
-3.20198	0.899289

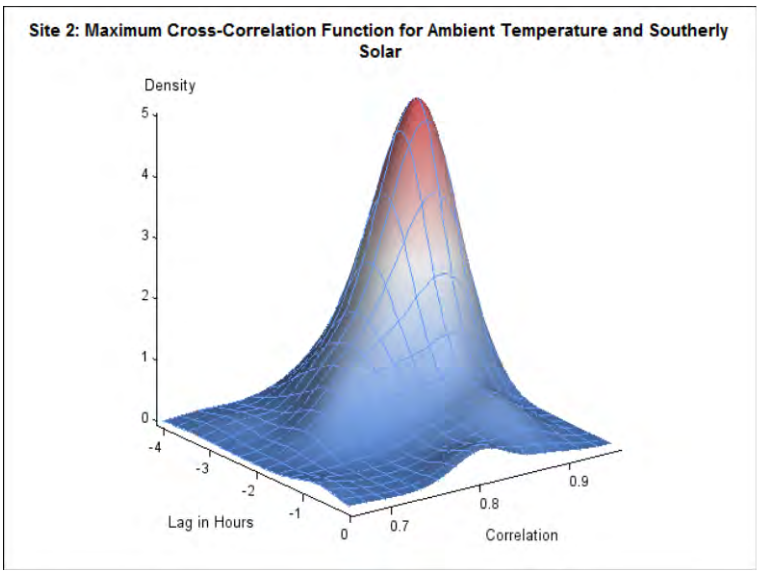

Southerly Solar & Temperature

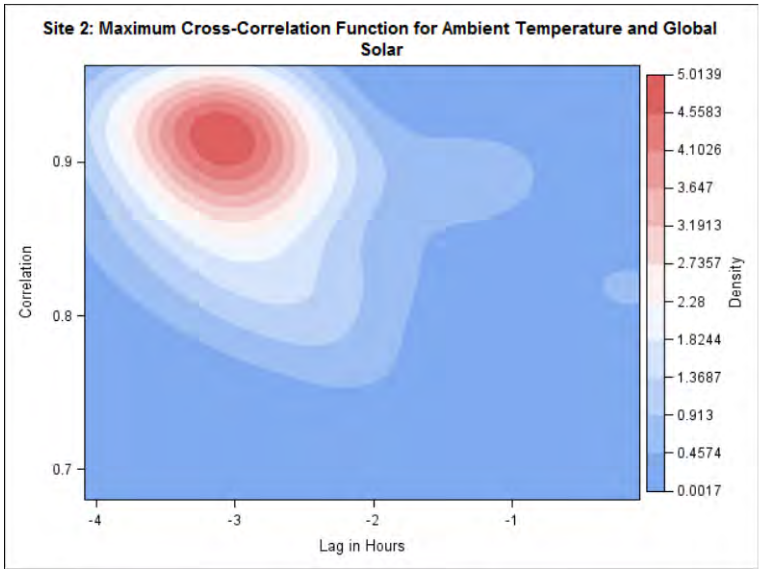

Lag	Correlation
-3.06638	0.915087

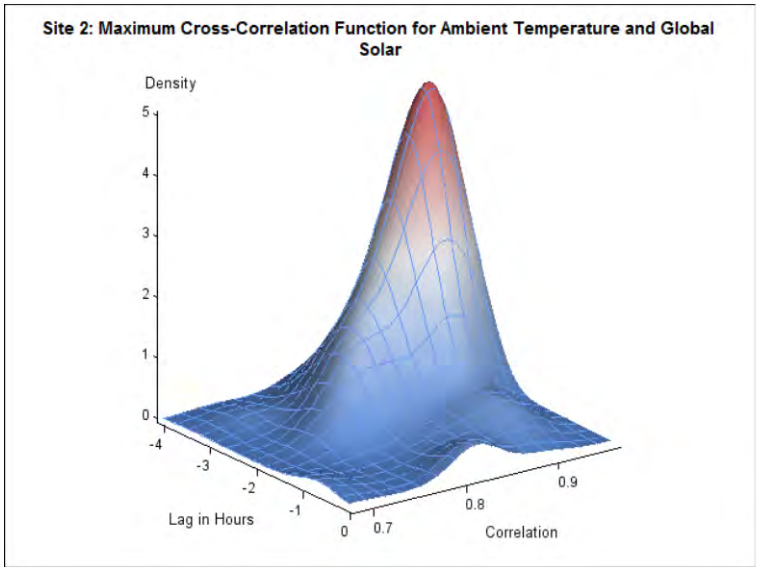

Global Solar & Temperature

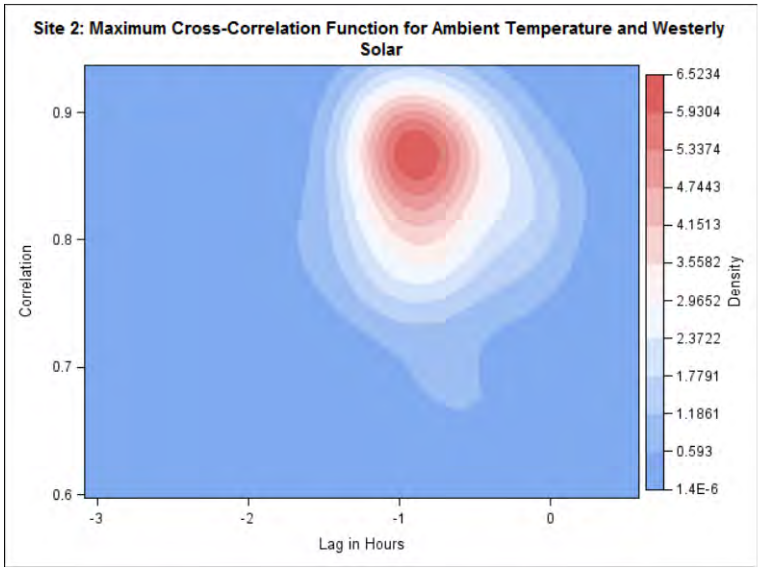

Lag	Correlation
-0.90819	0.86795

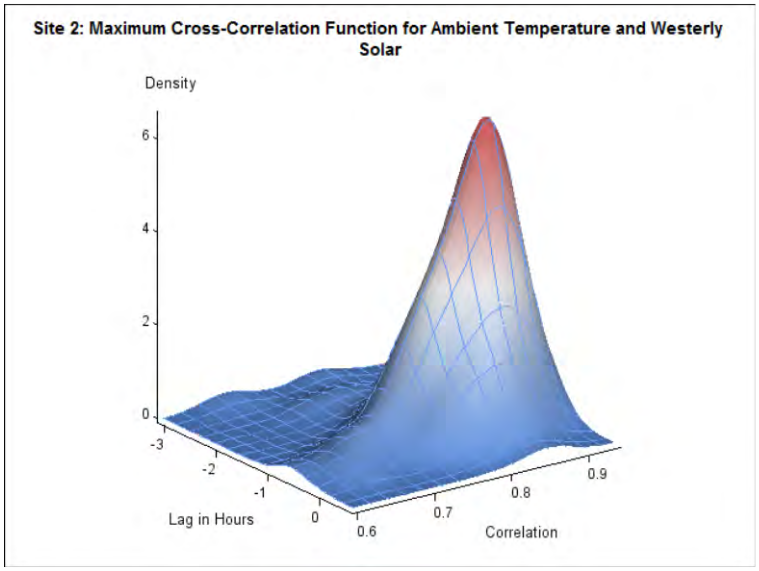

Westerly Solar & Temperature

Wind speeds and Irradiances

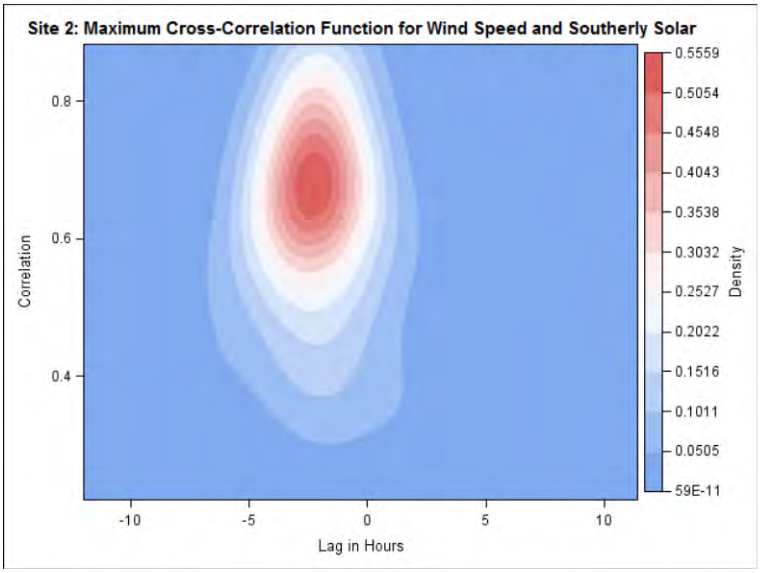

Lag	Correlation
-2.07768	0.680391

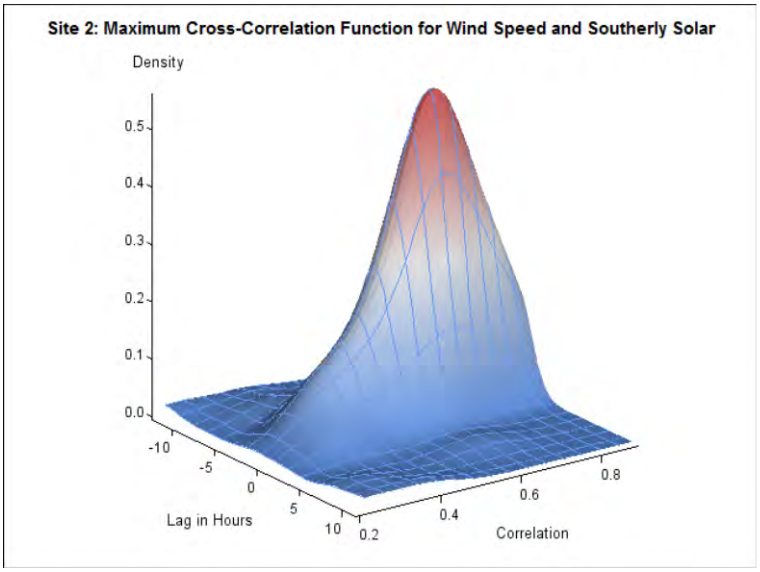

Southerly Solar & Wind Speeds

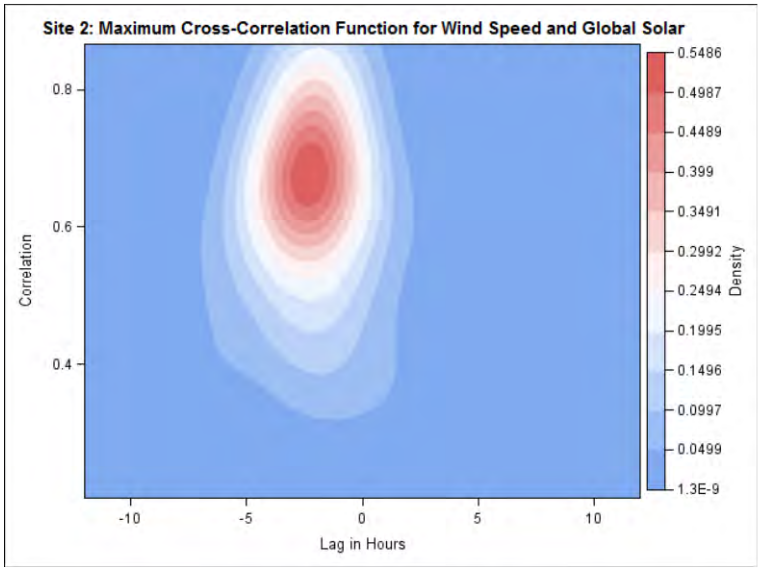

Lag	Correlation
-2.23729	0.675853

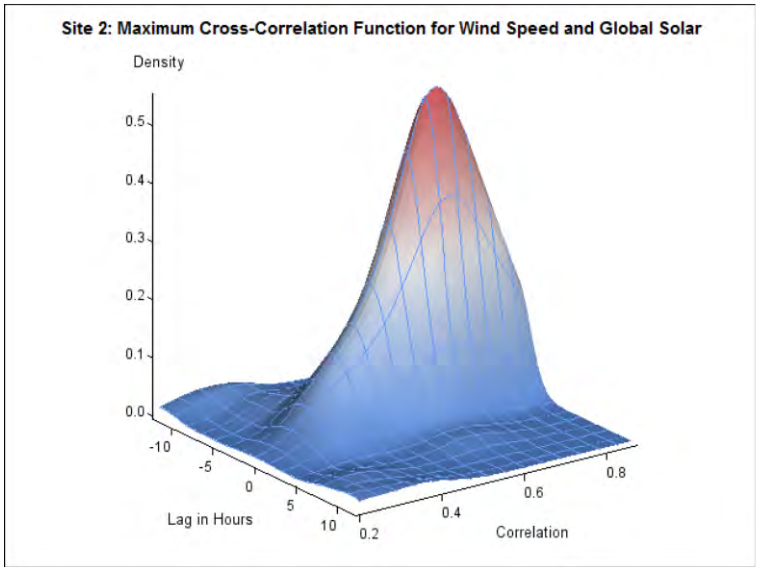

Global Solar & Wind Speeds

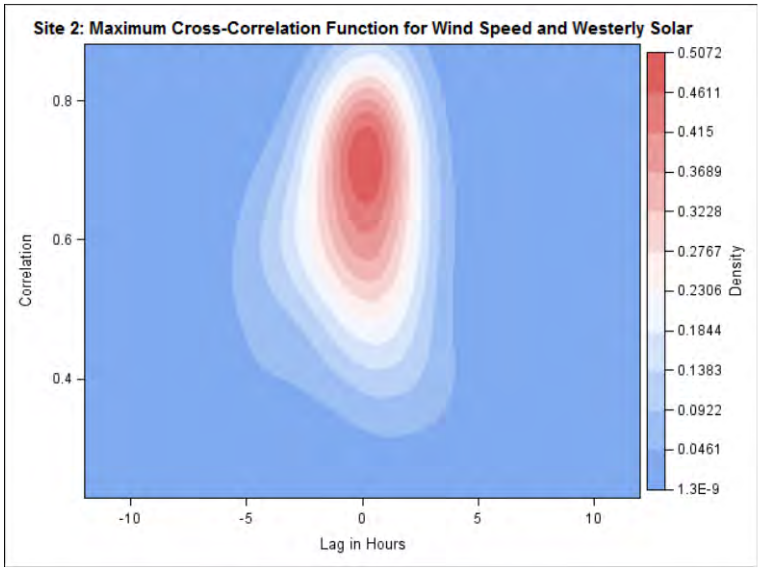

Lag	Correlation
0.20339	0.715771

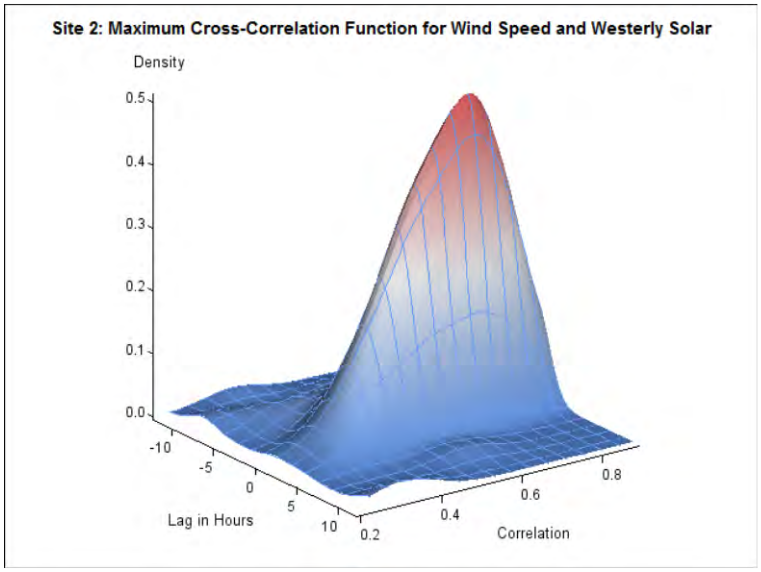

Westerly Solar & Wind Speeds

Other correlations

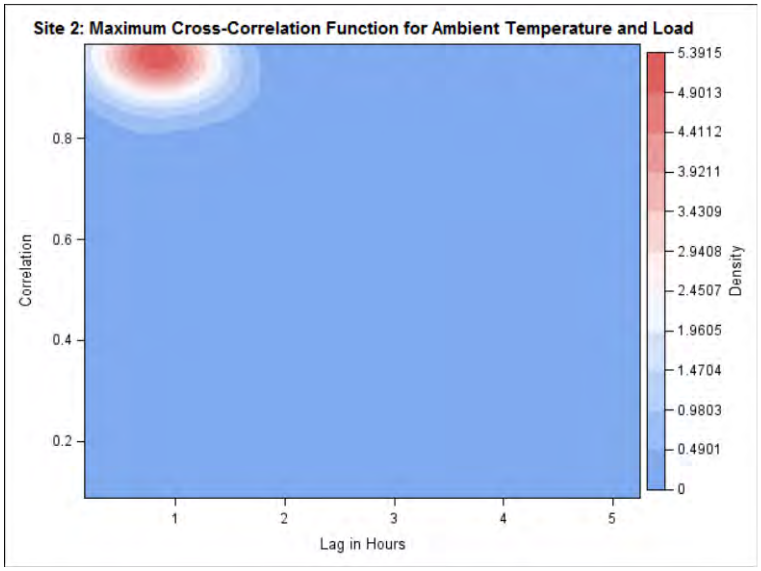

Lag	Correlation
0.855932	0.971897

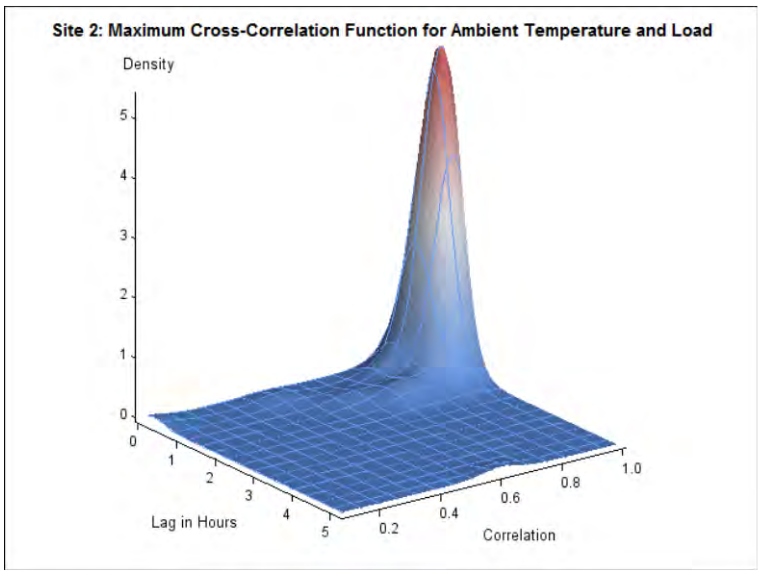

Temperature & Load

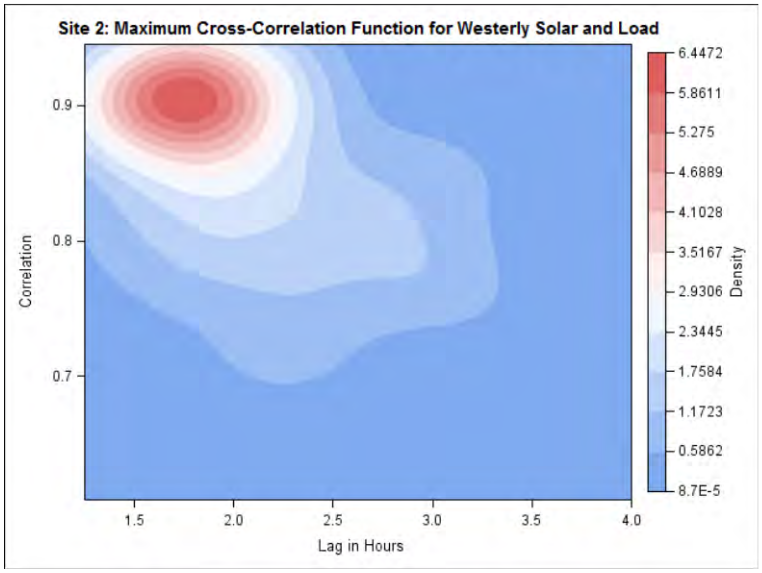

Lag	Correlation
1.90113	0.696714

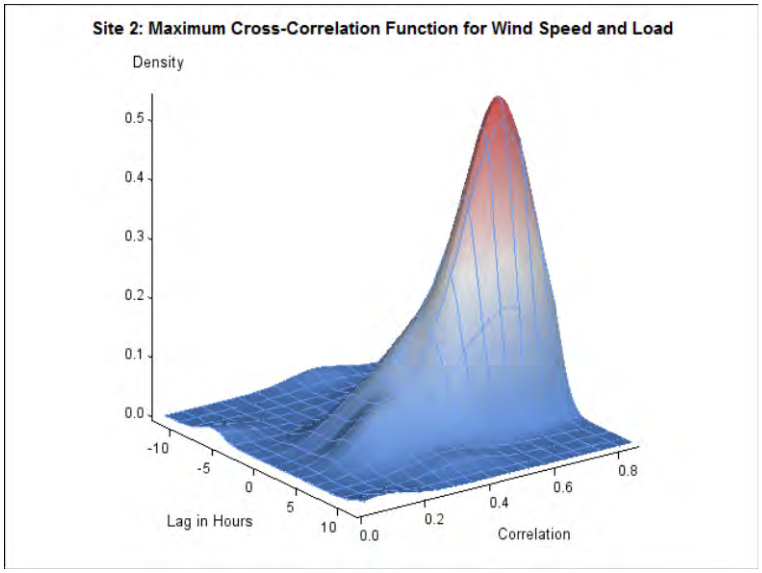

Wind Speed & Load

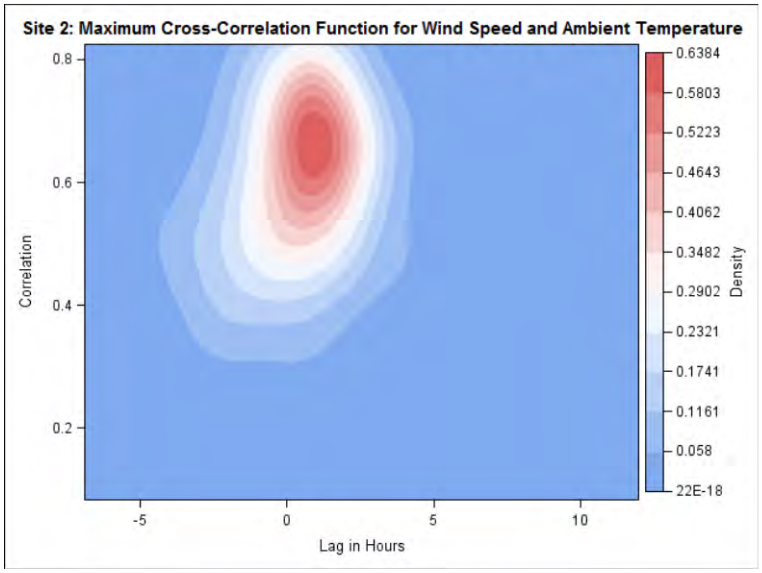

Lag	Correlation
1.09887	0.661522

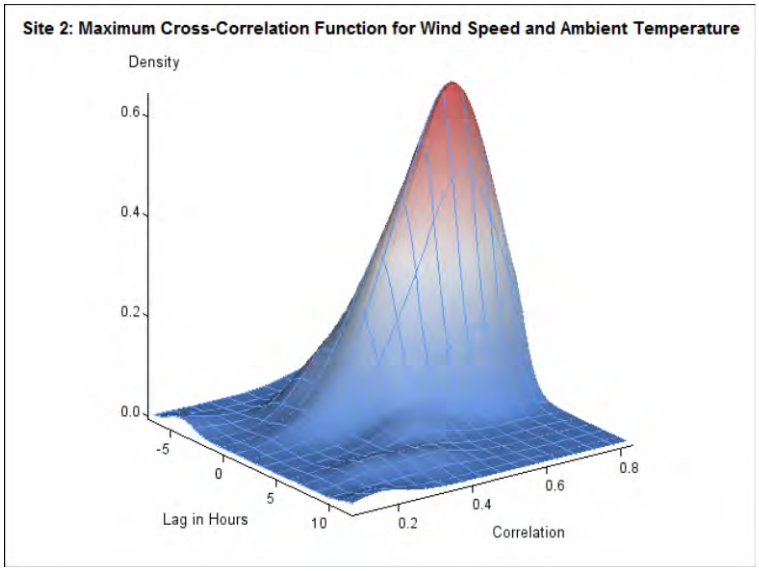

Wind Speed & Temperature

Summarized Results

SIWS02

Variable	Wind Speed	Ambient Temperature	Southerly Solar	Westerly Solar	Global Solar	Load
Wind Speed		0.66	0.68	0.72	0.68	0.70
Ambient Temperature	1.10		0.90	0.87	0.92	0.97
Southerly Solar	-2.08	-3.20		0.96	1.00	0.94
Westerly Solar	0.20	-0.91	2.61		0.94	0.91
Global Solar	-2.24	-3.07	0.00	-2.55		0.96
Load	1.90	0.86	4.13	1.76	4.02	

Wind Speed tends to lead Ambient Temperature by about 1.10 hours with a correlation of 0.66
Wind Speed tends to lag Southerly Solar by about 2.08 hours with a correlation of 0.68
Wind Speed tends to lead Westerly Solar by about 0.20 hours with a correlation of 0.72
Wind Speed tends to lag Global Solar by about 2.24 hours with a correlation of 0.68
Wind Speed tends to lead Load by about 1.90 hours with a correlation of 0.70

Ambient Temperature tends to lag Southerly Solar by about 3.20 hours with a correlation of 0.90
Ambient Temperature tends to lag Westerly Solar by about 0.91 hours with a correlation of 0.87
Ambient Temperature tends to lag Global Solar by about 3.07 hours with a correlation of 0.92
Ambient Temperature tends to lead Load by about 0.86 hours with a correlation of 0.97

Southerly Solar tends to lead Westerly Solar by about 2.61 hours with a correlation of 0.96
Southerly Solar tends to lead Global Solar by about 0.00 hours with a correlation of 1.00
Southerly Solar tends to lead Load by about 4.13 hours with a correlation of 0.94

Westerly Solar tends to lag Global Solar by about 2.55 hours with a correlation of 0.94
Westerly Solar tends to lead Load by about 1.76 hours with a correlation of 0.91

Global Solar tends to lead Load by about 4.02 hours with a correlation of 0.96

Appendix 3 — Graphs derived from SISW03 data

Loads and irradiances

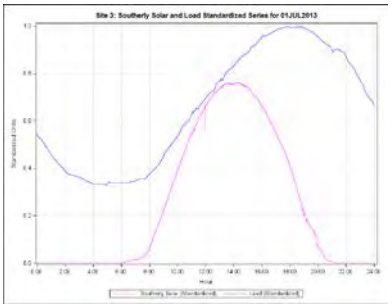

Southerly Solar & Load

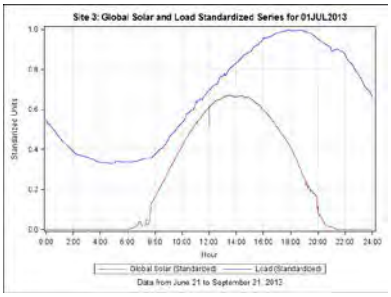

Global Solar & Load

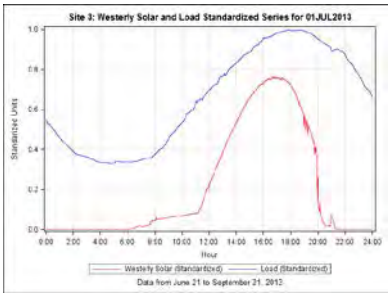

Westerly Solar & Load

07-01-2013, "max"

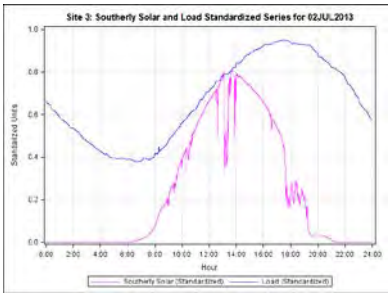

Southerly Solar & Load

Global Solar & Load

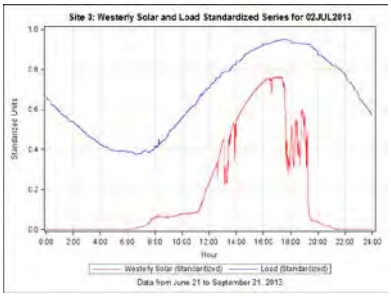

Westerly Solar & Load

07-02-2013, "max"

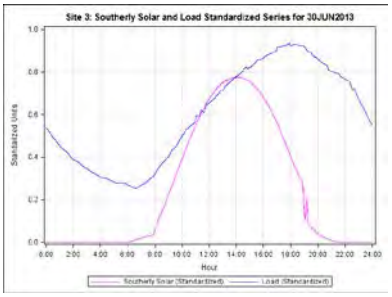

Southerly Solar & Load

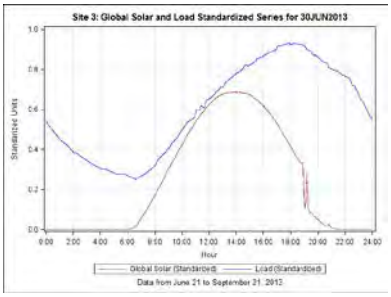

Global Solar & Load

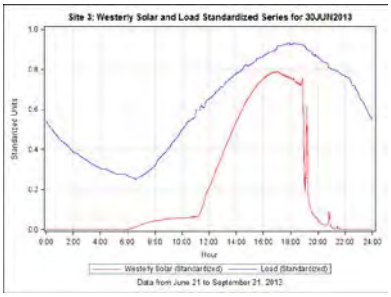

Westerly Solar & Load

6-30-2013, "max"

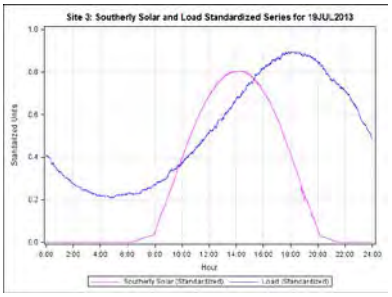

Southerly Solar & Load

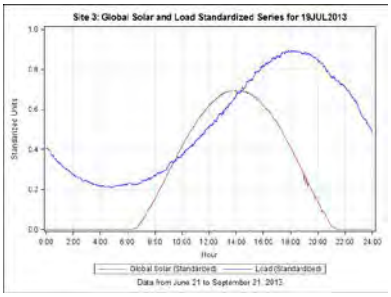

Global Solar & Load

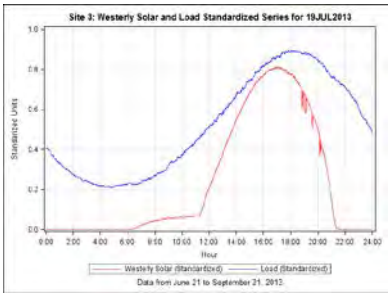

Westerly Solar & Load

7-19-2013, "max"

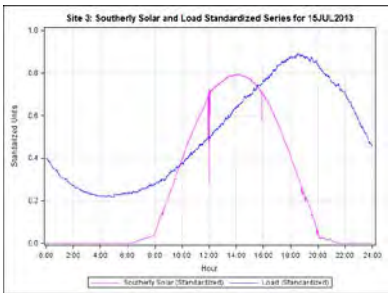

Southerly Solar & Load

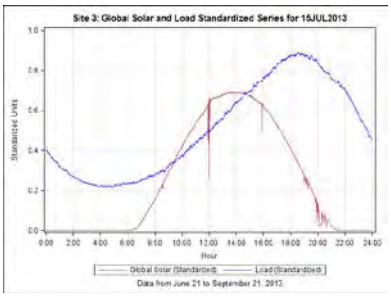

Global Solar & Load

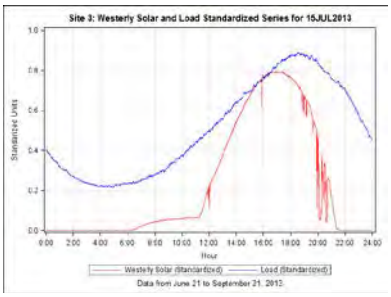

Westerly Solar & Load

7-15-2013, "max"

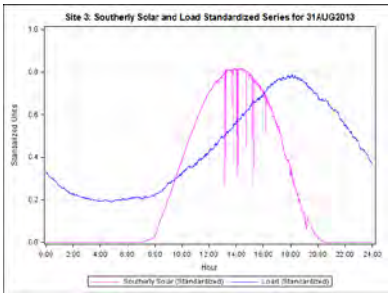

Southerly Solar & Load

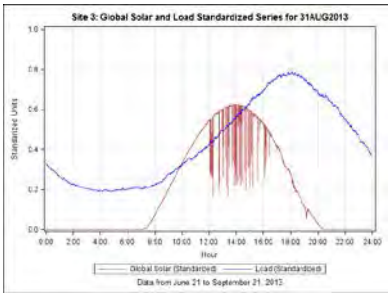

Global Solar & Load

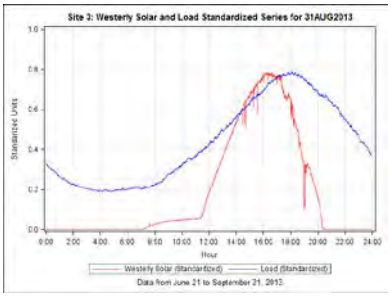

Westerly Solar & Load

8-31-2013, "mid"

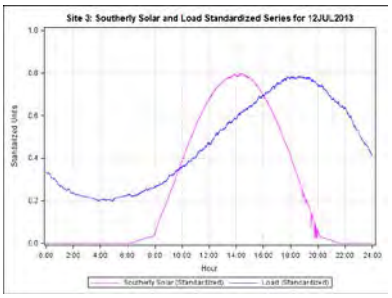

Southerly Solar & Load

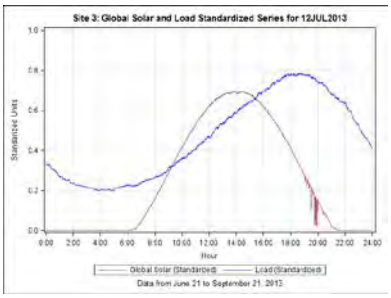

Global Solar & Load

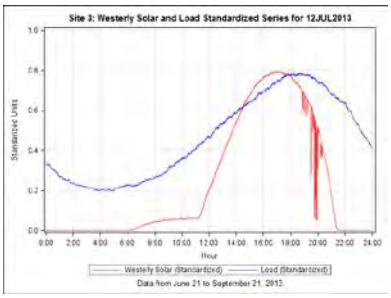

Westerly Solar & Load

7-12-2013, "mid"

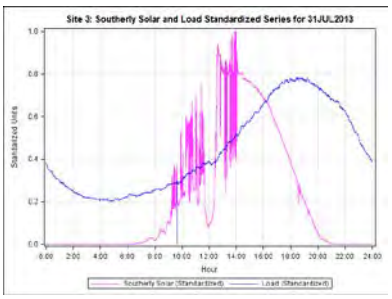

Southerly Solar & Load

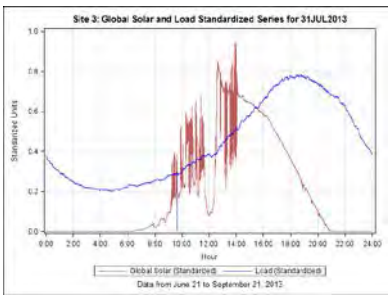

Global Solar & Load

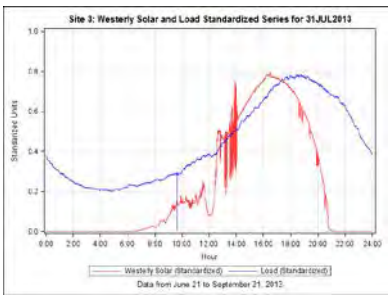

Westerly Solar & Load

07-31-2013, "mid"

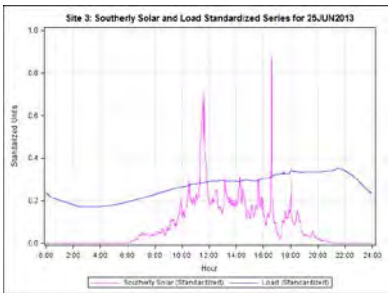

Southerly Solar & Load

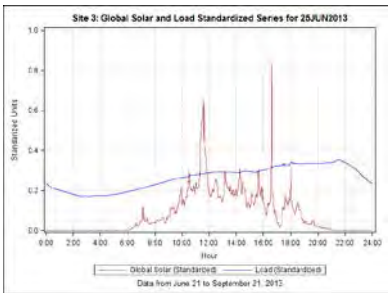

Global Solar & Load

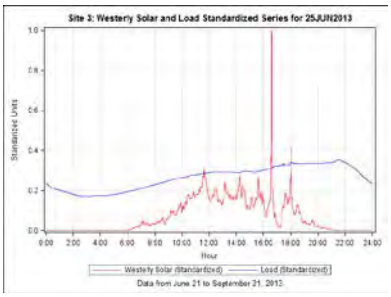

Westerly Solar & Load

06-25-2013, "min"

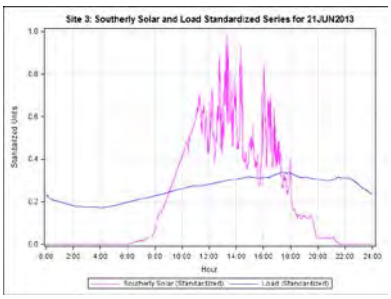

Southerly Solar & Load

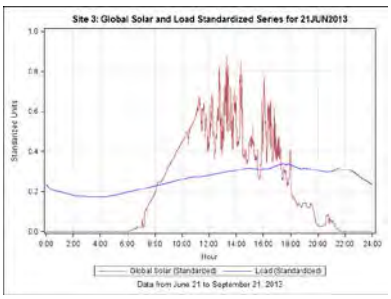

Global Solar & Load

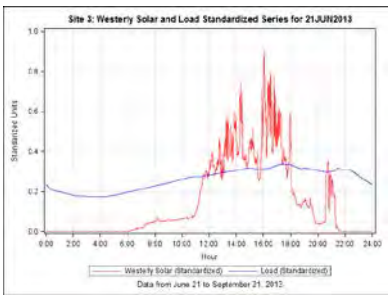

Westerly Solar & Load

6-21-2013, "min"

Auto-correlations of irradiances

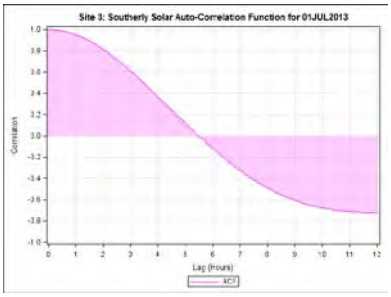

Southerly Solar

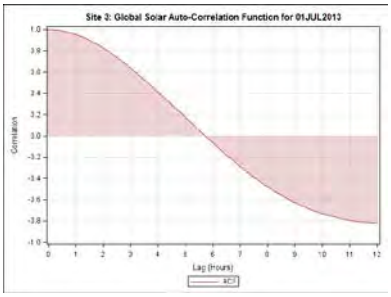

Global Solar

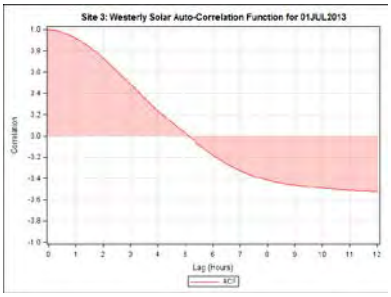

Westerly Solar

Mostly clear day: 07-01-2013

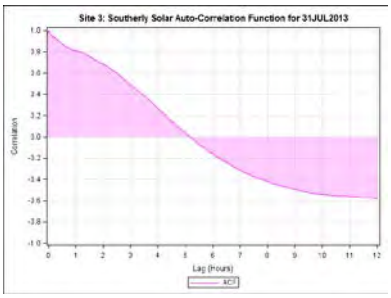

Southerly Solar

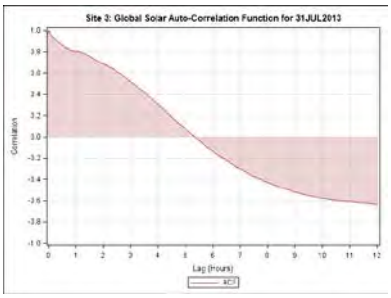

Global Solar

Westerly Solar

Moderately cloudy day: 07-31-2013

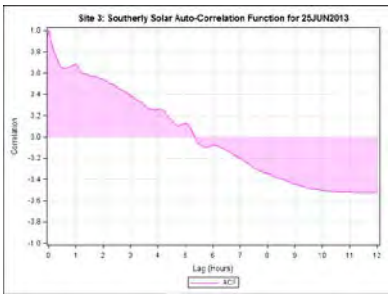

Southerly Solar

Global Solar

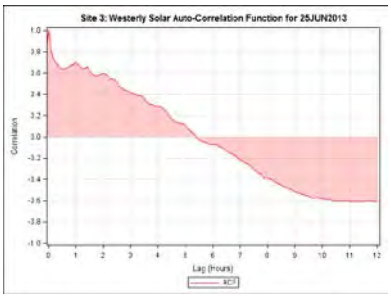

Westerly Solar

Very cloudy day: 06-25-2013

Cross-correlations between loads and irradiances

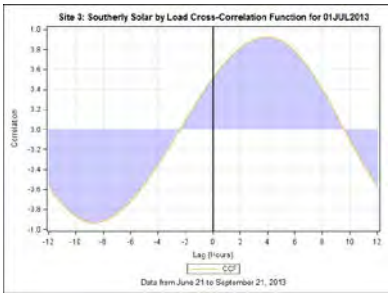

Southerly Solar & Load

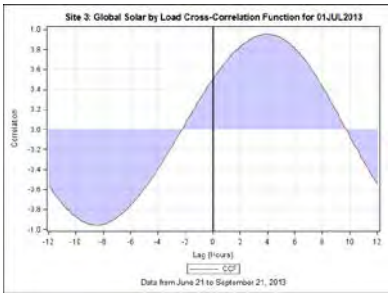

Global Solar & Load

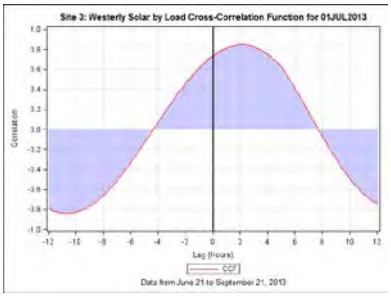

Westerly Solar & Load

Mostly clear day: 07-01-2013

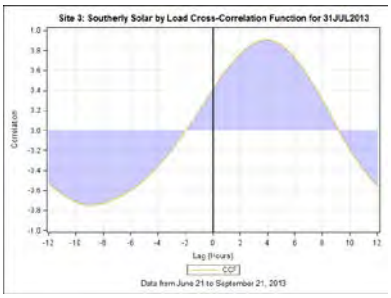

Southerly Solar & Load

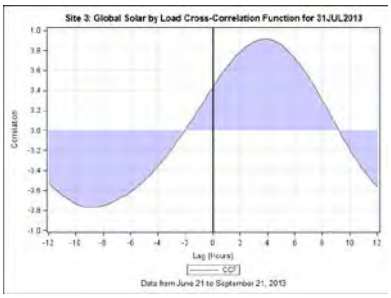

Global Solar & Load

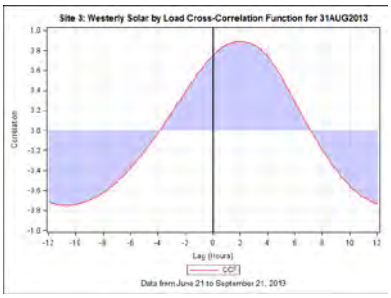

Westerly Solar & Load

Moderately cloudy day: 07-31-2013

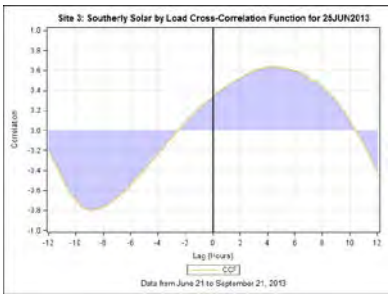

Southerly Solar & Load

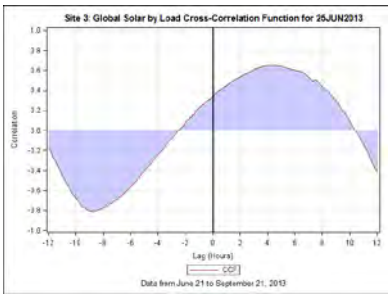

Global Solar & Load

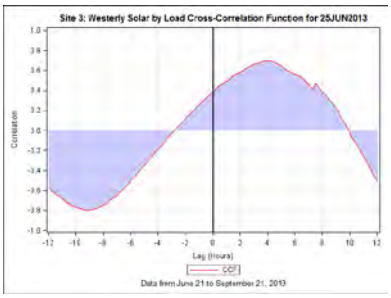

Westerly Solar & Load

Very cloudy day: 06-25-2013

Loads versus other weather factors

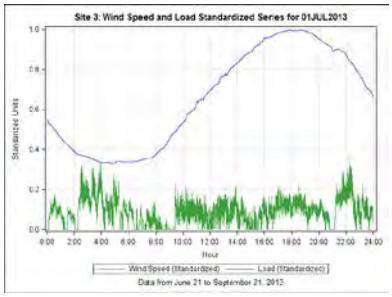

Wind Speed & Load

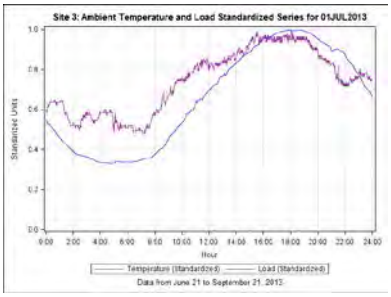

Ambient Temperature & Load

Mostly clear day: 07-01-2013

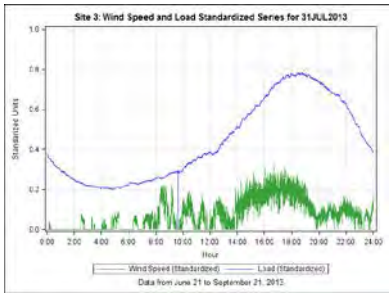

Wind Speed & Load

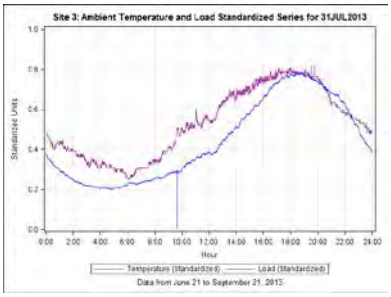

Ambient Temperature & Load

Moderately cloudy day: 07-31-2013

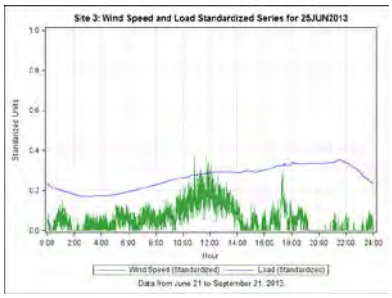

Wind Speed & Load

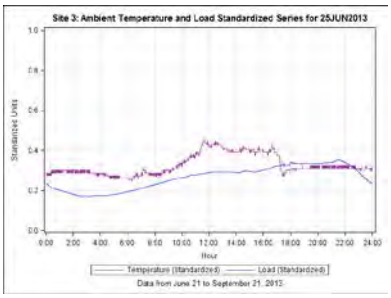

Ambient Temperature & Load

Very cloudy day: 06-25-2013

Auto-correlations of loads and other factors

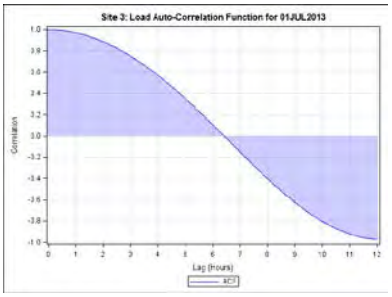

Load

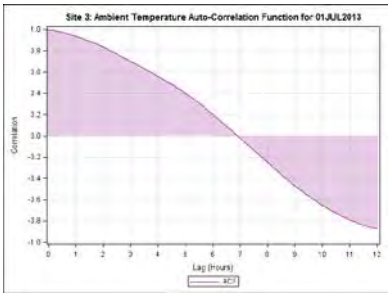

Ambient Temperature

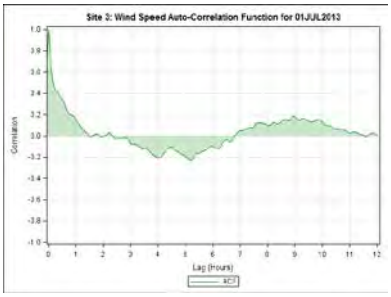

Wind Speed

Mostly clear day: 07-01-2013

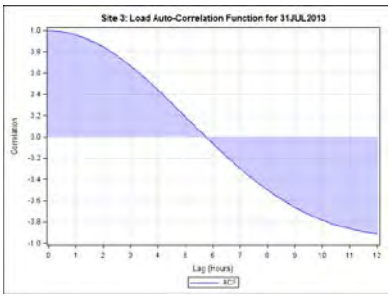

Load

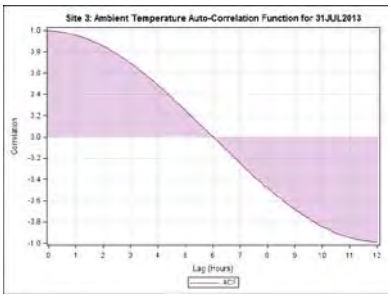

Ambient Temperature

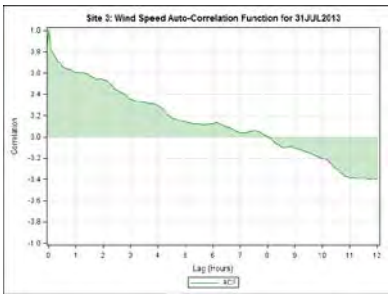

Wind Speed

Moderately cloudy day: 07-31-2013

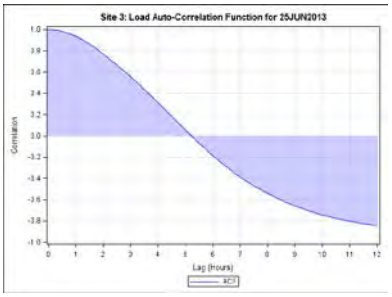

Load

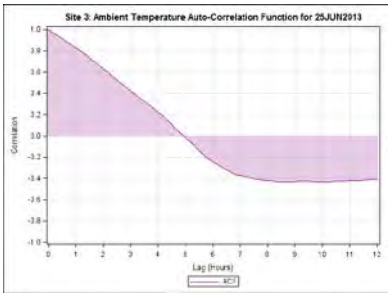

Ambient Temperature

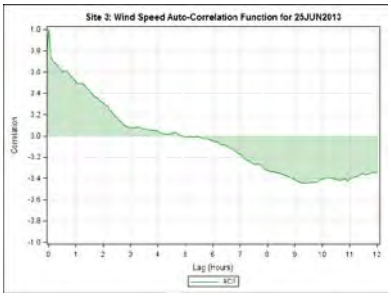

Wind Speed

Very cloudy day: 06-25-2013

Cross-correlations between loads and other weather factors

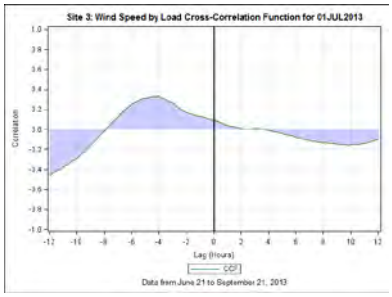

Wind Speed & Load

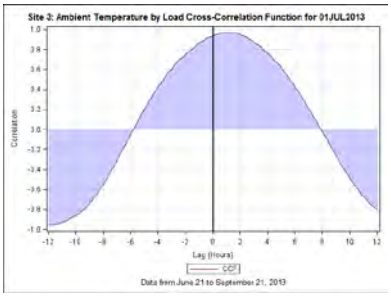

Ambient Temperature & Load

Mostly clear day: 07-01-2013

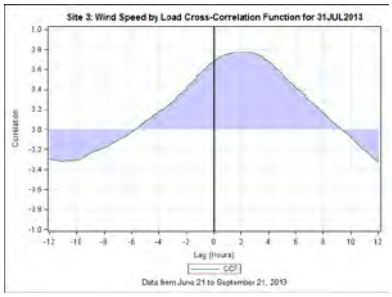

Wind Speed & Load

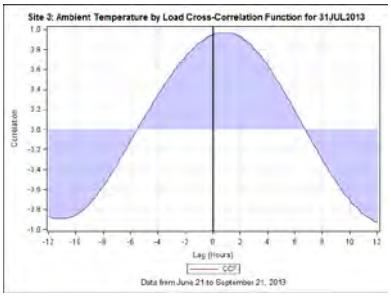

Ambient Temperature & Load

Moderately cloudy day: 07-31-2013

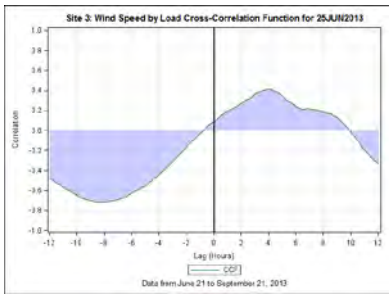

Wind Speed & Load

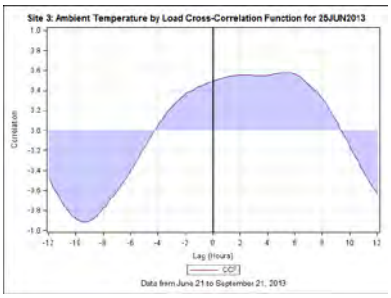

Ambient Temperature & Load

Very cloudy day: 06-25-2013

Maximum cross-correlations for the 93-day study period

Loads and irradiances

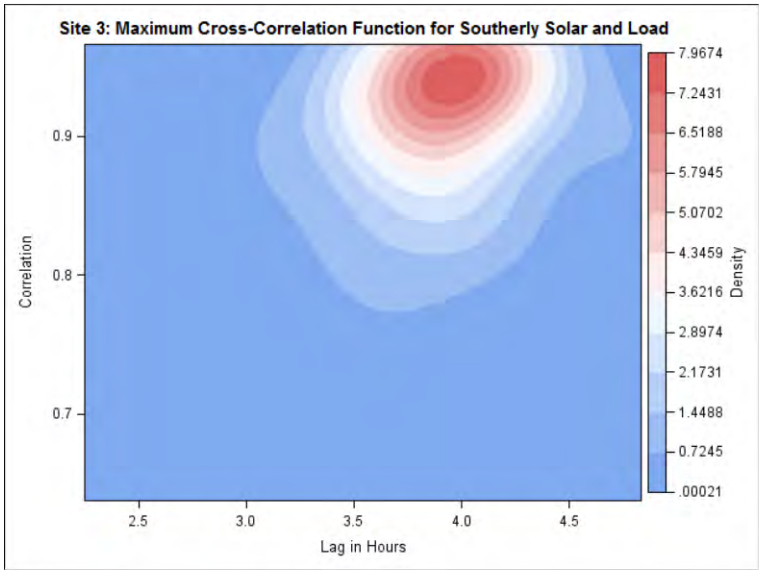

Lag	Correlation
3.957627	0.943656

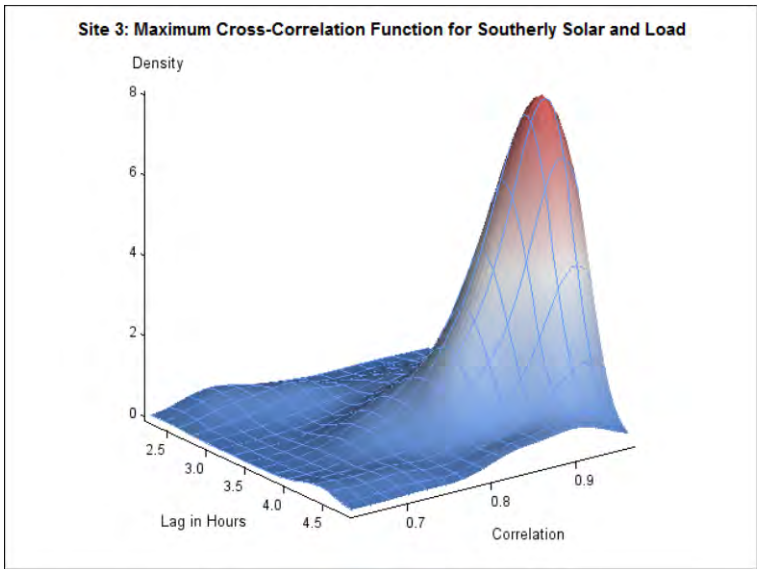

Southerly Solar & Load

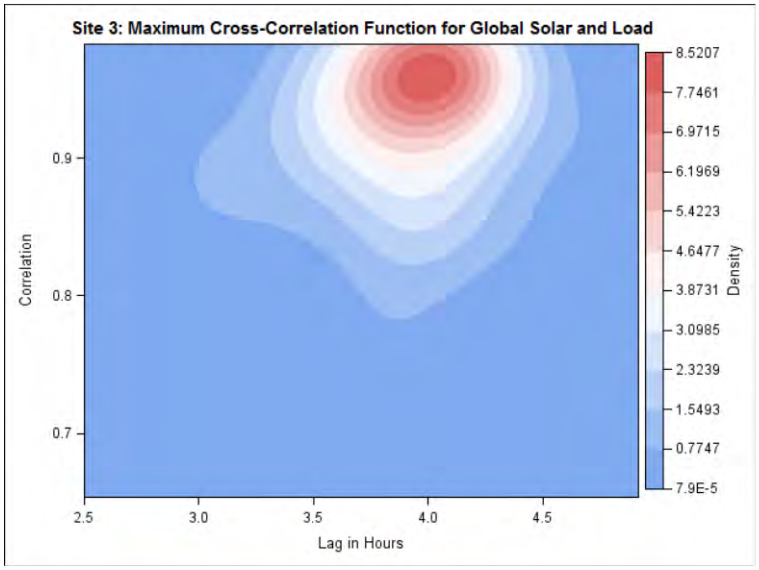

Lag	Correlation
4.015537	0.960693

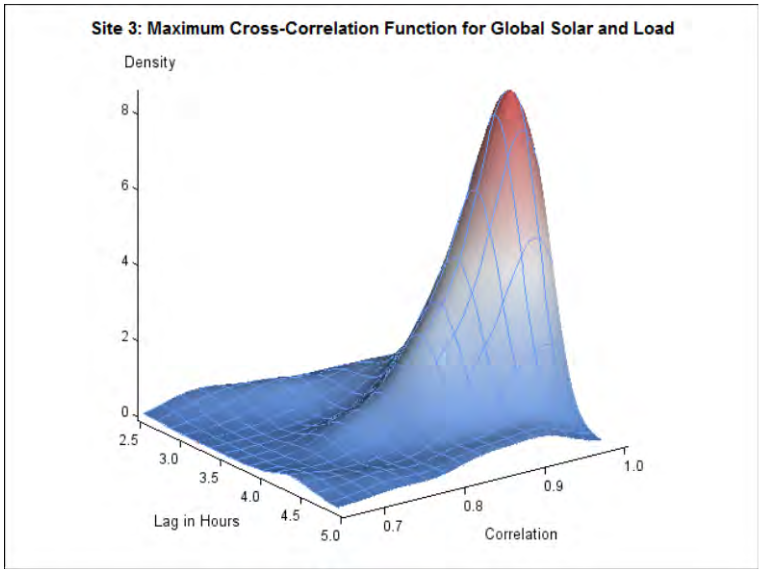

Global Solar & Load

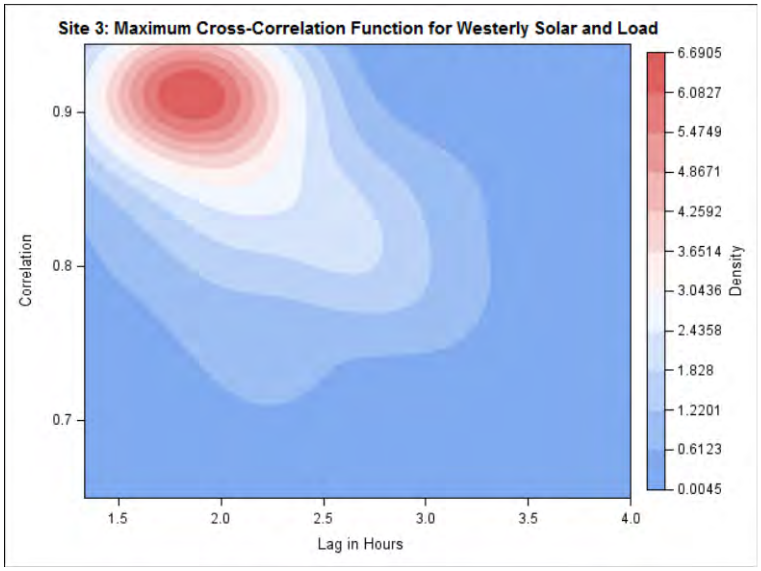

Lag	Correlation
1.830508	0.914068

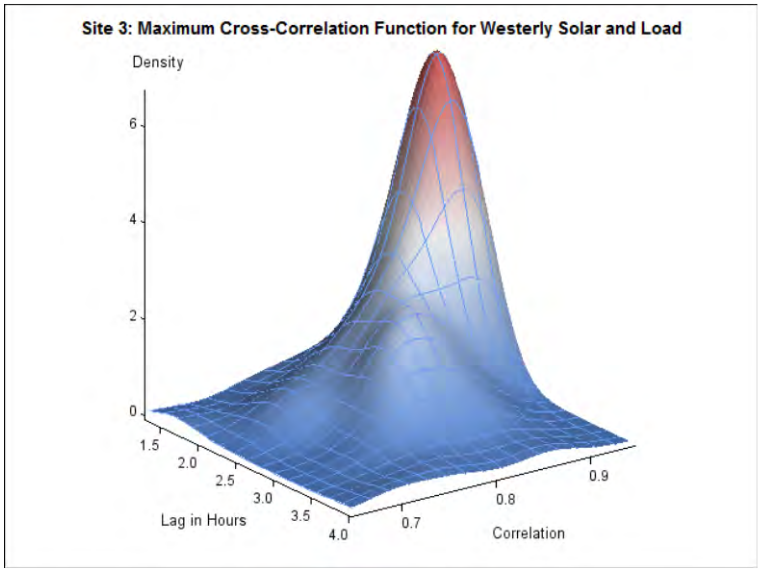

Westerly Solar & Load

Temperatures and irradiances

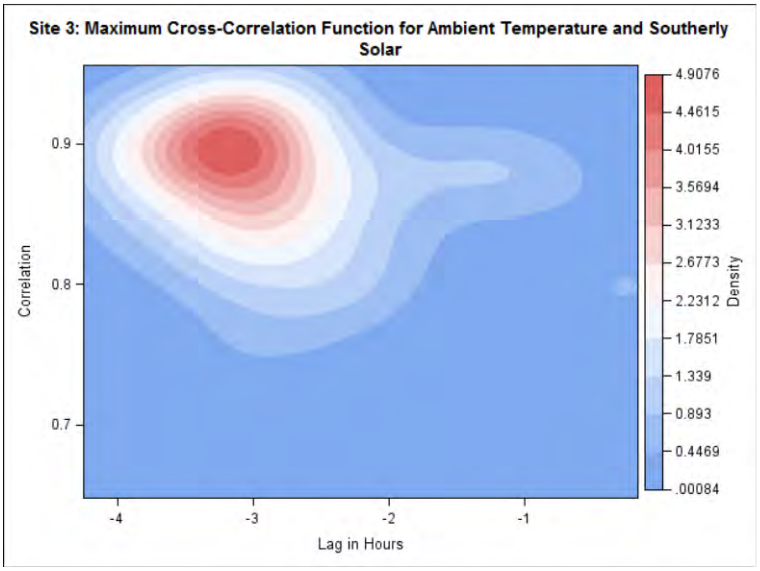

Lag	Correlation
-3.21186	0.898338

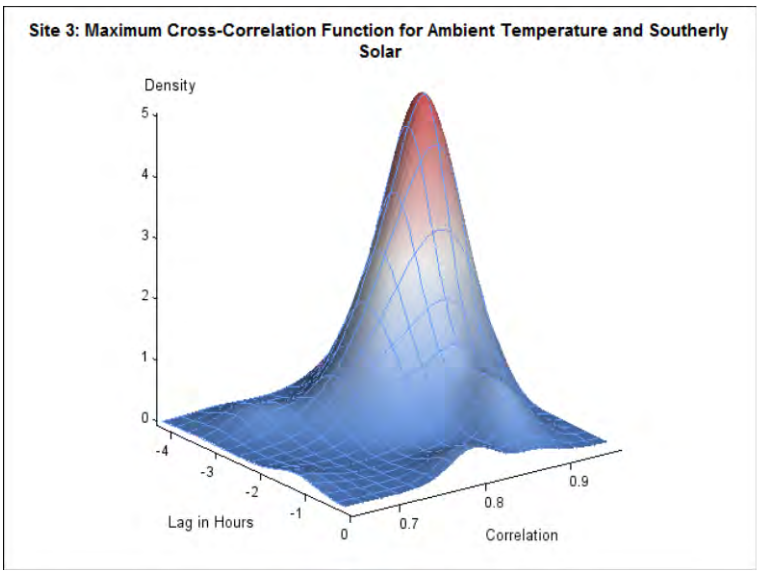

Southerly Solar & Temperature

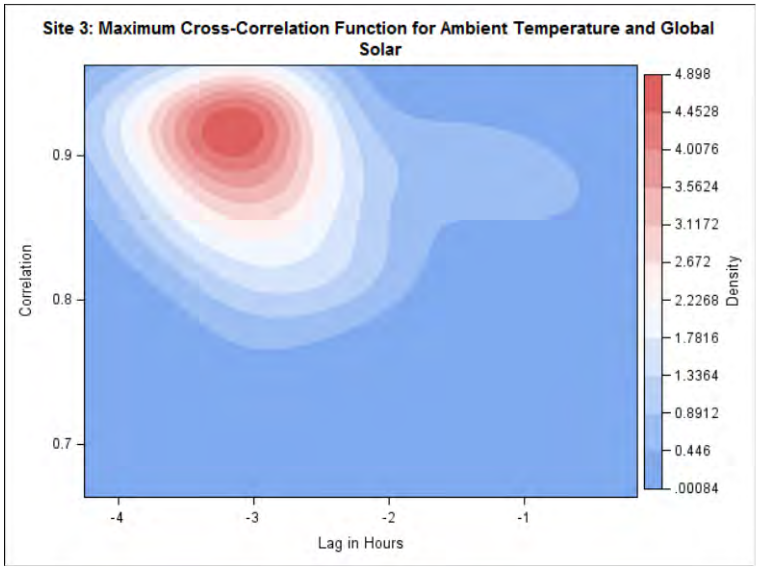

Lag	Correlation
-3.14266	0.916724

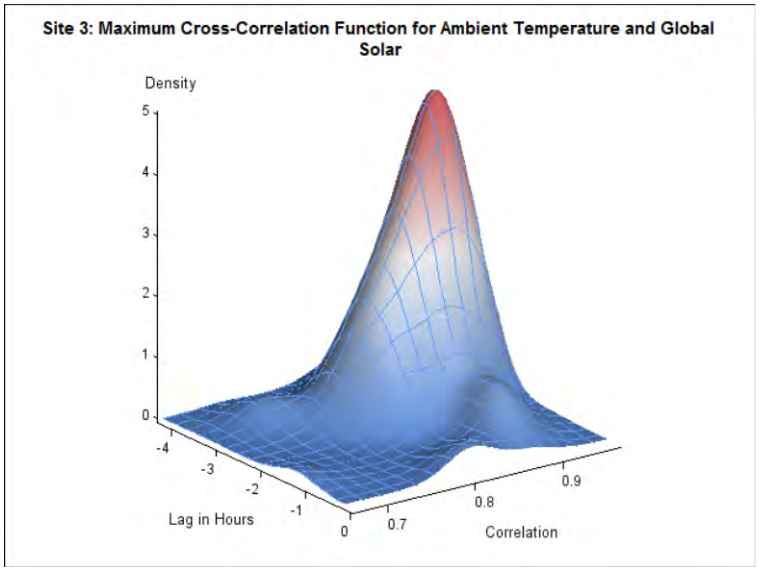

Global Solar & Temperature

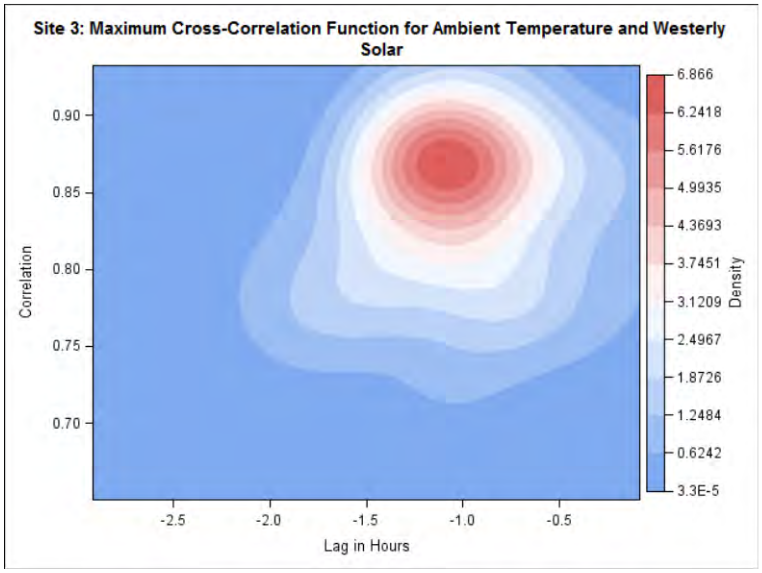

Lag	Correlation
-1.09181	0.870414

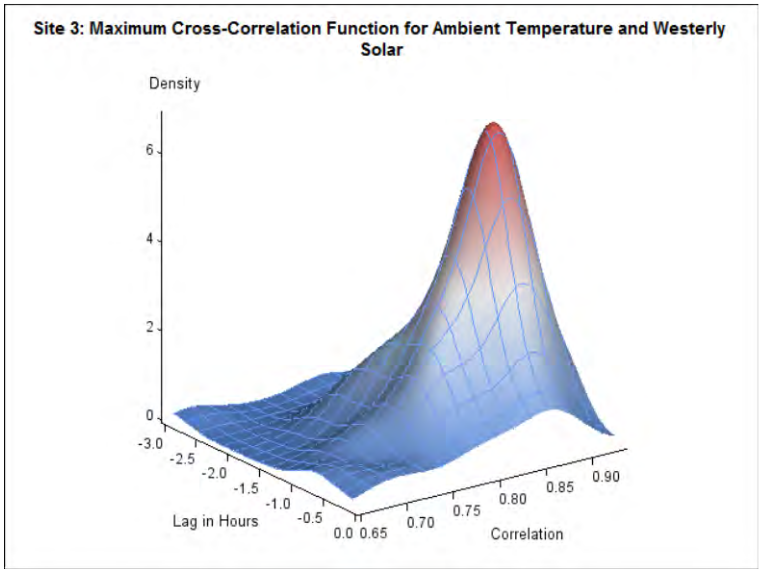

Westerly Solar & Temperature

Wind speeds and Irradiances

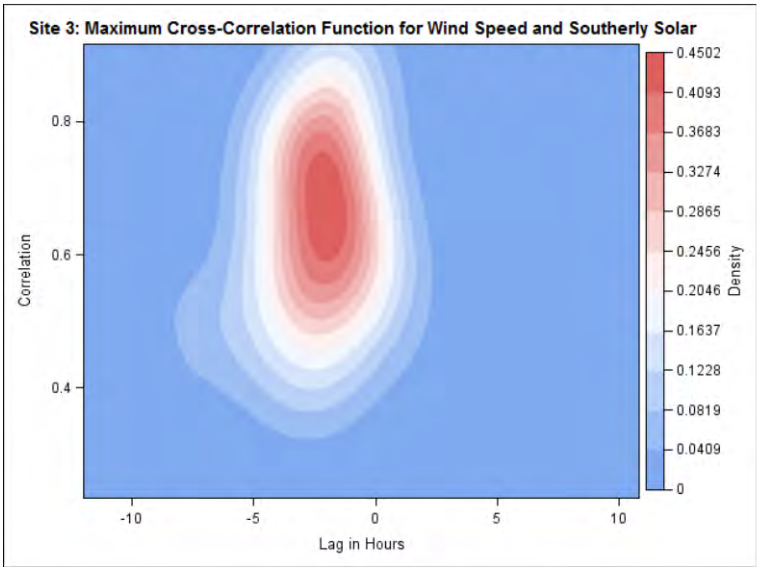

Lag	Correlation
-1.93785	0.673628

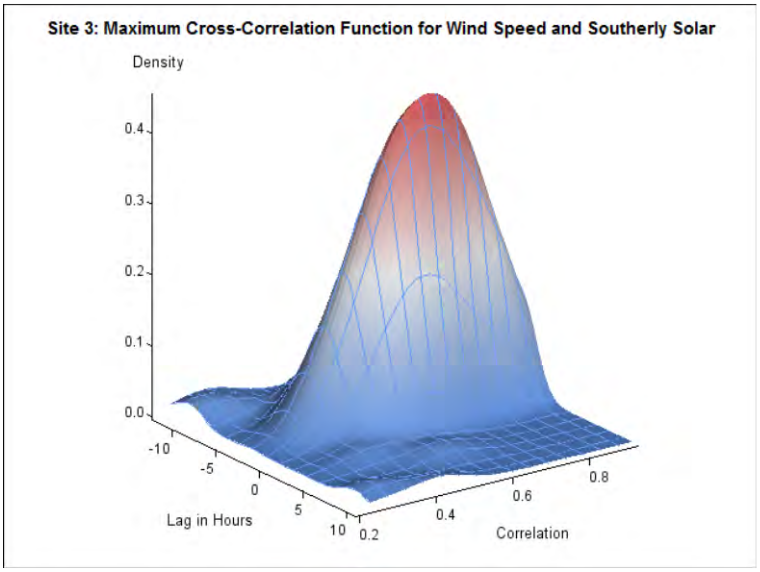

Southerly Solar & Wind Speeds

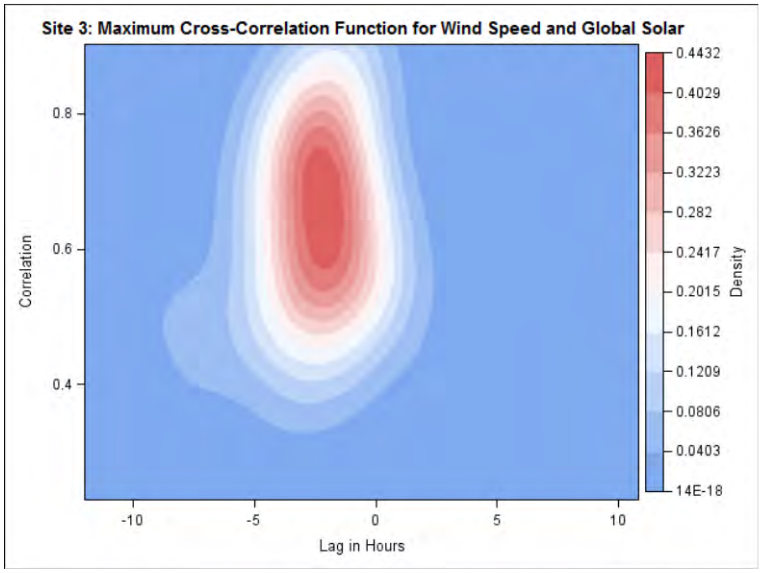

Lag	Correlation
-2.32486	0.674588

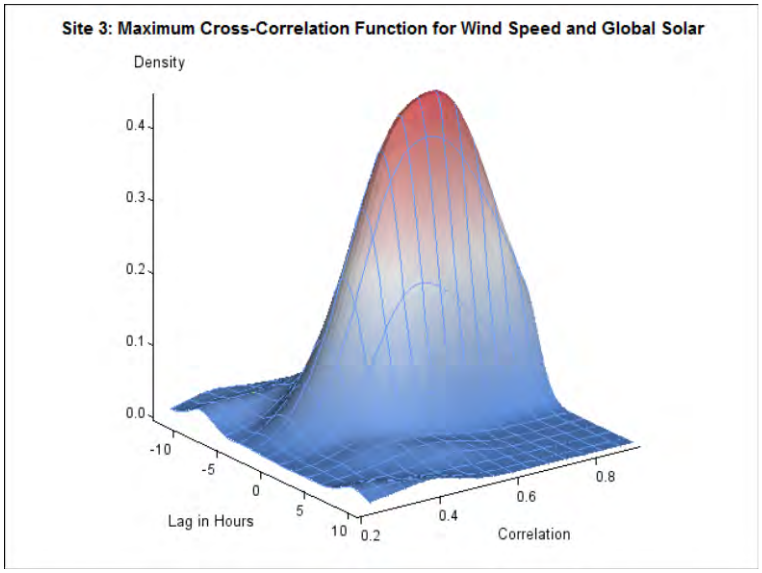

Global Solar & Wind Speeds

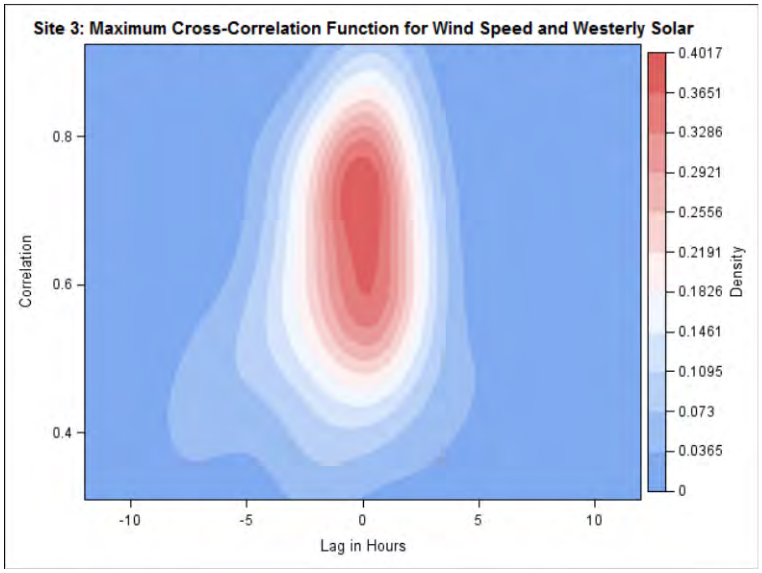

Lag	Correlation
-0.20339	0.716374

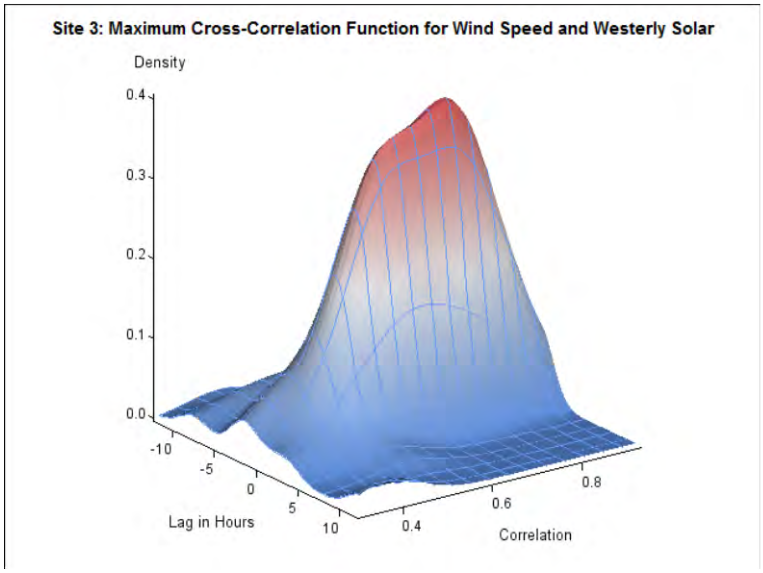

Westerly Solar & Wind Speeds

Other correlations

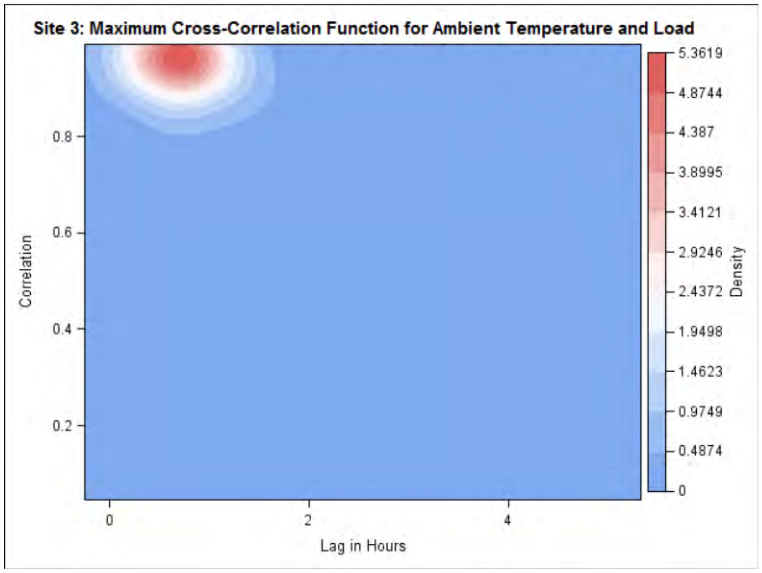

Lag	Correlation
0.696328	0.959052

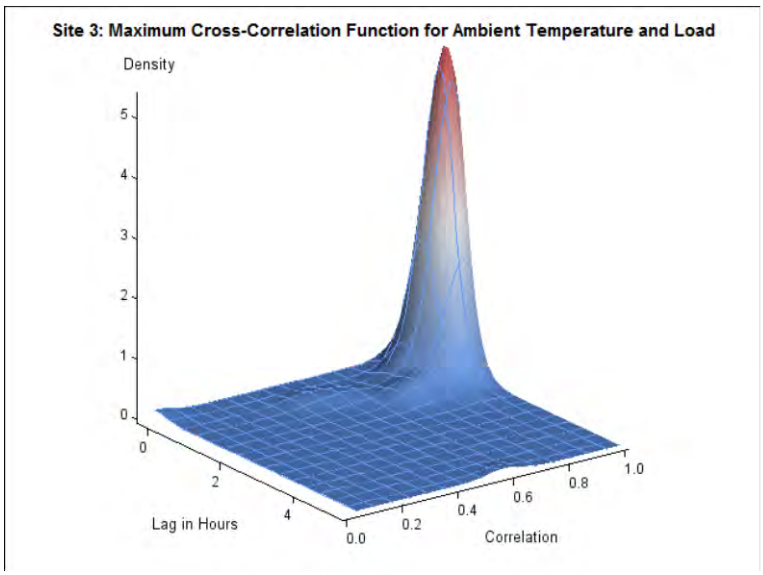

Temperature & Load

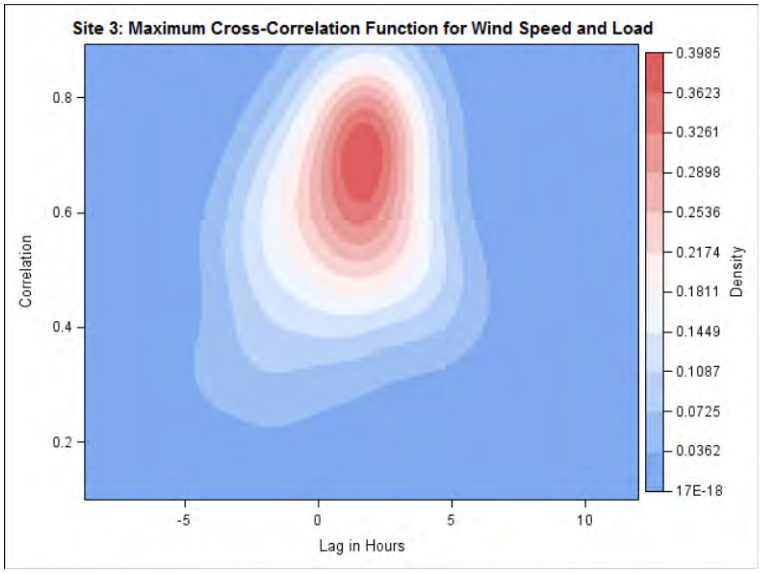

Lag	Correlation
1.800847	0.691447

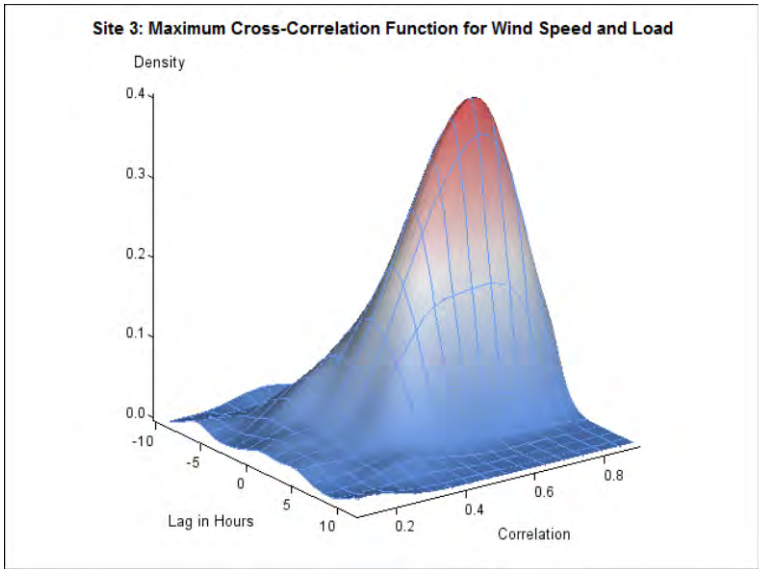

Wind Speed & Load

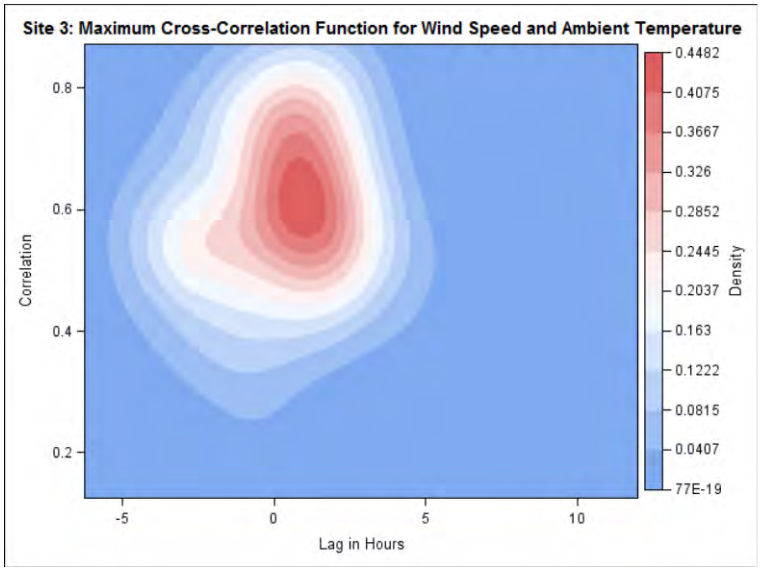

Lag	Correlation
0.864407	0.619116

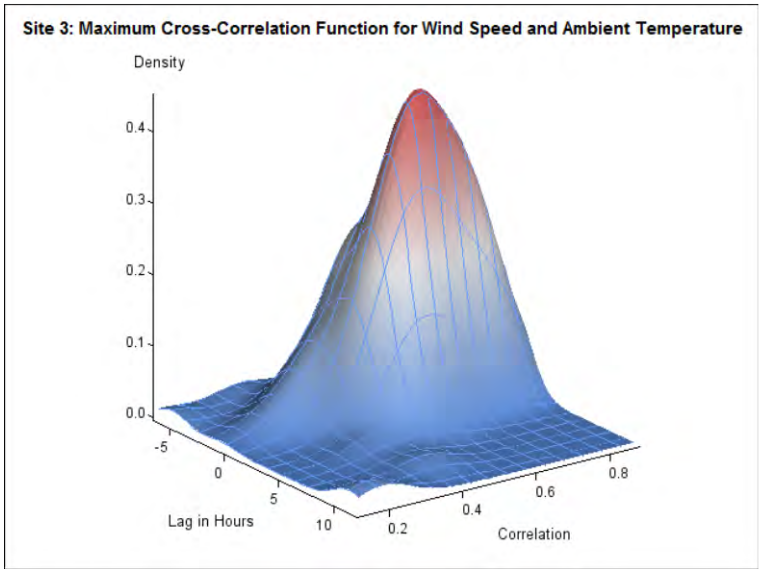

Wind Speed & Temperature

Summarized Results

SIWS03

Variable	Wind Speed	Ambient Temperature	Southerly Solar	Westerly Solar	Global Solar	Load
Wind Speed		0.62	0.67	0.72	0.67	0.69
Ambient Temperature	0.86		0.90	0.87	0.92	0.96
Southerly Solar	-1.94	-3.21		0.97	1.00	0.94
Westerly Solar	-0.20	-1.09	2.27		0.95	0.91
Global Solar	-2.32	-3.14	0.00	-2.32		0.96
Load	1.80	0.70	3.96	1.83	4.02	

Wind Speed tends to lead Ambient Temperature by about 0.86 hours with a correlation of 0.62
Wind Speed tends to lag Southerly Solar by about 1.94 hours with a correlation of 0.67
Wind Speed tends to lag Westerly Solar by about 0.20 hours with a correlation of 0.72
Wind Speed tends to lag Global Solar by about 2.32 hours with a correlation of 0.67
Wind Speed tends to lead Load by about 1.80 hours with a correlation of 0.69

Ambient Temperature tends to lag Southerly Solar by about 3.21 hours with a correlation of 0.90
Ambient Temperature tends to lag Westerly Solar by about 1.09 hours with a correlation of 0.87
Ambient Temperature tends to lag Global Solar by about 3.14 hours with a correlation of 0.92
Ambient Temperature tends to lead Load by about 0.70 hours with a correlation of 0.96

Southerly Solar tends to lead Westerly Solar by about 2.27 hours with a correlation of 0.97
Southerly Solar tends to lead Global Solar by about 0.00 hours with a correlation of 1.00
Southerly Solar tends to lead Load by about 3.96 hours with a correlation of 0.94

Westerly Solar tends to lag Global Solar by about 2.32 hours with a correlation of 0.95
Westerly Solar tends to lead Load by about 1.83 hours with a correlation of 0.91

Global Solar tends to lead Load by about 4.02 hours with a correlation of 0.96

Appendix 4 — Solar Energy Densities for all sites

Solar Energy Density (Generation per Day in w/m^2)									
	Global Solar Intensity			Southerly Solar Intensity			Westerly Solar Intensity		
Date	Site 1	Site 2	Site 3	Site 1	Site 2	Site 3	Site 1	Site 2	Site 3
6/21/2013	2,393,500.76	2,480,678.84	2,482,800.02	2,177,928.67	2,234,314.15	2,232,674.42	1,411,858.97	1,518,853.47	1,581,030.74
6/22/2013	3,106,574.73	3,137,294.47	3,137,503.60	2,842,223.44	2,843,267.69	2,865,093.79	2,274,724.07	2,346,037.85	2,362,602.93
6/23/2013	2,023,157.52	2,030,463.67	2,004,073.67	1,870,780.45	1,857,010.08	1,844,791.34	1,186,325.07	1,190,153.21	1,219,912.42
6/24/2013	1,264,348.41	1,275,460.70	1,262,991.78	1,082,382.08	1,069,278.46	1,074,596.77	870,962.69	851,951.34	822,391.53
6/25/2013	1,018,354.90	1,010,538.83	981,993.46	939,754.63	904,007.35	895,280.82	735,043.65	730,798.85	748,322.84
6/26/2013	2,819,039.33	2,926,368.94	2,814,779.80	2,646,576.75	2,693,493.19	2,620,556.94	2,480,342.67	2,677,602.48	2,558,846.36
6/27/2013	3,093,961.26	3,142,897.69	3,140,595.41	2,780,131.17	2,793,243.87	2,827,589.85	2,443,548.35	2,614,392.47	2,593,348.50
6/28/2013	3,083,778.90	3,129,868.60	3,128,957.90	2,773,336.49	2,787,653.98	2,819,698.72	2,421,815.36	2,587,471.21	2,572,355.35
6/29/2013	2,658,258.93	2,694,894.03	2,674,675.01	2,486,735.01	2,476,486.94	2,522,414.08	2,444,796.94	2,614,297.06	2,583,932.96
6/30/2013	2,957,074.83	2,985,415.00	2,984,363.94	2,737,682.00	2,751,261.75	2,772,333.48	2,066,652.83	2,148,558.06	2,184,045.56
7/1/2013	2,899,358.66	2,913,112.60	2,917,692.24	2,719,010.24	2,707,143.00	2,744,653.44	2,194,616.40	2,271,469.72	2,282,650.92
7/2/2013	2,670,267.99	2,703,219.70	2,716,251.19	2,537,583.30	2,546,437.16	2,589,067.59	1,913,278.01	1,965,765.38	1,993,060.94
7/3/2013	1,914,085.27	1,980,764.60	2,046,487.97	1,813,257.42	1,832,405.26	1,950,083.96	1,633,400.52	1,695,601.58	1,690,141.05
7/4/2013	2,458,116.80	2,434,651.97	2,540,880.84	2,359,768.40	2,321,067.50	2,445,524.46	1,697,925.51	1,705,773.10	1,788,001.07
7/5/2013	2,868,876.94	2,837,631.46	2,899,060.66	2,604,711.36	2,534,441.16	2,645,982.41	2,359,567.42	2,512,027.08	2,517,888.93
7/6/2013	2,863,386.41	2,939,219.03	3,051,291.43	2,603,114.99	2,646,057.50	2,787,865.81	2,425,941.78	2,608,378.28	2,602,896.61
7/7/2013	3,035,968.71	3,087,349.90	3,080,156.84	2,745,515.23	2,791,870.54	2,827,565.37	2,390,940.65	2,575,611.32	2,561,009.99
7/8/2013	2,770,578.22	2,797,670.85	2,881,821.18	2,564,185.79	2,579,389.38	2,714,254.88	2,402,484.88	2,589,245.14	2,577,867.85
7/9/2013	3,056,145.54	3,097,739.52	3,093,981.04	2,786,922.81	2,813,589.18	2,851,637.71	2,373,683.31	2,545,196.74	2,541,018.22
7/10/2013	2,973,422.35	2,995,203.62	2,974,374.68	2,756,606.85	2,747,090.44	2,769,878.29	2,353,016.62	2,520,282.05	2,493,082.08
7/11/2013	1,327,820.98	1,392,169.85	1,450,790.74	1,198,534.77	1,212,400.59	1,329,391.52	1,436,544.12	1,572,216.92	1,557,789.71
7/12/2013	3,002,853.69	3,049,687.83	3,039,366.14	2,754,851.51	2,784,752.71	2,818,540.38	2,343,005.25	2,543,119.05	2,527,231.99
7/13/2013	3,042,611.34	3,088,950.80	3,079,425.13	2,800,430.89	2,812,495.84	2,845,624.03	2,393,023.95	2,601,610.71	2,583,803.83
7/14/2013	3,052,047.49	3,097,437.34	3,085,036.07	2,805,185.29	2,831,387.34	2,864,741.85	2,397,127.03	2,598,534.20	2,582,535.15
7/15/2013	2,974,410.34	3,002,119.41	3,000,307.80	2,769,636.86	2,778,842.61	2,816,517.83	2,304,573.25	2,424,330.76	2,450,764.84
7/16/2013	2,361,811.59	2,406,095.00	2,440,494.56	2,246,178.86	2,272,441.59	2,318,650.03	1,492,807.40	1,551,108.35	1,648,815.59
7/17/2013	2,988,779.95	3,036,337.85	3,019,231.85	2,790,892.45	2,814,148.06	2,852,704.55	2,429,272.06	2,629,361.24	2,604,728.25
7/18/2013	3,049,328.24	3,095,702.74	3,072,353.98	2,828,931.46	2,859,298.22	2,890,213.02	2,447,147.42	2,638,152.98	2,617,791.08
7/19/2013	3,011,238.47	3,052,184.71	3,032,333.57	2,813,578.96	2,837,106.62	2,870,013.49	2,403,873.95	2,572,605.40	2,564,906.67
7/20/2013	2,985,642.42	3,021,313.66	3,004,955.96	2,803,558.61	2,820,345.74	2,859,292.74	2,405,959.98	2,567,573.29	2,565,946.32
7/21/2013	3,118,912.19	3,161,060.92	3,145,442.43	2,912,807.74	2,942,163.69	2,978,438.98	2,513,398.75	2,688,547.61	2,682,640.40
7/22/2013	3,071,843.22	3,105,558.93	3,086,481.13	2,884,944.89	2,910,608.67	2,942,600.51	2,452,159.50	2,615,391.34	2,607,950.21
7/23/2013	2,835,313.23	2,857,424.19	2,830,391.75	2,754,319.70	2,785,065.79	2,790,916.33	1,749,786.31	1,812,614.42	1,866,227.81
7/24/2013	1,889,311.85	1,882,764.91	1,694,727.56	1,763,662.62	1,738,773.04	1,600,564.53	1,620,319.54	1,635,370.62	1,433,045.93
7/25/2013	2,733,720.45	2,735,499.46	2,749,715.87	2,669,408.75	2,647,633.97	2,711,688.37	2,218,557.32	2,344,060.15	2,387,337.10
7/26/2013	2,268,856.59	2,221,350.32	2,209,002.41	2,169,323.58	2,096,241.71	2,116,930.93	1,735,391.97	1,796,303.33	1,854,144.47
7/27/2013	2,440,838.25	2,450,897.18	2,549,984.60	2,423,894.30	2,410,892.08	2,573,375.95	2,328,617.88	2,492,346.35	2,529,044.12
7/28/2013	2,773,002.31	2,791,158.00	2,798,049.10	2,728,430.66	2,732,914.36	2,794,913.20	2,168,526.38	2,301,535.08	2,344,255.14
7/29/2013	2,433,217.31	2,505,121.29	2,516,097.68	2,324,373.30	2,390,325.29	2,443,353.60	1,667,354.00	1,787,885.56	1,867,609.53
7/30/2013	2,842,802.82	2,853,269.58	2,797,910.12	2,774,963.72	2,765,580.62	2,779,364.13	2,313,395.33	2,412,071.29	2,372,032.40
7/31/2013	2,328,243.27	2,321,049.29	2,324,542.45	2,301,324.55	2,264,998.77	2,345,571.30	2,285,166.99	2,369,431.16	2,405,142.10
8/1/2013	2,489,131.29	2,444,995.73	2,369,076.91	2,514,411.73	2,462,750.50	2,459,050.63	2,128,629.73	2,149,355.33	2,078,912.19
8/2/2013	2,814,448.96	2,833,057.87	2,804,871.48	2,766,741.11	2,781,567.08	2,814,836.50	2,313,870.78	2,446,320.84	2,462,950.70
8/3/2013	2,796,912.06	2,816,046.71	2,781,514.11	2,768,123.26	2,782,157.90	2,805,092.94	2,253,471.36	2,385,879.00	2,396,402.21
8/4/2013	2,786,360.55	2,811,136.64	2,737,094.50	2,763,430.07	2,779,843.96	2,774,104.17	2,280,203.78	2,427,571.65	2,418,667.85
8/5/2013	2,787,162.28	2,801,388.05	2,773,826.59	2,779,959.54	2,788,210.16	2,815,455.03	2,268,839.78	2,406,737.33	2,418,843.15
8/6/2013	2,726,261.29	2,739,122.58	2,715,593.21	2,744,190.24	2,745,980.74	2,780,943.45	2,225,883.16	2,348,321.94	2,359,316.14
8/7/2013	2,298,855.18	2,349,664.17	2,398,434.55	2,346,388.76	2,382,230.33	2,461,639.31	1,648,023.22	1,741,780.55	1,770,508.76
8/8/2013	2,185,676.78	2,190,338.56	2,159,158.61	2,258,697.47	2,267,363.86	2,277,303.92	1,516,104.93	1,548,864.07	1,590,849.15
8/9/2013	2,654,630.48	2,664,251.49	2,637,026.14	2,706,599.68	2,717,882.31	2,751,589.53	2,248,036.57	2,384,918.36	2,371,828.94
8/10/2013	2,578,483.92	2,601,830.76	2,541,769.25	2,668,604.82	2,699,918.96	2,682,428.38	1,879,255.37	1,973,221.18	1,956,155.26
8/11/2013	2,149,049.39	2,149,673.63	2,049,083.68	2,216,986.49	2,220,053.09	2,136,167.09	1,281,786.71	1,307,025.99	1,407,366.90
8/12/2013	1,695,352.81	1,680,088.00	1,651,879.54	1,747,314.20	1,736,798.72	1,737,193.34	960,705.79	988,461.92	1,029,156.86
8/13/2013	2,445,423.77	2,447,197.03	2,323,220.06	2,535,369.24	2,525,174.79	2,435,743.51	1,951,097.59	2,047,967.49	1,907,062.75
8/14/2013	2,515,328.36	2,519,302.87	2,496,875.49	2,645,347.97	2,645,557.18	2,653,125.97	2,117,696.42	2,210,619.42	2,213,192.49
8/15/2013	2,496,730.84	2,543,864.08	2,529,355.82	2,597,925.96	2,657,576.14	2,686,789.37	2,146,717.74	2,302,553.76	2,293,890.23
8/16/2013	2,616,169.60	2,650,410.56	2,621,595.63	2,766,078.96	2,788,045.30	2,783,418.86	2,133,744.79	2,305,739.21	2,321,847.15
8/17/2013	2,225,312.63	2,167,539.37	2,136,271.94	2,298,162.40	2,242,967.35	2,261,251.13	1,755,388.25	1,848,568.97	1,948,480.34
8/18/2013	2,521,890.03	2,554,242.77	2,535,182.88	2,641,761.17	2,710,241.07	2,719,792.40	2,075,887.47	2,246,706.69	2,253,748.95
8/19/2013	2,300,942.48	2,336,631.68	2,353,552.65	2,429,944.72	2,497,967.45	2,545,777.30	1,712,824.97	1,851,825.27	1,885,870.01
8/20/2013	2,504,839.88	2,516,984.05	2,490,577.82	2,687,503.78	2,710,116.41	2,710,904.11	2,052,499.62	2,222,732.74	2,200,173.09
8/21/2013	2,005,628.02	2,048,097.03	1,990,500.53	2,136,996.98	2,199,096.84	2,146,402.77	1,281,423.33	1,340,714.47	1,316,016.35
8/22/2013	1,793,954.72	1,810,125.24	1,779,888.76	1,881,907.49	1,906,481.05	1,880,100.48	1,122,807.81	1,198,666.84	1,214,981.21
8/23/2013	2,349,118.27	2,372,391.61	2,367,923.85	2,543,402.91	2,573,899.72	2,607,981.12	1,886,233.80	2,076,432.63	2,103,520.43
8/24/2013	1,700,523.77	1,758,748.32	1,876,607.09	1,784,077.14	1,835,413.18	2,001,161.61	1,345,658.61	1,482,529.83	1,662,508.56
8/25/2013	1,979,316.46	1,966,717.81	1,947,185.99	2,143,014.86	2,140,879.06	2,146,877.85	1,333,602.79	1,361,188.62	1,391,852.81
8/26/2013	2,212,219.28	2,219,035.33	2,192,275.47	2,444,399.13	2,446,027.54	2,420,329.79	1,821,588.51	1,956,202.04	1,958,793.69
8/27/2013	2,154,283.43	2,278,212.81	2,135,795.34	2,376,579.35	2,513,185.77	2,431,428.45	1,806,205.13	2,020,600.92	1,979,556.09
8/28/2013	2,225,439.48	2,185,414.34	2,106,225.77	2,496,168.14	2,442,714.49	2,483,437.06	1,883,379.87	1,989,494.52	1,986,063.26
8/29/2013	2,252,607.30	2,222,002.68	2,170,996.69	2,510,513.12	2,481,338.14	2,535,252.42	1,869,702.04	2,011,122.81	2,000,826.75
8/30/2013	2,379,450.39	2,382,699.97	2,296,448.00	2,681,552.35	2,695,809.33	2,648,806.74	2,055,782.90	2,257,137.11	2,233,225.82
8/31/2013	2,386,140.56	2,404,337.74	2,342,241.78	2,735,329.51	2,749,740.79	2,742,749.77	1,871,276.78	2,017,821.14	2,033,922.11
9/1/2013	2,088,379.34	2,055,588.01	1,928,650.47	2,354,041.65	2,300,932.69	2,219,646.98	1,657,210.34	1,738,138.25	1,660,532.20
9/2/2013	1,067,389.32	1,105,683.78	1,212,620.07	1,117,372.51	1,148,109.28	1,316,459.58	982,244.90	1,030,487.21	1,154,074.39
9/3/2013	1,225,032.84	1,234,670.84	1,280,977.98	1,309,462.62	1,300,655.28	1,398,130.54	1,345,135.26	1,395,782.86	1,406,407.08
9/4/2013	1,958,033.43	1,938,605.09	1,823,495.64	2,265,605.84	2,257,108.27	2,157,828.23	1,191,538.78	1,230,376.34	1,226,103.14
9/5/2013	1,207,998.76	1,180,726.30	1,260,928.92	1,359,387.43	1,331,248.23	1,483,676.80	823,851.25	848,951.51	913,979.46
9/6/2013	2,320,182.27	2,335,137.17	2,299,850.05	2,728,714.37	2,744,582.54	2,747,563.02	1,979,153.33	2,130,725.65	2,127,437.96
9/7/2013	2,288,686.74	2,311,935.65	2,279,941.13	2,688,937.52	2,717,963.78	2,732,636.95	1,918,421.97	2,066,779.61	2,087,944.30
9/8/2013	2,224,492.18	2,239,291.80	2,210,227.45	2,612,425.53	2,654,460.49	2,668,338.56	1,942,870.56	2,081,123.19	2,096,541.71
9/9/2013	2,238,880.61	2,259,986.45	2,226,139.23	2,673,633.88	2,696,433.02	2,696,789.86	1,891,661.30	2,031,234.83	2,055,909.98
9/10/2013	2,203,703.84	2,218,284.61	2,191,552.79	2,650,288.17	2,672,195.31	2,678,211.77	1,866,212.57	2,004,268.72	2,040,615.09
9/11/2013	2,197,473.96	2,211,291.19	2,183,036.91	2,657,512.70	2,674,050.49	2,677,892.36	1,854,172.37	1,978,567.39	2,017,026.03
9/12/2013	1,431,517.50	1,402,193.71	1,491,068.12	1,604,968.09	1,625,843.43	1,777,218.32	1,151,013.57	1,190,923.90	1,382,738.90
9/13/2013	1,691,220.62	1,617,549.09	1,627,395.64	1,886,759.08	1,798,286.40	1,865,747.58	1,633,672.00	1,718,998.43	1,775,809.88
9/14/2013	1,937,484.57	1,908,180.85	1,956,539.75	2,369,880.24	2,334,260.36	2,428,444.12	1,467,188.49	1,619,425.57	1,811,081.68
9/15/2013	2,018,390.02	2,020,107.94	1,963,843.85	2,510,003.07	2,518,847.99	2,475,803.91	1,572,358.28	1,673,741.36	1,639,744.20
9/16/2013	2,113,568.69	2,120,842.63	2,105,602.03	2,628,700.70	2,671,134.25	2,693,265.14	1,831,178.39	1,959,245.57	2,003,025.23
9/17/2013	1,040,457.05	1,077,463.54	1,108,716.20	1,079,793.21	1,103,858.31	1,178,190.27	1,049,536.36	1,101,809.03	1,188,810.12
9/18/2013	1,784,107.33	1,840,595.50	1,841,481.94	2,162,085.08	2,245,860.89	2,290,163.61	1,664,357.96	1,824,335.25	1,899,760.95
9/19/2013	2,109,104.08	2,114,343.47	2,088,066.95	2,690,831.50	2,712,406.09	2,716,118.36	1,857,079.37	1,998,653.44	2,037,080.23
9/20/2013	2,062,663.50	2,069,414.59	2,035,357.08	2,618,616.59	2,675,584.48	2,667,416.67	1,745,981.91	1,855,600.63	1,906,618.17
9/21/2013	1,007,630.29	1,008,236.80	957,527.65	1,029,568.59	1,010,506.83	966,280.11	759,449.39	745,963.46	744,662.69
Totals	219,704,903.60	221,463,275.80	220,126,443.55	222,963,511.51	223,959,243.50	226,517,909.09	174,599,552.03	185,305,851.03	186,670,542.98
Average Total	220,431,540.98			224,480,221.36			182,191,982.01		

Appendix F.
Smart Grid Metrics

This page left blank intentionally.

Smart Grid Metrics

II. STATUS OF CURRENT SMART GRID INVESTMENTS

A. Transmission Network and Operations Enhancements

Transmission Situational Awareness Grid Operator's Monitoring and Control Assistant

Description: This project relates to the Linear State Estimator (LSE) and Region of Stability Existence (ROSE) tools. The LSE is a quasi-real-time state estimator solution based on phasor measurement unit (PMU) data. This provides for a non-iterative power flow solution of the (reduced) system. The ROSE tool will be fed by either the Peak RC state estimator or the LSE and will calculate real time a margin to voltage stability or to a Path System Operating Limit (SOL) violation.

Status: Ongoing

Benefits: Avoid drifting into voltage instability during unforeseen operating conditions

Cost: $157,321 as of April 2019*

Metric: Increased awareness of voltage stability to avoid the risk of operating in an unsafe operating mode. Also act as backukp to state estimator operated by Peak Reliability.

* Please note that in the *2017 Smart Grid Report*, the project cost was reported as $272,000. However, upon preparing the *2019 Smart Grid Report*, it was determined the cost of the project to date is $157,321.

II. STATUS OF CURRENT SMART GRID INVESTMENTS (*continued*)

A. Transmission Network and Operations Enhancements *(continued)*

Dynamic Line Capacity Pilot

Description: Transmission line ratings are static and are based on conservative and often worst-case environmental factors. A dynamic transmission line rating system is based on real time or near real time measured environmental conditions, such as ambient temperature, wind speed, and wind direction. This allows the line rating to be more accurate as it is based on actual conditions. An increase of at least 20 percent of the static line rating is often possible.

Status: Complete

Benefits: The potential to in increase transmission System operational flexibility and increased operating limits by replacing conservative assumptions with known measurements when needed in the future.

Cost: $474,000 total cost of project over 5 years

Metric: Identify the times when we make use of the additional capacity. (System was installed to validate the Dynamic Line Rating [DLR] Principal. The usefulness of DLR has been demonstrated and has the potential to be a tool to be used by Idaho Power when additional line capability is needed; however there are no capacity gains to claim yet.)

II. STATUS OF CURRENT SMART GRID INVESTMENTS (*continued*)

A. Transmission Network and Operations Enhancements *(continued)*

Power System Engineering Research Center

Description: This is a Power System Engineering Research Center (PSERC) High Impact Project: Life-cycle management of critical systems through certification, commissioning, in-service maintenance, remote testing, and risk assessment. The life-cycle management of critical systems is particularly complex since it requires tools and methodologies that are not readily available, so some custom approaches are typically taken, which may be costly. Typical examples are the deployment of synchrophasor based Wide Area Protection, Monitoring and Control (WAMPAC) and Special Protection System (SPS) where no standard tools for certification, commissioning, in-service maintenance and risk assessment are available. This project will deliver such tools and make some of them readily available for the industry to use at the host universities. Presently we are trying to create a non-disclosure agreement with Washington State University to be able to install and test their PMU remote testing software or PPA (PMU Performance Analyzer) and associated ERKIOS middleware software for remote end-to-end testing of mission critical systems.

Status: Completed

Benefits: Awareness and/or implementation of new projects, methods and technologies that can increase the operational and planning efficiencies

Cost: $100,000 total cost of project

Metric: Number of projects, methods, and technologies that become adopted by the company

# of Projects Adopted
0

II. STATUS OF CURRENT SMART GRID INVESTMENTS (*continued*)

A. Transmission Network and Operations Enhancements *(continued)*

Transmission and Distribution Line Inspections using Unmanned Aircraft Systems

Description: Using Unmanned Aircraft Systems (UAS) in the Transmission and Distribution Line inspection process as an additional tool to visually assess the condition of the Transmission and Distribution conductor, equipment and poles

Status: Complete

Benefits: Improves line inspection efficiency, safety, and reliability

Cost: $50,000 for initial equipment and training, $10,000/year O & M expense for software licensing, $50,000/year capital expense for additional equipment

Metric: UAS flights due to limited access or elevation conditions

# of Arial Flights	Time Period
416	April 2018–November 2018

II. STATUS OF CURRENT SMART GRID INVESTMENTS (*continued*)

B. Substation and Distribution Network and Operations Enhancements

Solar End-of-Feeder Project

Description: Explore and install a pilot project to determine the possible benefits of using energy storage, "smart" inverter technology and/or photovoltaic (PV) solar panels at the end of the feeder to improve distribution voltage.

Status: Complete

Benefits: Multiple customer voltage improvement

Cost: $114,000 total cost of project*

Metric: Deviations outside of ANSI C84.1

*Please note that in *2017 Smart Grid Report*, the project cost was estimated at $133,000. However, upon preparing the *2019 Smart Grid Report*, it was determined the total cost of the project is $113,758.

	2016	2017	2018
	(Pre-Project)	(Post Project / non-smart Inverter)	(Post Project / smart Inverter)
Deviations outside of ANSI C84.1			
	436	33	4

II. STATUS OF CURRENT SMART GRID INVESTMENTS (*continued*)

B. Substation and Distribution Network and Operations Enhancements *(continued)*

Volt/VAr InterTechnology Control Pilot

Description: Determine a strategy or set of strategies that can be used for optimizing the Volt/VAr characteristics on a distribution circuit.

Status: Complete

Benefits: Losses reduction

Cost: $203,000 over two years

Metric: Technical losses

	Circuit	Pre-Project	Post-Project	Change
Winter	AIKN-011	6.056%	5.622%	- 7.166%
	AIKN-013	1.905%	1.803%	- 5.350%
Summer	AIKN-011	8.265%	2.140%	-74.1%
	AIKN-013	5.175%	5.050%	-2.41%

II. B. Substation and Distribution Network and Operations Enhancements (*continued*)

Electric Vehicle Activities

Description: Offer incentives for the installation of home charging stations and workplace charging stations

Status: Ongoing

Benefits: Collect information on the barriers and opportunities related to home charging and charging behavior

Cost: This project was funded by shareholder dollars. No project costs were charged to customers

Metric: Number of stations installed

Electric Vehicle Program	# of Customers*	# of Sites*	# of Stations*
Home Electric Vehicle Charging Incentive Pilot	1	1	1
EV workplace Charging Station Incentive Program	19	26	46

2016-2018 results, 2019 pending

II. STATUS OF CURRENT SMART GRID INVESTMENTS (*continued*)

B. Substation and Distribution Network and Operations Enhancements (*continued*)

Jordan Valley Energy Storage Project

Description: Install an energy storage system as a non-wire alternative to a transformer replacement in Jordan Valley, Oregon

Status: Postponed

Benefits: Potential replacement cost reduction, gain experience with new technologies

Cost: $0 to date

Metric: None currently

II. STATUS OF CURRENT SMART GRID INVESTMENTS (*continued*)

B. Substation and Distribution Network and Operations Enhancements (*continued*)

700 MHz Field Area Network

Description: Install a 700 MHz licensed spectrum field area network (FAN) to provide secure, reliable, and sustainable communications to distribution field devices. Current scope of FAN buildout includes supporting the Integrated Volt/VAr Control system buildout. The number of communication devices planned below in the metrics.

Status: In Progress

Benefits: Reliable, secure, flexible and affordable communications to field devices

Cost: $12,000,000 total projected for 5 year project (2017–2021)

Metric: Number Master radios installed, Number field radios installed

Year	2017	2018	2019	2020	2021	Total
# Master Radios	1	1	14	14	27	**57**
# Field Radios	0	33	402	591	693	**1719**

II. STATUS OF CURRENT SMART GRID INVESTMENTS (*continued*)

B. Substation and Distribution Network and Operations Enhancements (*continued*)

Integrated Volt/VAr Control (IVVC) System Project

Description: The Installation of an Integrated Volt/VAr Control (IVVC) system is intended to replace the obsolete automated capacitor control (ACC) system and provide integrated control of capacitors, voltage regulators, and station load tap changers (LTC). IVVC system includes new IT network and infrastructure, smart field device controls and control software. New communications network required is listed as a separate project (700 MHz Field Area Network)

Status: Phase 1 (pilot) completed in 2018. Multi-year full deployment ongoing.

Benefits: Reduced feeder losses, improved situational awareness and control, optimize device operations count, flatten feeder voltage profile, manage system with two-way power flow from distributed generation.

Cost: $22,000,000, 5-year project cost

Metric: Number of substation controls upgraded, number of field device controls upgraded

Year	2018	2019	2020	2021	Total
# Substation Controls	2	41	36	44	**123**
# Field Controls	41	402	591	693	**1727**

II. STATUS OF CURRENT SMART GRID INVESTMENTS (*continued*)

B. Substation and Distribution Network and Operations Enhancements (*continued*)

Phased Implementation of Distribution Circuit Fault Locating

Description: Phased implementation of distribution circuit fault locating by installing mid-line reclosers, line sensors, and fault locators that will provide real-time data to SCADA.

Status: Ongoing

Benefits: Improved SAIDI, real-time fault locating, and situational awareness

Cost: $600,000 projected in 2019

Metric: SAIDI (Phase 1 of the distribution circuit fault locating project begin in 2018, future phases to follow.)

II. STATUS OF CURRENT SMART GRID INVESTMENTS (*continued*)

C. Customer Information and Demand-Side Management Enhancements

My Account (Web Portal for Customers)

Description: My Account gives customers on-line access to Bill and Payment History, Usage History, Daily And Hourly Energy Use, Energy Use vs Degree Days, Pay My Bill, Ways To Pay My Bill, Account Alerts, Add An Account, Electric Service Requests, My Account Profile, Understanding My Bill, FAQs, How My Usage Compares, How I Use Energy, and When I Use Energy.

Status: Ongoing

Benefits: Provides customers with direct access to their account information including energy consumption patterns. Enhances customers' ability to be engaged and educated on ways to use energy more effectively and efficiently. Facilitated by the Advanced Metering Infrastructure (AMI) system.

Cost: $507,000 total cost of project to-date

Metric: Number of Monthly log-ins, Number of My Account customers that logged in

Month	# of Log-ins	# of Customers that logged in	Avg Log-ins/Day
January 2018	279,279	105,304	9,009
February 2018	215,845	94,860	7,709
March 2018	246,098	102,581	7,939
April 2018	246,562	102,762	8,219
May 2018	254,803	103,334	8,215
June 2018	245,803	102,429	8,193
July 2018	268,987	106,414	8,677
August 2018	279,607	110,534	9,020
September 2018	258,321	107,517	8,611
October 2018	273,251	110,350	8,815
November 2018	272,679	109,825	9,089
December 2018	244,939	108,999	7,901

II. STATUS OF CURRENT SMART GRID INVESTMENTS (*continued*)

C. Customer Information and Demand-Side Management Enhancements *(continued)*

Customer Relationship Management (CRM)

Description: Idaho Power explored implementation of a CRM system integrated with the Customer Relationship and Billing (CR&B) system, however, the Company found the expense of integration and the ongoing maintenance to be greater than expected. In order to pursue some of the benefits that would have been gained through the CRM, Idaho Power developed a Customer Manager application in-house. While Idaho Power now has a tool available for email marketing and communication, there ismay still be a broader need for a centralized CRM system to be integrated with the CR&B system; the company continues to review vendors and offerings.

Status: Ongoing

Benefits: Manage and track customer interactions related to energy efficiency and other customer relations activities, manage prospective customers, improve efficiencies by centralizing information and automating processes, and manage and track marketing efforts

Cost: CRM Project: $421,804

Metric: Increased effectiveness of Idaho Power's energy efficiency program and service offerings

II. STATUS OF CURRENT SMART GRID INVESTMENTS (*continued*)

C. Customer Information and Demand-Side Management Enhancements *(continued)*

Demand Response (previously Direct Load Control)

Description: Idaho Power has offered optional direct load control, or DR, programs since 2004 and to all of its customer segments since 2009. The company offers an air conditioning (A/C) cycling program, A/C Cool Credit; an irrigation direct load control program, Irrigation Peak Rewards; and a commercial/industrial DR program, Flex Peak Program. The A/C Cool Credit uses smart grid technology, more specifically the power line carrier (PLC) technology, to activate load control devices installed on customer equipment. Irrigation Peak Rewards programs uses a combination of smart grid technology and secure cell phone technology to dispatch events. All three programs use the hourly load data made possible by AMI (excluding Irrigation Peak Rewards cell phone sites) to help determine the load reduction.

Status: Ongoing

Benefits: Demand response programs serve as a peaking resource during times of peak load on the Idaho Power system. They minimize or delay the needs to build supply-side peaking resources. The AMI system is used to facilitate these programs.

Cost: $8,817,529 in 2017 and $8,169,419 in 2018 of total annual expenses for demand response

Metric:

Demand Response Program	# of Participants	Demand Reduction (MW)
2017 A/C Cool Credit	28,214 Homes	29
2017 Flex Peak Program	141 Sites	36
2017 Irrigation Peak Rewards	2,307 Service Points	318

Demand Response Program	# of Participants	Demand Reduction (MW)
2018 A/C Cool Credit	26,182 Homes	29
2018 Flex Peak Program	140 Sites	33
2018 Irrigation Peak Rewards	2,335 Service Points	297

II. STATUS OF CURRENT SMART GRID INVESTMENTS (*continued*)

D. Disbtributed Resource and Renewable Resource Enhancements

Renewable Integration Tool

Description: The Renewable Integration Tool (RIT) was developed to provide the Load Serving Operators a more accurate wind generation forecast to utilize when balancing supply and demand. A wind generation forecast is generated for both day ahead and real time balancing purposes and displays the trends for both actual generation and the forecast generation for determining forecast accuracy. The day ahead and real time operators utilize this forecast to determine what resources are available and needed to serve firm system demand for the next day(s) and hour(s). The RIT is being expanded to forecast the solar generation that is scheduled to come on-line over the next few years.

Status: Complete

Benefits: Improved optimization of dispatchable resources

Cost: $470,000 wind forecast project, $60,000 solar forecast project

Metric: Number of curtailments of renewable generation, amount of energy curtailed, amount of generation acquired during the hour as a result of renewable generation deficit.

# of Curtailments	Amount of Energy Curtailed	Amount of Generation Acquired as a result of renewable generation deficit
0	0	0

III. FUTURE SMART GRID INVESTMENTS

B. Substation and Distribution Network and Operations Enhancements

Advanced Metering Infrastructure Expansion

Description: Install AMI to cover about 24 substations and 3,500 customers

Status: Future

Benefits: Affordable, Improved Customer Information and Billing, Enhance DSM Program, Improve Reliability

Improvement in Momentary Interruptions and Frequency Monitoring

Description: Develop data analytics and visualization tools to track momentary interruptions experiences by our customers. Use the data to identify root causes and identify mitigation methods to reduce the number of interruptions.

Status: Under consideration

Benefits: Improved customer satisfaction, create efficient tools used to identify and manage momentary interruptions

Jordan Valley Microgrid

Description: Install a microgrid to cover critical loads in Jordan Valley.

Status: Under consideration

Benefits: Increased resiliency, reliability, and expertise

Cost: Estimated at $834,000 as of June 2019

III. Future Smart Grid Investments *(continued)*

C. Customer Information and Demand-Side Management Enhancements

Personalized Customer Interaction and Customer Care Roadmap

Description: Proactively provide information to customers that is most important to them using email, text messaging, phone applications, and social media platform

Status: Under consideration

Benefits: Improved customer satisfaction, expand self-service options, deeper customer engagement

IV. Smart Grid Opportunities and Constraints

A. Transmission, Substation, Operations, and Customer Information Enhancements

None to report.

B. Evaluations and Assessments of Smart Grid Technologies

None to report.

COMPLETED PROJECTS

II. A. Transmission Network and Operations Enhancements

Transmission Situational Awareness Peak Reliability Hosted Advanced Application

Description: This provides remote access to Peak Reliability Coordinator (RC) state estimator as well as a set of displays used by Peak RC to monitor the interconnection. Peak Reliability's Hosted Advanced Applications (HAA) provides enhanced situational awareness of pre- and post-contingency system conditions that help Transmission Operators (TOPs) to reliably monitor their systems. The Hosted Advanced Applications File Management tool provides a means for HAA users to manage their files in the HAA environment including file transfer (state estimator solutions) between a local machine and the HAA environment.

Status: Complete

Benefits: The ability for the operators to determine whether a planned outage and/or forced outage (e.g., line out of service) would result in a system operating limit exceedance

Cost: $75,000 Annually

Metric: Number of potential SOL exceedances avoided

# of Potential SOL Exceedances Avoided
4

II. B. Substation and Distribution Network and Operations Enhancements

Conservation Voltage Reduction Enhancements

Description: Minimize voltages on transformers while maintaining customers' voltage levels to meet the National Service Voltage Standard (ANSI C84.1). conservation voltage reduction (CVR) would also be able to reduce demand on transformers during peak load periods in response to capacity requirements. The scope of the project includes the following: validate energy savings associated with CVR using measured instead of modeled values; quantify the costs and benefits associated with implementing CVR; determine methods for expanding the CVR program to additional feeders; pilot methods for making Idaho Power's CVR program more dynamic; and determine methods for ongoing measurement and validation of CVR effectiveness.

Status: Complete

Benefits: Validation of customer and utility energy and demand savings from CVR

Cost: $263,000 total cost of project

Metric: kWh and kW reduction between typical and CVR operated feeders

	Boise		Pocatello		Twin Falls		Ketchum		McCall		Ontario		Irrigation
	Commercial	Residential	Commercial	Residential	Commercial	Residential	Commercial	Residential	Commercial	Residential	Commercial	Residential	Irrigation
Energy	-2.16%	-2.39%	-1.75%	-1.28%	-0.89%	-0.57%	-2.47%	-2.58%	-0.61%	-1.21%	-0.31%	-1.50%	-0.52%
Demand	-3.12%		-4.95%		0.40%*		-1.58%		-3.39%		-1.85%		-2.98%

*Red numbers indicate data points where energy use increased under CVR. Examining this data may prove useful for making CVR more dynamic and informing Idaho Power which seasons, days of the week, times of the day and temperatures CVR works best in a particular weather zone.

II. B. Substation and Distribution Network and Operations Enhancements *(continued)*

Edge of Network Grid Optimization use for improving performance of CVR

Description: Evaluate Edge of Network Grid Optimization (ENGO) unit ability to mitigate voltage problems in place of more expensive solutions such as reconductoring or installing small voltage regulators

Status: Complete

Benefits: Improve ability to apply CVR to feeders that currently have voltages too low to qualify for CVR

Cost: $59,410 total cost of project

Metric: Customer voltage improvement

Customer voltage improvement	
Substation Phase Balance Improvement-Maximum Average Phase Difference Reduction	0.1939 V
Flatten Feeder Voltage—Maxium Decrease in Standard Deviation*	0.797 V
Voltage Increase End of feeder (max)	2.219 V
Low Voltage Mitigation when CVR ON - % Fewer Low Voltage Readings at monitored locations	80.83%
Technical Loss Reduction due to ENGO units while in CVR Mode	3.33%
Average CVR Factor for Energy**	1.5
Reduction of Energy Consumption due to CVR**	3.75%

*Decrease in standard deviation represents the difference between substation voltage and end of feeder voltage

**Calculation of CVR factor performed using day on/day off testing and calculating the difference in energy used from metering at substation end of feeder. This CVR factor is a combined number for all customer types connected to this feeder and represents only 4 weeks testing. No separation between customer classes performed. This CVR factor cannot be directly compared to CVR factors calculated in CVR Enhancements project and is only indicative of the positive potential for CVR.

II. B. Substation and Distribution Network and Operations Enhancements *(continued)*

Replace the Existing Outage Management System

Description:	Replace the existing Outage Management System (OMS). The new OMS will integrate into existing control and operating software platforms, including: the Geographic Information System (GIS), Supervisory Control and Data Acquisition (SCADA), Advance Meter Information (AMI), Mobile Workforce Management (MWM), and Customer Relationship and Billing (CR&B) systems.
Status:	Complete
Benefits:	Vendor Support of the application to accomplish faster identification of outage, more accurate count of customers impacted by the outage, enhanced outage communication with customers
Cost:	$3,060,332
Metric:	Faster identification of, and a more accurate scope of, customer outages

II. B. Substation and Distribution Network and Operations Enhancements *(continued)*

Automated Connect/Disconnect Capability

Description: Approximately 19,477 meters with remote controlled disconnect and reconnect capability have been installed at customer locations that historically required multiple visits annually. Remote connect/disconnect was implemented in Idaho on September 15, 2015 and in Oregon on August 16, 2016. In Oregon, Idaho Power only uses the remote disconnect functionality for customer requested disconnects.

Status: Complete

Benefits: Reduced connect/reconnect labor and expenses, collection labor and expenses, reduced reconnect fee in Idaho, reduced reconnect response time, improved employee safety

Cost: $1.0 million total cost of project

Metric: Change in head count, Number of remote meters installed, Number of remote disconnects, Number of remote reconnects, change in reconnect fee, and reconnect response time**

Jurisdiction	Year	Positions Reduced	# of Remote Meters Installed	# of Remote Disconnects	# of Remote Reconnects	Change in Reconnect Fee
Idaho	2015	5	13,728	3,178	3,201	-$7
	2016	0	15,145	10,211	10,144	$0
	2017	0	18,543	12,391	12,258	$0
	2018	0	18,874	10,856	10,764	$0
Oregon	2015	0	772	0	0	$0
	2016	0	811	41	129	$0
	2017	0	934	311	195	$0
	2018	0	946	292	161	$0

**Remote reconnects occur every hour, at the top of the hour

II. B. Substation and Distribution Network and Operations Enhancements *(continued)*

Implement Additional AMI Outage Scoping and Restoration Confirmation Functionality

Description:	Integrate the AMI system with the Smart Grid Monitoring System (formerly known as the Sentry System)
Status:	Complete
Benefits:	See "Replace the Existing Outage Management System"
Cost:	This work was included within the scope, cost, and schedule of the OMS replacement project.
Metric:	See "Replace the Existing Outage Management System"

II. C. Customer Information and Demand-Side Management Enhancements

Advanced Metering Infrastructure

Description: Idaho Power has deployed the Aclara Two-way Automated Communications System (TWACS) on 99 percent of the retail customers served, 99 percent in Idaho and 93 percent in Oregon. The TWACS technology is installed in the distribution substation and communicates with meters through the distribution power line.

Status: Complete

Benefits: Reduced cycle billing and customer movement meter reading, reduced bill estimates, reduced cancel re-bills, reduced trouble call mileage (pinging), enhanced failure and voltage monitoring. Daily and hourly energy use information for 99 percent of customers.

Cost: $71,281,847 total cost of project

Metric: Operation and Maintenance Cost Reduction (Docket No. UE 233, DR No. 343)

Operation and Maintenance Cost Reduction (Idaho & Oregon)	
O&M Costs Reductions Related to Metering Activity	$3,353,192
O&M Costs Reductions Related to Connect/Disconnects	$4,045,913
Total O&M Benefits	**$7,399,104**

II. C. Customer Information and Demand-Side Management Enhancements *(continued)*

Customer Outage Map

Description: Idaho Power's Outage Map application provides customers with near-real-time information about outages that impact their home or business. Idaho Power launched the online Outage Map application on April 28, 2015. The Outage Map is located on the Idaho Power website in the Outage Center. Customers can view either the full version if using a desktop computer or they can use the mobile version if using a mobile device. The map is tied to the Outage Management System and will be automatically updated every five minutes.

Status: Ongoing

Benefits: Improved customer service during electricity outages. The Outage Map enables Idaho Power to improve customer communication and better meet customer expectations. The following information will be available for known outages, both planned and unplanned: time the outage started, number of customers affected, the status of the restoration crew (in-route or on site), and the estimated time of restoration (ETR).

Cost: No additional costs were incurred by Idaho Power for this activity. The work was performed as regular work duties.

Metric: Number of visits to the Outage Map on the Idaho Power website

# of visits to Outage Map*	
Total Map Visits	**477,483**

*July 1, 2016 through June 30, 2017

II. E. General Business Enhancements

Idaho Power Enterprise Data Warehouse

Description: The Enterprise Data Warehouse (EDW) is a database for storing customer and meter data.

Status: Complete

Benefits: The EDW supports the Company's analytical and reporting, customer data viewing and analytics (see My Account), ensures that reporting activities do not adversely impact performance of the source systems

Cost: $1,591,000 total cost of project

Metric: # of types of data (meter data, customer data), # of fields within each type of data

Meter Data (# of fields)	Customer Data (# of fields)
217	2403

II. E. General Business Enhancements *(continued)*

Meter Data Management System Upgrade

Description: Upgrade the existing version of Itron Enterprise Edition (IEE) to the latest version.

Status: Complete

Benefits: Provided additional functionality - support of complex rate and billing options, enabled net metering rate option (validate and scale hourly data for net metered customers with negative #s). Moved IEE from the no longer supported Windows XP operating system to Windows 7 thereby eliminating certain security concerns. The upgrade also allowed Idaho Power to eliminate some customizations that are now part of the base product supported by Itron.

Cost: $351,738 total cost of project

Metric: Number of net metered customers in both Idaho and Oregon

Jurisdiction	Customer Group	# of Customers*
Idaho	Residential	1,092
Idaho	Commercial	117
Idaho	Industrial	3
Idaho	Irrigation	4
Oregon	Residential	15
Oregon	Commercial	8
Oregon	Industrial	0
Oregon	Irrigation	9

* Customer count as of June 30, 2017

II. E. General Business Enhancements *(continued)*

The Mobile Workforce Management System Upgrade

Description: Upgrade the existing version of PragmaCAD to the latest version to maintain vendor support and realize improvements in the functionality of the latest version.

Status: Complete

Benefits: Vendor Support of application to optimize scheduling of customer appointments by location, employee skill, levelizing work load

Cost: $1,246,468

Metric: Improved usability and a reduced number of software customizations which are now standard functionality

	Before Upgrade	After Upgrade
Number of Software Customizations	8	2

IV. B. Evaluations and Assessments of Smart Grid Technologies

Electric Vehicle Charging Impacts Study

Description: Evaluate the impact of residential EV charging on Idaho Power's distribution system.

Status: Complete in 2016

Benefits: Gain an understanding the likely impact to utility facilities of electric vehicle charging

Cost: $51,000 total cost of project

Metric: Increase in household demand at peak

Average Demand Increase (per participant)	
Peak Hours (13:00 – 21:00)	After Peak (22:00 – 24:00)
13.3%	21.9%

Maximum Demand Increase (per participant)	
Peak Hours (13:00 – 21:00)	After Peak (22:00 – 24:00)*
125%	800%

* Small home, energy efficient, likely only vampire (standby) loads

IV. B. Evaluations and Assessments of Smart Grid Technologies

Photovoltaic and Feeder Peak Demand Alignment Pilot

Description: Conduct a study of a residential/small commercial feeder to determine the number of weather stations, including solar intensity monitors that need to be installed along the feeder to gather and characterize the solar/weather patterns. Gather feeder load data and correlate the feeder load to the solar generation potential along the feeder. Includes purchase and installation of (probably) permanent solar intensity monitors, PV panels, and power metering and recording equipment.

Status: Complete in 2016

Benefits: Gain an understanding of the potential for solar PV generation to contribute to feeder peak load demand reduction.

Cost: $25,000 total cost of project

Metric: The cross correlation and time offset of the feeder load data in MW and the solar irradiance in Watt/m^2.

	Solar Peak Leads Load Peak (# of hours)
Southerly	3.96 to 4.13
Global	4.00 to 4.02
Westerly	1.76 to 1.94

IV. B. Evaluations and Assessments of Smart Grid Technologies

Solar-Powered Parking Lot Lighting

Description: High-pressure sodium lighting was replaced with high-efficiency LEDs in an employee parking lot. Solar panels were mounted on each light pole so that energy can be fed back onto Idaho Power's distribution system when the solar panels produce more energy than the LED lights consume.

Status: Complete

Benefits: Lighting for parking lot on a net-zero annual energy basis

Cost: This project was funded by shareholder dollars. No project costs were charged to customers.

Metric: Annual Net consumption/generation in kWh

Year 1

Month	Year	Net kWh Consumption	Running Total
September	2013	8	8
October	2013	(5)	3
November	2013	244	247
December	2013	383	630
January	2014	417	1047
February	2014	277	1324
March	2014	(0)	1323
April	2014	(157)	1167
May	2014	(359)	808
June	2014	(382)	426
July	2014	(359)	66
August	2014	(262)	(196)

Running Total (196)

Negative = net generation
Positive = net load

Year 2

Month	Year	Net kWh Consumption	Running Total
September	2014	(144)	(144)
October	2014	2	(142)
November	2014	217	75
December	2014	412	487
January	2015	307	794
February	2015	28	822
March	2015	(188)	634
April	2015	(344)	290
May	2015	(339)	(48)
June	2015	(438)	(487)
July	2015	(403)	(890)
August	2015	(329)	(1219)

Running Total (1,219)

Negative = net generation
Positive = net load

Year 3

Month	Year	Net kWh Consumption	Running Total
September	2015	(214)	(214)
October	2015	(9)	(222)
November	2015	189	(34)
December	2015	405	371
January	2016	291	662
February	2016	22	684
March	2016	(22)	662
April	2016	(304)	358
May	2016	(347)	11
June	2016	(391)	(381)
July	2016		
August	2016		

Running Total (381)

Negative = net generation
Positive = net load